ARIZONA STATE UNIVERSITY

PENETRATION OF HIGH INTENSITY RADIATED FIELDS (HIRF) INTO GENERAL AVIATION AIRCRAFT

Final Report
(June 1, 2001 - May 31, 2004)

by
Constantine A. Balanis
Craig R. Birtcher
Stavros V. Georgakopoulos
Anastasios H. Panaretos

Sponsored by

National Aeronautics and Space Administration
Langley Research Center
Hampton, VA
under
Cooperative Agreement NCC-1-01051

Prepared by

TELECOMMUNICATIONS RESEARCH CENTER
College of Engineering and Applied Sciences
PO BOX 877206, TEMPE, AZ 85287-7206

Contents

LIST OF TABLES iv
LIST OF FIGURES v

1 Introduction **1**

2 Fourth-Order Finite-Difference Time-Domain **9**
I. Introduction 9
II. Basic Principles 11
III. FDTD Schemes 13
A. The FDTD(2,2) scheme 13
B. The FDTD(2,4) scheme 14
C. Characteristics of the FDTD schemes 15
IV. FDTD(2,4) in 1-D Domains 23
V. Absorbing Boundary Conditions 27
A. Numerical experiments 29
VI. Applications 37
A. Array factor 37
B. Resonances of a rectangular cavity 41
C. Radiation pattern analysis 45
VII. Boundary Conditions 52
A. Problem definition 54
B. FDTD(2,4) 55
C. FDTD(2,4) with thin wire model of FDTD(2,2) 62
D. FDTD(2,4) with one-sided differences 67
E. Summary 68
VIII. Hybrid of FDTD(2,4) and Subgrid FDTD(2,2) 68
A. Method 69
B. Results 73
C. Conclusions 76
IX. Hybrid of Subgrid FDTD(2,2) and FDTD(2,4) 79
A. Method 81

3 Applications **86**
I. Introduction 86
II. An Improved FDTD Feed Model for Thin-Wire Antennas 87
A. Delta-gap source 87
B. Improved delta-gap source 90
III. Discrete Fourier Transform 94
IV. Analysis of Cavity-Backed Slot Antennas 98
A. FDTD modeling 100

B. Impedance . . . 104
C. Coupling . . . 105
D. Reduction of coupling . . . 107
E. Patterns . . . 118
F. Summary of coupling reduction methods . . . 118
G. Conclusions . . . 122

4 HIRF Penetration and PED Coupling Analysis 124
I. HIRF Penetration Through Apertures . . . 125
A. Definition of shielding effectiveness . . . 127
B. Problem definition . . . 128
C. Measurements . . . 130
D. Acceleration techniques . . . 132
E. Windowing . . . 136
F. Comparison for SE definitions . . . 144
G. Results . . . 148
H. Summary . . . 150
II. HIRF Penetration Through a Scaled Fuselage . . . 152
A. Construction and specifications of the geometry . . . 153
B. Measurements . . . 156
C. FDTD(2,2) predictions . . . 161
D. Hybrid of subgrid FDTD(2,2)/FDTD(2,4) . . . 180
E. Summary . . . 188
III. Personal Electronic Devices (PEDs) . . . 190
A. Geometry and setup of the measurements . . . 191
B. Measurements . . . 195
C. FDTD(2,2) predictions . . . 195
D. Hybrid subgrid FDTD(2,2)/FDTD(2,4) predictions . . . 209
E. Summary . . . 217
IV. Personal Electronic Devices (PEDs) . . . 218
A. Introduction . . . 218
B. Modifications to the "Simplified Fuselage" . . . 218
C. PED Measurements . . . 219

5 Measured Shielding Effectiveness of the Cylindrical Fuselage Model 233
I. The Cylindrical Fuselage . . . 233
II. Shielding Effectiveness Measurements . . . 235
A. Measurements . . . 237
B. Results . . . 238
III. Shielding Effectiveness Improvement . . . 240
IV. FDTD Predictions . . . 247
A. Cell size of 10 mm . . . 251
B. Cell size of 5 mm . . . 254
C. Cell size of 2.5 mm . . . 257
V. Conclusions . . . 263

6 Statistics of the Electromagnetic (EM) Field Inside the Simplified Fuselage **264**
I. Introduction . . . 264
II. Reverberation Chambers (RCs) . . . 265
A. Principles of Operation . . . 265
B. Statistical Characterization . . . 268
III. Mode-Stirrer Construction and Measurements . . . 285
A. Introduction . . . 285
B. The Mode Stirrer . . . 286
C. Measurements . . . 287
D. Predictions and Comparisons . . . 295
IV. Statistical and Probabilistic Analysis of Measurements . . . 305
A. Introduction . . . 305
B. Basic Statistical Processing . . . 306
C. Shielding Effectiveness: The Statistical Approach . . . 306
D. Data Statistical Independence . . . 314
E. CDFs and PDFs of Experimental Data . . . 317

7 Statistical Properties of an Overmoded Cavity as a Function of Frequency **325**
I. Introduction . . . 325
II. Statistical Field Theory of Complex Cavities . . . 327
III. Statistical Analysis of Experimental Data . . . 331
IV. The Lehman Model . . . 337

8 Frequency Stirring for Reverberation Chambers **340**
I. Introduction . . . 340
II. Frequency stirring . . . 341
III. Stochastic processes and noise . . . 346
A. Properties of white gaussian noise . . . 346
B. Filtering and spectral characteristics of band–limited white gaussian noise . . . 349
IV. Two-dimensional cavity excitation . . . 352
A. Simulation set-up . . . 352
B. Simulation Results . . . 355
V. Three-dimensional cavity excitation . . . 358
A. Simulation set-up . . . 362
B. Simulation results . . . 365

9 Summary and Conclusions **370**

10 Conclusions **381**

List of Tables

1.1 HIRF certification environment proposed by the EEHWG [1] 5

2.1 Simulation times and memory requirements 76
2.2 Memory requirements for the different regions of the computational domain for a cell size of 2.5 mm 84
2.3 Memory requirements for the different regions of the computational domain of box #1 for a cell size of 2.5 mm 85
2.4 Memory requirements for the different regions of the computational domain of box #2 for a cell size of 2.5 mm 85

3.1 Effective radius for the input impedance calculations 94
3.2 Efficiency of the two CBS antennas configuration for different thicknesses of the GDS superstrate 121
3.3 Gain of the two CBS antennas configuration at elevation angle $\theta = -60^o$ 121
3.4 Coupling reduction of the two CBS antennas configuration 122
3.5 Coupling reduction of the two CBS antennas configuration 122

4.1 Memory requirements for the different regions of the computational domain for a cell size of 2.5 mm 189

6.1 Normal distribution, $[x < k] = \gamma,\ x \sim N(\mu, \sigma^2)$. 282
6.2 Maximum, minimum, mean average and standard deviation, over all stirrer positions, of the electric field for points A, B, C and D, for different frequencies. 308
6.3 Mean average and standard deviation values of the maximum electric field value. 309
6.4 Kolmogorov-Smirnov test results. 319

8.1 Standard deviation and number of modes for different bandwidths, excitation frequencies and positions. 358
8.2 Standard deviation and number of modes for different bandwidths, excitation frequencies,electric field components and positions. 369

List of Figures

2.1 Computational molecule of a central second-order FD stencil. 14
2.2 The FDTD unit cell as proposed by Yee. 15
2.3 Computational molecule of a central fourth-order FD stencil. 16
2.4 Variation of the numerical phase velocity versus the propagation angle of a plane wave for FDTD(2,2). 20
2.5 Variation of the numerical phase velocity versus the propagation angle of a plane wave for FDTD(2,4). 20
2.6 Comparison of the error in the numerical phase velocity for FDTD(2,2) and FDTD(2,4). 21
2.7 Grid for a 1-D TM^z mode. 23
2.8 Comparison of the FDTD(2,2) and FDTD(2,4) calculations for a 1-D domain. 24
2.9 Field components around a PEC discontinuity. 24
2.10 1-D simulation results: (a) propagating pulse, (b) PEC plane implemented by setting the tangential E field to zero, (c) PEC plane one cell thick and (d) PEC plane implemented by setting the tangential E field to zero along with modification of the FDTD(2,4) stencil for the fields just beside the boundary by using image theory. 26
2.11 Dielectric discontinuity analysis: (a) FDTD(2,2) and (b) FDTD(2,4). 27
2.12 The two-dimensional computational domains for numerical testing of the effectiveness of PML. 30
2.13 Compact smooth pulse. 32
2.14 Global error in the 2-D test domain caused by the Berenger's PML for the FDTD(2,2) scheme. 33
2.15 Global error in the 2-D test domain caused by the anisotropic PML for the FDTD(2,2) scheme. 34
2.16 Global error in the 2-D test domain caused by the anisotropic PML for the FDTD(2,4) scheme. 34
2.17 Global error in the 3-D test domain caused by the anisotropic PML for the FDTD(2,2) scheme. 35
2.18 Maximum error, L^∞, in the 3-D test domain caused by the anisotropic PML for the FDTD(2,2) scheme. 35
2.19 Global error in the 3-D test domain caused by the anisotropic PML for the FDTD(2,4) scheme. 36
2.20 Maximum error, L^∞, in the 3-D test domain caused by the anisotropic PML for the FDTD(2,4) scheme. 36
2.21 Geometry of an array formed by two current elements positioned along the x-axis. 38
2.22 Distance $d = 5.5\lambda$. Toward zenith: (a) FDTD(2,2) -17 dB, (b) FDTD(2,4) -32 dB. 39

2.23 Distance $d = 10.5\lambda$. Toward zenith: (a) FDTD(2,2) -14 dB, (b) FDTD(2,4) -30 dB. 40
2.24 Distance $d = 20.5\lambda$. Toward zenith: (a) FDTD(2,2) -13 dB, (b) FDTD(2,4) -24 dB. 40
2.25 Resonances of a rectangular cavity predicted using FDTD(2,2) with a cell size of 100 mm. 42
2.26 Resonances of a rectangular cavity predicted using FDTD(2,2) with a cell size of 50 mm. 43
2.27 Resonances of a rectangular cavity predicted using FDTD(2,2) with a cell size of 25 mm. 44
2.28 Resonances of a rectangular cavity predicted using FDTD(2,4) with a cell size of 100 mm. 44
2.29 Geometry of a monopole mounted on the tail of the NASA scale-model helicopter. 46
2.30 Yaw plane radiation patterns of a monopole mounted on the tail of the NASA scale-model helicopter at 9.18 GHz. 47
2.31 Roll plane radiation patterns of a monopole mounted on the tail of the NASA scale-model helicopter at 9.18 GHz. 48
2.32 Pitch plane radiation patterns of a monopole mounted on the tail of the NASA scale-model helicopter at 9.18 GHz. 49
2.33 Geometry of a monopole mounted on a rectangular box. 50
2.34 Roll plane radiation patterns of a monopole mounted on a rectangular box at 2 GHz. 51
2.35 Pitch plane radiation patterns of a monopole mounted on a rectangular box at 2 GHz. 51
2.36 Geometry of two monopoles on a ground plane. 55
2.37 S_{11} of the 6 cm long monopole. 57
2.38 S_{22} of the 4 cm long monopole. 58
2.39 S_{12} between the two monopoles. 58
2.40 Phase of S_{11} of the 6 cm long monopole. 59
2.41 Phase of S_{22} of the 4 cm long monopole. 59
2.42 Phase of S_{12} between the two monopoles. 60
2.43 Phase of S_{12} between the two monopoles. 60
2.44 Input resistance of the 6 cm long monopole. 61
2.45 Input reactance of the 6 cm long monopole. 61
2.46 S_{11} of the 6 cm long monopole. 62
2.47 S_{22} of the 4 cm long monopole. 63
2.48 S_{12} between the two monopoles. 63
2.49 Phase of S_{11} of the 6 cm long monopole. 64
2.50 Phase of S_{22} of the 4 cm long monopole. 64
2.51 Phase of S_{12} between the two monopoles. 65
2.52 Phase of S_{12} between the two monopoles. 65
2.53 Input resistance of the 6 cm long monopole. 66
2.54 Input reactance of the 6 cm long monopole. 67
2.55 Two-dimensional view of the coarse and fine grids. 70
2.56 Respective locations in time of the electric and magnetic fields for both the coarse and the fine grids. 70
2.57 Electric field e_2 (near the boundary between the coarse and fine grids) that is linearly weighted. 71
2.58 S_{11} of the 6 cm long monopole. 74
2.59 S_{22} of the 4 cm long monopole. 74

2.60 S_{12} between the two monopoles. 75
2.61 Input resistance of the 6 cm long monopole. 78
2.62 Input reactance of the 6 cm long monopole. 78
2.63 Schematic visualization of the hybrid method of FDTD(2,4) and subgrid FDTD(2,2) presented in the previous section. 79
2.64 Schematic visualization of the hybrid method subgrid FDTD(2,2) and FDTD(2,4) presented in the this section. 80
2.65 Two-dimensional view of the coarse and fine grids. 82

3.1 The delta-gap source model. 88
3.2 Input impedance of a thin wire dipole with radius $a = \ell/500$. 89
3.3 Input impedance of a thin wire dipole with radius $a = \ell/150$. 90
3.4 Field locations and geometry for the sub-cell model of a thin wire. . . 91
3.5 Input impedance of a thin wire dipole with radius $a = \ell/500$. 93
3.6 Input impedance of a thin wire dipole with radius $a = \ell/150$. 93
3.7 Elevation radiation pattern of a monopole mounted on a rectangular ground plane at 300 MHz. 97
3.8 Elevation radiation pattern of a monopole mounted on a rectangular ground plane at 450 MHz. 97
3.9 Elevation radiation pattern of a monopole mounted on a rectangular ground plane at 600 MHz. 98
3.10 A three-dimensional view of an air-filled rectangular cavity-backed slot antenna fed with a probe oriented in the y-direction. 101
3.11 A two-dimensional view of an air-filled rectangular cavity-backed slot fed with a probe oriented in the y-direction. 101
3.12 A top view of a cavity-backed slot mounted on a ground plane (experimental configuration). 102
3.13 Current of the probe exciting the cavity-backed slot antenna for a resistance $R_s = 0$ 103
3.14 Current of the probe exciting the cavity-backed slot antenna for a resistance $R_s = 50$ ohms 103
3.15 Cross-section of the FDTD mesh of the CBS antenna for a cell size of 0.6 mm. 105
3.16 Input impedance of a cavity-backed slot antenna. (a) Resistance. (b) Reactance. 106
3.17 Geometry of two identical cavity-backed slot antennas mounted on a rectangular ground plane (for antenna specifications see Fig. 2). (a) 3-D view. (b) Top view. 107
3.18 S-parameters of two identical cavity-backed slot antennas mounted on a rectangular ground plane (for antenna specifications see Figure 1.4). 108
3.19 Geometry of two identical cavity-backed slot antennas mounted on a rectangular ground plane (for antenna specifications see Fig. 2). (a) Side view. (b) Top view. 109
3.20 Coupling with and without lossy superstrate. (a) 1.5 mm thick GDS. (b) 3.0 mm thick GDS. (c) 4.5 mm thick GDS. 110
3.21 Measured coupling for three different cases. 111
3.22 Total surface current density J_{tot} in dB, with no lossy superstrate at 11.92 GHz. 112
3.23 Total surface current density J_{tot} in dB, with a 1.5 mm thick GDS superstrate at 11.92 GHz. 112

3.24 Geometry of two cavity-backed slot antennas on a ground plane with a slit. 113
3.25 Coupling with a slit on the ground plane. (a) 2 mm wide slit. (b) FDTD predictions for different widths of the slits. 114
3.26 Coupling between two CBS antennas. (a) All the measurements. (b) All the FDTD predictions. 115
3.27 Top view of the two CBS antennas oriented along the H-plane. 115
3.28 Coupling between two CBS antennas for different separation distances. (a) Measurements. (b) FDTD predictions. 117
3.29 Measured coupling versus separation distance at different frequencies. 117
3.30 Patterns at 7.5 GHz. (a) With no superstrate. (b) 1.5 mm GDS thick superstrate. 119
3.31 Patterns at 11.92 GHz. (a) With no superstrate. (b) 1.5 mm GDS thick superstrate. 119
3.32 Measured patterns. (a) At 7.5 GHz. (b) At 11.92 GHz. 120

4.1 Geometries:(a) Cavity #1; (b) Cavity #2; and (c) Cavity #3. 129
4.2 Definition of: (a) incident angle, ϕ_i and θ_i, for SE computations using procedure #1; and (b) observation angle, ϕ_o and θ_o, for SE computations using procedure #2. 130
4.3 To accommodate multiple aperture configurations in the conducting enclosure, the front and back walls were constructed to accept flush-mounted aperture panels. 131
4.4 A photograph of the bottom of the enclosure, with the probe, and the auxiliary antenna inside the anechoic chamber. 132
4.5 The time-domain electric field at the center of cavity #2 for a normally incident wave ($\phi_i = 0^o$ and $\theta_i = 90^o$) and an artificial conductivity of (a) 0 S/m; and (b) 0.0032 S/m. 134
4.6 Time-domain far-field of cavity #2 at observation angle, $\phi_o = 0^o$ and $\theta_o = 90^o$, for (a) $R_s = 0$ ohms; and (b) $R_s = 200$ ohms. 136
4.7 (a) Rectangle window. (b) Its spectrum. 139
4.8 (a) Hanning window. (b) Its spectrum. 139
4.9 (a) 50% Tukey window. (b) Its spectrum. 140
4.10 (a) 75% Tukey window. (b) Its spectrum. 140
4.11 Time-domain far-field of cavity #2. (a) Top and sides of cavity present. (b) Top and sides of cavity absent. 141
4.12 Illustration of windowing procedure. (a) Time-domain far-field along with scaled (for plotting purposes) Hanning window (the actual maximum of the window is one). (b) Windowed time-domain far-field. . . 142
4.13 Shielding effectiveness of cavity #2 computed using (a) Rectangle; (b) Hanning; (c) 50% Tukey; and (c) 75% Tukey window. 143
4.14 Illustration of shielding effectiveness definitions (R_x=receiving point, T_x=transmitting point, •=center of cavity). (a) Procedure #1 (Plane Wave excitation-No probe); (b) Procedure #2 (Probe excitation); (c) Procedure #3 (Plane Wave excitation-receiving at a probe); and (d) Procedure #4 (Delta-gap excitation at the center). 145
4.15 Shielding effectiveness of cavity #1 using (a) Procedure #1 (Plane Wave excitation-No probe); (b) Procedure #2 (Probe excitation); (c) Procedure #3 (Plane Wave excitation-receiving at a probe); and (d) Procedure #4 (Delta-gap excitation at the center). 146
4.16 Shielding effectiveness of cavity #1. 149

4.17 Shielding effectiveness of cavity #2. 149
4.18 Shielding effectiveness of cavity #3 for incident angle (a) $\phi_i = 0^o$, $\theta_i = 90^o$; (b) $\phi_i = 60^o$, $\theta_i = 90^o$; (c) $\phi_i = 120^o$, $\theta_i = 90^o$; and (d) $\phi_i = 180^o$, $\theta_i = 90^o$. 151
4.19 Measured shielding effectiveness of cavity #3 for different incident angles. (a) Versus frequency. (b) Versus azimuth incident angle. 151
4.20 The construction of the simplified fuselage was conceived as being four panels joined together with epoxy applied to outside surfaces, as shown. Instead, the protrusions of the side panels beyond the top panel have been trimmed flush with the top, and the top panel is epoxied from the inside. This alteration extends the usefulness of the model by enabling meaningful scaled measurements of PED coupling to top-mounted aircraft antennae. 155
4.21 A photograph showing five of the six aluminum panels which form the simplified fuselage. 156
4.22 The first step in the assembly of the simplified fuselage was to epoxy the top and sides together from the inside. 157
4.23 The bottom panel was then epoxied to the assembly. 157
4.24 The top "rails" were removed using a rotary tool, files and sandpaper. 158
4.25 A front view of the completed "simplified fuselage" scale model. . . . 158
4.26 A floor plan view of the anechoic chamber illustrating the relationships between the simplified fuselage under test and the auxiliary antenna. This configuration is symmetric and does not suffer from feed spillover. Due to the small vertical dimensions of the apertures, the near-field response of the simplified fuselage in the azimuthal plane is the same as it would be in a field of cylindrical waves. 160
4.27 An absorber baffle was used to further reduce the illumination of the SPCR reflector by the back-lobes of the auxiliary antenna. The absorber reduced the signal scattered by the reflector by an average (over the band of interest) of about 15 dB, as observed by the monopole reference antenna. 161
4.28 Geometry of the simplified fuselage model 162
4.29 Shielding effectiveness of the scaled fuselage for azimuthal incident angle of 0^o (nose incidence). 164
4.30 Shielding effectiveness of the scaled fuselage for azimuthal incident angle of 0^o (nose incidence). 165
4.31 Shielding effectiveness of the scaled fuselage for azimuthal incident angle of 45^o. 166
4.32 Shielding effectiveness of the scaled fuselage for azimuthal incident angle of 45^o. 167
4.33 Shielding effectiveness of the scaled fuselage for azimuthal incident angle of 90^o (broadside incidence). 168
4.34 Shielding effectiveness of the scaled fuselage for azimuthal incident angle of 90^o (broadside incidence). 169
4.35 Shielding effectiveness of the scaled fuselage for azimuthal incident angle of 180^o (tail incidence). 170
4.36 Shielding effectiveness of the scaled fuselage for azimuthal incident angle of 180^o (tail incidence). 171
4.37 Shielding effectiveness of the scaled fuselage for azimuthal incident angle of 0^o. 173

4.38 Shielding effectiveness of the scaled fuselage for azimuthal incident angle of 0^o. 174
4.39 Shielding effectiveness of the scaled fuselage for azimuthal incident angle of 0^o. 175
4.40 Shielding effectiveness of the scaled fuselage for azimuthal incident angle of 0^o. 177
4.41 Shielding effectiveness of the scaled fuselage for azimuthal incident angle of 0^o. 178
4.42 Shielding effectiveness of the scaled fuselage for azimuthal incident angle of 0^o. 179
4.43 Shielding effectiveness of the scaled fuselage for azimuthal incident angle of 0^o. 180
4.44 Schematic visualization of the hybrid method subgrid FDTD(2,2) and FDTD(2,4) applied to the scaled fuselage. 181
4.45 Shielding effectiveness of the scaled fuselage for azimuthal incident angle of 0^o computed by the hybrid method. 182
4.46 Shielding effectiveness of the scaled fuselage for azimuthal incident angle of 0^o computed by the hybrid method. 183
4.47 Shielding effectiveness of the scaled fuselage for azimuthal incident angle of 0^o computed by the hybrid method. 184
4.48 Shielding effectiveness of the scaled fuselage for azimuthal incident angle of 0^o computed by the hybrid method. 185
4.49 Shielding effectiveness of the scaled fuselage for azimuthal incident angle of 0^o computed by the hybrid method. 186
4.50 Shielding effectiveness of the scaled fuselage for azimuthal incident angle of 0^o computed by the hybrid method. 187
4.51 Shielding effectiveness of the scaled fuselage for azimuthal incident angle of 0^o computed by the hybrid method. 188
4.52 The externally mounted antenna was built into a pedestal to accommodate the RF connector and cable, and to allow the antenna to be relocated easily. 192
4.53 The construction of the simulated PED allows the calibration to be performed as close as possible to the PED connector. 192
4.54 The top of the pedestal for the simulated PED screws on to the bottom of the pedestal with counter-bored allen head screws. 193
4.55 To more easily describe the locations of the PED and external antenna, a letter designation is assigned to the locations of the simplified fuselage cabin windows. 194
4.56 The PED is located against the starboard side wall of the simplified fuselage, while the external antenna is mounted on the top of the fuselage, along the centerline. Both the PED and external antenna are centered on station C. 194
4.57 The PED measurements were performed within the anechoic chamber with the S-parameter test set located immediately beneath the simplified fuselage, the RF cable losses were reduced to an acceptable level. 196
4.58 Reflection coefficient of the PED antenna (station C). 199
4.59 Reflection coefficient of the antenna mounted on the exterior of the fuselage (station C). 199
4.60 Coupling between the PED antenna and the antenna mounted on the exterior of the fuselage (station C). 200

4.61 Coupling between the PED antenna and the antenna mounted on the exterior of the fuselage (station C). 200
4.62 Coupling between the PED antenna and the antenna mounted on the exterior of the fuselage (station C). 201
4.63 Coupling between the PED antenna and the antenna mounted on the exterior of the fuselage (station C). 202
4.64 Coupling between the PED antenna and the antenna mounted on the exterior of the fuselage (station C). 203
4.65 Coupling between the PED antenna and the antenna mounted on the exterior of the fuselage (station C). 204
4.66 Coupling between the PED antenna and the antenna mounted on the exterior of the fuselage (station A). 204
4.67 Coupling between the PED antenna and the antenna mounted on the exterior of the fuselage (station A). 205
4.68 Coupling between the PED antenna and the antenna mounted on the exterior of the fuselage (station A). 206
4.69 Coupling between the PED antenna and the antenna mounted on the exterior of the fuselage (station A). 207
4.70 Coupling between the PED antenna and the antenna mounted on the exterior of the fuselage (station A). 208
4.71 Coupling between the PED antenna and the antenna mounted on the exterior of the fuselage at stations A and C. 209
4.72 Schematic visualization of the hybrid method subgrid FDTD(2,2) and FDTD(2,4) applied to the scaled fuselage. 210
4.73 Reflection coefficient of the PED antenna (station C). 211
4.74 Reflection coefficient of the antenna mounted on the exterior of the fuselage (station C). 211
4.75 Coupling between the PED antenna and the antenna mounted on the exterior of the fuselage (station C). 212
4.76 Coupling between the PED antenna and the antenna mounted on the exterior of the fuselage (station C). 212
4.77 Coupling between the PED antenna and the antenna mounted on the exterior of the fuselage (station C). 213
4.78 Coupling between the PED antenna and the antenna mounted on the exterior of the fuselage (station C). 214
4.79 Coupling between the PED antenna and the antenna mounted on the exterior of the fuselage (station C). 215
4.80 Coupling between the PED antenna and the antenna mounted on the exterior of the fuselage (station C). 216
4.81 The original epoxied construction of the Simplified Fuselage was found to provide imperfect shielding. The new design includes 1 cm square aluminum bars in each of the upper corner to which the top and side panels can be screwed, and an increase in the thickness of the bottom panel to which the bottom edges of the side panels is screwed. 219
4.82 The top and side plates of the fuselage were screwed to two 1 cm square aluminum bars. 220
4.83 For this series of measurements, the cockpit and all but one cabin windows were sealed. The window that is open is denoted by a letter designation. In this photograph, window "I" is open. 221
4.84 The S_{12} was collected for ten external antenna locations along the top of the fuselage, as shown. 222

4.85 The raw S_{12} data plotted as a contour plot is very difficult to interpret due to the extremely rapid variations in magnitude with frequency. . 222
4.86 Smoothing the S_{12} with respect to frequency by 5% reveals the trends of the data. 223
4.87 With all of the windows covered with copper tape, the "leakage floor" measurement shows that the modified fuselage is well shielded. There is some residual leakage at the taped-on fuselage end plates, but the leakage along most of the top of the fuselage is below -80 dB. 224
4.88 The S_{12} between the simulated PED and the external antenna when only window "D" is open. 225
4.89 The S_{12} between the simulated PED and the external antenna when only window "F" is open. 225
4.90 The S_{12} between the simulated PED and the external antenna when only window "I" is open. 226
4.91 The S_{12} between the simulated PED and the external antenna when only the cockpit window is open. 226
4.92 A close-up photograph of a brass screen with a mesh size of 3 mm (2.36" full-scale) applied to window "F." 227
4.93 The S_{12} between the simulated PED and the external antenna when window "F" is screened with a 3 mm brass mesh, and all other windows are sealed. The maximum coupling is reduced 27.3 dB compared to the case of window "F" open. 228
4.94 A close-up photograph of a brass screen with a mesh size of 2 mm (1.57" full-scale) applied to window "F." 229
4.95 The S_{12} between the simulated PED and the external antenna when window "F" is screened with a 2 mm brass mesh, and all other windows are sealed. The maximum coupling is reduced 33.3 dB compared to the case of window "F" open. 230
4.96 A close-up photograph of a brass screen with a mesh size of 0.75 mm (0.59" full-scale) applied to window "F." 231
4.97 The S_{12} between the simulated PED and the external antenna when window "F" is screened with a 0.75 mm brass mesh, and all other windows are sealed. The maximum coupling is reduced 36.2 dB compared to the case of window "F" open. 232
4.98 The coupling observed when external antenna is located at the same station as window "F" as a function of frequency for the three applied screens. 232

5.1 The cylindrical fuselage began as a sheet of aluminum that was custom welded into a tube. 235
5.2 The cabin windows were designed to be the same number and configuration as those in the Simplified Fuselage. However, some discrepancies occurred in the physical realization. 236
5.3 Aluminum caps were machined to fit within the ends of the cylinder. The nose end cap features the same 8 cm by 18 cm "cockpit window" as the Simplified Fuselage. 236
5.4 The shielding effectiveness (relative to a monopole) of the cylindrical fuselage (blue) compared to that of the Simplified Fuselage (red), at nose incidence and observed at a point 50 cm from the nose. 240

5.5 A detailed view of the comparison between the cylindrical fuselage and the Simplified Fuselage shielding effectiveness between 0.5 GHz and 1.5 GHz. No correlation in the peaks and nulls are observed. 241
5.6 With the shielding effectiveness smoothed by 3% (with respect to frequency), it is more evident that the SE of the cylindrical fuselage is nearly identical to that of the Simplified Fuselage in this averaged, quasi-statistical sense. 241
5.7 Shielding effectiveness measurements were made with the cockpit window sealed with a brass plate and copper tape to observe the relative penetration through this aperture, and as a comparison for when the cockpit window is covered with a wire screen. 242
5.8 The shielding effectiveness increased by approximately 20 dB by sealing the cockpit window. 243
5.9 Replacing the brass with an aluminum wire screen should still be effective at reducing the penetration into the fuselage, if the screen wire spacing is small relative to the wavelength. 244
5.10 As the frequency goes up, the shielding effectiveness of the wire screen decreases, but it is just as effective as the brass plate below 4.5 GHz. 244
5.11 Adding the wire screens to the cabin windows should reduce the penetration into the fuselage still further. 245
5.12 A close-up view of the screen applied to the cabin windows. 245
5.13 But curiously, at frequencies above 4.5 GHz, the shielding effectiveness actually decreases. 246
5.14 The cockpit window screen was replaced with the brass plate, in an attempt to better understand this seemingly anomalous behavior. . . 246
5.15 Now the shielding effectiveness has increased above that for the case of the cabin windows open and the cockpit window sealed, as expected. 247
5.16 The entire window treatment series of measurements was repeated with the observation point moved to 1.25 m from the nose. 248
5.17 The resulting SE plots demonstrate that the same trends occur as when the observation point was at 50 cm from the nose. 248
5.18 Geometry of the cylindrical fuselage 249
5.19 Side view of the cylindrical fuselage 249
5.20 Front view of the cylindrical fuselage 250
5.21 Probe location in the cylindrical fuselage 250
5.22 Shielding effectiveness of the scaled fuselage for azimuthal incident angle of 0°, cell size 10 mm 252
5.23 Shielding effectiveness of the scaled fuselage for azimuthal incident angle of 0°, cell size 10 mm 252
5.24 Shielding effectiveness of the scaled fuselage for azimuthal incident angle of 0°, cell size 10 mm 253
5.25 Shielding effectiveness of the scaled fuselage for azimuthal incident angle of 0°, cell size 10 mm 253
5.26 Shielding effectiveness of the scaled fuselage for azimuthal incident angle of 0°, cell size 5 mm 255
5.27 Shielding effectiveness of the scaled fuselage for azimuthal incident angle of 0°, cell size 5 mm 255
5.28 Shielding effectiveness of the scaled fuselage for azimuthal incident angle of 0°, cell size 5 mm 256
5.29 Shielding effectiveness of the scaled fuselage for azimuthal incident angle of 0°, cell size 5 mm 256

5.30 Shielding effectiveness of the scaled fuselage for azimuthal incident angle of 0°, cell size 2.5 mm 257
5.31 Shielding effectiveness of the scaled fuselage for azimuthal incident angle of 0°, cell size 2.5 mm 258
5.32 Shielding effectiveness of the scaled fuselage for azimuthal incident angle of 0°, cell size 2.5 mm 258
5.33 Shielding effectiveness of the scaled fuselage for azimuthal incident angle of 0°, cell size 2.5 mm 259
5.34 Shielding effectiveness of the scaled fuselage for azimuthal incident angle of 0°, cell size 2.5 mm 259
5.35 Shielding effectiveness of the scaled fuselage for azimuthal incident angle of 0°, cell size 2.5 mm 260
5.36 Shielding effectiveness of the scaled fuselage for azimuthal incident angle of 0°, cell size 2.5 mm 260
5.37 Shielding effectiveness of the scaled fuselage for azimuthal incident angle of 0°, cell size 2.5 mm 261
5.38 Shielding effectiveness of the scaled fuselage for azimuthal incident angle of 0°, cell size 2.5 mm 261
5.39 Shielding effectiveness of the scaled fuselage for azimuthal incident angle of 0°, cell size 2.5 mm 262
5.40 Shielding effectiveness of the scaled fuselage for azimuthal incident angle of 0°, cell size 2.5 mm 262

6.1 Reverberation Chamber geometry. 266
6.2 One vector component of the angular spectrum of the electric field. . 270
6.3 Reverberation Chamber: (a) Top view (b) Side view. 273
6.4 Normal/Gaussian distributions: (a) probability density functions (b) cumulative density functions 275
6.5 Chi-square distributions: (a) probability density functions (b) cumulative density functions. 277
6.6 Confidence Interval vs. Stirrer Positions. 284
6.7 Probability for $|\rho| > |\rho_0| = e^{-1}$. 284
6.8 The mode stirrer blades are made from 0.010″ thick brass. Their asymmetrical dimension are intended to enhance the randomization of the penetrated fields. 287
6.9 The brass cross piece is constructed with 0.5 cm square tubing. Short lengths of brass tubing soldered to the edges of each blade are tight slip fits into the ends of the cross piece. 288
6.10 The construction was designed to enable the variable orientation of each blade in elevation. 289
6.11 Here, the blades are shown at approximately 45° elevation angle. . . . 290
6.12 This photograph shows the expanded polystyrene blocks supporting the Simplified Fuselage, and the dielectric shaft which connects the positioner to the mode stirrer. 292
6.13 The measured relative variations of field penetration at Probe B with respect to mode stirrer orientation. 293
6.14 The measured relative variations, with respect to mode stirrer orientation, of the field penetration at Probe C. 294
6.15 The calibrated penetration measured at probe B when the mode stirrer orientation is fixed at 0° versus frequency. 294
6.16 Simplified scale model fuselage with the mode-stirrer and the four probes 296

6.17 Measurement setup at ASU EMAC 296
6.18 Shielding effectiveness of the scaled fuselage with the mode-stirrer for azimuthal incident angle of 0° at probe A 297
6.19 Shielding effectiveness of the scaled fuselage with the mode-stirrer for azimuthal incident angle of 0° at probe A 297
6.20 Shielding effectiveness of the scaled fuselage with the mode-stirrer for azimuthal incident angle of 0° at probe A 298
6.21 Shielding effectiveness of the scaled fuselage with the mode-stirrer for azimuthal incident angle of 0° at probe A 298
6.22 Shielding effectiveness of the scaled fuselage with the mode-stirrer for azimuthal incident angle of 0° at probe B 299
6.23 Shielding effectiveness of the scaled fuselage with the mode-stirrer for azimuthal incident angle of 0° at probe B 299
6.24 Shielding effectiveness of the scaled fuselage with the mode-stirrer for azimuthal incident angle of 0° at probe B 300
6.25 Shielding effectiveness of the scaled fuselage with the mode-stirrer for azimuthal incident angle of 0° at probe B 300
6.26 Shielding effectiveness of the scaled fuselage with the mode-stirrer for azimuthal incident angle of 0° at probe C 301
6.27 Shielding effectiveness of the scaled fuselage with the mode-stirrer for azimuthal incident angle of 0° at probe C 301
6.28 Shielding effectiveness of the scaled fuselage with the mode-stirrer for azimuthal incident angle of 0° at probe C 302
6.29 Shielding effectiveness of the scaled fuselage with the mode-stirrer for azimuthal incident angle of 0° at probe C 302
6.30 Shielding effectiveness of the scaled fuselage with the mode-stirrer for azimuthal incident angle of 0° at probe D 303
6.31 Shielding effectiveness of the scaled fuselage with the mode-stirrer for azimuthal incident angle of 0° at probe D 303
6.32 Shielding effectiveness of the scaled fuselage with the mode-stirrer for azimuthal incident angle of 0° at probe D 304
6.33 Shielding effectiveness of the scaled fuselage with the mode-stirrer for azimuthal incident angle of 0° at probe D 304
6.34 Maximum and minimum E-field variation vs. frequency for points A and B. 307
6.35 Maximum and minimun E-field variation vs. frequency for points C and D. 307
6.36 Maximum and mean SE variation versus frequency, points A and B. 310
6.37 Maximum and mean SE variation versus frequency, points C and D. 310
6.38 Stirrer effectiveness, points A and B. 312
6.39 Stirrer effectiveness, points C and D. 312
6.40 Stirring ratio of points A and B. 313
6.41 Stirring ratio of points C and D. 313
6.42 Schematic representation of data clustering for the run-test. 315
6.43 Scatter plot for point A at 1 GHz. 316
6.44 Scatter plot for point A at 8 GHz. 316
6.45 PDF of $|E_z|^2$ at 1 GHz. 321
6.46 CDF of $|E_z|^2$ at 1 GHz. 321
6.47 PDF of $|E_z|^2$ at 8 GHz. 322
6.48 CDF of $|E_z|^2$ at 8 GHz. 322

6.49 PDF of SE at 5 GHz. 323
6.50 CDF of SE at 5 GHz. 323
6.51 PDF of SE at 8 GHz. 324
6.52 CDF of SE at 8 GHz. 324

7.1 Fuselage geometry along with the mode-stirrer and the four probes. . 331
7.2 $|E_z|^2$ vs. frequency, point A. 333
7.3 Empirical and theoretical-exponential CDFs at point A. 333
7.4 $|E_z|^2$ vs. frequency, point B. 334
7.5 Empirical and theoretical-exponential CDFs at point B. 334
7.6 $|E_z|^2$ vs. frequency, point C. 335
7.7 Empirical and theoretical-exponential CDFs at point C. 335
7.8 $|E_z|^2$ vs. frequency, point D. 336
7.9 Empirical and theoretical-exponential CDFs at point D. 336
7.10 Empirical and theoretical (exponential and Lehman) CDFs : (a) Point A (b) Point B. 339
7.11 Empirical and theoretical (exponential and Lehman) CDFs : (a) Point C (b) Point D. 339

8.1 Cavity geometries. (a) Empty (unperturbed). (b) With a rotating perturbing body. 343
8.2 Mode distributions. (a) Empty cavity. (b) Cavity including perturb body. 344
8.3 Three realizations of a stochastic process. 348
8.4 Noise band-pass filtering. (a) Power spectral density of white noise. (b) Block diagram of noise filtering. 350
8.5 Noise band-pass filtering. (a) Band-pass filter transfer function. (b) Time response of noise band-pass filtering. 351
8.6 Two dimensional cavity geometry. 352
8.7 Excitation signal generation. 353
8.8 Raised cosine pulse. (a) Time waveform. (b) Spectrum. 355
8.9 Spectrum of excitation signal. (a) 1 MHz bandwidth. (b) 5 MHz bandwidth. (c) 10 MHz bandwidth. (d) 50 MHz bandwidth. 356
8.10 Electric field homogeneity at 1 GHz for different noise bandwidths. (a)0 MHz versus 1 MHz. (b) 0 MHz versus 5 MHz. (c) 0 MHz versus 10 MHz. (d) 0 MHz versus 50 MHz. 359
8.11 Electric field homogeneity at 4 GHz for different noise bandwidths. (a)0 MHz versus 1 MHz. (b) 0 MHz versus 5 MHz. (c) 0 MHz versus 10 MHz. (d) 0 MHz versus 50 MHz. 360
8.12 Electric field homogeneity for different y positions. (a) Center frequency 1 GHz and bandwidth 50 MHz. (b) Center frequency 4 GHz and bandwidth 50 MHz. 361
8.13 Three dimensional cavity. 363
8.14 Dipole details. (a) Front view. (b) Top view. 364
8.15 Observation points. 365
8.16 Electric field homogeneity at 3 GHz for different noise bandwidths. (a) Center frequency 3 GHz and bandwidth 10 MHz. (b) Center frequency 3 GHz and bandwidth 50 MHz. 367
8.17 Electric field homogeneity for different y positions. Center frequency 3 GHz and bandwidth 50 MHz. 368
8.18 Electric field isotropy. Center frequency 3 GHz and bandwidth 50 MHz. 368

Chapter 1

Introduction

The ability to design and achieve electromagnetic compatibility is becoming more challenging with the rapid development of new electronic products and technologies. The importance of electromagnetic interference (EMI) and electromagnetic compatibility (EMC) issues stems from the fact that the ambient electromagnetic environment has become very hostile; that is, it increases both in density and intensity, while the current trend in technology suggests the number of electronic devices increases in homes, businesses, factories, and transportation vehicles. Furthermore, the operating frequency of products coming into the market continuously increases. While cell phone technology has exceeded 1 GHz and Bluetooth operates at 2.4 GHz, products involving satellite communications operate near 10 GHz and automobile radar systems involve frequencies above 40 GHz. The concern about higher frequencies is that they correspond to smaller wavelengths, therefore electromagnetic waves are able to penetrate equipment enclosure through apertures or even small cracks more easily. In addition, electronic circuits have become small in size, and they are usually placed on motherboards or housed in boxes in very close proximity. Cosite interference and coupling in all electrical and electronic circuit assemblies are two essential issues that have to be examined in every design.

According to IEEE, EMC is defined as "the capability of electrical and electronic systems, equipments, and devices to operate in their intended electromagnetic environment within a defined margin of safety, and at design levels of performance without suffering of causing unacceptable degradation as a result of electromagnetic interference" [2]. According to the same source, EMI is defined as "any electromag-

netic disturbance, whether intentional or not, that interrupts, obstructs, or otherwise degrades or limits the effective performance of electronic or electrical equipment."

From the above definitions the strong relation between EMC and EMI is evident. As a matter of fact it is EMI control along with susceptibility control that lead to EMC. EMI and susceptibility control are achieved by emission reduction from sources that are controllable, and increase of sensitive equipment immunity, respectively. Therefore, the focus of today's work in EMC is on standardization. Several technical organizations and committees such as the International Electrotechnical Commission (IEC), the International Standards Organization (ISO), and the International Telecommunications Union (ITU) are responsible for setting EMC and EMI standards for all electronic devices, as well as standards for measurement and test methods necessary for repeatable standards.

EMI is caused by dynamic factors, such as spurious emissions, space weather, or geomagnetic and atmospheric conditions. In other words, electromagnetic disturbances that affect electronic systems equate to EMI. A broader definition of EMI would encompass more static causes, such as geographical and man - made obstructions. Potential EMI threats can come from a jamming device, malfunctioning equipment, or improper system operation. A mountaintop, a clump of trees, or a building can also be contributing factors. What occurs much more frequently is interference from extraneous navigation and telecommunications systems, and other sources.

The area of modern technology that EMI and EMC issues are of particular interest and importance is aviation. This is because a large number of antennas are mounted on various platforms, such as helicopters, airplanes, etc., to support and provide crucial operational services, such as video and audio communications, high frequency (HF) beyond line - of - sight communications, GPS, radar altimeter, etc. In specific applications, very advanced communication systems are required (e.g., communication systems of helicopters or aircraft). For example, pilots of airplanes (or helicopters) depend substantially on guidance systems that check the alignment and the position of the airplane (or helicopter) during landing, especially at night or in poor visibility conditions. Consequently, in order to ensure safety, the communications instrumentation should be extremely reliable. However, when many antennas are placed on the same structure (e.g., helicopter or airplane airframe), the problem

of interference and coupling between transmitting and/or receiving elements can influence the operation and integrity of the communication systems. Interference can corrupt the signals with noise and deteriorate the quality of the communications. In addition, it can cause jamming of the systems, followed by complete interruption of already established communications. Therefore, the investigation of mutual coupling and the interpretation of coupling mechanisms is of great importance. Understanding the behavior of coupling helps us provide guidelines to minimize interference. This will significantly contribute to the design of communication systems with improved quality and reliability.

Another critical EMI/EMC issue that is relevant to all aviation, and which has lately attracted a lot of attention concerns the penetration of High Intensity Radiated Fields (HIRF) into conducting enclosures via apertures. In numerous occasions it has been proven that EM sources external to the aircraft have caused several problems to the equipment of airplanes, such as disrupted communications, disabled navigation equipment, etc. Sophisticated digital avionics are increasingly used in safety critical equipment of all types of modern aircraft. Regardless of digital avionics usefulness for critical and essential aircraft functions, they are susceptible to electronic upset if subjected to certain electromagnetic (EM) environments. Additionally, under regular flight conditions, the aircraft is exposed to the radiation of numerous EM sources covering the entire spectrum. Therefore, for the safety of the flight it is evident that aircraft is required to be immune to various EM interferences (EMI) and hence operate without adverse effects. EMI to an aircraft can be created by internal sources such as the installed on - board systems and passengers' personal electronic devices, as well as by external ones, such as high power communication systems (satellite links), radars and other aircraft. Such radiations are of significant interest, and they are referred to as HIRF sources.

More precisely, HIRF encompasses man - made sources of electromagnetic radiation generated external to the aircraft considered as possible interference toward the safety of aircraft flight. The easiest way to distinguish HIRF from other types of EMI is to state what it is not. HIRF does not include interference among on - board systems; this type of interference is referred to as an EMC issue. HIRF does not include EMI effects caused by portable electronic devices (PEDs) carried by pas-

sengers, such as cellular telephones, laptop computers and portable radios [1]. HIRF does not include the effects of lightning [3] [4], nor the effects of static electricity generated on the airplane; this is called Electrostatic Discharge (ESD). HIRF sources are only those emitters that intentionally generate emissions. Non - intentional (and in some cases non - licensed) emissions in the passband of aircraft navigation and communication systems have been known to cause interference problems, sometimes with serious consequences, but are not considered HIRF. These types of emissions are regulated by Federal Communications Commission (FCC). HIRF sources include radio and TV transmitters, airport and weather radar and various military systems, both grounded - based and airborne, such as surveillance radar, electronic warfare (EW) systems and electromagnetic weapons. The HIRF environment proposed for certifying safety critical systems in fixed wing aircraft and helicopters is shown in Table 1.1. As this table suggests, the HIRF frequency spectrum divides into distinctly different halves around 400 MHz. Below this frequency, most high - power use of the electromagnetic spectrum is by communication and navigation devices which radiate signals that are weakly directional and continuously on the air. This includes AM and HF or "short wave" broadcasts and FM and TV broadcasts. Most high - power use of the spectrum above 400 MHz is by radar, satellites and weapon systems. Radiation associated with these systems is generally of narrow beamwidth and often pulsed. In spite of the much higher peak levels associated with signals in the GHz range, experience has shown that the region of greatest sensitivity for electrical and electronic systems on aircraft is between a few MHz and a few hundred MHz.

This research project was primarily intended to develop analytical/numerical techniques to examine HIRF penetration into cavities. The parameter that was used to judge HIRF penetration in a cavity is shielding effectiveness (SE). Our research primarily focused on cavities with apertures because they better resemble aircraft fuselages while the mechanism of field penetration is the same in both cases. In such structures, an external signal penetrates through the apertures and directly couples energy into the interior. Although there are many possible mechanisms contributing to the penetration of fields into an aircraft, it is the windows that allow the greatest

[1] Rapid increases in the technology of personal communications causes concern about the potential EMI threat posed by PEDs however.

Frequency	Field Strength (V/m)	
	Peak	Average
10 kHz - 2 MHz	50	50
2 MHz - 30 MHz	100	100
30 MHz - 100 MHz	50	50
100 MHz - 400 MHz	100	100
400 MHz - 700 MHz	700	50
700 MHz - 1 GHz	700	100
1 GHz - 2 GHz	2000	200
2 GHz - 6 GHz	3000	200
6 GHz - 8 GHz	1000	200
8 GHz - 12 GHz	3000	300
12 GHz - 18 GHz	2000	200
18 GHz - 40 GHz	600	200

Table 1.1: HIRF certification environment proposed by the EEHWG [1]

penetration.

The drawback of this method is that in high - Q cavities, such as that of an aircraft, SE changes rapidly with respect to space and frequency, while the mode density is extremely high. As a result, adequate information regarding HIRF penetration in such cavities requires that measurements be performed at several points inside them. An alternative to this method would be to measure the SE of a single point while varying the impinging wave angle of incidence. The aforementioned methods, in addition to being time consuming, are also not practically feasible when, for example, the size of the equipment under test is of the order of meters. Moreover the methods mentioned previously cannot give a reliable estimate of the EM field maximum value, or the range over which it varies, at a specified region of the cavity. The latter may result in misjudgments when one wants to properly shield sensitive electronic equipment of an aircraft and ensure safe flight conditions.

The numerical techniques that were developed in this project are based on the Finite Difference Time - Domain (FDTD) method, and they were used to predict the field penetrating inside a fuselage when the structure is illuminated by an impinging electromagnetic wave. In addition, simplified experimental models were built and measurements were performed in ASU's Electro - Magnetic Anechoic Cham-

ber (EMAC) in order to compare them with predictions and validate the accuracy of the proposed computational methods. Initially, the standard FDTD scheme was implemented and shielding effectiveness (SE) predictions are performed for small conducting boxes with apertures. After successfully completing this task, the same numerical technique was used for SE predictions of a simplified scaled model fuselage of rectangular cross section. Moreover, for the simplified scaled model fuselage, coupling of personal electronic devices was studied and predictions as well as measurements, were performed. Then a hybrid numerical technique was suggested which combines a higher - order FDTD scheme with the standard one. The new method was implemented and all the aforementioned problems were studied. In addition, reverberation chamber techniques, along with statistical and probabilistic methods, were developed to test the statistical properties of the electromagnetic field inside cavities. Since the field inside a complex cavity strongly depends on frequency, position, angle of incidence of the impinging wave and other parameters, the need for a different approach was recognized in order to better predict it. Both measurements and predictions were performed, and the resulting data were statistically processed and compared with probabilistic models provided by the theory of statistical electromagnetics. Cumulative density function (CDF) plots are presented for field quantities in the fuselage, as well as for its SE.

The structural documentation of this report is now outlined. In Chapter 2, the basic theory of the higher - order FDTD will be presented. The concepts of stability, as well as dispersion, will be defined and analyzed. The Perfectly Matched Layer ABC will be implemented in the context of the fourth - order FDTD, and its accuracy will be verified through numerical experiments. Fourth - order FDTD will be applied initially to the analysis of two simple but interesting 3 - D problems, including array factor and cavity resonances computations. Then, FDTD(2,4) will be used for radiation pattern analysis. Boundary conditions in the context of higher - order schemes will be discussed, and their limitations and restrictions will be readily outlined. These issues will be numerically examined through simulations of monopole antennas mounted on finite ground planes. Moreover, a hybrid technique of fourth - order FDTD, with the standard second - order FDTD, will be implemented following a subgrid formulation. The accuracy and efficiency of this new hybrid method will

be verified and validated using again the analysis of coupling between two monopoles mounted on ground planes. The calculations of the hybrid method will be compared to measurements as well as to predictions using the standard second - order FDTD method. Finally, a second hybrid method will be formulated between subgrid FDTD(2,2) and FDTD(2,4) which provides significant computational savings when applied to the analysis of electrically large rectangular enclosures.

In Chapter 3 the FDTD method is applied to antenna problems. Initially, an improved feed model for thin - wire antennas will be examined, and it will be compared with the delta - gap feed model. Furthermore, the discrete Fourier transform (DFT) will be compared to the fast Fourier transform (FFT) in the context of the FDTD method. Then, cavity - backed slot (CBS) antennas will be analyzed. FDTD will be used to predict various antenna characteristics of such antennas, such as input impedance, coupling, and radiation patterns. Different coupling reduction techniques, such as inclusion of lossy material superstrates, ground plane discontinuities (slits), and disorientation of the elements, will be introduced and compared. Certain computational difficulties concerning the simulation of CBS antennas will be addressed and resolved in the context of FDTD.

In Chapter 4, the penetration of High Intensity Radiated Fields (HIRF) into conducting enclosures via apertures will be presented. The FDTD method will be used to predict the shielding effectiveness of conducting enclosures with apertures. Several techniques that speed the simulation of highly resonant and high quality factor (high - Q) structures, such as windowing and acceleration techniques, will also be introduced and applied. Also, the penetration through a scaled model fuselage will be examined and simulated by the standard FDTD(2,2) and the hybrid of subgrid FDTD(2,2) and FDTD(2,4). Finally, the coupling generated by on - board personal electronic devices (PEDs) will be analyzed by both methods. In Chapter 5 the penetration through a circular cross - section scaled model fuselage will be examined. Measurements were performed, and they are compared with FDTD predictions.

In Chapter 6, a statistical approach for the HIRF penetration problem will be presented. As mentioned previously, field penetration and SE of aircraft are issues of great importance. Previous studies and experience have shown that in order to properly investigate this problem, its statistical nature should be taken into account.

Therefore a statistical approach is used that utilizes a reverberation chamber technique. A reverberation chamber is a measurement facility within which the field is uniformly and isotropically distributed. In order to achieve such field conditions, a rotatable scatterer, referred to as mode - stirrer, is used. The role of the mode - stirrer is to perturb the existing modes in the chamber and give the field a stochastic nature. Therefore a mode - stirrer was constructed and installed in the scaled model fuselage. Measurements were performed for different mode - stirrer orientations, and the field was probed in various locations in the fuselage. The collected data was statistically processed and its statistical properties was compared with the theoretical expected ones. Moreover, basic statistical analysis was performed where the maximum and mean values of the field over all stirrer positions were plotted versus frequency. Also several aspects of reverberation chamber theory will be presented, and an overview of their principles of operation will be given.

In Chapter 7, an additional statistical approach (different from that of Chapter 6) to the HIRF penetration problem is presented. This approach is based on the work of Price and Davis [5] who state that the power received by a dipole antenna located within an overmoded cavity will be distributed exponentially. This exponential power distribution occurs when either the frequency is swept while the location of the dipole antenna is fixed, or when the frequency is held constant and the dipole is translated in position. An improvement on this rigorous theory of exponential power distribution within overmoded cavities, developed by Lehman [6], is briefly discussed. The Price and Lehman approaches are applied to the "Simplified Fuselage" scale model geometry as a function of frequency for the four monopole observation points. These predicted power distributions compare well with the measured data.

Finally, in Chapter 8 the frequency stirring technique is presented which is an alternate to mechanically stirred reverberation chambers. The technique's theoretical principles are presented while afterwards it is applied for the excitation initially of a 2-D and then a 3-D cavity. The statistical properties of the electromagnetic field inside the cavity are calculated and compared with those of a reverberation chamber.

Chapter 2

Fourth-Order Finite-Difference Time-Domain

I. Introduction

The technological advancements of the last few decades have triggered new engineering problems and challenges. With the clock speed of all electronic equipment increasing, communication systems operate at higher frequencies. Therefore, the antenna elements become smaller whereas the platforms they operate on, e.g., helicopter airframes, become electrically larger. These problems yield large computational domains and require significant computational resources, such as memory and execution time. Traditional finite methods (FDTD and FEM) are second-order accurate, thereby restricting the size of the domains that can be handled efficiently.

The standard FDTD method was introduced by Yee [7] in 1966. The classical FDTD method as proposed by Yee [7] is second-order accurate both in time and space [FDTD(2,2)] thereby requiring many grid points per wavelength to accurately model the wave propagation. The FDTD method, as is typical for discrete methods, is dispersive; the phase velocity on the FDTD grid is not the same as the phase velocity of the physical continuous problem. In order to reduce dispersion errors, a finer discretization is required. On the other hand, finer discretizations demand larger memory and increased computational time, thereby restricting yet further the problems that can be solved. Consequently, mesh refinement is not an efficient solution and sometimes is not even possible.

Numerous attempts have been made in the field of FDTD research to minimize

phase errors [8]-[10]. One of the most promising approaches is based on higher-order accuracy schemes [11]-[17]. Such schemes theoretically exhibit lower dispersion errors and can utilize coarser grids as compared to those needed to achieve comparable levels of accuracy with a second-order scheme. Moreover, coarser meshes yield smaller computational spaces, reduced computational times and require less computational resources. Thus, ideally, the implementation of higher-order FDTD schemes will enable the efficient analysis of electrically larger problems.

In this chapter, the theory of FDTD is presented for both second- and fourth-order accurate schemes. Their different characteristics, such as dispersion and stability are described and compared. The accuracy of the different FDTD schemes is initially examined through numerical experiments in one-dimensional (1-D) domains. Then, the implementation of absorbing boundary conditions, such as the Perfectly Matched Layer (PML), is implemented in the context of a fourth-order accurate FDTD method. Furthermore, fourth-order FDTD is applied in 3-D problems including, array analysis, cavity resonances and radiation pattern computations, and its accuracy is compared to the accuracy of the second-order FDTD. The limitations of fourth-order FDTD related to boundary conditions, and thin geometric features are discussed through simulations of coupling analysis between two monopole antennas mounted on ground planes.

A hybrid technique of fourth-order FDTD with the standard second-order FDTD is implemented following a subgrid formulation. The accuracy and efficiency of this new hybrid method is verified, and validated using again the analysis of coupling between two monopoles mounted on ground planes. The calculations of the hybrid method are compared to measurements as well as results of the standard second-order FDTD method.

Finally, the reverse hybrid of the subgrid FDTD(2,2) with the FDTD(2,4) is formulated to accommodate simulations of electrically large rectangular boxes. It is shown that this new hybrid yields significant memory and/or time savings when applied to shielding effectiveness analysis of large fuselages.

II. Basic Principles

The relations and variations of the electric and magnetic fields, charges and currents associated with electromagnetic waves are governed by physical laws, which are known as Maxwell's equations. These equations can be written either in differential or in integral form. For a source-free region, the differential form of Maxwell's equations can be written as

$$\nabla \times \mathbf{E} = -\mathbf{M} - \frac{\partial \mathbf{B}}{\partial t} \tag{2.1}$$

$$\nabla \times \mathbf{H} = \mathbf{J} + \frac{\partial \mathbf{D}}{\partial t} \tag{2.2}$$

$$\nabla \cdot \mathbf{D} = 0 \tag{2.3}$$

$$\nabla \cdot \mathbf{B} = 0 \tag{2.4}$$

where $\mathbf{E}$ is the electric field intensity in (volts/meter), $\mathbf{H}$ is the magnetic field intensity in (amperes/meter), $\mathbf{D}$ is the electric flux density in (coulombs/square meter), $\mathbf{B}$ is the magnetic flux density in (webers/square meter), $\mathbf{J}$ is the conduction electric current density in (amperes/square meter), $\mathbf{M}$ is the conduction magnetic current density in (volts/square meter). It should be pointed out that a complete description of the fields at any point (including the discontinuities) at any time requires not only Maxwell's equations in differential form but also the associated boundary conditions.

The integral form of Maxwell's equations for a source-free region can be written as

$$\oint_C \mathbf{E} \cdot d\mathbf{l} = -\iint_S \mathbf{M} \cdot d\mathbf{s} - \frac{\partial}{\partial t} \iint_S \mathbf{B} \cdot d\mathbf{s} \tag{2.5}$$

$$\oint_C \mathbf{H} \cdot d\mathbf{l} = \iint_S \mathbf{J} \cdot d\mathbf{s} + \frac{\partial}{\partial t} \iint_S \mathbf{D} \cdot d\mathbf{s} \tag{2.6}$$

$$\oint_S \mathbf{D} \cdot d\mathbf{s} = 0 \tag{2.7}$$

$$\oint_S \mathbf{B} \cdot d\mathbf{s} = 0 \tag{2.8}$$

In materials with constitutive parameters that are independent of time the electric and magnetic flux densities $\mathbf{D}$ and $\mathbf{B}$ can be related to the electric and magnetic field intensities $\mathbf{E}$ and $\mathbf{H}$, respectively, using the constitutive relations

$$\mathbf{D} = \epsilon \mathbf{E} \tag{2.9}$$

$$\mathbf{B} = \mu \mathbf{H} \tag{2.10}$$

where ϵ is the electrical permittivity in (farad/meter) and μ is the magnetic permeability in (henries/meter). Furthermore, the conduction electric current density $\mathbf{J}$ and the conduction magnetic current density $\mathbf{M}$ are related to the electric and magnetic intensities $\mathbf{E}$ and $\mathbf{H}$, respectively, using the constitutive relations

$$\mathbf{J} = \sigma \mathbf{E} \tag{2.11}$$

$$\mathbf{M} = \rho \mathbf{H} \tag{2.12}$$

where σ is the electrical conductivity in (siemens/meter) and ρ is the magnetic resistivity in (ohms/meter). Substituting (2.9)-(2.12) into the differential form of Maxwell's equations (2.1) and (2.2), the following two equations are obtained

$$\frac{\partial \mathbf{H}}{\partial t} = -\frac{1}{\mu} \nabla \times \mathbf{E} - \frac{\rho}{\mu} \mathbf{H} \tag{2.13}$$

$$\frac{\partial \mathbf{E}}{\partial t} = \frac{1}{\epsilon} \nabla \times \mathbf{H} - \frac{\sigma}{\epsilon} \mathbf{E} \tag{2.14}$$

Assuming that ϵ, μ, σ and ρ are linear and isotropic, (2.13) and (2.14) can be written as a system of six coupled scalar equations in Cartesian coordinates as follows:

$$\frac{\partial H_x}{\partial t} = \frac{1}{\mu} \left(\frac{\partial E_y}{\partial z} - \frac{\partial E_z}{\partial y} - \rho H_x \right) \tag{2.15}$$

$$\frac{\partial H_y}{\partial t} = \frac{1}{\mu} \left(\frac{\partial E_z}{\partial x} - \frac{\partial E_x}{\partial z} - \rho H_y \right) \tag{2.16}$$

$$\frac{\partial H_z}{\partial t} = \frac{1}{\mu}\left(\frac{\partial E_x}{\partial y} - \frac{\partial E_y}{\partial x} - \rho H_z\right) \tag{2.17}$$

$$\frac{\partial E_x}{\partial t} = \frac{1}{\epsilon}\left(\frac{\partial H_z}{\partial y} - \frac{\partial H_y}{\partial z} - \sigma E_x\right) \tag{2.18}$$

$$\frac{\partial E_y}{\partial t} = \frac{1}{\epsilon}\left(\frac{\partial H_x}{\partial z} - \frac{\partial H_z}{\partial x} - \sigma E_y\right) \tag{2.19}$$

$$\frac{\partial E_z}{\partial t} = \frac{1}{\epsilon}\left(\frac{\partial H_y}{\partial x} - \frac{\partial H_x}{\partial y} - \sigma E_z\right) \tag{2.20}$$

The system of six coupled partial differential equations of (2.15)-(2.20) forms the basis of the FDTD algorithm for solving problems of electromagnetic wave interactions in the three-dimensional (3-D) space. Notice that the FDTD algorithm need not explicitly enforce the Gauss's Law relations indicating zero free electric and magnetic charge, (2.3) and (2.4), as these relations are theoretically a direct consequence of the curl equations (2.1) and (2.2).

III. FDTD Schemes

FDTD methods attempt to solve the differential form of Maxwell's equations and therefore their implementation consists of finite-difference (FD) approximations to spatial and time derivatives. Consequently, the accuracy of FDTD solutions depends on the accuracy of the FD schemes that are used. FD stencils appeared initially in the field of mathematics and numerous schemes have been examined exhibiting their own advantages and disadvantages. In this section two schemes are considered; the standard second-order FD scheme both in time and space [FDTD(2,2)] and the second-order in time and fourth-order in space scheme [FDTD(2,4)]. The characteristics of the two schemes are presented and compared.

A. The FDTD(2,2) scheme

In 1966, Kane Yee presented a set of finite difference equations for the system of Maxwell's curl equations for lossless materials [7]. Yee introduced the following notation for a function of space and time on a Cartesian grid

$$F(x, y, z, t) = F(i\Delta x, j\Delta y, k\Delta z, n\Delta t) = F^n(i, j, k) \tag{2.21}$$

where Δx, Δy and Δz are the grid sizes in the x, y and z directions, respectively; Δt is the time increment; and i, j, k and n are integers. Yee used central finite difference expressions for the space and time derivatives that are second-order accurate in space and time, respectively:

$$\frac{\partial F(i,j,k)}{\partial x} \simeq \frac{F^n(i+\frac{1}{2},j,k) - F^n(i-\frac{1}{2},j,k)}{\Delta x} + O\ (\Delta x^2) \tag{2.22}$$

$$\frac{\partial F(i,j,k)}{\partial t} \simeq \frac{F^{n+\frac{1}{2}}(i,j,k) - F^{n-\frac{1}{2}}(i,j,k)}{\Delta t} + O\ (\Delta t^2) \tag{2.23}$$

FD schemes are commonly visualized using the so called *computational molecules.* The computational molecule corresponding to the second-order central FD of (2.22) or (2.23) is illustrated in Fig. 2.1.

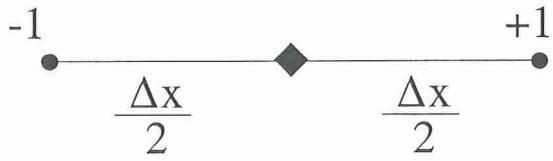

Figure 2.1: Computational molecule of a central second-order FD stencil.

A representative unit cell of Yee's algorithm with the positions of several field components is illustrated in Fig. 2.2. The electric and magnetic components are staggered by half-cell dimension in each direction within the grid. A similar staggering is applied in time. The electric field components are evaluated at integer time steps, $n\Delta t$, and the magnetic field components at $(n + 1/2)\Delta t$ time steps (leapfrog algorithm). Moreover, in order to be able to implement the leapfrog algorithm, Yee utilized the following time averaging scheme:

$$F^{n+\frac{1}{2}}(i,j,k) = \frac{F^{n+1}(i,j,k) + F^n(i,j,k)}{2} \tag{2.24}$$

B. The FDTD(2,4) scheme

More accurate approximations to derivatives are provided by higher order FD schemes. Here a second-order in time and fourth-order in space scheme [FDTD(2,4)] is described. In this scheme the positions of the electric and magnetic field components remain the same with the ones of the FDTD(2,2) scheme. The FDTD(2,4) stencil

uses central finite differences fourth-order accurate in space and second-order accurate in time, respectively:

$$\frac{\partial F(i,j,k)}{\partial x} \simeq \frac{9}{8}\frac{F^n(i+\frac{1}{2},j,k)-F^n(i-\frac{1}{2},j,k)}{\Delta x} - \frac{1}{24}\frac{F^n(i+\frac{3}{2},j,k)-F^n(i-\frac{3}{2},j,k)}{\Delta x} + O\left(\Delta x^4\right) \tag{2.25}$$

$$\frac{\partial F(i,j,k)}{\partial t} \simeq \frac{F^{n+\frac{1}{2}}(i,j,k)-F^{n-\frac{1}{2}}(i,j,k)}{\Delta t} + O\left(\Delta t^2\right) \tag{2.26}$$

The computational molecule of a central fourth-order FD stencil corresponding to (2.25) is shown in Fig. 2.3.

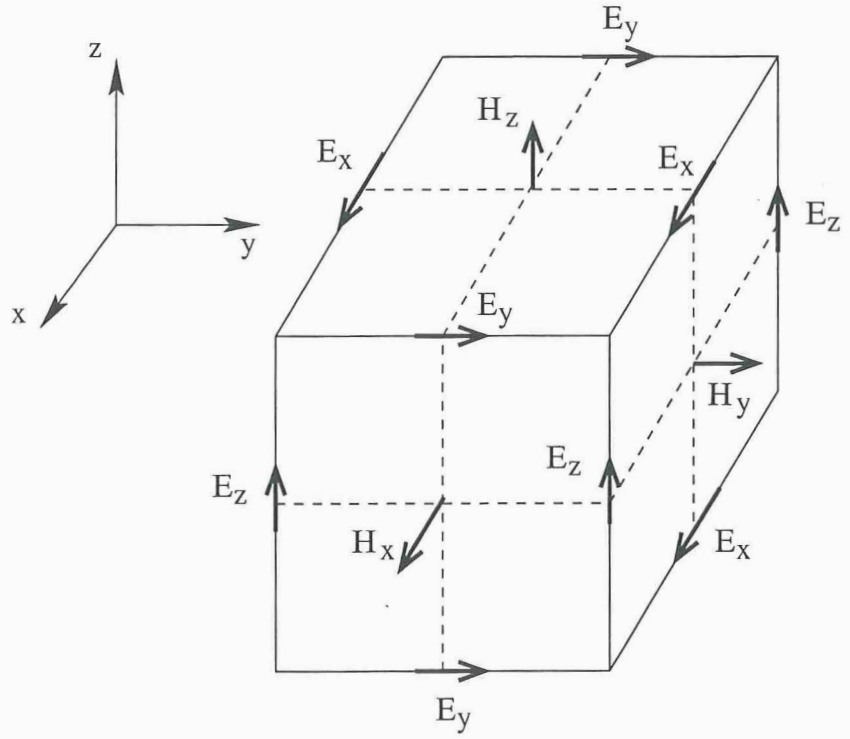

Figure 2.2: The FDTD unit cell as proposed by Yee.

C. Characteristics of the FDTD schemes

Any FDTD scheme exhibits its own strengths and weaknesses. The order of accuracy of a scheme dominates its characteristics and is directly related to the numerical

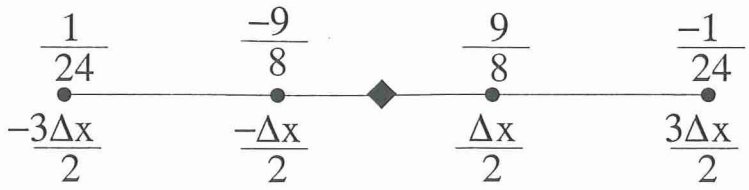

Figure 2.3: Computational molecule of a central fourth-order FD stencil.

dispersion. Another important characteristic of a scheme is its stability criterion which defines the largest time-step that can be used in order for the scheme to be stable. Additionally, the memory requirements and computational cost of schemes are also used to evaluate their practicality. In the following subsections, the stability and the dispersion of the FDTD(2,2) and FDTD(2,4) schemes are described and compared.

1. Numerical stability

Finite-Difference schemes require that the time increment Δt has a specific bound relative to the spatial discretization, Δx, Δy and Δz. This bound is necessary to prevent numerical instability, which is an undesirable feature of explicit differential equation schemes. Numerical instability can cause the computed results to spuriously increase without limit as time-stepping progresses thereby yielding meaningless solutions. It should be pointed out that many implicit schemes are stable for any choice of time-step which is a very advantageous feature.

An investigation of the numerical stability of Yee's algorithm [FDTD(2,2)] was initially presented in [18] and detailed afterwards in [19]. The stability analysis is based upon finding the Fourier numerical modes in the grid for both the electric and magnetic field components and requiring that each Fourier mode is stable for arbitrary angles of propagation through the mesh. Enforcing the stability in the 3-D FDTD(2,2) algorithm provides the following constraint on the algorithm's time-step, relative to the space grid increments

$$\Delta t \leq \frac{1}{c\sqrt{\frac{1}{\Delta x^2}+\frac{1}{\Delta y^2}+\frac{1}{\Delta z^2}}} \tag{2.27}$$

where $c = 1/\sqrt{\mu\epsilon}$ is the speed of light in the homogeneous material being modeled. For a uniform grid with equal cell size in all dimensions ($\Delta x = \Delta y = \Delta z = \Delta$), (2.27)

reduces to

$$\Delta t \leq \frac{\Delta}{c\sqrt{3}} \tag{2.28}$$

The stability criterion for the FDTD(2,4) scheme was derived by Fang [13] who based his formulations on the Von Neumann analysis suitable for systems of equations and multi-step schemes. This analysis requires the eigenvalues of the amplification matrix to be bounded. However, this is only a necessary but not sufficient condition for stability. A necessary and sufficient condition for stability is that the norm of the amplification matrix is bounded. Therefore, after a stability constraint has been obtained by the eigenvalue analysis, it should be checked if the norm of the amplification matrix remains bounded under the same constraint. The stability constraint for the FDTD(2,4) scheme derived by Fang is:

$$\Delta t \leq \frac{6}{7} \frac{1}{c\sqrt{\frac{1}{\Delta x^2} + \frac{1}{\Delta y^2} + \frac{1}{\Delta z^2}}} \tag{2.29}$$

It is apparent that the stability criterion of FDTD(2,4) is more constraining than the one of FDTD(2,2). For a uniform grid with equal cell size in all dimensions ($\Delta x = \Delta y = \Delta z = \Delta$), (2.29) becomes

$$\Delta t \leq \frac{6}{7} \frac{\Delta}{c\sqrt{3}} \tag{2.30}$$

2. Numerical dispersion

Numerical algorithms that solve Maxwell's equations using finite-difference approximations cause dispersion of the simulated wave modes in the computational mesh. This dispersion phenomenon originates from the deviation of the phase velocity of the numerical wave modes in the FDTD grid from the speed of light in vacuum, in terms of wavelength, direction of propagation, and grid discretization. As Taflove suggests in [19] "A useful way to view this phenomenon is that the FDTD algorithm effectively embeds the electromagnetic wave interaction structure of interest in a tenuous 'numerical aether' having a permittivity very close to vacuum, but not quite. This 'aether' causes propagating waves to accumulate delay or phase errors that can lead to non-physical results, such as broadening and ringing of single-pulse waveforms, imprecise

cancellation of multiple scattered waves, spurious anisotropy, and pseudo-refraction". Furthermore, different wave components propagate at different velocities inside the numerical domain, and hence the wave is dispersed. Therefore, numerical dispersion is an important factor in FDTD modeling that should be taken into account, especially for electrically large structures where the accumulation of phase errors can be significant. The dispersion characteristic of the FDTD algorithm is readily analyzed in [19] and involves the substitution of monochromatic traveling-wave trial solutions into the finite-difference equations. This procedure yields an equation that relates the numerical wave-vector components, the wave frequency, and the grid space increments. This equation is usually referred to as the numerical dispersion relation. In this subsection the dispersion characteristics of FDTD(2,2) and FDTD(2,4) are examined and compared.

The dispersion equation for FDTD(2,2) was derived in [19] as

$$\left[\frac{1}{c\Delta t}\sin\left(\frac{\omega\Delta t}{2}\right)\right]^2 = \left[\frac{1}{\Delta x}\sin\left(\frac{k_x\Delta x}{2}\right)\right]^2 + \left[\frac{1}{\Delta y}\sin\left(\frac{k_y\Delta y}{2}\right)\right]^2 + \left[\frac{1}{\Delta z}\sin\left(\frac{k_z\Delta z}{2}\right)\right]^2 \tag{2.31}$$

To quantitatively assess the dependence of numerical dispersion upon the FDTD grid discretization, Taflove [19] examined a two-dimensional (2-D) TM mode, assuming for simplicity square cells ($\Delta x = \Delta y = \delta$) and wave propagation at an angle θ with respect to the positive x-axis ($k_x = kcos\theta; k_y = ksin\theta$). The numerical dispersion relation in this case simplifies to

$$\left(\frac{\delta}{c\Delta t}\right)^2 sin^2\left(\frac{\omega\Delta t}{2}\right) = sin^2\left(\frac{\delta kcos\theta}{2}\right) + sin^2\left(\frac{\delta ksin\theta}{2}\right) \tag{2.32}$$

where c is the speed of light in vacuum. Using Newton's method iterative procedure, (2.32) can be solved for the wave-vector k at any wave propagation angle θ:

$$k_{i+1} = k_i - \frac{sin^2(Ak_i) + sin^2(Bk_i) - C}{Asin(2Ak_i) + Bsin(2Bk_i)} \tag{2.33}$$

where k_{i+1} is the improved estimate of k, k_i is the previous estimate of k, and A, B and C are coefficients determined by the wave propagation angle and the FDTD grid

discretization:

$$A = \frac{\delta cos\theta}{2}, \qquad B = \frac{\delta sin\theta}{2}, \qquad C = \left(\frac{\delta}{c\Delta t}\right)^2 sin^2\left(\frac{\omega\Delta t}{2}\right) \tag{2.34}$$

Assuming that the numerical stability criterion, $c\Delta t = \delta/2$, is used and that the wavelength is set to 1 meter, $\lambda = 1$ m, (2.33) can be used to quantify the numerical dispersion. For this case, the normalized numerical phase velocity v_p is given by

$$\frac{v_p}{c} = \frac{2\pi}{k_{final}} \tag{2.35}$$

where k_{final} is the final result of Newton's method iterations. Fig. 2.4 shows the numerical phase velocity relative to the speed of light in the vacuum versus the propagation angle of a plane wave traveling in a 2-D FDTD(2,2) mesh. Evidently, the numerical phase velocity is always less than c and the error decreases as the discretization becomes finer.

The dispersion equation for FDTD(2,4) was derived by Fang [13] as

$$\begin{aligned}\left[\frac{1}{c\Delta t}\sin\left(\frac{\omega\Delta t}{2}\right)\right]^2 &= \left(\frac{1}{\Delta x}\right)\left[\frac{9}{8}\sin\left(\frac{k_x\Delta x}{2}\right) - \frac{1}{24}\sin\left(\frac{3k_x\Delta x}{2}\right)\right]^2 \\ &+ \left(\frac{1}{\Delta y}\right)\left[\frac{9}{8}\sin\left(\frac{k_y\Delta y}{2}\right) - \frac{1}{24}\sin\left(\frac{3k_y\Delta y}{2}\right)\right]^2 \\ &+ \left(\frac{1}{\Delta z}\right)\left[\frac{9}{8}\sin\left(\frac{k_z\Delta z}{2}\right) - \frac{1}{24}\sin\left(\frac{3k_z\Delta z}{2}\right)\right]^2 \end{aligned} \tag{2.36}$$

Following a similar approach as illustrated before for FDTD(2,2), the numerical phase velocity of FDTD(2,4) can be accessed for a 2-D lattice. By choosing the same parameters as for FDTD(2,2) ($c\Delta t = \delta/2$ and $\lambda = 1$ m), (2.36) can be solved to obtain the numerical phase velocity. Fig. 2.5 shows the computed phase velocity for a 2-D FDTD(2,4) grid. Fig. 2.6 also illustrates a comparison between the errors in the numerical phase velocities of FDTD(2,2) and FDTD(2,4). It is observed, as expected, that FDTD(2,4) exhibits substantially reduced dispersion compared to FDTD(2,2). Therefore, FDTD(2,4) can be used to accurately model electrically larger domains than the ones that can be simulated by FDTD(2,2). Another interesting observation

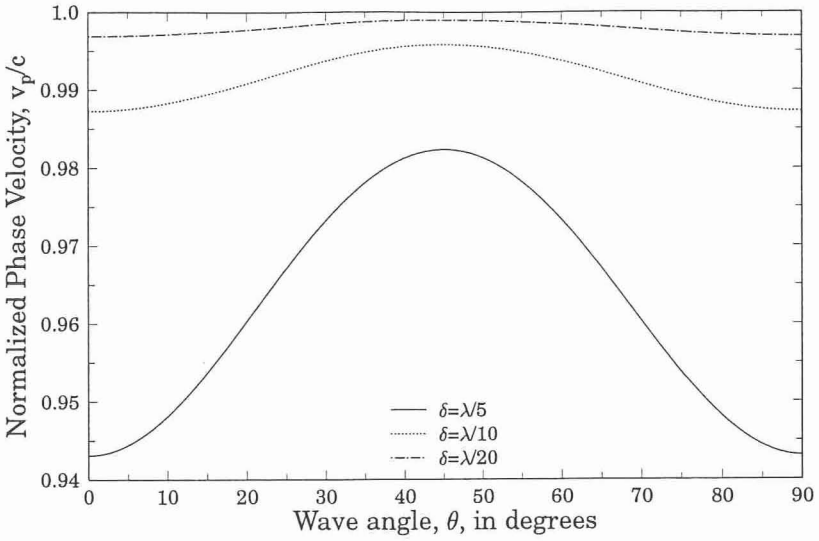

Figure 2.4: Variation of the numerical phase velocity versus the propagation angle of a plane wave for FDTD(2,2).

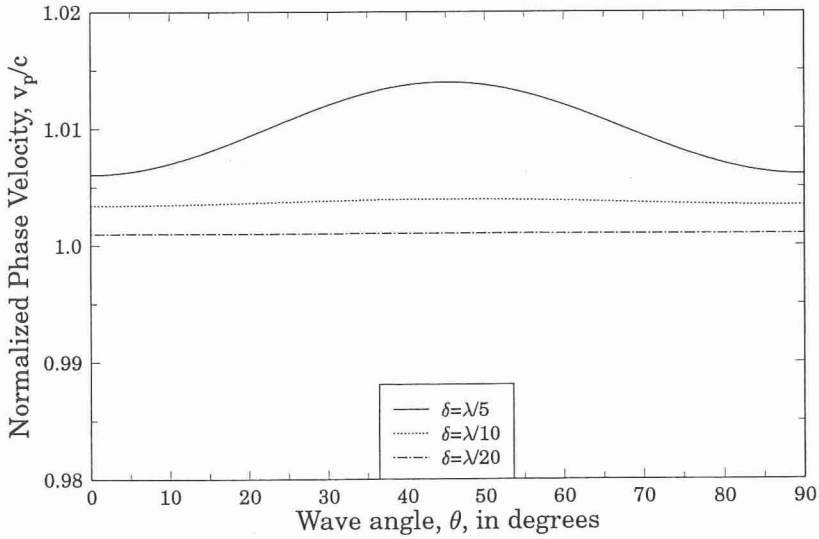

Figure 2.5: Variation of the numerical phase velocity versus the propagation angle of a plane wave for FDTD(2,4).

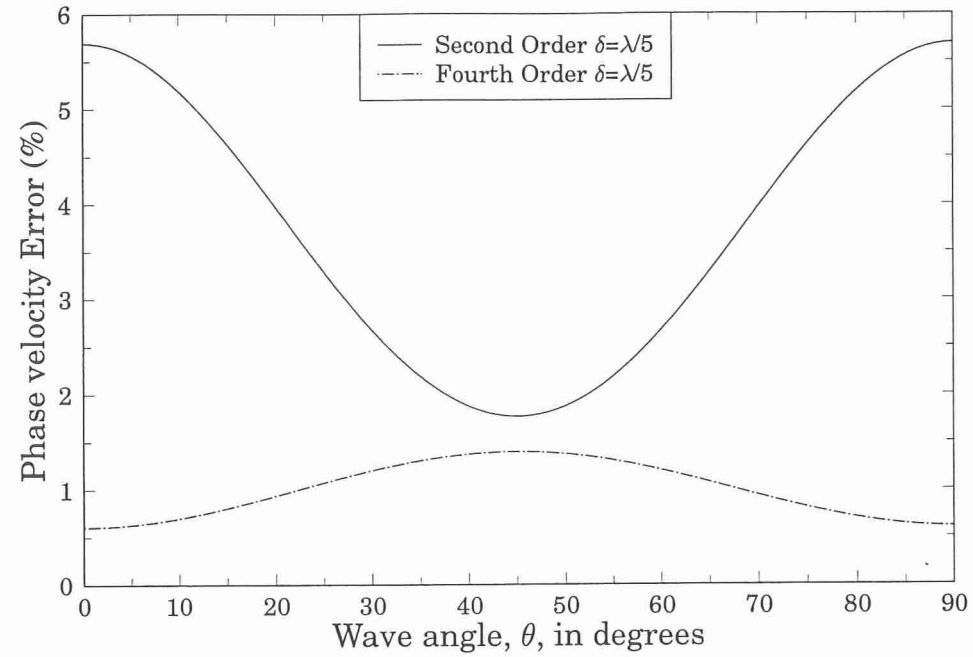

(a)

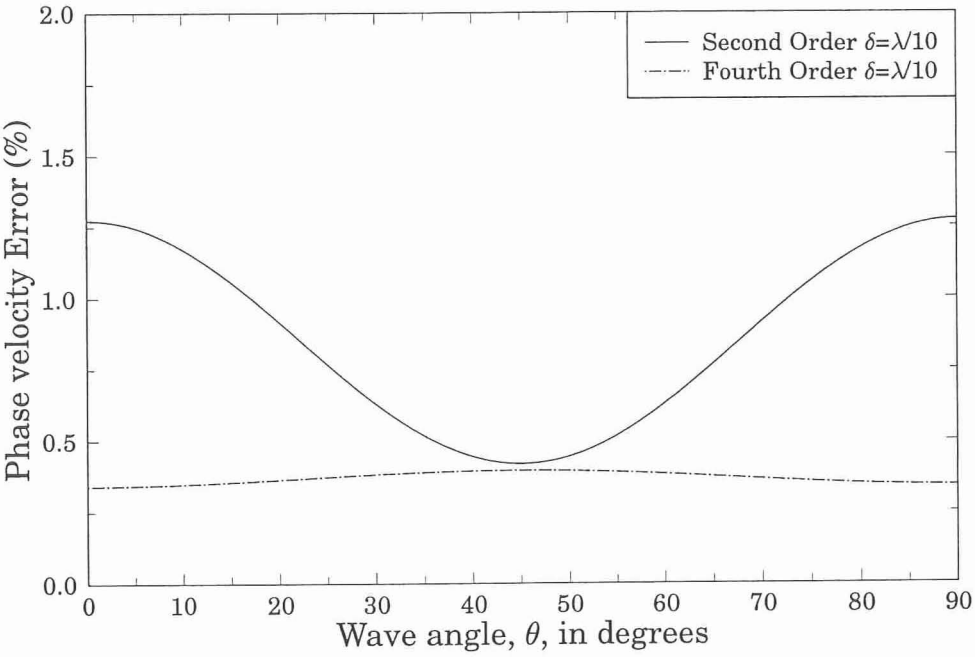

(b)

Figure 2.6: Comparison of the error in the numerical phase velocity for FDTD(2,2) and FDTD(2,4).

based on Figs. 2.4 and 2.5 is that the numerical phase velocity varies with the angle of wave propagation thereby generating a numerical anisotropy which is an inherent characteristic of the FD schemes.

IV. FDTD(2,4) in 1-D Domains

In this section, numerical experiments are performed in one-dimensional domains using FDTD(2,2) and FDTD(2,4) in order to qualitatively access the performance characteristics of FDTD(2,4) and compare them with the ones of FDTD(2,2). All the

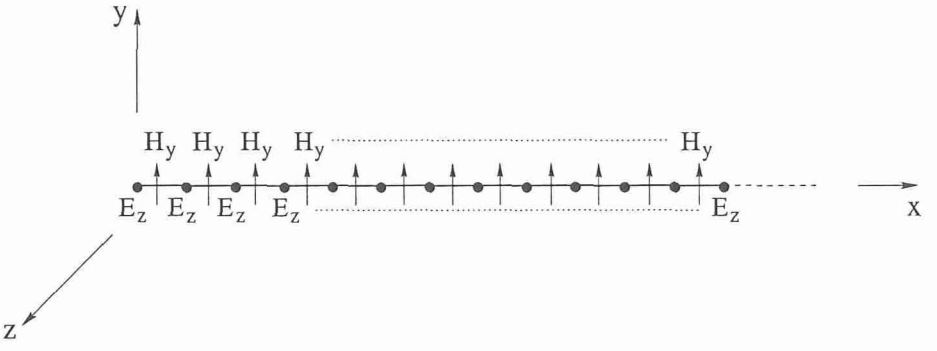

Figure 2.7: Grid for a 1-D TM^z mode.

simulations presented here are solving the 1-D TM^z mode (see Fig. 2.7), and the time-step for both FDTD(2,2) and FDTD(2,4) computations is chosen such that $c\Delta t = \delta/2$ ($\Delta x = \Delta y = \delta$). The time-step in the case of FDTD(2,2) was not chosen to be equal to the upper limit of the Courant stability criterion because it would correspond to the "magic" time-step, and therefore it would yield results equal to the exact solution. Initially, the 1-D lattice was excited by a sinusoidal wave at the left boundary and was terminated using the perfectly matched layer (PML) absorbing boundary condition at the right boundary. The computational domain was twenty wavelengths long (20λ). Both the FDTD(2,2) and FDTD(2,4) schemes were used to analyze this problem and the results are compared with the exact solution at the last 2λ portion of the domain in Fig. 2.8. The discretization for both schemes was $\Delta x/10$. It is apparent that the phase errors due to dispersion have severely affected the accuracy of the FDTD(2,2) computations whereas these errors are still reasonable for the FDTD(2,4) calculations considering that the wave has traveled 20 wavelengths through the numerical lattice. Also, notice that the FDTD(2,2) predictions are behind the exact solution whereas the FDTD(2,4) are ahead of it. Therefore, both predictions are not dispersed since in 1-D domains the waves propagate only at one angle exhibiting no numerical dispersive anisotropies.

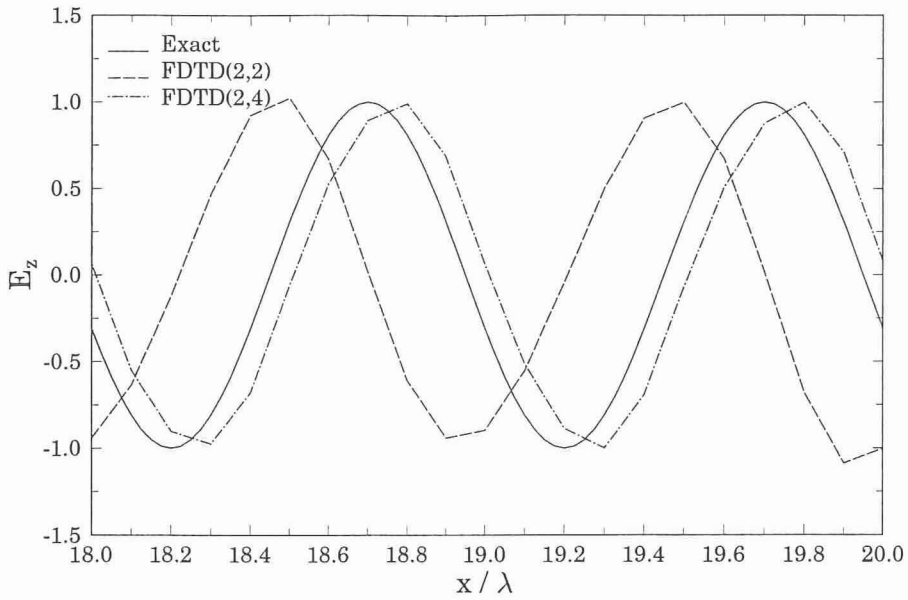

Figure 2.8: Comparison of the FDTD(2,2) and FDTD(2,4) calculations for a 1-D domain.

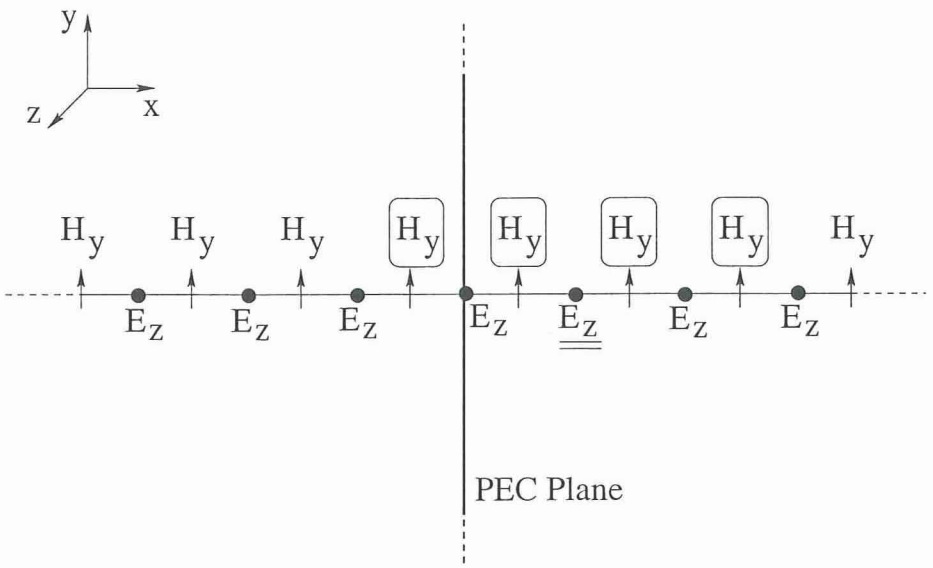

Figure 2.9: Field components around a PEC discontinuity.

Another important concern related to the performance of FDTD(2,4) is its accuracy in the modeling of discontinuities. Here, two types of discontinuities are examined, a perfect electric conductor (PEC) and a dielectric discontinuity, respectively. The FDTD(2,4) is expected to fail to accurately model infinitesimally thin PEC films. This can be seen in Fig. 2.9 where a 1-D grid is shown with a PEC plane separating two regions of free space. The fields on one side of the PEC plane when updated using the FDTD(2,4) stencil will couple to the fields on the other side of the plane. This is illustrated graphically in Fig. 2.9 for one of the E_z components (doubly underlined in the figure) located on the left of the PEC plane. This E_z component is updated using the H_y components which are inscribed in a box. It is clearly seen that the stencil reaches across the PEC boundary and therefore coupling occurs from one side of the PEC boundary to the other. Such coupling is not physical and should not happen for a PEC boundary. To investigate numerically this characteristic of FDTD(2,4), a 1-D TM mode was again used. The 1-D domain was excited at the left boundary using a Gaussian pulse and was terminated with PML on the right boundary. Also, a PEC boundary with no thickness was placed at the center of the domain by forcing the tangential electric field, E_z, to be zero. The pulse initially propagates to the right [see Fig. 2.10(a)] until it hits the PEC boundary and is reflected back [see Fig. 2.10(b)]. Notice though that the pulse was able to "penetrate" through the PEC plane and the fields on the right of the boundary are not zero as they should ideally have been (the maximum of the E_z field at the right of the PEC boundary was 1% of the maximum of the excitation pulse). This agrees with what was discussed above and is due to the length of the FDTD(2,4) stencil. Two ways to overcome this problem were examined. The first one implements a PEC boundary one-cell thick whereas the second one uses image theory to modify the FDTD(2,4) stencil for the fields just beside the PEC. Both ways do not allow the fields from one side of the PEC plane to couple to the other and this was verified by the numerical computations (see Fig. 2.10(c) and 2.10(d), respectively). For details on the use of image theory implementation see Haussmann [20].

Another type of discontinuity occuring in electromagnetic problems is formed between different dielectric materials. To examine the accuracy of the FDTD(2,4) scheme around such discontinuities a 1-D domain was used. The left half of the

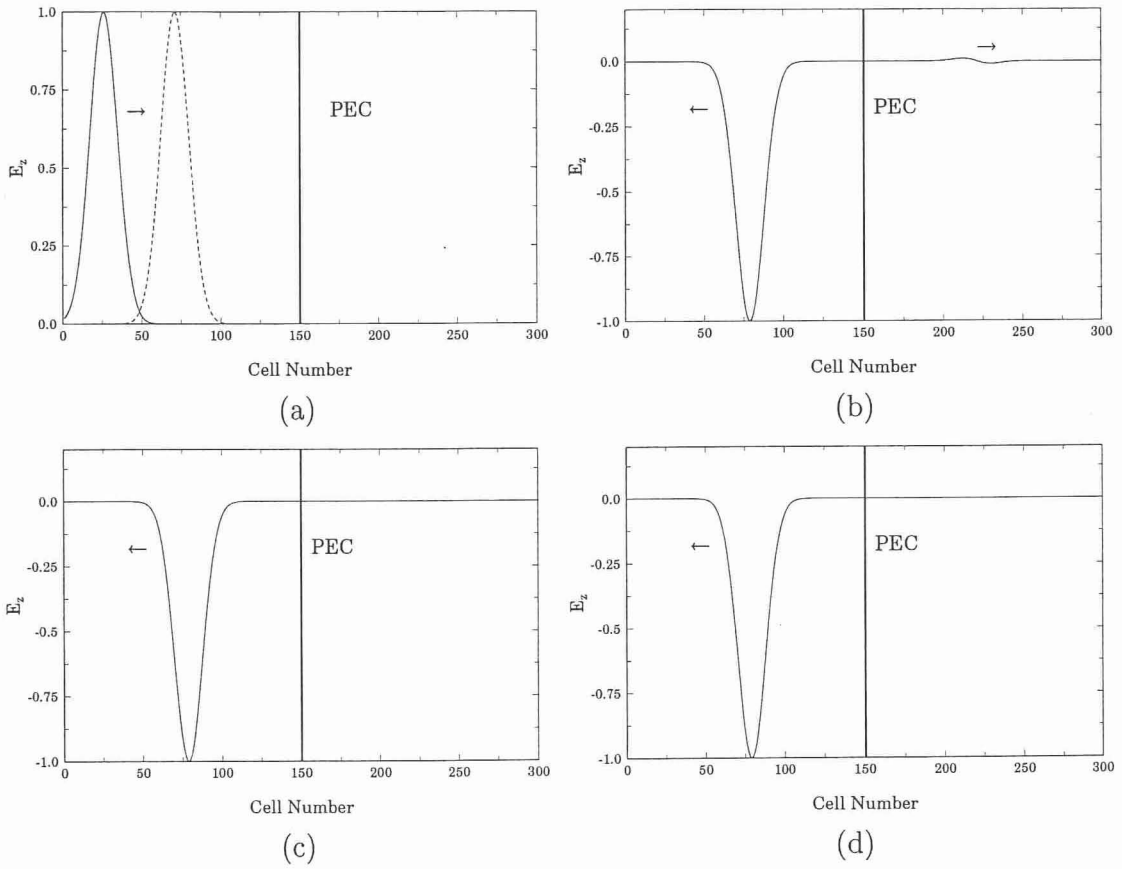

Figure 2.10: 1-D simulation results: (a) propagating pulse, (b) PEC plane implemented by setting the tangential E field to zero, (c) PEC plane one cell thick and (d) PEC plane implemented by setting the tangential E field to zero along with modification of the FDTD(2,4) stencil for the fields just beside the boundary by using image theory.

domain corresponded to free space and the right half corresponded to a dielectric material thereby creating a discontinuity at the center of the computational domain. Again a Gaussian pulse excited the right boundary of the domain and by using the reflected and transmitted pulses the numerical reflection and transmission coefficients were computed for both FDTD(2,2) and FDTD(2,4). These numerical coefficients were also compared to the theoretical values. By the results it was found that the accuracy of both schemes was very good and no scheme was particularly more accurate than the other. A sample of the computations is illustrated in Fig. 2.11 were an instant of the reflected and transmitted waves are plotted for a dielectric material with $\epsilon_r = 9$ for both schemes. Note that for this case the theoretical reflection and transmission coefficient are $R = -0.5$ and $T = 0.5$, respectively.

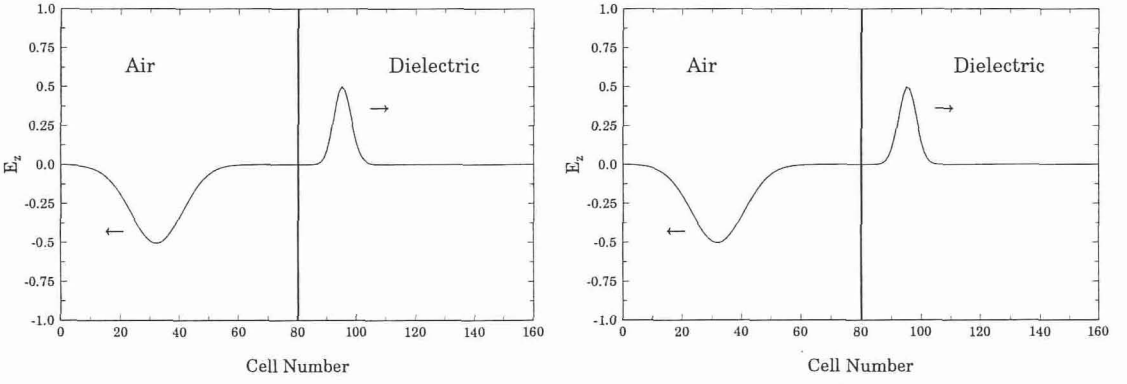

Figure 2.11: Dielectric discontinuity analysis: (a) FDTD(2,2) and (b) FDTD(2,4).

V. Absorbing Boundary Conditions

The FDTD method is based on a quite general formulation as it solves directly the differential form of Maxwell's equations, and it can treat arbitrary and elaborate problems. However, it should be kept in mind that for a partial differential equation (PDE) problem to be well posed an appropriate number of boundary and initial conditions need to be specified. This is usually stated in electromagnetic textbooks as the requirement of both the Maxwell's equations in differential form and the boundary and initial conditions in order to completely describe the fields in a region. In the

context of electromagnetic principles this is described by the uniqueness theorem that requires the specification of the tangential components of the electric, **E**, or magnetic, **H**, field (or a combination of the two) over the boundary of a domain to suffice a unique solution. Therefore, it becomes clear that the boundary conditions are an integral part of a PDE problem and should always accompany the FDTD formulation. This inflicts particular concerns when the problem under examination is a so called "open" space or unbounded problem , e.g., radiation, scattering, etc., meaning that the domain of interest is unbounded in one or more spatial coordinate directions. For such problems there are not any exact boundary conditions known. In addition, no computer can store an unlimited amount of data, and therefore, the computational domain should always be finite in size.

The correct treatment of such problems is to simulate a computational domain large enough to enclose the structure of interest, and truncate it by applying appropriate artificial boundary conditions on the outer perimeter of the domain, which simulate its extension to infinity. These boundary conditions should allow the outward propagating wave to exit the domain and suppress spurious reflections of this wave to an acceptable level. Depending upon their theoretical basis, outer grid boundary conditions of this type have been called either radiation boundary conditions (RBCs) or absorbing boundary conditions (ABCs). Initially, ABCs were obtained by applying the theory of one-way wave equations derived by Engquist and Majda [21]. Mur [22] introduced one of the most popular ABCs for FDTD applications based on the work of Engquist and Majda. The major drawback of Mur's ABCs is that the computational boundaries must be placed sufficiently far from the sources of scattered waves so that the boundary conditions operate on outward propagating plane waves. For example, Mur's second-order ABCs generally require approximately one wavelength of computational space on all sides of the radiator or scatterer to be accurate. Tirkas, Balanis and Renaut [23], based on the work of Lindman [24], Higdon [25], [26], Halpern and Trefethen [27], and Renaut and Petersen [28], presented a more accurate higher-order absorbing boundary condition (HOABC) which allows the size of the computational space from the radiating element or scatterer to be reduced from λ to $\lambda/4$.

Recently, a novel and pioneering ABC was introduced by Berenger [29], who used a non-physical absorbing (lossy) material adjacent to the computational boundary to

truncate the domain, and he called this approach *Perfectly Matched Layer* (PML). This method is based upon splitting the electric and magnetic components in the PML region. The PML exhibits characteristics that permit electromagnetic waves of arbitrary frequency and angle of incidence to be absorbed while maintaining the impedance and velocity of a lossless dielectric. Berenger reported reflection coefficients for PML in two dimensions significantly better than second- and third-order one-way wave equation (OWWE) based ABCs. The PML method was extended to three dimensions by Katz et al. [30], who verified that PML is at least 40 dB more accurate than second-order Mur ABCs. Andrew et al. [31] compared the PML to the HOABCs in both the time and frequency domains. Andrew et al. showed that PML significantly reduces reflections from the truncation of the computational grid when compared to 7th order Lindman ABCs. Also, higher-order ABCs were proven no better than 2nd order Mur ABCs at low frequencies. In the field of the Finite Element method (FEM) the PML truncation technique was initially implemented by Pekel and Mittra [32], [33].

The initial PML based on the splitting of the field components was followed by formulations that properly characterize the PML as a uniaxially anisotropic medium. These formulations were introduced by Sacks et al. [34] in FEM, and extended afterwards by Zhao and Cangellaris in [35], [36] and Gedney in [37], [38] in FDTD. They have the advantage that they can implement the perfectly matched layer in the FDTD scheme without splitting of the fields. The effectiveness of the anisotropic PML in FEM was examined by Polycarpou et al. [39], who later presented an optimized anisotropic PML for the analysis of microwave circuits [40].

As far as higher order FDTD schemes the PML was implemented for the standard fourth-order FDTD in [41], [42]. Also, the PML was used along with the modified FDTD(2,4) method to truncate both 2-D [17], [43] and 3-D lattices [20]. Here, the accuracy of the anisotropic PML technique is examined for both the FDTD(2,2) and FDTD(2,4) methods by examining 2-D as well as 3-D domains.

A. Numerical experiments

In this section, various numerical simulations are performed to illustrate the effectiveness of PML and they are all based on the same procedure. To judge the effectiveness

of the method, the procedure used here is the same as the one published in [44] and used in most papers introducing and discussing ABCs and consists of the following steps:

a. A test domain Ω_T terminated by PML is excited at its center with a pulse and the solution is computed.

b. A reference domain Ω_R is also excited at its center with a pulse to provide us with a reference solution that is free of truncation errors. This is achieved by choosing domain Ω_R large enough so that any reflections from its grid truncation are totally isolated from all points of comparison between the two solution domains. An example of such a configuration is shown in Fig. 2.12.

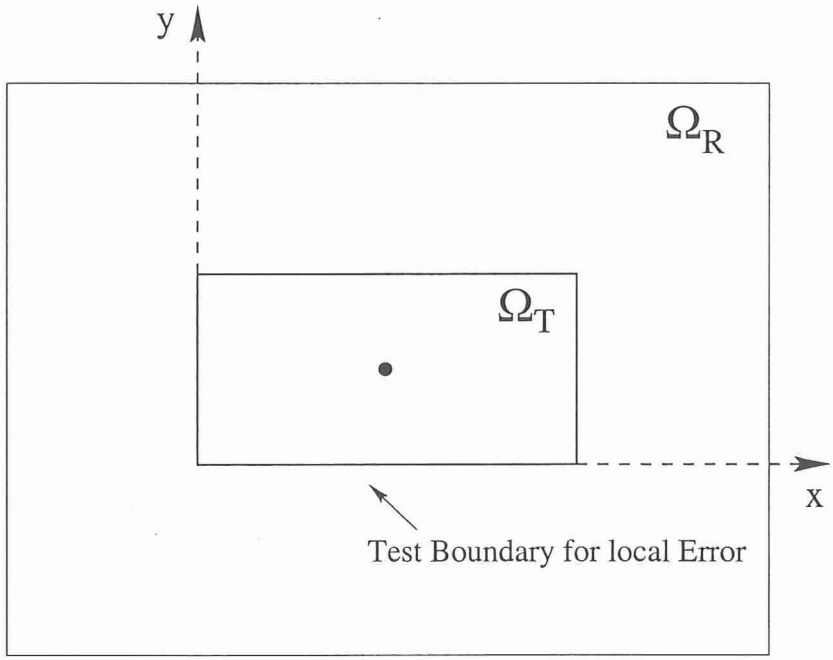

Figure 2.12: The two-dimensional computational domains for numerical testing of the effectiveness of PML.

Then the local error of the computed field in Ω_T due to reflections from the PML is obtained by subtracting the field at any point within Ω_T at a given time step, from the field at the corresponding space-time point in Ω_R. Here, the z-component of the

magnetic field, H_z, is used to define the error

$$e(i,j) = H_z^R(i,j) - H_z^T(i,j) \tag{2.37}$$

where $H_z^T(i,j)$ is the magnetic field component in the test domain Ω_T and $H_z^R(i,j)$ is the magnetic field component in the large reference domain Ω_R. Furthermore, the global error was defined by Berenger [29] as the square of the L^2 norm of the error as

$$e_{glob} = \sum_i \sum_j e^2(i,j) \tag{2.38}$$

Here, the effectiveness of the PML is illustrated by using either the global error as defined in (2.38) or the L^∞ norm of the error. Recall that the L^2 and L^∞ norms are defined as follows for a vector $x \in \Re^n$:

$$L^\infty = \|x\|_\infty = \max_{1 \le i \le n} |x_i| \tag{2.39}$$

$$L^2 = \|x\|_2 = \sqrt{\sum_{i=1}^{n} x_i^2} \tag{2.40}$$

In all the cases examined here the excitation is a pulse exhibiting very smooth transition to zero as used in [44] and defined as follows:

$$H_z(\text{at center of domain}) = \begin{cases} \alpha[10 - 15cos(\omega_1 \xi) + 6cos(\omega_2 \xi) - cos(\omega_3 \xi)] & \xi \le \tau \\ 0 & \xi > \tau \end{cases} \tag{2.41}$$

where

$$\alpha = \frac{1}{320}, \quad \tau = 10^{-9}, \quad \xi = n\Delta t, \quad \omega_m = \frac{2\pi m}{\tau}, \quad m = 1,2,3 \tag{2.42}$$

This pulse is often called *compact smooth pulse* and is shown in Fig. 2.13.

Initially, a 2-D test domain, 100×50 cells long, is examined. A square cell is used with $\Delta x = \Delta y = 0.015$ meters and the time-step is chosen based to a relaxed stability criterion, $\Delta t = \Delta x/2c = 2.5 \times 10^{-11}$ sec, where c is the speed of light in vacuum. The test grid Ω_T is terminated by PML with theoretical reflection coefficient 10^{-6} backed by PEC walls. Three different cases are considered. In the first case, the PML as

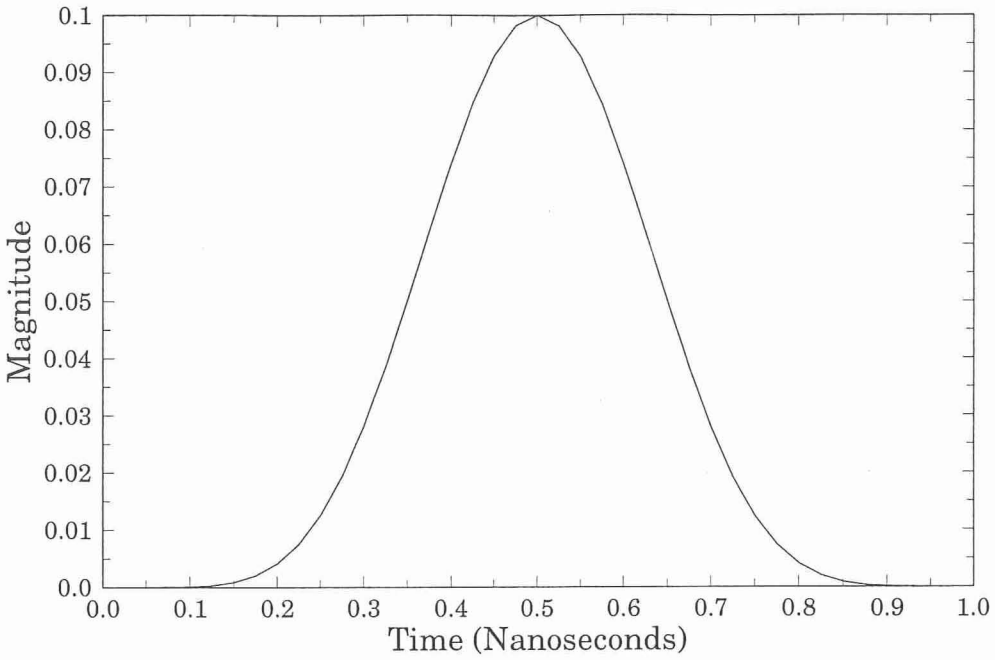

Figure 2.13: Compact smooth pulse.

proposed by Berenger [29] is used to truncate a grid of the FDTD(2,2) scheme. In the second and third cases, the anisotropic PML as proposed by Gedney [37] is used to truncate the grid of the FDTD(2,2) and FDTD(2,4) schemes, respectively. The global error of the solution caused by the PML in these three cases is illustrated in Figs. 2.15 and 2.16, respectively. Evidently, the PML for the FDTD(2,2) scheme as proposed by Berenger performs equally well with the anisotropic PML formulated by Gedney for both the FDTD(2,2) and FDTD(2,4) schemes.

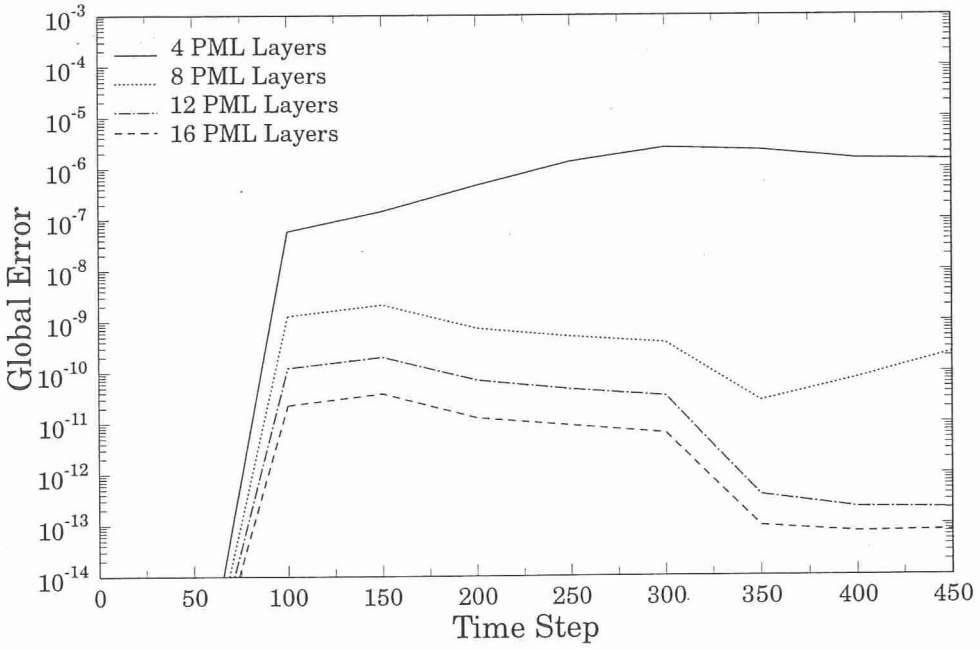

Figure 2.14: Global error in the 2-D test domain caused by the Berenger's PML for the FDTD(2,2) scheme.

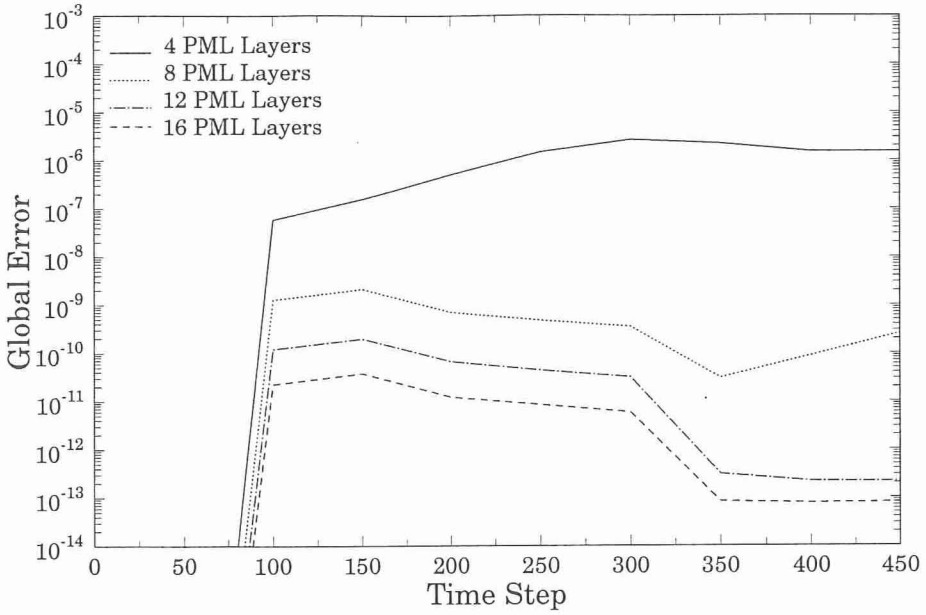

Figure 2.15: Global error in the 2-D test domain caused by the anisotropic PML for the FDTD(2,2) scheme.

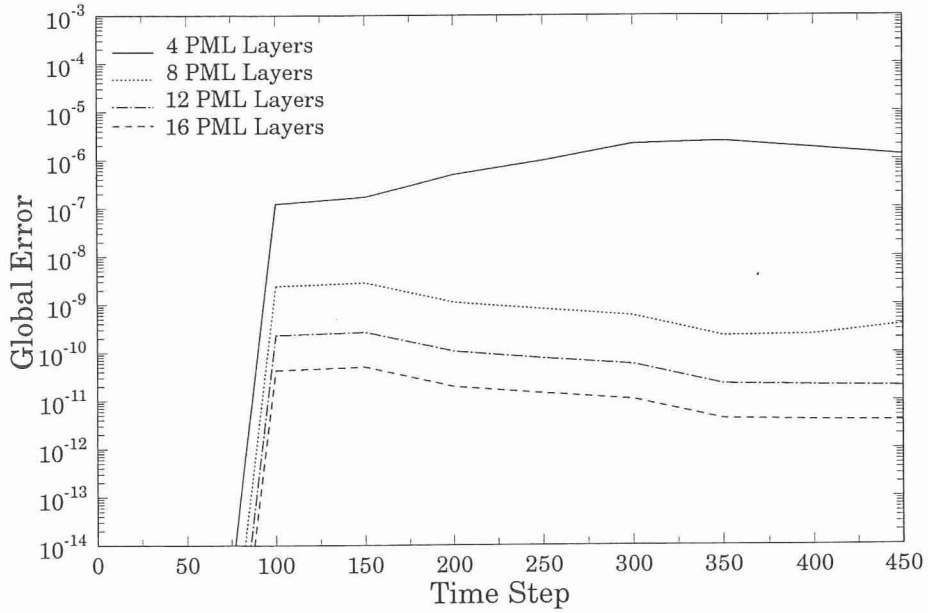

Figure 2.16: Global error in the 2-D test domain caused by the anisotropic PML for the FDTD(2,4) scheme.

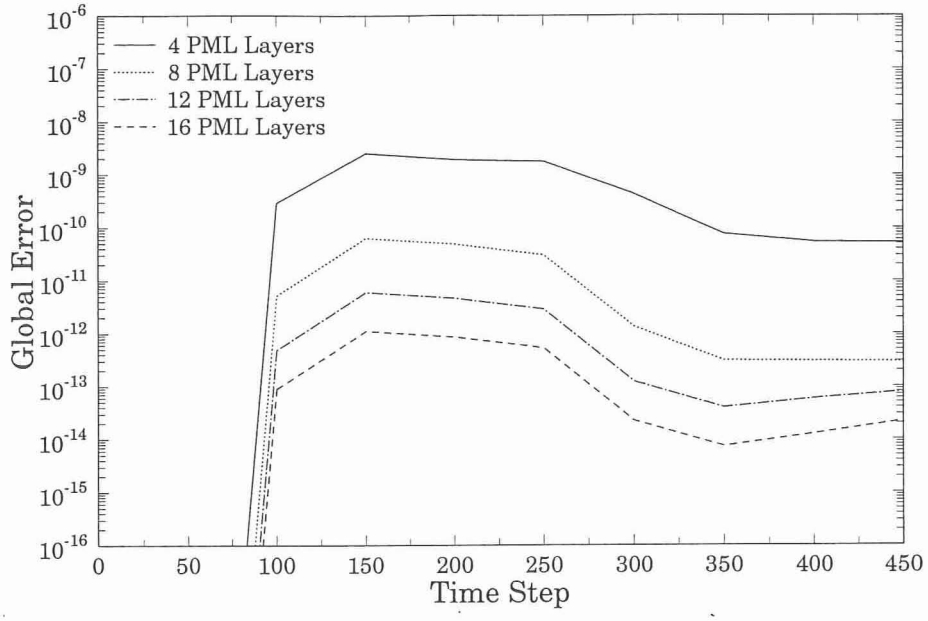

Figure 2.17: Global error in the 3-D test domain caused by the anisotropic PML for the FDTD(2,2) scheme.

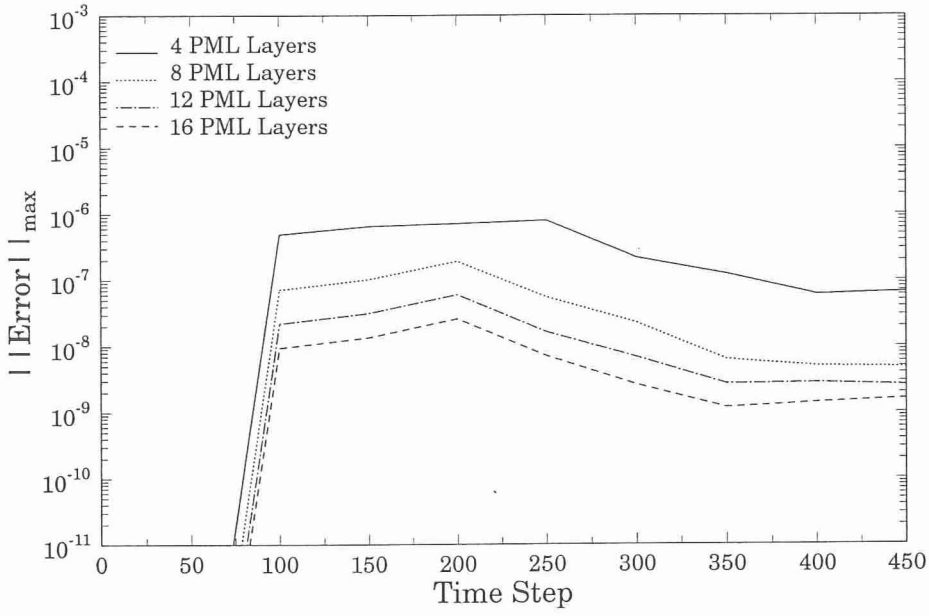

Figure 2.18: Maximum error, L^{∞}, in the 3-D test domain caused by the anisotropic PML for the FDTD(2,2) scheme.

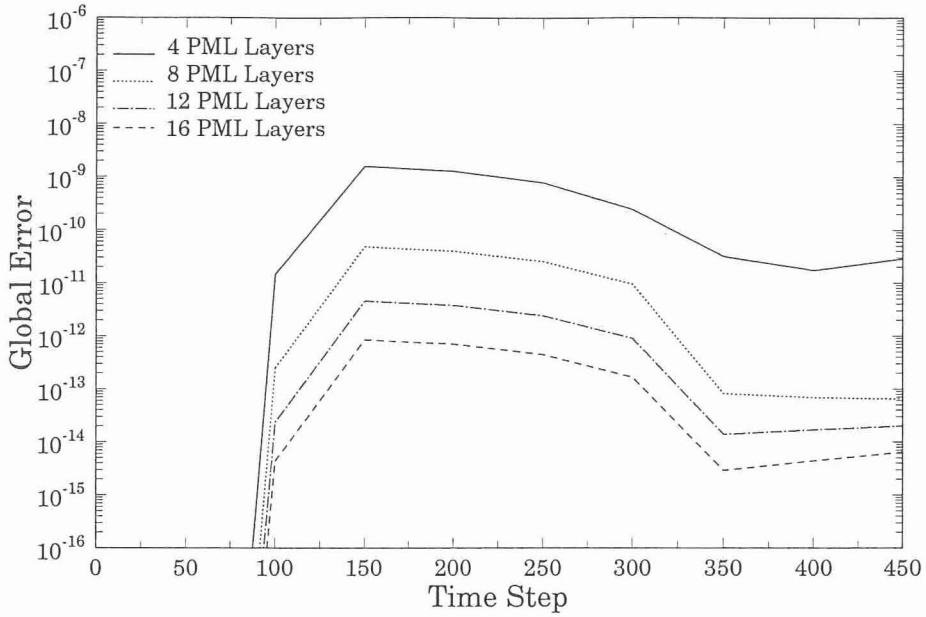

Figure 2.19: Global error in the 3-D test domain caused by the anisotropic PML for the FDTD(2,4) scheme.

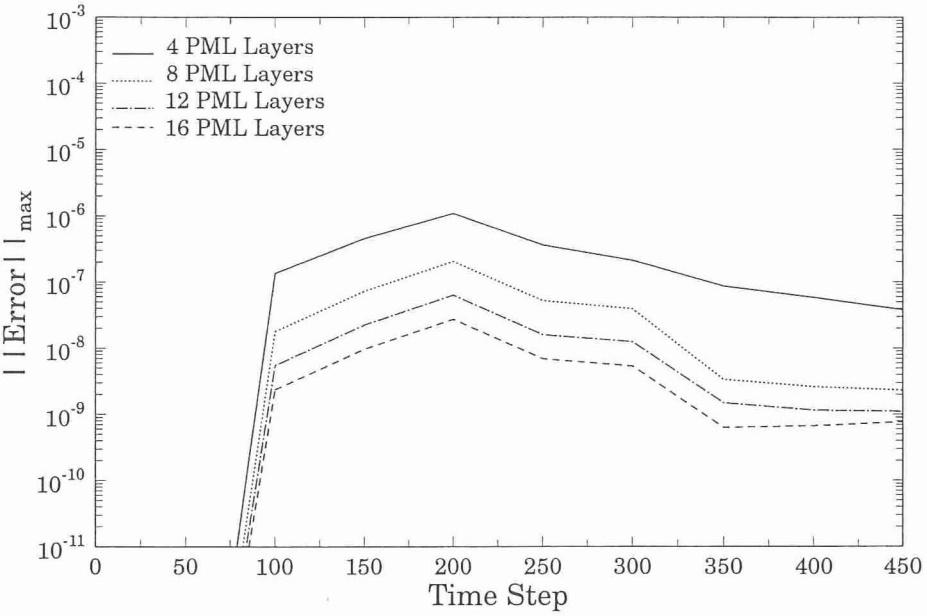

Figure 2.20: Maximum error, L^{∞}, in the 3-D test domain caused by the anisotropic PML for the FDTD(2,4) scheme.

Furthermore, a 3-D domain test domain, $50 \times 50 \times 51$ cells long, is considered. A square cell is used with $\Delta x = \Delta y = \Delta z = 0.015$ meters and the time-step is chosen based to a relaxed stability criterion, $\Delta t = \Delta x/3c$ sec, where c is the speed of light in vacuum. The test grid Ω_T is terminated by PML with theoretical reflection coefficient 10^{-6} backed by PEC walls. The anisotropic PML again is used to truncate the computational domain for both the FDTD(2,2) and FDTD(2,4) stencils. The global error [defined by (2.38)] and the maximum norm of the error [defined by (2.39)] caused by the PML on either the FDTD(2,2) or FDTD(2,4) domain are shown in Figs. 2.17-2.20. These figures illustrate clearly that the anisotropic PML provides an effective termination of an FDTD computational domain for both schemes. Also, it should be pointed out that in some of the curves the error of the PML increases at certain time-steps. This can be attributed to the formation of standing waves between the PML truncation and the source. This explanation is supported by the observation that the error does not increase in time for all different numbers of PML layers.

VI. Applications

Here, the FDTD(2,4) scheme, which is second-order accurate in time and fourth-order accurate in space, is initially applied in the analysis of two simple 3-D problems of practical interest. The first problem, although simplified to illustrate the principle, consists of the pattern computation of an array whereas the second problem involves the calculation of the resonances of a rectangular cavity. Then, FDTD(2,4) is applied in radiation pattern analysis of monopoles on helicopter airframes as well as rectangular boxes. The accuracy of FDTD(2,4) is compared with the accuracy of FDTD(2,2) and measurements.

A. Array factor

In this section, an array consisting of two x-oriented current filaments, J_x, is considered. The geometry configuration is illustrated in Fig. 2.21. The phase difference between the two currents is set to zero, whereas their separation distance d is chosen according to the following equation:

$$d = n\lambda + \lambda/2, \quad n = 0, 1, 2, ... \tag{2.43}$$

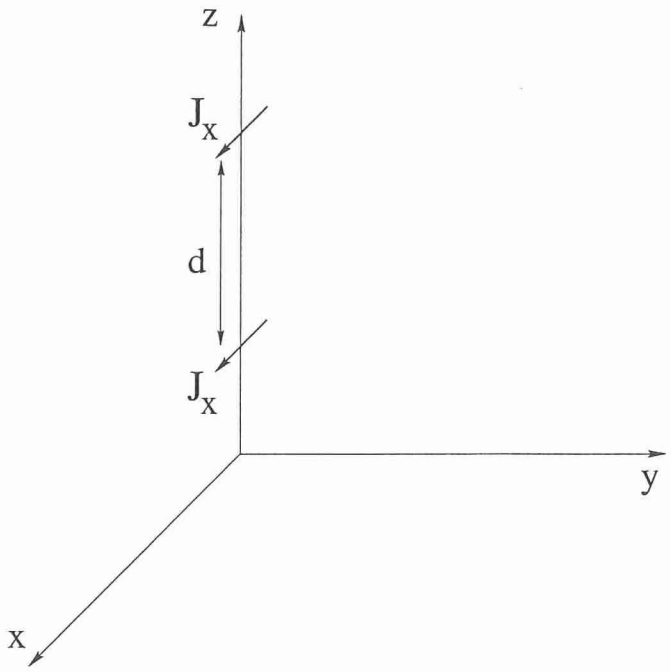

Figure 2.21: Geometry of an array formed by two current elements positioned along the x-axis.

in order for the array to exhibit nulls toward $\theta = 0^o$ and $\theta = 180^o$. From basic antenna theory it is well known that the total far-zone field of an array of identical elements, neglecting coupling, is equal to the product of the field of a single element and the array factor of that array [45]. However, in our example the array pattern on the yz-plane is solely determined by the array factor because the two current elements J_x have omni-directional yz-plane pattern. The pattern of our two-element array is computed using both the FDTD(2,2) as well as the FDTD(2,4) schemes. In all numerical simulations a cell size of $\Delta = \lambda/10$ is used. The accuracy of the finite difference calculations (FD) is affected by the phase errors which are inherent in all FD stencils. These phase errors are expected to significantly affect the pattern computations of our example in particular toward $\theta = 0^o$ and $\theta = 180^o$ due to two reasons:

- The array factor exhibits nulls toward these directions.
- The phase difference between two waves emanating from the two current elements is larger toward these directions.

Array pattern computations were performed for three different element separation distances: (a) $d = 5.5\lambda$, (b) $d = 10.5\lambda$, and (c) $d = 20.5\lambda$. The numerical pattern computations of both FDTD(2,2) and FDTD(2,4) are compared with the analytical calculations of the array factor in Figs. 2.22-2.24. It is apparent that toward $\theta = 0^o$ and $\theta = 180^o$ the pattern accuracy is significantly affected by the phase errors especially for the FDTD(2,2) computations. In the case where the distance d between the two elements is equal to $d = 5.5\lambda$ the pattern calculated by FDTD(2,2) exhibits a peak of -17 dB toward zenith instead of a null (see Fig. 2.22). On the contrary the pattern calculated by FDTD(2,4) exhibits a null of -32 dB and is in excellent agreement with the analytical results (see Fig. 2.22). In the same way for $d = 10.5\lambda$ and toward zenith, the pattern computed by: (a) FDTD(2,2) has a peak of -14 dB, and (b) FDTD(2,4) has a null of -30 dB (see Fig. 2.23). Finally, for $d = 20.5\lambda$ and toward zenith, the pattern computed by: (a) FDTD(2,2) has a peak of -13 dB, and (b) FDTD(2,4) has a peak of -24 dB (see Fig. 2.24). Considering all the

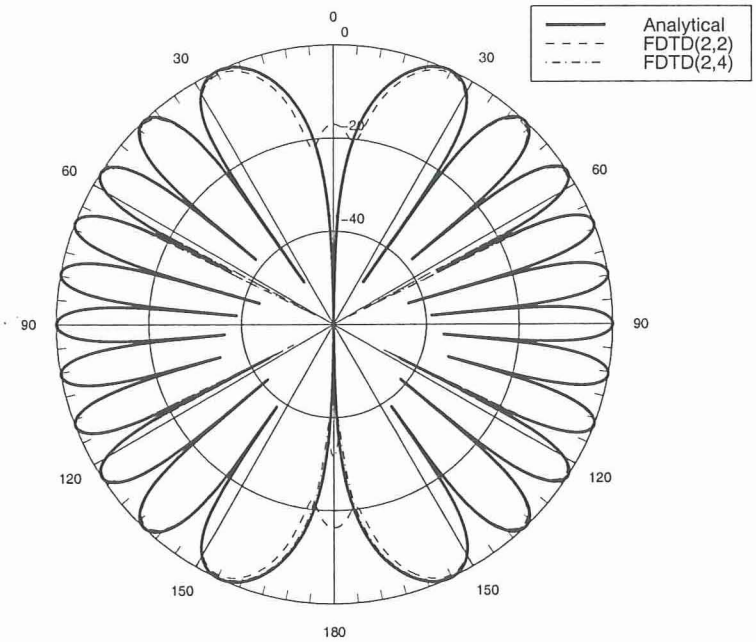

Figure 2.22: Distance $d = 5.5\lambda$. Toward zenith: (a) FDTD(2,2) -17 dB, (b) FDTD(2,4) -32 dB.

comparisons between the two FD methods, FDTD(2,2) and FDTD(2,4), and the analytical results, it can be concluded that FDTD(2,4) provided excellent accuracy

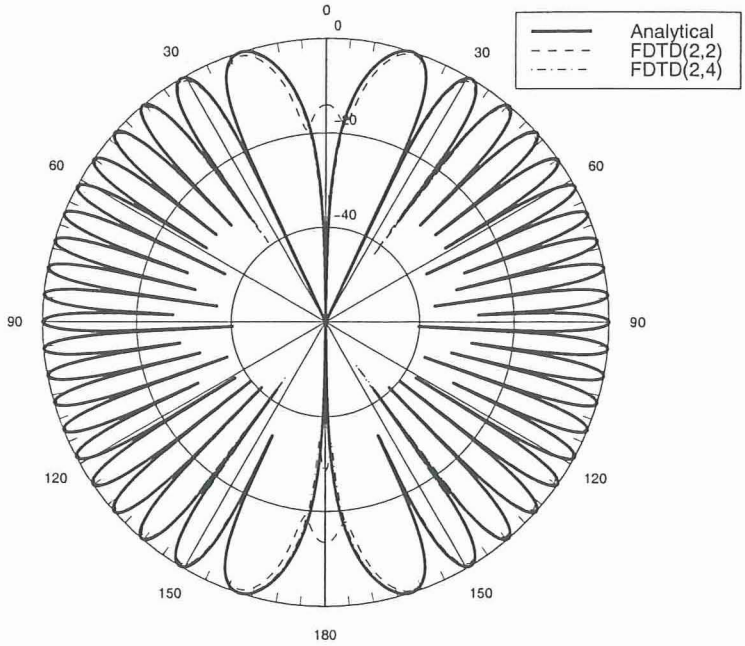

Figure 2.23: Distance $d = 10.5\lambda$. Toward zenith: (a) FDTD(2,2) -14 dB, (b) FDTD(2,4) -30 dB.

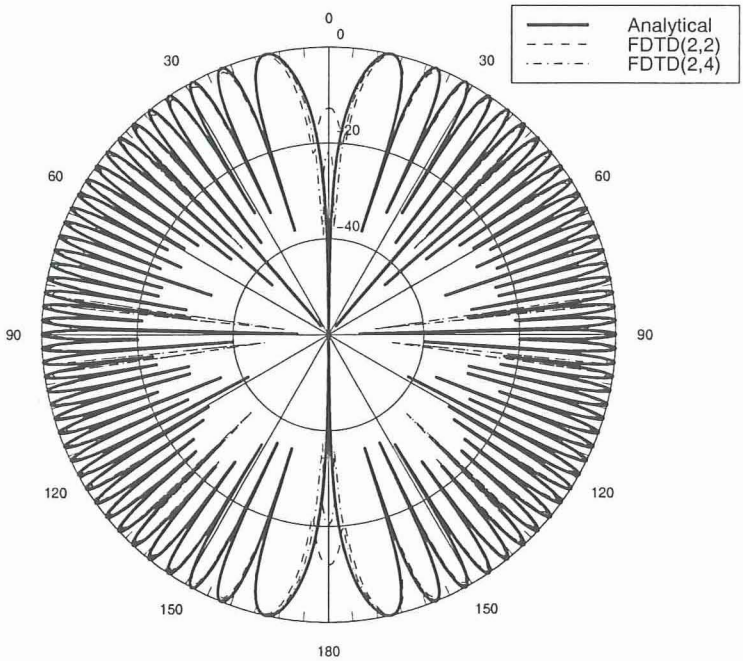

Figure 2.24: Distance $d = 20.5\lambda$. Toward zenith: (a) FDTD(2,2) -13 dB, (b) FDTD(2,4) -24 dB.

and outperformed FDTD(2,2). The phase errors of FDTD(2,2) are larger than the ones of FDTD(2,4) and contribute to the unsatisfactory accuracy of the FDTD(2,2) computations. Furthermore, FDTD(2,4) required reduced computational time and memory compared to the ones needed by FDTD(2,2) to achieve satisfactory accuracy.

B. Resonances of a rectangular cavity

In this section, the resonances of a rectangular cavity are analyzed. The dimensions of the cavity are 1 m $\times$ 1 m $\times$ 1 m. Both FDTD(2,2) and FDTD(2,4) are used in the numerical analysis. The resonances are computed by exciting the cavity at a point using all three components of the electric field and by Fourier transforming the time history of the electric field components at another point. The Fourier transform is performed using a discrete Fourier transform (DFT) of 1201 frequency points in the range 200-500 MHz yielding a frequency resolution of 0.25 MHz for all numerical simulations. Furthermore, the simulation time is $t_s = 3.656\ \mu s$ and remains the same for all predictions by choosing appropriate number of time-steps.

The FDTD(2,2) method used three different cell sizes of: (a) $\Delta x = 100$ mm or $\lambda/6$ at 500 MHz, (b) $\Delta x = 50$ mm or $\lambda/12$ at 500 MHz, and (c) $\Delta x = 25$ mm or $\lambda/24$ at 500 MHz and the time-step was chosen according to the upper limit of the stability criterion:

$$\Delta t \leq \frac{\Delta}{c\sqrt{3}} \tag{2.44}$$

The computed results are illustrated in Figs. 2.25-2.27 for the three different discretizations and they are compared with the analytically calculated resonances of the cavity [46]. Obviously, the coarser mesh of $\Delta x = 100$ mm (or $\lambda/6$ at 500 MHz) was not able to accurately resolve the resonances of the cavity. Then the finer discretization of $\Delta x = 50$ mm (or $\lambda/12$ at 500 MHz) provides predictions of very good accuracy in the lower frequency band and of poor accuracy in the higher frequency band. Finally, the finest mesh of $\Delta x = 25$ mm (or $\lambda/24$ at 500 MHz) gives results that exhibit excellent agreement with the analytical computations in the entire frequency range.

In addition, FDTD(2,4) used a cell size of $\Delta x = 100$ mm or $\lambda/6$ at 500 MHz, and the time-step was chosen to be smaller than the upper limit of the stability criterion

$$\Delta t \leq \frac{6}{7}\frac{\Delta}{c\sqrt{3}} \tag{2.45}$$

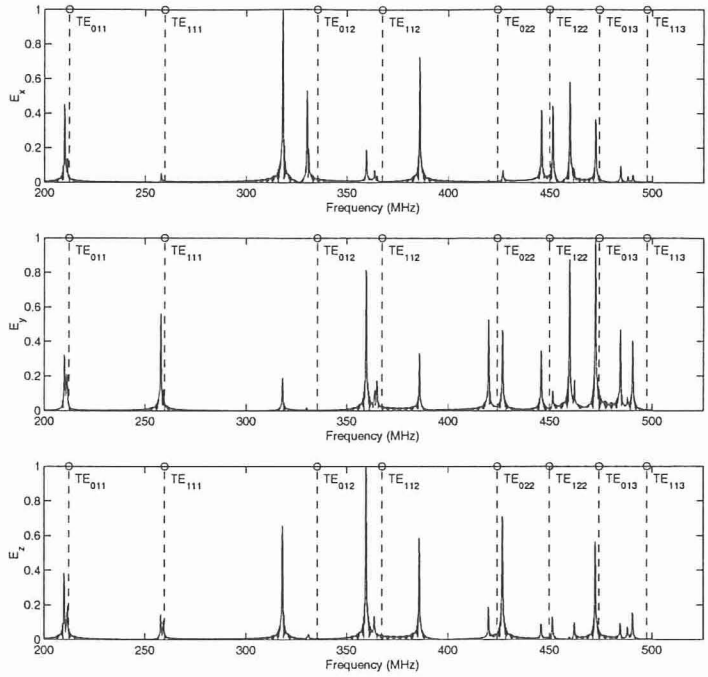

Figure 2.25: Resonances of a rectangular cavity predicted using FDTD(2,2) with a cell size of 100 mm.

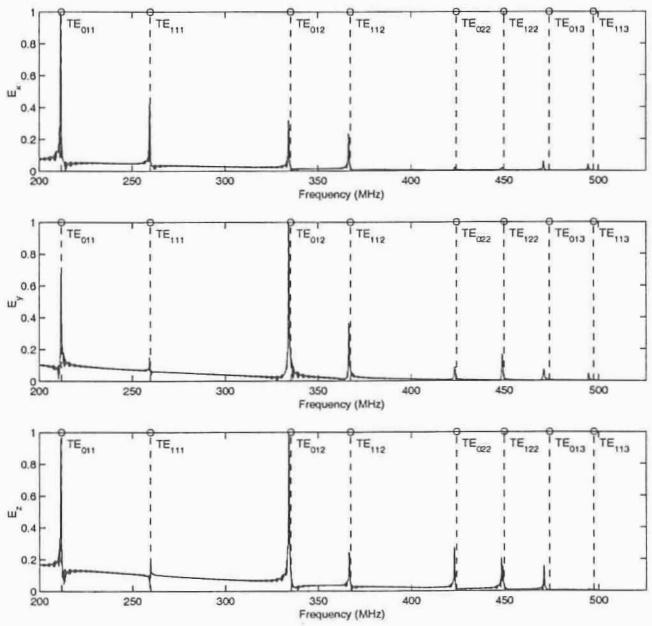

Figure 2.26: Resonances of a rectangular cavity predicted using FDTD(2,2) with a cell size of 50 mm.

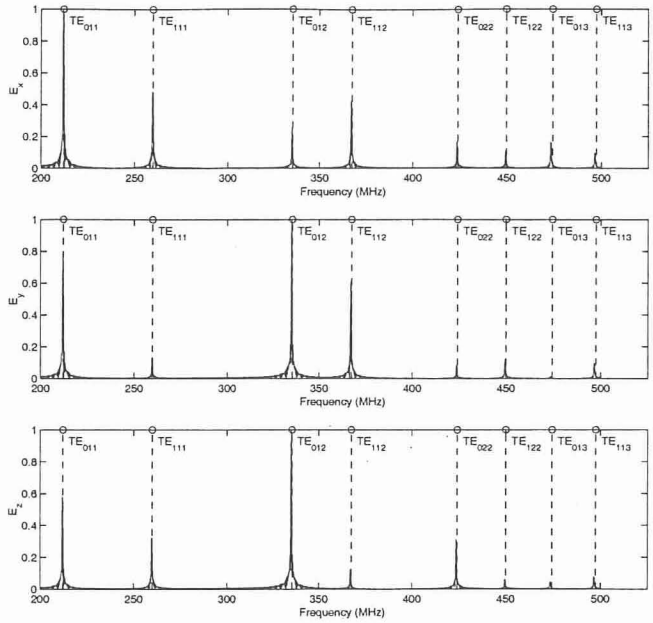

Figure 2.27: Resonances of a rectangular cavity predicted using FDTD(2,2) with a cell size of 25 mm.

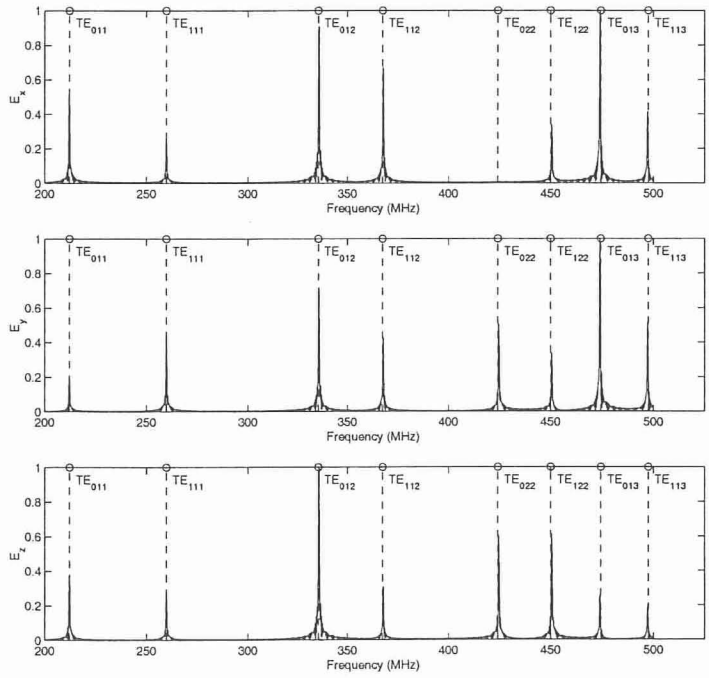

Figure 2.28: Resonances of a rectangular cavity predicted using FDTD(2,4) with a cell size of 100 mm.

in order to reduce errors related to time-derivative computations. Specifically, it was chosen to be approximately three times smaller than the upper limit of (2.45)

$$\Delta t = \frac{1}{6}\frac{\Delta}{c} \tag{2.46}$$

In this example, where the excitation consists of a Gaussian pulse which varies rapidly in time, time-differentiation can introduce large errors. Using a smaller time-step than the upper limit of (2.45) was found necessary in order to retain the higher accuracy of the FDTD(2,4) stencil, which is fourth-order accurate in space but only second-order accurate in time. The numerical calculations from this simulation are shown in Fig. 2.28, and they agree very well with the analytical results.

In summary, it is shown that the fourth-order stencil, FDTD(2,4) provides excellent accuracy using a cell size of $\Delta x = 100$ mm or $\lambda/6$ at 500 MHz, whereas the traditional second-order accurate FDTD(2,2) requires 4 times smaller cell size ($\Delta x = 25$ mm or $\lambda/24$ at 500 MHz) in order to accurately resolve all the cavity resonances. Therefore, FDTD(2,4) required reduced computational time and memory compared to the ones needed by FDTD(2,2) to achieve satisfactory accuracy.

C. Radiation pattern analysis

Here, some radiation problems are examined in order to investigate and illustrate possible advantages of FDTD(2,4) versus FDTD(2,2). Initially, the radiation patterns of a monopole antenna mounted on the tail of the NASA scale model helicopter are computed at 9.18 GHz. The NASA helicopter, which is sometimes called as Generic Advanced Attack Helicopter (GAAH), exhibits many common characteristics of operational full-scale helicopters. In addition, the NASA airframe represents approximately a 10:1 scale model of full-scale helicopters. Therefore, it can be used along with appropriately scaled frequencies to perform scale measurements in an indoors anechoic chamber. Scale measurements are more convenient and cheaper than full scale measurements, but their main drawback consists of the difficulty to build accurate scaled geometries. However, scale model measurements remain very useful as they can provide information about the radiation characteristics of candidate antennas on the operational helicopter. Moreover, the radiation patterns of a monopole antenna mounted on top of a rectangular box are calculated at 2 GHz. Both problems

are analyzed using either FDTD(2,4) or FDTD(2,2,) and the numerical results are compared with measurements.

The first problem consists of a quarter-wavelength long monopole at 9.18 GHz, mounted on the tail of the NASA scale-model helicopter. The geometry is shown in Fig. 2.29. The principal radiation patterns of this monopole on the NASA helicopter were measured in the Electromagnetic Anechoic Chamber facility at Arizona State University. The physical length of the monopole was 8.17 mm ($\lambda/4$ at 9.18 GHz), the cell size was 4 mm ($\lambda/8$) and the computational domain was $184 \times 440 \times 98$ cells or $21\lambda \times 51\lambda \times 11\lambda$ long. Both FDTD(2,2) and FDTD(2,4) were used to compute the principal plane patterns of the monopole. The numerical calculations are illustrated in Figs. 2.30-2.32, where the predicted yaw, roll, and pitch plane patterns are compared with measurements. Considering these computations, it seems that FDTD(2,4) does not provide a significantly better accuracy than FDTD(2,2). The main reason for this is that the discretization errors of each method are mixed with staircasing errors. The artificial corners that have been created on the simulation geometry through staircasing become diffraction points that affect substantially the shape of the radiation patterns. This effect becomes more dominant at high frequencies, as the one used in this simulation. Through a closer examination of the results, it seems though that FDTD(2,4) exhibits a slightly better accuracy than FDTD(2,2). This improved accuracy of FDTD(2,4) can be observed, for example, on the yaw pattern calculations, and on the top, bottom and port side of the roll plane.

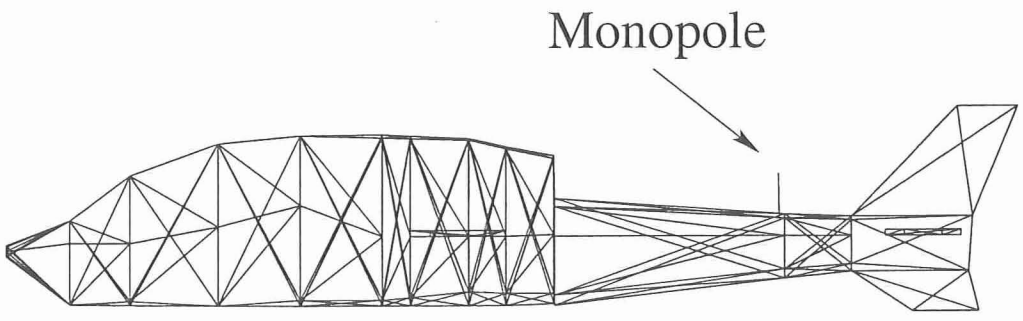

Figure 2.29: Geometry of a monopole mounted on the tail of the NASA scale-model helicopter.

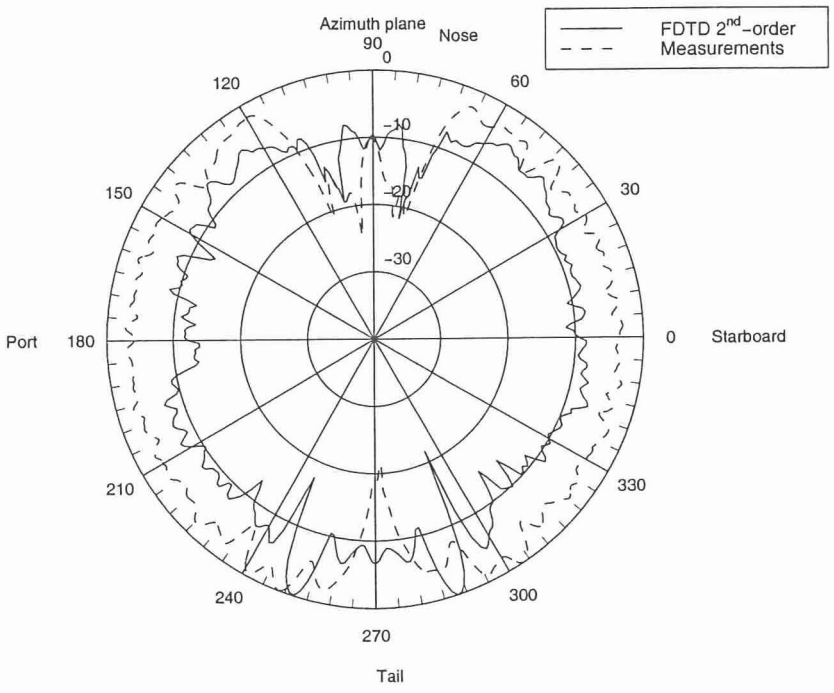

(a)

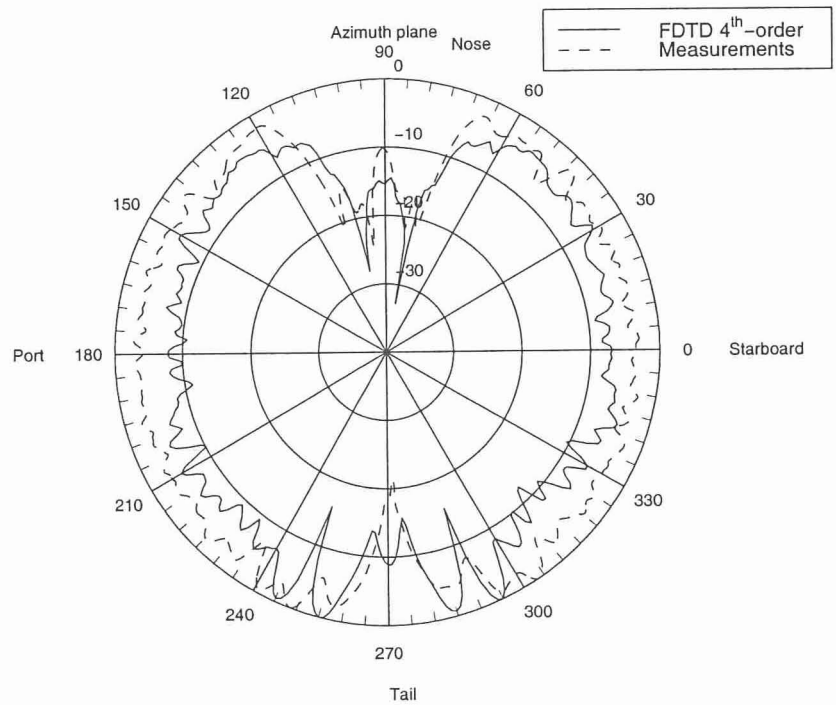

(b)

Figure 2.30: Yaw plane radiation patterns of a monopole mounted on the tail of the NASA scale-model helicopter at 9.18 GHz.

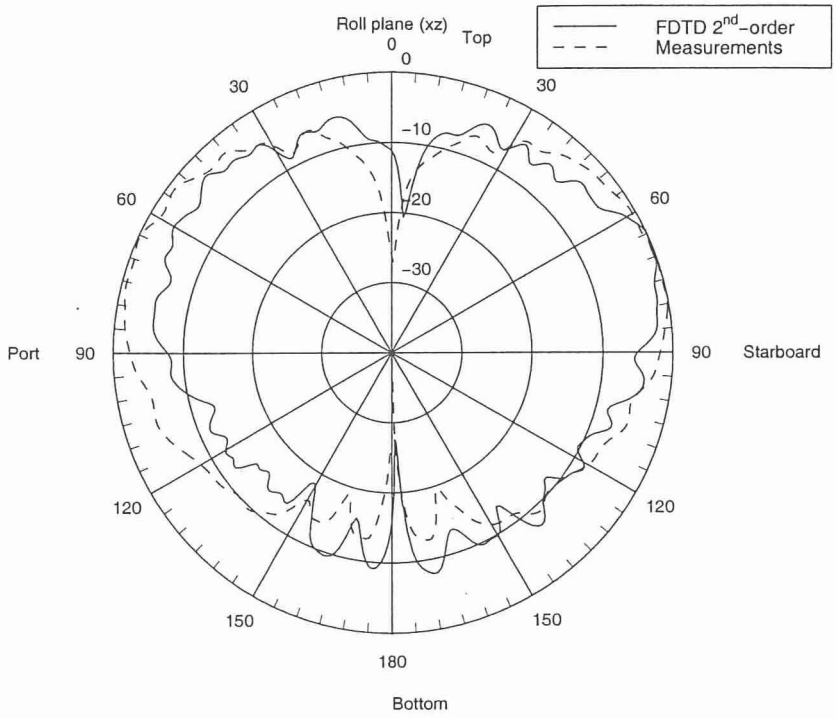

(a)

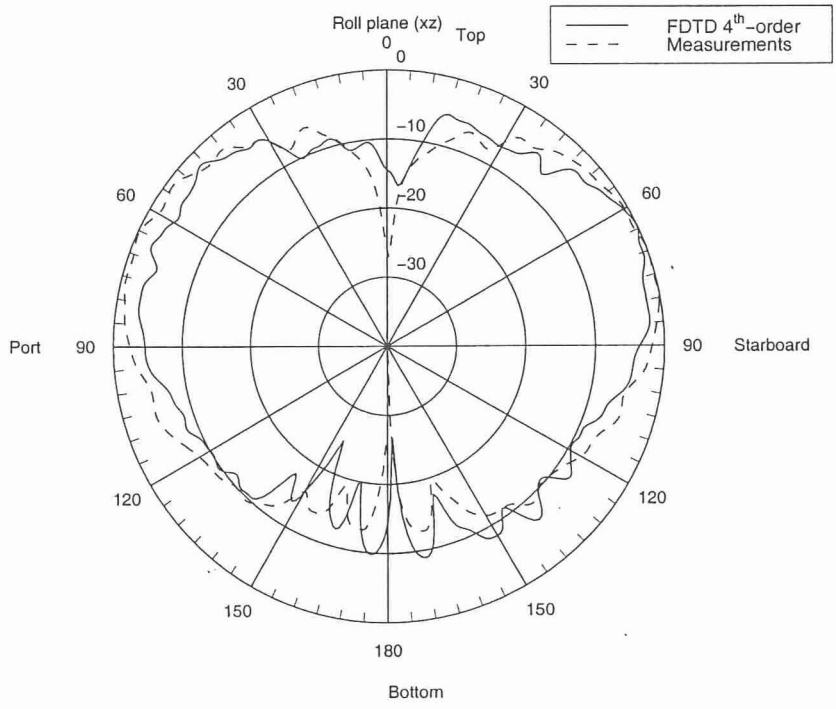

(b)

Figure 2.31: Roll plane radiation patterns of a monopole mounted on the tail of the NASA scale-model helicopter at 9.18 GHz.

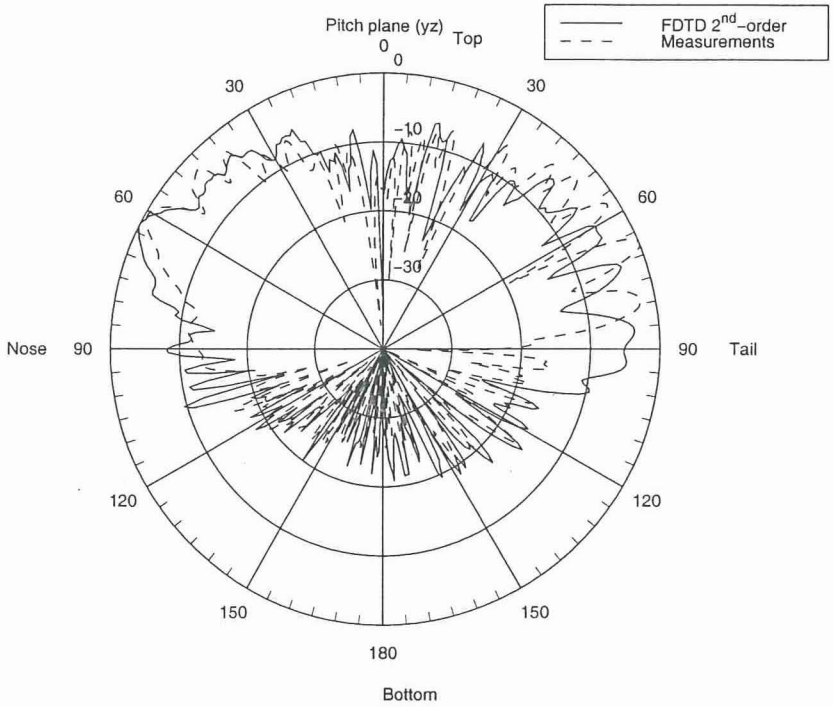

(a)

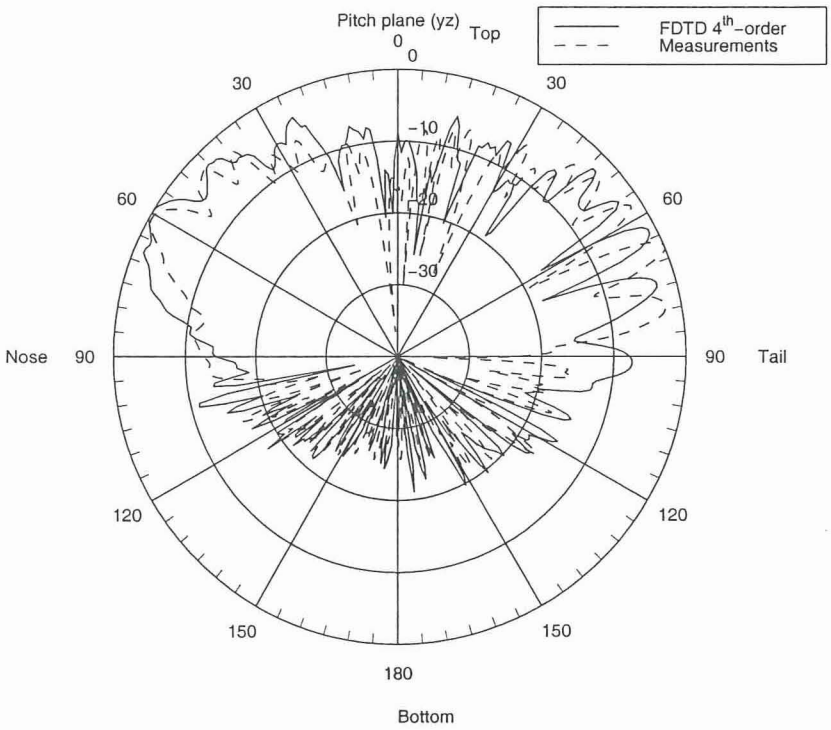

(b)

Figure 2.32: Pitch plane radiation patterns of a monopole mounted on the tail of the NASA scale-model helicopter at 9.18 GHz

Because of the coexistence of discretization and staircasing errors in the previous example, it was not clear which method is more accurate. Therefore, another problem, which is free of staircasing errors, was chosen to be analyzed. This problem consists of a monopole mounted on a rectangular box of dimensions $11\lambda \times 5\lambda \times 2\lambda$ at 2 GHz (see Fig. 2.33). The physical length of the monopole was 60 mm ($\lambda/2.5$), the cell size was chosen either 20 mm ($\lambda/7.5$) or 5 mm ($\lambda/30$), and the computational domain was $92\times54\times34$ cells or $320\times168\times88$, respectively. Both FDTD(2,2) and FDTD(2,4) were used to compute the principal plane patterns of the monopole. The FDTD(2,2) code was run for both cell sizes (20 mm and 5 mm) whereas the FDTD(2,4) code was run only for the coarser mesh (20 mm). The predictions of the simulation with the finer

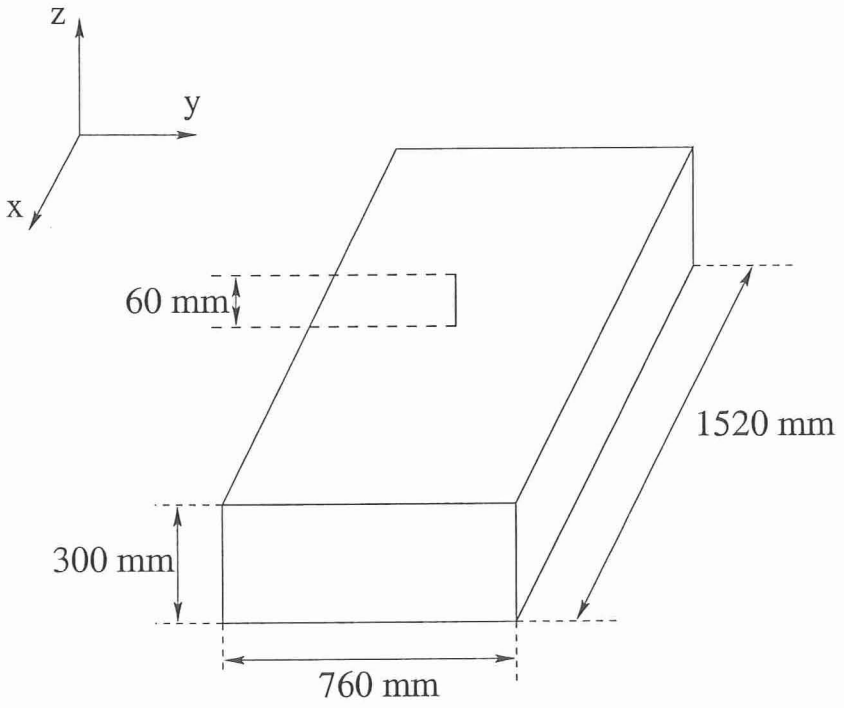

Figure 2.33: Geometry of a monopole mounted on a rectangular box.

discretization (5 mm or $\lambda/30$) were used as a reference to determine the accuracy of all simulations performed with the coarser discretization (20 mm or $\lambda/7.5$). The results of FDTD(2,2) and FDTD(2,4) for the coarser mesh are compared in Figs. 2.34 and 2.35 with the FDTD(2,2) predictions obtained for the finer mesh. From these figures, it is obvious that even with such a coarse discretization of $\lambda/7.5$, FDTD(2,4) still predicts

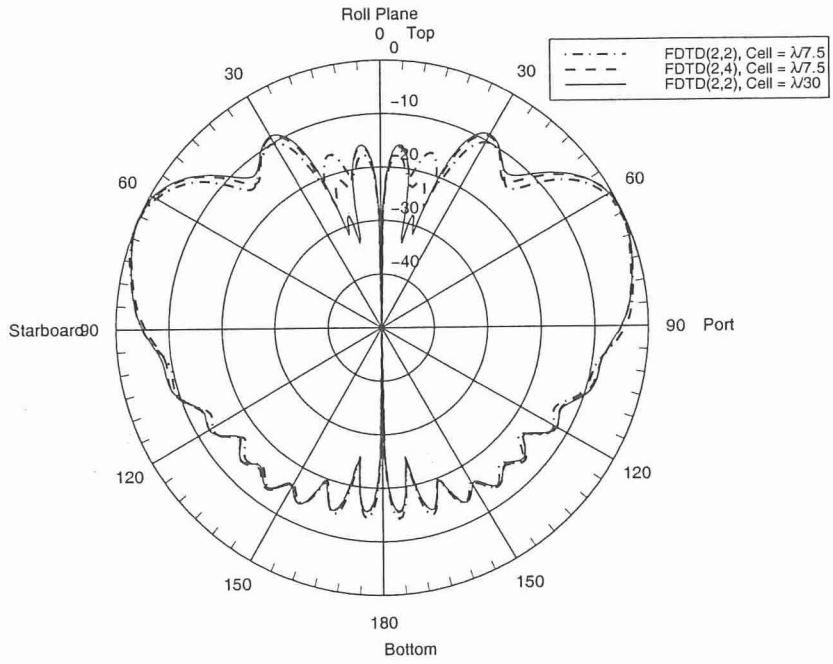

Figure 2.34: Roll plane radiation patterns of a monopole mounted on a rectangular box at 2 GHz.

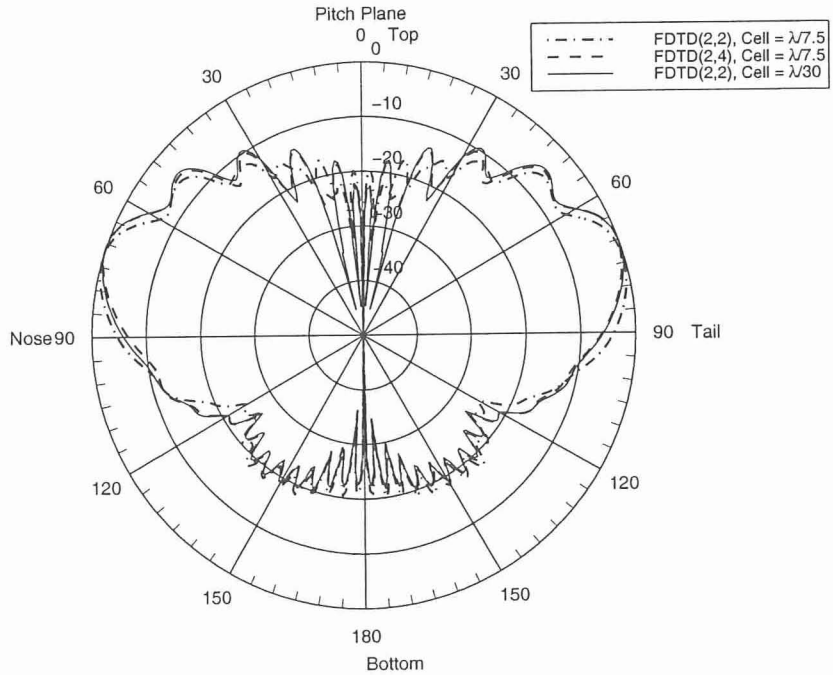

Figure 2.35: Pitch plane radiation patterns of a monopole mounted on a rectangular box at 2 GHz.

very accurately all principal patterns, whereas FDTD(2,2) fails to predict some of the peaks and nulls in these patterns. This example clearly illustrates that FDTD(2,4) outperforms FDTD(2,2) in terms of accuracy. Furthermore, it is expected that as frequency increases, the accuracy of FDTD(2,2) will decline even further whereas FDTD(2,4) will still provide satisfactory results. Additional simulations at higher frequencies were not performed as it was impossible to run a fine enough mesh, such as $\lambda/30$ at a frequency higher than 2 GHz with the available computational resources. In the future, measurements in the anechoic chamber may be performed at higher frequencies in order to provide reference for comparison.

VII. Boundary Conditions

The modeling of complex structures introduces additional challenges in high-order FDTD for the correct formulations of boundary conditions (BCs) and discontinuities. Many different approaches for the treatment of boundary conditions have been proposed in the literature. Most of this work has appeared in the field of computational mathematics and physics. The common method of dealing with the two issues of BCs and discontinuities is to implement one-sided higher-order finite differences. However, such one-sided stencils cause instabilities which are usually very difficult to resolve.

When boundary conditions are applied, there are two main numerical issues that have to be addressed; accuracy and stability. In [47], it was shown that in order to retain the formal accuracy of a higher-order scheme, boundary conditions should be implemented with either the same accuracy as the one of the interior scheme or at least one order less. For Cartesian meshes and for most problems, BCs that satisfy the overall accuracy of the interior scheme are usually possible to derive. However, the difficulty is to derive high-order accurate and *stable* operators.

When a problem is numerically solved, convergence of the numerical solution to the exact solution is desired. Lax's equivalence theorem states that a numerical scheme is convergent when it satisfies both stability as well as consistency for a well posed PDE. Time stability can be defined through two different approaches when dealing with time numerical integration of partial differential equations (PDEs). The first approach is described by the behavior of the numerical solution as the cell size Δx tends to zero for a fixed time T. This procedure defines stability in the *classical* sense.

Classical stability is ensured when the Lax's equivalence theorem is satisfied, i.e., the numerical solution converges to the analytical solution as the cell size Δx tends to zero, and for a fixed time T. This stability definition not only does not exclude error growth in time but it actually permits exponential growth of error in time. Therefore, this stability definition can be weak, and not ensure stability especially for long simulation times. The second stability definition addresses these issues, and is characterized by the behavior of the numerical solution for a fixed cell size Δx as the time T tends to infinity. This procedure defines stability in the *strict* sense. Strict stability is achieved by requiring that for a fixed cell size Δx, all eigenvalues of the differential operator (which is a matrix) have a non-positive real part. Note that the stability of a scheme can be significantly influenced by the imposition of boundary conditions.

Carpenter et al. [48] examined the stability characteristics of various compact fourth- and sixth-order spatial operators by applying the theory of Gustafsson, Kreiss and Sundstrom (G-K-S) [49]. It was shown that many higher-order schemes that are G-K-S stable (stable in the classical sense) are not stable in the strict sense. Moreover, it was found later in [50] that most high-order schemes that were strictly stable for scalar problems, were unstable for systems of equations. A new method, for designing higher-order schemes stable both in the classical and the strict sense, was also proposed in [50]. This method uses the summation-by-parts (SAT) procedure to construct derivative operators that satisfy the summation-by-parts formula. For higher-order explicit formulations the work by Strand [51] was used, whereas for higher-order compact schemes a new methodology was derived. It was proven that compact schemes satisfying just the SAT formula are not necessarily strictly stable unless a specific procedure of imposing boundary conditions is followed. This approach was recently generalized to two-dimensional problems in [52], [53]. Boundary conditions in the context of higher-order schemes have also been discussed in [54]-[56].

In [57] instabilities caused by one-sided high-order boundary conditions were resolved by using an artificial dissipation. This approach of incorporating an artificial dissipation or viscosity is a common way of stabilizing higher-order schemes. In [58] a compact higher-order scheme was combined with boundary conditions implemented by one-sided differences, and a dissipative temporal integration method (Runge-Kutta

fourth-order). In [59] the instabilities were eliminated through a filtering approach. Additionally, artificially dissipative schemes have been discussed in [60]-[63].

A method of dealing with 2-D material discontinuities was presented in [64]. Special one-sided difference operators were derived and applied to both metal and dielectric interfaces. However, the analysis was limited to one- and two-dimensional examples with metal and/or dielectric interfaces, and a 3-D free-space example.

All methods that appeared in the papers discussed above, although promising, have not yet been verified for complex three-dimensional problems for which boundary conditions may be required not only on the external boundary of the computational space but also in the interior of the domain. Their analysis was restricted to one- and two-dimensional free-space problems with boundary conditions needed only on the outer boundary of the domain. However, in most practical engineering problems, imposition and treatment of boundary conditions is mainly needed inside the computational domain for both two- and three-dimensional problems. Such problems cannot be solved using methods that have already been proposed in the literature.

In this section, some of the issues related to boundary conditions, and simulation of thin geometric features in the context of FDTD(2,4) are discussed.

A. Problem definition

To illustrate the accuracy of FDTD(2,4) in simulation of thin wires, a geometry of two monopole antennas mounted on a finite ground plane is analyzed. The specifications of the geometry are shown in Fig. 2.36, and the radius of the two monopoles is 0.60325 mm. The distance between the two monopoles was set to 32 cm so that it would be electrical large at the frequencies of interest [i.e., 32 cm is approximately 21 wavelengths (λ) at 20 GHz].

The analysis of this geometry addresses two issues. The first issue relates to the capability and accuracy of FDTD(2,4) to simulate thin wires. Until today, there are not any available thin or subcell models derived for FDTD(2,4) that would be able to implement thin geometric features in the computational space. Moreover, the accuracy of thin wire analysis, e.g., input impedance, coupling, etc., depends greatly on the radius of the wires under investigation. However, the radius of the wires cannot be taken into account in FDTD(2,4) unless higher-order thin wire models are devel-

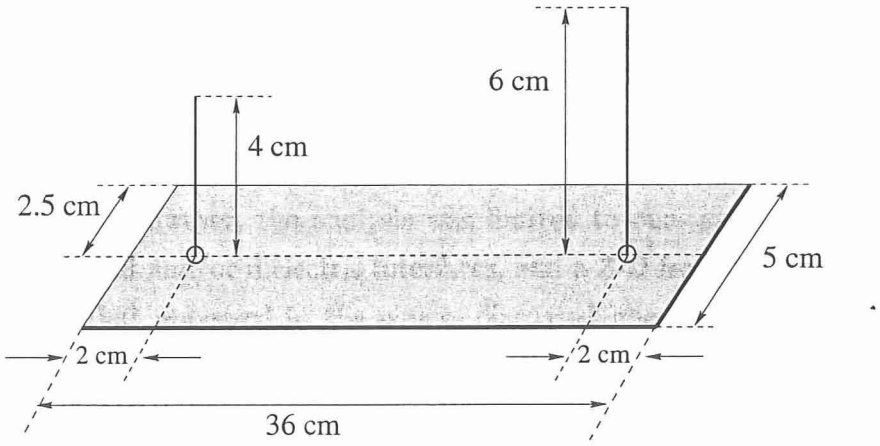

Figure 2.36: Geometry of two monopoles on a ground plane.

oped. The second issue, related to the analysis of the two monopoles, concerns the accuracy of coupling computations. Coupling represents the energy that is coupled from one wire to the other. The accuracy of coupling calculations greatly depends on the accuracy of simulating the wave propagation from one wire to the other. Therefore, it can be very challenging to accurately compute coupling between wires that are separated by electrically large distances due to errors from numerical dispersion. Especially, when using a low-order scheme, such as FDTD(2,2), dispersion errors can degrade the accuracy of the solutions, and provide inaccurate coupling computations.

In the subsections that follow, the S-parameters of the monopoles illustrated in Fig. 2.36 are computed through different ways to address all these issues. Also, all FDTD(2,4) computations are compared with FDTD(2,2) calculations and measurements performed in the Electromagnetic Anechoic Chamber facility (EMAC) at Arizona State University (ASU). The S-parameters were computed by using the procedure described in [65]. To speed the simulation times all sources used a internal resistance of 50 ohms [65]. All following simulations use a cell size of 1.67 mm (or $\lambda/9$ at 20 GHz).

B. FDTD(2,4)

In this subsection, the S-parameters of the monopoles illustrated in Fig. 2.36 are calculated using either FDTD(2,2) or FDTD(2,4). The radius of the monopoles is taken into account in the FDTD(2,2) simulations both along the wire (using a thin

wire model) and the excitation (using a source based on the radial electric fields). The formulation of the thin wire model will be examined in detail in Chapter 3. However, the radius of the wires in the FDTD(2,4) computations are not implemented due to the lack of higher-order thin wire models.

The results of FDTD(2,2) are illustrated in Figs. 2.37-2.43, and they are compared with the FDTD(2,4) computations, and measurements. S_{11} and S_{22} represent the reflection coefficients of the 6 mm and 4 mm long monopoles, respectively. S_{12} represents the coupling between the two monopoles. The accuracy of S_{11} and S_{22} is governed by the modeling of each wire and the discretization near each wire. Moreover, the accuracy of S_{12} is governed by the accuracy of the FDTD stencil used to simulate the wave propagation from one element to the other. Figs. 2.37-2.39 illustrate the magnitude of the S-parameters, and Figs. 2.40-2.43 show their corresponding phase. It can be concluded that FDTD(2,4) predicted the resonances of S_{11} and S_{22} more accurately that FDTD(2,2) due to its reduced dispersion. Also, the magnitude and the phase of coupling, i.e., S_{12}, computed using FDTD(2,4) are more accurate than the ones calculated by FDTD(2,2). This was expected as FDTD(2,4) simulates the wave propagation from one wire to the other more accurately than FDTD(2,2).

Next, the input impedance of the 6 mm long monopole is computed in order to see more clearly the effect of not simulating the radius of the wires in FDTD(2,4). This input impedance is represented by the Z_{11} parameter, and it is calculated by converting the S-parameters to Z-parameters through the well known two-port network relations. Figs. 2.44 and 2.45 illustrate the input resistance and reactance of the 6 mm long monopole, respectively. It can be seen that the computations of FDTD(2,4) are not as accurate as the ones of FDTD(2,2). This is expected, since input impedance calculations depend strongly on the radius of the wires, and FDTD(2,4) did not simulate the radius of the wires. However, FDTD(2,2) took into account the radius of the wires using a thin wire model thereby providing more accurate input impedance predictions.

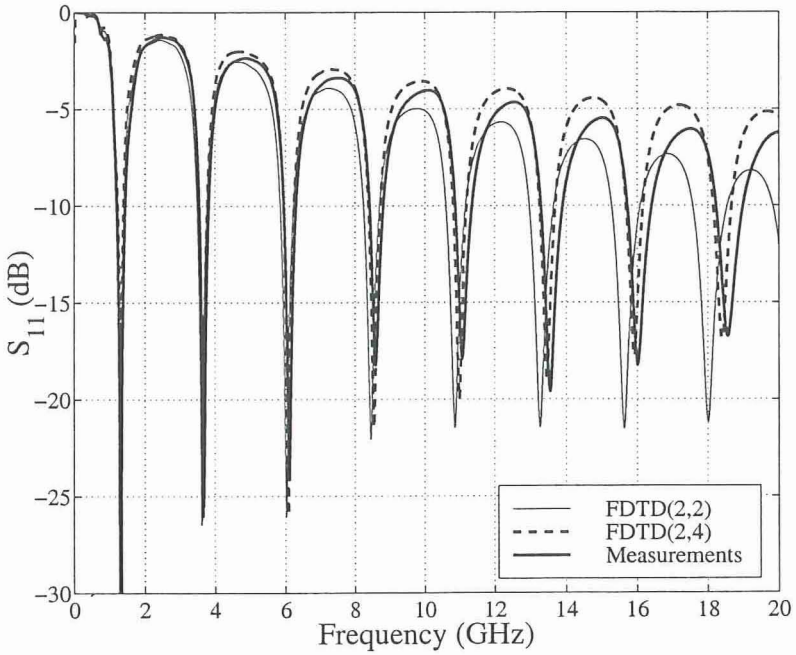

Figure 2.37: S_{11} of the 6 cm long monopole.

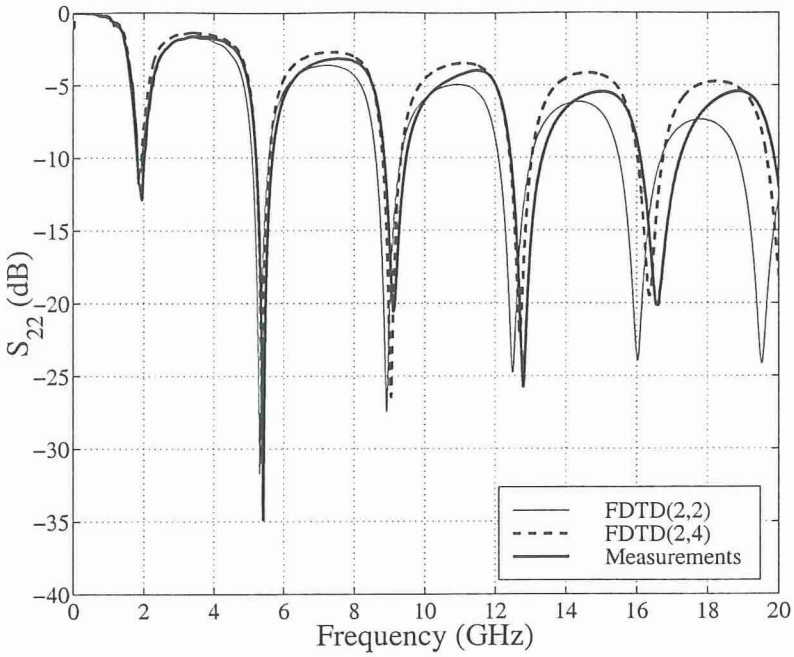

Figure 2.38: S_{22} of the 4 cm long monopole.

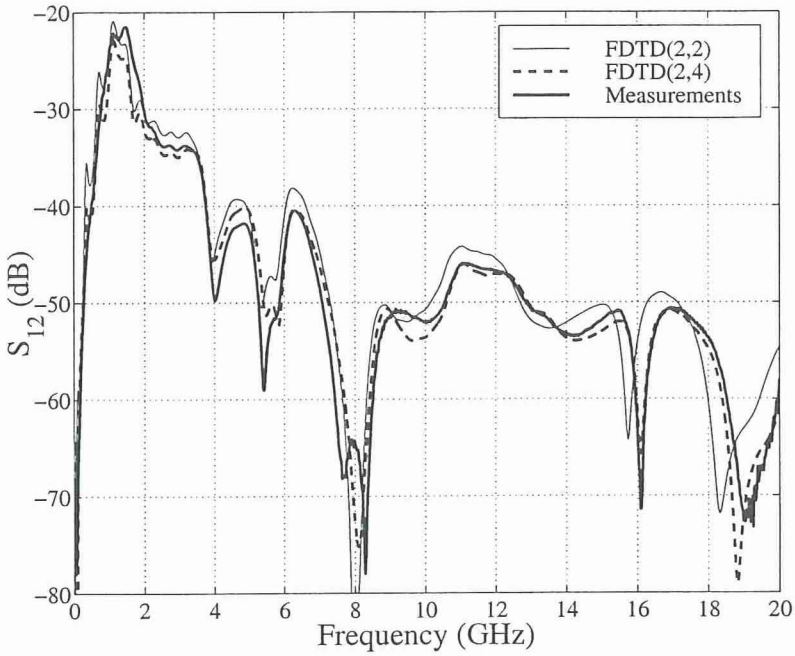

Figure 2.39: S_{12} between the two monopoles.

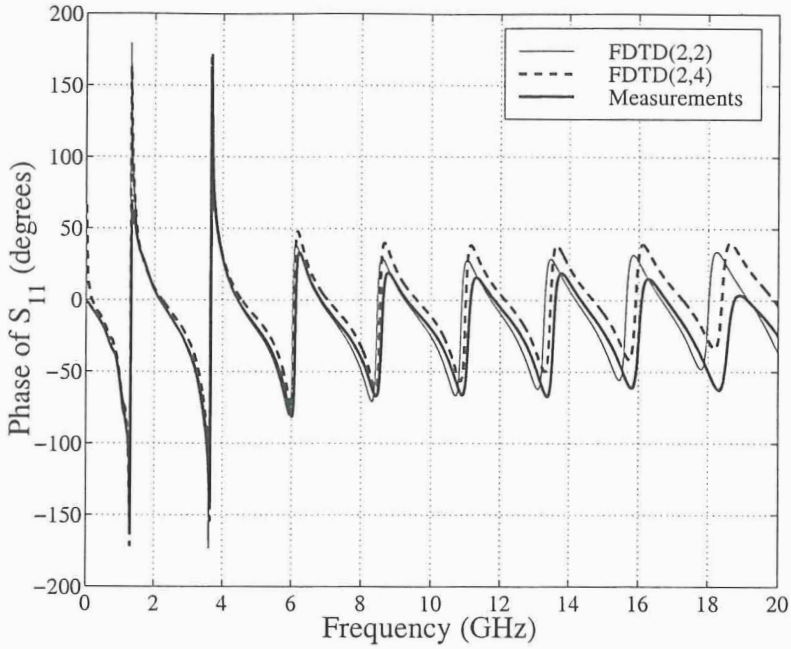

Figure 2.40: Phase of S_{11} of the 6 cm long monopole.

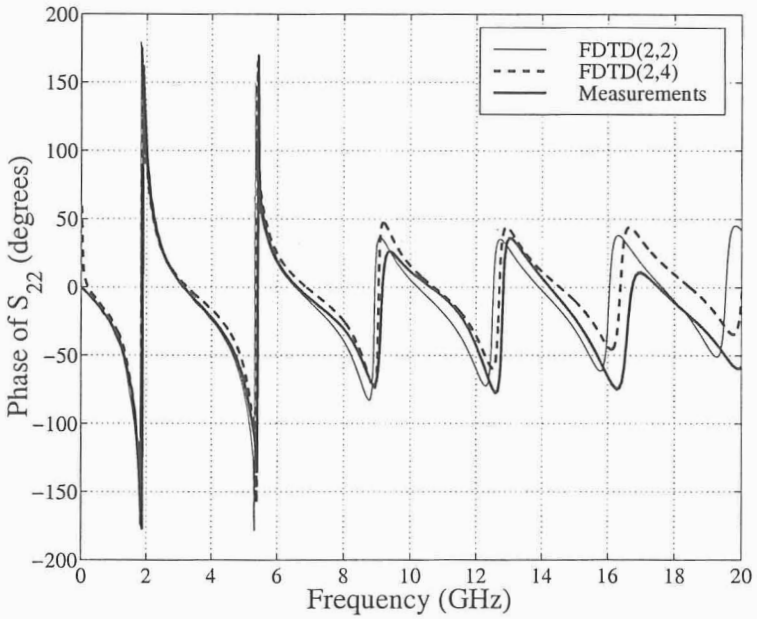

Figure 2.41: Phase of S_{22} of the 4 cm long monopole.

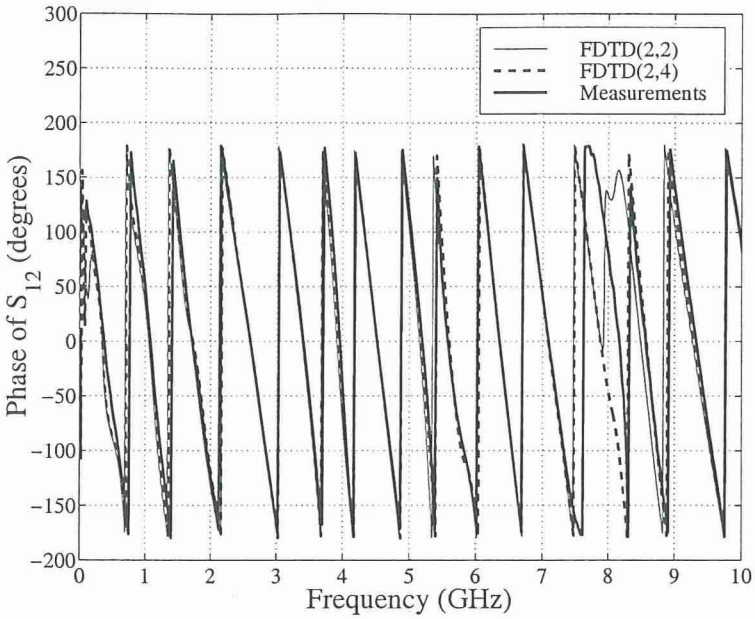

Figure 2.42: Phase of S_{12} between the two monopoles.

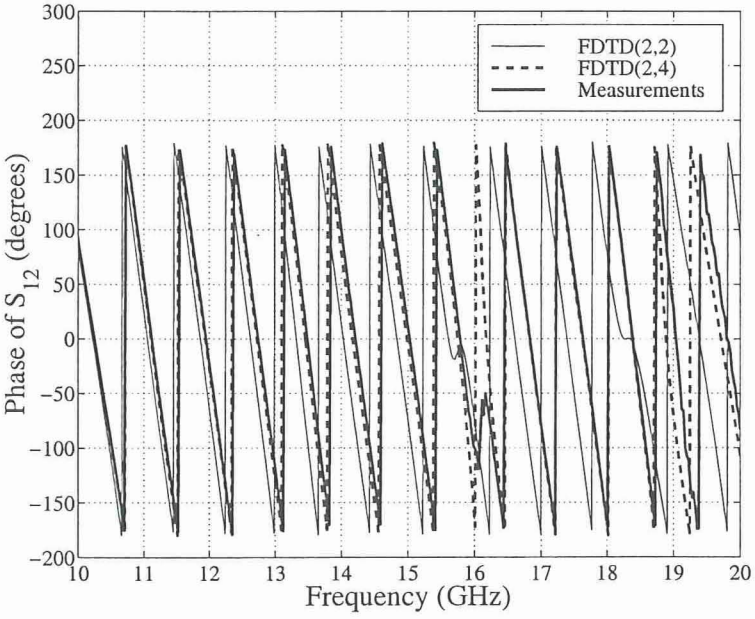

Figure 2.43: Phase of S_{12} between the two monopoles.

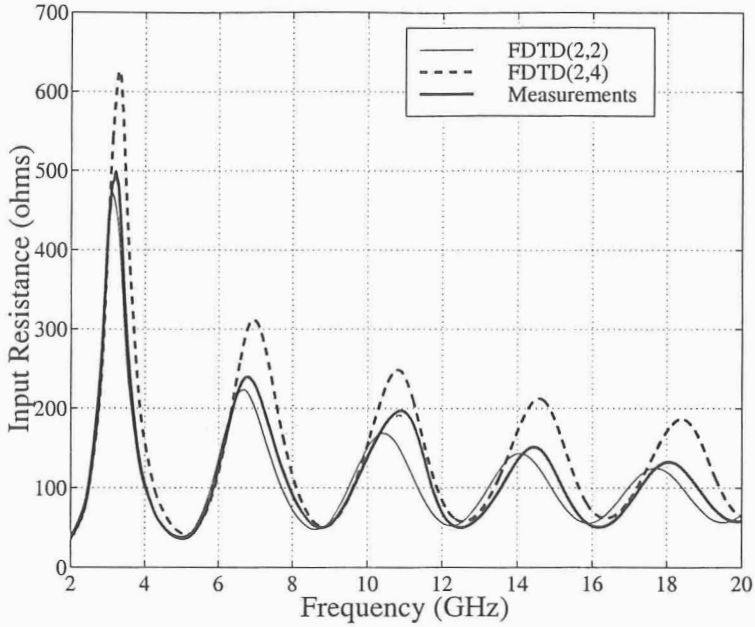

Figure 2.44: Input resistance of the 6 cm long monopole.

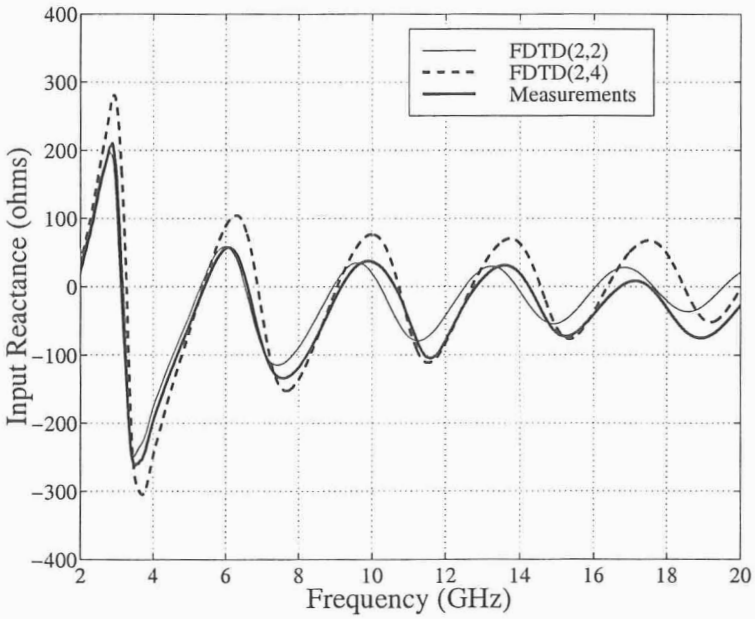

Figure 2.45: Input reactance of the 6 cm long monopole.

C. FDTD(2,4) with thin wire model of FDTD(2,2)

In this subsection, the S-parameters of the monopoles illustrated in Fig. 2.36 are again calculated using either FDTD(2,2) or FDTD(2,4). The radius of the monopoles is taken into account in the FDTD(2,2) simulations both along the wire (using a thin wire model) and the excitation (using a source based on the radial electric fields). Also, the radius of the wires is implemented in the FDTD(2,4) computations using the FDTD(2,2) thin wire model.

The results of FDTD(2,2) are illustrated in Figs. 2.46-2.52, and they are compared with FDTD(2,4) and measurements. It can be concluded that using the FDTD(2,2) thin wire model in conjunction with FDTD(2,4) degrades the accuracy of FDTD(2,4) alone [compare Figs. 2.37-2.43, which correspond to the FDTD(2,4) without any thin wire model, with Figs. 2.46-2.52, which correspond to the FDTD(2,4) with the FDTD(2,2) thin wire model].

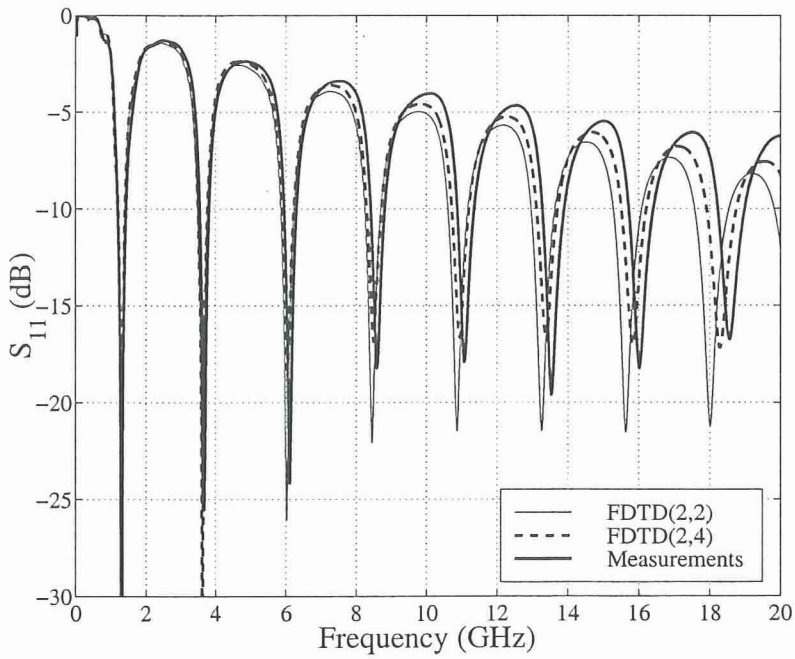

Figure 2.46: S_{11} of the 6 cm long monopole.

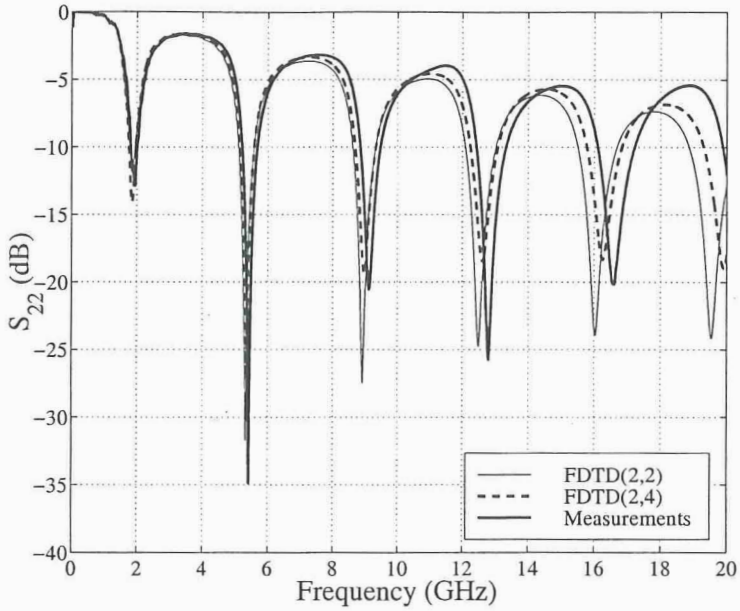

Figure 2.47: S_{22} of the 4 cm long monopole.

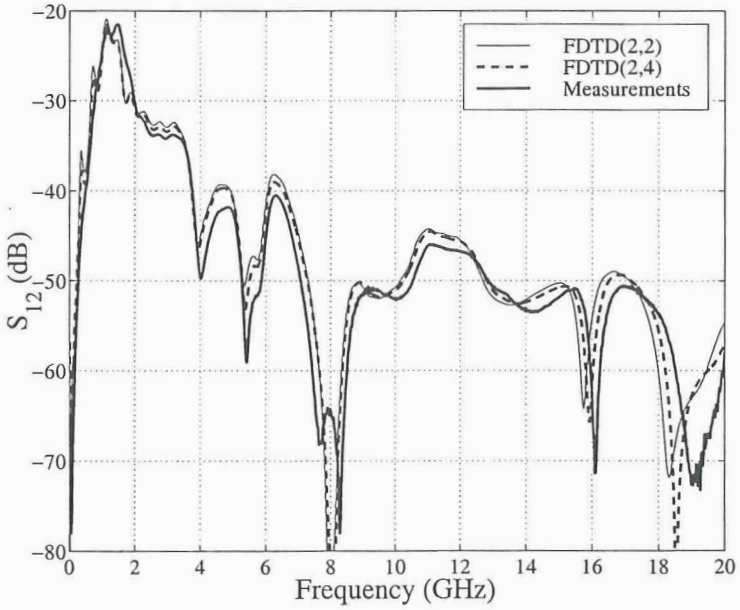

Figure 2.48: S_{12} between the two monopoles.

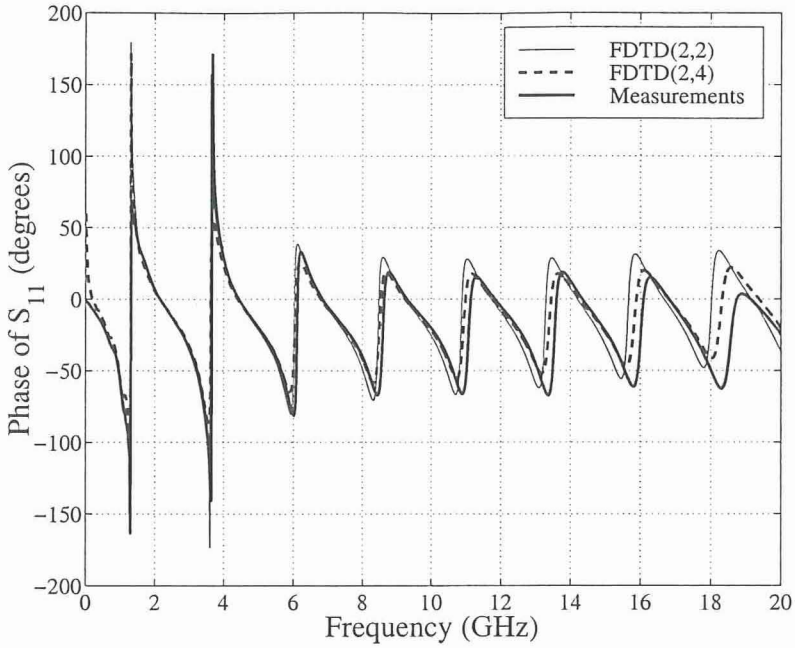

Figure 2.49: Phase of S_{11} of the 6 cm long monopole.

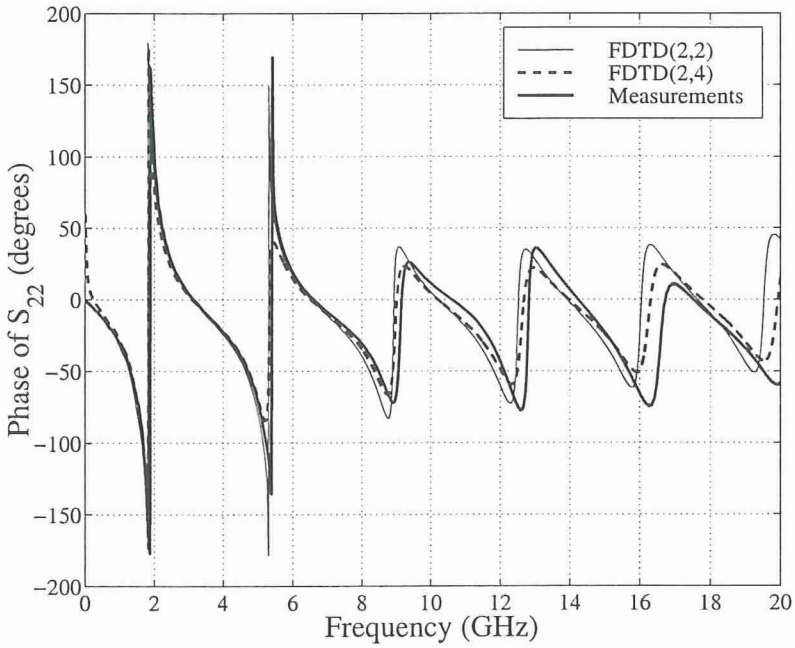

Figure 2.50: Phase of S_{22} of the 4 cm long monopole.

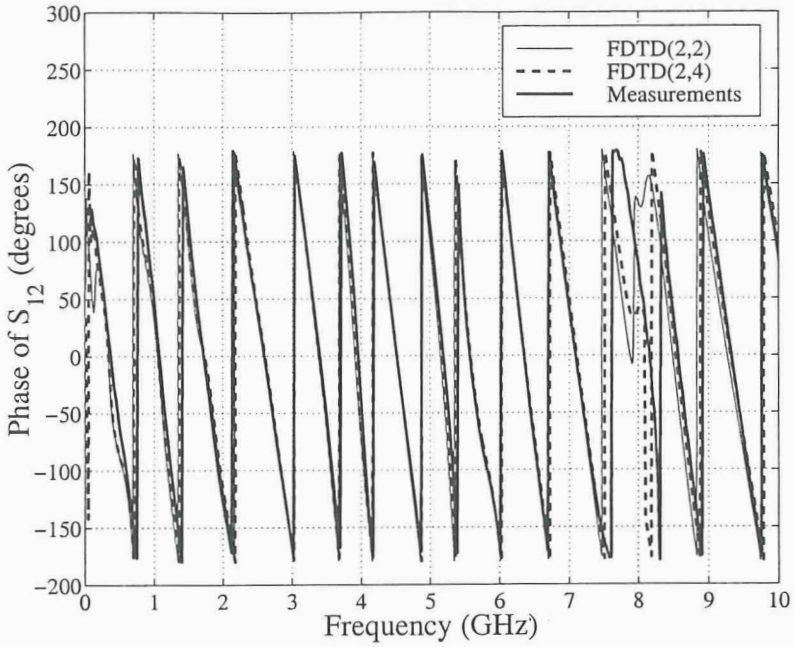

Figure 2.51: Phase of S_{12} between the two monopoles.

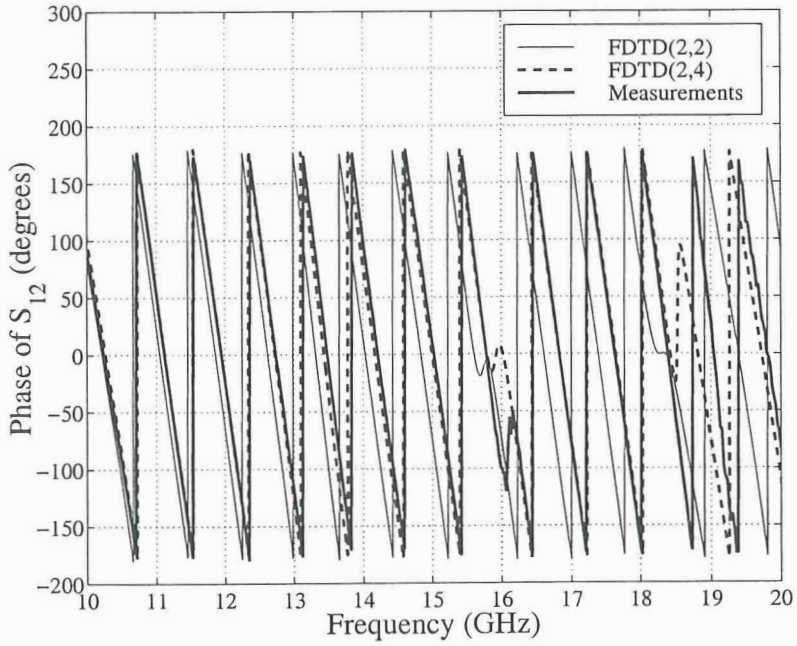

Figure 2.52: Phase of S_{12} between the two monopoles.

When the FDTD(2,2) thin wire model is used along with FDTD(2,4) the resonances of the monopoles, and their coupling, are not predicted as accurately as in FDTD(2,4) alone. Actually, the results of this hybrid resemble more the FDTD(2,2) computations. This accuracy degradation is due to the fact that the FDTD(2,2) thin wire model introduces second-order errors in the FDTD(2,4) solution. Therefore, it is seen that by using the FDTD(2,2) thin wire model combined with FDTD(2,4), the accuracy of the S-parameters is degraded.

However, by using the FDTD(2,2) thin wire model combined with FDTD(2,4), it is expected that the accuracy of the FDTD(2,4) input impedance results should improve compared to the FDTD(2,4) with no consideration of the wires' radius. The new input impedance calculations of FDTD(2,4) are illustrated in Figs. 2.53 and 2.54. Apparently, the accuracy of the new FDTD(2,4) impedance computations [incorporating the FDTD(2,2) thin wire model] is improved compared to the computations of the previous subsection (compare Figs. 2.44 and 2.45 with Figs. 2.53 and 2.54)

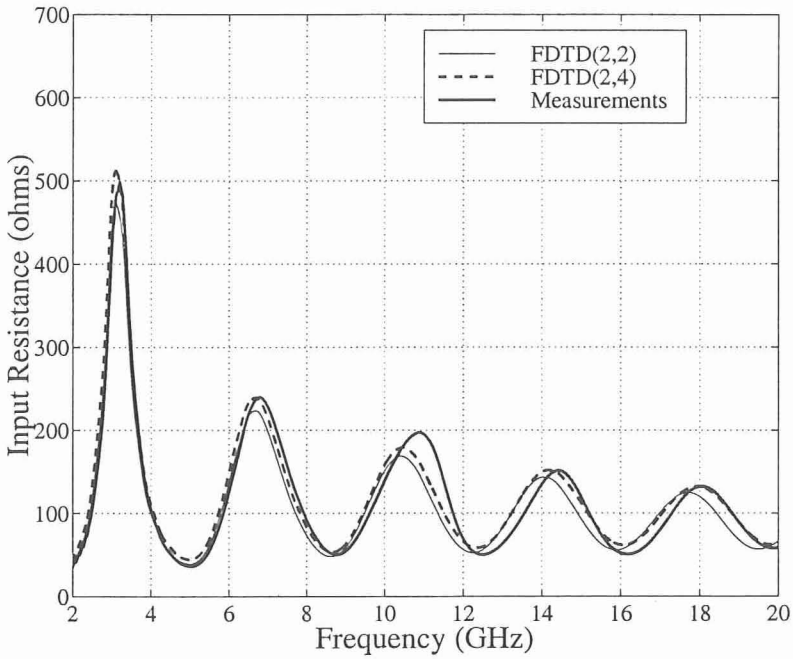

Figure 2.53: Input resistance of the 6 cm long monopole.

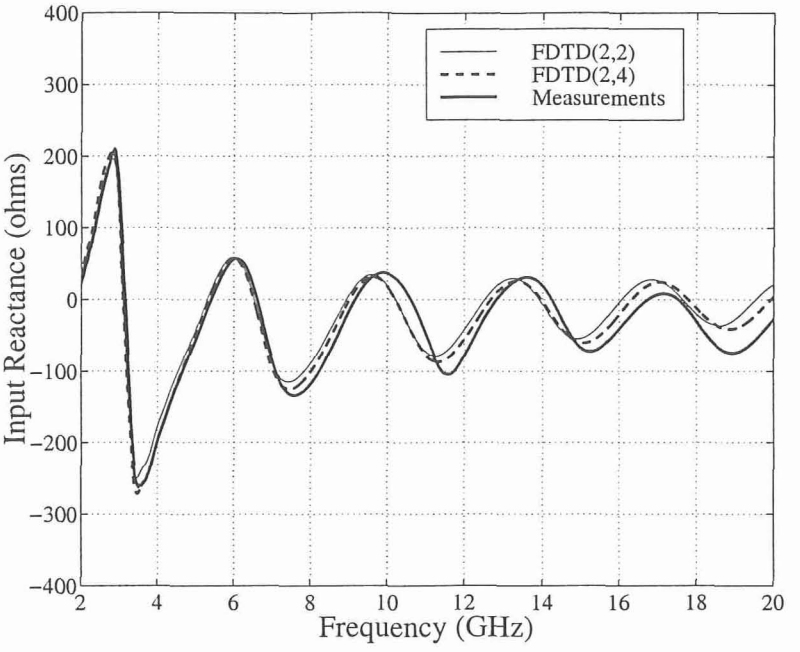

Figure 2.54: Input reactance of the 6 cm long monopole.

D. FDTD(2,4) with one-sided differences

One-sided higher-order differences are incorporated in this subsection around each wire. All the different one-sided schemes that have been implemented during this research were found to be unstable. This finding is supported by the literature review of similar work that was discussed in the beginning of this section (Section VII.). Other papers that have appeared in the literature have encountered similar instability problems when one-sided differences were used. The instability issue stems from the interaction of the one-sided difference schemes with the central difference schemes, and it is usually difficult to resolve. It should be pointed out that stencils can generate parasitic solutions which can lead to instabilities when they are used in conjunction with other stencils. Such instabilities can still occur even when the parasitic solutions are damped for the individual stencils. Therefore, one-sided differences will not be pursued further during this research.

E. Summary

In the previous three subsections, FDTD(2,4) was applied to analyze the problem of two monopoles on a ground plane. Initially, FDTD(2,4) was applied alone without being able to simulate the radius of the wires. The S-parameters computed in this case by FDTD(2,4) were more accurate than FDTD(2,2). However, the input impedance FDTD(2,4) calculations were not as accurate as the ones of FDTD(2,2), since FDTD(2,4) did not simulate the radius of the wires.

Then, FDTD(2,4) was combined with the FDTD(2,2) thin wire model and the S-parameters computed for this case were not as accurate as the ones that used only FDTD(2,4). In addition, the input impedance calculations exhibited improved accuracy in this case compared to the ones that used FDTD(2,4) alone. Basically, when FDTD(2,4) was combined with the FDTD(2,2) thin wire model, it provided results very similar to the calculations of FDTD(2,2) alone. This can be attributed to the fact that the FDTD(2,2) thin wire model is second-order accurate thereby degrading the accuracy of FDTD(2,4).

Also, one-sided differences were applied around each wire, but they were found unstable. After long experimentation with various one-sided schemes, it was decided to pursue other ways to expand the capabilities of FDTD(2,4).

In conclusion, it is clear that there is a need for a higher-order method that can simulate thin geometric features without loosing its high-order of accuracy. In the next section, a method that benefits from the advantages of both FDTD(2,2) and FDTD(2,4) is presented.

VIII. Hybrid of FDTD(2,4) and Subgrid FDTD(2,2)

The proposed approach in this section consists of combining a subgridding technique with a higher-order scheme. Subgridding techniques have been used in the past in the context of the standard FDTD. These methods divide the simulation space into two separate grids; a fine one and a coarse one. In [9] the first subgridding technique was introduced, and it required two separate FDTD calculations one for the fine and one for the coarse grid. Then, Kim et al., [66], derived a subgrid method with a 4:1 resolution such that only one simulation was needed. In 1991, Zivanovic et al.,

[67], developed a method that used a 2:1 resolution, and implemented the coupling between coarse and fine region through time and space interpolations of both magnetic and electric fields. Also, they applied the homogeneous traveling wave equation to achieve matching between the coarse and the fine region with a 3:1 ratio of cell sizes. A more efficient implementation of the approach presented in [67] was discussed in [68]. Finally, Chevalier et al. presented in [69] a new subgridding technique that allows the boundary between the coarse and the fine grid to be located in an inhomogeneous dielectric region. Moreover, odd integer-cell ratios were used, e.g., 1:3, 1:5, 1:7, etc., so that the fields in the coarse and fine grids stay synchronized in time and collocated in space. The time and space arrangement of the fields in the fine and coarse domains for a 1:3 cell ratio are depicted graphically in Figs. 2.55 and 2.56 respectively.

Here, the subgridding method of [69] is used in conjunction with the second-order accurate in time and fourth-order accurate in space FDTD(2,4). On the fine grid, the standard FDTD(2,2) is used to handle any of the fine features of the structure, whereas on the coarse grid FDTD(2,4) is used. Thus existing successfully-applied techniques in FDTD(2,2) for the incorporation of discontinuities, boundary conditions, and thin features are available for use on the fine grid. On the coarse mesh, away from phenomena associated with the complex structure, FDTD(2,4) is used to mainly simulate the wave propagation in homogeneous media. Following, this approach, high accuracy is obtained both around fine geometric features, such as thin wires, thin slots, etc., as well as in the wave propagation which is simulated by a higher-order scheme, i.e., FDTD(2,4).

A. Method

The method developed here uses a modification of the subgridding technique of [69]. The boundary between the fine and the coarse grid is collocated with electric field components instead of magnetic field components. The ratio between the coarse and the fine grid cell sizes is chosen to be 1:3 as in [69]. A two-dimensional view of the grid is shown in Fig. 2.55.

To make the method stable, the two types of weighting used in [69] are applied.

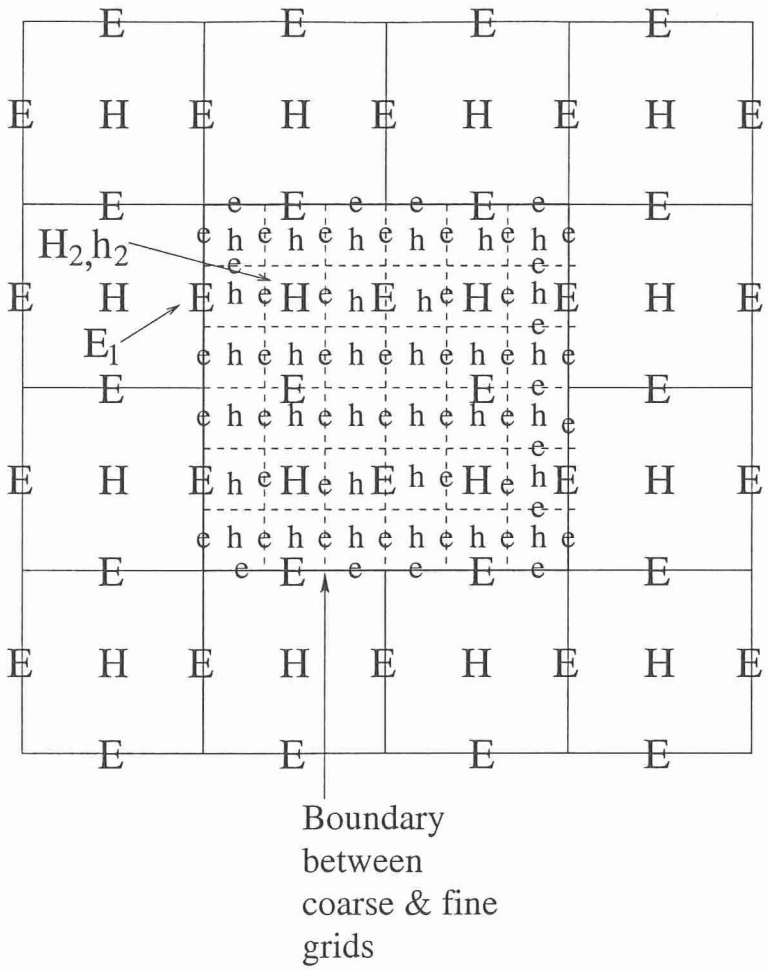

Figure 2.55: Two-dimensional view of the coarse and fine grids.

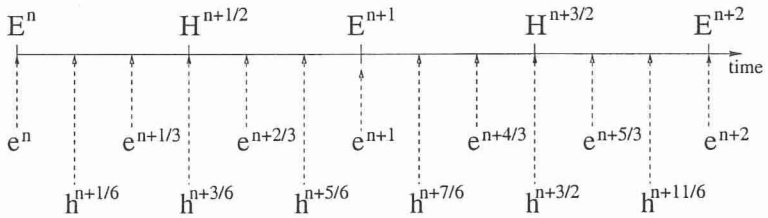

E, H: Coarse grid fields
e, h : Fine grid fields

Figure 2.56: Respective locations in time of the electric and magnetic fields for both the coarse and the fine grids.

First, the electric fields near the coarse-fine boundary are weighted as:

$$e_2 = 0.95\ e_{2fine} + 0.05\ \frac{E_1 + e_3}{2} \tag{2.47}$$

where e_2 is the weighted electric field value of the fine grid just adjacent to the coarse-fine grid boundary, e_{2fine} and e_3 are the fields computed by FDTD(2,2) in the fine grid, and E_1 is the field computed by time and space interpolation of FDTD(2,4) fields on the coarse-fine grid boundary (see Fig. 2.57). The coefficients were empirically found in [69]. This type of weighting can be considered effectively as a smoothing of the electric field values when transitioning from the coarse to the fine domain.

The second type of weighting that is used relates to the coarse grid magnetic field values adjacent to the coarse-fine domain boundary and inside the fine grid region (see Fig. 2.55). It is done using the following equations:

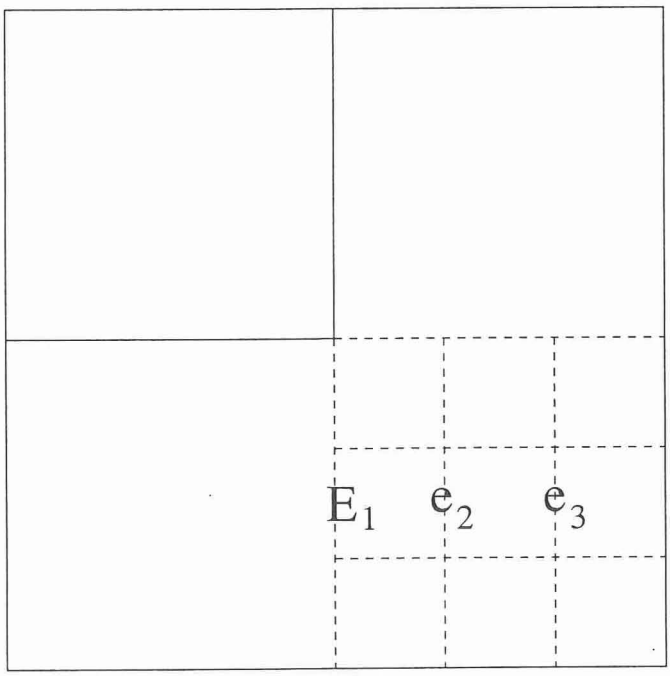

Figure 2.57: Electric field e_2 (near the boundary between the coarse and fine grids) that is linearly weighted.

$$H_2 = 0.7\ H_{2coarse} + 0.3\ h_{2fine} \tag{2.48}$$

$$h_2 = 0.3\ H_{2coarse} + 0.7\ h_{2fine} \tag{2.49}$$

where the locations of H_2 and h_2 are illustrated in Fig. 2.55, and the subscripts *coarse* and *fine* correspond to the coarse and fine field values computed from FDTD(2,4) and FDTD(2,2), respectively.

The time interpolation of the fine grid electric field values on the boundary is performed using the following third-order accurate relations:

$$E^{n+2+1/3} = \frac{2}{9} E^n - \frac{7}{9} E^{n+1} + \frac{14}{9} E^{n+2} \tag{2.50}$$

$$E^{n+2+2/3} = -\frac{1}{9} E^{n+1} + \frac{5}{9} E^{n+2} + \frac{5}{9} E^{n+3} \tag{2.51}$$

The respective locations in time of the electric and magnetic fields for both the coarse and the fine grids are shown in Fig. 2.56.

Also, in order to ensure stability the Courant stability upper limit of the fourth-order FDTD was reduced by a factor of 1.25 as follows:

$$\Delta t \leq 0.8 \frac{6}{7} \frac{\Delta}{c\sqrt{3}} \tag{2.52}$$

A brief description of the procedure is given as follows (see also [69]):

a. Apply FDTD(2,4) on all the main grid points (including the ones inside the fine grid) and obtain $H^{n+1/2}$.

b. Apply FDTD(2,2) on the fine grid to obtain $h^{n+1/6}$.

c. Apply FDTD(2,2) on the fine grid to obtain $e^{n+1/3}$. Update $e^{n+1/3}$ on the coarse-fine boundary using space and time interpolation. Apply (2.47) to weight $e^{n+1/3}$ one cell inside the fine grid.

d. Apply FDTD(2,2) on the fine grid to obtain $h^{n+3/6}$. Use (2.48) and (2.49) to weight $h^{n+3/6}$ and $H^{n+1/2}$ collocated one coarse grid cell into the fine domain.

e. Update E^{n+1} at the coarse-fine boundary using the obtained values for $H^{n+1/2}$ from step 4.

f. Repeat step 3 to obtain $e^{n+2/3}$, step 2 to obtain $h^{n+5/6}$, and step 3 again to obtain e^{n+1}. Correct the coarse-fine grid boundary values of e^{n+1} using space interpolation of E^{n+1}.

g. Transfer all fine grid e field values to the corresponding collocated coarse grid E field values.

Capital letters E and H represent coarse grid field values, and small letters e and h represent fine grid field values.

B. Results

To illustrate the accuracy of the hybrid FDTD(2,4)-subgrid FDTD(2,2), the geometry of the two monopole antennas mounted on a finite ground plane, shown in Fig. 2.36, is analyzed.

Three test simulations were performed by using:

a. FDTD(2,2) with a cell size of 4 mm (or approximately $\lambda/4$ at 20 GHz),

b. FDTD(2,2) with a cell size of 1.67 mm (or $\lambda/9$ at 20 GHz), and

c. The hybrid FDTD(2,4)-subgrid FDTD(2,2) with a coarse grid cell size of 4 mm (or approximately $\lambda/4$ at 20 GHz) and a fine grid cell size 4/3 mm$\simeq$1.334 mm (or $\lambda/11$ at 20 GHz).

These three simulations are labeled 1, 2, and 3 respectively. Notice that in simulation 3, a fine grid was applied around each wire and the rest of the space used a coarse grid. The fine grid extended two coarse grid cells (or six fine grid cells) around each wire. The radius of the monopoles was taken into account in all three simulations both along the wire (using a thin wire model) and the excitation (using a source based on the radial electric fields). The S-parameters were computed by using the procedure described in [65]. To speed the simulation times, all sources used an internal resistance of 50 ohms [65].

The results of the three simulations are illustrated in Figs. 2.58-2.60 where the S-parameters of the two monopoles are compared against measurements performed in the Electromagnetic Anechoic Chamber facility (EMAC) at Arizona State University (ASU). S_{11} and S_{22} represent the reflection coefficients of the 6 cm and 4 cm long monopoles, respectively. S_{12} represents the coupling between the two monopoles. The accuracy of S_{11} and S_{22} is governed by the modeling of each wire and the discretization

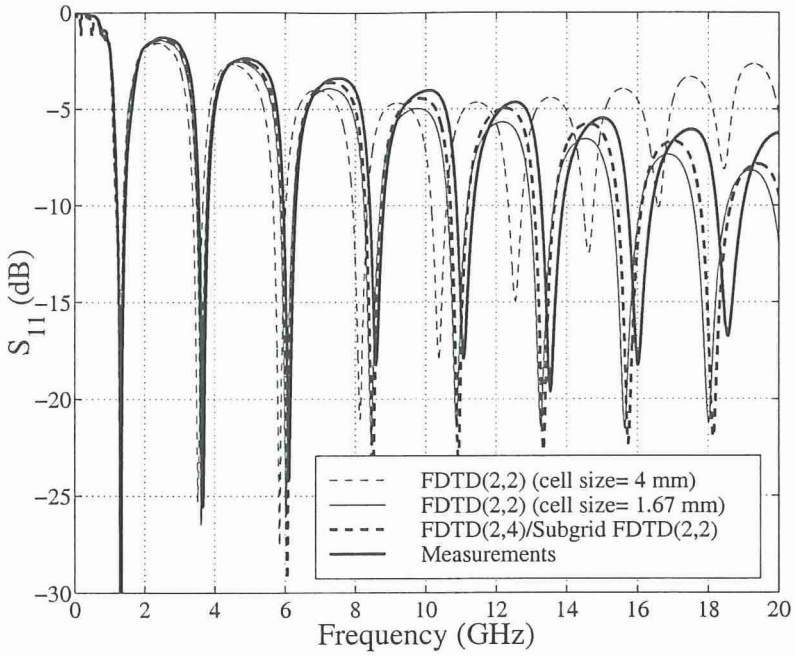

Figure 2.58: S_{11} of the 6 cm long monopole.

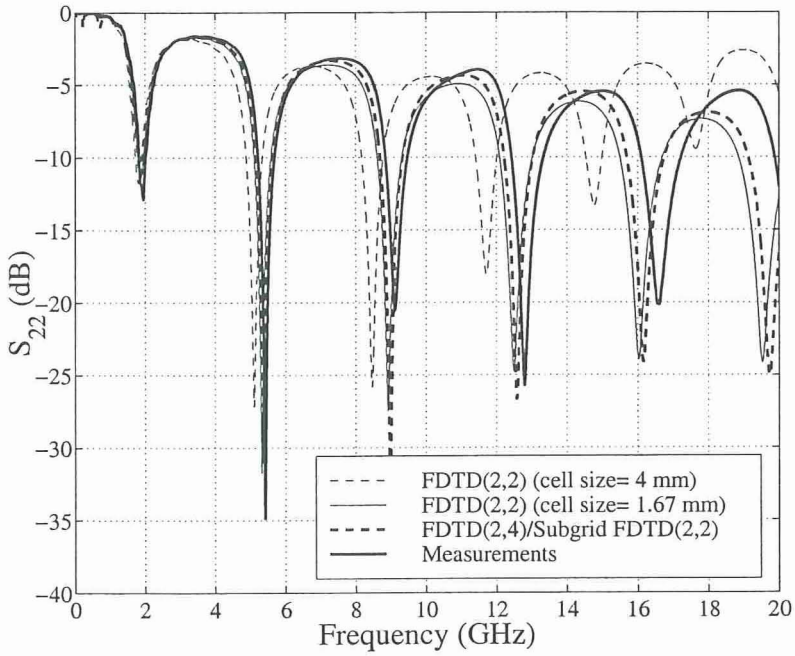

Figure 2.59: S_{22} of the 4 cm long monopole.

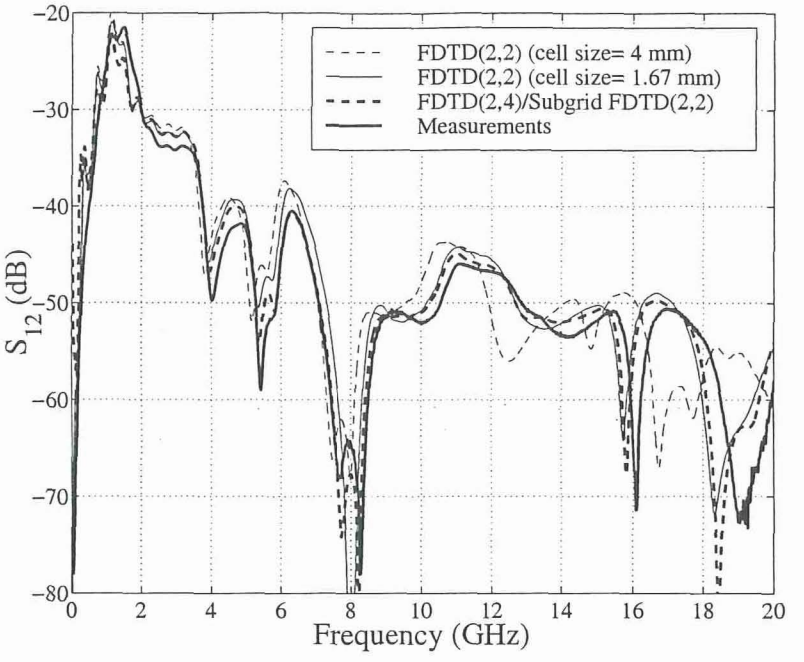

Figure 2.60: S_{12} between the two monopoles.

near each wire whereas the accuracy of S_{12} is governed by the accuracy of the FDTD stencil used to simulate the wave propagation from one element to the other.

All S-parameter computations of simulation 1 [FDTD(2,2) with $\Delta x = 4$ mm] do not agree well with the measurements due to the poor discretization (only $\lambda/4$ at 20 GHz). However, simulations 2 and 3 provided predictions that are in very good agreement with measurements. Simulation 2 used FDTD(2,2) and $\Delta x = 1.67$ mm (or $\lambda/9$ at 20 GHz) which is a good discretization of our structure. Simulation 3 used the hybrid FDTD(2,4)-subgrid FDTD(2,2) and provided very good results for S_{11} since the discretization of the wires was done with a fine grid ($\Delta x = 4/3$ mm or $\lambda/11$ at 20 GHz). Furthermore, the hybrid FDTD(2,4)-subgrid FDTD(2,2) computations for S_{12} were also accurate since the wave propagation from one element to the other was performed using the higher-order stencil FDTD(2,4), with $\Delta x = 4$ mm (or $\lambda/4$ at 20 GHz). Therefore, it can be concluded that in the hybrid approach the field variations around thin geometric features, such as wires, are captured using the standard FDTD(2,2) and the available sub-cell models on a fine grid. Moreover, the

field propagation for large distances is accurately modeled by a higher-order FDTD stencil [FDTD(2,4) in our case] on a coarse grid.

For the computation of S-parameters, two simulations must be performed for each of our cases. The simulation times, as well as the memory requirements for each simulation, for cases 1, 2, and 3, are depicted and compared in Table 2.1. To obtain accurate results with FDTD(2,2), a cell size of 1.67 mm had to be used (case 2). This case required almost two and a half times more time, and three and a half times more memory than the respective time and memory of case 3, which used the hybrid FDTD(2,4)-subgrid FDTD(2,2). It should be noted that the computational savings will be significantly larger in cases where the computational domain is electrically large in all three directions (in our geometry, see Fig. 2.36, the domain is electrically large along one direction only).

Table 2.1: Simulation times and memory requirements

Case	Simulation Time (min)	Memory (Mbytes)
1	15	3.5
2	118	14.0
3	48	3.9

Also, to validate the accuracy of the hybrid FDTD(2,4)-subgrid FDTD(2,2) method for input impedance calculations, the S-parameters computed above were converted to Z-parameters. Specifically, the input impedance of the 6 cm monopole is represented by Z_{11}. This input impedance is compared for the three simulations 1-3 with measurements in Figs. 2.61 and 2.62. It is clearly, shown that the hybrid FDTD(2,4)-subgrid FDTD(2,2) approach provides very accurate input impedance results due to the use of the FDTD(2,2) thin wire model in the fine grid.

C. Conclusions

An accurate hybrid method of FDTD(2,4) coupled with FDTD(2,2) on a subgrid has been presented. The results indicate great computational savings both in memory and time. Moreover, this hybrid approach is very promising for other practical situations because of the flexibility for the inclusion of all existing thin and sub-cell models with FDTD(2,2). Simultaneously, the method offers the high accuracy of

FDTD(2,4) for the propagation of waves over electrically large distances. Finally, this hybrid approach was found to be stable after several thousands of time-steps when the procedures of [69] were incorporated.

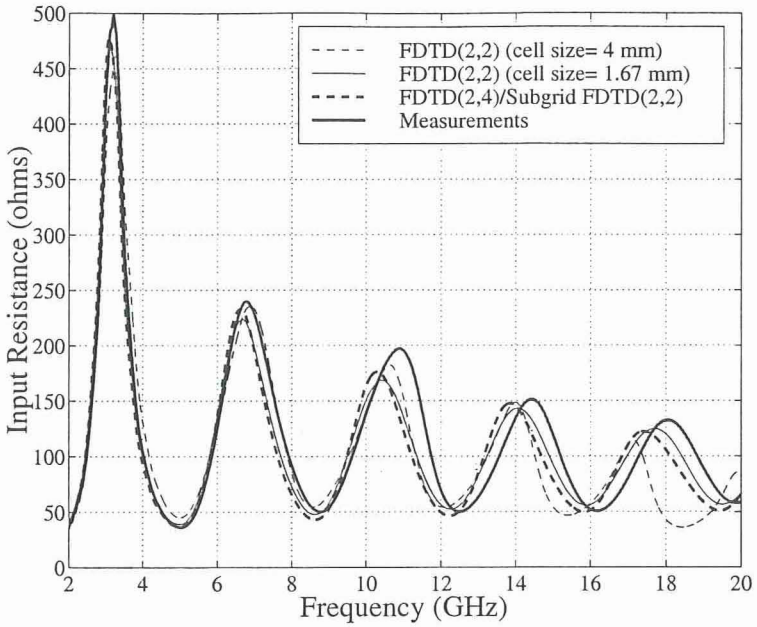

Figure 2.61: Input resistance of the 6 cm long monopole.

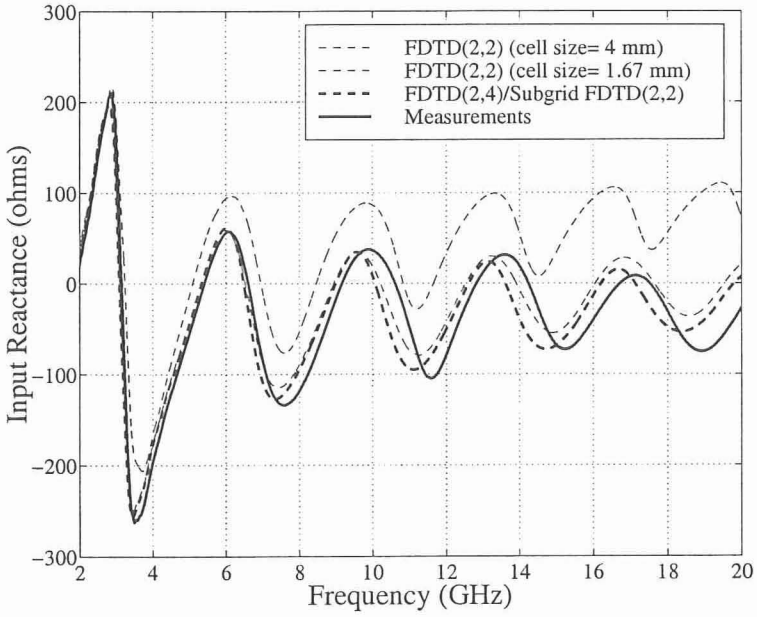

Figure 2.62: Input reactance of the 6 cm long monopole.

IX. Hybrid of Subgrid FDTD(2,2) and FDTD(2,4)

In the previous section, a hybrid formulation of FDTD(2,4) and subgrid FDTD(2,2) was presented. The code that was written to implement that hybrid method assumed that everywhere in the domain FDTD(2,4) is applied except small areas of the domain where subgrid FDTD(2,2) is used. These parts where subgrid FDTD(2,2) is used were assumed to be internal to the entire FDTD(2,4) domain. For example, see in Fig. 2.63 the domain of the two monopoles that was previously analyzed, and notice that subgrid FDTD(2,2) was used only around the two monopoles. The areas where subgrid FDTD(2,2) was applied are obviously included in the FDTD(2,4) domain.

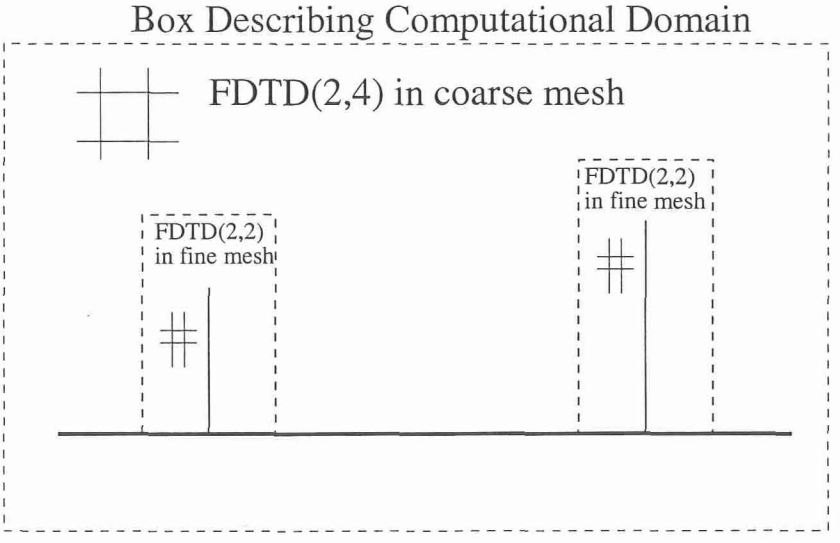

Figure 2.63: Schematic visualization of the hybrid method of FDTD(2,4) and subgrid FDTD(2,2) presented in the previous section.

However, there might exist problems where the opposite configuration of meshes (coarse and thin) occurs, i.e., the area where FDTD(2,4) is used is contained in the subgrid FDTD(2,2) domain. One example of such a case comes from shielding effectiveness analysis of electrically large rectangular enclosures. In these cases, the largest part of the computational domain is the interior of the enclosures, and the problem of boundary conditions arises near the walls of the enclosures. In such cases, it is desired to simulate the propagation inside the box using a higher-order method, such as FDTD(2,4). In addition, near the walls of the boxes a subgrid

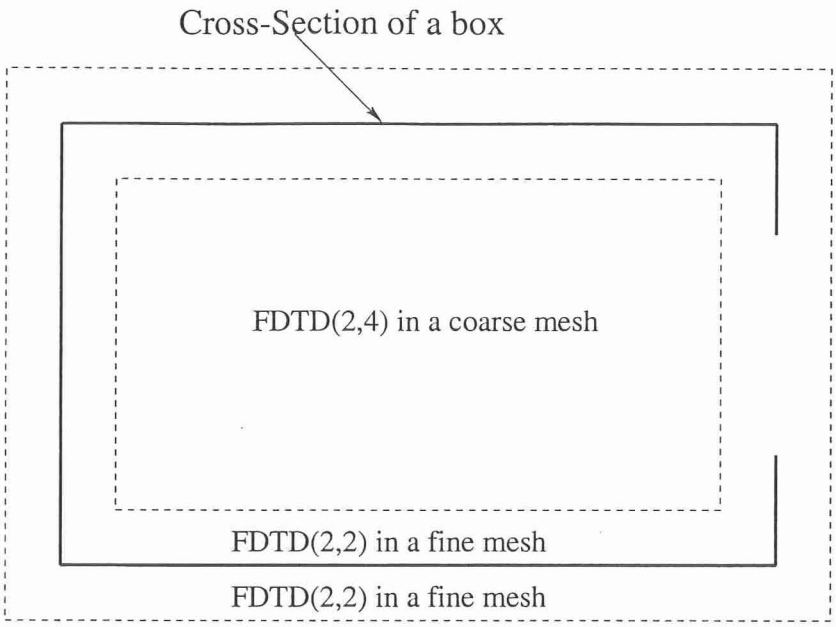

Figure 2.64: Schematic visualization of the hybrid method subgrid FDTD(2,2) and FDTD(2,4) presented in the this section.

FDTD(2,2) method should be used in order to represent accurately the PEC boundary conditions, and successfully simulate the penetration mechanisms. FDTD(2,2) is used near the walls instead of FDTD(2,4) since FDTD(2,4) exhibits an inherent artificial penetration through thin PEC films. This artificial penetration is attributed to the length of the FDTD(2,4) stencil which allows fields from one side of the PEC to couple on the other side of the PEC. Also, as discussed in Section VII. stable higher-order boundary conditions that would simulate correct PEC discontinuities do not exist and they are very challenging to derive. Therefore, subgrid FDTD(2,2) is hybridized with FDTD(2,4) to resolve all these issues. Following such a procedure yields tremendous savings in memory and/or time depending on the particular problem. A schematic representation of such a problem is depicted in Fig. 2.64. In order to implement this new type of hybrid, a new code has to be implemented. This new hybrid is named subgrid FDTD(2,2)/FDTD(2,4) which is the reverse of the name of the hybrid method in the previous section.

A. Method

This new hybrid method resembles the hybrid method presented in the previous section. The boundary between the fine and the coarse grid is collocated with electric field components. The ratio between the coarse and the fine grid cell sizes is chosen to be 1:3.

A two-dimensional view of the grid is shown in Fig. 2.65 which represents a cross-section of the computational grid. In Fig. 2.65 several features should be pointed out as follows:

a. The external thick line represents the walls of the conducting enclosure. On and outside this boundary only subgrid FDTD(2,2) is used on a fine grid.

b. The internal thick line represents the boundary between the fine and the coarse grid domains. On and inside this boundary only FDTD(2,4) is used on a coarse grid. The domain that is described by this boundary is labeled *domain* #1 for reference purposes.

c. In the area between the two thick lines both subgrid FDTD(2,2) (on a fine grid) and FDTD(2,4) (on a coarse grid) are applied. This area is labeled *domain* #2 for reference purposes.

d. The distance between the walls of the conducting enclosure and the coarse-fine grid boundary is chosen to be 3 coarse grid cells, so that the standard FDTD(2,4) using central finite difference spatial scheme can be applied on the coarse-fine grid boundary.

To make the method stable, the electric fields near the coarse-fine boundary are weighted in the same manner presented in the previous section and described by (2.47). Also, another weighting that is used relates to the coarse grid magnetic field values adjacent to the coarse-fine domain boundary and inside the fine grid region (see Fig. 2.65). The locations of the magnetic fields where this weighting occurs is illustrated by the black dots shown in Fig. 2.65. It is done using (2.48) and (2.49). The time interpolation of the fine grid electric field values on the boundary is performed using the same third-order accurate relations, (2.50) and (2.51), used in the previous section.

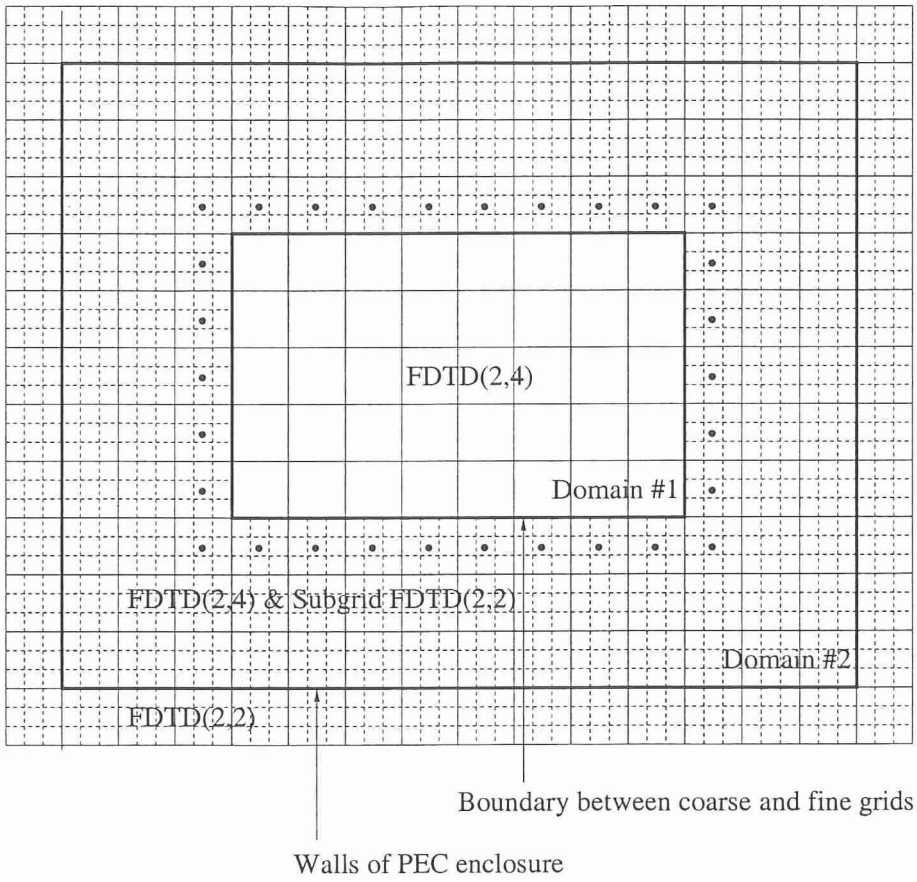

Figure 2.65: Two-dimensional view of the coarse and fine grids.

Also, in order to ensure stability the Courant stability upper limit of the fourth-order FDTD was reduced by a factor of 2 as follows:

$$\Delta t \leq 0.5 \, \frac{6}{7} \frac{\Delta}{c\sqrt{3}} \tag{2.53}$$

A brief description of the procedure is given as follows (see also [69]):

a. Apply FDTD(2,4) on all the main grid points (including the ones inside the shared area by both the coarse and fine grid, i.e., domains #1 and #2) and obtain $H^{n+1/2}$.

b. Apply FDTD(2,2) on the fine grid to obtain $h^{n+1/6}$.

c. Apply FDTD(2,2) on the fine grid to obtain $e^{n+1/3}$. Update $e^{n+1/3}$ on the coarse-fine boundary using space and time interpolation. Apply (2.47) to weight $e^{n+1/3}$

one cell inside the fine grid.

d. Apply FDTD(2,2) on the fine grid to obtain $h^{n+3/6}$. Use (2.48) and (2.49) to weight $h^{n+3/6}$ and $H^{n+1/2}$ collocated one coarse grid cell into the fine domain. Transfer all fine grid $h^{n+3/6}$ field values to the corresponding collocated coarse grid $H^{n+1/2}$ in the area shared by both the coarse and fine grids (domain #2) except the fields included in the area described by the black dots (see Fig. 2.65).

e. Update E^{n+1} at the coarse-fine boundary using the obtained values for $H^{n+1/2}$ from step 4.

f. Repeat step 3 to obtain $e^{n+2/3}$, step 2 to obtain $h^{n+5/6}$, and step 3 again to obtain e^{n+1}. Correct the coarse-fine grid boundary values of e^{n+1} using space interpolation of E^{n+1}.

g. Transfer all fine grid e field values to the corresponding collocated coarse grid E field values in the area that is commonly shared by the fine and coarse grids (domain #2).

Capital letters E and H represent coarse grid field values, and small letters e and h represent fine grid field values. It should be pointed out that the space interpolation of the coarse grid values on the coarse-fine boundary is performed using a standard second-order accurate interpolation.

To illustrate the savings that can result in the numerical FDTD analysis of shielding effectiveness by using this new hybrid method some examples are presented. One of the main purposes of this research is to be able to efficiently and accurately analyze the shielding effectiveness of a full-scale fuselage. Results for such analyses will be presented in Chapter 3 where a simplified scaled model of a Boeing 757 aircraft is examined. This scaled model has the following dimensions: 155 cm long by 20 cm wide by 24 cm high. In order to accurately simulate this problem with the standard FDTD(2,2) up to 9 GHz, a cell size of 2.5 mm (or $\lambda/13$ at 9 GHz) has to be used. This mesh yields a very large computational domain; $620 \times 80 \times 96$ cells. This domain requires $M_{FDTD(2,2)} = 114$ Mbytes just for the electric and magnetic field components. Therefore, simulating this problem requires a very large amount of computational resources, memory as well as time. Especially, the memory issue is more restrictive

since if the required memory for a simulation is not available, then the simulation cannot be performed.

However, if the new hybrid method of subgrid FDTD(2,2)/FDTD(2,4) is applied to the same problem, significant savings in memory are achieved. The hybrid applies FDTD(2,4) to the entire fuselage but on a coarse grid with a cell size three times larger than the one required by FDTD(2,2), i.e., a cell size of 7.5 mm (or $\lambda/4$ at 9 GHz). This FDTD(2,4) part of the hybrid code (domains #1 and #2) requires only 4 Mbytes of memory. Furthermore, the subgrid FDTD(2,2) is only applied on a region between the wall of the fuselage and the coarse-fine grid boundary (domain #1 in Fig. 2.65) and has a thickness of only 9 cells. This subgrid FDTD(2,2) part of the hybrid code requires 44 Mbytes of memory. Therefore, the total amount of memory for the hybrid subgrid FDTD(2,2)/FDTD(2,4) method is only M_{hybrid} = 4+44=48 Mbytes which is 2.5 times smaller than the memory required by the standard FDTD(2,2) code (114 Mbytes). This reduction in memory results by not applying FDTD(2,2) along with a fine cell size in the part of the computational domain that solely corresponds to the coarse domain (domain #2 in Fig. 2.65), which would have required M_2^{fine} = 70 Mbytes. Instead, the FDTD(2,4) is applied on the coarse domain using a coarse cell size allocating only M_2^{coarse} = 2.5 Mbytes. The comparison of the specific numerics are illustrated in Table 2.2 where M_1 and M_2 are the memory requirements for domains #1 and #2, respectively.

Table 2.2: Memory requirements for the different regions of the computational domain for a cell size of 2.5 mm

		Hybrid subgrid FDTD(2,2)/FDTD(2,4)	
Memory (Mbytes)	FDTD(2,2)	subgrid FDTD(2,2)	FDTD(2,4)
M_1	70	-	2.5
M_2	44	44	1.5
M_{total}	114	48	
Savings Factor	$114/48 \simeq 2.5$		

The example that was presented exhibited dimensions that were extremely long only in one direction, since the fuselage is a very long rectangular box. However, in cases where the geometry is large in two or in all three directions, then the memory

savings are even more significant. Tables 2.3 and 2.4 show the corresponding memory savings achieved by the hybrid method for two boxes with the following dimensions, respectively: a) 155 cm long by 155 cm wide by 24 cm high (box #1), and b) 155 cm long by 155 cm wide by 155 cm high (box #2). As expected, the memory savings are tremendous when the domains become large in all three directions.

Table 2.3: Memory requirements for the different regions of the computational domain of box #1 for a cell size of 2.5 mm

		Hybrid subgrid FDTD(2,2)/FDTD(2,4)	
Memory (Mbytes)	FDTD(2,2)	subgrid FDTD(2,2)	FDTD(2,4)
M_1	678	-	25.0
M_2	207	207	7.6
M_{total}	885	240	
Savings Factor	$885/240 \simeq 3.7$		

Table 2.4: Memory requirements for the different regions of the computational domain of box #2 for a cell size of 2.5 mm

		Hybrid subgrid FDTD(2,2)/FDTD(2,4)	
Memory (Mbytes)	FDTD(2,2)	subgrid FDTD(2,2)	FDTD(2,4)
M_1	5,236	-	194
M_2	484	484	18
M_{total}	5,720	696	
Savings Factor	$5,720/696 \simeq 8.2$		

The hybrid method of subgrid FDTD(2,2)/FDTD(2,4) that was presented in this section will be validated and applied in Chapter 4 in the context of shielding effectiveness analysis.

Deriving a stable hybrid is a very challenging task. The hybridization procedure, which was outlined above, is the result of long experimentation with different time and space interpolation schemes. For the results presented in this manuscript, the hybrid method was found stable up to several tens of thousands of time-steps for different applications.

Chapter 3

Applications

I. Introduction

The standard second-order accurate FDTD is still a very powerful method especially for problems of moderate electrical size. The FDTD method has exhibited a wide range of applications due to its robustness, simplicity and ability to simulate complex structures. Some of the most important categories of FDTD applications are the following:

- Analysis of microwave circuits and devices [70]-[77]
- Analysis of waveguide structures [78]-[84]
- Analysis of electromagnetic wave interactions with biological tissues [85]-[92]
- Scattering and radar cross section analysis [93]-[96]
- Antenna analysis and design [97]-[102]
- Analysis and design of cavity resonators [103]-[108]

In this chapter, FDTD is applied in antenna problems. Initially, an improved feed model for thin-wire antennas is examined, and it is compared with the delta-gap feed model. Furthermore, the discrete Fourier transform (DFT) is compared to the fast Fourier transform (FFT) in the context of the FDTD method. The pros and cons of these two time-to-frequency domain conversion methods are presented through examples.

Then, cavity-backed slot (CBS) antennas are examined. CBS antennas are commonly used in earth-based and space-borne applications. They are relatively easy to manufacture, lightweight and often small in size. Here, FDTD is used to analyze different antenna characteristics of such elements including input impedance, coupling, and radiation patterns. Emphasis is given on coupling calculations, especially on different methods to reduce coupling.

Specifically, coupling reduction is attempted using lossy material superstrates or ground plane discontinuities, such as slits. Numerical issues concerning the analysis of CBS antennas in the context of FDTD are also discussed. Moreover, the effect of distance and orientation on coupling is examined through FDTD simulations and measurements. All the different coupling reduction techniques are compared through their radiation characteristics, such as gain, efficiency and coupling reduction. The numerical results are validated by comparison with measurements and few available finite element method (FEM) calculations.

II. An Improved FDTD Feed Model for Thin-Wire Antennas

A wire antenna is one of the most common radiating elements. In FDTD, wire antennas are usually excited by using a delta-gap. Furthermore, wire antennas exhibit radius much smaller than the cell size and a thin-wire model is needed to model it correctly. However, until now a thin-wire model has been used to simulate the radius only along the wire but not at the feed point. In a recently published paper [109], a thin wire model at the feed point was implemented, and it was illustrated that this modeling together with the standard thin-wire modeling along the element gives more accurate results. This thin-wire model at the feed-point is examined here and compared to the delta-gap source.

A. Delta-gap source

The standard delta-gap source imposes a voltage by using the electric field located at the feed point which is specified by the following equation (assuming that the wire is

located along the z-direction):

$$E(gap) = -\frac{V(t)}{\Delta z} \tag{3.1}$$

where $V(t)$ is the desirable voltage source and Δz is the cell size in the direction of the gap. Fig. 3.1 illustrates this type of source. The magnetic fields around the

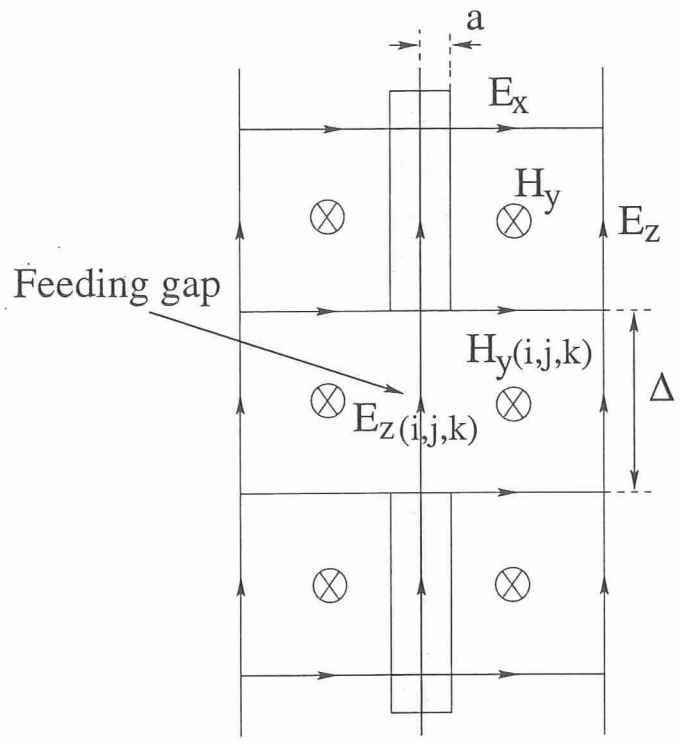

Figure 3.1: The delta-gap source model.

gap are updated using the electric field which imposes the source. For example, by substituting (3.1) into the regular FDTD update equations, the magnetic field component H_y located at the right side of the gap can be written as

$$H_y|_{i,j,k}^{n+1/2} = H_y|_{i,j,k}^{n-1/2} + \frac{\Delta t}{\mu}\left(\frac{E_z|_{i+1,j,k}^{n} + V^n/\Delta z}{\Delta x} - \frac{E_x|_{i,j,k+1}^{n} - E_x|_{i,j,k}^{n}}{\Delta z}\right) \tag{3.2}$$

The other magnetic field components surrounding the delta-gap are updated in a similar way.

To examine the accuracy of the delta-gap feed modeling, the input impedance of two dipole antennas was computed by FDTD and it is compared with NEC computations. Both dipoles had length ℓ which was varied in terms of wavelength in the

range $\lambda/10 \leq \ell \leq 2\lambda$. The first dipole had a radius $a = \ell/500$ whereas the second one had a radius $a = \ell/150$. The radius of each dipole was simulated in FDTD by using the thin wire model along each element. FDTD calculations were performed for different discretizations $\Delta = \ell/11,\ \ell/21,\ \ell/41,\ \ell/81$. The Moment-Method [110] (NEC) simulations used, 255 segments along the wire with radius $a = \ell/500$ in one case, and 71 segments along the wire with radius $a = \ell/150$ in the other case.

The results are compared in Figs. 3.2 and 3.3 for the two dipoles, respectively. It can be concluded that the accuracy of the input impedance predicted by using this delta-gap source depends on the cell size. Notice also that a finer discretization does not always result in higher accuracy. For the dipole with radius $a = \ell/500$, $\Delta = \ell/81$ seems to provide the best agreement with the NEC, whereas for the dipole with radius $a = \ell/150$, $\Delta = \ell/21$ gives the best results. This observation will be explained in the next section after the presentation of the improved delta-gap feed.

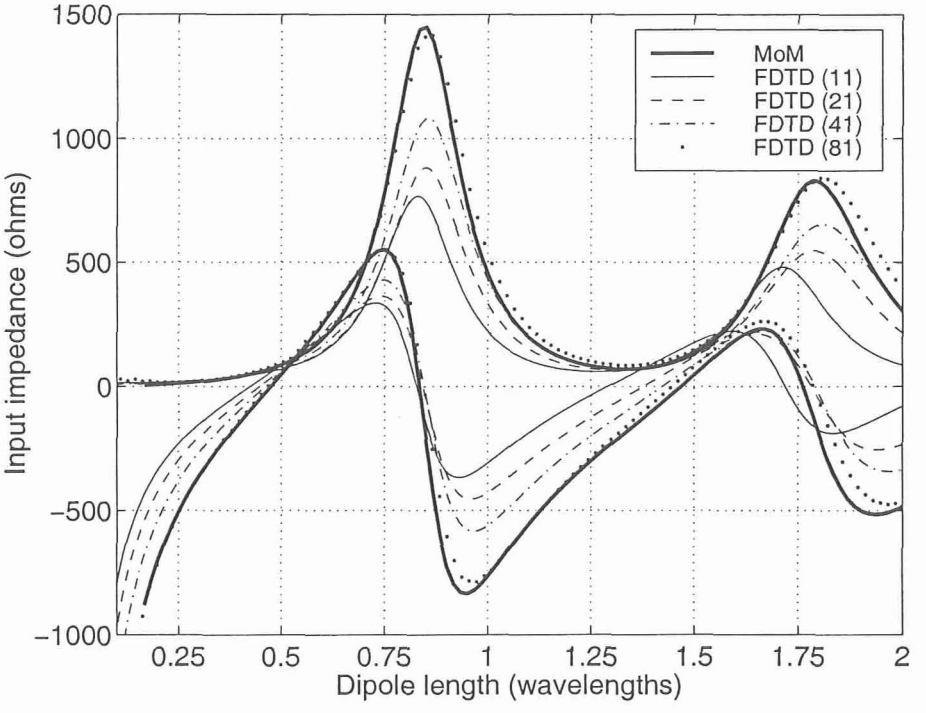

Figure 3.2: Input impedance of a thin wire dipole with radius $a = \ell/500$.

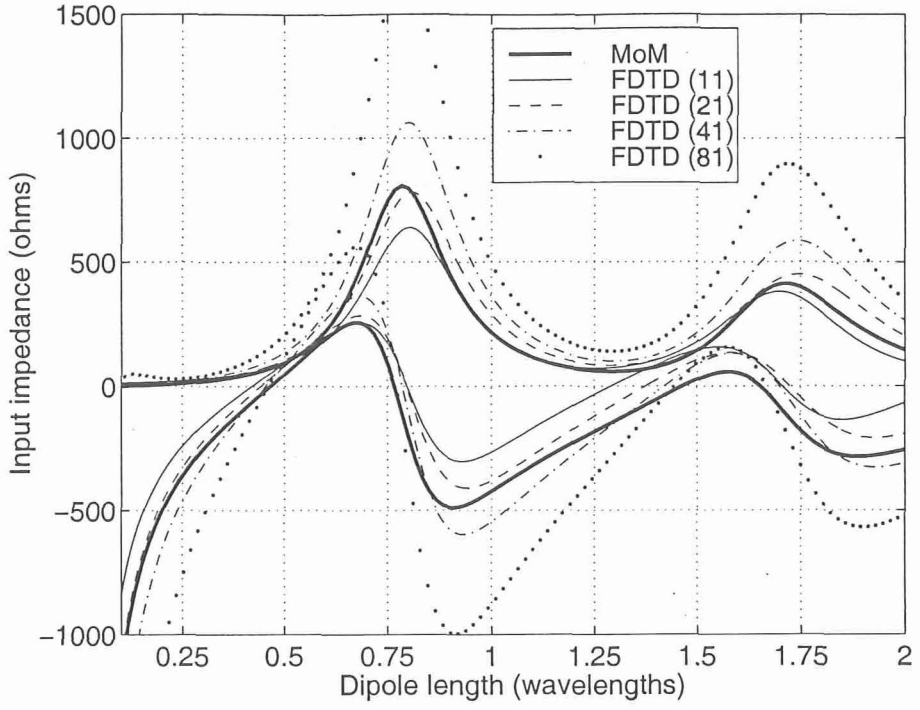

Figure 3.3: Input impedance of a thin wire dipole with radius $a = \ell/150$.

B. Improved delta-gap source

In the paper by Watanabe et al. [109] an improved delta-gap model was proposed that takes into account the radius of the wire antenna at the feed point. Their idea is based on the standard FDTD thin wire model. Therefore, before presenting their modeling, the thin wire model will be briefly discussed.

Fig. 3.4 demonstrates a PEC wire of radius a superimposed on a Yee grid and aligned with the z-axis. The assumption that the wire radius is much smaller than 0.5 Δx was made. Furthermore, since Δx must be much smaller than the wavelength in order for the FDTD algorithm to be stable, the wire radius should also be smaller than the wavelength. This justifies the assumption that the radial electric and circumferential magnetic fields in the vicinity of the wire exhibit a 1/r dependence. With the above assumptions, the spatial dependence of the fields in the vicinity of the wire can be approximated as

$$H_y(r, j, k) \simeq H_y(i, j, k)\frac{\Delta x}{2r} \tag{3.3}$$

$$E_x(r, j, k) \simeq E_x(i, j, k)\frac{\Delta x}{2r} \tag{3.4}$$

$$E_x(r, j, k+1) \simeq E_x(i, j, k+1)\frac{\Delta x}{2r} \tag{3.5}$$

$$E_z(i, j, k) = 0 \tag{3.6}$$

$$E_z(i+1, j, k) = \text{constant} \tag{3.7}$$

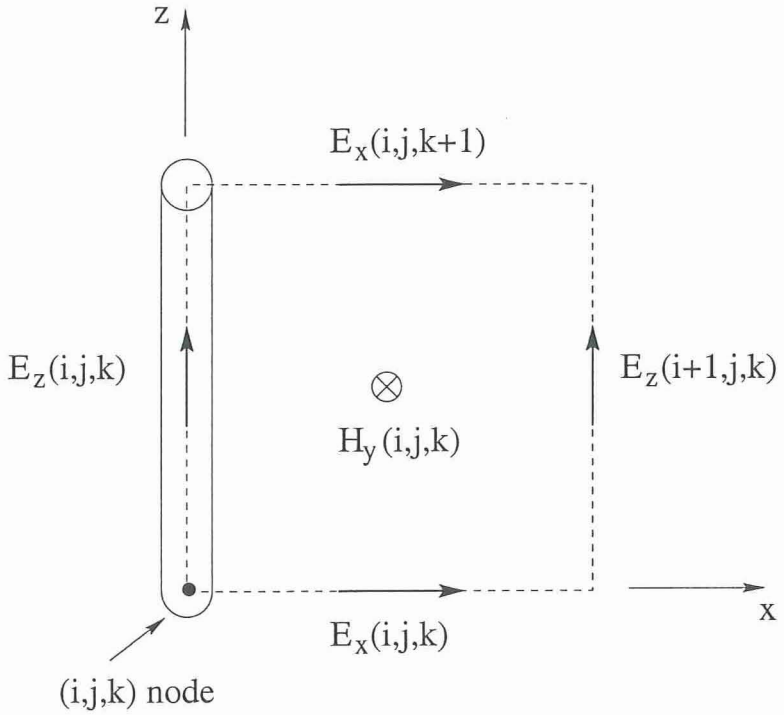

Figure 3.4: Field locations and geometry for the sub-cell model of a thin wire.

Applying the integral form of Faraday's law to the contour path which passes through the four electric field locations yields

$$0 + \int_a^{\Delta x} E_x(i, j, k+1)\frac{\Delta x}{2r}dr - E_z(i+1, j, k)\Delta z - \int_a^{\Delta x} E_x(i, j, k)\frac{\Delta x}{2r}dr$$

$$= -\mu\Delta z\frac{\partial}{\partial t}\int_a^{\Delta x} H_y(i, j, k)\frac{\Delta x}{2r}dr \tag{3.8}$$

After carrying out the integrations, (3.8) reduces to

$$\frac{\Delta x}{2}\ln\left(\frac{\Delta x}{a}\right)E_x(i,j,k+1)-\frac{\Delta x}{2}\ln\left(\frac{\Delta x}{a}\right)E_x(i,j,k)-E_z(i+1,j,k)\Delta z$$

$$=-\frac{\mu\Delta x\Delta z}{2}\ln\left(\frac{\Delta x}{a}\right)\frac{\partial H_y(i,j,k)}{\partial t} \quad (3.9)$$

Discretizing the magnetic field time derivative and rearranging the terms gives the modified update equations for the H_y field components circulating a z-directed wire; i.e.,

$$H_y|_{i,j,k}^{n+1/2} = H_y|_{i,j,k}^{n-1/2}+\frac{\Delta t}{\mu}\left(\frac{E_z|_{i+1,j,k}^{n}}{\frac{\Delta x}{2}\ln\left(\frac{\Delta x}{a}\right)}-\frac{E_x|_{i,j,k+1}^{n}-E_x|_{i,j,k}^{n}}{\Delta z}\right) \quad (3.10)$$

The improved delta-gap feed modeling can be derived by applying again the integral form of Faraday's law in a similar way. By noticing that the integration along the edge where $E_z(i,j,k)$ coincides should be equal to the voltage source V [and not zero as in (3.8)], the update equation for the magnetic field beside the delta-gap source takes the form

$$H_y|_{i,j,k}^{n+1/2} = H_y|_{i,j,k}^{n-1/2}+\frac{\Delta t}{\mu}\left(\frac{E_z|_{i+1,j,k}^{n}+V^n/\Delta z}{\frac{\Delta x}{2}\ln\left(\frac{\Delta x}{a}\right)}-\frac{E_x|_{i,j,k+1}^{n}-E_x|_{i,j,k}^{n}}{\Delta z}\right) \quad (3.11)$$

This equation provides a more accurate delta-gap excitation as it takes into account the radius of the wire at the feed point. Similar equations to (3.11) can be easily derived for the other magnetic field components surrounding the source edge.

In order to illustrate the accuracy of this source modeling, the same dipoles as the ones analyzed in the previous subsection were examined by using the same FDTD parameters. Notice that in this case the radius of the wire was simulated along the wire using the thin wire model, and also at the feed point using the improved delta-gap source described by (3.11). The results of these computations are shown in Figs. 3.5 and 3.6 and compared with the NEC predictions. It is apparent that the new delta-gap modeling yields input impedances that do not depend on the cell size as strongly as the results of the standard delta-gap source, and then agree very well with the MoM computations.

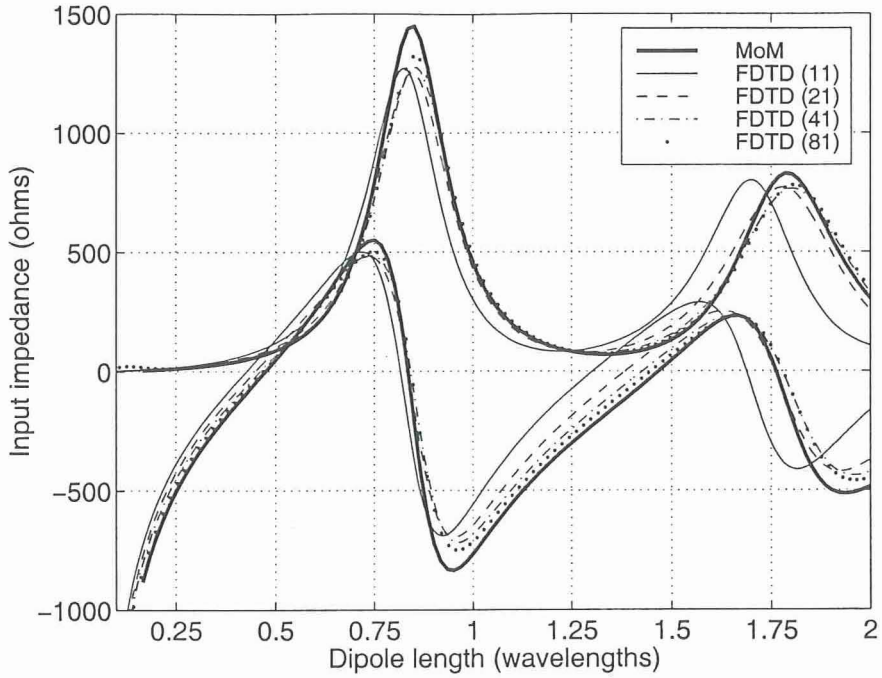

Figure 3.5: Input impedance of a thin wire dipole with radius $a = \ell/500$.

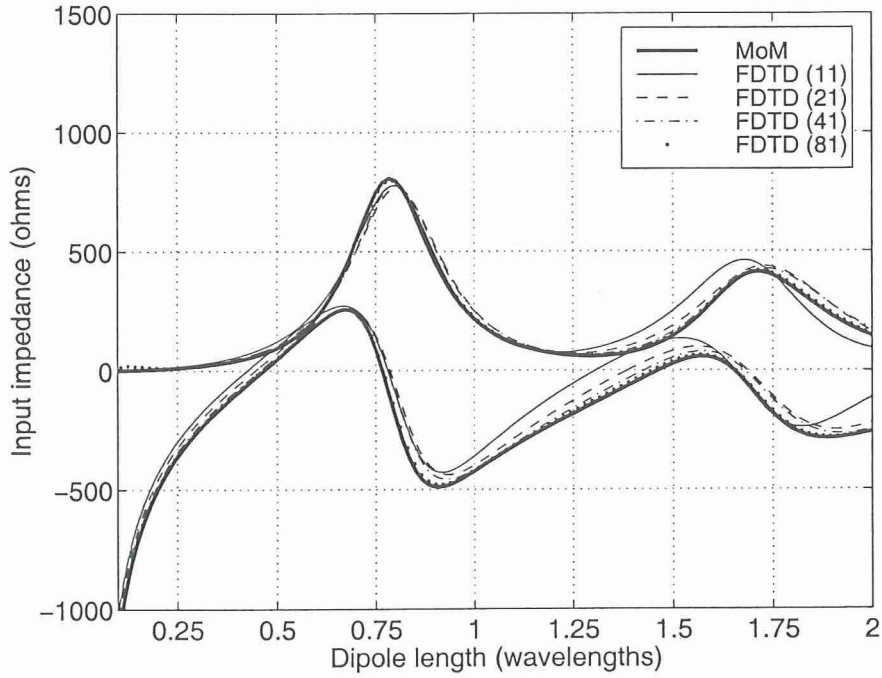

Figure 3.6: Input impedance of a thin wire dipole with radius $a = \ell/150$.

By comparing now the two delta-gap feed models described by (3.2) and (3.11), respectively, it is seen that the only difference is the coefficient $2/\ln(\Delta x/a)$ on the denominator of the first fraction of (3.11), which does not exist in (3.2). Therefore, this coefficient is assumed to be unity in (3.2), and this condition can give us an effective radius that is simulated by the delta-gap model of (3.2)

$$\frac{2}{\ln\left(\frac{\Delta x}{a_{eff}}\right)} = 1 \Rightarrow a_{eff} = \frac{\Delta x}{e^2} \simeq 0.135\Delta x \tag{3.12}$$

Table 3.1 gives the effective radius for the different discretizations. It is expected that when the effective radius is close to the actual radius of the wire, the most accurate results will be obtained. This is verified by the observations made in the previous section where the best accuracy in the impedance calculations was observed for the cell size $\Delta = \ell/81$ for the wire with radius $a = \ell/500$ and for the cell size $\Delta = \ell/21$ for the wire with radius $a = \ell/150$. Therefore, in cases where the improved delta-gap source is not used, the cell size should be chosen such that it yields an effective radius equal to the actual radius of the wire.

Table 3.1: Effective radius for the input impedance calculations

Δ	$\ell/11$	$\ell/21$	$\ell/41$	$\ell/81$
a_{eff}	$\ell/81.3$	$\ell/155$	$\ell/303$	$\ell/599$

III. Discrete Fourier Transform

Although it is widely believed that FFT is faster than DFT, this is not always true, especially for FDTD applications. The DFT series summation is given by

$$G(f) = \Delta t \sum_{n=0}^{N} g(n\Delta t)\ e^{-j2\pi f n\Delta t} \tag{3.13}$$

where $g(n\Delta t)$ is a time-domain response at discrete time instants $t = n\Delta t, n = 0, .., N$, $G(f)$ represents the Fourier transform of $g(t)$ at frequency f, and Δt is the time-step. This summation is updated at every FDTD time-step and is often called "on the fly

DFT". Therefore, it is not necessary to store the entire time history. On the other hand, FFT requires storage of the complete time history of the fields of interested. This is a major disadvantage of FFT for some FDTD applications.

A thorough comparison of the DFT and FFT in the context of FDTD was presented in [111]. Here, the pros and cons of these two time-to-frequency domain conversion methods are briefly outlined. Suppose that the cell size in a FDTD simulation is chosen according to the rule of thumb of being at least a tenth of wavelength at the maximum frequency of interest, $\Delta x = \lambda_{min}/10 = c/(10 f_{max})$. The time-step is taken to be $\Delta t = \Delta x/(2\ c)$ for stability of the algorithm, yielding $\Delta t = 1/(20 f_{max})$. Therefore, FFT computes the response up to frequencies 20 times larger than the one accurately modeled by FDTD. On the contrary, DFT computes the response only at the frequencies of interest, thereby eliminating this waste of resources.

Another important advantage of DFT over FFT is its ability to compute the transform at any frequency whereas FFT is limited to the choice of frequencies. The efficiency of FFT is based on the fact that the number of time-domain samples, N, must be a power of an integer. In particular, the very popular radix-2 FFT assumes that $N = 2^n$, and this in a way limits the frequencies that can be obtained. Suppose that a monopole antenna is under examination and the frequencies of interest are 300 MHz and 305 MHz. Therefore, the number of points, N, that the FFT will use, must be chosen so that the results will exhibit a 5 MHz frequency resolution. For a cell size of 25 mm, the time-step is 4.8 ps and $N = 4096$. The FFT for such a discretization gives results at 299.31 MHz and 304.38 MHz approximating the frequencies of interest, which are 300 MHz and 305 MHz, respectively. On the contrary, DFT provides calculations at the exact frequencies of interest. Furthermore, the number of time-steps needed for the FDTD simulation transients to decay to zero is usually smaller than the required number of samples by the FFT to give certain frequency resolution. For the previous example of the monopole antenna, the required FDTD simulation time is 1000 time-steps, and thus the DFT will only use so many samples, whereas the FFT, as it was explained above, has to use at least 4096 time-domain values for a frequency resolution of 5 MHz. Consequently, the DFT is proven again more efficient.

As far as memory requirements, the DFT as already mentioned above, does not

need to store the entire time-history of the fields thereby yielding significant saving in memory. In order to compute patterns at multiple frequencies, the fields at the equivalent surface are needed. For the monopole antenna example discussed previously with a computational domain of $50 \times 50 \times 20$ cells, the entire time history (4096 samples) of the fields at 9000 locations on the equivalence surface is required when the FFT is used. This amount of memory is 700 times larger than the one required by FDTD and 4096 times larger than the one used by the DFT. Obviously, the FFT memory requirements are enormous compared to the memory allocated by FDTD, discouraging its use in pattern computations.

In summary, DFT is more efficient than FFT and requires far less additional storage. Moreover, the frequency resolution of the FFT is controlled by the number of time samples whereas the DFT can provide results at the precise frequencies of interest.

In order to verify the implementation of the DFT for pattern computations, the monopole antenna problem discussed above was analyzed. The length of the monopole was 0.25 m or quarter wavelength at 300 MHz. One pulse simulation was executed and patterns were calculated using the newly implemented DFT at 300, 450 and 600 MHz. Also, single frequency simulations were run at each of these frequencies to provide a reference for comparison. The results are illustrated in Figs. 3.7-3.9. It can be clearly seen that the DFT yielded identical patterns with the single frequency calculations. This new feature is very useful and efficient, because it can compute patterns at as many frequencies are needed only in a single simulation.

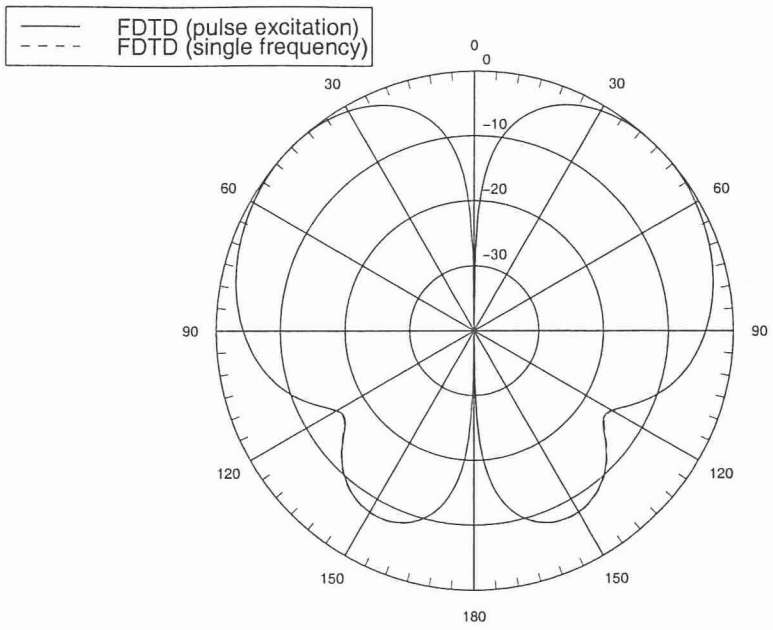

Figure 3.7: Elevation radiation pattern of a monopole mounted on a rectangular ground plane at 300 MHz.

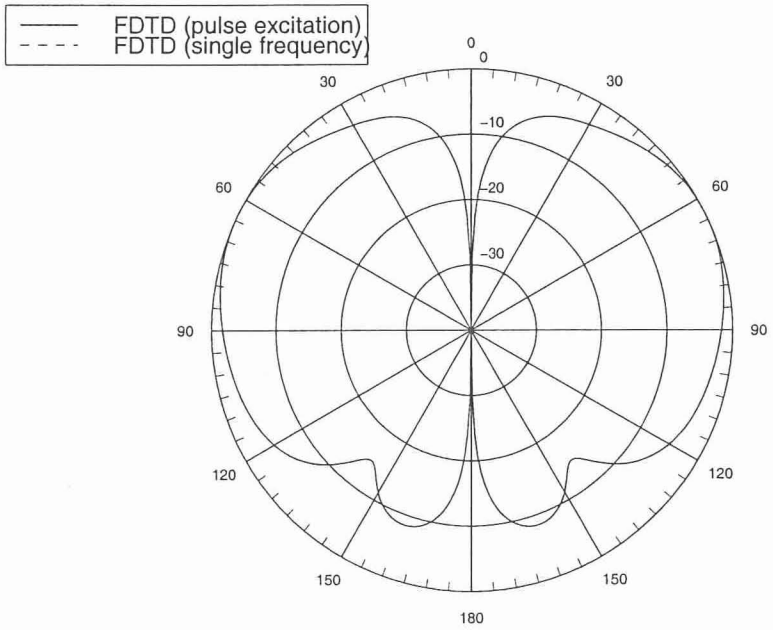

Figure 3.8: Elevation radiation pattern of a monopole mounted on a rectangular ground plane at 450 MHz.

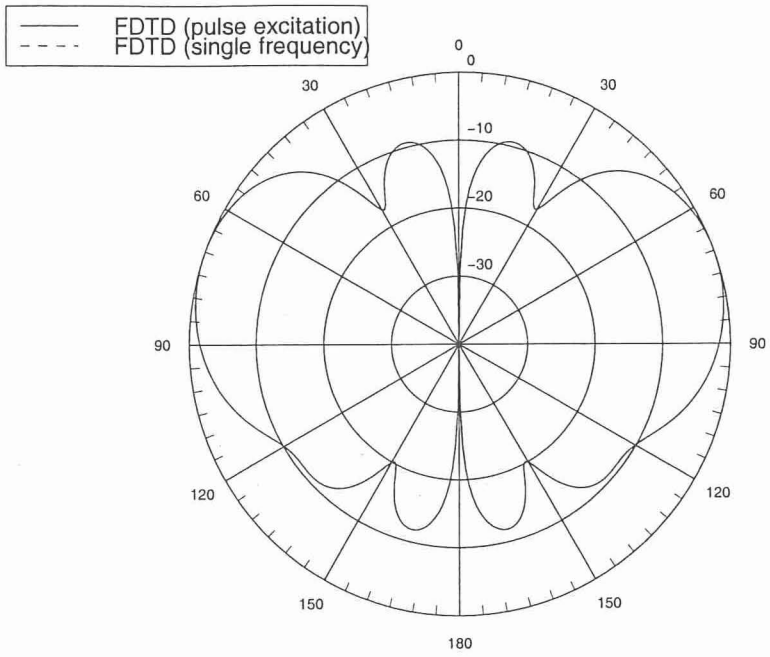

Figure 3.9: Elevation radiation pattern of a monopole mounted on a rectangular ground plane at 600 MHz.

IV. Analysis of Cavity-Backed Slot Antennas

Cavity-backed slot (CBS) antennas have been widely used in different types of applications within the microwave band, including radars, satellite communications, mobile telephony, broadcast TV, and aircraft/spacecraft communications. They are relatively easy to manufacture, lightweight and often small in size. Their low profile is an important characteristic, especially for aircraft, missile and spacecraft applications, because they can be flush-mounted on the surface of airborne vehicles without affecting the vehicle's aerodynamic profile.

Coupling is an important factor in today's communication systems which have become more complex and use a large number of antennas to support all required services. The reliability and integrity of communication systems can be significantly affected by coupling between transmitting and/or receiving elements, that are mounted on the same structure such as a helicopter or an aircraft airframe. Especially when several antennas are collocated on the same structure of finite dimensions, interac-

tion, referred to as *cosite interference*, can deteriorate the quality of communications and corrupt the signals with noise. This leads to an extremely critical EMI/EMC problem. In addition, airborne communications require extremely reliable systems that sustain continuous operation without jamming or interruption. In such airborne communication systems, the installation of a new antenna appears to be a challenging task. Its mounting location is influenced not only by the type of service the antenna will provide, but also by the mounting locations of the already existing antennas on the airframe. Therefore, the interaction between the new antenna and other radiating elements should be analyzed in order to optimize its position, such that coupling satisfies specific requirements. It can be concluded that coupling mechanisms are very important in the design of reliable communication systems.

Cavity backed slot antennas have been analyzed in numerous papers using different methods. Two of the early efforts to analyze such antennas were presented by Calejs in [112] and by Adams in [113]. The equivalence principle along with the generalized network formulation have been used in [114] to form the integral equation for a CBS antenna which was then solved by a method of moments formulation. The finite-difference time-domain (FDTD) method was applied to the analysis of a single CBS antenna by Omiya et al. [115]. Furthermore, coupling between two CBS antennas was examined in [116] using FDTD combined with the Kirchhoff transformation. However in this section, although using FDTD, the various issues related to computational time and accuracy, are discussed and resolved using appropriate modeling. Furthermore, calculations are performed to examine the dependence of coupling on the frequency of operation. In addition, coupling reduction techniques are also presented including incorporation of lossy superstrates and ground plane slits.

Lossy materials have been used to suppress the surface currents induced in conducting bodies and reduce the radar cross section of structures, such as airplanes or antennas. In [117] a lossy coating was used to suppress the undesirable side-lobes of a paraboloidal reflector antenna. Also, lossy materials have been used in the design of horn antennas to improve side-lobe levels, equalize the E- and H-plane radiation patterns and reduce the cross-polarized radiation [118]-[121]. In [122] the contour path FDTD was used to analyze pyramidal horn antennas with and without composite E-plane inner walls. Planar and cylindrical arrays of open-ended waveguides have been

analyzed in the presence of a lossy ground in [123]. In [124] the radiation of a rectangular waveguide mounted on a lossy flange was examined, and it was shown that the lossy flange improves the E-plane radiation pattern as well as the cross-polarized radiation. Here, lossy superstrates are used to suppress surface currents and reduce coupling between antennas that are flush-mounted on a ground plane. Moreover, the effect of distance and orientation on coupling is examined through FDTD simulations and measurements. All the different coupling reduction techniques are compared through their radiation characteristics, such as gain, efficiency and coupling reduction. The numerical results are validated by comparison with measurements and few available finite element method (FEM) calculations.

A. FDTD modeling

FDTD analysis of electromagnetic problems usually involves post-processing that transforms the time-domain data to the frequency domain. This transformation is performed using a discrete Fourier transform (DFT) procedure. However, in order for the DFT to give accurate results, the FDTD simulation time must be chosen long enough for all the transient phenomena to decay. This requirement can be restrictive, especially in highly resonant and high quality factor (Q) structures where the transients may need a prohibitive simulation time to decay. A very effective technique that resolves this problem is based on a source with an internal resistance which provides the excitation [97],[125],[126]. The basic characteristics of FDTD are well documented and will not be repeated here. Instead, the emphasis will be placed on the modeling of the cavity-backed slot antennas, their radiation characteristics, and coupling reduction techniques.

In order to illustrate the effectiveness of a voltage source with an internal resistance, it was decided to compute the input impedance of an air-filled cavity-backed slot antenna originally analyzed in [127]. A three-dimensional (3-D) view of the cavity under consideration is exhibited in Fig. 3.10, and a detailed description of the geometry is shown in Fig. 3.11. Notice that the CBS antenna is formed by an open-ended standard X-band waveguide. The input impedance of the cavity-backed slot antenna was measured in the Electromagnetic Anechoic Chamber facility at Arizona State University. In the experiment, the aperture antenna was mounted on a finite

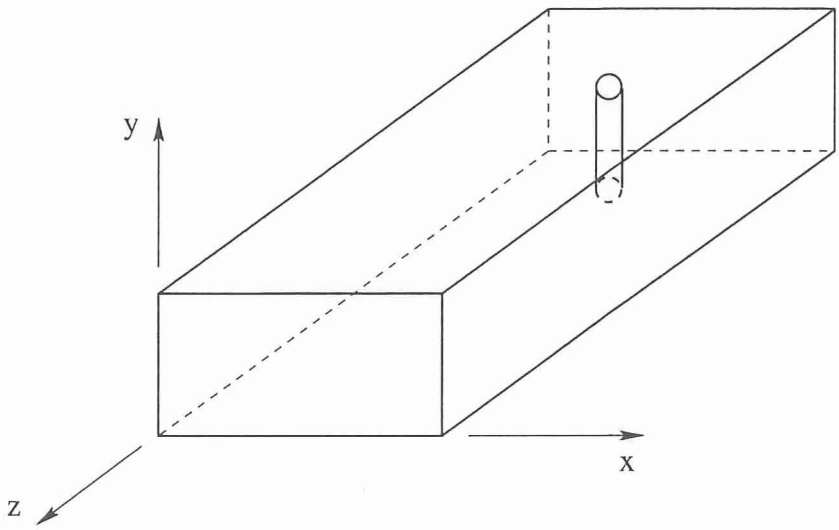

Figure 3.10: A three-dimensional view of an air-filled rectangular cavity-backed slot antenna fed with a probe oriented in the y-direction.

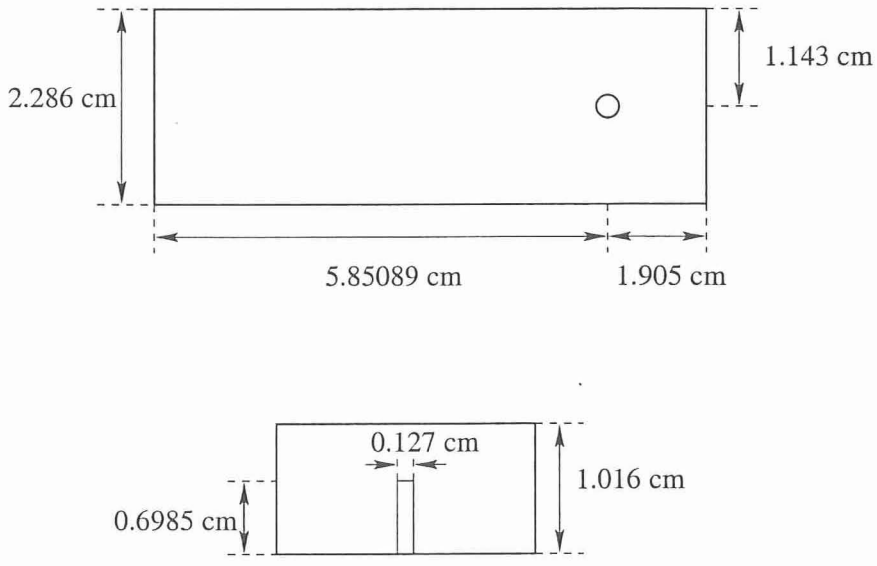

Figure 3.11: A two-dimensional view of an air-filled rectangular cavity-backed slot fed with a probe oriented in the y-direction.

ground plane of dimensions 24 × 24 in (60.96 × 60.96 cm), and the sharp edges were covered with a strip of absorbing material to reduce diffractions (see Fig. 3.12). Additionally, the antenna was rotated at an angle with respect to the principal axes and offset, relative to the center of the ground, to direct the edge diffractions away from the aperture. Moreover, the input impedance of the same aperture mounted on an infinite ground plane was calculated in [127] using a hybridization of the Finite Element Method (FEM) with the Moment Method (MoM) and compared very well with measurements. In this report, it was shown that the dimensions of the ground plane do not have a profound effect on the value of the input impedance.

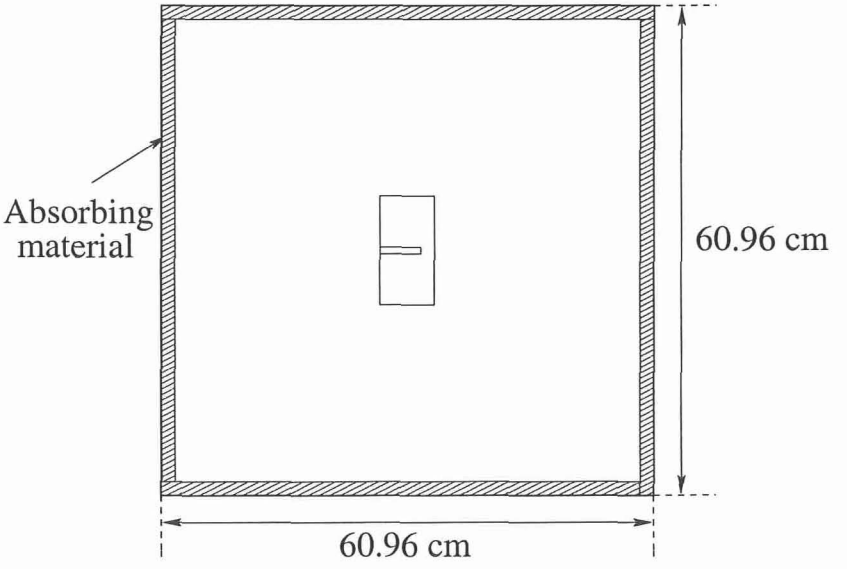

Figure 3.12: A top view of a cavity-backed slot mounted on a ground plane (experimental configuration).

In the FDTD simulations, this aperture antenna was mounted on a 9 × 9 cm finite ground plane, which is smaller than the one used in the measurements to reduce the size of the computational space. In order to determine the input impedance of the antenna, the voltage and current at the feeding probe of the cavity-backed slot antenna have to be computed. The simulation time should allow the transient effects in both the voltage and current to decay, so that they can be accurately Fourier transformed. The voltage is a user defined function of time that decays quickly to zero, whereas the current may need a long time to decay. Two FDTD simulations were performed,

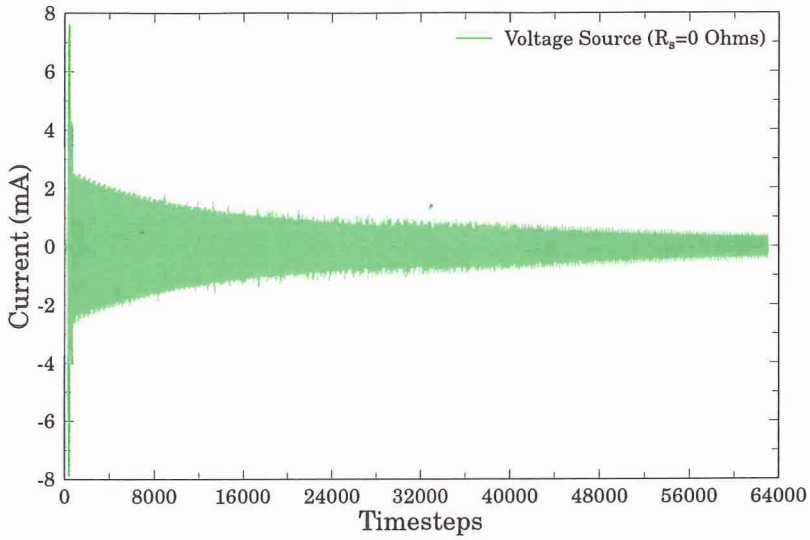

Figure 3.13: Current of the probe exciting the cavity-backed slot antenna for a resistance $R_s = 0$

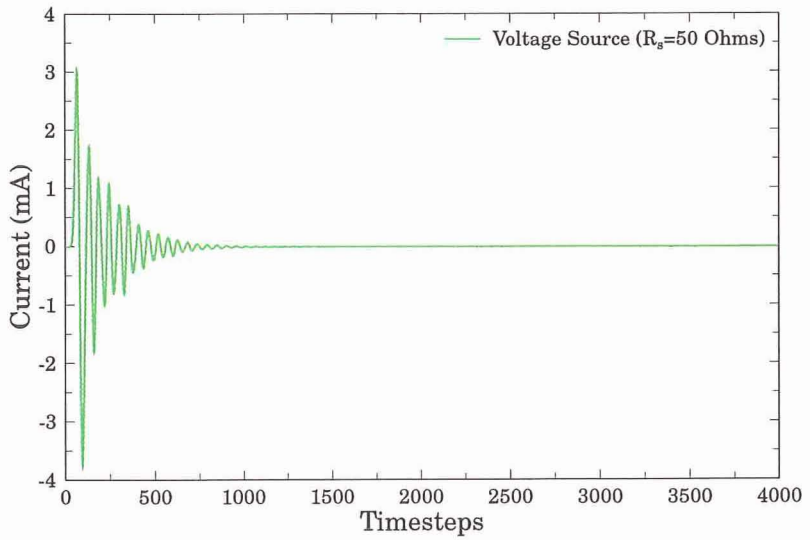

Figure 3.14: Current of the probe exciting the cavity-backed slot antenna for a resistance $R_s = 50$ ohms

and for both the cell size was 1.5 mm. In the first case, the voltage source had zero internal resistance ($R_s = 0$), and in the second case, R_s was set equal to 50 ohms. Figs. 3.13 and 3.14 show the computed current at the probe exciting the cavity for the two cases, respectively. Obviously, the current in the case with no internal resistance ($R_s = 0$) did not decay to zero even after 64,000 time steps, indicating the resonant behavior and the high quality factor, Q, of the antenna. On the contrary, in the second simulation ($R_s = 50$ ohms), the source current converged to zero very fast and the FDTD calculation time reduced significantly. Based on our experience, the use of an internal resistance is essential for efficient simulations of CBS antennas. The internal resistance is usually chosen close to the characteristic impedance of the transmission line and the larger it is, the faster the transient phenomena decay. However, the internal resistance cannot be chosen very large since it may lead to instabilities due to the interaction of the source with the numerical scheme or due to the neglect of the displacement current through the FDTD cell which includes the source [126].

B. Impedance

In order to examine the accuracy of FDTD results which are computed using a source with an internal resistance, the input impedance of the CBS antenna examined in Subsection A. was computed for three different cases. In all the cases, the feeding probe was excited by a voltage source with R_s equal to 50 ohms. In the first case, the radius of the probe (0.0635 cm) was not modeled and the cell size was 1.5 mm. In the second case, the radius was taken into account by using the thin-wire model and the cell size was 1.5 mm. In the third case, the cell size was 0.6 mm, and the probe itself was discretized along with the remaining geometry (see Fig. 3.15). Fig. 3.16 illustrates the computed input resistance and reactance of the aperture antenna for the three different cases. Also, the FDTD calculations are compared with measurements as well as with results obtained by the FEM/MoM hybrid formulation reported in [127]. Evidently, the accuracy of the FDTD predictions depends greatly on the wire modeling of the probe that excites the antenna. Excellent agreement between the FDTD computations and measurements is observed in the case where the probe was discretized (third case). The improved accuracy of this third FDTD simulation can be attributed to the finer discretization and the enhanced modeling of the probe.

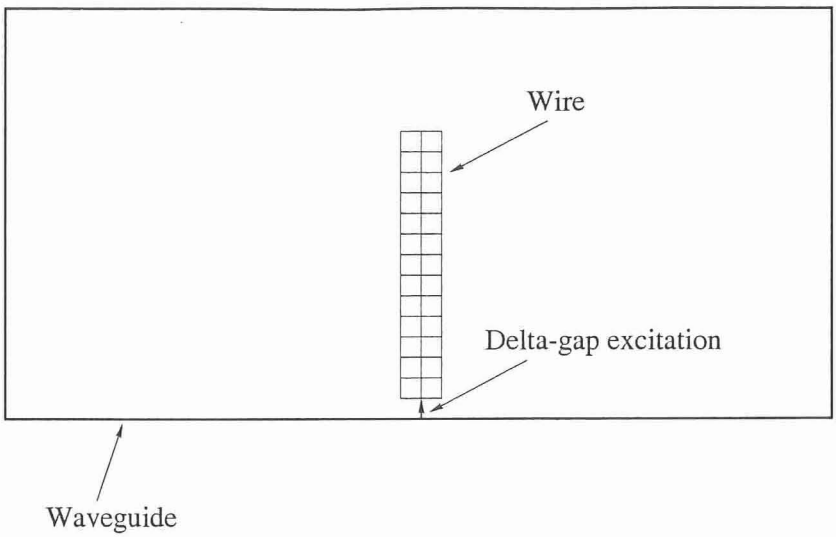

Figure 3.15: Cross-section of the FDTD mesh of the CBS antenna for a cell size of 0.6 mm.

C. Coupling

The coupling between two identical cavity-backed slot antennas (whose specifications are defined in Fig. 3.11) mounted on a rectangular 10×6 cm ground plane, 25 mm apart from each other, was also analyzed. The geometry of the two cavities along with the dimension specifications are shown in Fig. 3.17. FDTD simulated the physical dimensions of the finite ground plane whereas the FEM/MoM hybrid method simulated an infinite ground plane.

The S parameters of the two antennas were calculated using both methods; FDTD and FEM. S_{11} and S_{22} correspond to the reflection coefficient of each antenna, and they are equal because the two antennas are identical and the geometry is symmetrical. Furthermore, S_{12} and S_{21} correspond to the coupling between the antennas, and they are also identical due to reciprocity. The numerical results of both methods are compared with measurements in Fig. 3.18, and they all exhibit very good agreement. The discrepancies at the higher end of the band are attributed to discretization errors. In these simulations the FEM mesh consisted of 75,874 elements with average edge size 0.16 cm whereas the FDTD used a cell size of 0.6 mm and a computational domain of $160 \times 160 \times 142$ cells. Notice that two different FDTD methods were used. The first one, denoted as FDTD(2,2), represents a second-order accurate FDTD both

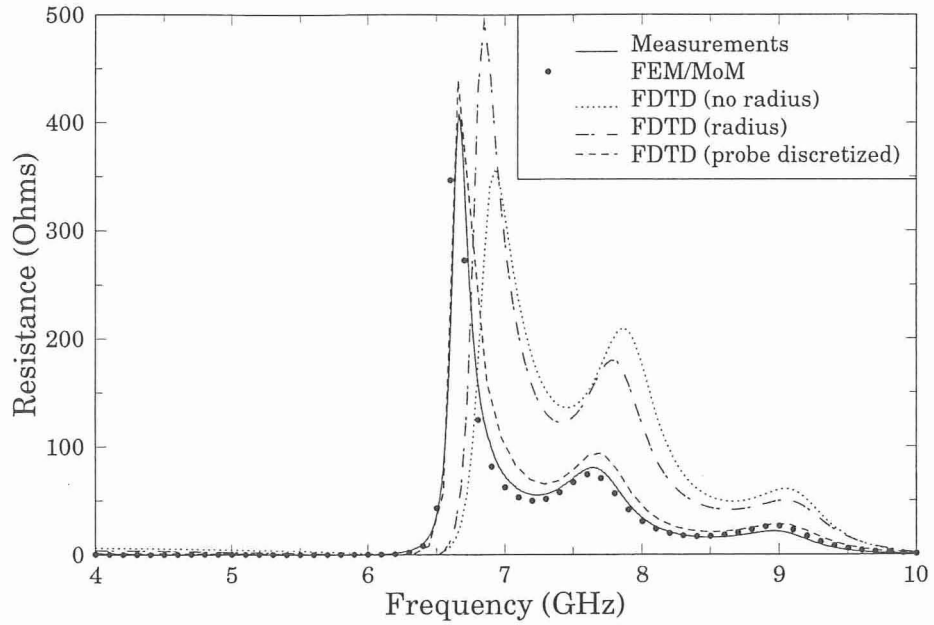

(a)

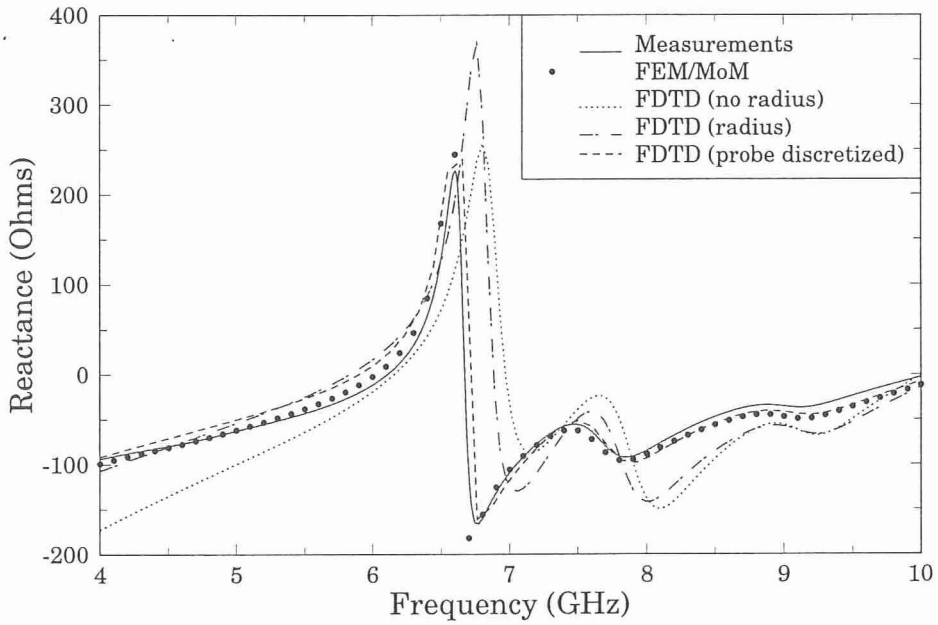

(b)

Figure 3.16: Input impedance of a cavity-backed slot antenna. (a) Resistance. (b) Reactance.

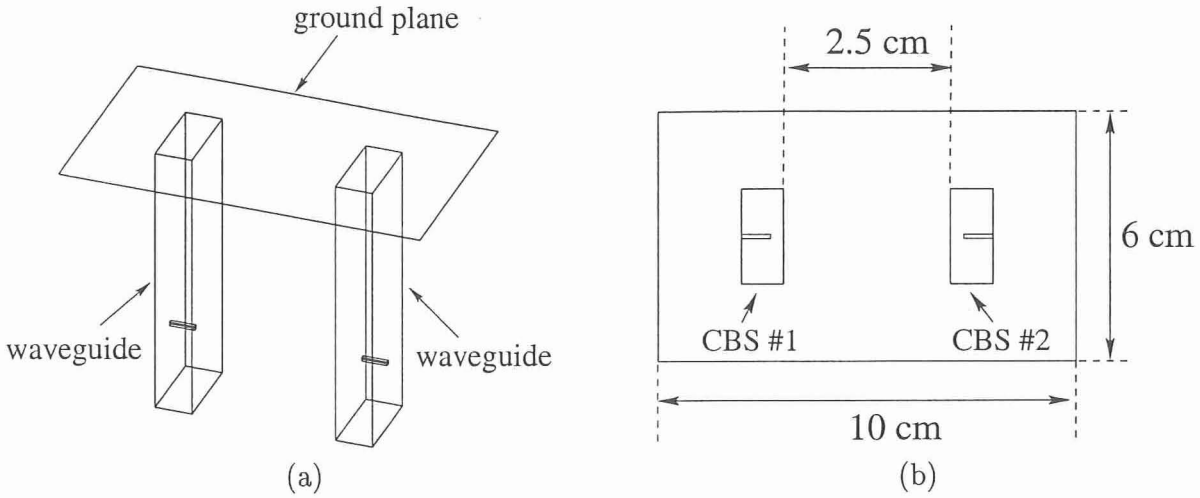

Figure 3.17: Geometry of two identical cavity-backed slot antennas mounted on a rectangular ground plane (for antenna specifications see Fig. 2). (a) 3-D view. (b) Top view.

in time and space. The second one, denoted as FDTD(2,4), represents a second-order accurate in time and and fourth-order accurate in space FDTD. It can be observed that the FDTD(2,4) scheme does not provide a dramatic improvement in accuracy compared to the FDTD(2,2) scheme. However, it is expected that as the distance between the two apertures becomes large in terms of the wavelength, FDTD(2,4) should outperform FDTD(2,2).

D. Reduction of coupling

In this subsection, different methods of coupling reduction are examined. The geometry under examination is shown in Fig. 3.19. The separation between the two apertures of the CBS antennas is 4 cm, and the space between the two apertures is covered with a superstrate. Initially, coupling was calculated using FDTD without any superstrate, and this case is labeled "blank" for reference purposes. Then a superstrate of lossy material was placed on top of the ground plane, filling the space between the two apertures. The superstrate was constructed using a number of layers of 1.5 mm thick ECCOSORB GDS electric/magnetic composite material. Three different superstrates were used with thicknesses of 1.5, 3.0, and 4.5 mm consisting of one, two or three GDS material layers, respectively. Coupling computations were again

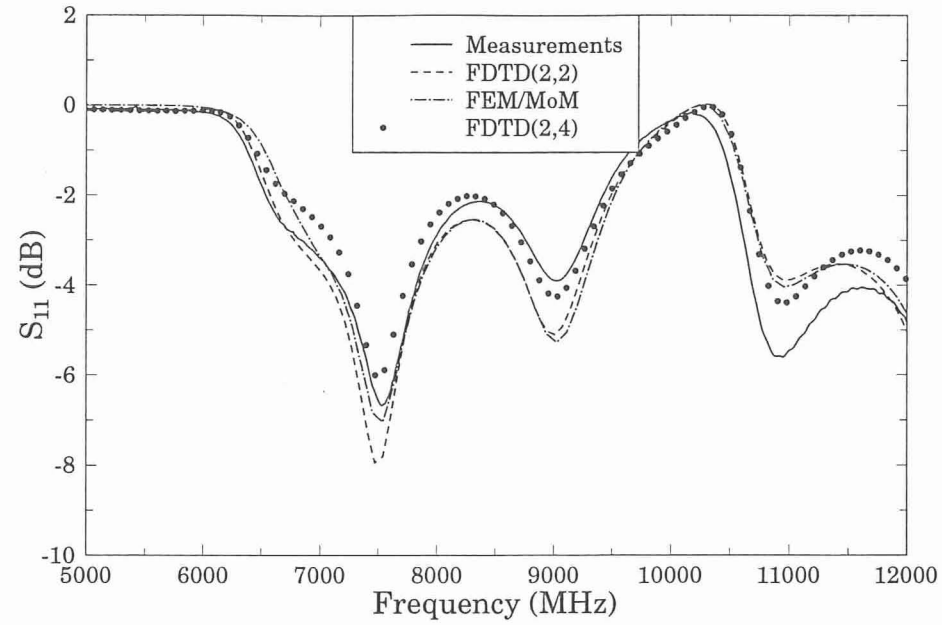

(a)

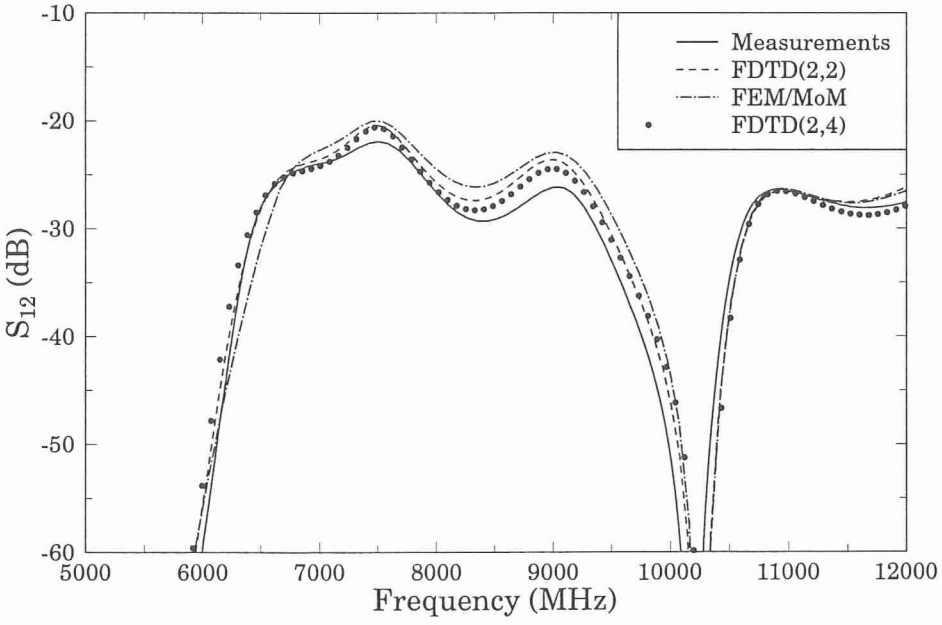

(b)

Figure 3.18: S-parameters of two identical cavity-backed slot antennas mounted on a rectangular ground plane (for antenna specifications see Figure 1.4).

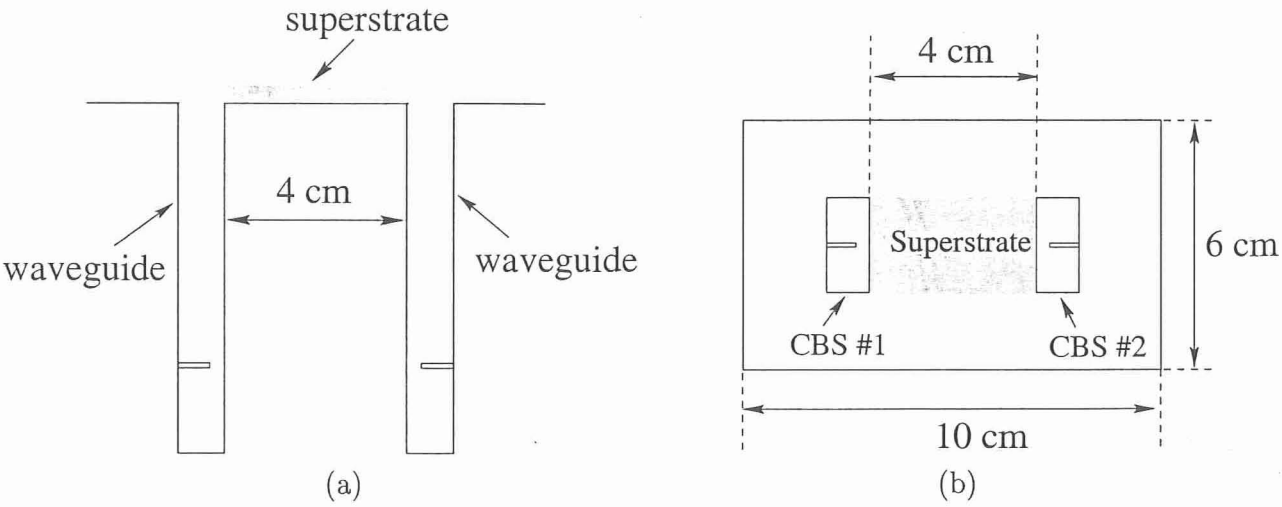

Figure 3.19: Geometry of two identical cavity-backed slot antennas mounted on a rectangular ground plane (for antenna specifications see Fig. 2). (a) Side view. (b) Top view.

performed by FDTD for all three superstrates. Although, the GDS material does not have constant material properties along the entire band of interest, its properties do not exhibit large variations. Therefore, in the FDTD simulations constant material properties (found by averaging the maximum and minimum values) were used. These properties are: $\epsilon_r = 13.4$, $\sigma = 0.17$ S/m, $\mu_r = 1.5$, and $\sigma^* = 95,000$ ohm/m, where σ and σ^* are the electrical and magnetic conductivities, respectively.

All the FDTD predictions of coupling for the GDS material are illustrated in Fig. 3.20 along with the predictions for the case with no superstrate (blank case), and they are also compared with the corresponding measurements. The FDTD calculations for all cases compare very well with measurements even at levels below -30 dB with maximum discrepancies ranging from 1 to 2 dB. It is also observed that adding the lossy superstrate substantially reduces coupling. Specifically, the maximum coupling decreased 4 dB for the 1.5 mm thick GDS, 6 dB for the 3.0 mm thick GDS, and 7 dB for the 4.5 mm thick GDS (the maximum coupling for each case is defined as the maximum over the entire band of frequencies). This reduction of coupling can be attributed to the minimization of surface currents on the ground plane which couple energy from one CBS antenna to the other. In addition, to examine if the blockage created by the physical presence of the superstrate contributes to the

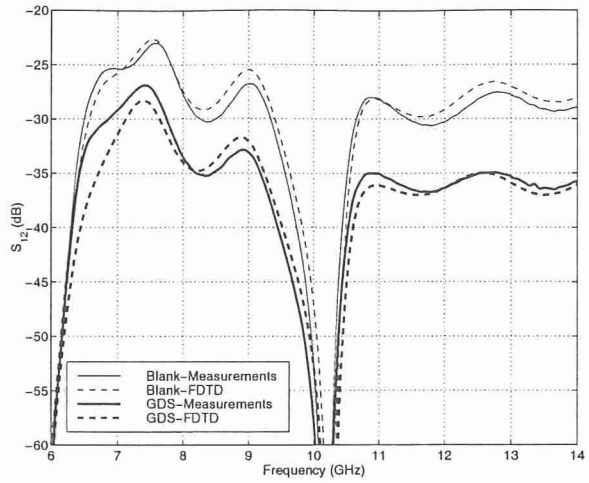

(a)

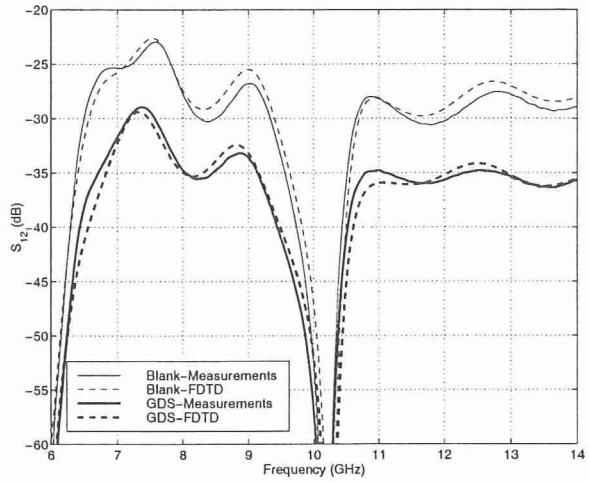

(b)

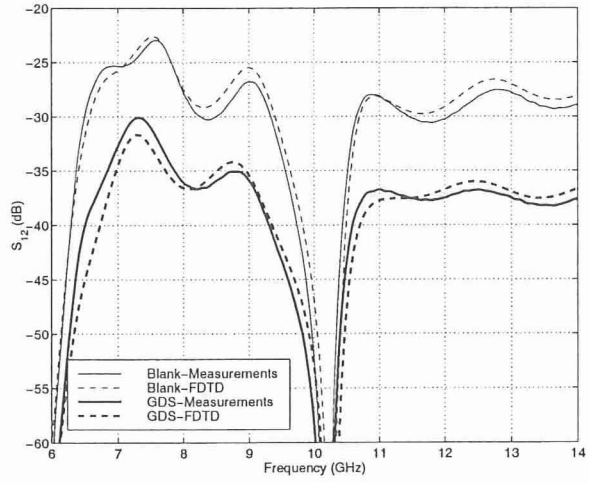

(c)

Figure 3.20: Coupling with and without lossy superstrate. (a) 1.5 mm thick GDS. (b) 3.0 mm thick GDS. (c) 4.5 mm thick GDS.

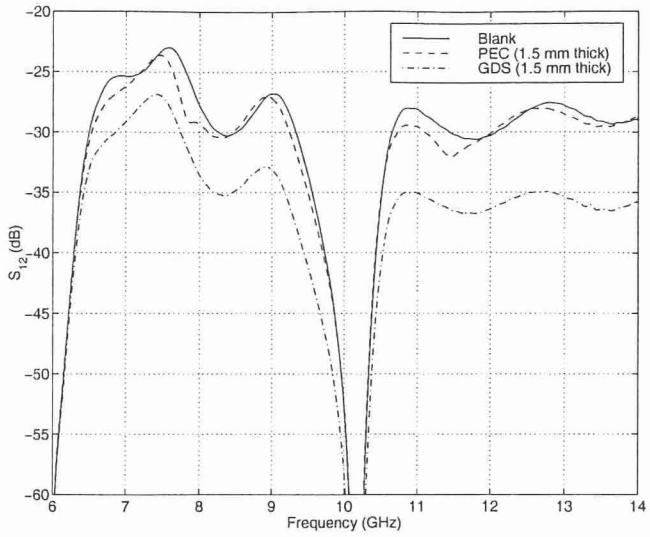

Figure 3.21: Measured coupling for three different cases.

coupling reduction, an 1.5 mm thick piece of PEC (perfect electric conductor) was placed between the apertures replacing the lossy superstrate. The measured coupling for this case is plotted in Fig. 3.21 and compared with measurements of the equal thickness GDS superstrate and the case with no superstrate (blank). Apparently, the inclusion of the PEC piece does not seem to reduce the maximum coupling even though it introduces maximum blockage. Therefore, it can be concluded that the reduction of coupling in the case of the lossy superstrate is mainly attributed to the minimization of the surface currents and not the blockage.

To better understand the mechanism of coupling reduction in the case of lossy superstrates, the induced surface current densities on the ground plane of the two CBS antennas were computed for two cases: (a) with a one-layer (1.5 mm thick) GDS superstrate, and (b) no superstrate, at 11.92 GHz. In both cases only CBS #1 was excited (see Fig. 3.19). Figs. 3.22 and 3.23 illustrate the normalized total surface current densities on the ground plane in dB. It is apparent that in the case with no loss (see Fig. 3.22) the surface current densities in the area between the two apertures are intense (as high as -15 dB) thereby establishing a strong coupling mechanism. However, in the case with the lossy superstrate (see Fig. 3.23) the surface current densities in the area between the two apertures have been significantly reduced exhibiting levels as low as -25 dB. Therefore, it is clear that lossy superstrates weaken

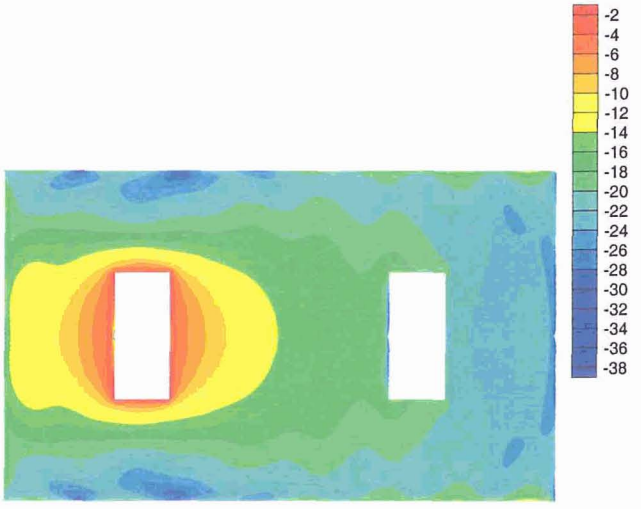

Figure 3.22: Total surface current density J_{tot} in dB, with no lossy superstrate at 11.92 GHz.

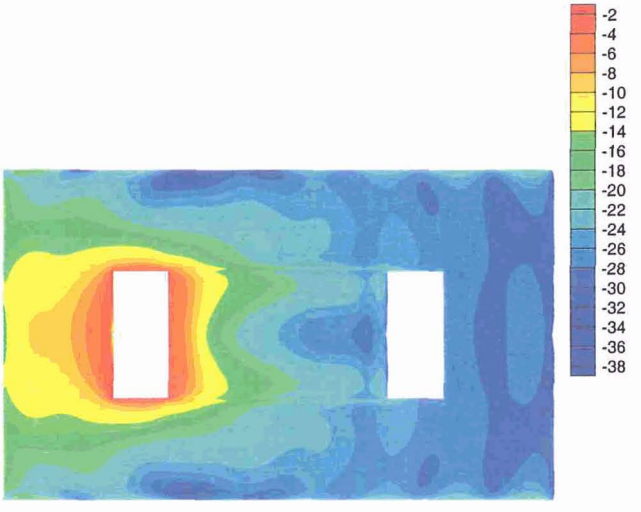

Figure 3.23: Total surface current density J_{tot} in dB, with a 1.5 mm thick GDS superstrate at 11.92 GHz.

the coupling mechanism supported by surface current densities.

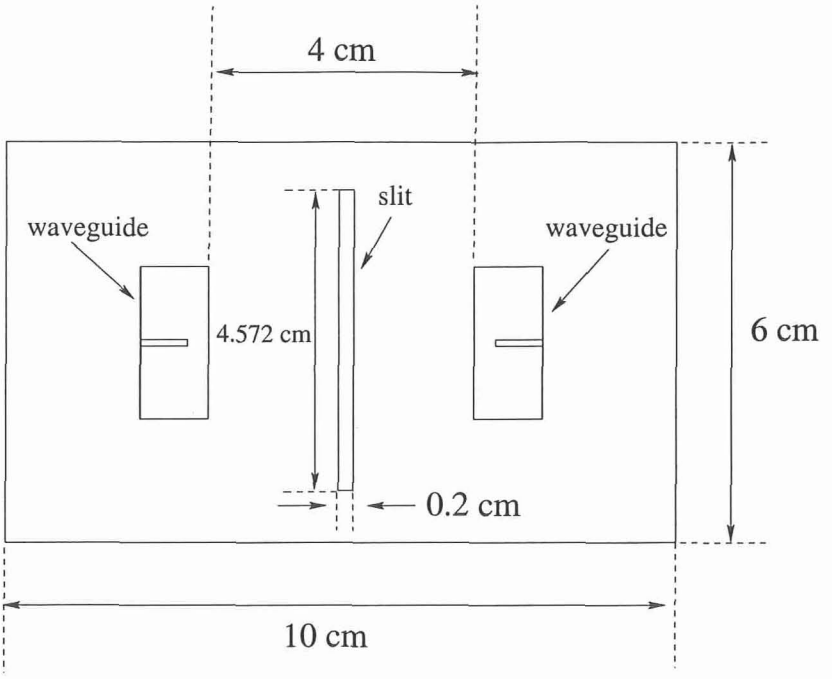

Figure 3.24: Geometry of two cavity-backed slot antennas on a ground plane with a slit.

Another method of reducing coupling through surface currents is to introduce a discontinuity, such as a thin slit, on the ground plane between the two apertures. A 2 mm wide slit was symmetrically cut at the center of the ground plane as shown in Fig. 3.24. The FDTD calculations for this case are plotted against measurements in Fig. 3.25(a), and they exhibit excellent agreement. During our coupling studies, the width of the original slit (2 mm) was increased to 4 mm and 8 mm, sequentially. The FDTD predictions for these cases are illustrated and compared in Fig. 3.25(b).

It is observed that the wider the slit is, the smaller the coupling becomes. However, the reduction of coupling did not change dramatically when the width of the slit became two or four times larger than the original 2 mm wide slit. Moreover, it appears that as the slit becomes wider the reduction of coupling is larger at higher frequencies. This can be possibly attributed to the fact that the slit is electrically larger at higher frequencies thereby disrupting the surface currents on the ground plane for a larger electrical distance. Specifically, the 2 mm and 8 mm slits are $\lambda/20$

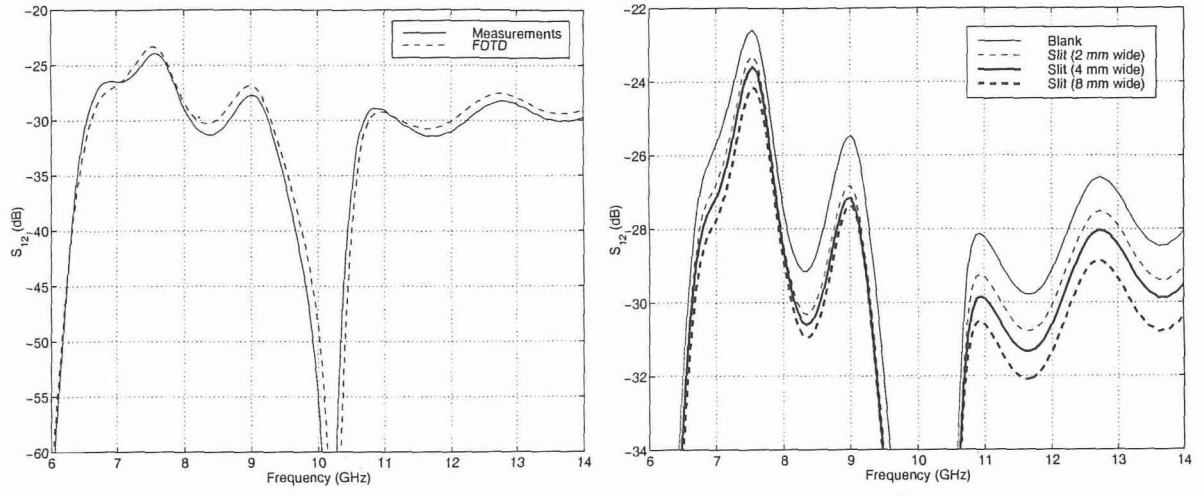

Figure 3.25: Coupling with a slit on the ground plane. (a) 2 mm wide slit. (b) FDTD predictions for different widths of the slits.

and $\lambda/5$ wide, respectively, at 7.5 GHz. However the same slits, 2 mm and 8 mm are approximately $\lambda/12$ and $\lambda/3$ wide, respectively, at 12 GHz. The incorporation of a 2 mm slit caused a 1 dB reduction of the maximum coupling as illustrated in Fig. 3.26 which presents the comparison of four different cases of measured [see Fig. 3.26(a)] or calculated [see Fig. 3.26(b)] coupling. Conclusively, the largest reduction of coupling occurs for the thickest GDS superstrate of 4.5 mm whereas the smallest reduction happens for the slit. Therefore, a lossy superstrate can be very effective in minimizing the coupling between aperture antennas by reducing the surface currents on the ground plane. Moreover, superstrates are very practical because they can be flush mounted, and they do not affect the mechanical strength of the ground plane as slits do. Dis-orienting the two CBS antennas is another technique that can be used to reduce coupling. The configuration of the aperture antennas examined above (seen in Fig. 3.19) is called E-plane configuration. The H-plane configuration is formed by rotating both aperture antennas 90^o (see Fig. 3.27). Pozar in [128] examined the mutual coupling between two rectangular microstrip patches for both E-plane and H-plane configurations. He demonstrated that the E-plane configuration exhibits the smallest coupling for electrically small separation distances, while the H-plane configuration exhibits the smallest coupling for electrically large separation distances. Therefore, it

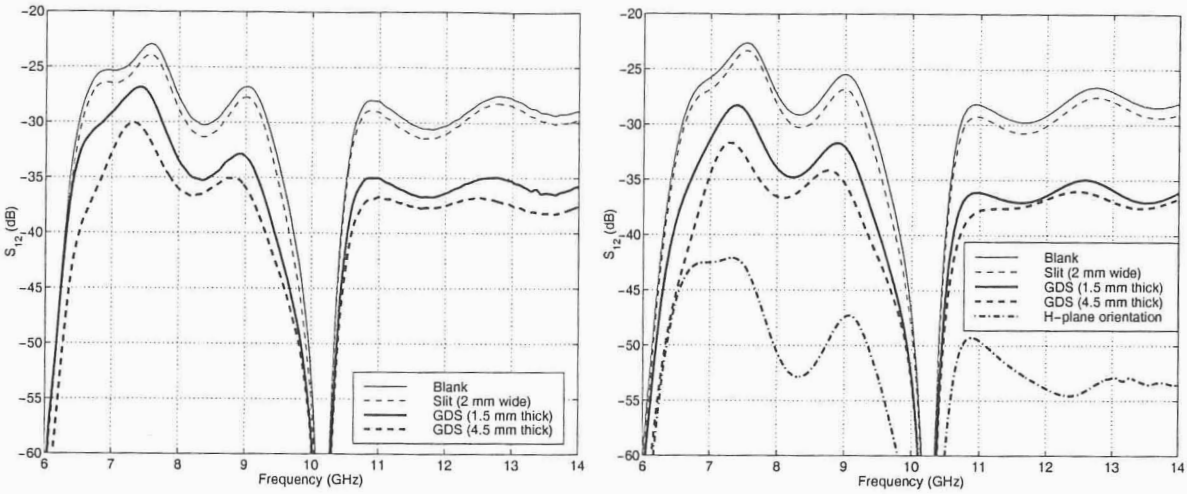

Figure 3.26: Coupling between two CBS antennas. (a) All the measurements. (b) All the FDTD predictions.

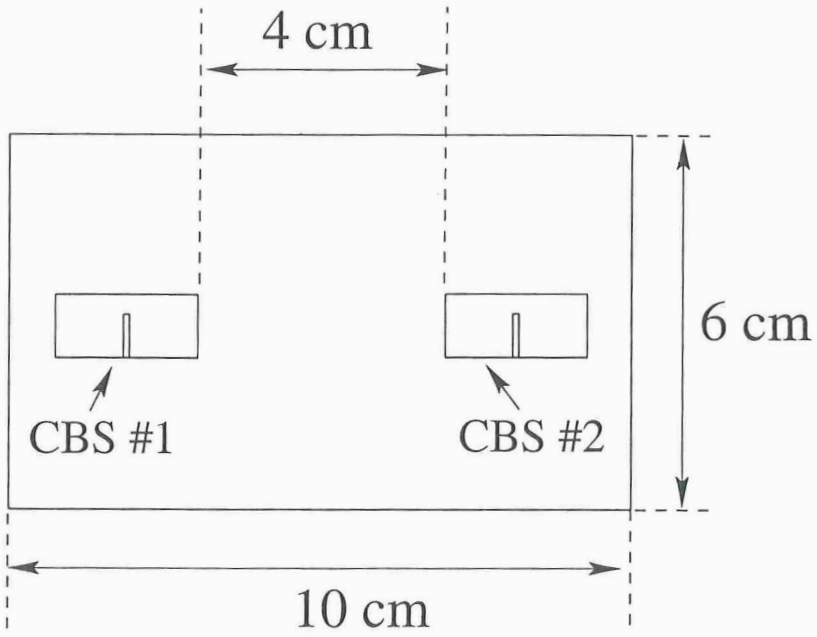

Figure 3.27: Top view of the two CBS antennas oriented along the H-plane.

is expected that coupling of the H-plane configuration of two CBS antennas will be much smaller than the coupling of the E-plane configuration, especially for separation distances that are not very small in terms of wavelength. This mechanism of coupling reduction is also discussed in [45], and it can be explained by comparing the coupling of two side-by-side versus two collinear dipoles. Alternatively, the pattern of a CBS antenna in the H-plane nearly vanishes along the ground plane due to boundary conditions. In the E-plane the pattern does not have to vanish along the ground plane unless the dimension of the aperture in that plane is a multiple of wavelength [45]. Hence, the mutual effects between two CBS antennas which are oriented along the H-plane are less intense because the antennas are placed in the direction of minimum radiation. One FDTD simulation was performed to verify this line of thought by calculating the coupling between two CBS antennas oriented along the H-plane (see Fig. 3.27). The results of this simulation are illustrated in Fig. 3.26(b). It is observed that the coupling of the H-plane configuration is 20 dB less than the coupling of the E-plane configuration (labeled "blank"), which is a substantial reduction.

Finally, dependence of coupling on the separation distance between two CBS antennas is examined. Coupling was measured for various separation distances by placing the two antennas on a larger ground plane (1×1 m). The measured results are illustrated in Fig. 3.28(a) for a range of distances from 25 mm to 160 mm at increments of 15 mm. As expected, coupling decreases as the separation between the two antennas becomes larger. FDTD simulations were also performed for few selected cases of separation distances (25 mm, 40 mm, and 55 mm), and the computed results are illustrated in Fig. 3.28(b). The predictions agreed very well with the measurements and exhibited similar variation. Also, the measured coupling was plotted at four selected frequencies versus the separation distance in Fig. 3.29. The coupling decreased following a variation similar to $1/r$ at all four frequencies exhibiting a total reduction of about 14 dB when the separation was increased from 25 mm to 160 mm (see Fig. 3.29).

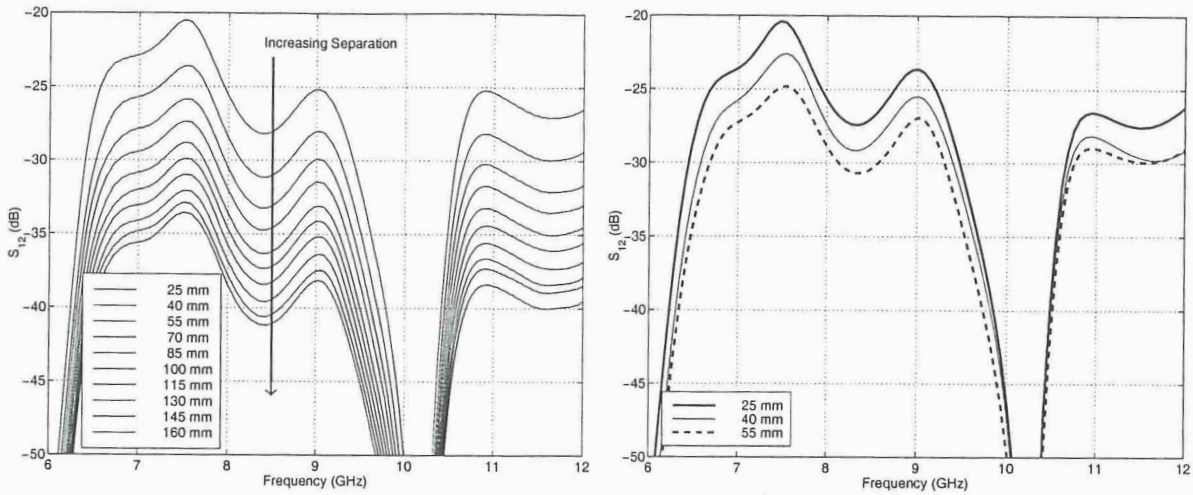

Figure 3.28: Coupling between two CBS antennas for different separation distances. (a) Measurements. (b) FDTD predictions.

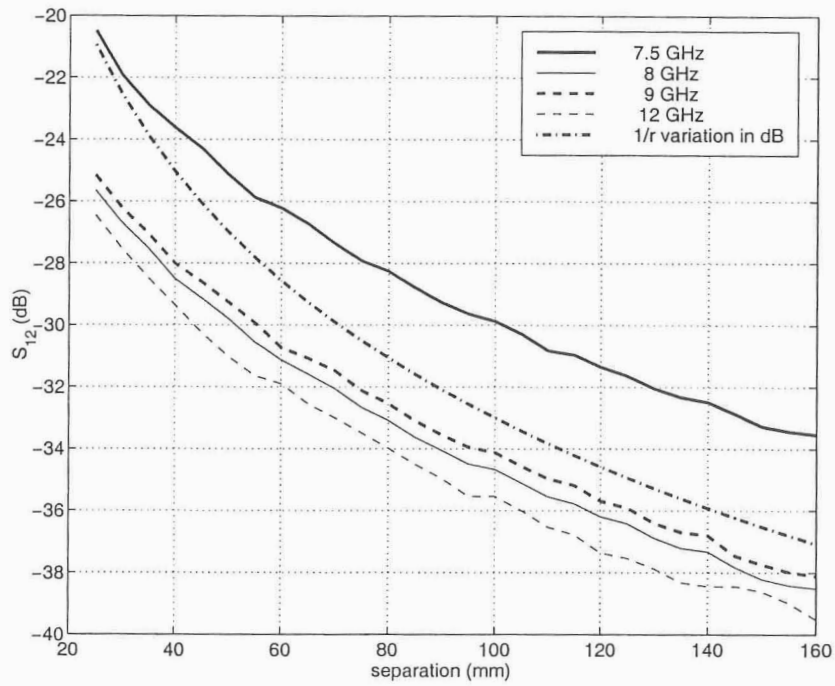

Figure 3.29: Measured coupling versus separation distance at different frequencies.

E. Patterns

In the previous subsection, various methods of minimizing coupling between two CBS antennas were investigated. Lossy superstrates, as well as slits, on the ground plane were implemented and analyzed. However, these alterations of the physical geometry also change the radiation characteristics of the antennas. Especially, the presence of composite superstrates introduces losses which can potentially reduce the antenna gain. Radiation patterns of the E-plane were computed using FDTD for two cases: (a) with a one-layer (1.5 mm thick) GDS superstrate, and (b) no superstrate, at two frequencies of 7.5 GHz and 11.92 GHz. In both cases only CBS #1 was excited (see Fig. 3.19). The GDS material properties used in the single frequency FDTD simulations were picked to be equal to the measured material properties at the corresponding frequency. These properties are: (a) at 7.5 GHz; $\epsilon_r = 13.4$, $\sigma = 0.09$ S/m, $\mu_r = 1.75$, and $\sigma^* = 74,000$ ohm/m, and (b) at 11.92 GHz; $\epsilon_r = 13.4$, $\sigma = 0.25$ S/m, $\mu_r = 1.35$, and $\sigma^* = 110,000$ ohm/m. The numerical results are illustrated in Figs. 3.30 and 3.31, and the predictions are compared with measurements. All radiation patterns were calculated as well as measured by exciting only one of the two CBS antennas. The agreement between the measurements and the numerical calculations is very satisfactory and the maximum discrepancy ranges from 1 to 2 dB. Finally, the measured gain of the antennas for the cases with and without the lossy superstrate are compared for both frequencies of 7.5 GHz and 11.92 GHz in Fig. 3.32. It is observed that the introduction of a lossy superstrate causes a reduction of the antenna gain which can be as high as 5 dB for some observation angles. Consequently, when incorporating lossy materials, there is a trade-off between minimizing the coupling and maintaining high efficiency. Furthermore, the E-plane radiation patterns of the two CBS antennas on the ground with and without the 2 mm slit are essentially identical (especially when the observation angle is on the top of the ground plane, i.e., for elevation angles $-90^o \leq \theta \leq 90^o$) and therefore they are not illustrated and compared through a figure.

F. Summary of coupling reduction methods

Different coupling reduction techniques were presented and analyzed. Traditionally, the most intuitive way to reduce coupling between two antennas is to increase their

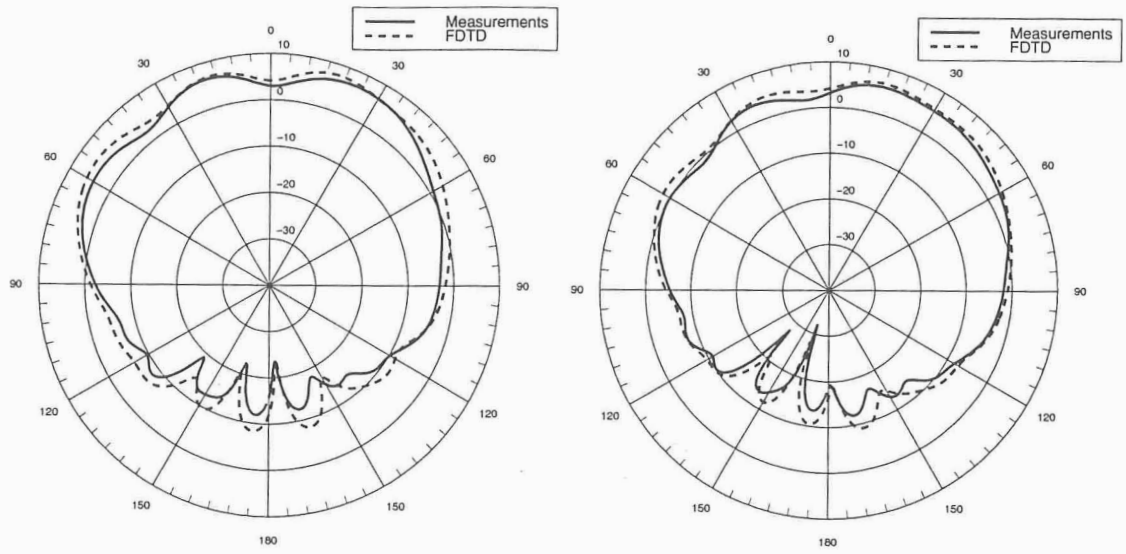

(a) (b)

Figure 3.30: Patterns at 7.5 GHz. (a) With no superstrate. (b) 1.5 mm GDS thick superstrate.

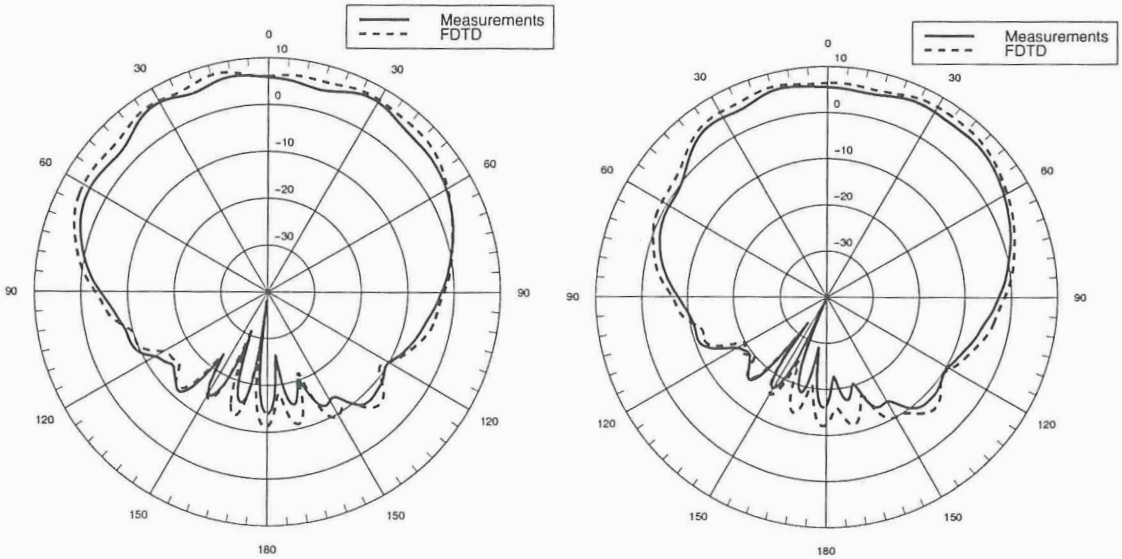

(a) (b)

Figure 3.31: Patterns at 11.92 GHz. (a) With no superstrate. (b) 1.5 mm GDS thick superstrate.

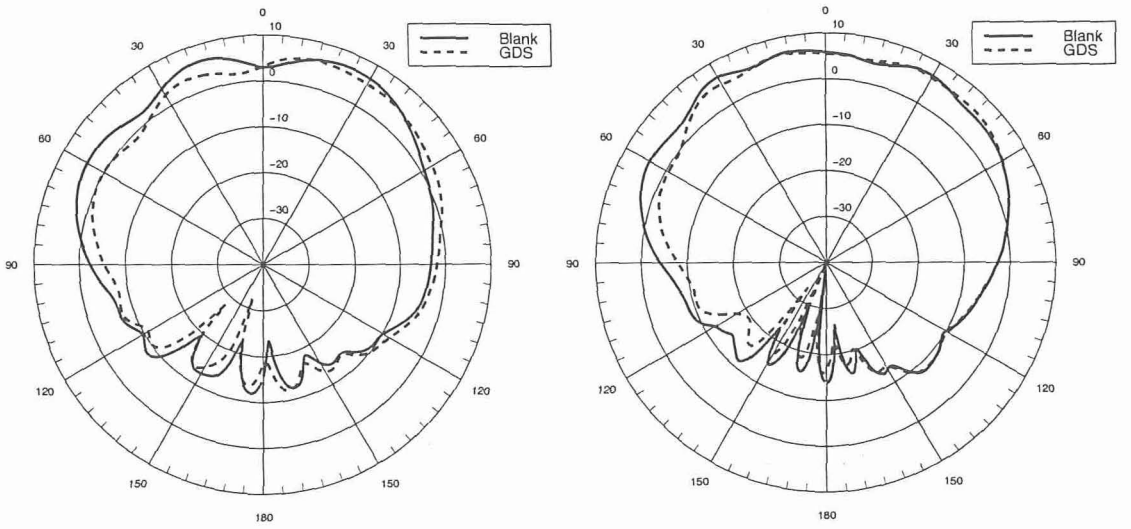

(a) (b)

Figure 3.32: Measured patterns. (a) At 7.5 GHz. (b) At 11.92 GHz.

separation distance. Measurements and simulations illustrated the decreasing behavior of coupling for increasing separation distances (see Subsection D.) which was very similar to a 1/r variation (see Fig. 3.29).

Other more novel techniques of coupling reduction were also examined such as the introduction of ground discontinuities, e.g., slits, and the use of lossy superstrates between the two antennas. Slits were found to be less effective in reducing coupling than lossy superstrates. However, the incorporation of lossy materials significantly influences the radiation characteristics of an antenna. To illustrate the different advantages and disadvantages of using lossy superstrates, some of the results are tabulated and they correspond to the configuration of the two CBS antennas examined in the previous subsections. Gain and efficiency computations were performed by exciting only CBS #1 (see Fig. 3.19).

In Table 3.2 the antenna efficiency is shown for the three different thicknesses of GDS material used in our analysis above at 7.5 GHz and 11.92 GHz. At 7.5 GHz the efficiency ranges from 70%-74%, and at 11.92 GHz it ranges from 83%-88%. In Table 3.3 the antenna gain at an elevation angle of $\theta = -60^o$ (where the minus corresponds to the left side of the elevation pattern) is shown for different superstrate thicknesses. It is also compared to the antenna gain with no lossy superstrate present

at 7.5 GHz and 11.92 GHz. The elevation angle of $\theta = -60^o$ was used chosen for our comparison because at this angle the gain exhibited the larger decrease when lossy materials were used (see Fig. 3.32). When the thickest GDS superstrate (4.5 mm thick) was used, the gain decreased 4.6 dB at 7.5 GHz and 6.1 dB at 11.92 GHz compared to the gain with no superstrate. Notice though that the gain toward zenith was almost the same for the cases with or without lossy superstrates (see for example Fig. 3.32).

Table 3.2: Efficiency of the two CBS antennas configuration for different thicknesses of the GDS superstrate

	Thickness of GDS superstrate		
Frequency	1.5 mm	3.0 mm	4.5 mm
7.5 GHz	74%	73%	70%
11.92 GHz	88%	85%	83%

Table 3.3: Gain of the two CBS antennas configuration at elevation angle $\theta = -60^o$

	No Loss	Thickness of GDS superstrate		
Frequency		1.5 mm	3.0 mm	4.5 mm
7.5 GHz	5.8 dB	1.9 dB	2.0 dB	1.2 dB
11.92 GHz	5.6 dB	1.2 dB	0.8 dB	-0.5 dB

Apparently, the use of lossy superstrates yields a decrease in the antenna gain and efficiency but provides a coupling reduction in return. The achieved coupling reduction for the different superstrates is depicted in Table 3.4. These coupling reductions were obtained by comparing the cases with and without lossy superstrates. At 7.5 GHz the coupling was reduced by 3.9 dB for the thinest superstrate of 1.5 mm, and by 7.8 dB for the thickest superstrate of 4.5 mm. At 11.92 GHz the coupling was reduced by 6.1 dB for the thinest superstrate of 1.5 mm, and by 7.2 dB for the thickest superstrate of 4.5 mm. Additionally, the average coupling reduction over the entire band of 6-14 GHz was 5.8 dB for the thinest superstrate of 1.5 mm, and 8.2 dB for the thickest superstrate of 4.5 mm. A similar table is constructed for the cases

that incorporated a slit in the ground plane (see Table 3.5). As mentioned earlier, the coupling reduction in the cases of the slits is not as significant as in the cases of the lossy superstrates.

Table 3.4: Coupling reduction of the two CBS antennas configuration

	Thickness of GDS superstrate		
Frequency	1.5 mm	3.0 mm	4.5 mm
7.5 GHz	3.9 dB	6.2 dB	7.8 dB
11.92 GHz	6.1 dB	5.4 dB	7.2 dB
Average Coupling Reduction over the band 6-14 GHz	5.8 dB	6.4 dB	8.2 dB

Table 3.5: Coupling reduction of the two CBS antennas configuration

	Width of the ground plane slit		
Frequency	2.0 mm	4.0 mm	8.0 mm
7.5 GHz	0.7 dB	1.0 dB	1.5 dB
11.92 GHz	0.9 dB	1.5 dB	2.4 dB
Average Coupling Reduction over the band 6-14 GHz	1.0 dB	1.4 dB	2.5 dB

Radiation characteristics, such as coupling, efficiency and gain, are critical to the design of an antenna and must be taken into consideration. In a practical configuration there is always a compromise between coupling reduction and maintenance of high efficiency and gain. Decisions regarding a design should take into account the communication system operation requirements.

G. Conclusions

In this section, the analysis of cavity-backed slot antennas in the context of FDTD was presented. Different numerical issues related to the modeling of such antennas were described. It was found that the use of a voltage source with an internal resistance in FDTD is indispensable for efficient computations. Both FDTD and FEM/MoM were used to compute the input impedance of a single CBS antenna, and coupling

between two elements, and they compared very well with measurements. However, it was found that for coupling versus distance calculations, the hybrid FEM/MoM is faster than the pure FDTD. This is attributed to the fact that FEM/MoM does not discretize the space between the two cavities but rather treats the open-space interaction within the MoM formulation. Therefore, the FEM/MoM computational space remains constant because only the CBS antennas need to be discretized in the hybrid methodology. On the contrary, FDTD has to also account for the space between the two antennas thereby yielding very large domains especially for large distances.

A very comprehensive study of coupling between two CBS antennas was also performed through measurements and simulations. The dependence of coupling on the separation distance between the two antennas was investigated. Dis-orienting the antennas was also found to be a very effective method of coupling reduction. Specifically, the H-plane configuration exhibited significantly smaller levels of coupling than the E-plane configuration. Moreover, other alternative methods of reducing coupling were examined including incorporation of lossy superstrates as well as ground plane discontinuities, such as slits. It was illustrated that lossy material superstrates can be very effective in decreasing the coupling between two antennas, but they cause a reduction of the antenna gain. In Subsection F. some of these trends were reported. Therefore, in a practical design there is always a compromise between reduction of coupling and maintenance of a sufficiently high gain.

Chapter 4

HIRF Penetration and PED Coupling Analysis

In this chapter, the penetration of High Intensity Radiated Fields (HIRF) into conducting enclosures via apertures is presented. HIRF penetration is an EMI issue that is relevant to all aviation. The stories are numerous, of disrupted communications, disabled navigation equipment, etc., due to the effects of EM sources external to the aircraft. Here, the FDTD method is used to predict the shielding effectiveness of conducting enclosures with apertures, and the numerical results are compared with measurements. Several issues related to the FDTD analysis of highly resonant and high quality factor (high-Q) structures, such as windowing and acceleration techniques, are examined and described.

Furthermore, the shielding effectiveness of a scaled model of a Boeing 757 aircraft is calculated. Both the standard FDTD(2,2) and the hybrid of subgrid FDTD(2,2) and FDTD(2,4) are used for the predictions which are validated by comparison with measurements. Finally, the coupling of personal electronic devices (PEDs) is examined for the scaled fuselage by modeling the coupling between a PED antenna inside the fuselage and an antenna mounted on the exterior skin of the fuselage. Again both the standard FDTD(2,2) and the hybrid of subgrid FDTD(2,2)/FDTD(2,4) are applied for the predictions which are validated by comparison with measurements.

I. HIRF Penetration Through Apertures

Penetration of High Intensity Radiated Fields (HIRF) into cavities through apertures is an important EMI issue. Electronic equipment that supports communications and navigation systems of airplanes is usually shielded in order to increase reliability and integrity. Additionally, electronic equipment is commonly housed into boxes that have openings. In such structures, an external signal can penetrate through these apertures and directly couple energy in the interior. Moreover, the electromagnetic environment of electronics consists of multiple friendly and threat signals that can cause problems to their operation; e.g., jamming in communication systems. Therefore, the shielding effectiveness of boxes with apertures is a crucial issue and should be taken into account during an installation.

In addition, the field penetration into airborne structures, such as helicopters or airplanes, is another crucial issue which has lately attracted a lot of attention. The design of new generation aircraft, such as the Boeing 777 and the Airbus A320, is based on "fly-by-wire" technology (FBW), in which the mechanical links between the pilot's controls and the airplane's flight surfaces have been replaced by electronic links. Digital avionic systems, such as navigation computers, flight data computers, engine control computers, digital autopilots, collision avoidance systems, etc., are even incorporated on older generation airplanes which are currently built. Future designs of airplanes seek the incorporation of electronic avionics that perform even more complicated functions, such as stability augmentation, gust load alleviation, satellite-guided navigation, etc. All these trends illustrate that safe operation of an airplane relies substantially on digital avionic systems. Therefore, the susceptibility of such systems to electromagnetic interference (EMI) is of great concern and interest.

In particular, EMI generated from man-made radio frequency (RF) sources external to the airplane, such as radars, radio stations, and other radiating sources, need to be carefully studied. Such sources are known as HIRF or High Intensity Radiated Field sources [129]. While an aircraft is flying, it is subject to HIRF sources which can potentially upset its electronic equipment. Although there are many possible mechanisms contributing to penetration of fields into an aircraft (including direct penetration through composites, penetration through cracks and joints, conduction along cabling, etc.), it is usually the windows which allow the greatest. Consequently,

it is of paramount importance to understand and be able to predict the field penetration through apertures. The research presented here was instigated and generated from projects related to HIRF studies of commercial airplanes [129].

In this section, the shielding effectiveness (SE) of cavities with apertures is examined. Mendez [130], in 1970, analytically formulated the SE of a cavity using a theory that applies at frequencies below the first cavity resonance. The radiation of apertures which are mounted on conducting boxes was also derived, based on the equivalence principle in [131]. Furthermore, another analytical formulation of SE of conducting enclosures has been recently presented in [132], but the results were for frequencies below the first cavity resonance. Method of moments was successfully used in [133] for SE analysis. As far as FDTD, few papers have applied it in SE studies. In [134] FDTD was applied to sinusoidal steady state penetration problems, and a small loss was introduced in the cavities to accelerate the simulation convergence to steady state. A hybrid Moment Method/FDTD approach was reported in [135] and applied to coupling and penetration into complex structures. Furthermore, a subcell model for thin wires was presented in [136] along with the concept of equivalent radius which was used to replace bundles of wires. Induced currents on wires and multi-conductor bundles placed into cavities were also computed. Additionally, in [137], FDTD models for narrow slots and lapped joints were derived. Different FDTD subcellural modeling of thin slots were examined and compared in [138]. In [139] the EMI through perforation patterns in shielding enclosures was investigated using the FDTD and compared with measurements.

The emphasis of this section is to address various issues related to the FDTD analysis of penetration. Specifically, problems related to the Fourier transform of time-domain data are discussed, and different techniques that can accelerate a simulation are examined. The procedure of windowing is introduced and applied to FDTD computations of shielding effectiveness. Although windowing has been used before in the context of FDTD [115], its capabilities were not thoroughly examined. Moreover, results are presented and compared with measurements. Finally, various definitions of SE are presented and their respective differences are analyzed.

A. Definition of shielding effectiveness

In this section, two definitions of electric shielding effectiveness of conducting enclosures with apertures are considered in the context of FDTD. The first one is based on a plane wave excitation and the following procedure:

a. Excite the cavity with an incident pulse plane wave and record the electric field at the position of interest.

b. Excite an empty space computational domain with the same incident pulse plane wave and record the electric field at the position of interest.

c. Fourier transform the time-domain data.

d. Compute the shielding effectiveness in dB using the following definition:

$$SE = 20 \log \left(\frac{\text{empty space frequency response}}{\text{problem space frequency response}} \right) \tag{4.1}$$

where the frequency response is defined as the magnitude of the electric field component of interest. This first definition of SE will be labeled *procedure* #1 for reference purposes.

The second way of defining SE assumes that the cavity is excited by a probe, and follows a similar procedure:

a. Excite the cavity using a probe and find the time-domain far-field at the observation angle of interest using the near to far field time-domain transformation.

b. Assume that the top of the cavity along with its sides are removed and only the bottom part is kept along with the excitation probe (forming essentially a geometry of a monopole on a ground plane). Find its time-domain far-field at the observation angle of interest using again the near to far field time-domain transformation.

c. Fourier transform the far-field time-domain data.

d. Compute the shielding effectiveness using the definition of (4.1).

For convenience, throughout this section, the case with the top and the sides of the cavity present will be referred to as "with the cavity" case, whereas the case without the top of the cavity will be referred to as "without the cavity" case. This second definition of SE will be labeled *procedure* #2 for reference purposes.

Assuming that the presence of the probe does not significantly affect the field distribution in the cavity, and that the field distribution at the center of the cavity is uniform from top to bottom, the two procedures of calculating SE can be approximately considered reciprocal. An incentive for computing SE using the second procedure is that this approach is in accordance with the way measurements were performed at ASU's Electromagnetic Anechoic Chamber (EMAC) facility. Therefore, by simulating in FDTD the actual experiment, a better agreement is expected. These two procedural definitions of SE will be compared in Subsection F.

B. Problem definition

In this section, the SE of three different geometries are examined. The conducting enclosure consists of a 30 cm wide, by 30 cm deep, by 12 cm high (inside dimensions) box. Three aperture configurations are considered: a single 20 cm x 3 cm [132], a single 10 cm x 0.5 cm [132], and one of each of these apertures. The three geometries are illustrated in Fig. 4.1. The analysis presented here involves FDTD SE computations of all three geometries at the center of the conducting enclosures, using the two different definitions of SE described in Subsection A.. When using procedure #1 (plane wave excitation), there is no probe in the cavity. In this case, SE is computed at the center of the cavity for a vertically polarized plane wave incident to the aperture at an angle ϕ_i and θ_i [see Fig. 4.2(a)]. Reciprocally, when using procedure #2 (probe excitation), a monopole mounted at the cavity's bottom side is present. The probe is always located at the center of the cavity and is 3 cm long, which is in accordance with the measurement configuration. In this case, the probe will excite the cavity, and the vertical electric field component in the far-field zone will be computed at the observation angle ϕ_o and θ_o [see Fig. 4.2(b)]. Also, note that all FDTD simulations presented in this section used a cell size of 2.5 mm (or $\lambda/80$ at 1.5 GHz), besides the windowing studies (shown in Subsection E. which used a cell size of 5 mm (or $\lambda/40$ at 1.5 GHz).

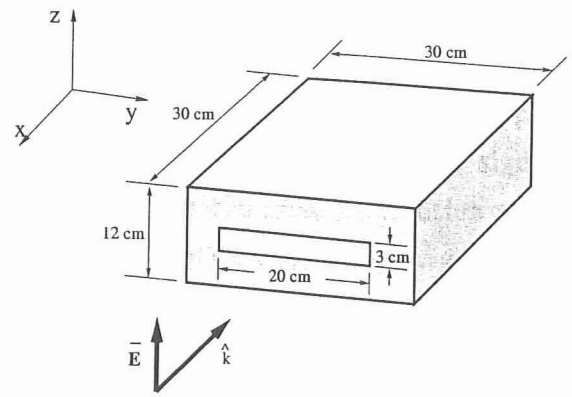

(a)

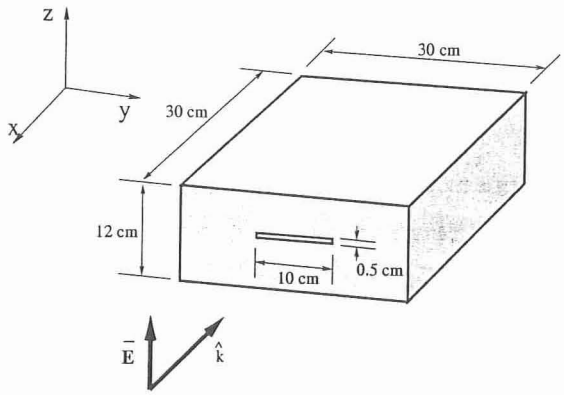

(b)

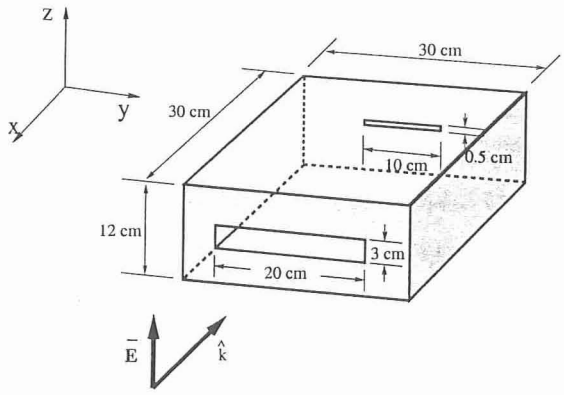

(c)

Figure 4.1: Geometries:(a) Cavity #1; (b) Cavity #2; and (c) Cavity #3.

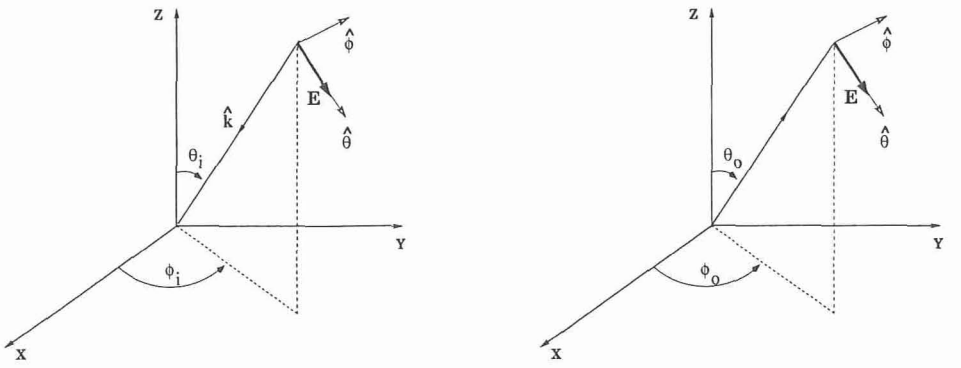

Figure 4.2: Definition of: (a) incident angle, ϕ_i and θ_i, for SE computations using procedure #1; and (b) observation angle, ϕ_o and θ_o, for SE computations using procedure #2.

C. Measurements

The conducting enclosure, described in the Subsection B., is constructed of brass plates. All the side and top joints were soldered together and then covered on the outside with copper tape. Because more than one aperture configuration was intended, the front and back walls were constructed with interchangeable panels containing the apertures. The panels and front and back walls were made with matching steps machined into their interfacing edges so that the panels installed flush into the front and back walls. This is illustrated schematically in Fig. 4.3. A film of uncured silver-bearing epoxy was used on the contact surfaces between the wall and the aperture panel as a flexible RF gasket. The panel was held in place and further sealed with copper tape over the outside seams.

Four aperture panels were constructed. Two of the panels were blank (no aperture). One of the blank panels was installed in the back wall for configurations consisting of only one aperture. The second blank panel was used with the first to verify the fidelity of the enclosure. If a significant signal had been measured when both blanks were installed, that would signify an incompletely sealed enclosure. Over the frequencies measured, the electric field inside the enclosure when both blanks were installed was found to be just discernibly above the noise floor, and the enclosure was judged to be free of significant "leaks". One of the aperture panels had a 20 cm wide by 3 cm high aperture [see Fig. 4.1(a) and (c)]. The final panel had a 10 cm wide by

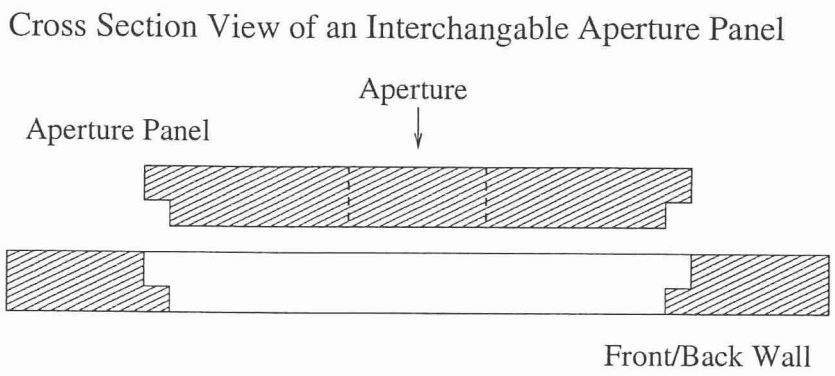

Figure 4.3: To accommodate multiple aperture configurations in the conducting enclosure, the front and back walls were constructed to accept flush-mounted aperture panels.

0.5 cm high aperture [see Fig. 4.1(b) and (c)].

A wire probe (monopole) with a 0.021 in (0.5334 mm) diameter was mounted at the bottom of the box in order to measure the electric field inside the box. The length of the wire probe started at slightly more than half the height of the box (approximately 7 cm). However, the first resonant frequency of the cavity was measured and exhibited a shift (from the theoretical) of approximately 30 MHz. The measured resonant frequency increased as the height of the probe was reduced, until the length of the probe approached one quarter of the height of the cavity (3 cm). Near that height, the first measured resonant frequency seemed to change very little with additional changes in the height of the probe, and was in close agreement with the first theoretical resonant frequency.

The procedure for measuring the shielding effectiveness was performed as follows. The bottom of the enclosure, with the electric field probe, was mounted on an expanded polystyrene column inside the anechoic chamber. An auxiliary antenna was mounted on another polystyrene support, at a distance of approximately 2.5 m from the enclosure. The auxiliary antenna was aligned in height, azimuthal orientation, and polarization. The field received by the probe was measured as a function of frequency. This measurement represents the electric field at the box location, when the box is not present (the incident field). Any effects due to the ground plane formed by the bottom of the box are ignored. The remainder of the box (the assembly consisting of the top and sides) was then fitted onto the bottom. Then, the fields that

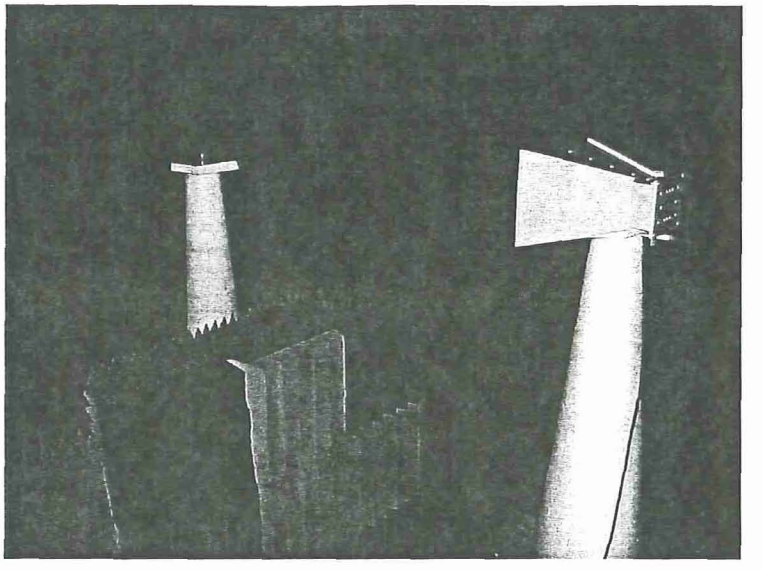

Figure 4.4: A photograph of the bottom of the enclosure, with the probe, and the auxiliary antenna inside the anechoic chamber.

have penetrated into the box were measured. The ratio of the incident fields to the penetrated fields is the shielding effectiveness. The bottom of the enclosure with the probe is shown in Fig. 4.4, with the auxiliary antenna in the foreground.

The measurements were performed over 801 frequency points between 250 MHz and 1.5 GHz. The three aperture configurations, illustrated in Fig. 4.1, were considered. The SE was measured, for each of the three aperture configurations, over a number of incidence angles. Two of the aperture cases that were measured are identical to those examined by Robinson et al., [132]: the single 10 cm by 0.5 cm, and the single 20 cm by 3 cm apertures. Due to the limitations of their facilities, these measurements exhibited filled nulls and approximately 5 dB of ripple. The ASU measurements exhibit a significant improvement in quality, as evidenced by the marked reduction in ripple and the deeper nulls.

D. Acceleration techniques

In electromagnetic analysis various quantities which describe different characteristics of a problem; e.g., gain, input impedance, scattering (RCS), shielding effectiveness, etc., are defined in the frequency domain. Therefore, a transformation must be used to convert the fields computed by time-domain methods (like the FDTD) into the the

frequency domain. This transformation is usually performed using a Fourier process (either FFT or DFT). The basic requirement for the FFT to work is to allow sufficient simulation time for the transient phenomena to decay. This requirement comes from the formula of DFT

$$G(f) = \Delta t \sum_{n=0}^{N} g(n\Delta t)\ e^{-j2\pi f n\Delta t} \tag{4.2}$$

where $g(n\Delta t)$ is a time-domain response at discrete time instants $t = n\Delta t, n = 0, .., N$, $G(f)$ represents the Fourier transform of $g(t)$ at frequency f, and Δt is the time-step. Theoretically, the DFT summation has to be infinite in extent ($N = \infty$). In practice though, the DFT summation has to be of finite extent, which introduces errors in the computations. For this reason FDTD simulations usually have to allow sufficient time for the transients to decay, so that the DFT summation can be accurately truncated without introducing large errors. However, one of the main difficulties involved in FDTD simulations is that in some applications, e.g., resonant lossless structures, tens or even hundreds of thousands of time-steps may be required for the transient fields to decay. In the case of SE computations, a prohibitive simulation time may be needed for transients to converge to zero, especially for conducting enclosures with high quality factor, Q.

In this subsection, two different techniques that can be used to overcome this problem, are proposed. Their respective advantages and disadvantages are also reported. To illustrate the use of these acceleration techniques, the geometry of the cavity with the thin aperture (cavity #2) is analyzed due to its higher Q compared to the other two geometries.

1. Artificial Losses

Here, the SE of cavity #2 is examined using procedure #1. SE is computed at the center of the cavity for a normally incident plane wave ($\phi_i = 0^o$, $\theta_i = 90^o$). The field at the center of the cavity was recorded and Fourier transformed. After executing the simulation for 131,000 time steps, the time-domain electric field amplitude at the center of the box has only decayed to a value of 0.03 V/m, as seen in the inset of Fig. 4.5(a). Therefore, this electric field cannot be accurately Fourier transformed. One possible solution is to introduce some additional loss mechanism into the solution

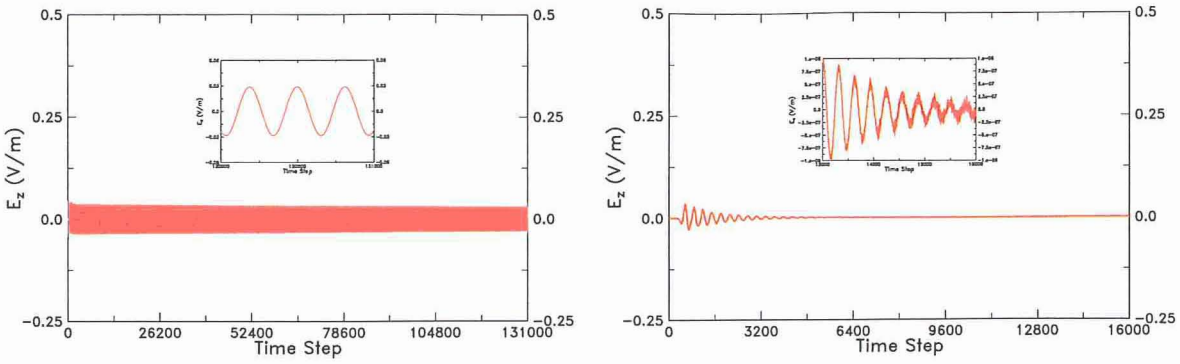

Figure 4.5: The time-domain electric field at the center of cavity #2 for a normally incident wave ($\phi_i = 0^o$ and $\theta_i = 90^o$) and an artificial conductivity of (a) 0 S/m; and (b) 0.0032 S/m.

space. A sufficiently lossy lumped element inside the enclosure would alter the field distribution from that of the empty cavity. Instead, a very small value of loss is distributed throughout the solution space by artificially assigning a conductivity to the free-space cells of the FDTD mesh. This approach was first published in [134], and it was also used in [129].

The FDTD prediction for cavity #2 was computed again, but with the free-space cells artificially assigned a conductivity of 0.0032 S/m, and the number of time steps was reduced to 16,000. In Fig. 4.5(b), the time-domain fields at the center of the cavity are shown versus number of time steps, and the last 3,000 time steps are shown in the inset. The late-time fields have now been driven almost to zero within 16,000 time steps and an FFT can be performed accurately. Therefore, the introduction of a small artificial conductivity can resolve the problem of extremely large simulation times of high Q structures.

The inclusion of artificial losses in a problem is expected to alter its physical response. However, it has been found in our SE studies that this method can provide very accurate results for small artificial conductivities. Based on observations from these studies, several speculative conclusions can be drawn. When the free-space cells are assigned a very low value of conductivity, the loss experienced by the pulse is cumulative over a large number of time steps, and the greatest effect is on the late-time fields. When the free-space cells are assigned a higher value of conductivity,

the initial pulse response of the cavity is altered, and the accuracy of the prediction is degraded. However, if the conductivity of the free-space cells is increased as a function of time steps from an initial value of zero, the initial pulse response of the cavity is virtually unaltered from its true free-space response. The artificial loss then increases to values that are effective in forcing the late-time fields to zero. The introduction of a linearly increasing artificial loss to the free-space cells of an FDTD problem consisting of a cavity with apertures was found to greatly reduce the computation time of the calculations, reduce the computer memory requirements, enable the solution of otherwise possibly intractable problems, and yield results that are in excellent agreement with measurements.

2. Voltage Source with Internal Resistance

Here, the SE of cavity #2 is examined using procedure #2. Therefore, the cavity is excited by a 3 cm probe and the far-field is computed along the normal outward direction to the aperture ($\phi_o = 0^o$, $\theta_o = 90^o$). A very effective technique that reduces the simulation time is based on a source with an internal resistance that provides the excitation [97],[125],[126],[140]. This source inserts losses in the computational domain by incorporating a resistance in its excitation and thereby forcing the transients in a resonant structure to decay rapidly.

To illustrate the effectiveness of this type of excitation, the time-domain far-field is plotted for cavity #2 for a voltage source with internal resistance, $R_s = 0$ and 200 ohms, in Fig. 4.6. Obviously, the field in the case with no internal resistance ($R_s = 0$) has not decayed to zero even after 60,000 time steps, indicating the resonant behavior and the high quality factor, Q, of the cavity. On the contrary, in the second simulation ($R_s = 200$ ohms), the field converged to zero very fast and the FDTD calculation time significantly reduced. The approach that was proposed in the previous subsection, inserts artificial losses in the computational domain in order to accelerate the simulation and decrease the required time for the transients to decay. However, the source with the internal resistance has the advantage of not altering or modifying the physical problem by including artificial losses. The only limitation of the source with the internal resistance is that it must be attached to a probe (monopole or dipole) which exists in the domain. If such a probe does not exist

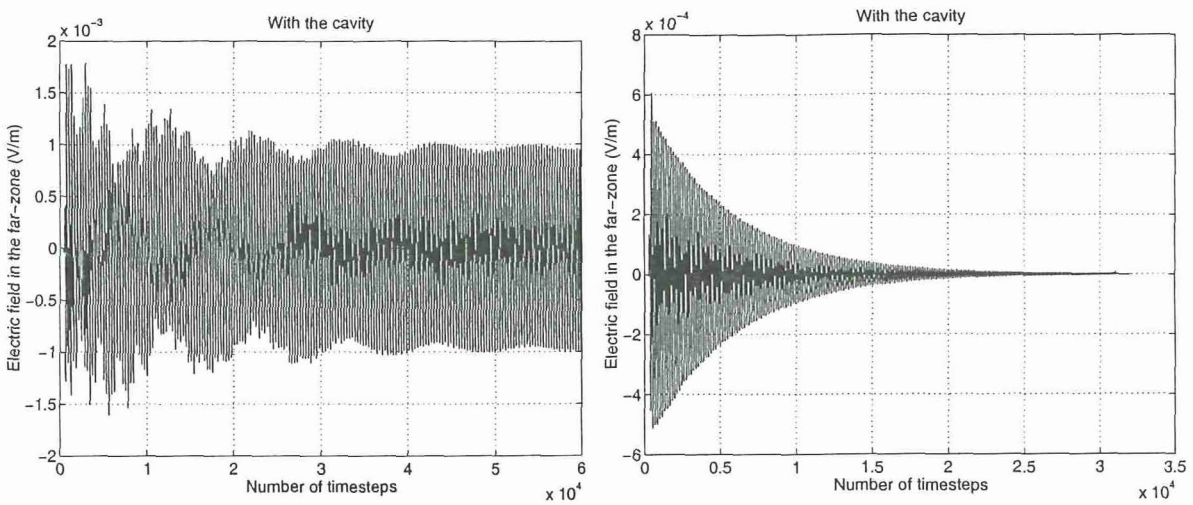

(a) (b)

Figure 4.6: Time-domain far-field of cavity #2 at observation angle, $\phi_o = 0^o$ and $\theta_o = 90^o$, for (a) $R_s = 0$ ohms; and (b) $R_s = 200$ ohms.

in the computational domain, then this source cannot be used. However, it should be pointed out that a cavity can potentially be excited using a infinitesimal dipole, which is implemented as a delta-gap source. An internal resistance can be connected to this source, in order to accelerate the simulation, without effectively having a probe (metallic wire) present in the cavity (see also Subsection F.). Usually, when studying SE of cavities, probes are not present in the physical geometry. Although, when measurements of SE are performed, a probe should always be used to sample the fields in the cavity.

E. Windowing

Harmonic analysis, such as the Fourier transform (FT), is based on the projection of a signal on a basis set which spans the time interval of interest. In the case of FT this basis is formed either by exponential functions alone or by sine and cosine functions. The selection of a finite time interval and of the orthogonal basis functions over this interval causes one of the main problems of harmonic analysis. The signal of interest spans a band of frequencies from which, only those that coincide with the basis will project on a single basis function, whereas all other frequencies will have non zero projections on the entire basis set. This phenomenon is often called spectral

leakage [141]. One of the common approaches that attempts to resolve the problem of spectral leakage and which has been extensively used in the field of signal processing is windowing. Windows are weighting functions that multiply the signal of interest and aim in the reduction of discontinuities at the boundaries. This is usually accomplished by matching as many derivatives as possible at the boundary. Naturally, the most straightforward way to do this matching is by setting the value of these derivatives to zero or near zero [141]. Windowing was introduced in FDTD simulations in [115], without though presenting a thorough elaboration of its capabilities and drawbacks.

Let the signal of interest be $f(t)$ and the window $w(t)$. Then the windowed signal, $f_w(t)$, can be written as

$$f_w(t) = f(t)\ w(t) \tag{4.3}$$

From basic theory of signals and systems, it is well known that the FT of the windowed signal, $f_w(t)$, is the convolution of the FTs of $f(t)$ and $w(t)$

$$F_w(\omega) = F(\omega) * W(\omega) \tag{4.4}$$

The spectrum of most windows usually resembles a sinc function, i.e., it exhibits a main lobe and multiple side lobes. Windowing of a signal causes spectral leakage which results in biasing of the amplitude and the position of the harmonic estimate. This bias is particularly important in the detection of small signals in the presence of nearby large signals [141]. This biasing effect is less severe for windows that exhibit low amplitude side-lobes far from the main lobe, and a rapid transition to the low side lobes. Another problem that can occur by windowing is masking of resonances that are located closely to each other. This happens because the window imposes an effective bandwidth on each resonance. The resolution that a window can provide is related to its main lobe beamwidth; e.g., a 3-dB beamwidth criterion is commonly used in signal processing. This criterion means that two equal strength main lobes separated in frequency by less than their 3-dB beamwidths will give a single resonance and will not be resolved as two distinct resonances [141]. Therefore, if a particular problem exhibits very sharp resonances, then a window with narrow main lobe beamwidth should be used in order to be able to resolve them. It is apparent, that there must be a compromise between side lobe level and beamwidth when a window is chosen or designed.

Numerous types of windows, have been used in the field of signal processing, such as Hanning, Blackman-Harris, Kaizer, Hamming, etc., [141]. Here, only few of the most common windows are examined for illustration purposes. Assuming that the windows are centered at time zero and are sampled using $N+1$ equally spaced samples, i.e., $w(n)$, $n = -N/2, ..., 0, ..., N/2$, they can be written as

a. Rectangle window

$$w(n) = 1.0 \tag{4.5}$$

This window and its spectrum are illustrated in Fig. 4.7 for $N = 10,000$. The FFT frequency resolution was $\Delta f = 1.68$ MHz (obtained by zero padding of the window so that the total number of time samples would be 2^{16}). These parameters are also used for the other window illustration examples that follow.

b. Hanning window

$$w(n) = \cos^2\left(\frac{\pi n}{N}\right) \tag{4.6}$$

This window and its spectrum are illustrated in Fig. 4.8.

c. Tukey window

$$w(n) = \begin{cases} 1.0, & 0 \leq |n| \leq a\dfrac{N}{2} \\ 0.5\left[1.0 + \cos\left(\dfrac{\pi\left(|n| - a\dfrac{N}{2}\right)}{(1-a)\dfrac{N}{2}}\right)\right], & a\dfrac{N}{2} < |n| \leq \dfrac{N}{2} \end{cases} \tag{4.7}$$

The Tukey window is a tapered cosine. The window as well as its spectrum are shown in Figs. 4.9 and 4.10 for $a = 0.5$ and 0.75, respectively.

To illustrate the use and application of windowing in the context of FDTD, the shielding effectiveness of a cavity #2 [see Fig. 4.1(b)] is examined. To compute the SE, procedure #2 is used. The observation point in the far-field is along the normal outward direction to the aperture ($\phi_o = 0^o$ and $\theta_o = 90^o$). Remember that in order to compute the SE two simulations are needed; one in the presence and

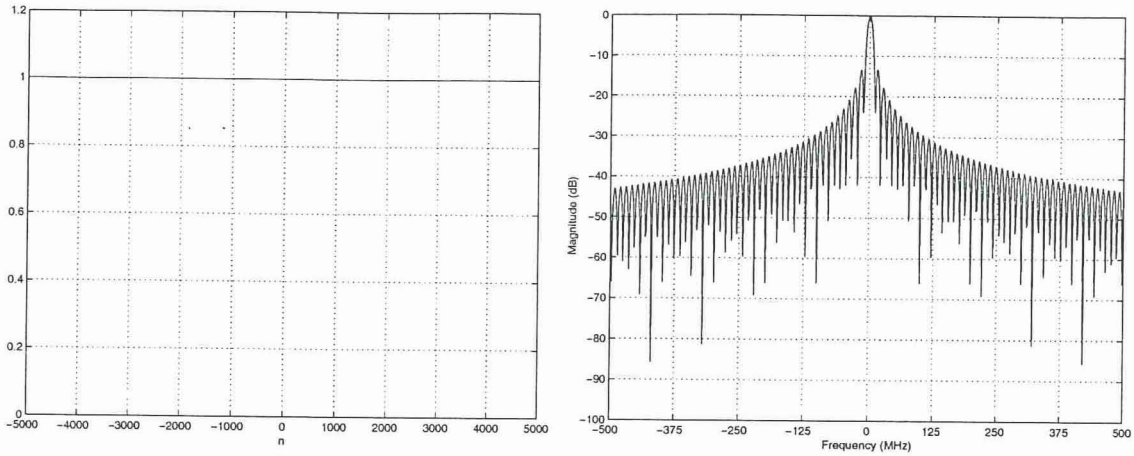

(a) (b)

Figure 4.7: (a) Rectangle window. (b) Its spectrum.

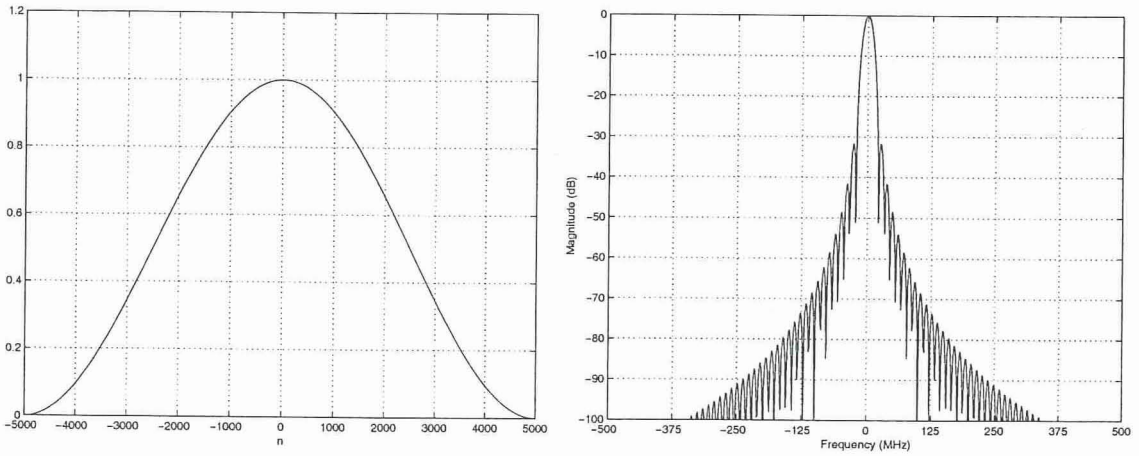

(a) (b)

Figure 4.8: (a) Hanning window. (b) Its spectrum.

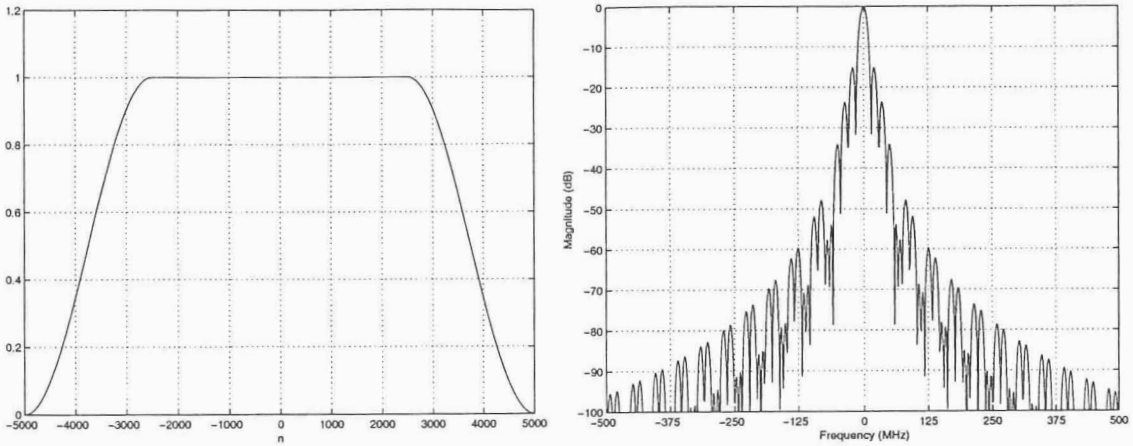

(a) (b)

Figure 4.9: (a) 50% Tukey window. (b) Its spectrum.

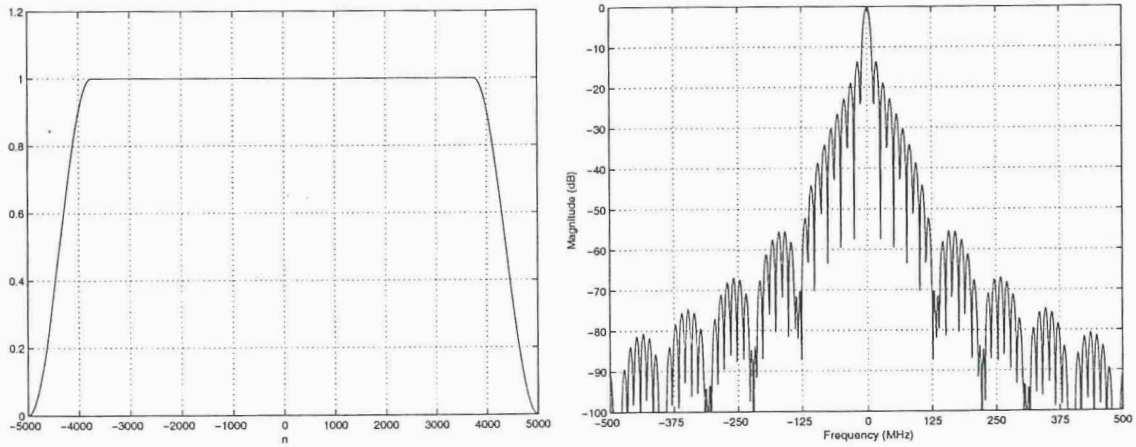

(a) (b)

Figure 4.10: (a) 75% Tukey window. (b) Its spectrum.

one in the absence of the cavity. The simulation times for the two cases with and without the cavity (for the meaning of the expressions with and without the cavity see Subsection A.) were chosen such that the transients would decay to zero and they were 32,000 and 6,000 time-steps, respectively. These simulation times were achieved using a voltage source with internal resistance $R_s = 200$ ohms. The corresponding time-domain far-fields are illustrated in Fig. 4.11. Notice, that the more time consuming simulation is the one with the cavity present, where the Q of the structure is high and the transients need a longer time to decay to zero. Using these FDTD results SE was computed and this calculation is used as a reference.

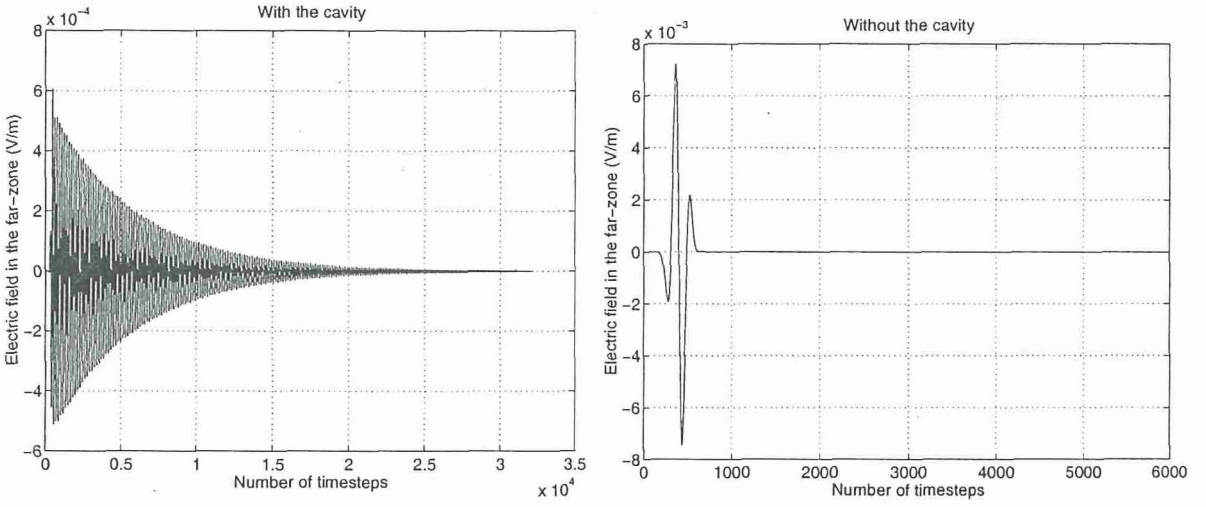

Figure 4.11: Time-domain far-field of cavity #2. (a) Top and sides of cavity present. (b) Top and sides of cavity absent.

Furthermore, to present the use of windowing, it is assumed that FDTD simulations were run for both geometries, with and without the cavity, only for 5,000 time-steps. Obviously, for the case without the cavity there is no impact of chopping the time response, because the far-field has already decayed to zero and therefore it can be Fourier transformed without significant errors. However, for the case with the cavity the far-field after 5,000 time-steps has not decayed to zero yet and is still highly oscillatory. As a result, if this response is directly Fourier transformed (equivalent to rectangular windowing), then significant error will be introduced in the computation of SE. Alternatively, different windowing can be applied to the far-field response

before the FFT is used. The length of the window is 10,001 time-steps including both the negative- and positive-time samples. However, only the positive-time samples of the window are used because it is assumed that the FDTD response is zero for negative times. The windowed time-domain FDTD response is formed by multiplying the positive time half of the window with the first 5,001 time-domain points (including time, $t = 0$) of the entire FDTD response (see Fig. 4.12). Also, before FFT is used the windowed data are padded with zeros to increase the frequency resolution.

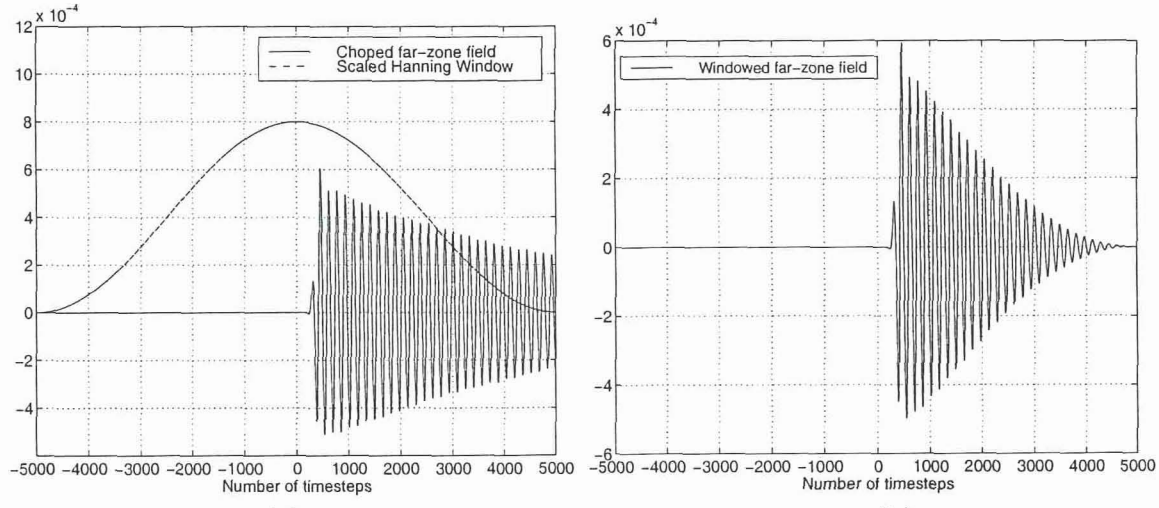

Figure 4.12: Illustration of windowing procedure. (a) Time-domain far-field along with scaled (for plotting purposes) Hanning window (the actual maximum of the window is one). (b) Windowed time-domain far-field.

Fig. 4.13(a) illustrates the SE computed using the rectangle window. Obviously, there are significant oscillations in the response due to the high side lobe level (-13 dB) of the rectangle window. The oscillations are so high at some frequencies that they mask the actual resonances of the response. This problem is resolved by using other types of windows. Fig. 4.13(b) shows the SE calculated using the Hanning window. Figs. 4.13(c) and 4.13(d) illustrate the SE using the Tukey window for $a = 0.5$, and 0.75, respectively. All the figures also compare the results with the reference FDTD calculations (labeled as no windowing in the graphs) that used the entire time-domain responses. Obviously, a computation performed using one of the windows, besides the rectangle, yields better results and gives more reasonable agreement with the

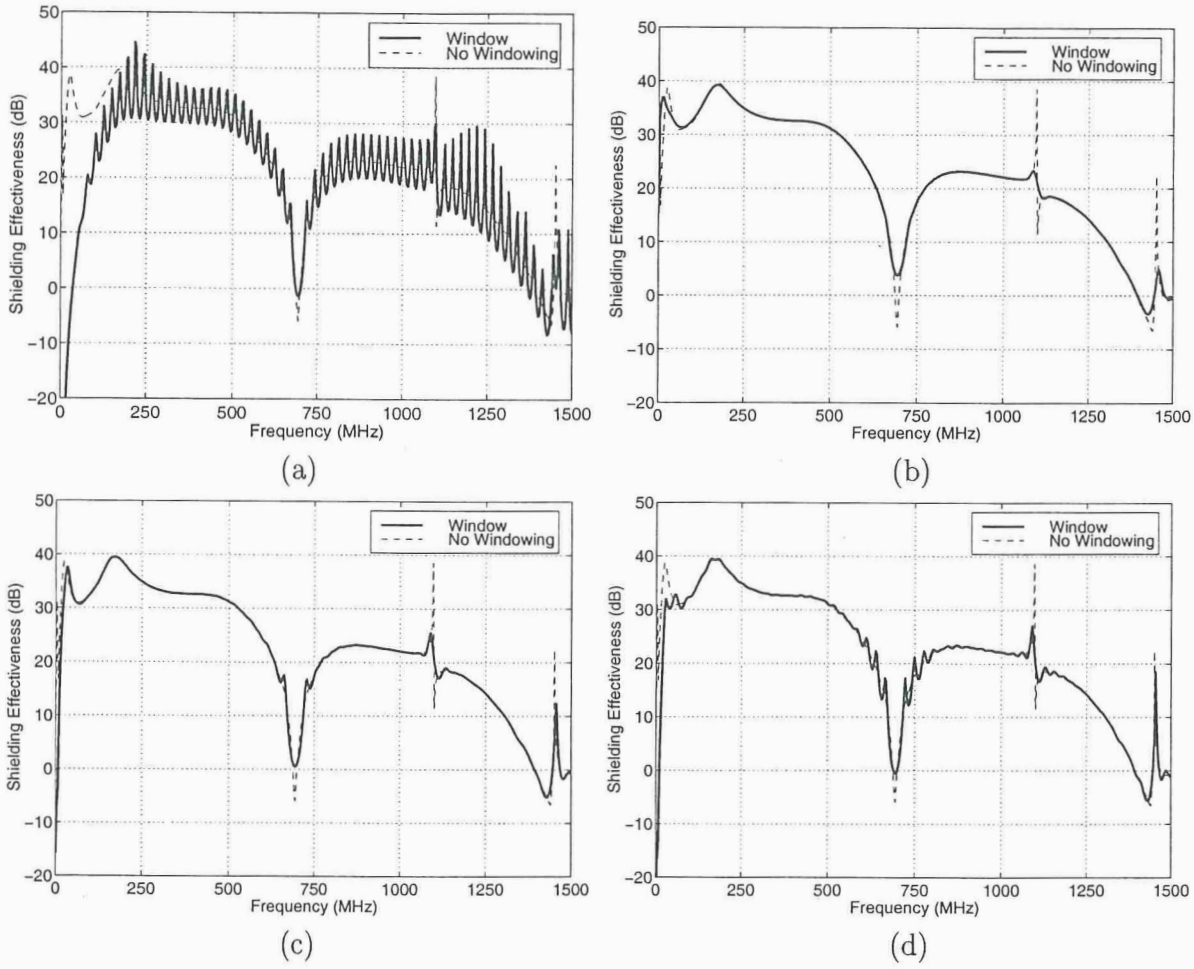

Figure 4.13: Shielding effectiveness of cavity #2 computed using (a) Rectangle; (b) Hanning; (c) 50% Tukey; and (c) 75% Tukey window.

actual (reference) FDTD response. This improvement and absence of oscillations in the SE computations is due to the reduced side lobe level of the windows. Another effect, that is observed in the results computed using certain windows (Hanning), is the substantial broadening of the resonances. This is due to the increased beamwidth of the main lobe of these windows. For this example, it seems that the Tukey window performs the best (especially for $a = 0.5$). Furthermore, the sharpness of the Tukey window is adjustable by the parameter a, providing additional flexibility. It should be pointed out that windowing is a post-processing procedure and therefore experimenting with different types of windows, when performing FFTs, is possible.

It can be concluded that windowing can be very helpful when transforming time-domain data to frequency domain, especially if the time response has not decayed to zero. From another viewpoint, windowing can contribute in computational savings by reducing the simulation time required to obtain accurate Fourier transforms. Essentially, in the example presented here it was shown that the shielding effectiveness computed using windowing needed only 5,000 time-steps whereas the standard approach of FFT (no windowing) required 32,0000 time-steps. The two different approaches, provided identical results except at the resonances. Therefore, it can be claimed that windowing provided a savings factor of 6.

F. Comparison for SE definitions

In this subsection, the different definitions of SE presented in Subsection A. are examined and compared. Fig. 4.14(a) and (b) illustrate the two first procedures #1 and #2 that were already used above to compute SE. Revisiting the definitions of SE following procedures #1 and #2, which were presented in Subsection A., two alternative procedures can be defined. The first one, which can be considered reciprocal definition of procedure #2, is the same with the one of procedure #1 but instead of collecting the data at the center of the cavity, the field is sampled at the base of an open-circuited probe existing in the cavity [see Fig. 4.14(c)]. This procedure is labeled procedure #3. Similarly, the second alternative definition of SE is reciprocal of procedure #1 and is exactly the same with procedure #2 except the fact that the cavity is not excited using a probe but rather a delta-gap excitation at its center [see Fig. 4.14(d)]. This procedure is labeled procedure #4.

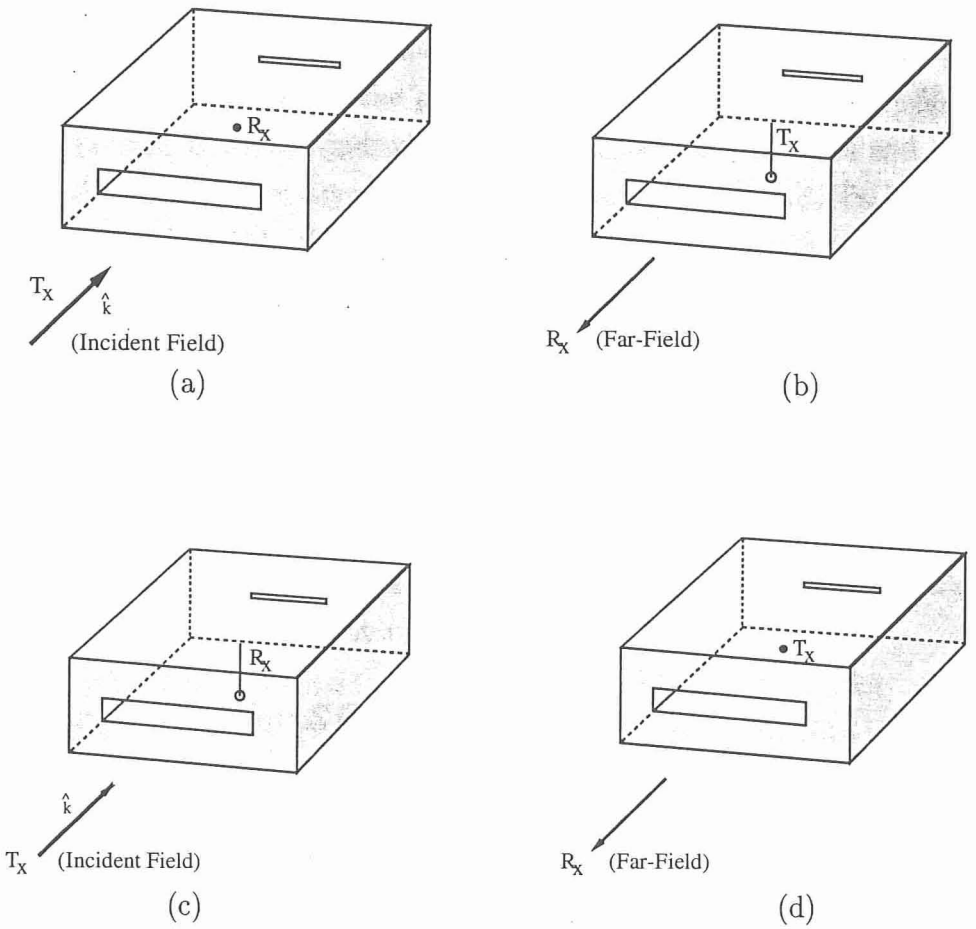

Figure 4.14: Illustration of shielding effectiveness definitions (R_x=receiving point, T_x=transmitting point, •=center of cavity). (a) Procedure #1 (Plane Wave excitation-No probe); (b) Procedure #2 (Probe excitation); (c) Procedure #3 (Plane Wave excitation-receiving at a probe); and (d) Procedure #4 (Delta-gap excitation at the center).

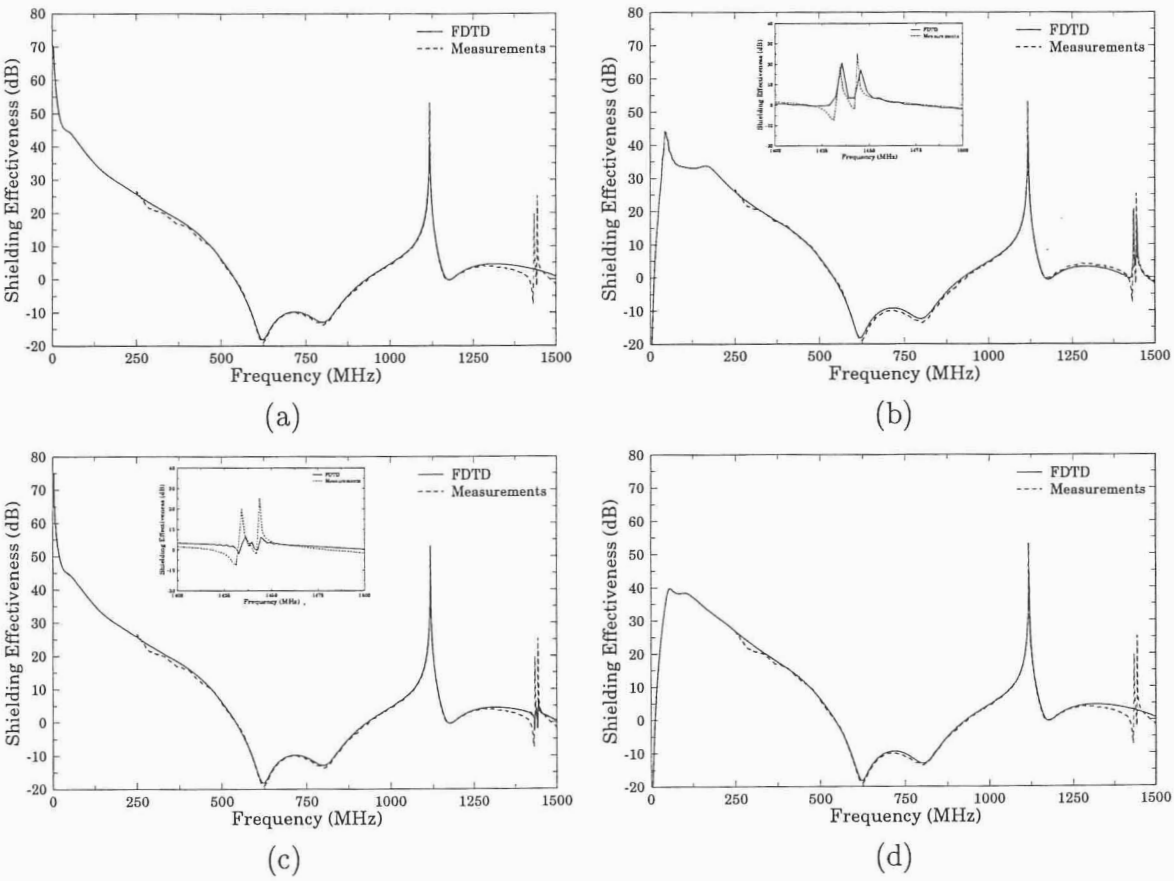

Figure 4.15: Shielding effectiveness of cavity #1 using (a) Procedure #1 (Plane Wave excitation-No probe); (b) Procedure #2 (Probe excitation); (c) Procedure #3 (Plane Wave excitation-receiving at a probe); and (d) Procedure #4 (Delta-gap excitation at the center).

For this study, the SE of cavity #1 is computed for normal incidence ($\phi_i = 0^o$ and $\theta_i = 90^o$ when using procedure #1, or $\phi_o = 0^o$ and $\theta_o = 90^o$ when using procedure #2). First, procedure #1 is used and the predicted SE is plotted along with the measurements in Fig. 4.15(a). The agreement between FDTD and measurements is excellent except near 1.4 GHz where the computations do not exhibit the resonance that appeared in the measurements. This resonance is attributed to the probe feeding the cavity in the measurements which was absent in the FDTD calculations that followed procedure #1 [see Fig. 4.14(a)]. Therefore, it is expected that any effects of the probe itself will not be predicted by FDTD. However, when procedure #2, which uses a probe to excite the cavity [see Fig. 4.14(b)] as done in the measurements, was used to compute the SE, FDTD predicted accurately the resonance at the higher end of the band. The result of this simulation is shown in Fig. 4.15(b). Obviously, the presence of the probe has an effect on the SE of a cavity, especially at higher frequencies where it is electrically longer and higher-order modes exist in the cavity.

The two new procedures #3 and #4, were also used to predict the SE of cavity #1, and the results are illustrated in Figs. 4.15(c) and 4.15(d), respectively. It can be concluded that procedures #2 and #3, which include the probe in the simulation, were able to predict the resonance associated with the probe. On the contrary, procedures #1 and #4, which do not include the probe in the simulation, did not predict the resonance attributed to the probe. Both types of SE definitions, including or excluding a probe, are useful. The ones including the probe are appropriate for direct comparison with measurements (which commonly use a probe). However, the ones excluding the probe are advantageous because SE of cavities usually need to be evaluated without probes existing in the cavities (unless the probes are in the physical geometry). Therefore, in the next results one representative of each type of SE definitions (procedure #1 and #2), are used to illustrate the SE of cavities with and without the probe.

Finally, notice the different low frequency variations of SE computed by the four procedures. Procedures #2 and #4, which used either a probe or a delta gap excitation, provided predictions of SE that exhibited deep nulls near DC [see Figs. 4.15(b) and (d)]. These nulls can be attributed to either the use of hard sources in the cavity or artifacts of the FDTD excitation models at low frequencies. On the contrary,

procedures #1 and #3, which used plane wave excitations, provided SE predictions that exhibited peaks near DC [as expected; see Figs. 4.15(a) and (c)].

G. Results

In this subsection, the SE of the three cavities illustrated in Fig. 4.1 are examined. It should be pointed out again that the SE of each of these cavities is computed following either procedure #1 or #2 presented in Subsection A.

For cavities #1 and #2, a normally incident plane wave to the aperture is used as an excitation for procedure #1 ($\phi_i = 0^o$, $\theta_i = 90^o$), or equivalently the observation point in the far-field is along the normal outward direction to the aperture for procedure #2 ($\phi_o = 0^o$, $\theta_o = 90^o$). Notice again, the reciprocity of the excitation and observation points for the two procedural definitions. The predictions are compared with measurements for cavity #1 in Fig. 4.16. The agreement of the FDTD calculations with the measurements is excellent. Also, FEM predictions are plotted in the same graph, and they compare very well both with FDTD and measurements. These FEM predictions and some other ones have been reported in [142]. The simulation based on procedure #1 did not use any artificial conductivity and needed 25,000 time-steps for the transients to converge to zero. The simulation based on procedure #2 and with the cavity, which is highly resonant, needed only 16,000 time-steps for the transients to decay. This was accomplished using the probe excitation of the cavity with an internal resistance of 100 ohms.

Similar comparisons are illustrated for cavity #2 in Fig. 4.17. In this case the use of either artificial conductivity (when using procedure #1), or a probe excitation with an internal resistance (when using procedure #2) is indispensable due to the high Q of the cavity. This is explained in detail in Subsection D.. In procedure #1 a linearly increasing artificial conductivity profile was used with a maximum of 0.064 S/m reached after 16,000 time-steps. In procedure #2 an internal resistance of 200 ohms was used and the simulation time was 62,000. Both procedures gave excellent agreement with measurements. The simulation time required for procedure #2 was significantly greater than the one of procedure #1. Note though, that the voltage source with an internal resistance facilitates the examination of structures with high quality factor Q, without changing the material properties of the physical geometry.

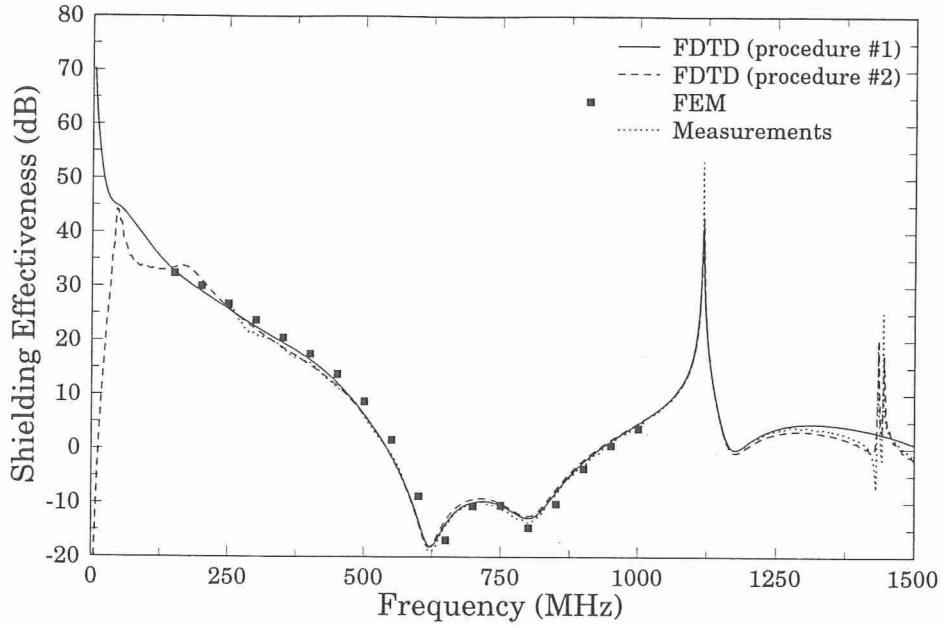

Figure 4.16: Shielding effectiveness of cavity #1.

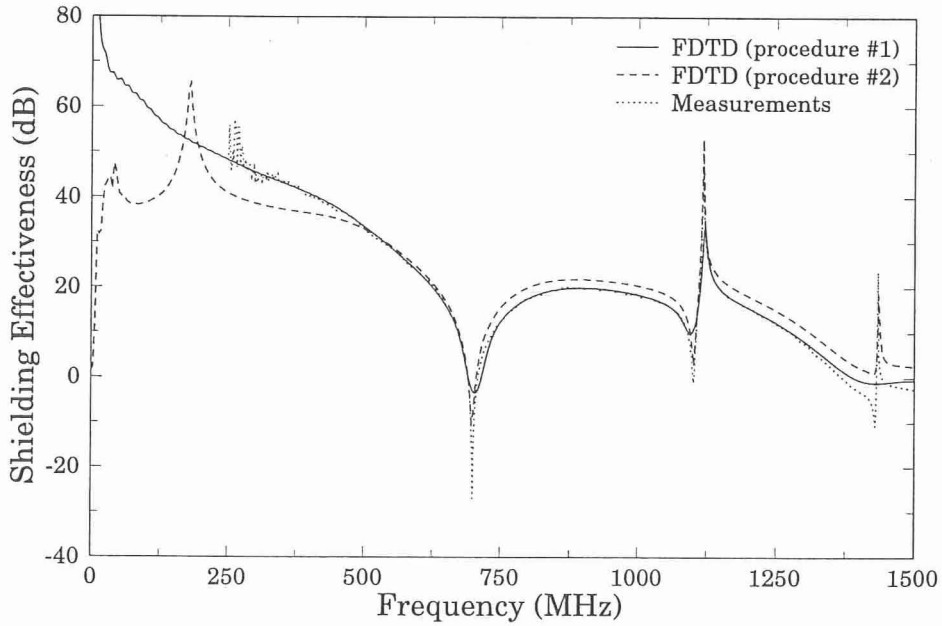

Figure 4.17: Shielding effectiveness of cavity #2.

Finally, for cavity #3, SE is computed for different incident azimuthal angles, ϕ_i, and for elevation angle $\theta_i = 90^o$ (describing the xy-plane). The FDTD computations are shown and compared with measurements for various angles ϕ_i in Fig. 4.18. The agreement is again very good. Measurements were performed for every 10^o of azimuth angle. Moreover, Fig. 4.19(a) illustrates the measured shielding effectiveness of cavity #3 for different incident angles, ϕ_i, versus frequency. It can be concluded, that at most of the frequencies SE is less when the field penetrates in the cavity from the front than from the back for symmetric azimuthal angles of incidence, ϕ_i, about $\phi = 90^o$. This is attributed to the significantly larger aperture located at the front wall compared to the one located at the back wall. Fig. 4.19(b) plots the measured SE of cavity #3 versus ϕ_i for few frequencies. Some of these frequencies where selected to be the ones where the SE exhibited nulls (622, 800, and 1155 MHz). An interesting observation is that the maximum of SE does not occur for all frequencies at normal incidence ($\phi_i = 90^o$).

For all three cavities, the FDTD simulations that used procedure #2 provided predictions which exhibited some nulls and peaks at the lower band of the frequencies and a deep null close to DC. These peaks and nulls can be attributed to either the effects of the probe in the cavities or artifacts of the FDTD probe excitation model at low frequencies.

H. Summary

In this section, shielding effectiveness analysis was performed for cavities with apertures. Various acceleration techniques were presented. The probe excitation by a voltage source with an internal resistance enabled the analysis of highly resonant structures. Also, the introduction of small artificial loss proved to be very useful when analyzing high Q structures using the plane wave excitation.

Furthermore, issues related to the Fourier transform of time-domain data were discussed. Windowing approaches were introduced and applied in FDTD computations. Different windows were presented and their advantages as well as their drawbacks were reported. Also, general guidelines for choosing windows were analyzed and explained in detail. It was found that windowing can be very useful, especially when FFTs of time-domain data that have not converged to zero are performed. Win-

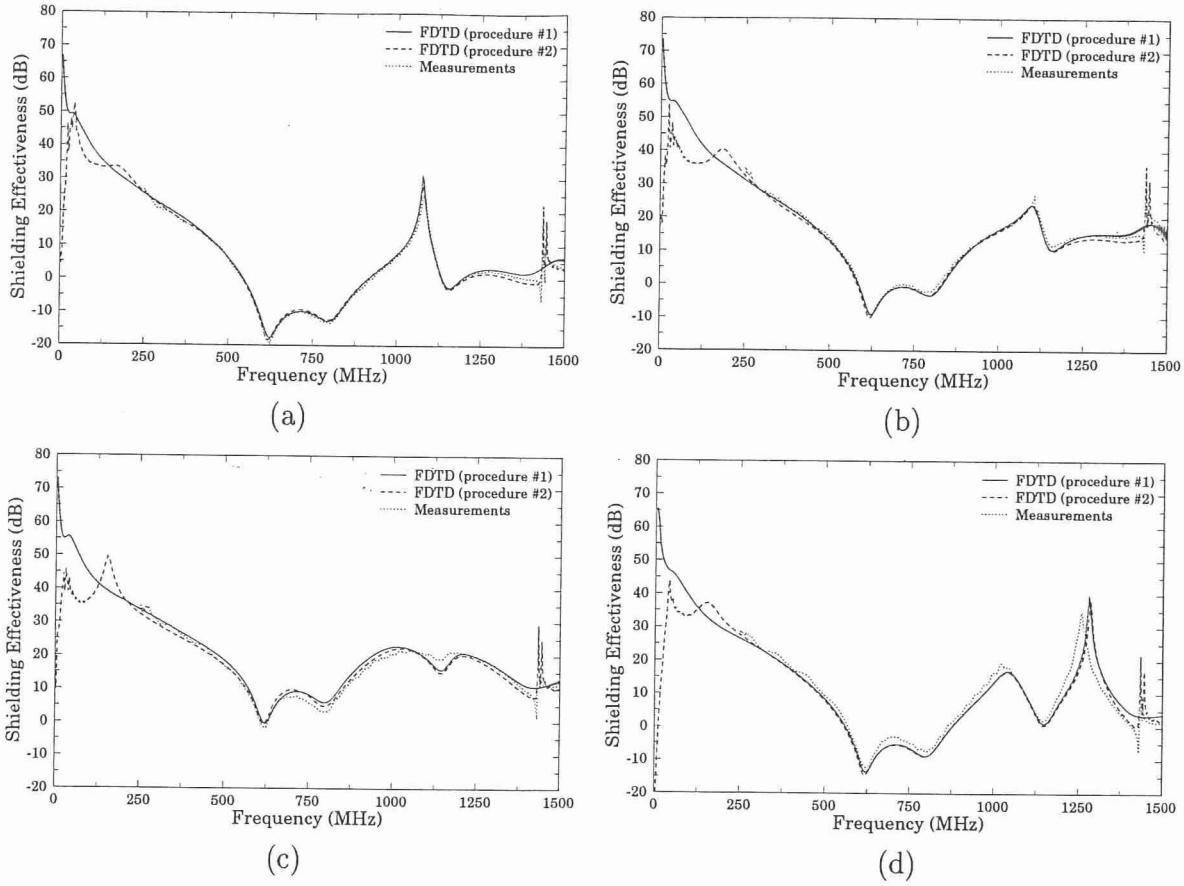

Figure 4.18: Shielding effectiveness of cavity #3 for incident angle (a) $\phi_i = 0^o$, $\theta_i = 90^o$; (b) $\phi_i = 60^o$, $\theta_i = 90^o$; (c) $\phi_i = 120^o$, $\theta_i = 90^o$; and (d) $\phi_i = 180^o$, $\theta_i = 90^o$.

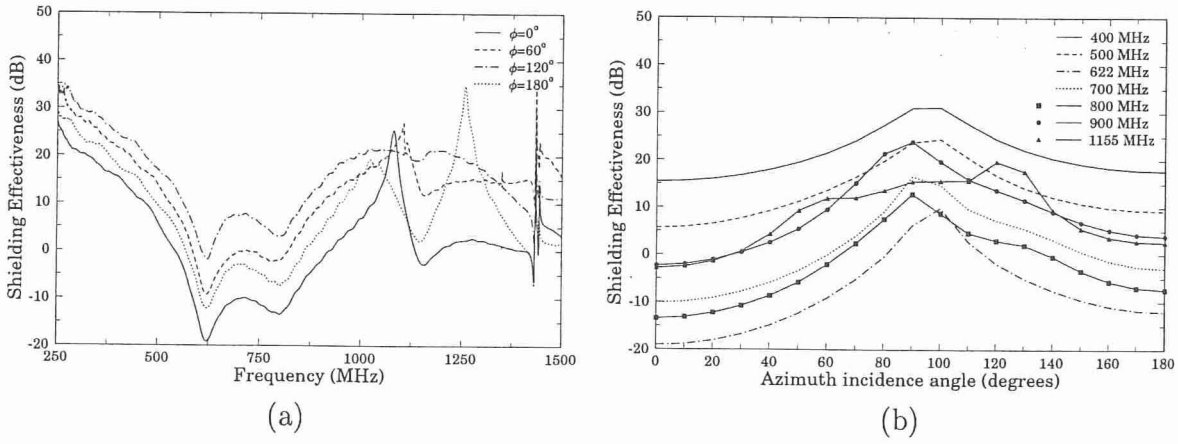

Figure 4.19: Measured shielding effectiveness of cavity #3 for different incident angles. (a) Versus frequency. (b) Versus azimuth incident angle.

dows reduce the discontinuities at the boundaries of data sets and effectively resolve problems associated with spectral leakage. It was illustrated that even when severe discontinuities occur at the end of time-domain data sets, windowing can be used and provide very accurate results as long as the set of data is sufficiently long to describe the response of a structure. Windowing can be particularly beneficial in the analysis of both large and high Q structures where the transients need a prohibitive simulation time to decay. In such cases windowing is probably the only way that can provide predictions of reasonable accuracy.

Finally, different possible shielding effectiveness definitions in the context of FDTD were presented and compared. Their respective pros and cons were analyzed. All numerical results were compared with measurements and exhibited excellent agreement. Shielding effectiveness was computed and measured for different incident angles at a band of frequencies covering up to 1.5 GHz.

II. HIRF Penetration Through a Scaled Fuselage

By examining the shielding effectiveness of various simple configurations of boxes with apertures in the previous section, the FDTD method has been validated and proven accurate through comparison of the FDTD predictions with measurements. In this section, a more complex and realistic problem of penetration is considered. As discussed above, the HIRF problem has been of tremendous interest for airborne applications. Penetration of high intensity fields into commercial airplanes is a challenging problem, and it has stimulated a significant amount of research.

Direct analysis of HIRF penetration into a full-scale model of a fuselage is a very complicated problem consisting of a plethora of different materials and very complex geometric features. In addition, uncertainty for the accuracy of CAD models for full-scale airplanes as well as uncertainty of the various measurement parameters in full-scale setups makes the modeling and numerical simulation of such geometries very challenging. Especially, when numerical results are being validated, a controlled geometric setup as well as measurement environment are desired. This is the reason that stimulated the construction and analysis of a simplified scaled model of a Boeing 757 aircraft.

The geometry of the scaled model was constructed and measured in the ASU

anechoic chamber thereby providing a completely controlled environment. This model will be used for validation of the accuracy of FDTD predictions for HIRF penetration into complex models.

A. Construction and specifications of the geometry

The simplified fuselage is much larger than the simple boxes that were examined in the previous section. Its internal dimensions are 155 cm long by 20 cm wide by 24 cm high. These dimensions are sufficient to enclose a 1:20 scale model of a Boeing 757 fuselage that is shortened by 25%.

The construction plan for the simplified fuselage was to machine six flat panels using 0.061" thick aluminum stock, and then assemble the panels into a rectangular box. The two side panels would be grooved near the top and bottom edges so as to accept the edges of the top and bottom panels. The rectangular tube so formed would then be epoxied together as depicted in Fig. 4.20. A photograph of the aluminum panels is shown in Fig. 4.21.

The grooves in the side panels help to accurately locate the top and bottom panels, and the parts of the side panels which extend beyond the top and bottom would provide surfaces with which the assembly could be epoxied without altering the interior of the model. However, it was decided that the model could also be useful for scaled measurements of EMI between passenger carried Portable Electronic Devices (PEDs) and antennas mounted on the top of the fuselage if the "rails" extending beyond the top of the model were removed. To remove the top "rails," the top corners of the model had to be epoxied from the inside. A conservative estimate of the epoxy volume needed in the top inside corners of the model is less than 0.21% of the total interior volume of the model. Furthermore, the epoxy is a dielectric that will be at locations of relatively low field intensity, so it is expected that this deviation from the ideal will have a negligible impact on shielding effectiveness measurements.

The first step in assembling the fuselage was to clean the aluminum panels. The effectiveness of epoxies depends on the preparation of the materials to be joined. Considerable effort was expended in cleaning the panels and their grooves. After cleaning, sandpaper was used to apply a fine cross hatching into the surfaces on which the epoxy was to be applied. The top and sides were clamped together in an

upside down orientation, as shown in Fig. 4.22, and epoxy was applied to the interior corners. Note in the photograph that expanded polystyrene ribs were used to aid in

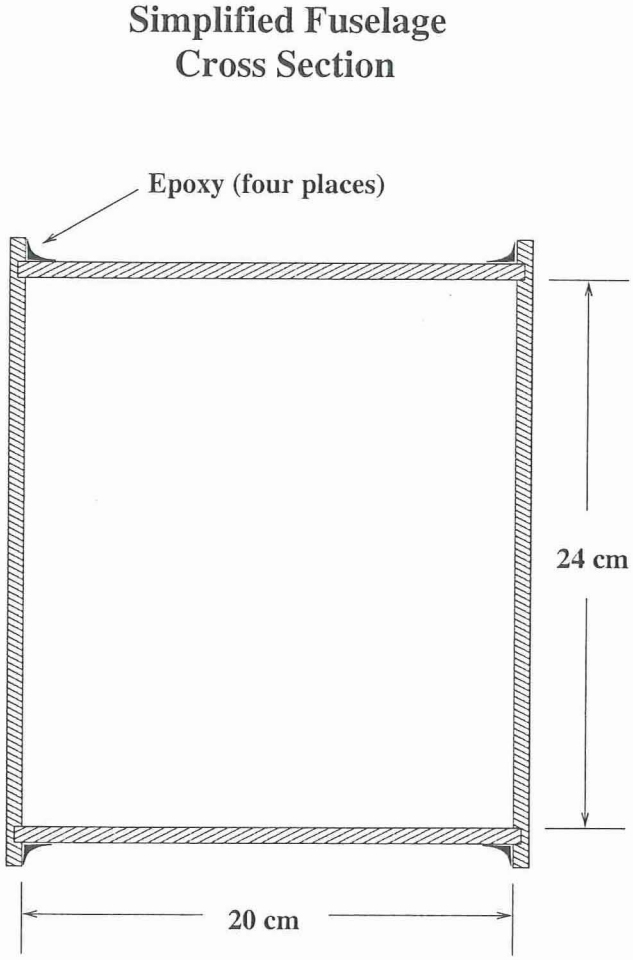

Figure 4.20: The construction of the simplified fuselage was conceived as being four panels joined together with epoxy applied to outside surfaces, as shown. Instead, the protrusions of the side panels beyond the top panel have been trimmed flush with the top, and the top panel is epoxied from the inside. This alteration extends the usefulness of the model by enabling meaningful scaled measurements of PED coupling to top-mounted aircraft antennae.

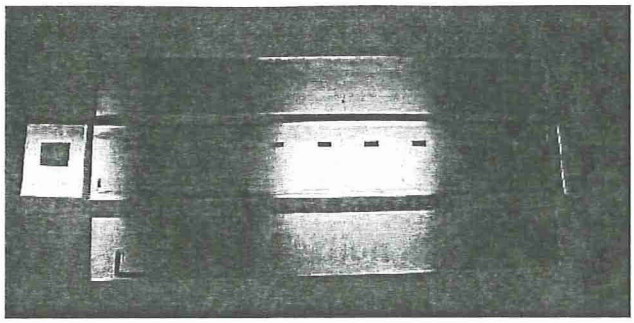

Figure 4.21: A photograph showing five of the six aluminum panels which form the simplified fuselage.

keeping the sides and top orthogonal to one another.

Next, the bottom panel was fitted to the assembly, and was epoxied into place. Here the epoxy was applied on the outside surfaces, as was originally envisioned. A photograph of the bottom panel being installed is shown in Fig. 4.23. The top "rails" were then removed (Fig. 4.24), and the top corners were covered over with aluminum tape.

The top, bottom, and sides were now in the form of a rectangular tube. The front and back ends are attached with aluminum tape, enabling them to be removed so as to provide access to the inside. A front view of the completed model is shown in Fig. 4.25. An *sma* connector was installed in the bottom panel, 50 cm from the front and on the centerline of the fuselage, as a probe for the preliminary measurements. The connector has a non-captivated center conductor so that the wire probe can be easily removed and replaced. For all the measurements and predictions, the probe length was 6 cm.

B. Measurements

The measurements were performed in ASU's anechoic chamber in very much the same manner as were the SE measurements of the small box. The new shielding effectiveness measurement configuration is again a direct illumination of the simplified fuselage by an auxiliary antenna. The fuselage was placed equidistantly from the rear and side walls of the chamber. The auxiliary antenna was located on the longitudinal center of the chamber. This configuration is illustrated in Fig. 4.26. With this

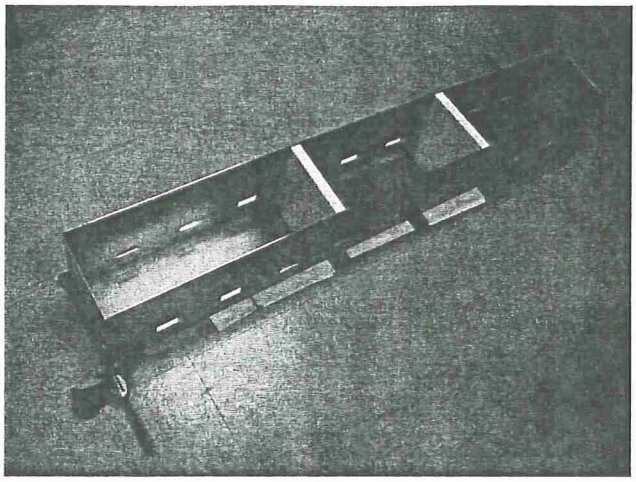

Figure 4.22: The first step in the assembly of the simplified fuselage was to epoxy the top and sides together from the inside.

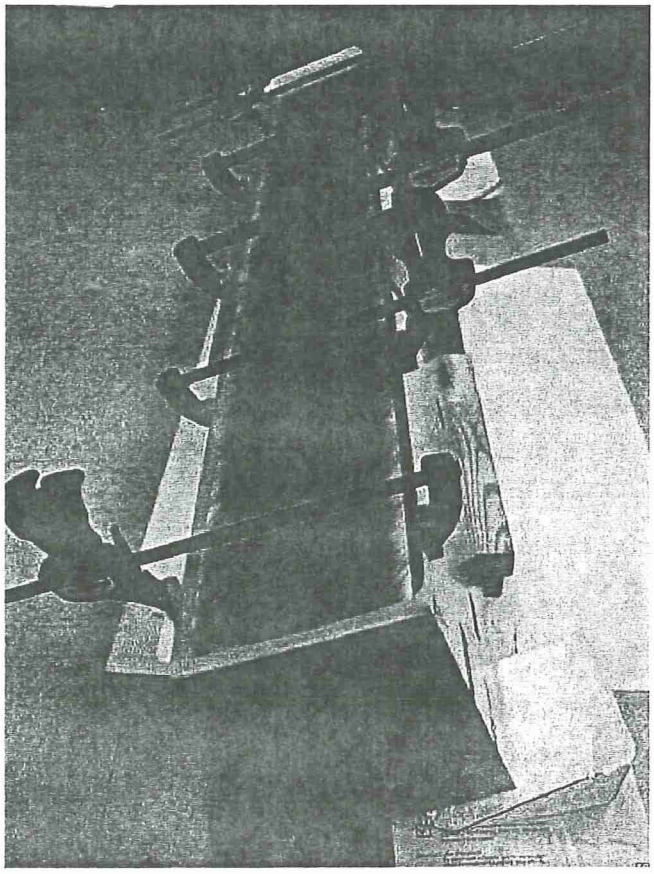

Figure 4.23: The bottom panel was then epoxied to the assembly.

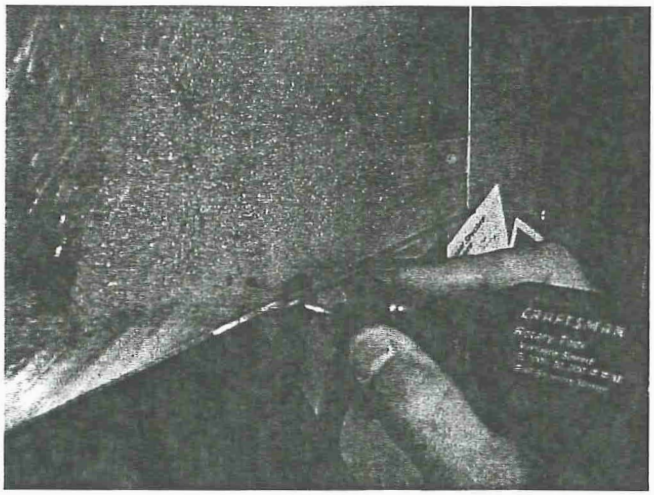

Figure 4.24: The top "rails" were removed using a rotary tool, files and sandpaper.

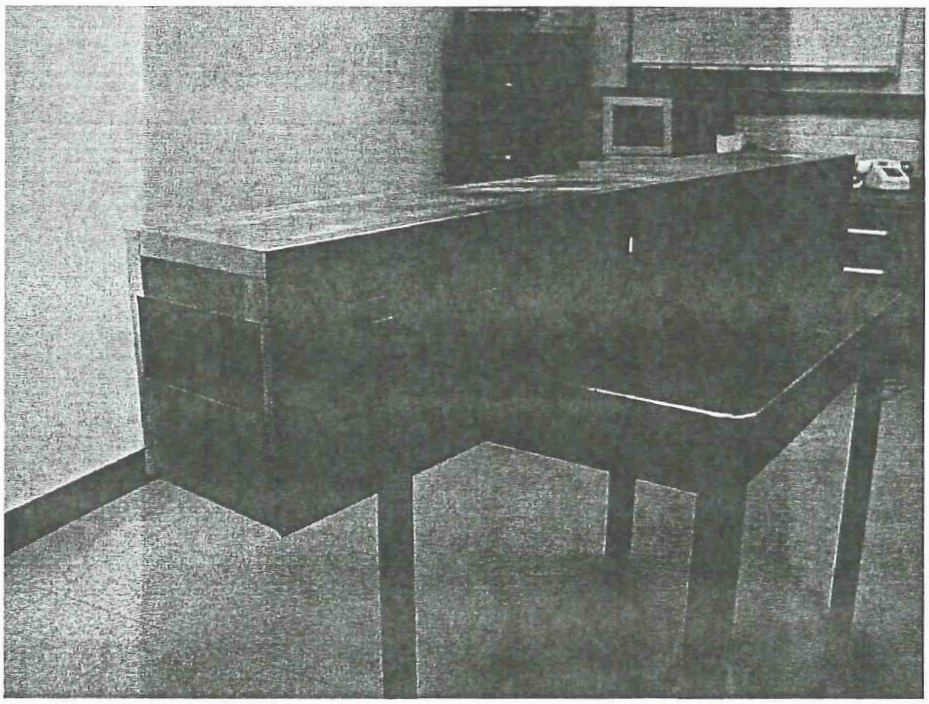

Figure 4.25: A front view of the completed "simplified fuselage" scale model.

setup, there is no feed spillover. The only sources of asymmetry in this configuration are the SPCR, and its feed and feed support tower. The feed tower was concealed using carbon loaded foam microwave absorbing material. The auxiliary antenna was deliberately oriented so as to place the SPCR reflector in its back lobe. To further reduce the illumination of the reflector, an absorber baffle was placed between it and the auxiliary antenna. A photograph of the auxiliary antenna and absorber baffle is shown in Fig. 4.27. Also, due to the reduced distance between the auxiliary antenna and the simplified fuselage, the response of the desired signal path is enhanced relative to any undesired scattering from the room as compared to the previous configuration using the SPCR reflector.

At a separation distance of 3.8 m, the simplified fuselage was very much in the near field of the auxiliary antenna. However, the illuminating phase-fronts, due to their small vertical dimensions, are practically linear (in the vertical plane) over the extent of the model's apertures. Therefore, for this particular geometry (in this xy-plane), there is no significant difference between its spherical and cylindrical near-field responses. Thus, the use of the cylindrical NF/FF transformation is justifiable and valid.

The HP8510 network analyzer can acquire 801 frequency points per measurement. This resolution is insufficient to accurately sample the rapid variations in the frequency response of the model. Therefore, 1 GHz bands were measured with 801 frequency point resolution, up to 11 GHz. An IF averaging factor of up to 1024 was used to reduce the effects of noise. The synthesizer was phase-locked to each measured frequency and produced an output power of +11 dBm.

However, in order to perform the NF/FF transformation, an increased azimuthal sampling rate was required due to the shortened separation distanced between the simplified fuselage and the auxiliary antenna. For frequencies up to 2 GHz, the angular spacing between measured points was one degree. Between 2 GHz and 6 GHz, this spacing was reduced to 0.4 degrees. Above 6 GHz, the necessary sample spacing was 0.2°. This resulted in the collection and processing of over 10.5 million complex near-field data points.

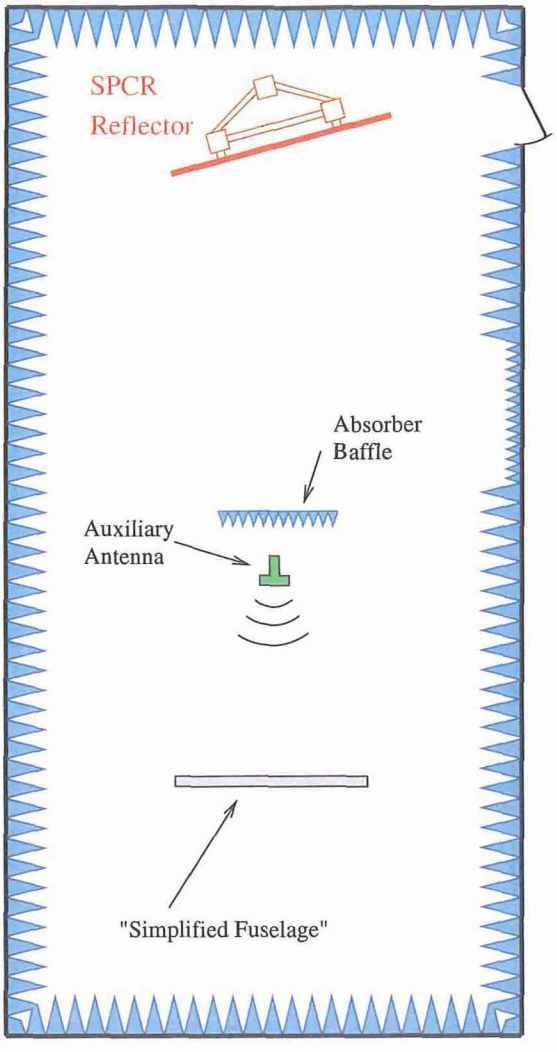

Figure 4.26: A floor plan view of the anechoic chamber illustrating the relationships between the simplified fuselage under test and the auxiliary antenna. This configuration is symmetric and does not suffer from feed spillover. Due to the small vertical dimensions of the apertures, the near-field response of the simplified fuselage in the azimuthal plane is the same as it would be in a field of cylindrical waves.

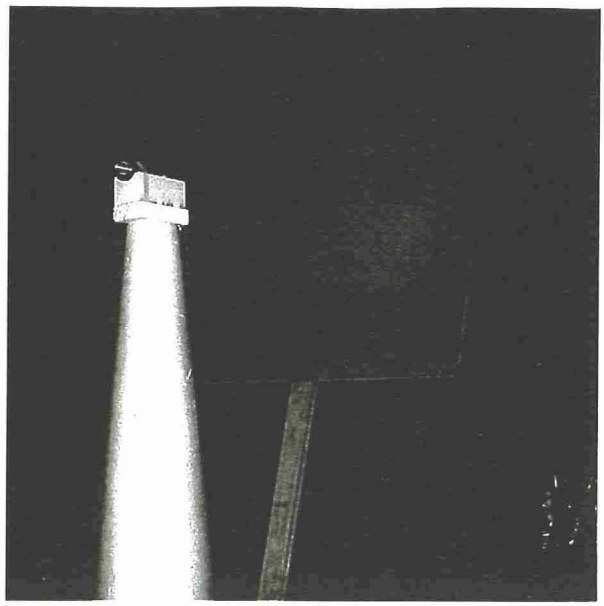

Figure 4.27: An absorber baffle was used to further reduce the illumination of the SPCR reflector by the back-lobes of the auxiliary antenna. The absorber reduced the signal scattered by the reflector by an average (over the band of interest) of about 15 dB, as observed by the monopole reference antenna.

C. FDTD(2,2) predictions

In this subsection, predictions of the shielding effectiveness for the simplified fuselage are presented. All the predictions are performed using the standard second-order accurate both in time and space FDTD(2,2) method. Three different cell sizes are used depending on the frequency range of the predictions. All the predictions are compared with measurements. Predictions are also performed for different angles of incidence. The computations of shielding effectiveness (SE) are based on the definition described by *procedure* #2 presented in Subsection A.. This procedure is in accordance with the measurements. The CAD model of the simplified fuselage is illustrated in Fig. 4.28.

1. Cell size of 10 mm

Initially, all FDTD predictions are performed using a cell size of 10 mm (or $\lambda/10$ at 3 GHz). Therefore, it is expected that these FDTD calculations will provide accurate results at most up to 3 GHz. The memory required for storing all the field components

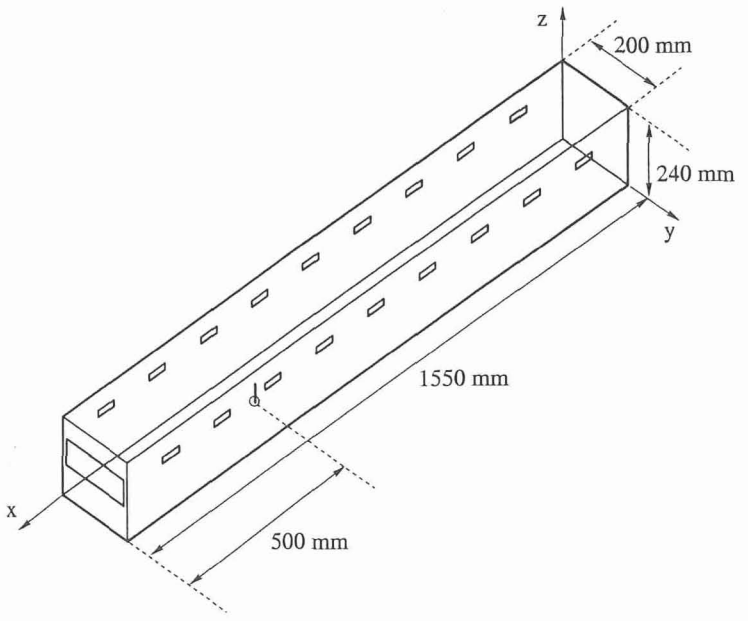

Figure 4.28: Geometry of the simplified fuselage model

that describe the dimensions of the box is approximately 2 Mbytes.

First, SE predictions are computed for an azimuthal angle of incidence of 0^o (nose incidence). The results of the FDTD(2,2) method are illustrated in Figs. 4.29 and 4.30. Fig. 4.29(a) depicts SE in the entire frequency range of 0-2.8 GHz, whereas Figs. 4.29(b), and 4.30(a) and 4.30(b) provide three zoom views in the bands 0.7-1.4 GHz, 1.4-2.1 GHz, and 2.1-2.8 GHz, respectively. It can be seen that the FDTD results are in excellent agreement with the measurements up to 2.1 GHz. Discrepancies between the measurements and the predictions are observed in the last frequency band of 2.1-2.8 GHz [see 4.30(b)]. These inaccuracies are attributed to FDTD(2,2) dispersion errors. Even though the cell size of 10 mm corresponds to $\lambda/10$ at 3 GHz, this mesh is proven insufficient for the last frequency band of 2.1-2.8 GHz. This happens because the domain of the fuselage is electrically very large causing accumulation of dispersion errors which significantly restricts the accuracy of FDTD(2,2).

The good agreement between FDTD(2,2) calculations and measurements validates the accuracy of the FDTD(2,2) method for SE analysis of fuselages of moderate complexity. It should also be pointed out that the SE waveform consists of rapid frequency variations with multiple peaks and valleys. This is due to the electrical

dimensions of the simplified fuselage which establish several resonances in the frequency band of interest. These rapid frequency variations complicate even more the analysis of this problem. Already the physical dimensions of the problem make it very challenging to analyze due to the memory and time required by the simulations. Especially, as the frequency of interest increases, these resources requirements will become even more demanding.

Similarly, FDTD computations are performed for three additional azimuthal angles of incidence; 45^o, 90^o, and 180^o, where 90^o is normal to the broad side of the fuselage. The results of the FDTD(2,2) method for an incident angle of 45^o are illustrated in Figs. 4.31 and 4.32. Fig. 4.31(a) depicts SE in the entire frequency range of 0-2.8 GHz, whereas Figs. 4.31(b), and 4.32(a) and 4.32(b) provide three zoom views in the bands 0.7-1.4 GHz, 1.4-2.1 GHz, and 2.1-2.8 GHz, respectively. In a similar manner, the computations for incident angles of 90^o and 180^o are shown in Figs. 4.33 and 4.34, and Figs. 4.35 and 4.36, respectively. All FDTD predictions agree very well with measurements for all the different angles of incidence. This again validates the accuracy of FDTD for SE computations. The largest discrepancies between FDTD calculations and measurements are exhibited in the last frequency band of 2.1-2.8 GHz [see Figs. 4.32(b), 4.34(b), and 4.36(b)]. These inaccuracies are again attributed to dispersion errors indicating an insufficiently fine mesh.

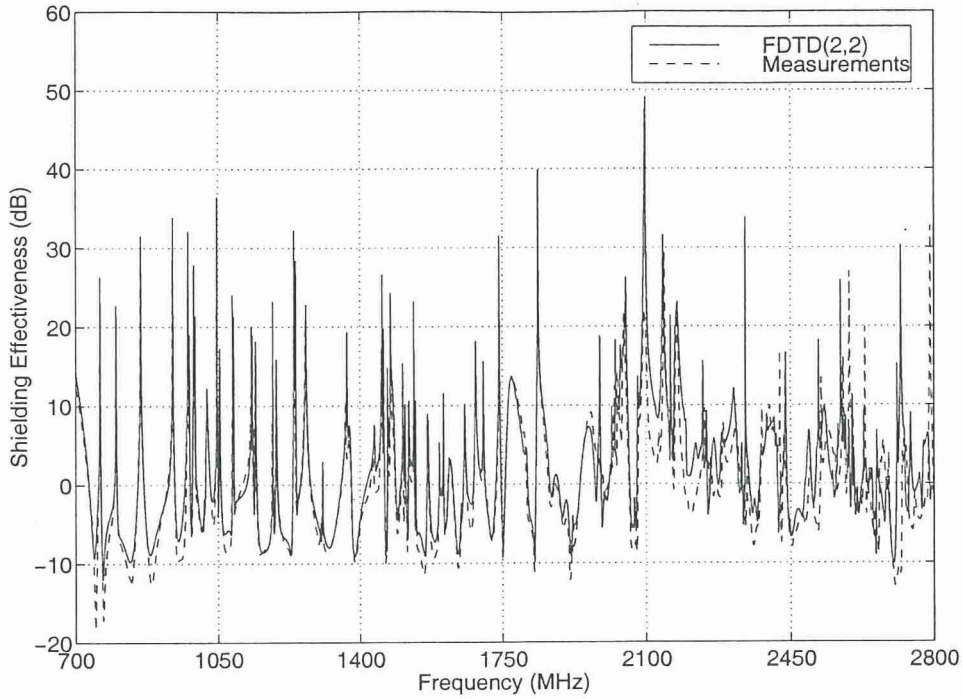

(a)

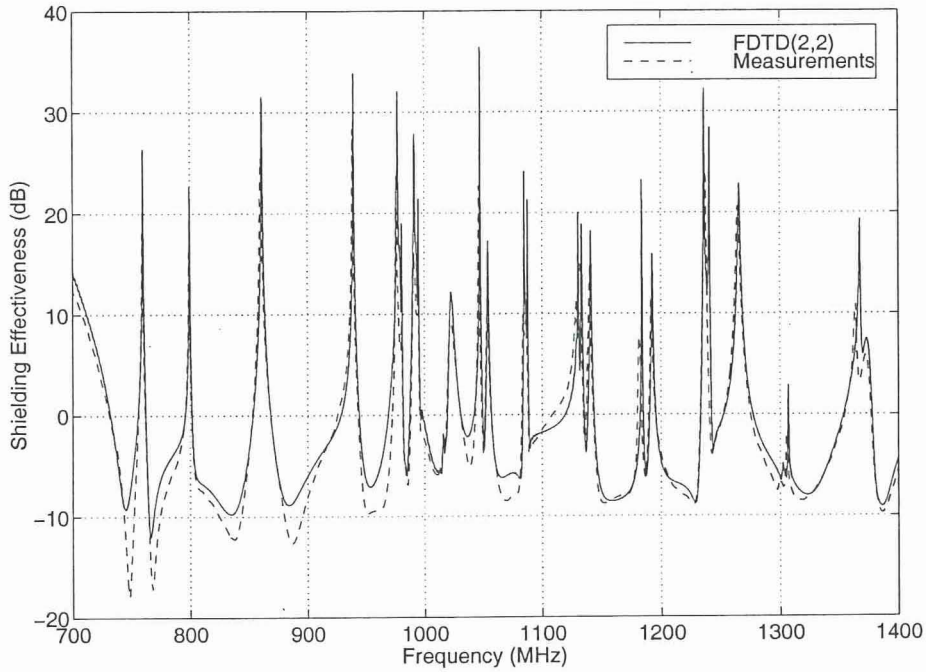

(b)

Figure 4.29: Shielding effectiveness of the scaled fuselage for azimuthal incident angle of 0^o (nose incidence).

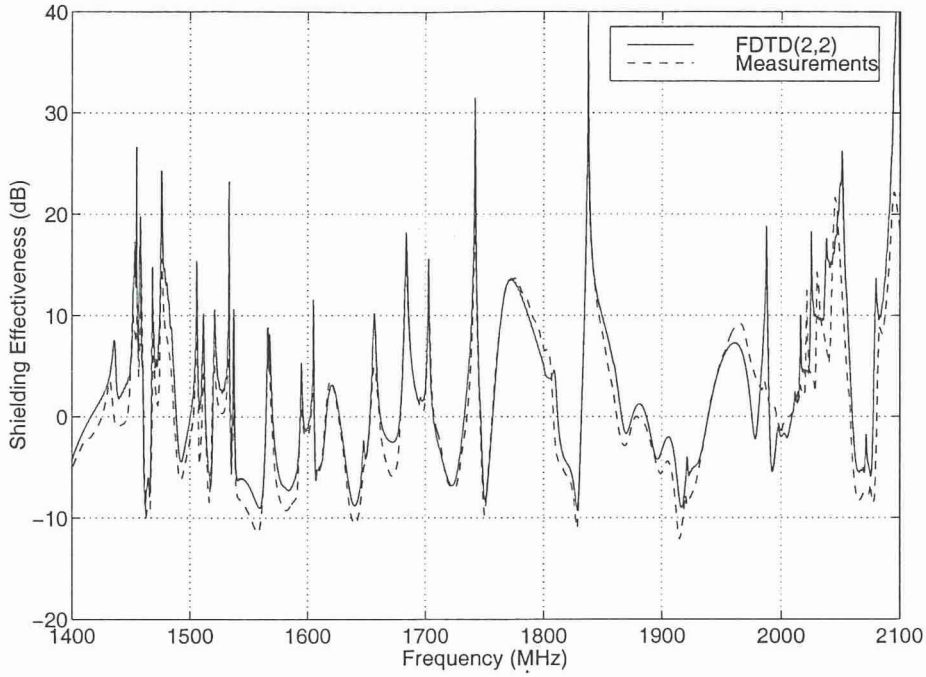

(a)

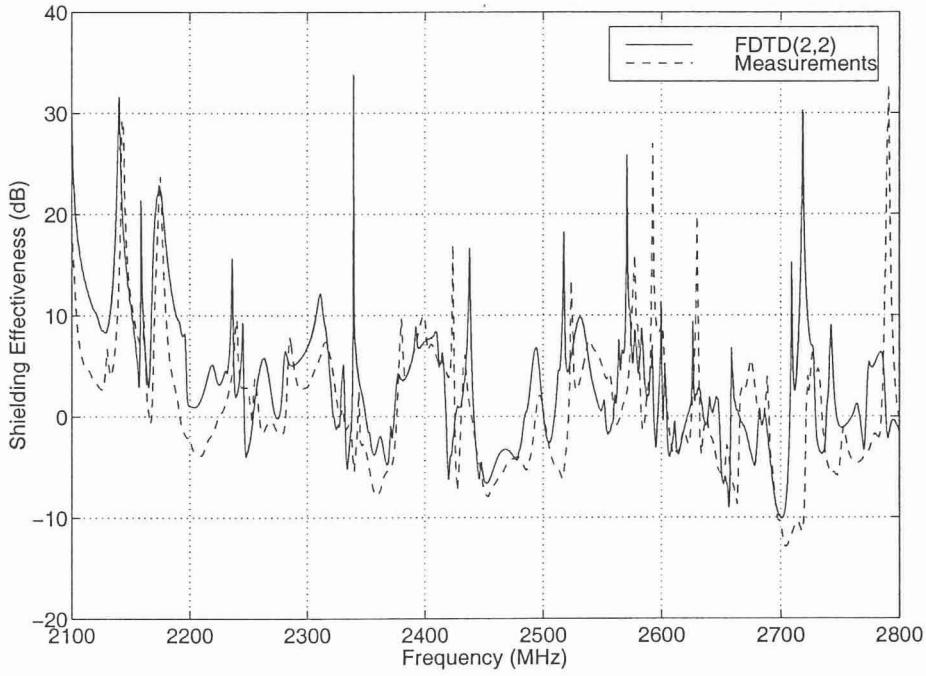

(b)

Figure 4.30: Shielding effectiveness of the scaled fuselage for azimuthal incident angle of 0^o (nose incidence).

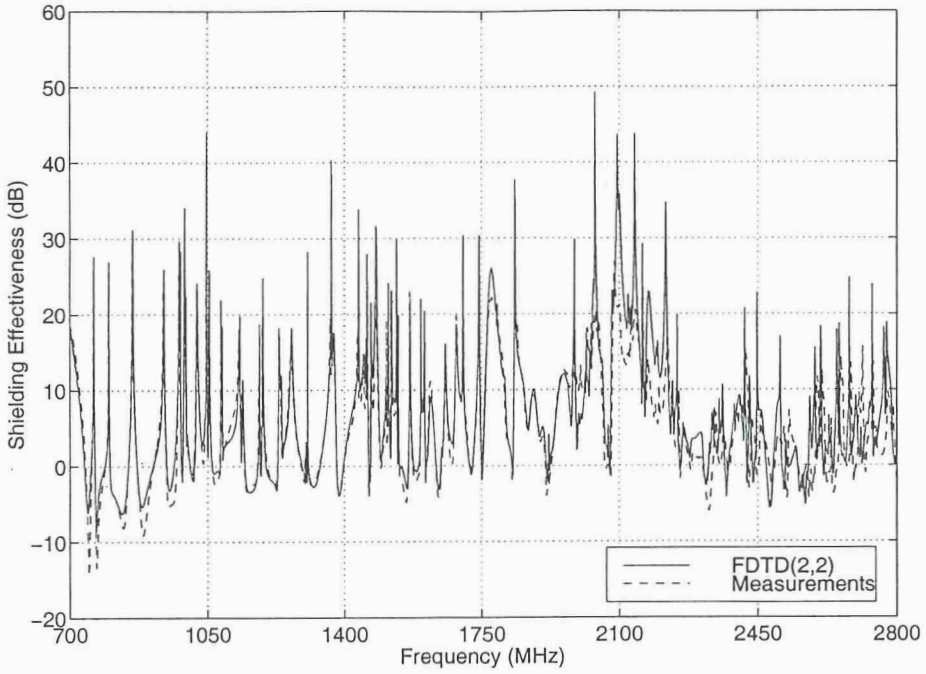

(a)

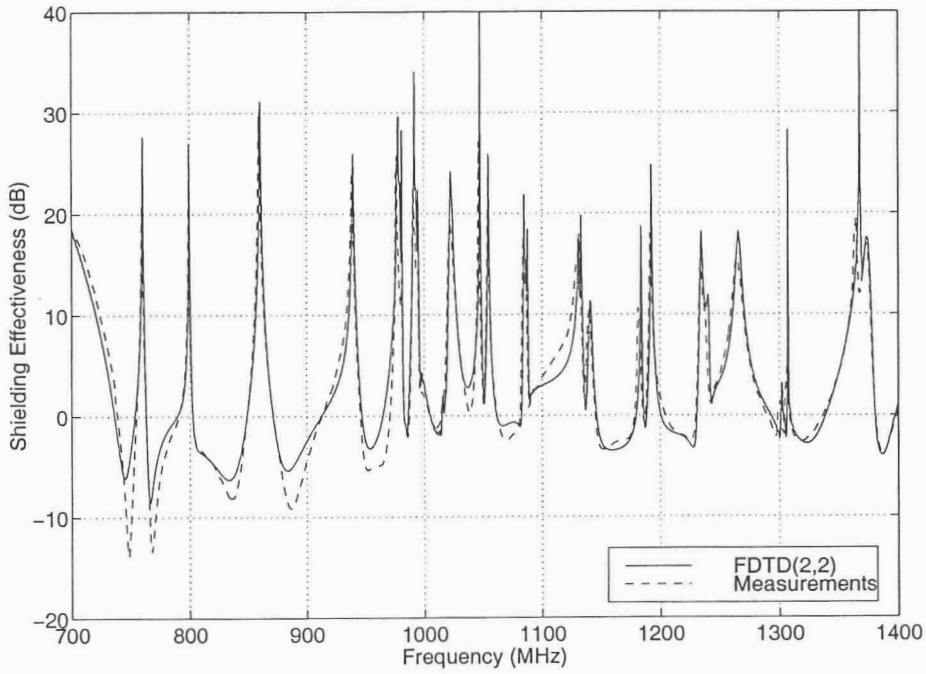

(b)

Figure 4.31: Shielding effectiveness of the scaled fuselage for azimuthal incident angle of 45^o.

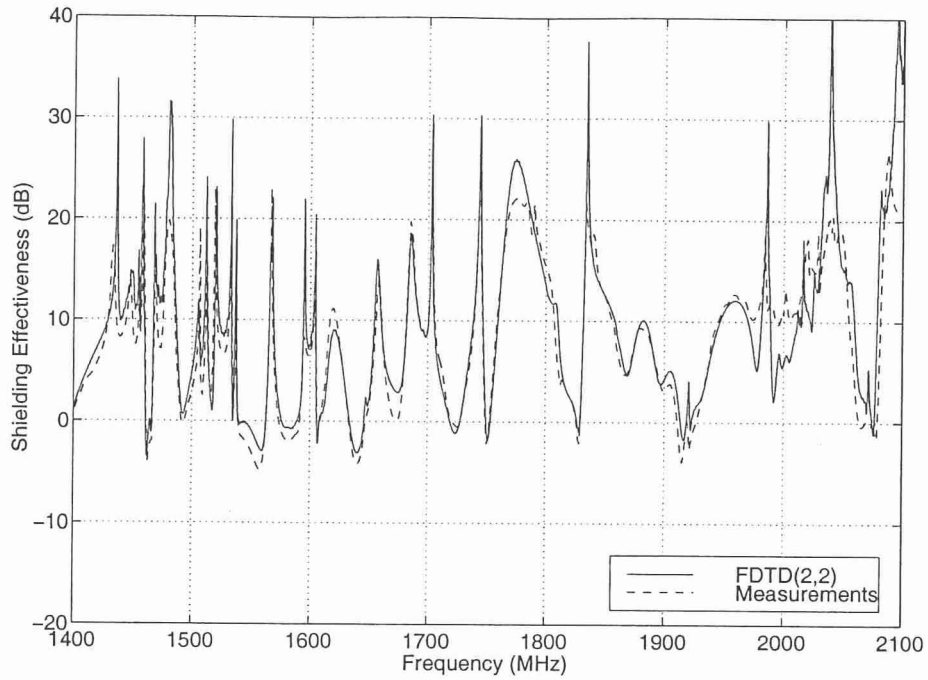

(a)

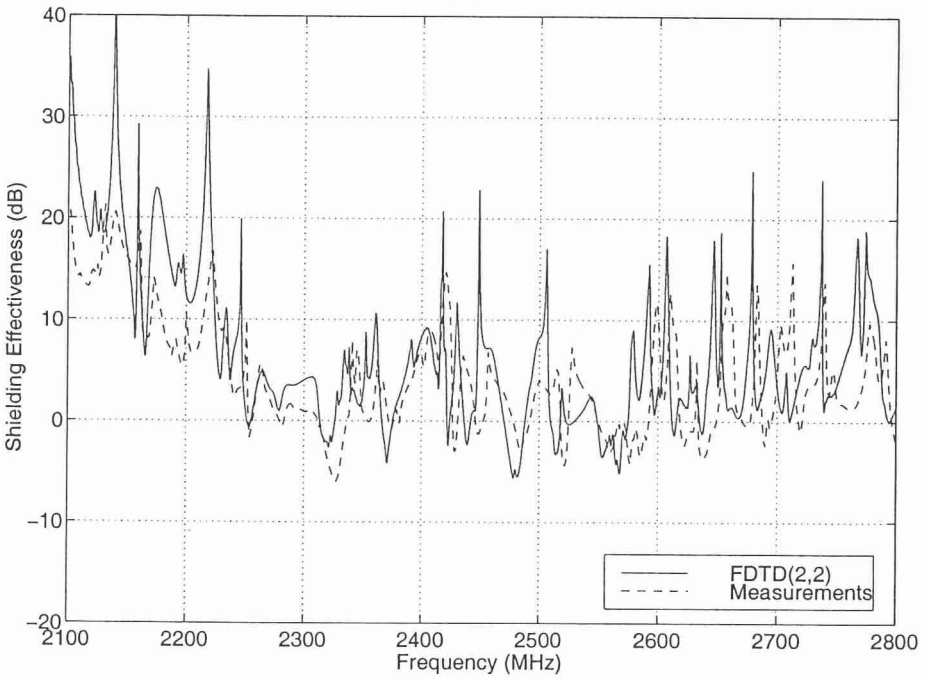

(b)

Figure 4.32: Shielding effectiveness of the scaled fuselage for azimuthal incident angle of 45^o.

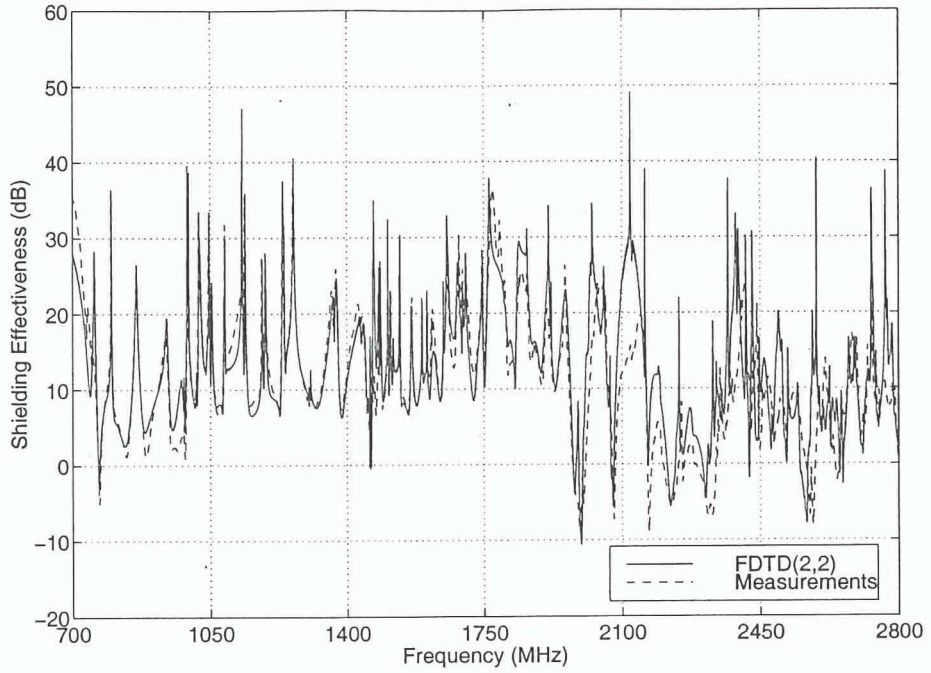

(a)

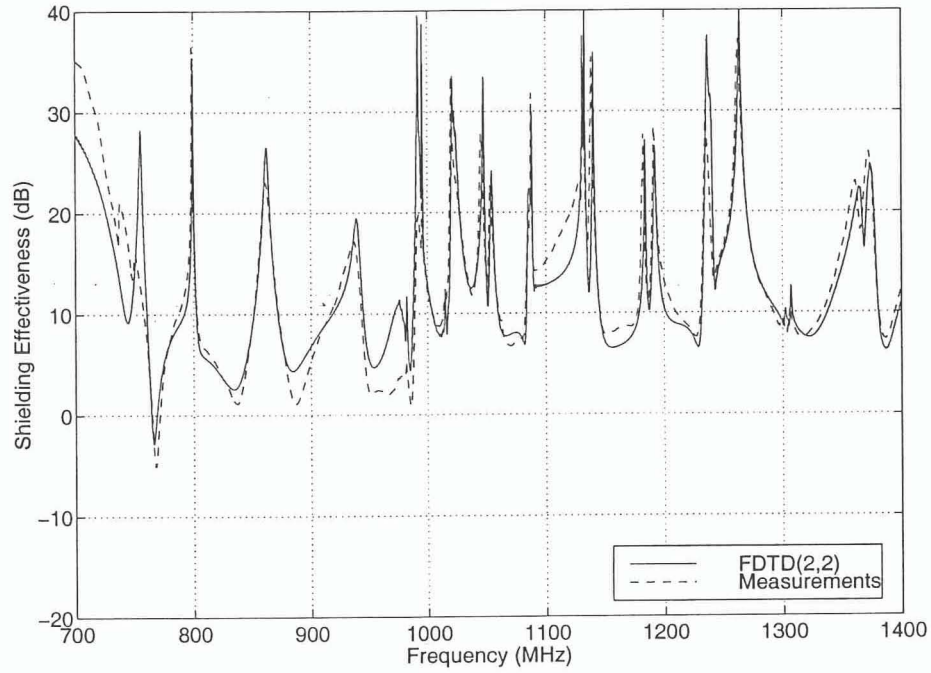

(b)

Figure 4.33: Shielding effectiveness of the scaled fuselage for azimuthal incident angle of 90^o (broadside incidence).

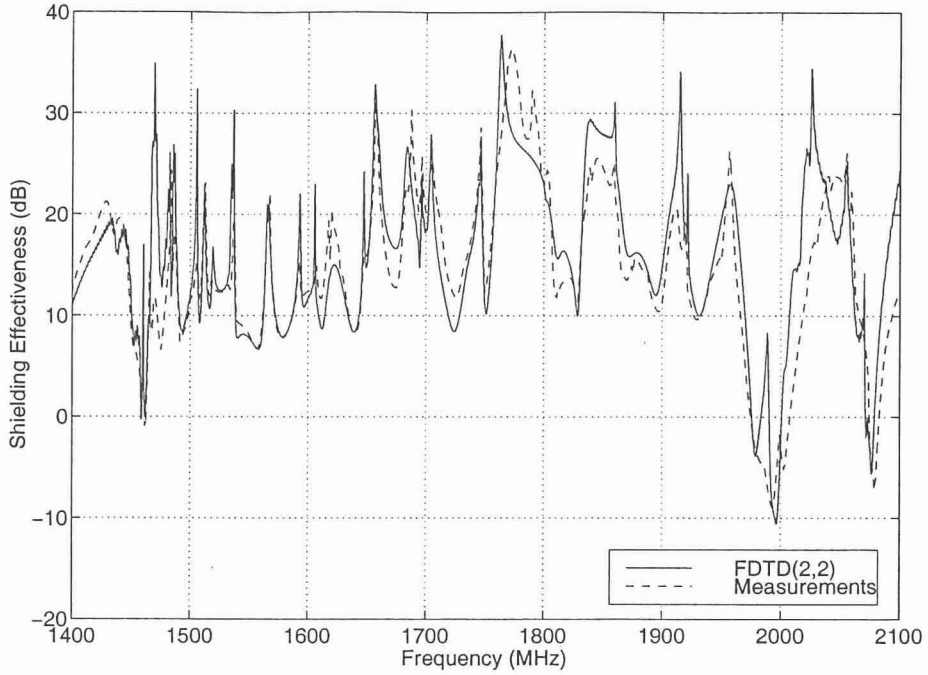

(a)

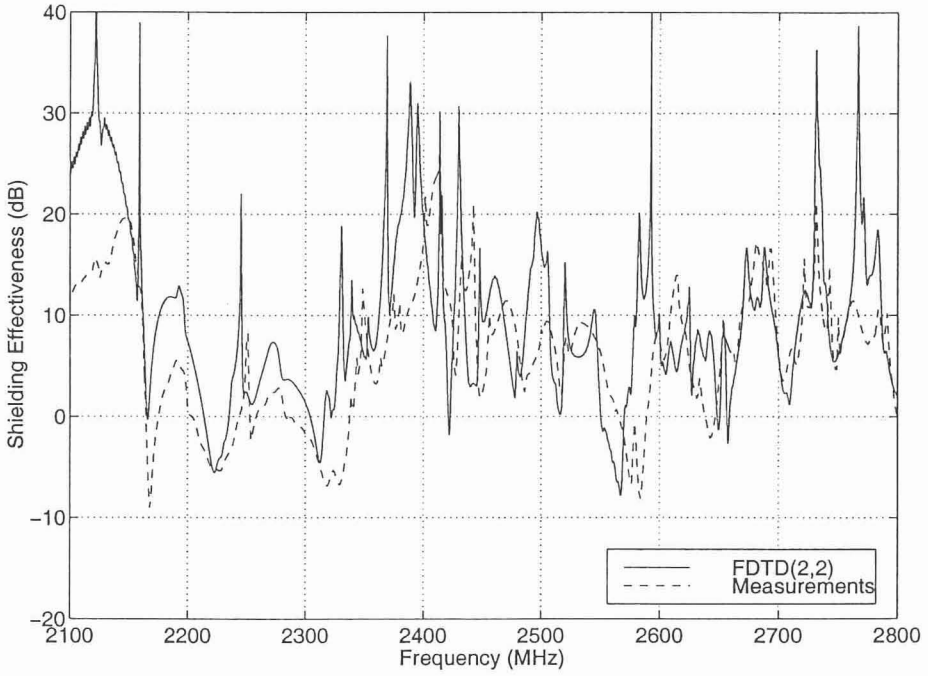

(b)

Figure 4.34: Shielding effectiveness of the scaled fuselage for azimuthal incident angle of 90^o (broadside incidence).

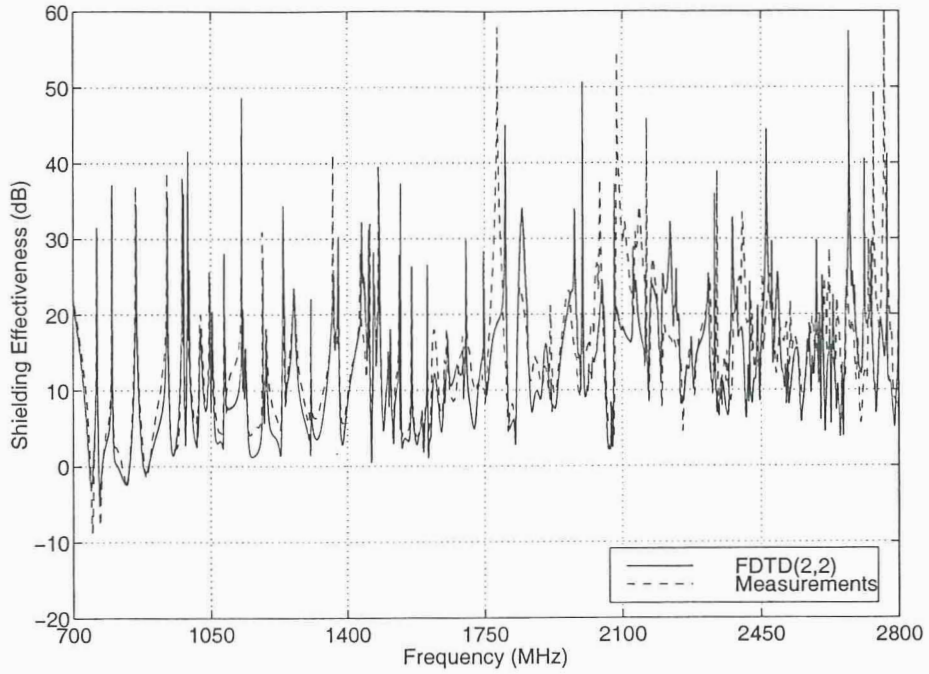

(a)

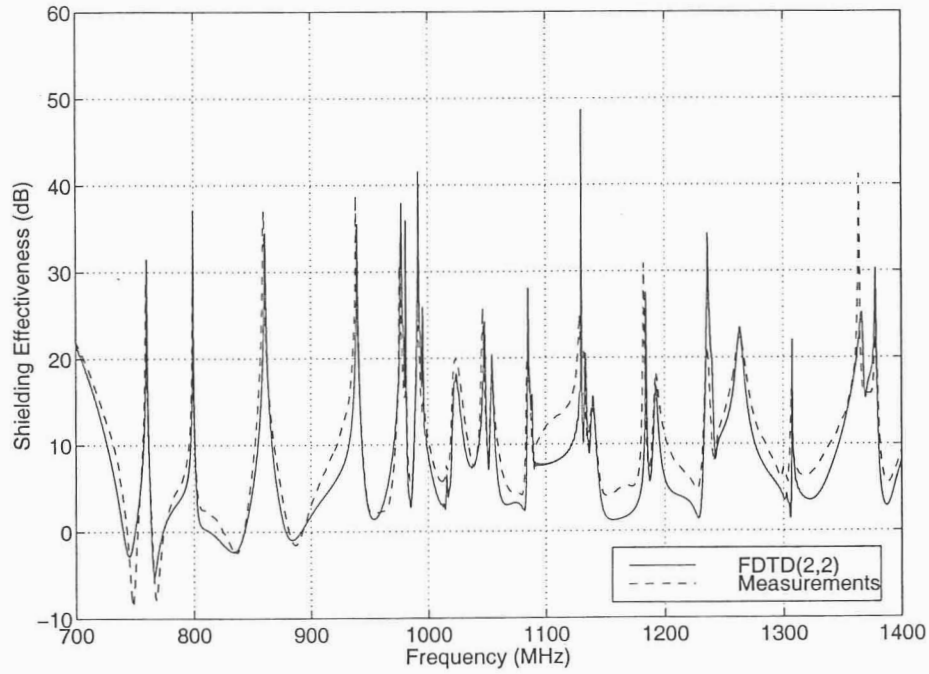

(b)

Figure 4.35: Shielding effectiveness of the scaled fuselage for azimuthal incident angle of 180^o (tail incidence).

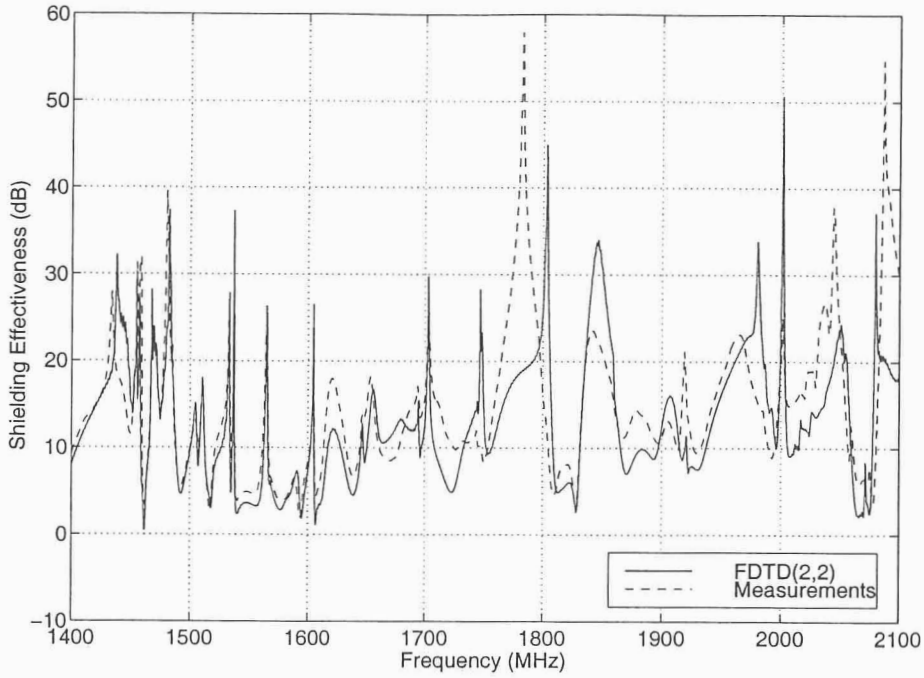

(a)

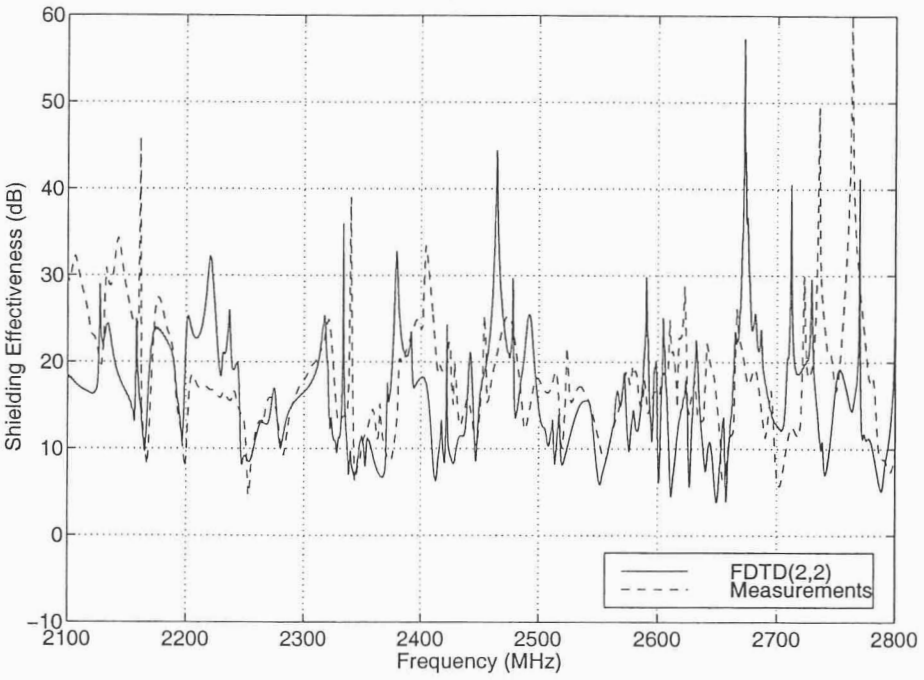

(b)

Figure 4.36: Shielding effectiveness of the scaled fuselage for azimuthal incident angle of 180^o (tail incidence).

2. Cell size of 5 mm

The inaccuracies of the FDTD computations shown above were attributed to dispersion errors. In order to reduce dispersion errors and expand the accuracy of FDTD at higher frequency bands, finer meshes have to be used. Finer meshes provide more accurate results but they yield large computational domains which require significant computational resources. Here, all FDTD predictions are performed using a cell size of 5 mm (or $\lambda/10$ at 6 GHz). Therefore, it is expected that these FDTD calculations will provide accurate results at most up to 6 GHz. The memory required for storing all the field components that describe the dimensions of the box is approximately 14 Mbytes. All the predictions are performed only for nose incidence (azimuthal angle of 0^o).

The FDTD computations are shown and compared to measurements in Figs. 4.37 and 4.38. It can be observed that the numerical results agree very well with measurements up to 3.5 GHz. However, their accuracy is already degraded in the 3.5-4.2 GHz band [see Fig. 4.38(b)], even though the cell size of 5 mm corresponds to $\lambda/15$ at 4 GHz. Numerical experiments along with analytical derivations of the phase velocity in the discrete space have shown that a cell size of $\lambda/10$ provides satisfactory accuracy for moderate problems when using FDTD(2,2). However, this rule of thumb may not be representative for electrically large spaces where the accumulation of phase errors due to dispersion becomes significant and deteriorates the accuracy of the FDTD solution. The simplified fuselage has electrical dimensions of approximately $31\lambda \times 4\lambda \times 5\lambda$ at 6 GHz, which make the fuselage an electrically very large domain. This justifies the inaccurate results of FDTD(2,2) in the frequency band of 3.5-6 GHz. Even though, the discretization is at least $\lambda/10$ at 6 GHz, the accumulation of phase errors through the domain make this discretization insufficient. However, the finer mesh of 5 mm, that is used here, provides predictions that exhibit better accuracy than the accuracy of the predictions performed for a cell size of 10 mm (presented in the previous section). This can be observed by comparing Figs. 4.30(b) and 4.37(b).

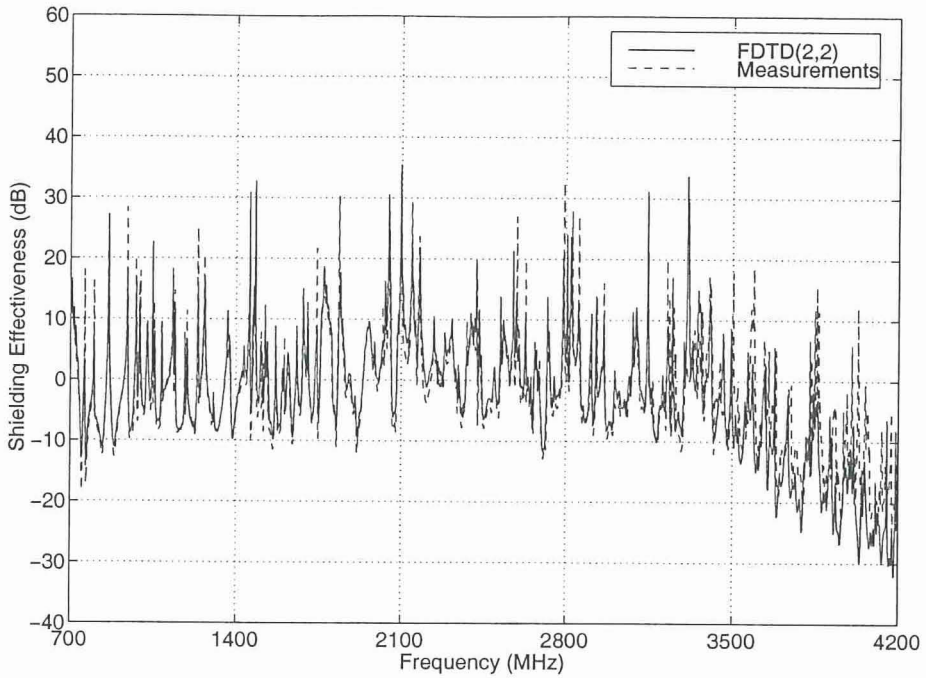

(a)

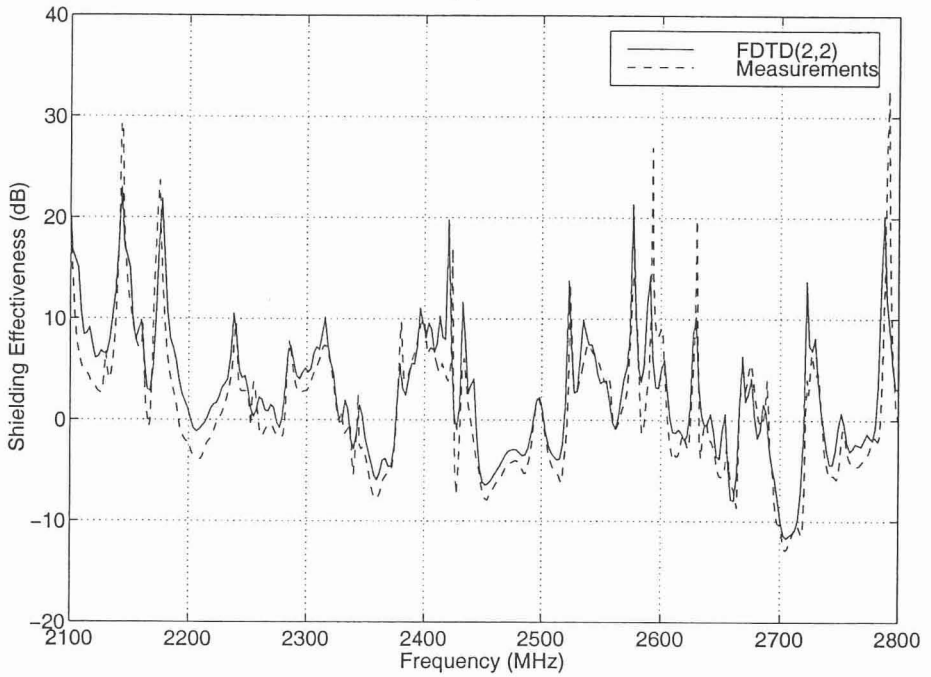

(b)

Figure 4.37: Shielding effectiveness of the scaled fuselage for azimuthal incident angle of 0^o.

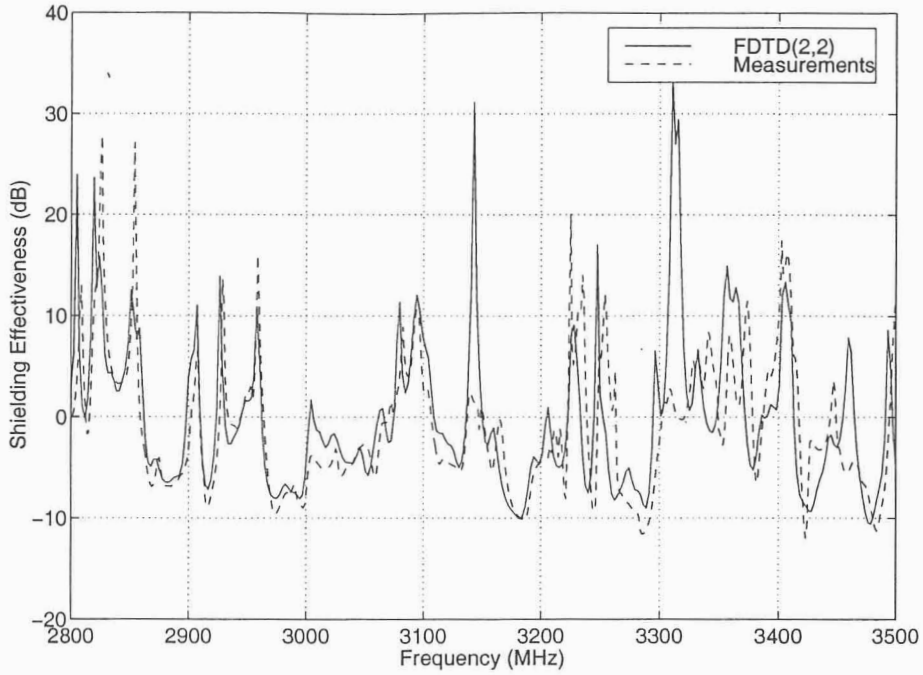

(a)

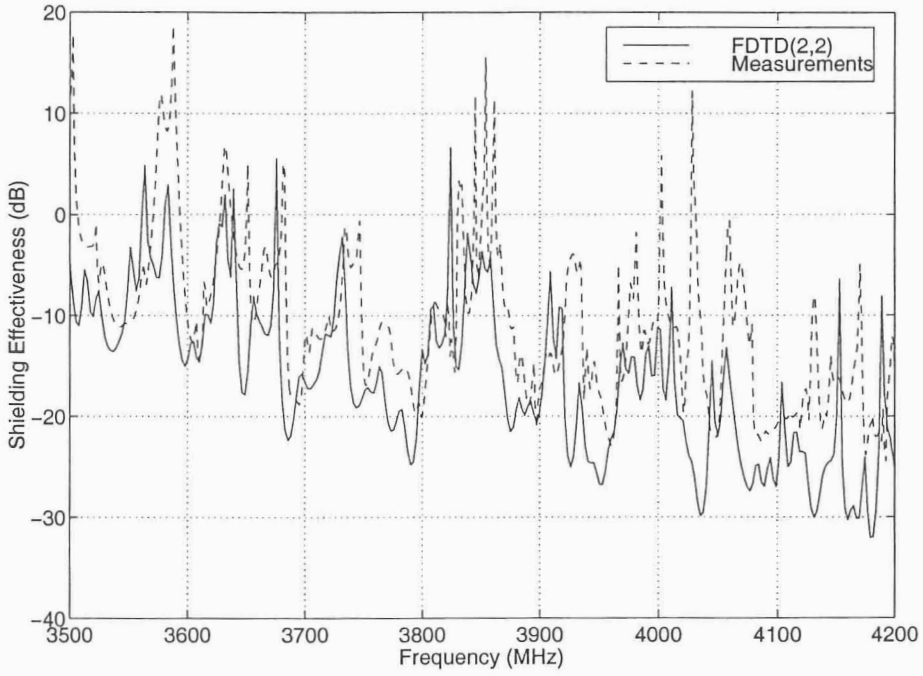

(b)

Figure 4.38: Shielding effectiveness of the scaled fuselage for azimuthal incident angle of 0^o.

3. Cell size of 2.5 mm

In the previous section, the FDTD mesh was refined from 10 mm to 5 mm and this refined mesh provided results of improved accuracy. In order to reduce even further the dispersion error and expand the accuracy of the FDTD predictions at higher frequency bands, the mesh is again refined. Here, all FDTD predictions are performed using a cell size of 2.5 mm (or $\lambda/13$ at 9 GHz). Therefore, it is expected that these FDTD calculations will provide accurate results at most up to 9 GHz. The memory required for storing all the field components that describe the dimensions of the box is approximately 114 Mbytes. For validation purposes, all the predictions are performed only for nose incidence (azimuthal angle of 0^o).

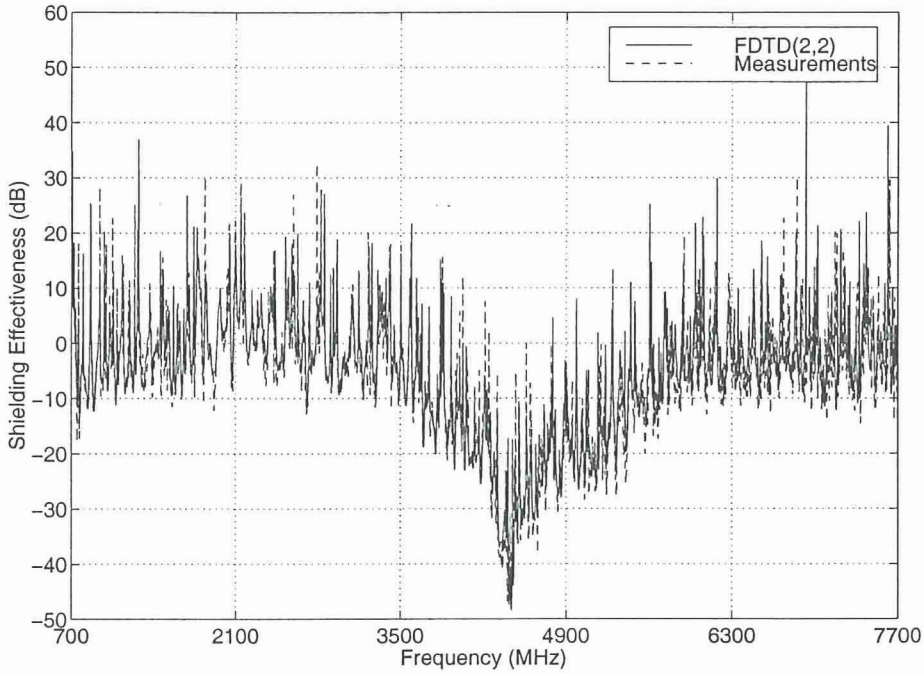

Figure 4.39: Shielding effectiveness of the scaled fuselage for azimuthal incident angle of 0^o.

The FDTD computations are shown and compared to measurements in Figs. 4.39-4.43. It can be observed that the numerical results agree very well with measurements up to 5.6 GHz. However, their accuracy is already degraded in the 5.6-7.7 GHz band (see Figs. 4.42 and 4.43). Again, even though the discretization is at least $\lambda/13$ at 9 GHz, the accumulation of phase errors through the domain make this

discretization insufficient. Note that the simplified fuselage has electrical dimensions of approximately $47\lambda \times 6\lambda \times 7\lambda$ at 9 GHz, which make the fuselage an extremely electrically large domain.

Also, it should be pointed out that the refinement of the fuselage's mesh provides again results of improved accuracy, as expected. This is attributed to the fact that finer meshes exhibit less dispersion errors. However, as mentioned before, as the cell size becomes smaller the memory and time requirements grow larger. Therefore, refinement is not always the best remedy to dispersion. In the following section, a new hybrid method that provides accurate results for shielding effectiveness computations is presented. This new hybrid technique requires much less memory to achieve the same accuracy as the one of FDTD(2,2).

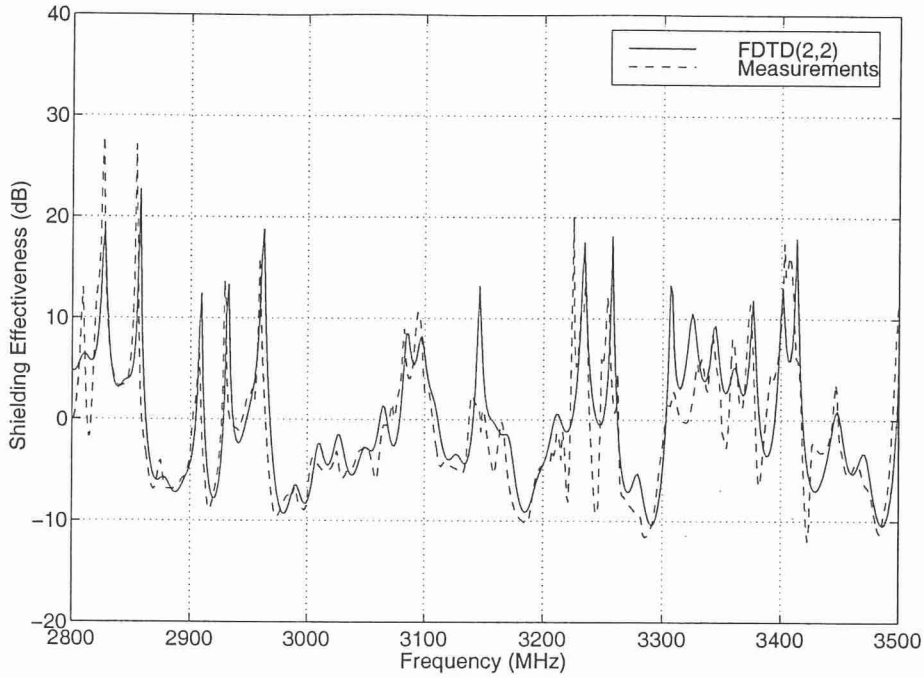

(a)

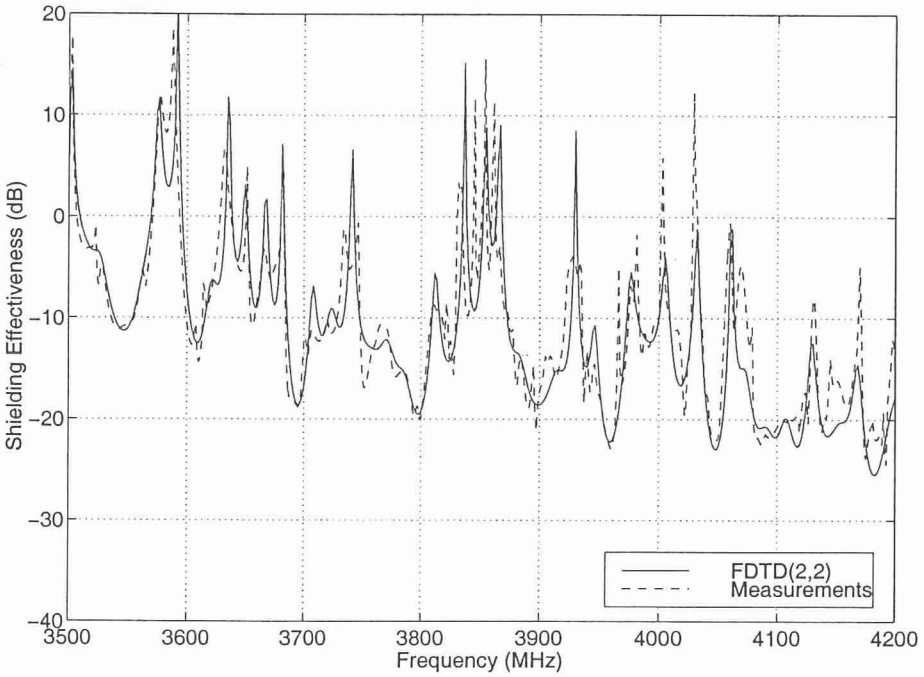

(b)

Figure 4.40: Shielding effectiveness of the scaled fuselage for azimuthal incident angle of 0^o.

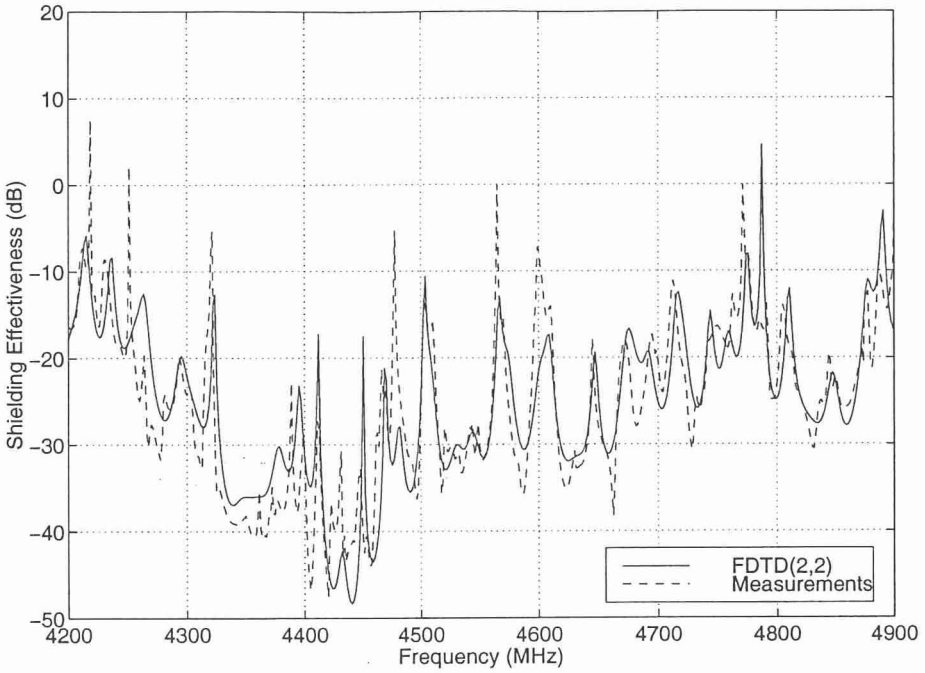

(a)

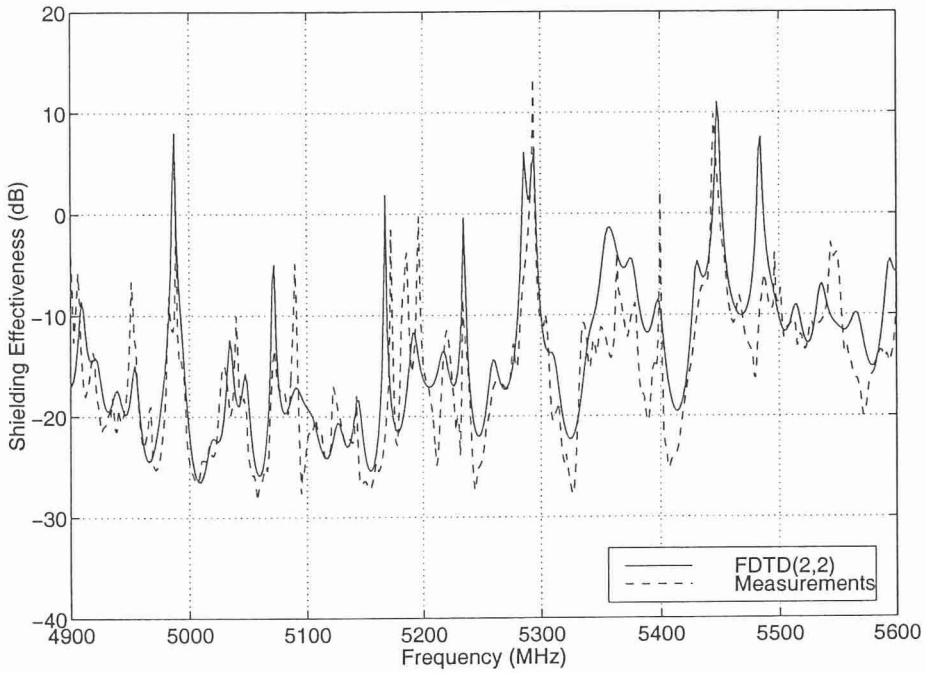

(b)

Figure 4.41: Shielding effectiveness of the scaled fuselage for azimuthal incident angle of 0^o.

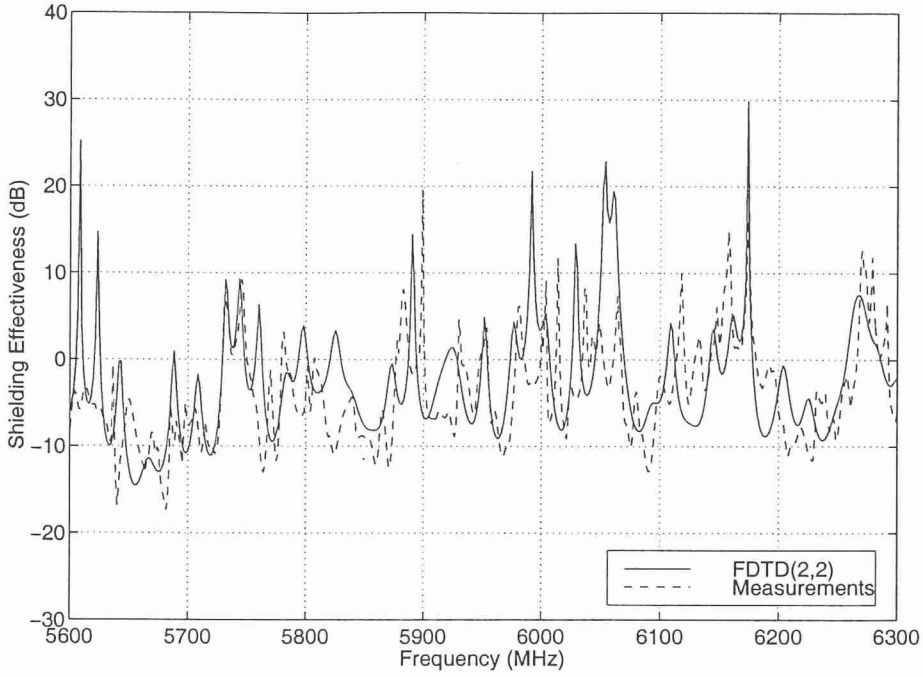

(a)

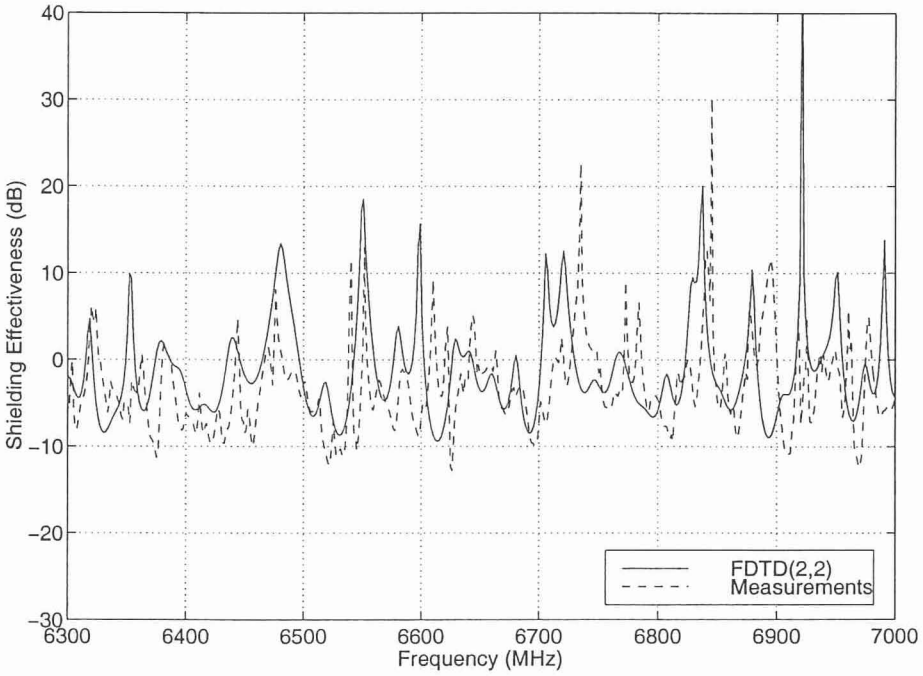

(b)

Figure 4.42: Shielding effectiveness of the scaled fuselage for azimuthal incident angle of 0^o.

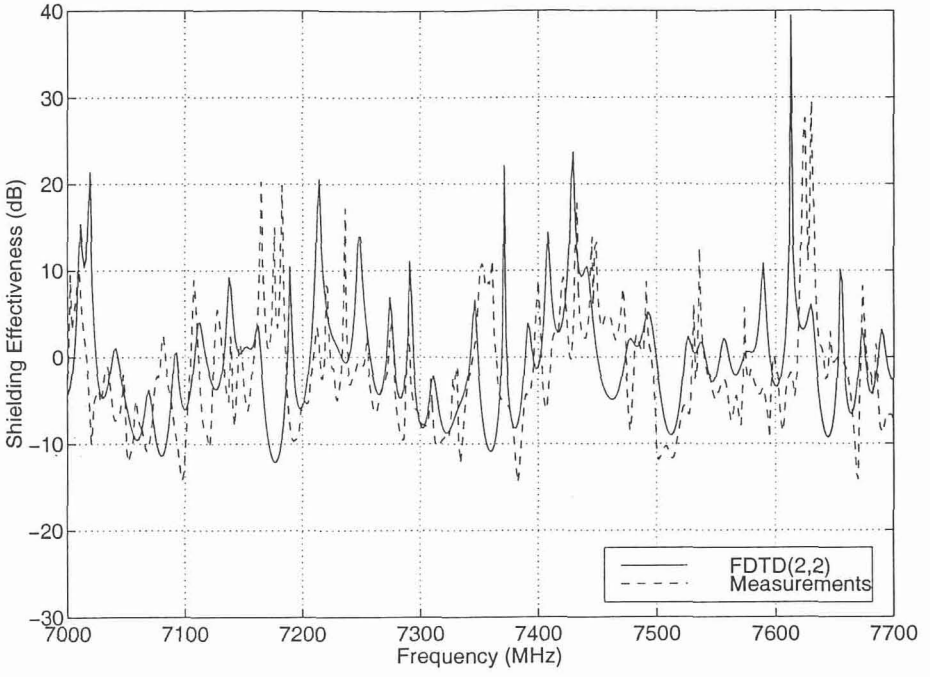

Figure 4.43: Shielding effectiveness of the scaled fuselage for azimuthal incident angle of 0^o.

D. Hybrid of subgrid FDTD(2,2)/FDTD(2,4)

In this subsection, the hybrid method of subgrid FDTD(2,2)/FDTD(2,4), presented in Section IX. is applied to compute the shielding effectiveness of the scaled fuselage. In Section IX., it was shown that significant memory savings can result when this hybrid method is used. The spatial layout of the methods used by the hybrid in the computational domain is depicted in Fig. 4.44. It is seen that the probe exciting the cavity is included in the fine region where subgrid FDTD(2,2) is applied. This is done in order to simulate the fields near and on the probe very well by representing the probe with many cells (fine grid).

Different cell sizes are used in the analysis presented here. The smaller the cell size is the more significant the memory savings are (compared to the memory required by the standard FDTD(2,2) for the same fine grid cell size). For validation purposes, all predictions are performed for nose incidence.

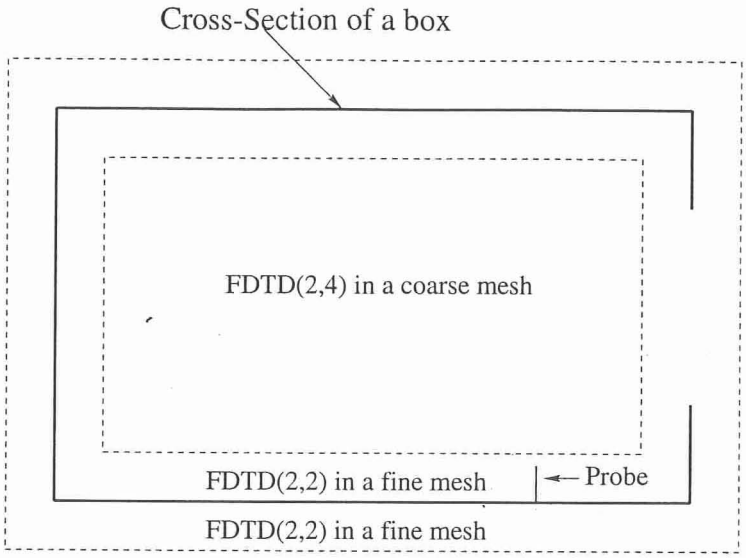

Figure 4.44: Schematic visualization of the hybrid method subgrid FDTD(2,2) and FDTD(2,4) applied to the scaled fuselage.

1. Hybrid 5mm

Initially, for validation purposes, a cell size of 5 mm (or $\lambda/10$ at 6 GHz) for the fine grid, and of 15 mm (or $\lambda/3$ at 6 GHz) for the coarse grid. Therefore, it is expected that these FDTD calculations will provide accurate results at most up to 6 GHz. The memory required for storing all the field components that describe the dimensions of the box is approximately 14 Mbytes which is approximately the same as the one required by FDTD(2,2) alone when a cell size of 5 mm is used (see Subsection C.). For this cell size, no memory savings occur since the cell size of 5 mm does not yield a large computational domain. However, the results of this simulation are used as validation of the hybrid method, and therefore they are very important.

By comparing Figs. 4.45 and 4.46 with Figs. 4.37 and 4.38, it is observed that the hybrid method gives almost identical results for shielding effectiveness as the ones of the standard FDTD(2,2) alone (with a cell size of 5 mm). Notice that even though most of the interior of the fuselage is simulated using a very coarse cell size of 15 mm, the accuracy is retained as a higher-order scheme is applied [FDTD(2,4)]. This clearly proves one more time the effectiveness of higher-order schemes.

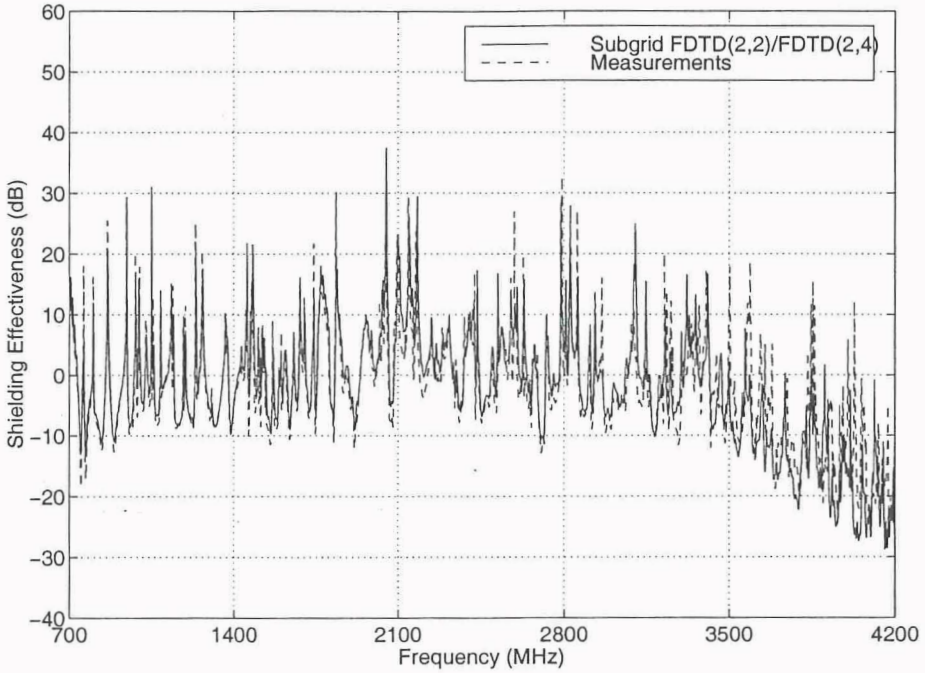

(a)

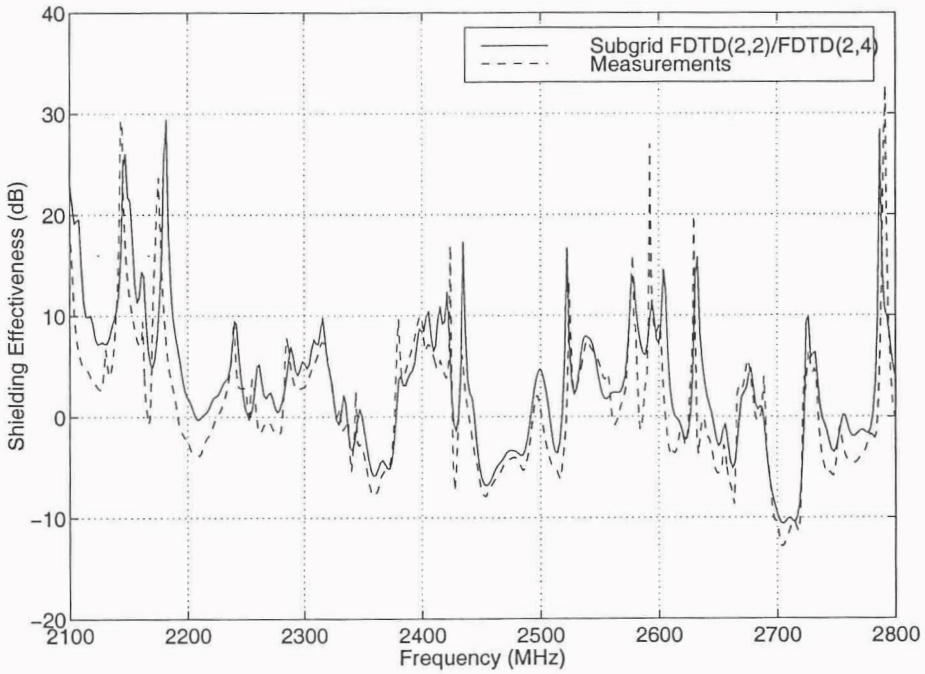

(b)

Figure 4.45: Shielding effectiveness of the scaled fuselage for azimuthal incident angle of 0^o computed by the hybrid method.

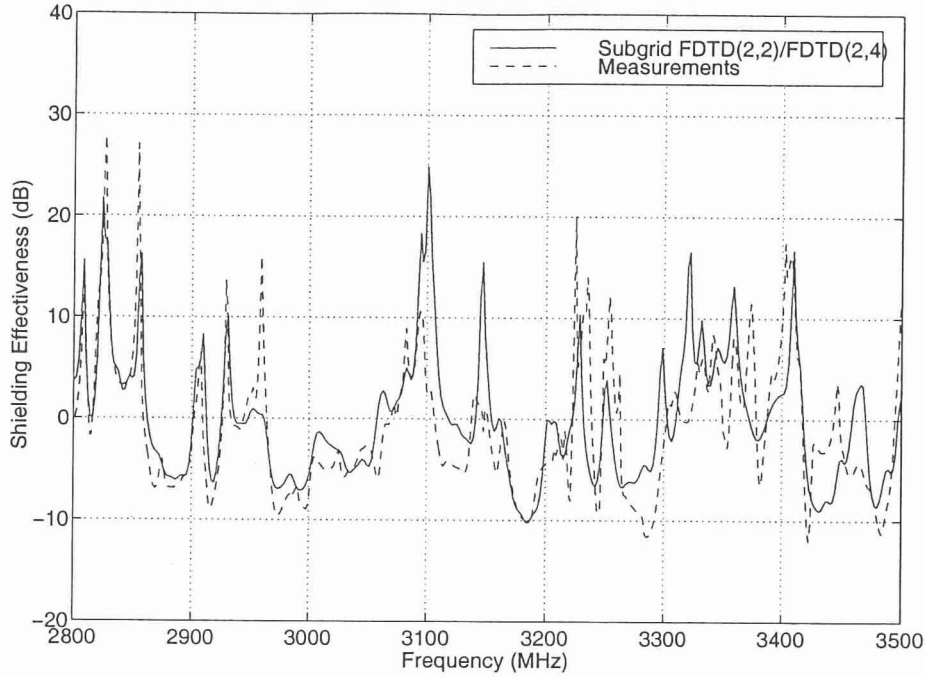

(a)

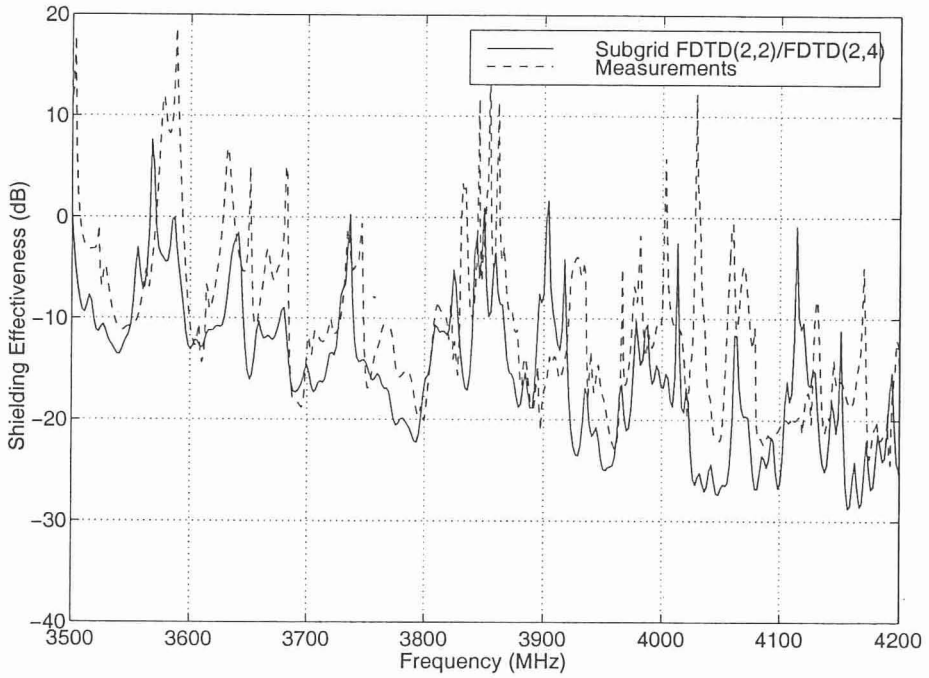

(b)

Figure 4.46: Shielding effectiveness of the scaled fuselage for azimuthal incident angle of 0^o computed by the hybrid method.

2. Hybrid 2.5mm

To clearly illustrate the memory advantages of the new hybrid, a refined mesh is used in this section. Here, all FDTD predictions are performed using a cell size of 2.5 mm (or $\lambda/13$ at 9 GHz) for the fine grid, and of 7.5 mm (or $\lambda/3$ at 9 GHz) for the coarse grid. Therefore, it is expected that these FDTD calculations will provide accurate results at most up to 9 GHz. The memory required for storing all the field components that describe the dimensions of the box is approximately only 48 Mbytes which is almost 2.5 times smaller than the memory (114 Mbytes) required by FDTD(2,2) alone when a cell size of 2.5 mm is used (see Subsection C.). This represents a significant amount of reduction in memory attributed to the hybrid scheme of subgrid FDTD(2,2)/FDTD(2,4).

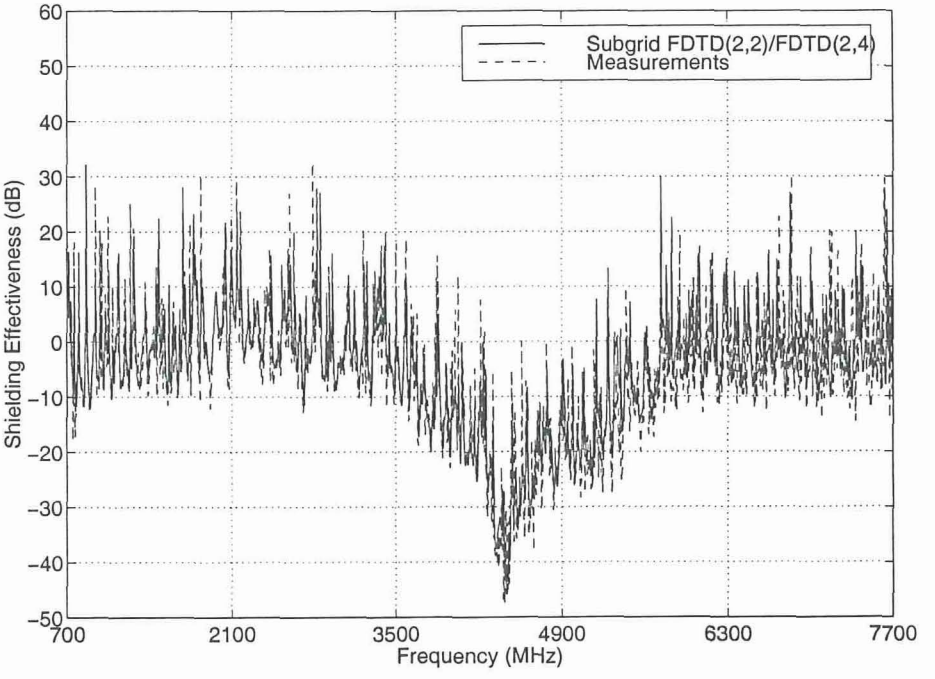

Figure 4.47: Shielding effectiveness of the scaled fuselage for azimuthal incident angle of 0^o computed by the hybrid method.

By comparing Figs. 4.47-4.51 with Figs. 4.39-4.43, it is observed that the hybrid method gives very similar results for shielding effectiveness as the ones of the standard FDTD(2,2) alone (with a cell size of 2.5 mm). Notice that even though most of the interior of the fuselage is simulated using a quite coarse cell size of 7.5 mm,

the accuracy is retained as a higher-order scheme is applied [FDTD(2,4)]. Also, the predictions of the hybrid method agree very well with the measurements. This simulation again verifies the accuracy and efficacy of the hybrid method.

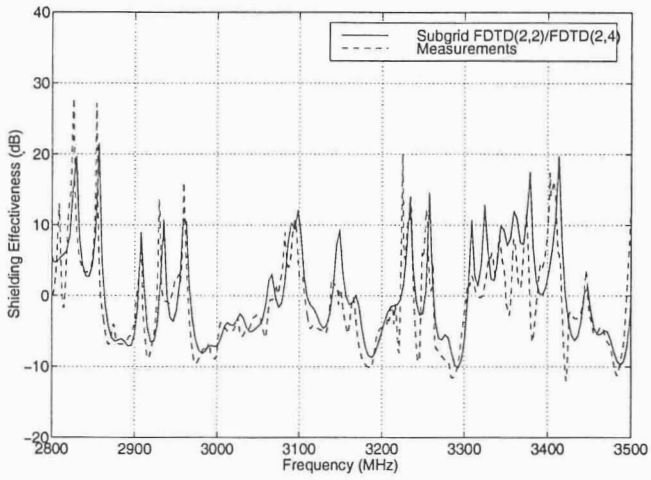

(a)

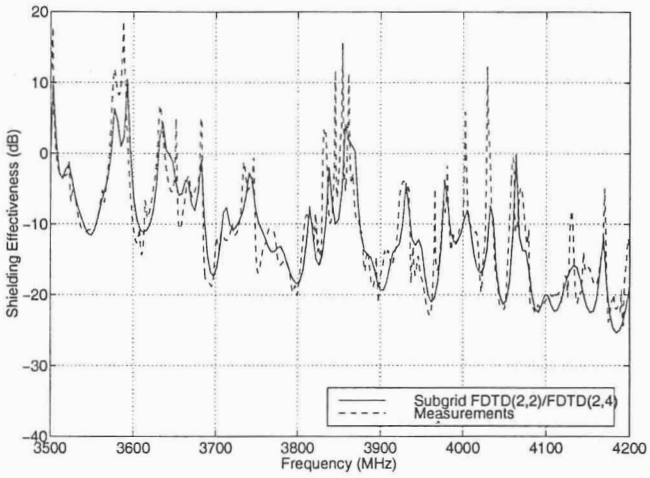

(b)

Figure 4.48: Shielding effectiveness of the scaled fuselage for azimuthal incident angle of 0^o computed by the hybrid method.

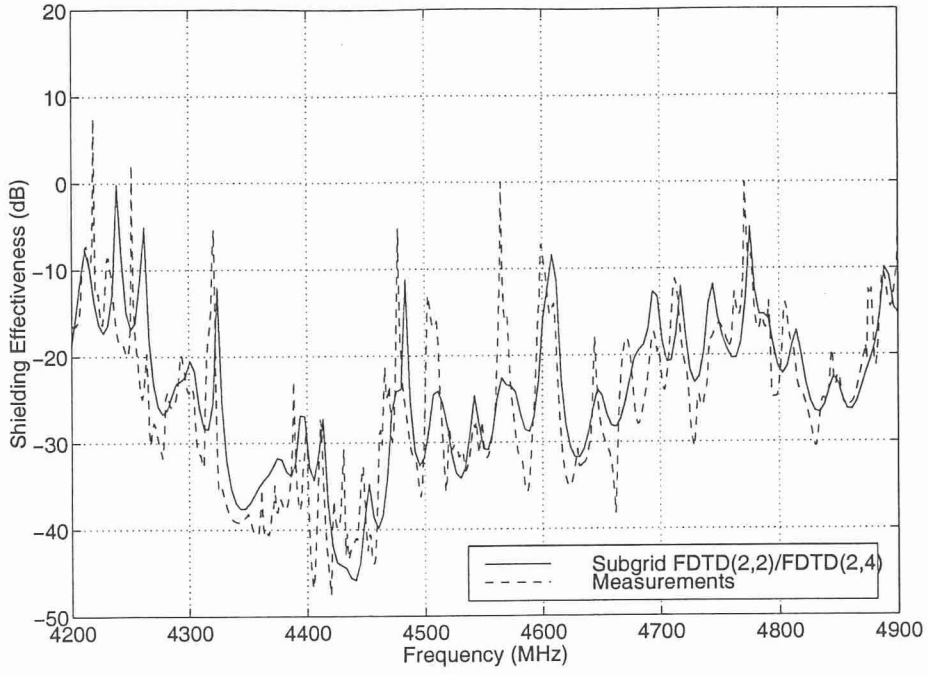

(a)

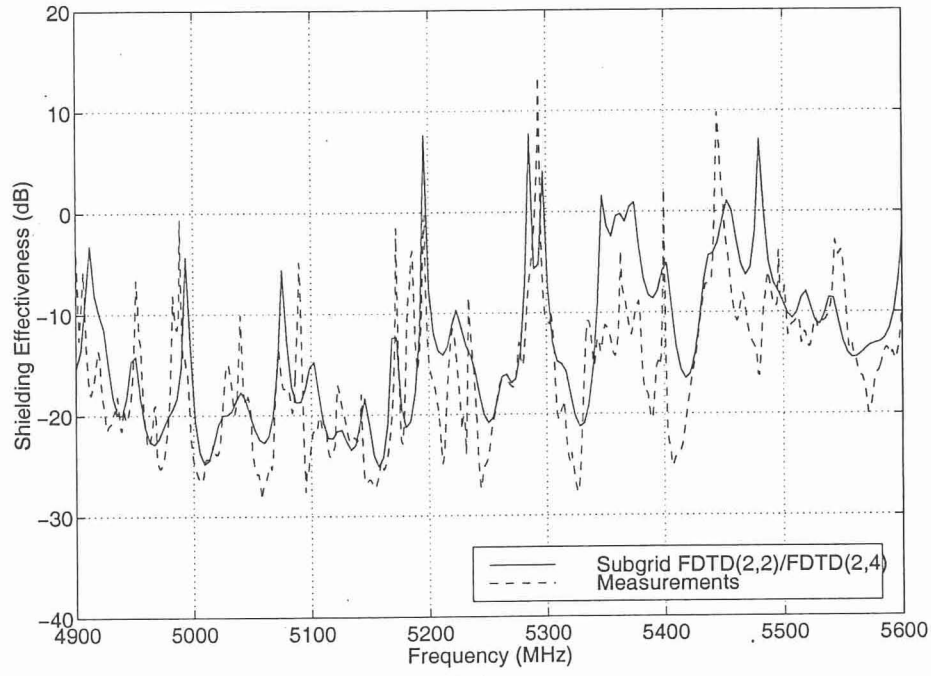

(b)

Figure 4.49: Shielding effectiveness of the scaled fuselage for azimuthal incident angle of 0^o computed by the hybrid method.

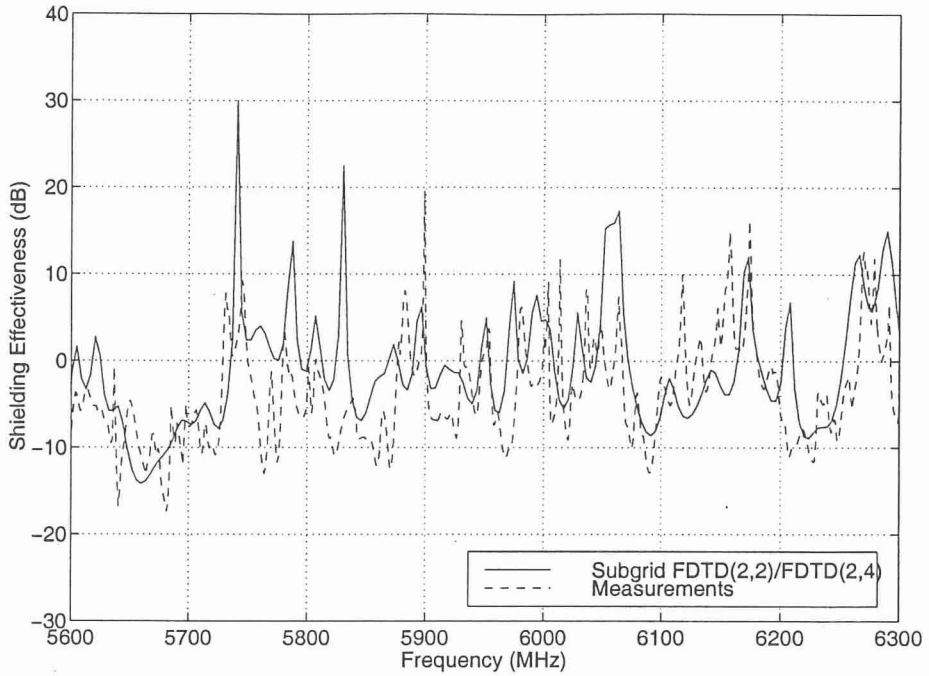

(a)

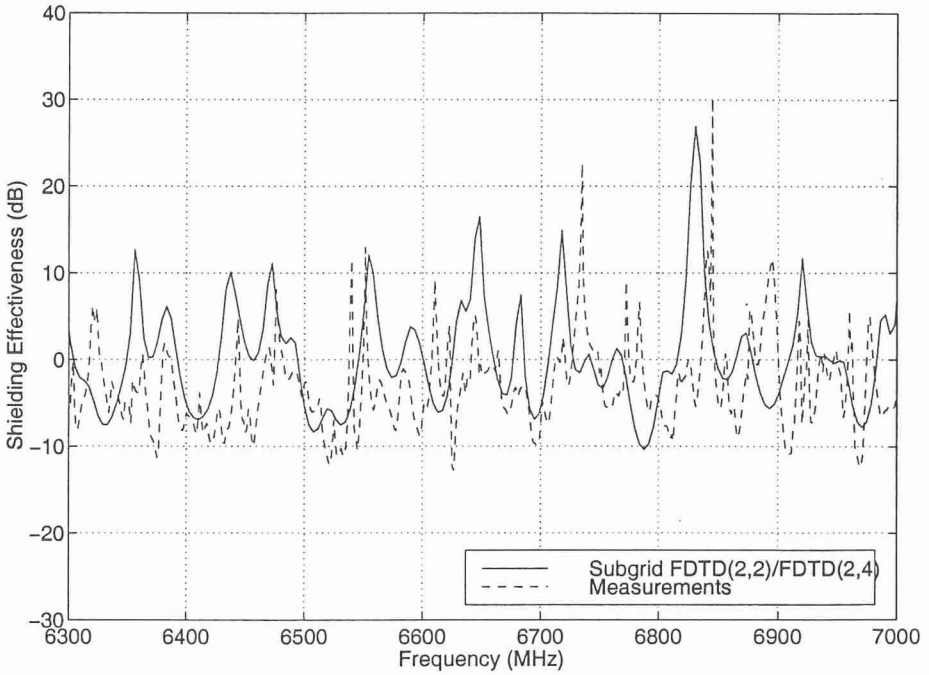

(b)

Figure 4.50: Shielding effectiveness of the scaled fuselage for azimuthal incident angle of 0^o computed by the hybrid method.

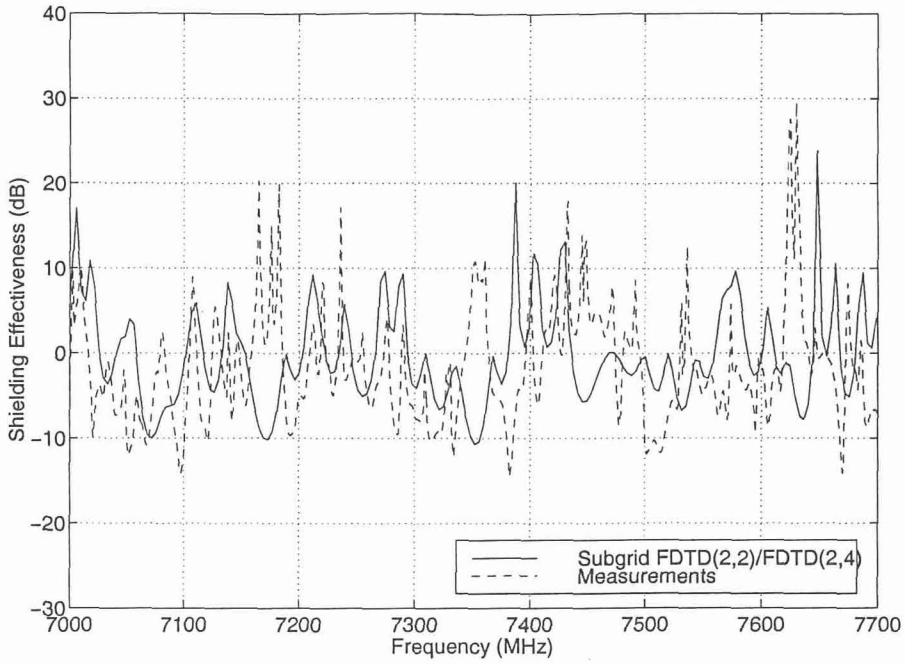

Figure 4.51: Shielding effectiveness of the scaled fuselage for azimuthal incident angle of 0^o computed by the hybrid method.

E. Summary

In this section, the shielding effectiveness of a simplified scaled model of a Boeing 757 aircraft is modeled. It was shown that this geometry generates very large computational domains, especially as the frequency of interest increases and the mesh becomes finer. For example the simplified fuselage has electrical dimensions of approximately $47\lambda \times 6\lambda \times 7\lambda$ at 9 GHz, which make the fuselage an extremely electrically large domain. This domain, discretized with a cell size of 2.5 mm (or $\lambda/13$ at 9 GHz), yields a very large computational domain; $620 \times 80 \times 96$ cells.

First, the standard FDTD(2,2) was used to compute the SE of the scaled fuselage and it was found to be very accurate when the cell size was chosen fine enough for the frequency band of interest. However, as the mesh became finer, the memory requirements became significantly larger, i.e., every time the mesh is refined by a factor of 2, the memory requirements just for the electric and magnetic field components that describe the fuselage became larger by a factor of $2^3 = 8$.

However, when the hybrid method of Subgrid FDTD(2,2)/FDTD(2,4) presented in Section IX. was applied to the same problem, significant savings in memory were achieved. This happens because the largest part of the computational domain is the interior of the fuselage, and the problem of boundary conditions arises only near the walls of the enclosures. Therefore, it is desired to simulate the propagation inside the fuselage using a higher-order method such as FDTD(2,4). In addition, near the walls of the fuselage a subgrid FDTD(2,2) method should be used in order to represent accurately the PEC boundary conditions, and successfully simulate the penetration mechanisms. FDTD(2,2) is used near the walls instead of FDTD(2,4) since FDTD(2,4) exhibits an inherent artificial penetration through thin PEC films. This artificial penetration is attributed to the length of the FDTD(2,4) stencil which allows fields from one side of the PEC to couple on the other side of the PEC. Also, as discussed in Section VII. stable higher-order boundary conditions that would simulate correct PEC discontinuities do not exist and they are very challenging to derive. Therefore, subgrid FDTD(2,2) is hybridized with FDTD(2,4) to resolve all these issues. Following such a procedure yields tremendous savings in memory and/or time depending on the particular problem. The memory requirements for both FDTD(2,2) and the hybrid method are summarized in Table 4.1 for a cell size of 2.5 mm. For

Table 4.1: Memory requirements for the different regions of the computational domain for a cell size of 2.5 mm

Memory (Mbytes)	FDTD(2,2)	Hybrid Subgrid FDTD(2,2)/FDTD(2,4)	
		Subgrid FDTD(2,2)	FDTD(2,4)
M_1	70	-	2.5
M_2	44	44	1.5
M_{total}	114	48	
Savings Factor	$114/48 \simeq 2.5$		

more examples about the memory savings that result from the application of the hybrid method of Subgrid FDTD(2,2)/FDTD(2,4) see Section IX.. Furthermore, the results of the hybrid method were found to be very accurate even though the interior of the fuselage was always simulated using coarse meshes for the frequency bands of interest. This validates the high accuracy of FDTD(2,4) which requires much fewer points per wavelength than FDTD(2,2) to accurately simulate the wave phenomena.

III. Personal Electronic Devices (PEDs)

Besides the penetration of man-made radio frequency (RF) signals external to the airplane into the fuselage (HIRF), another very important EMI issue concerns interference that can occur on-board. Such EMI can potentially be generated by personal electronic devices (PEDs), such as laptop computers, cell phones, etc. It is a common policy of all commercial airlines to prohibit the use of PEDs during at least the very sensitive phases of take-off and landing, if not for the entire duration of flights. This policy has been established because it is believed that radiated emissions from PEDs can interfere with on-board electronics and cause problems to their operation; e.g., jamming in communication systems. In fact, the policy statement of the Federal Communications Commission (FCC) and Federal Aviation Administration (FAA) about PEDs is as follows:

- "Cellulars, Laptops and Computer Games

    a. The FCC and FAA ban cell phones for airborne use because its signals could interfere with critical aircraft instruments. Radios and televisions are also prohibited.

    b. Laptops and other personal electronic devices (PEDs) such as hand-held computer games and tape or CD players are also restricted to use above 10,000 feet owing to concerns they could interfere with aircraft instrumentation."

Clearly, the investigation of the effects of EMI caused by PEDs is of paramount importance. Especially, as wireless communications become a part of everyday life, it is desired that cell phones and other portable electronic devices be allowed at any environment, even inside airplanes. However, before the strict policies about PEDs change, thorough examination of the effects of EMI, generated by PEDs, to the safety and operation of aircraft should be performed.

One possible mechanism for this PED interference can be established via the antennas which are mounted on the fuselage and support different types of communication. Electromagnetic fields radiated by PEDs can be transmitted to the exterior of an aircraft through the fuselage apertures (windows). Furthermore, these RF fields

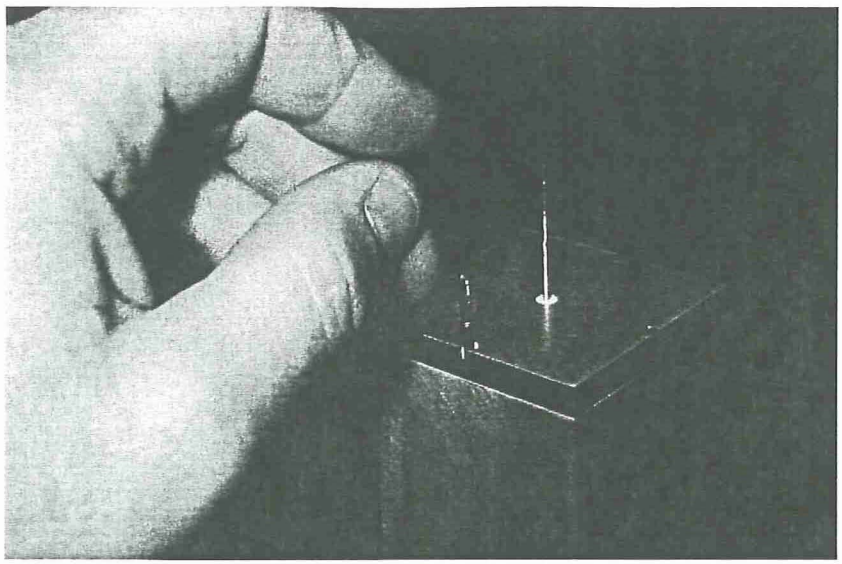

Figure 4.54: The top of the pedestal for the simulated PED screws on to the bottom of the pedestal with counter-bored allen head screws.

A hole was drilled through the bottom of the simplified fuselage through which the PED cable passes. To move the PED to another location, a new hole will have to be drilled through the fuselage at that location. Since it is desirable to minimize such holes, the existing PED location will be fixed for now. To facilitate the description of the PED and external antenna locations, a letter designation is associated with each of the cabin windows, as shown in Fig. 4.55. The current PED location is against the starboard side wall adjacent to window "C."

A drawing of the fuselage cross section (Fig. 4.56) illustrates the relationships of the simulated PED and the external antenna. In this view, both are at station C. This is the configuration for which measurements are compared with FDTD predictions later in this section. Note that both the PED element and the monopole externally mounted to the fuselage are 3 cm tall and have a radius of 0.60325 mm.

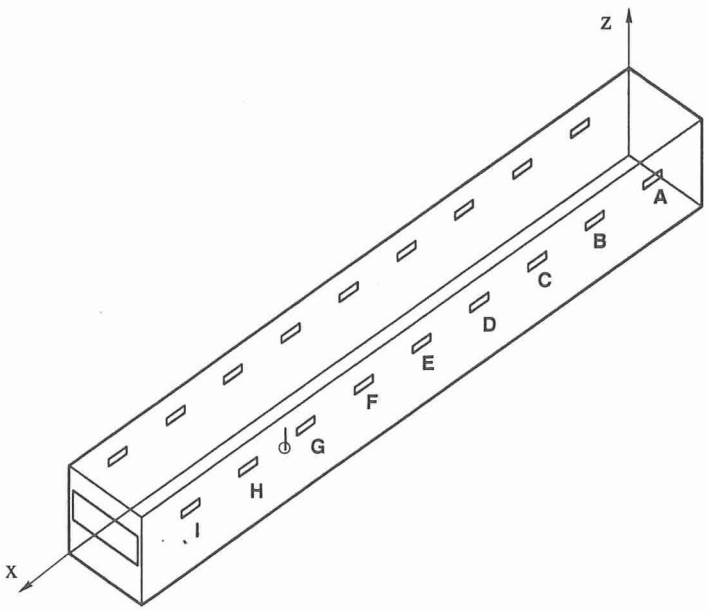

Figure 4.55: To more easily describe the locations of the PED and external antenna, a letter designation is assigned to the locations of the simplified fuselage cabin windows.

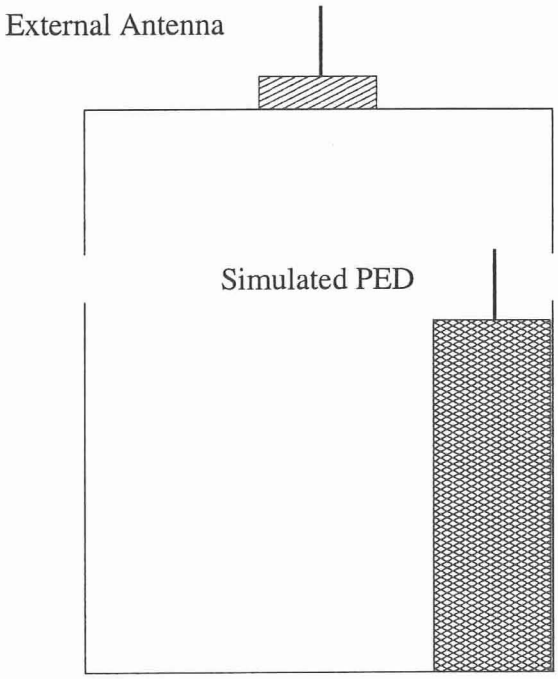

Figure 4.56: The PED is located against the starboard side wall of the simplified fuselage, while the external antenna is mounted on the top of the fuselage, along the centerline. Both the PED and external antenna are centered on station C.

B. Measurements

Again, due to the highly overmoded nature of this large cavity, the coupling between the PED and external antenna exhibit extremely rapid variations as a function of frequency. In order to resolve those variations, a large number of frequency points were measured.

The network analyzer is capable of measuring 801 frequency points per measurement/calibration. The only option available to increase the frequency resolution is to decrease the bandwidth of the measurement. To cover the frequency range of 0.05 GHz to 11 GHz (scaled frequencies of 2.5 MHz to 550 MHz), it is broken into many 801-point bands. In some cases, 14 calibration/measurements of 800 MHz bandwidth were performed. In other cases, seven 1.6 GHz band measurements were used.

The measurements were performed inside the anechoic chamber, with the instrumentation just outside the door. Originally, 15 and 19 foot long RF cables were used to connect the S-parameter test set with the simplified fuselage, but the losses of those cables were found to be excessive. Instead, while the source and receiver remained outside of the chamber, the test set was relocated to a position immediately under the simplified fuselage. This enabled the to use RF cables of four and five feet in length, greatly reducing the cable losses. A photograph of the measurement setup is shown in Fig. 4.57.

Measurements were performed for the purpose of validating FDTD predictions of coupling between the PED and external antenna. For these measurements, both the PED and external antenna were located at station C, as depicted in Fig. 4.56.

C. FDTD(2,2) predictions

Here, the predictions for the coupling between the PED antenna and the antenna mounted on the exterior of the fuselage are presented. A cell size of 5 mm (or $\lambda/10$ at 6 GHz) is used. The radius of the two monopoles is 0.60325 mm, and it is taken into account in all simulations both along the wire (using a thin wire model) and the excitation (using a source based on the radial electric fields). To speed the simulation times, all sources used internal resistances [65]. The S-parameters are computed using the following procedure described in [65]:

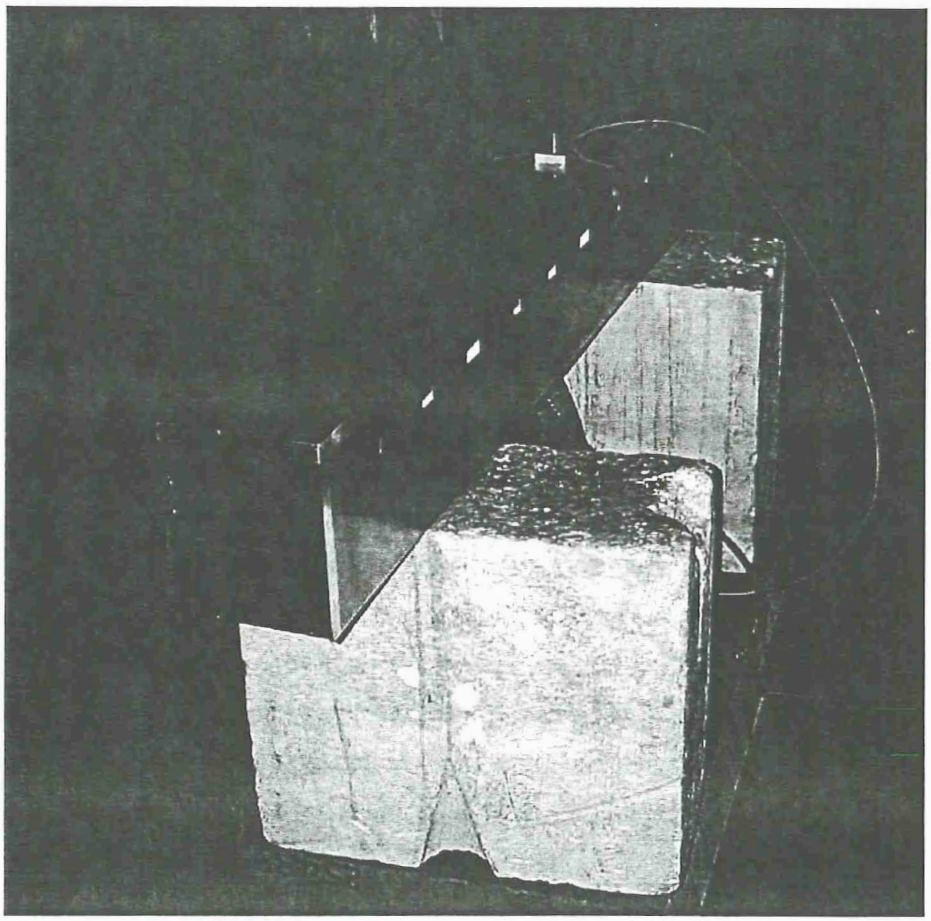

Figure 4.57: The PED measurements were performed within the anechoic chamber with the S-parameter test set located immediately beneath the simplified fuselage, the RF cable losses were reduced to an acceptable level.

a. Augment the system of the two antennas by connecting at their inputs two voltage sources with internal resistors.

b. Calculate the Y-parameters of the entire system including the antennas and the load resistors. This is accomplished by two simulations that implement the definition of the Y-parameters, i.e., excite one antenna and short circuit the other to compute Y_{11} and Y_{21} and vice versa to compute Y_{22} and Y_{12}.

c. From the Y-parameters of the entire system the Y-parameters of the antennas can be extracted using the properties of two-port networks connected in cascade along with $ABCD$-parameters [143].

d. The Y-parameters of the antennas are converted to S-parameters by taking into account the characteristic impedance of the transmission line, e.g., 50 ohms for a coaxial cable.

This procedure results in major computational savings because the internal resistors force the input current transients of the two antennas to decay fast. It should be mentioned that the internal resistance of the voltage sources was $R_s = 100$ ohms.

The complete set of S-parameters of the two antennas is illustrated in Figs. 4.58-4.60. Both the PED and external antenna are located at station C (see Fig. 4.56) as in the measurements. The FDTD(2,2) predictions are compared with measurements. For the S_{11} and S_{22} parameters which represent the reflection coefficients of the two antennas, measurements are available only up to 4 GHz, and they agree very well with the FDTD(2,2) calculations. It is observed that there is a shift between the measured and predicted resonant frequency of S_{22} which can be attributed to numerical dispersion or measurement errors. However, the parameter that is the focus of a PED analysis is the coupling between the two antenna elements. Coupling measures the amount of energy that a PED antenna can couple to an antenna that belongs to the communication system of an aircraft, and it is represented by the S_{12} and S_{21} parameters, which are equal due to reciprocity.

To illustrate more clearly the variation of coupling as well as the agreement between the FDTD(2,2) calculations and the measurements, figures that plot coupling in different frequency bands are constructed (see Figs. 4.61-4.65). It is observed that

FDTD(2,2) predicts very accurately the coupling between the PED antenna and the antenna mounted on the exterior of the airplane up to 4.5 GHz.

There are some discrepancies between the predictions and the measurements at low frequencies (see Figs. 4.61). This can be possibly attributed to the number of time-steps, since the accuracy of the FFT of the FDTD results is greatly affected at lower frequencies by the number of time-steps. Also, the discrepancies can be due to the low levels of coupling (below -80 dB) at the lower end of the frequency band, which make both the measurements and the predictions questionable.

The levels of coupling exhibit a highly oscillatory behavior due to the large number of resonances present inside the fuselage. Also, the maximum level of coupling is approximately -30 dB and occurs at several frequencies. This level of -30 dB can represent a threat to the communication systems of the airplane. However, the definite interpretation of effects of such coupling levels are left to the engineers that deal with and design the communication systems of the aircraft.

Also, to illustrate the effects of the location of the receiving external antenna another coupling configuration is examined. Specifically, the external antenna is moved on station A (see Fig. 4.55) along the centerline of the fuselage. Coupling calculations are performed again using FDTD(2,2) and the results are compared with measurements in Figs. 4.66-4.70. Again the predictions agree very well with measurements. Also, the coupling computations for stations A and C are compared in Fig. 4.71. Obviously, the coupling between the PED antenna and the external antenna is larger when the external antenna is located on station C than when it is located on station A. This is expected, because as the distance between the two antennas increases the coupling between them decreases.

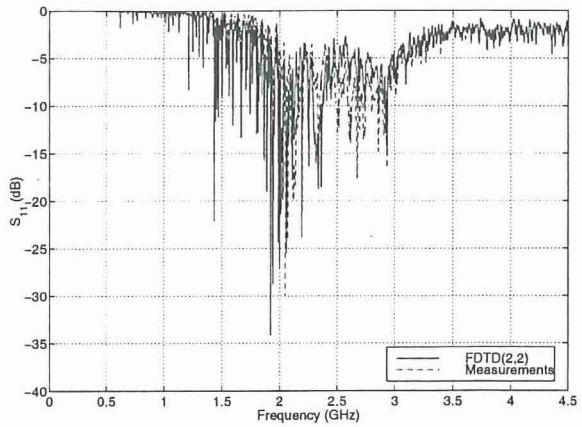

Figure 4.58: Reflection coefficient of the PED antenna (station C).

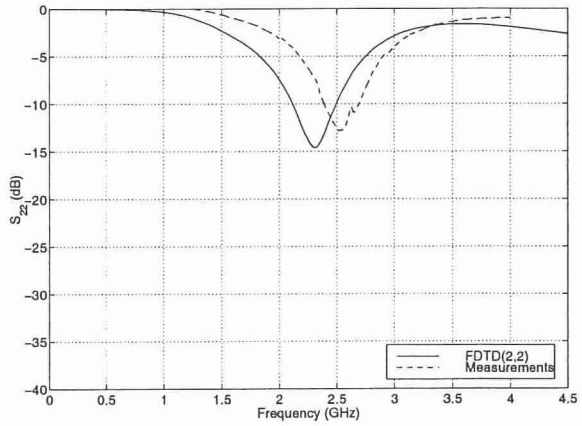

Figure 4.59: Reflection coefficient of the antenna mounted on the exterior of the fuselage (station C).

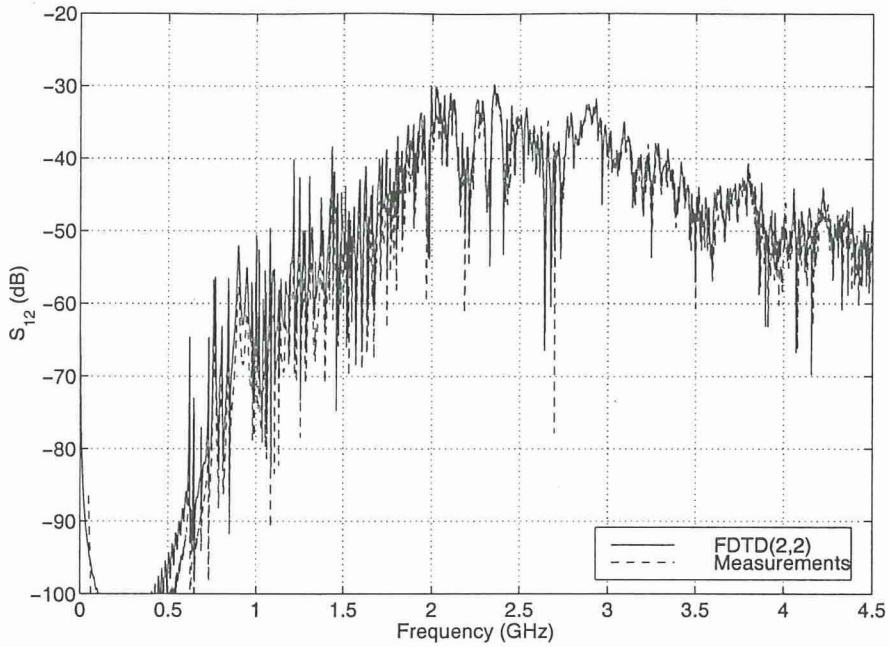

Figure 4.60: Coupling between the PED antenna and the antenna mounted on the exterior of the fuselage (station C).

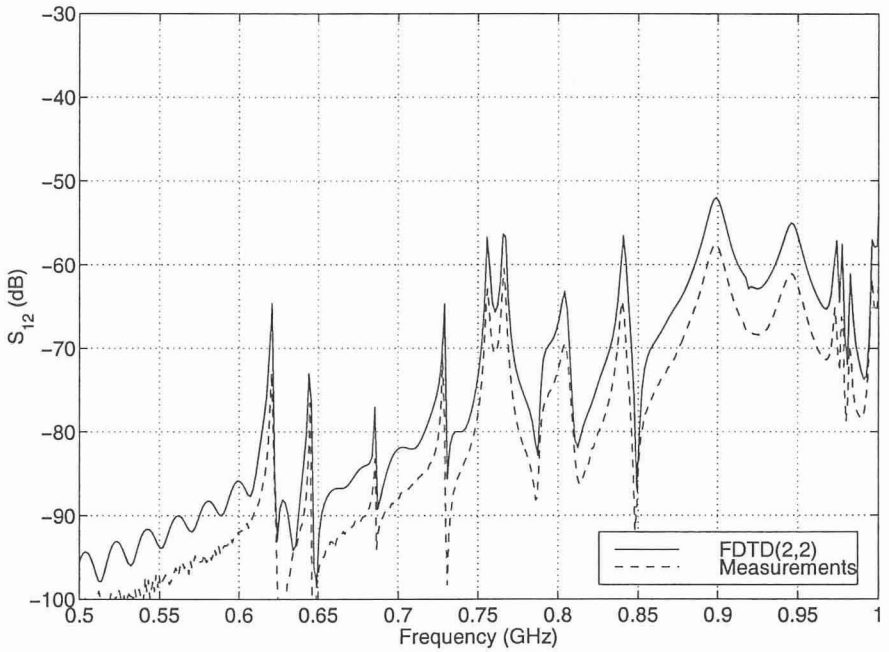

Figure 4.61: Coupling between the PED antenna and the antenna mounted on the exterior of the fuselage (station C).

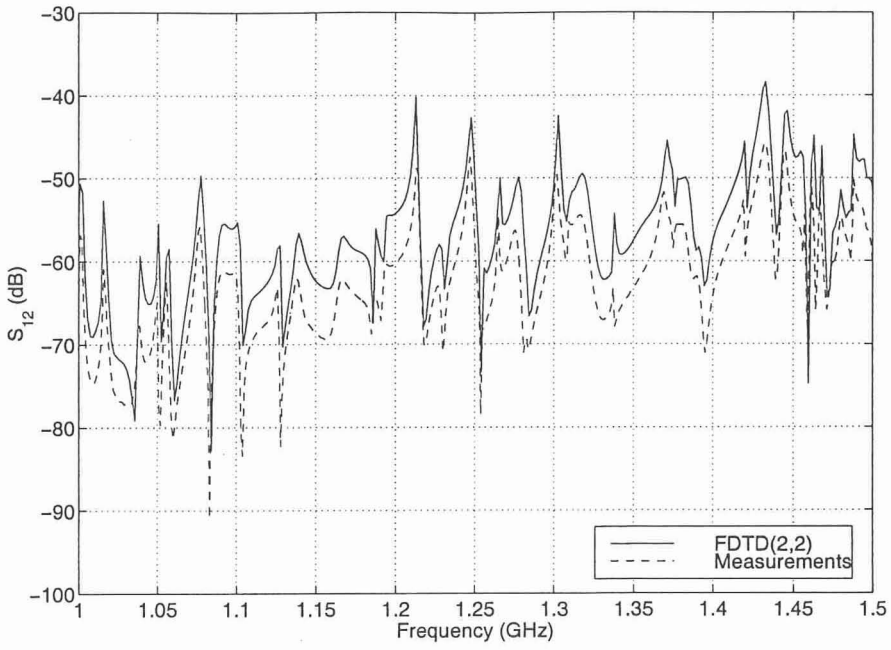

(a)

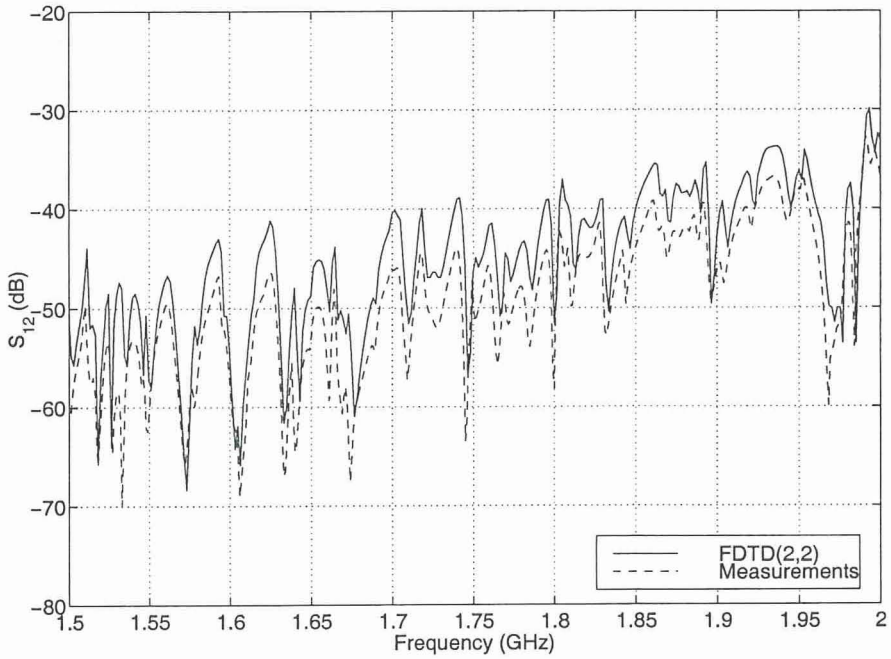

(b)

Figure 4.62: Coupling between the PED antenna and the antenna mounted on the exterior of the fuselage (station C).

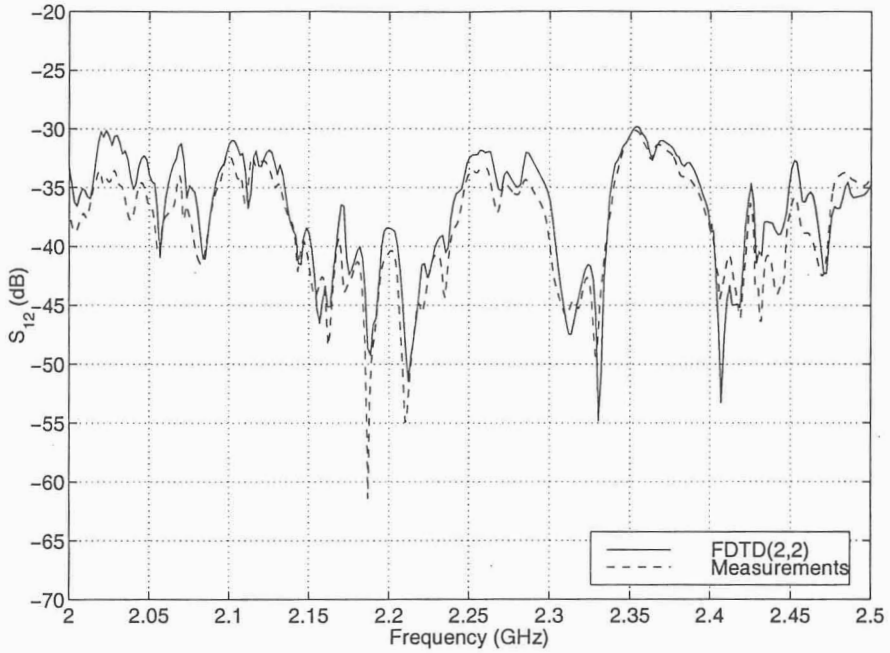

(a)

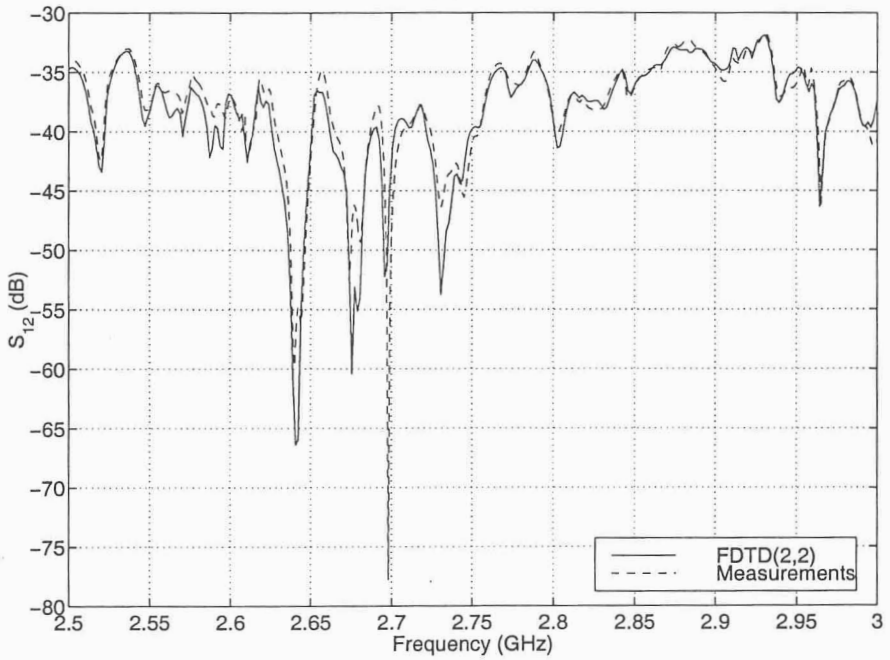

(b)

Figure 4.63: Coupling between the PED antenna and the antenna mounted on the exterior of the fuselage (station C).

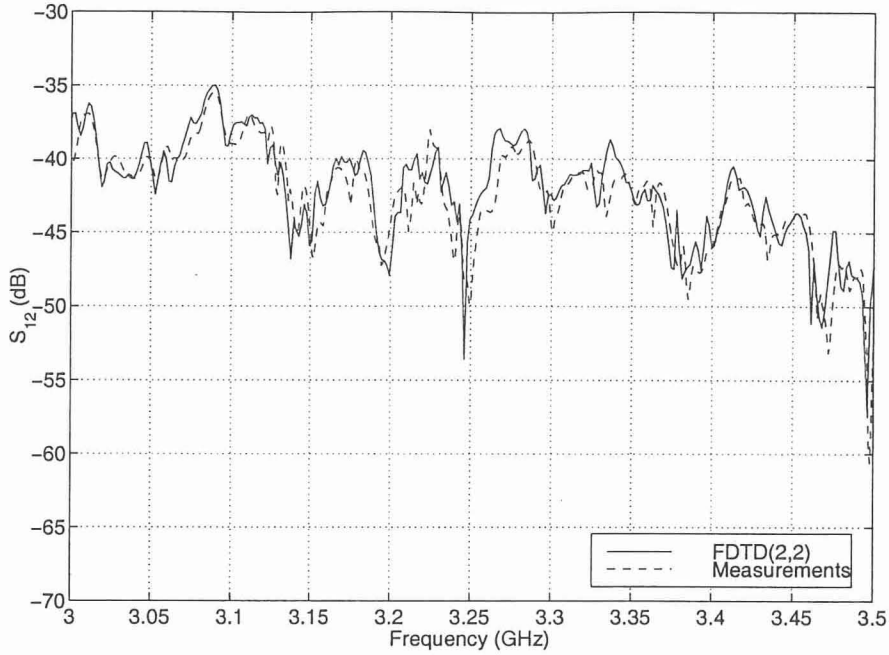

(a)

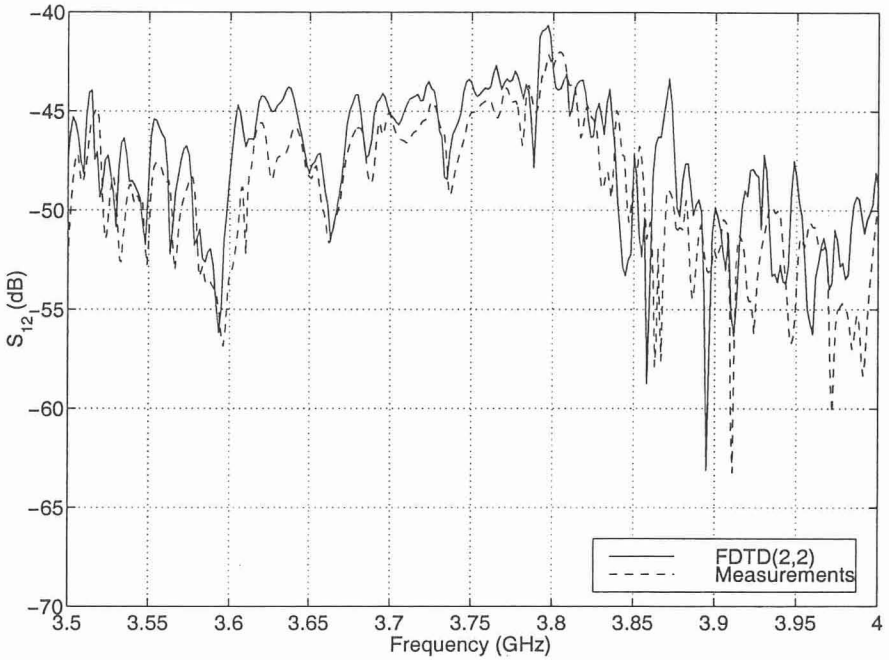

(b)

Figure 4.64: Coupling between the PED antenna and the antenna mounted on the exterior of the fuselage (station C).

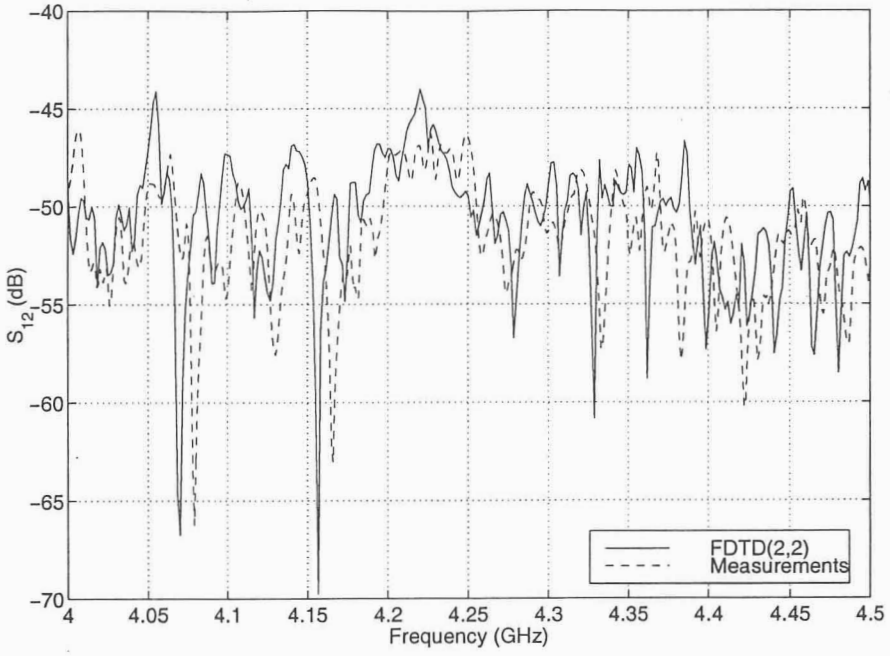

Figure 4.65: Coupling between the PED antenna and the antenna mounted on the exterior of the fuselage (station C).

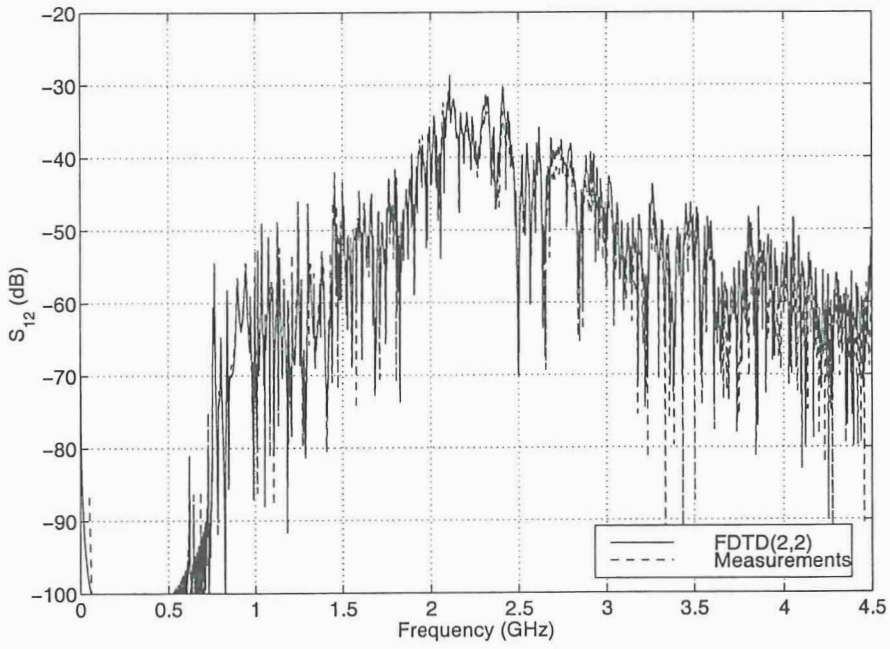

Figure 4.66: Coupling between the PED antenna and the antenna mounted on the exterior of the fuselage (station A).

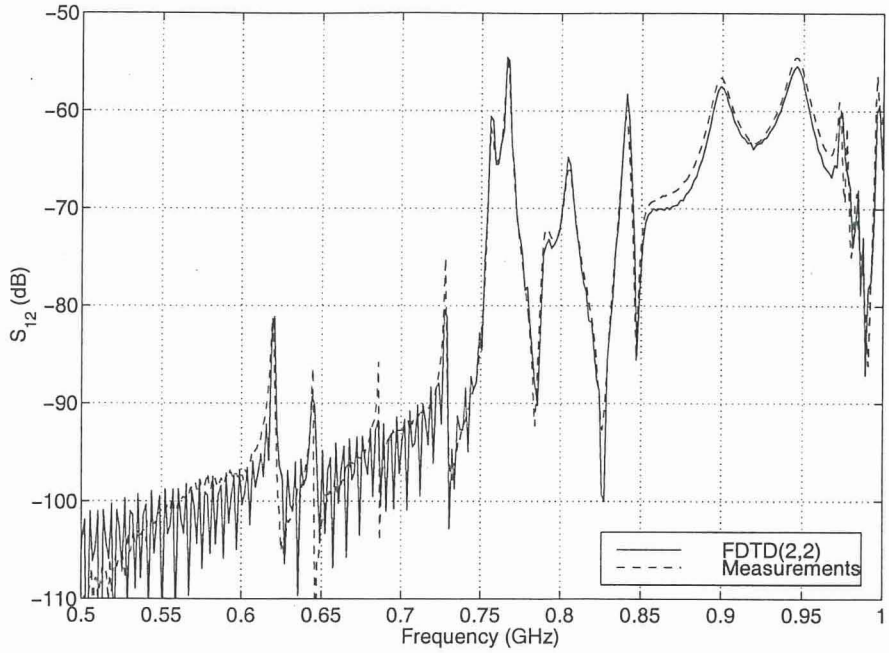

(a)

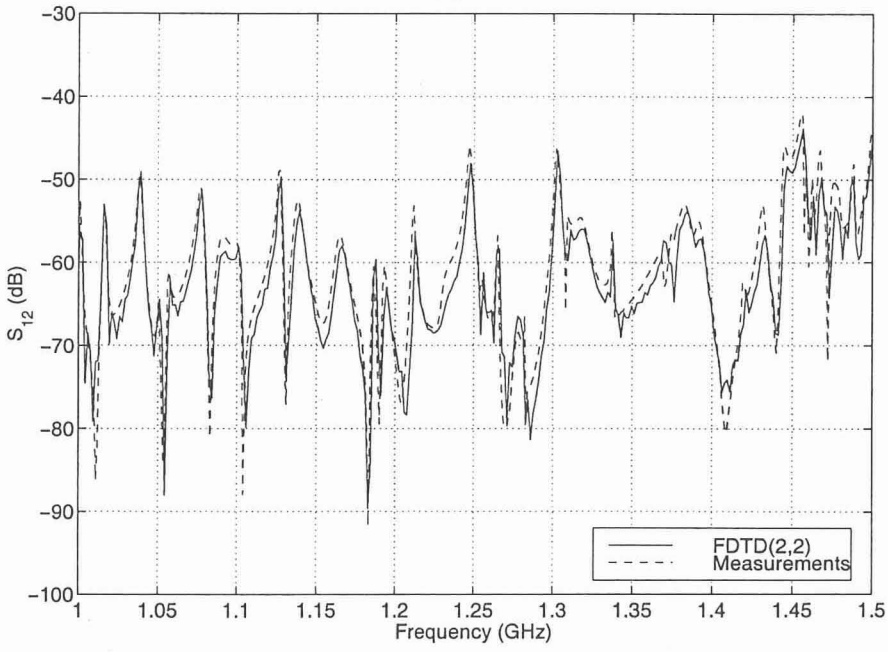

(b)

Figure 4.67: Coupling between the PED antenna and the antenna mounted on the exterior of the fuselage (station A).

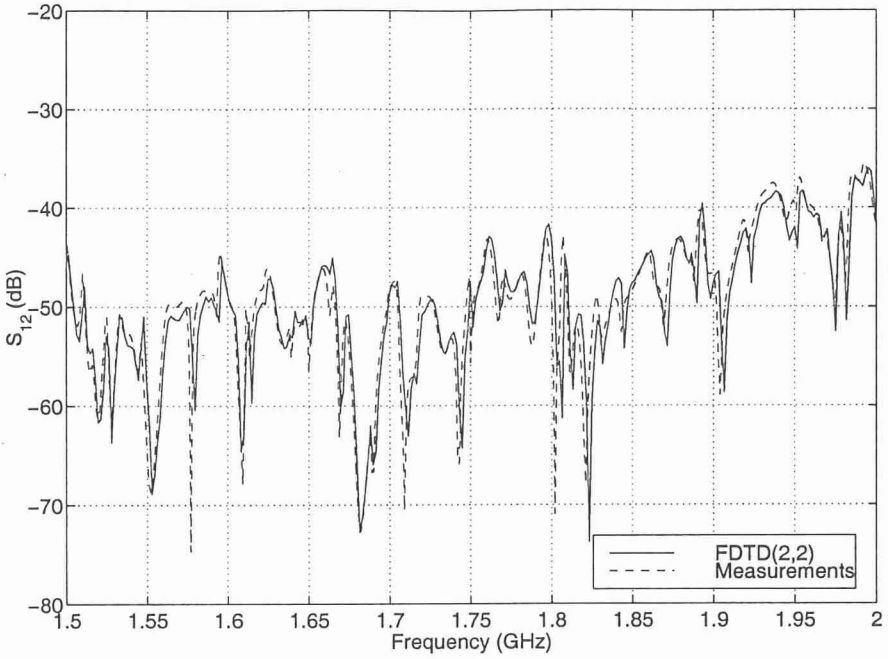

(a)

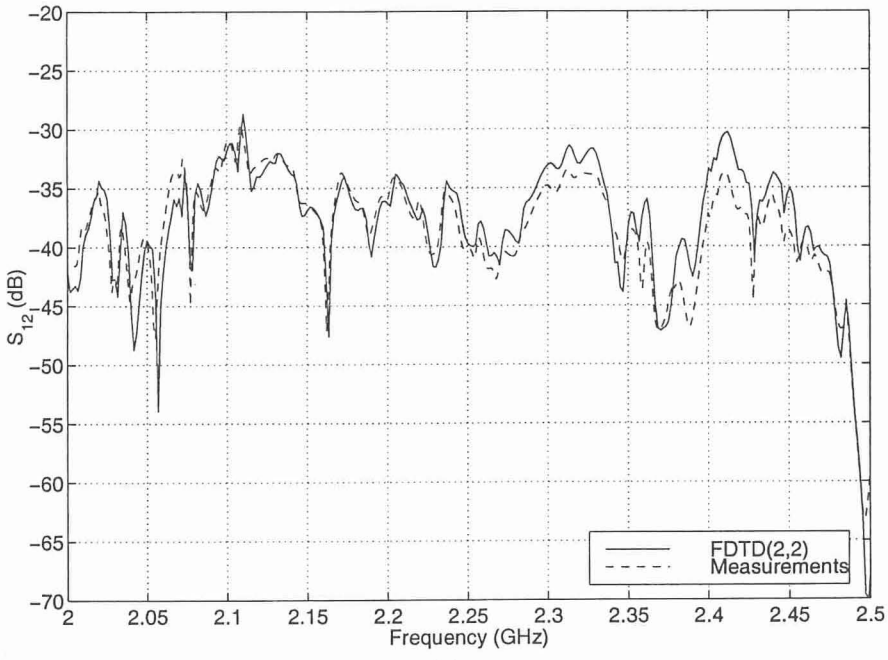

(b)

Figure 4.68: Coupling between the PED antenna and the antenna mounted on the exterior of the fuselage (station A).

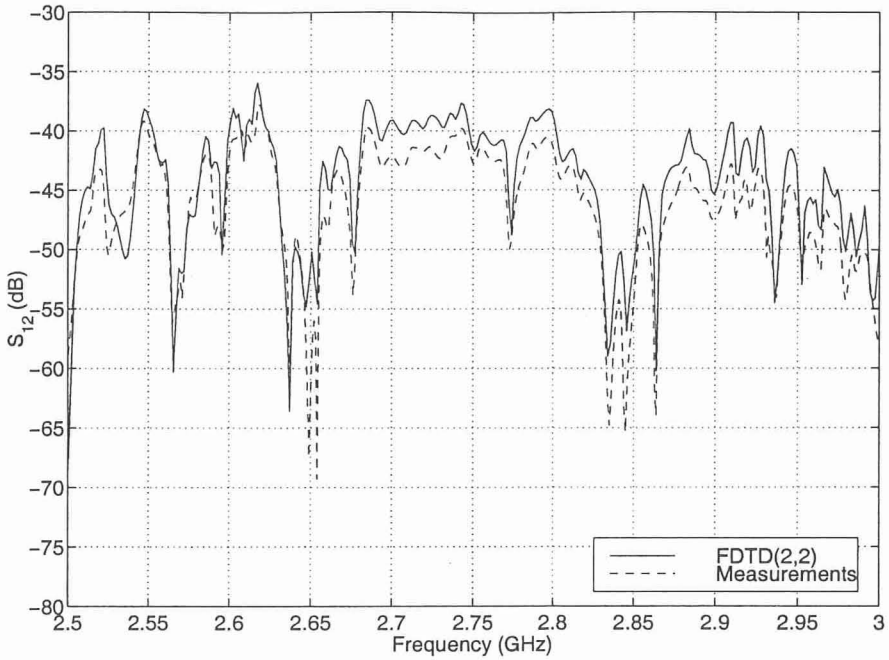

(a)

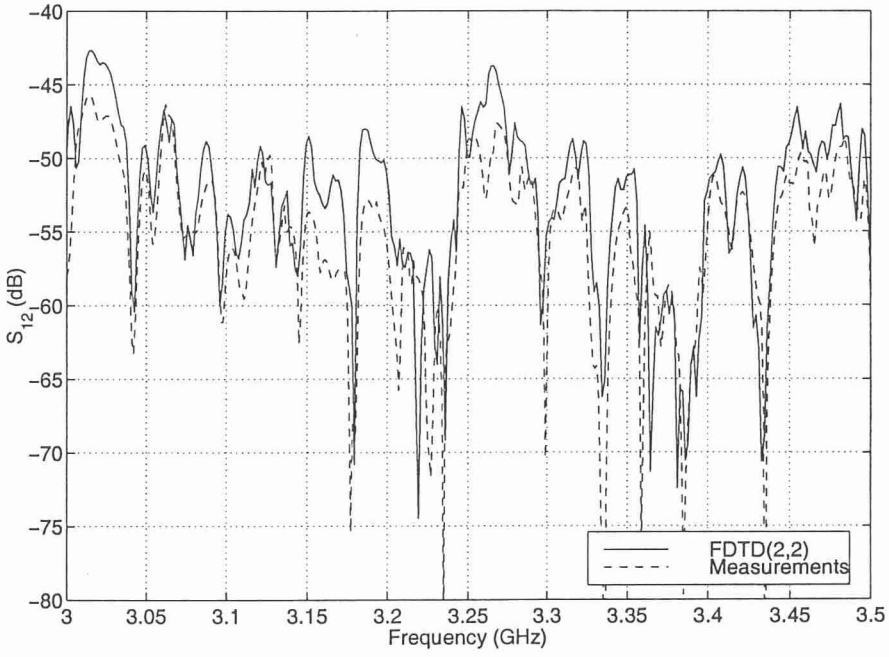

(b)

Figure 4.69: Coupling between the PED antenna and the antenna mounted on the exterior of the fuselage (station A).

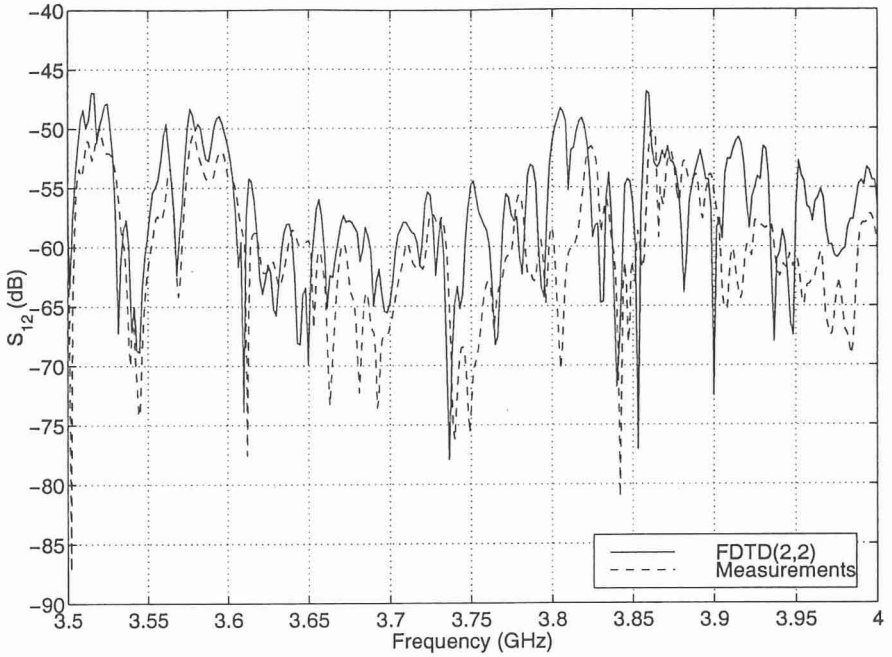

(a)

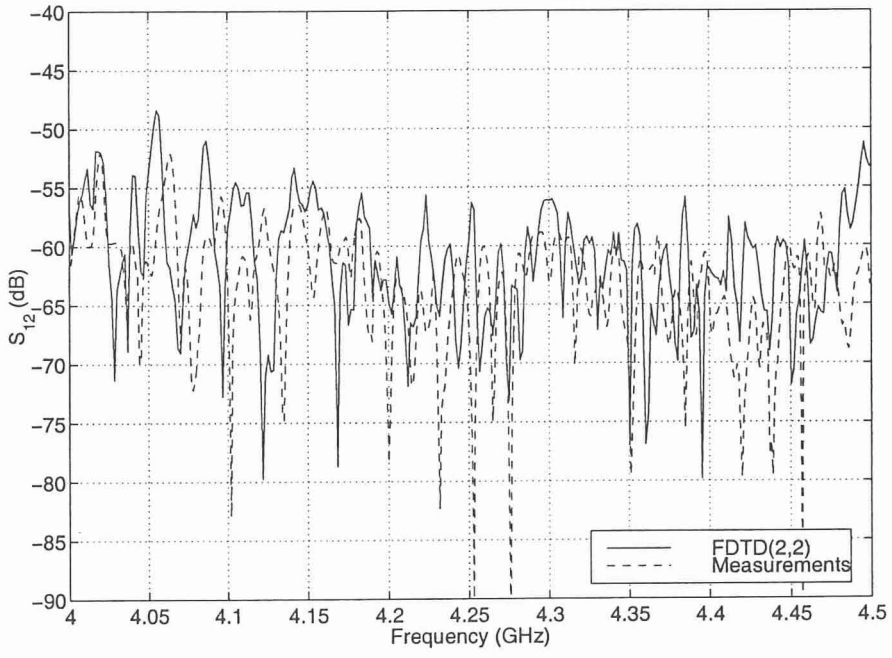

(b)

Figure 4.70: Coupling between the PED antenna and the antenna mounted on the exterior of the fuselage (station A).

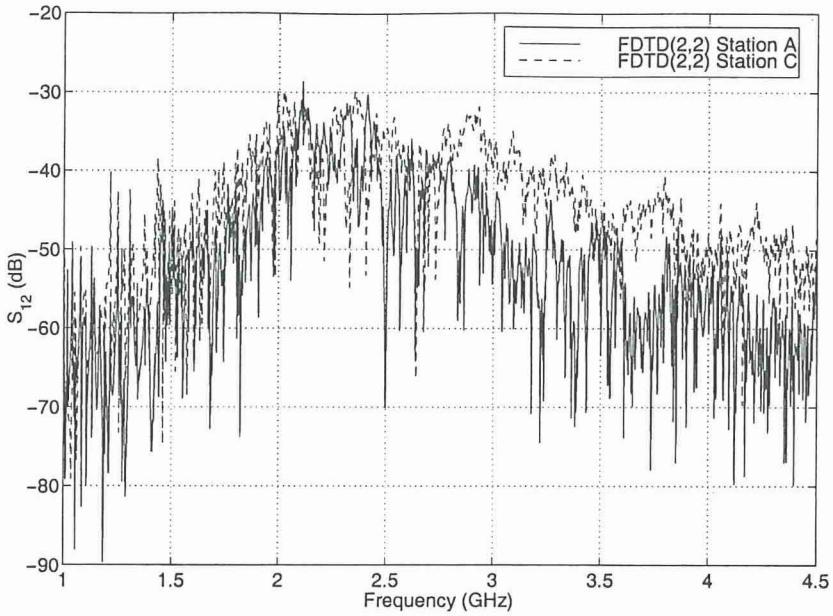

Figure 4.71: Coupling between the PED antenna and the antenna mounted on the exterior of the fuselage at stations A and C.

D. Hybrid subgrid FDTD(2,2)/FDTD(2,4) predictions

In the previous section, the hybrid method of subgrid FDTD(2,2)/FDTD(2,4) presented in Section IX. was applied and validated for shielding effectiveness computations. It was shown that great memory savings can be achieved by using this hybrid when the fuselage is analyzed at high frequencies. In this section, this hybrid method is applied to the analysis of the PED problem for station C.

The spatial layout of the methods used by the hybrids in the computational domain is depicted in Fig. 4.72. It is seen that both antennas are included in the fine region where subgrid FDTD(2,2) is applied. This was done in order to simulate the fields near and on the probes very well by representing the probes with many cells (fine grid).

Initially, for validation purposes a cell size of 5 mm (or $\lambda/10$ at 6 GHz) for the fine grid and of 15 mm (or $\lambda/3$ at 6 GHz) for the coarse grid is used. Therefore, it is expected that these FDTD calculations will provide accurate results at most up to 6 GHz. The memory required for storing all the field components that describe the dimensions of the box is approximately 14 Mbytes which is approximately the

same as the one required by FDTD(2,2) alone when a cell size of 5 mm is used (see Subsection C.). For this cell size no memory savings occur since the cell size of 5 mm does not yield a large computational domain. However, this simulation results are used as validation of the hybrid method.

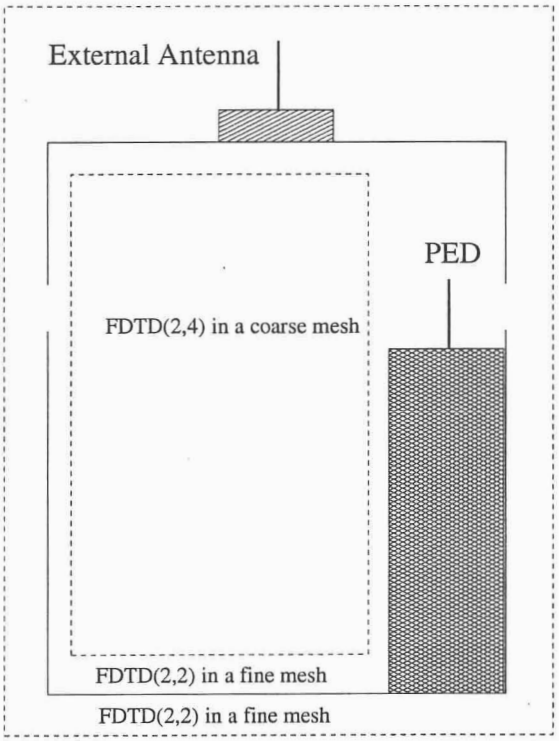

Figure 4.72: Schematic visualization of the hybrid method subgrid FDTD(2,2) and FDTD(2,4) applied to the scaled fuselage.

By comparing Figs. 4.73-4.80 with Figs. 4.58-4.65, it is observed that the hybrid method gives almost identical results for PED analysis as the ones of the standard FDTD(2,2) alone (with a cell size of 5 mm). Notice that even though most of the interior of the fuselage is simulated using a very coarse cell size of 15 mm, the accuracy is retained as a higher-order scheme is applied [FDTD(2,4)]. This, once again, proves the effectiveness of higher-order schemes.

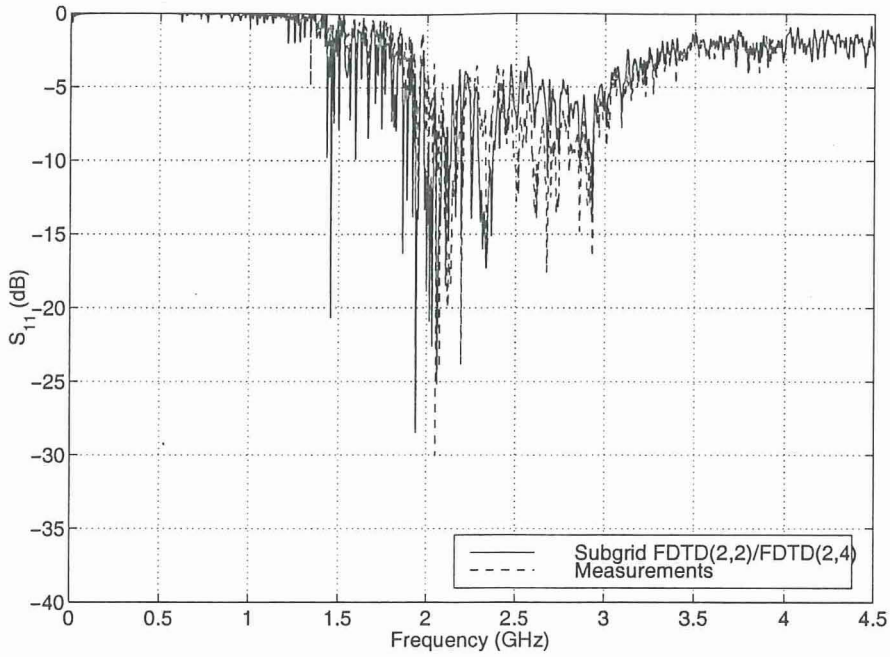

Figure 4.73: Reflection coefficient of the PED antenna (station C).

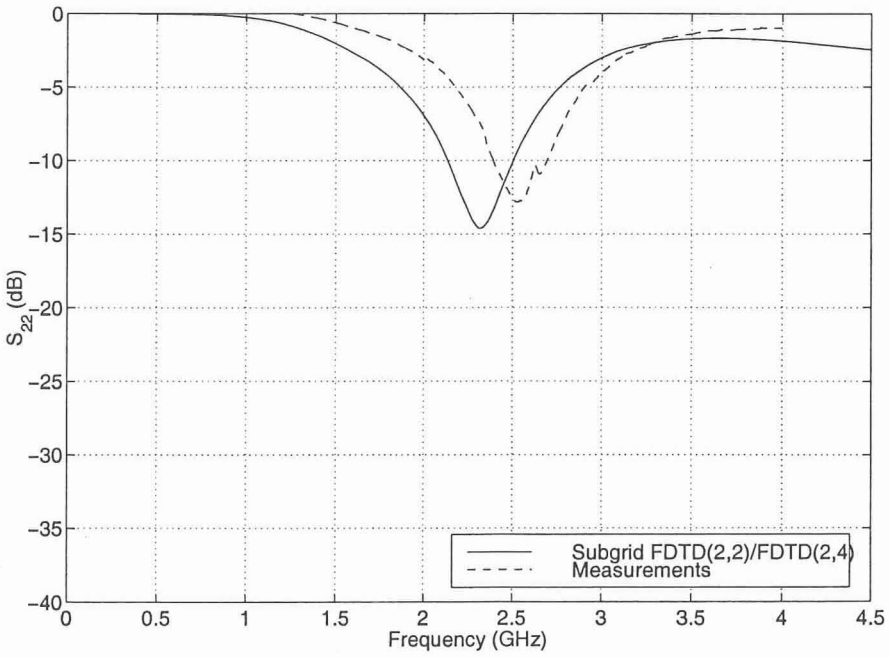

Figure 4.74: Reflection coefficient of the antenna mounted on the exterior of the fuselage (station C).

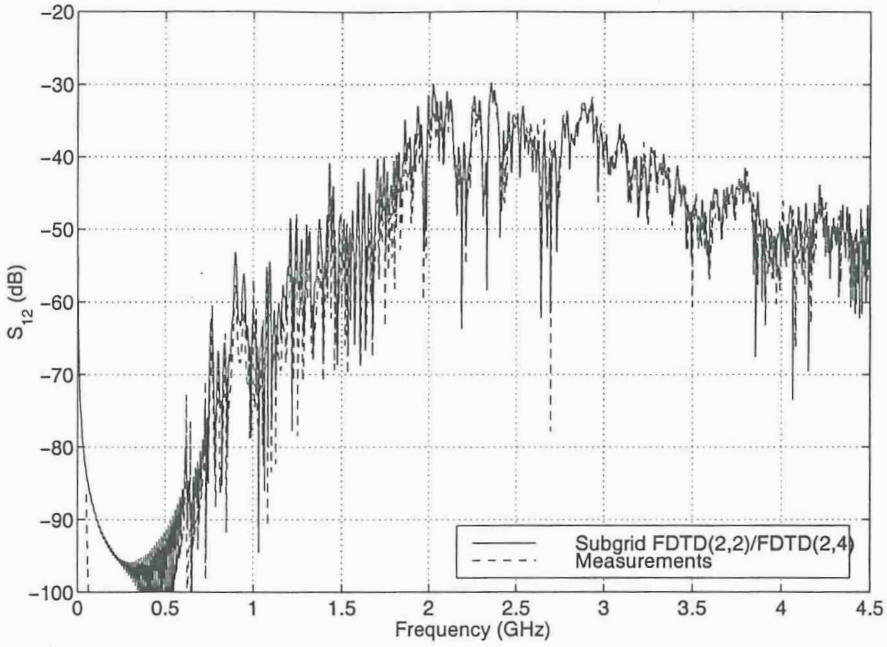

Figure 4.75: Coupling between the PED antenna and the antenna mounted on the exterior of the fuselage (station C).

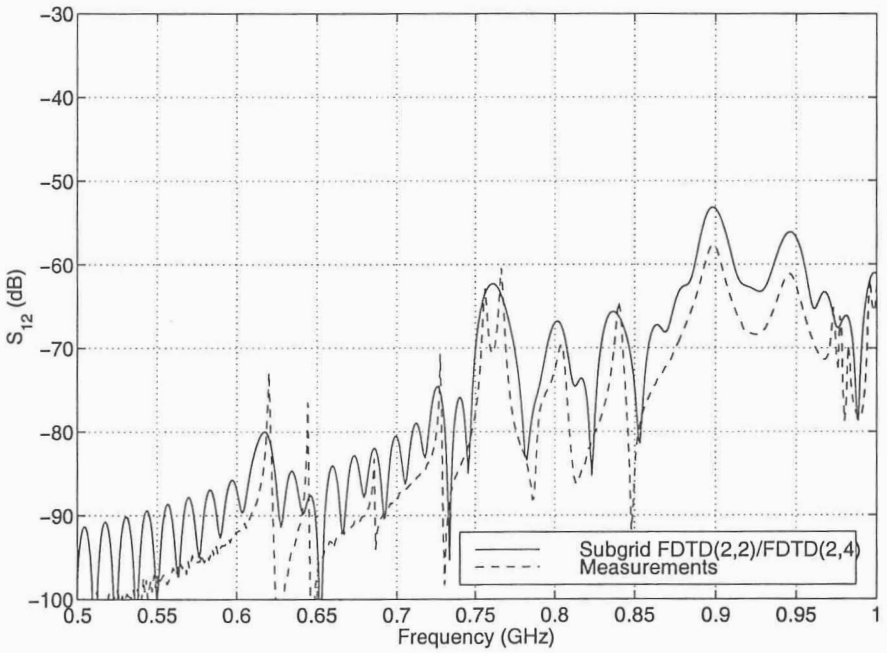

Figure 4.76: Coupling between the PED antenna and the antenna mounted on the exterior of the fuselage (station C).

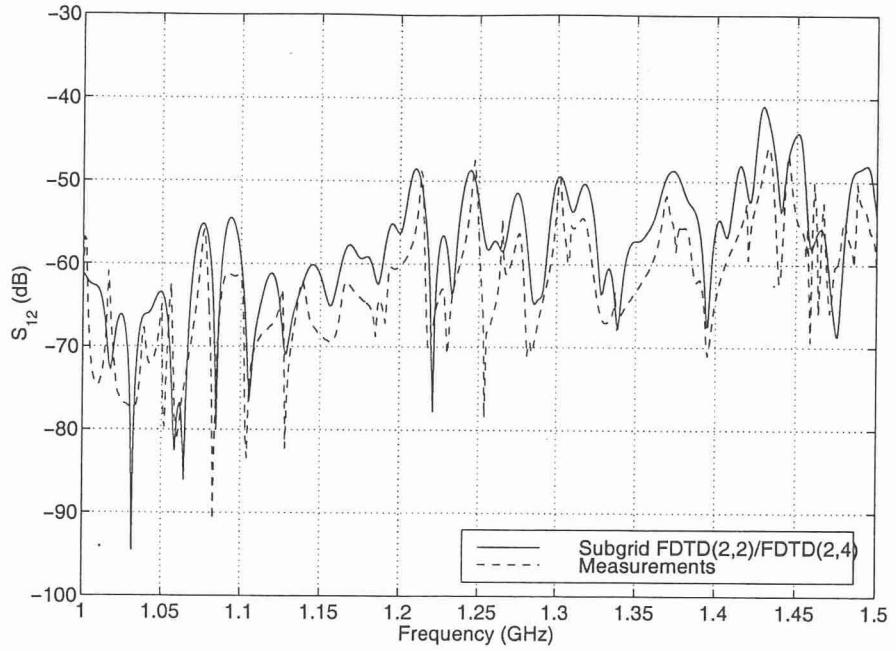

(a)

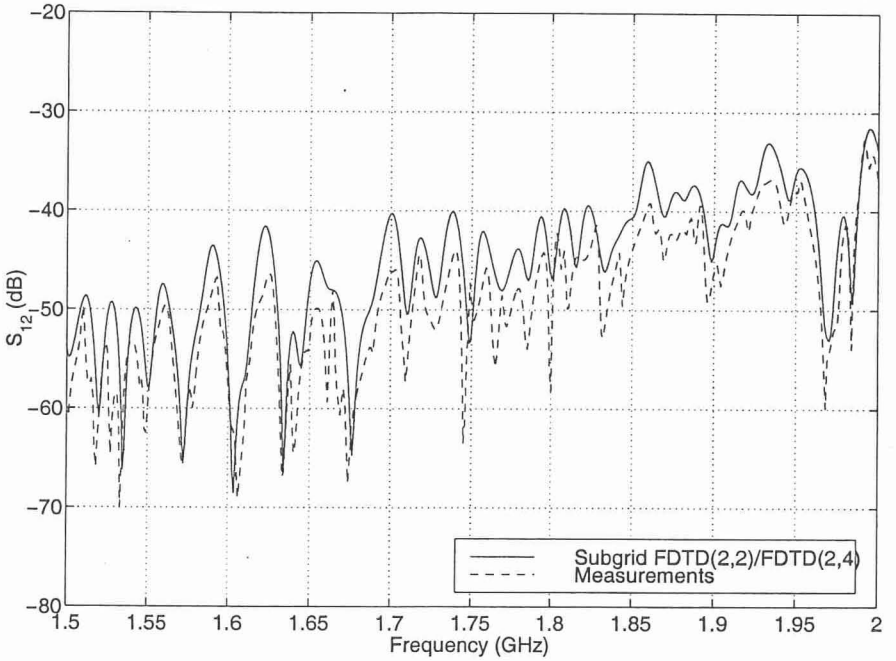

(b)

Figure 4.77: Coupling between the PED antenna and the antenna mounted on the exterior of the fuselage (station C).

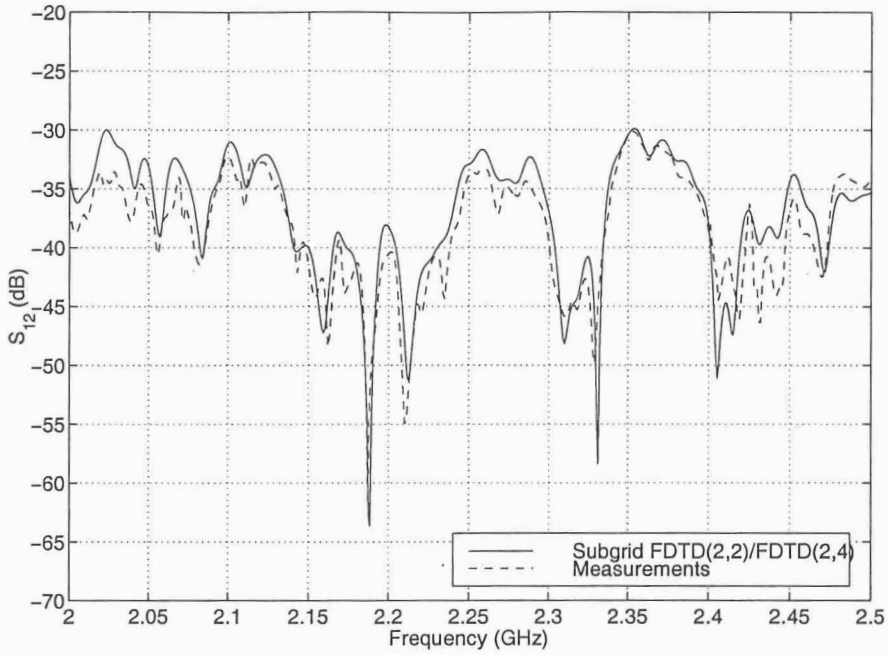

(a)

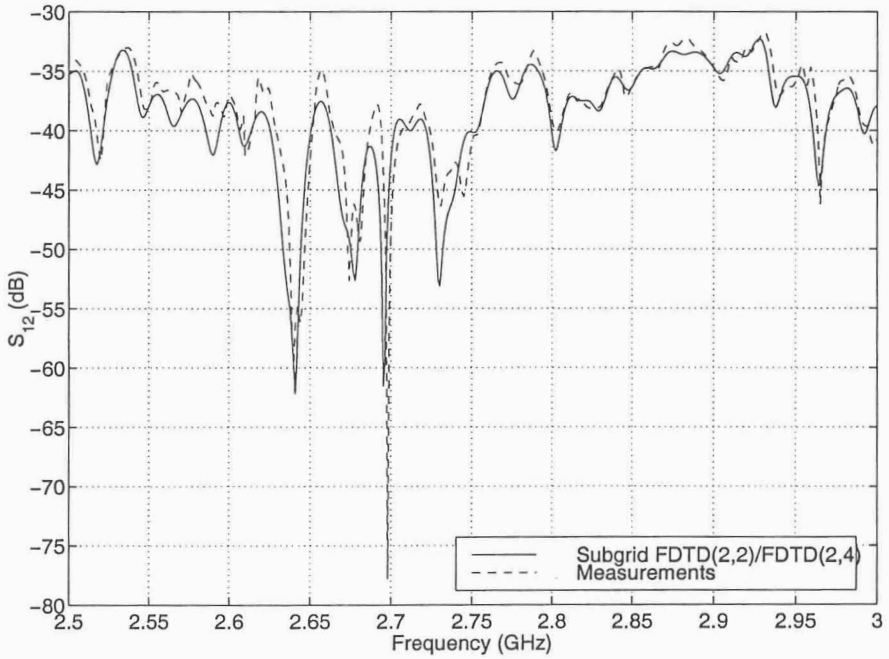

(b)

Figure 4.78: Coupling between the PED antenna and the antenna mounted on the exterior of the fuselage (station C).

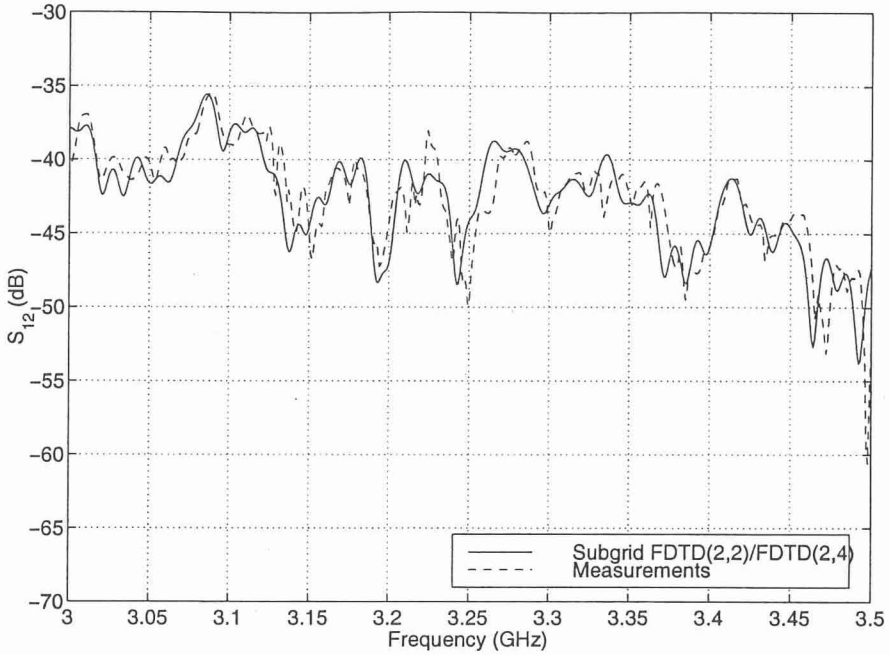

(a)

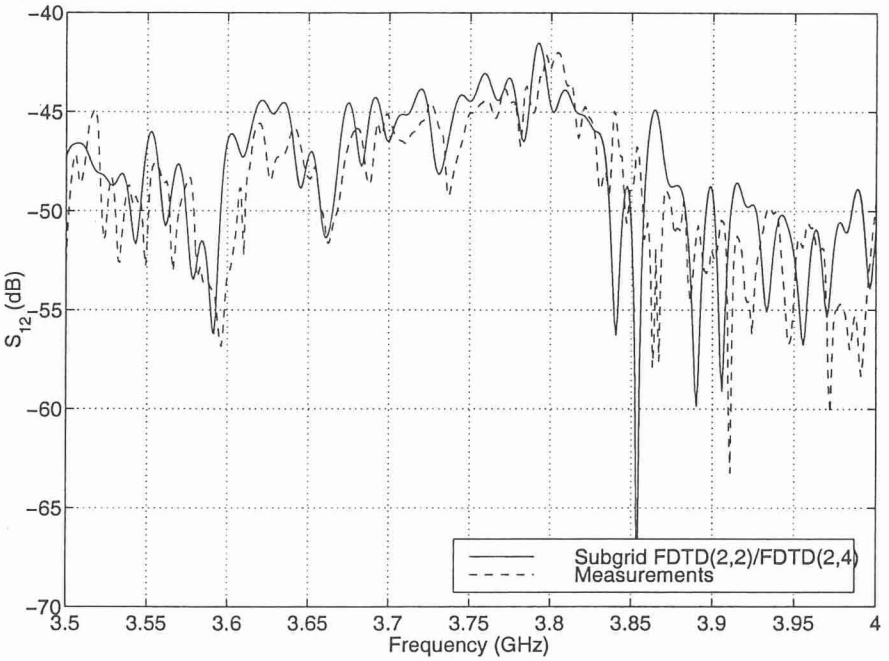

(b)

Figure 4.79: Coupling between the PED antenna and the antenna mounted on the exterior of the fuselage (station C).

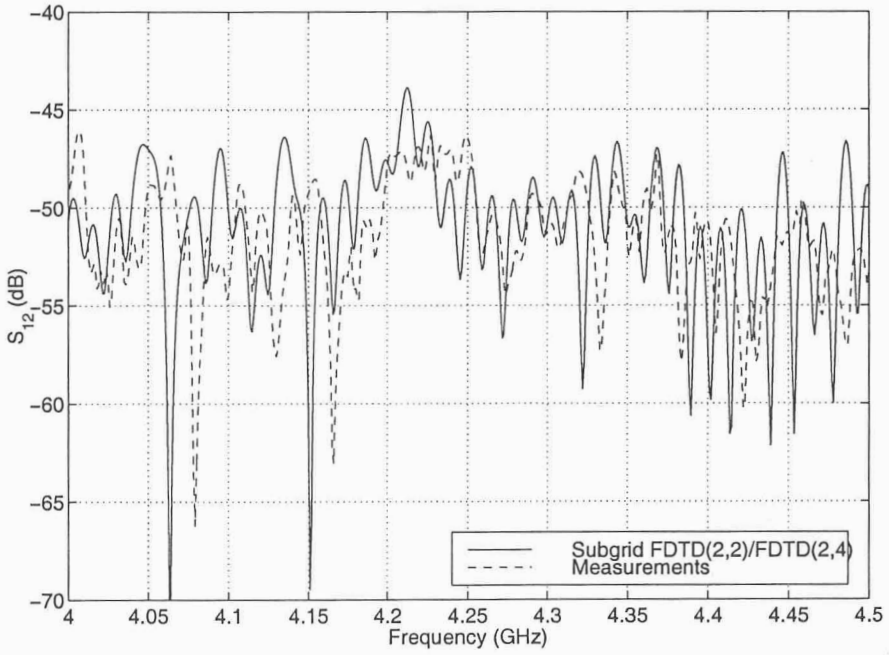

Figure 4.80: Coupling between the PED antenna and the antenna mounted on the exterior of the fuselage (station C).

E. Summary

In this section, the problem of EMI generated by PEDs was examined. Specifically, a PED antenna was mounted in the fuselage close to one of the windows whereas the receiving antenna was mounted on the exterior of the fuselage. The coupling between the PED element and the external antenna simulates the potential EMI threat signal to the communications systems of the aircraft. This coupling was both predicted as well as measured.

First, the standard FDTD(2,2) was applied and the numerical computations compared very well with the measurements up to frequencies for which the discretization was fine enough. These results validate for first time the ability of FDTD(2,2) to accurately simulate coupling in a complex geometrical setting. Furthermore, the fuselage is electrically very large thereby allowing a plethora of modes and resonances to be established. All these issues make the modeling of coupling even more challenging. However, FDTD(2,2) was proven very accurate for the analysis of such problems.

As mentioned in the previous section, the use of the hybrid subgrid FDTD(2,2) and FDTD(2,4) method yields significant memory savings. Therefore, the hybrid method was also applied here in order to be validated in the context of the PED analysis. Again, the hybrid method was found to be as accurate as the FDTD(2,2) scheme alone when the same fine grid cell size was used.

IV. Personal Electronic Devices (PEDs)

A. Introduction

In this section modifications to the simplified fuselage are presented. A new method is described to cover the upper long corners of the fuselage tube. The new method, in contrast to the previous one, results in less field leakage when PED measurements are performed with the window apertures covered. Additionally, a series of measurements are performed to explore the contribution of individual passenger windows to the coupling of fields from a simulated PED to an externally mounted antenna on the top of the fuselage, as well as the distribution of the coupled fields along the length of the fuselage.

B. Modifications to the "Simplified Fuselage"

The Simplified Fuselage was originally constructed by epoxying together four aluminum plates to form a rectangular cross section tube. The four long corners of the tube were covered with aluminum tape, and the ends of the tube were closed with aluminum plates that were aluminum taped in place.

This construction worked well for shielding effectiveness and PED measurements when all of the apertures were open, but it was found that the aluminum tape covered, epoxied corners were "leaking" when PED measurements were performed with the apertures covered with copper tape. Part of the problem was that the epoxy was failing, allowing the plates to separate. Another issue was related to the aluminum tape. This particular tape has an adhesive that is not electrically conductive, and the aluminum did not contact the body of the fuselage through the adhesive. Measurements with an ohm meter verified that the tape was not electrically continuous (at dc) to the fuselage. While changing to a type of copper tape having conductive adhesive may have yielded a significant improvement, the failure of the epoxy was still problematic. It was decided to implement yet another revision to the design of the Simplified Fuselage.

The design change is shown schematically in the illustration of Figure 4.81. The original epoxied construction is shown on the left. The new construction involves the addition of a 1 cm square bar in each of the upper corners to which the top and side

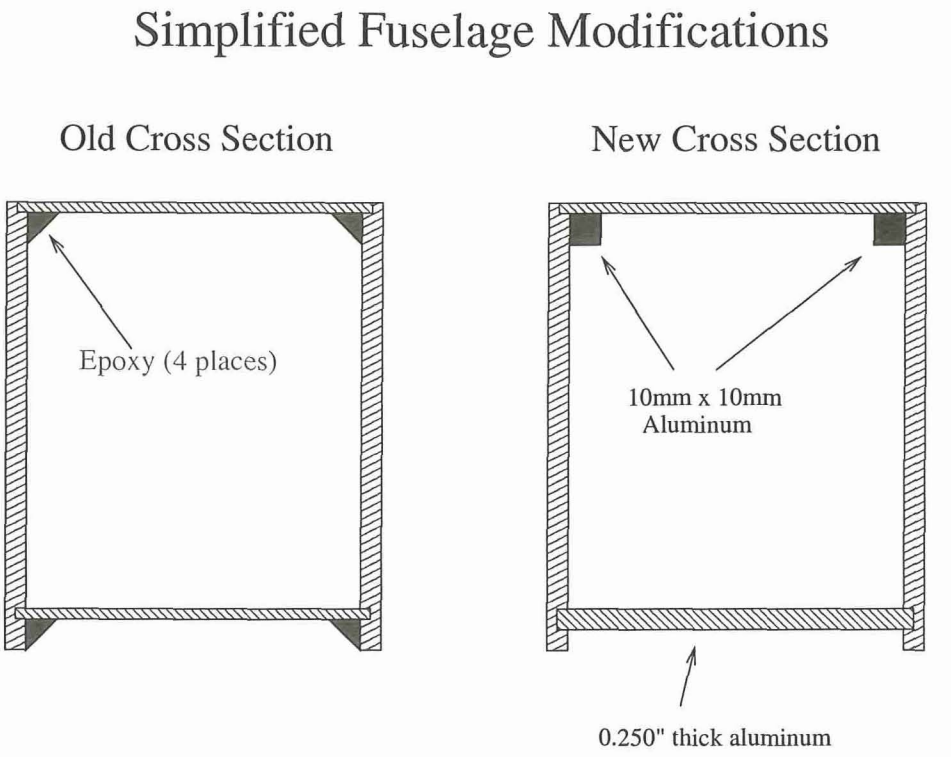

Figure 4.81: The original epoxied construction of the Simplified Fuselage was found to provide imperfect shielding. The new design includes 1 cm square aluminum bars in each of the upper corner to which the top and side panels can be screwed, and an increase in the thickness of the bottom panel to which the bottom edges of the side panels is screwed.

panels are screwed. The bottom panel was replaced with one having a thickness of 0.25 inches to which the bottom edges of the side panels is screwed. A photograph of one end of the modified fuselage in which the aluminum bars are visible is shown in Figure 4.82. The new bottom plate is seen in Figure 4.23. As seen in the photographs, the small screws are very close together. Over 900 screws and washers were used in the assembly of the fuselage. The nose and tail panels were taped in place as before, but using copper tape with conductive adhesive. These modifications were also implemented in the CAD model (neglecting the screw heads).

C. PED Measurements

A series of measurements was performed to explore the contribution of individual

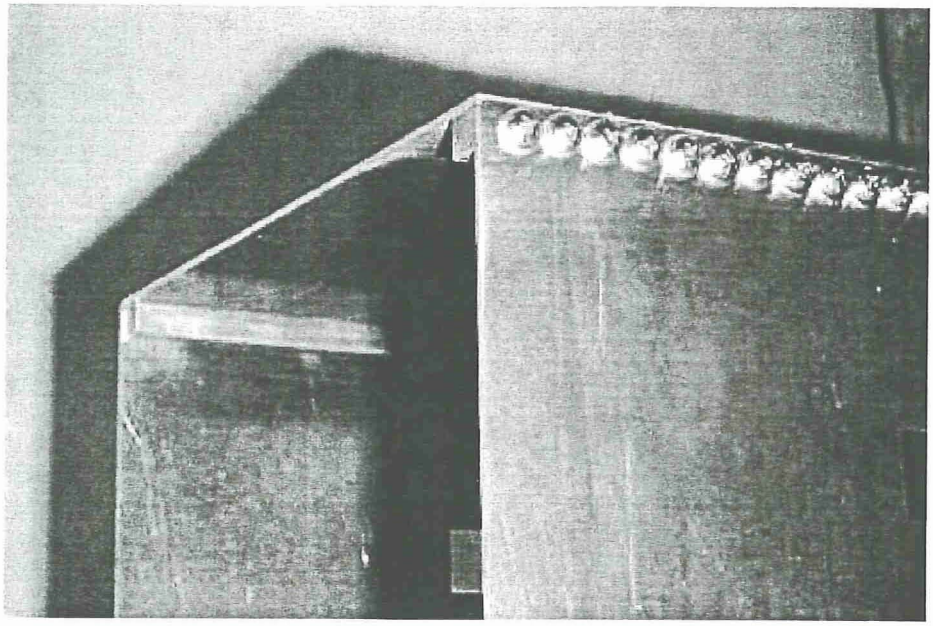

Figure 4.82: The top and side plates of the fuselage were screwed to two 1 cm square aluminum bars.

passenger windows to the coupling of fields from a simulated PED to an externally mounted antenna on the top of the fuselage, as well as the distribution of the coupled fields along the length of the fuselage.

To better describe this series of measurements, two photographs are shown in Figures 4.83 and 4.84. The PED measurement setup is shown in the photo of Figure 4.83. Notice that the cockpit window is sealed with a brass plate copper taped in place, and that all but one of the cabin windows are sealed with copper tape. Superimposed on the photograph are letter designations for each of the cabin windows. The window closest to the nose of the fuselage is denoted as "I", and the window closest to the tail is window "A." The external antenna is a 4 cm long monopole mounted on the 5 cm square by 1.5 cm high pedestal. The simulated PED is a 3 cm long vertical monopole on an aluminum pedestal (as before) located adjacent to window "C." The location of the PED is fixed, while the external antenna is moved from one position to the next along the top of the fuselage. Coupling measurements were obtained for ten external antenna locations, as indicated in Figure 4.84. For each external antenna location, S_{12} data was collected from 0.05 GHz to 20.0 GHz at 4001 frequencies. These measurements were repeated with all of the windows sealed with copper tape

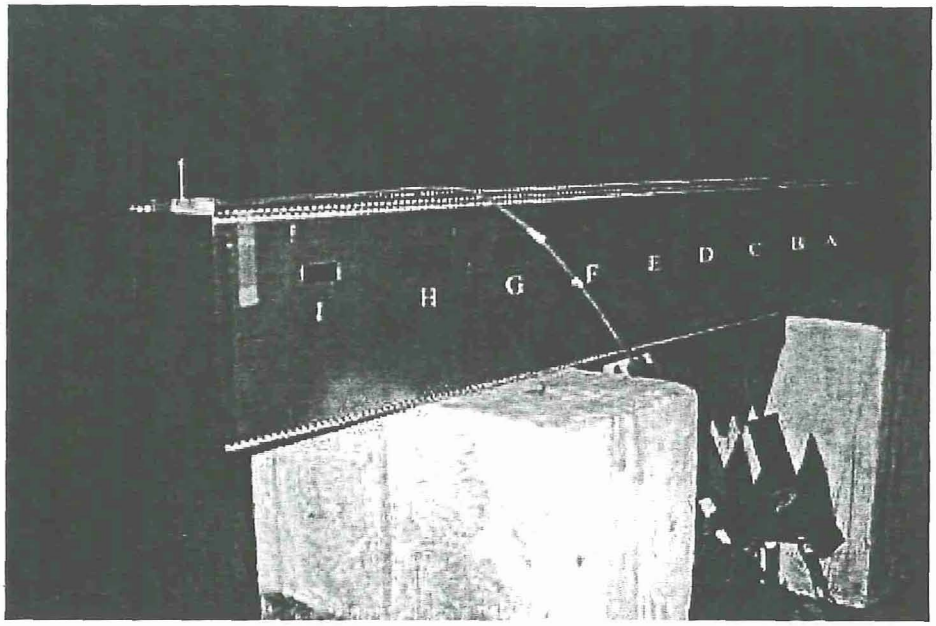

Figure 4.83: For this series of measurements, the cockpit and all but one cabin windows were sealed. The window that is open is denoted by a letter designation. In this photograph, window "I" is open.

except for individual selected cabin windows on the port side of the fuselage.

The results are formatted as color contour plots as a function of frequency and external antenna location. A typical plot is shown in Figure 4.85. Due to the extremely rapid variations in the coupling with frequency, the trends of the data are impossible to see. However, if the data is smoothed with respect to frequency by 5%, the amplitude contours are made clear, as in Figure 4.86. Consequently, the data in all of the following plots has been so smoothed.

To determine a baseline on the coupling, a measurement was made with all of the windows covered with copper tape. The results shown in Figure 4.87 verify that the shielding of the modified fuselage is very effective, with a maximum leakage of -65 dB from the fuselage end plates. Over the majority of the length of the fuselage, the "leakage floor" is below -80 dB.

The coupling from only windows "D", "F", and "I" being open are shown in Figures 4.88, 4.89, and 4.90, respectively. The location at which the maximum occurs is not surprisingly adjacent to the open window. More interesting is that the maximum

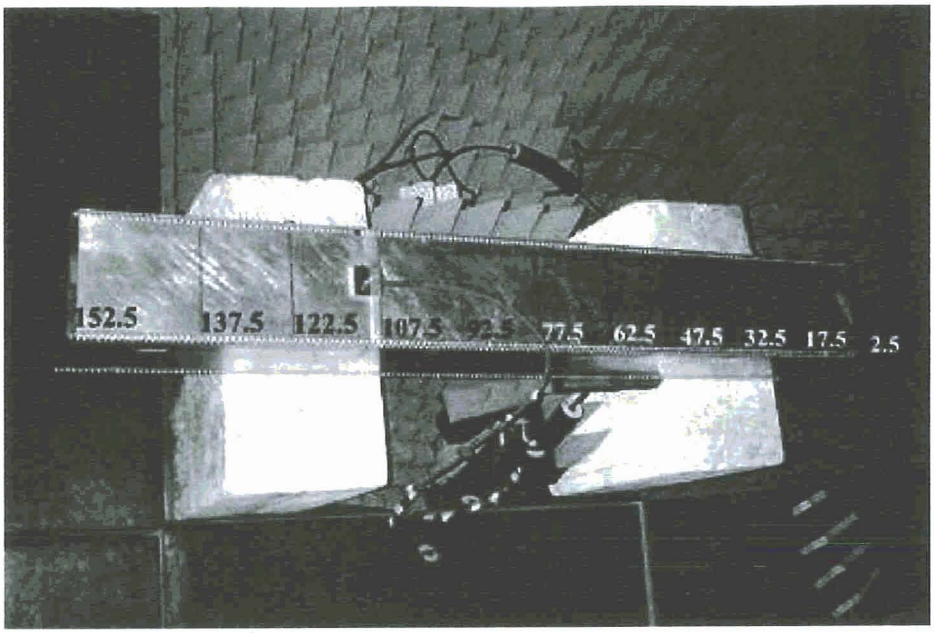

Figure 4.84: The S_{12} was collected for ten external antenna locations along the top of the fuselage, as shown.

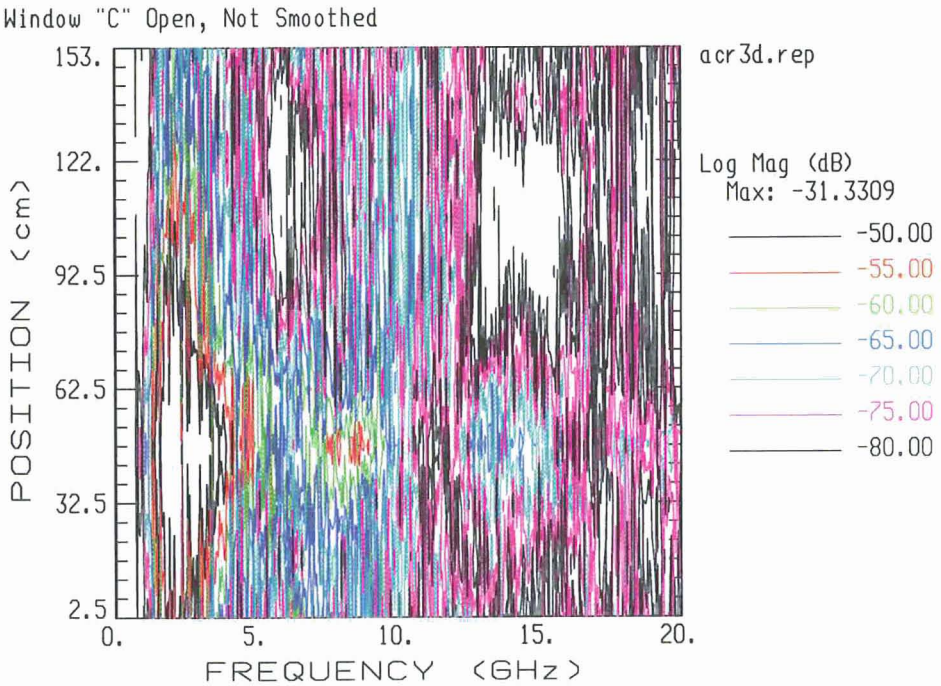

Figure 4.85: The raw S_{12} data plotted as a contour plot is very difficult to interpret due to the extremely rapid variations in magnitude with frequency.

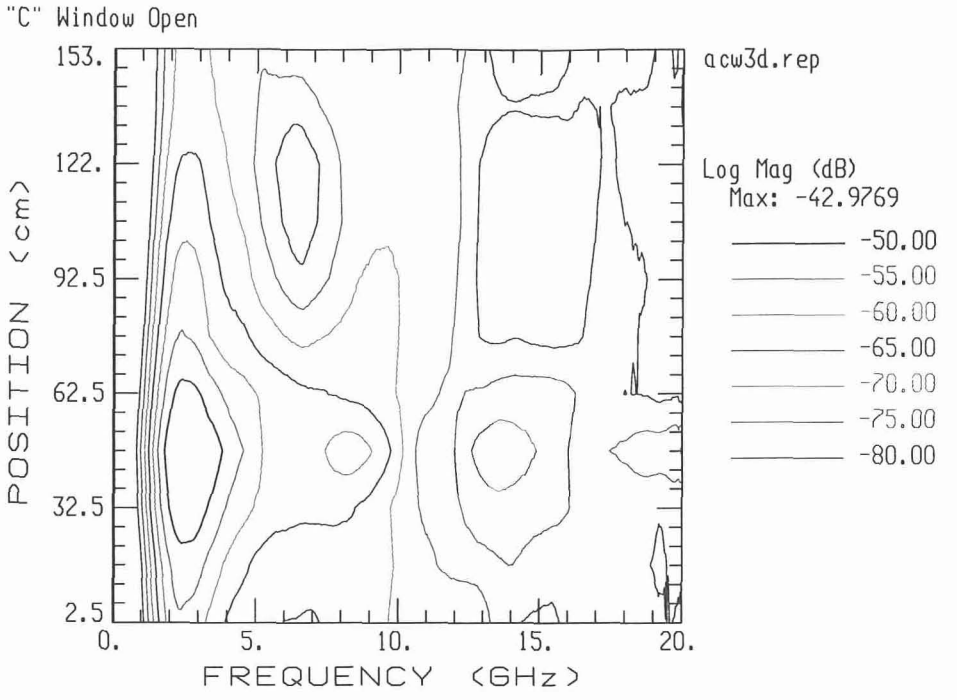

Figure 4.86: Smoothing the S_{12} with respect to frequency by 5% reveals the trends of the data.

values between these four cases differ by less than 6 dB.

If only the cockpit window is open, the maximum value of the coupling observed by the external antenna is 4.3 dB greater than that observed when only the window adjacent to the PED is opened, as seen in Figure 4.91.

Finally, screens of different mesh size are applied to the otherwise only open window "F." The screens are comprised of etched brass. The most coarse is shown in Figure 4.92. This screen has a mesh size of 3 mm which corresponds to a full-scale size of 2.36". The coupling through this screen is shown in Figure 4.93, and exhibits a reduction of 27.3 dB in the maximum coupling compared to the completely open window. A 2 mm screen (1.57" full-scale mesh size) was applied to window "F" next, as seen in Figure 4.94. The resulting coupling is plotted in Figure 4.95. With this screen the coupling was reduced by 33.3 dB. The final screen used had a mesh size of 0.75 mm (0.59" full-scale). A photograph of the installed screen is shown in Figure 4.96. The coupling through this screen is reduced to nearly the leakage level of the fuselage, as shown in Figure 4.97. These reductions are summarized graphically in the plot of coupling versus frequency at the external antenna location adjacent to

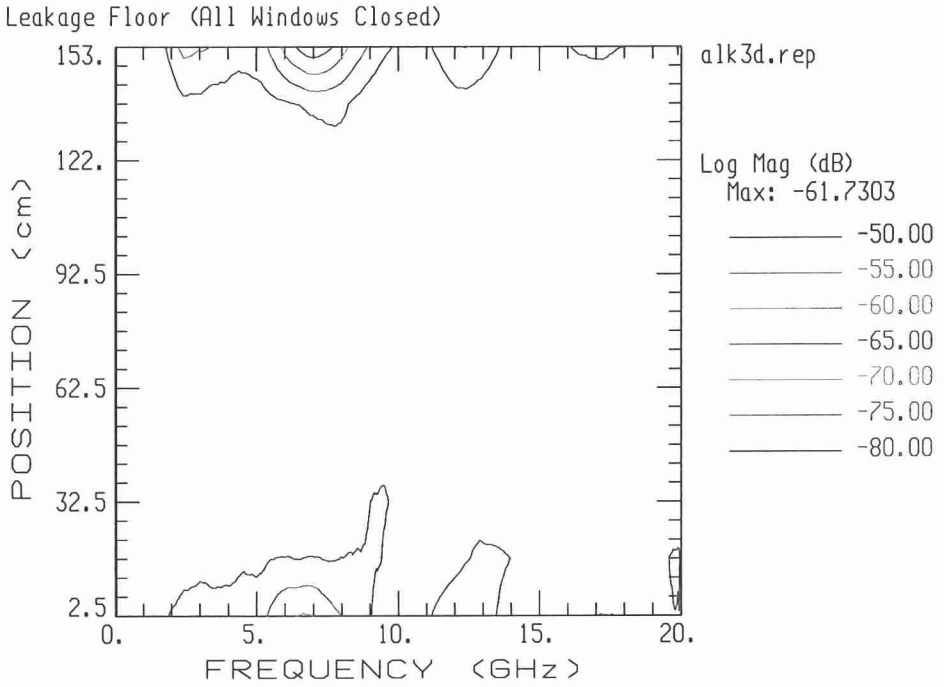

Figure 4.87: With all of the windows covered with copper tape, the "leakage floor" measurement shows that the modified fuselage is well shielded. There is some residual leakage at the taped-on fuselage end plates, but the leakage along most of the top of the fuselage is below -80 dB.

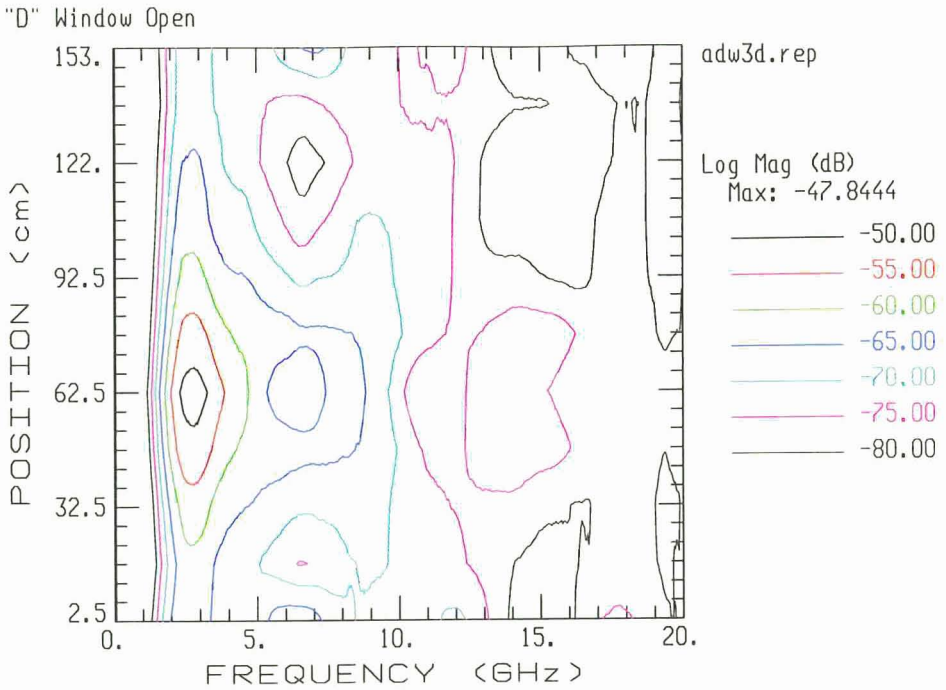

Figure 4.88: The S_{12} between the simulated PED and the external antenna when only window "D" is open.

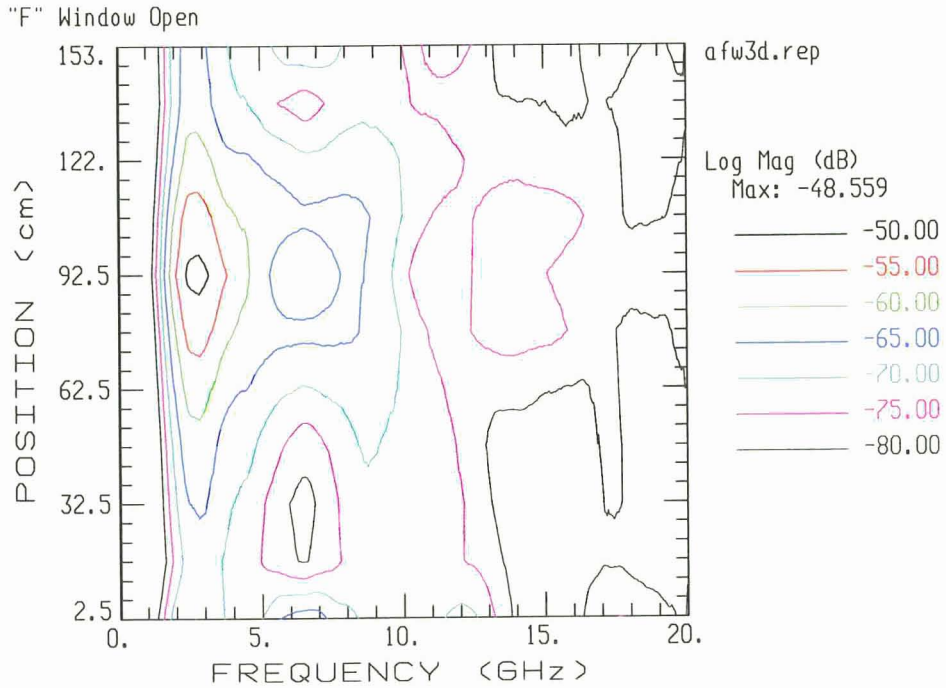

Figure 4.89: The S_{12} between the simulated PED and the external antenna when only window "F" is open.

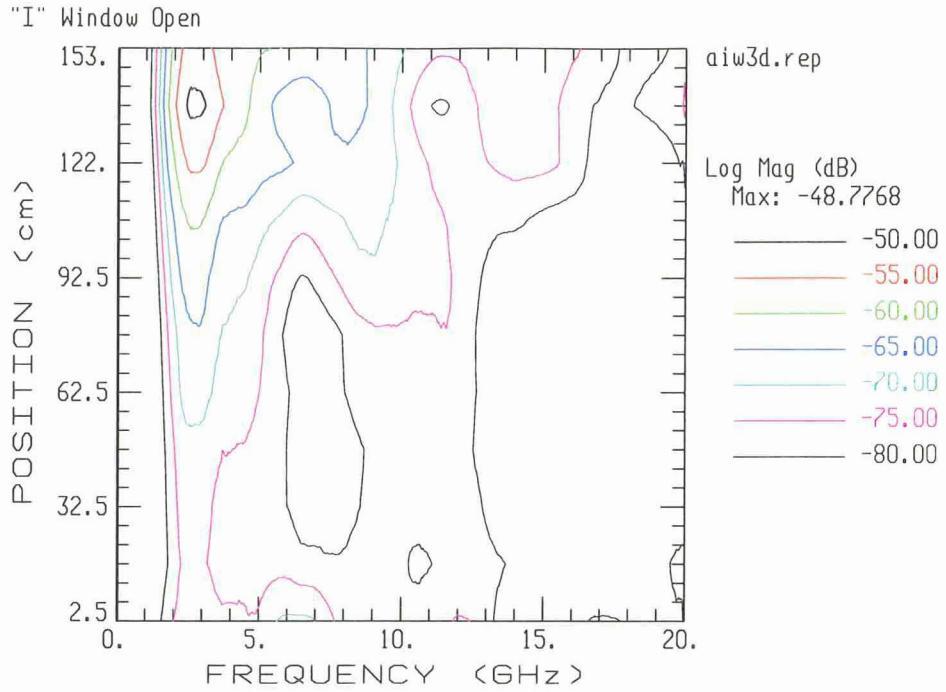

Figure 4.90: The S_{12} between the simulated PED and the external antenna when only window "I" is open.

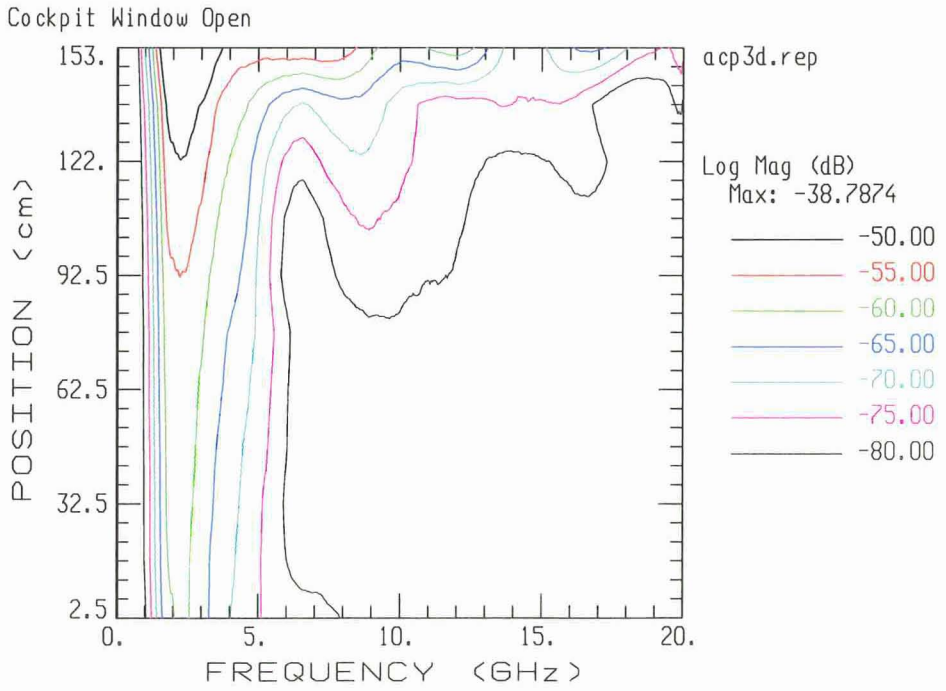

Figure 4.91: The S_{12} between the simulated PED and the external antenna when only the cockpit window is open.

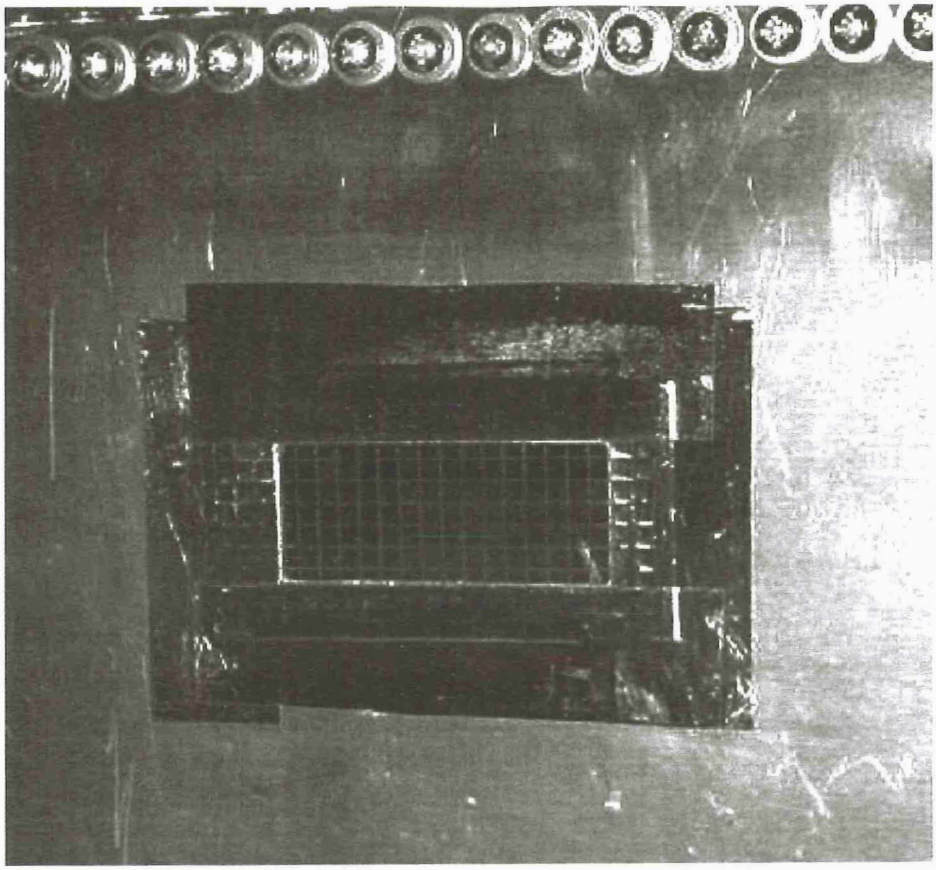

Figure 4.92: A close-up photograph of a brass screen with a mesh size of 3 mm (2.36" full-scale) applied to window "F."

window "F" shown in Figure 4.98.

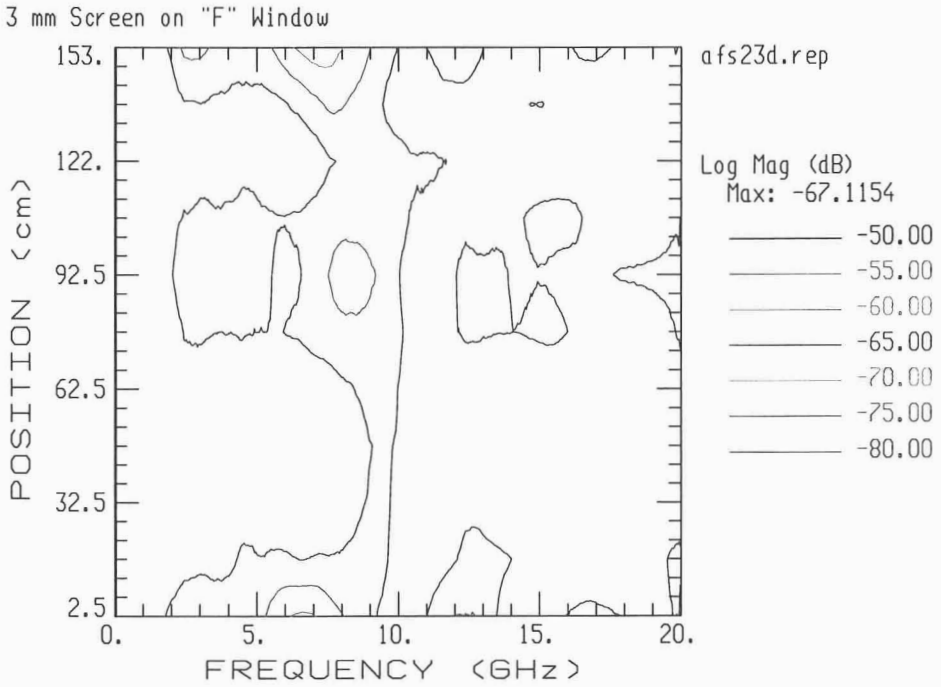

Figure 4.93: The S_{12} between the simulated PED and the external antenna when window "F" is screened with a 3 mm brass mesh, and all other windows are sealed. The maximum coupling is reduced 27.3 dB compared to the case of window "F" open.

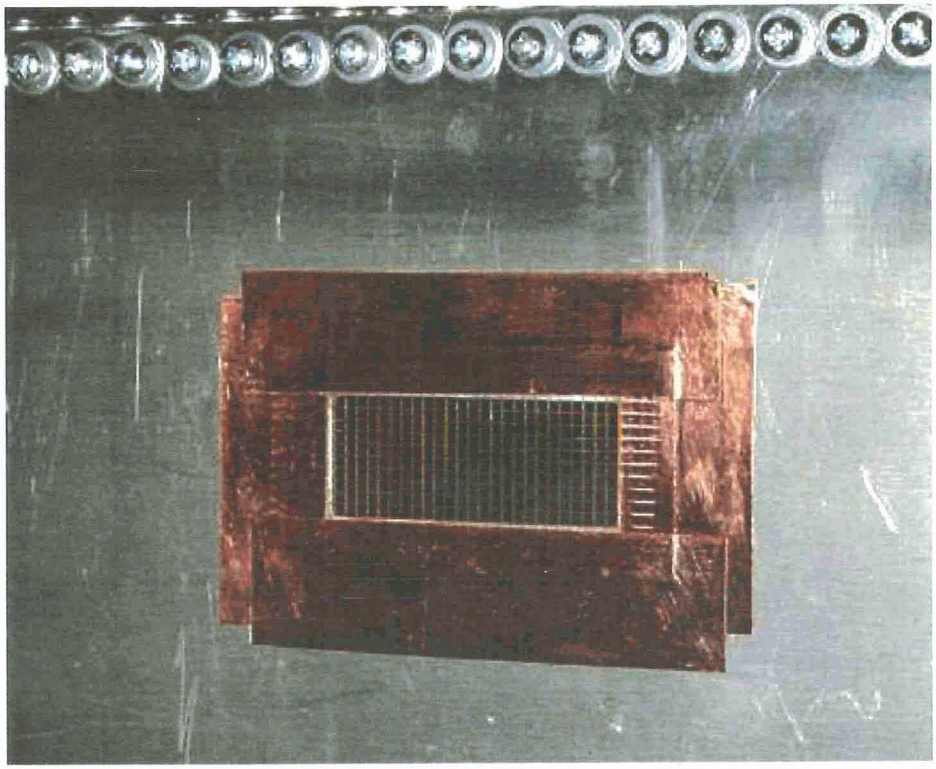

Figure 4.94: A close-up photograph of a brass screen with a mesh size of 2 mm (1.57" full-scale) applied to window "F."

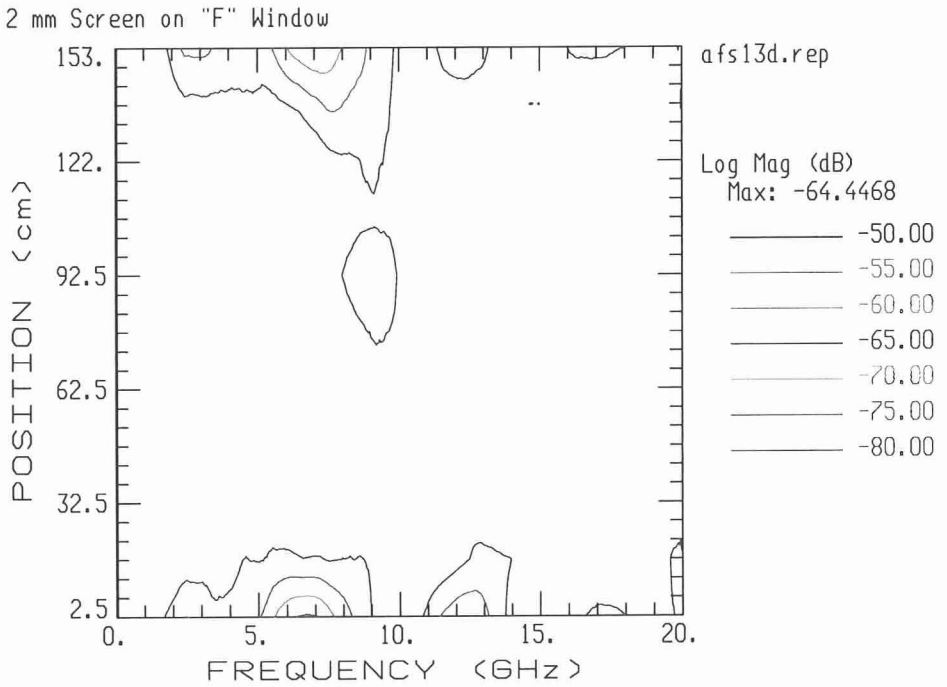

Figure 4.95: The S_{12} between the simulated PED and the external antenna when window "F" is screened with a 2 mm brass mesh, and all other windows are sealed. The maximum coupling is reduced 33.3 dB compared to the case of window "F" open.

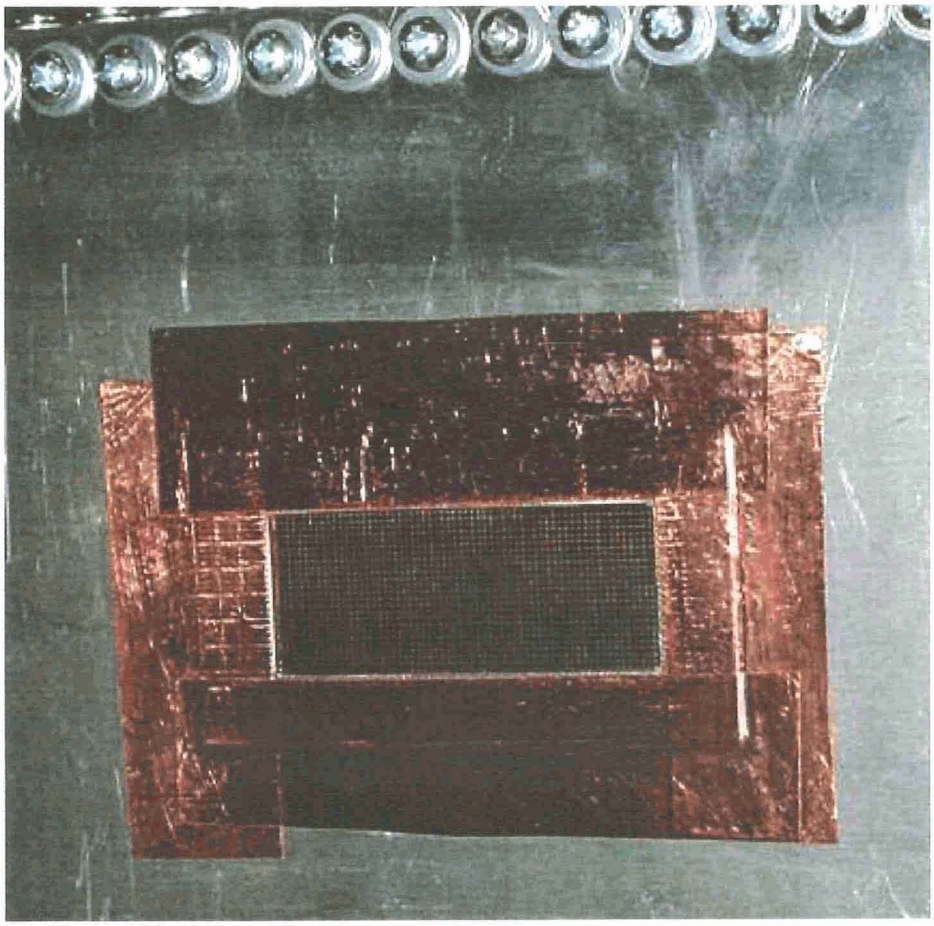

Figure 4.96: A close-up photograph of a brass screen with a mesh size of 0.75 mm (0.59" full-scale) applied to window "F."

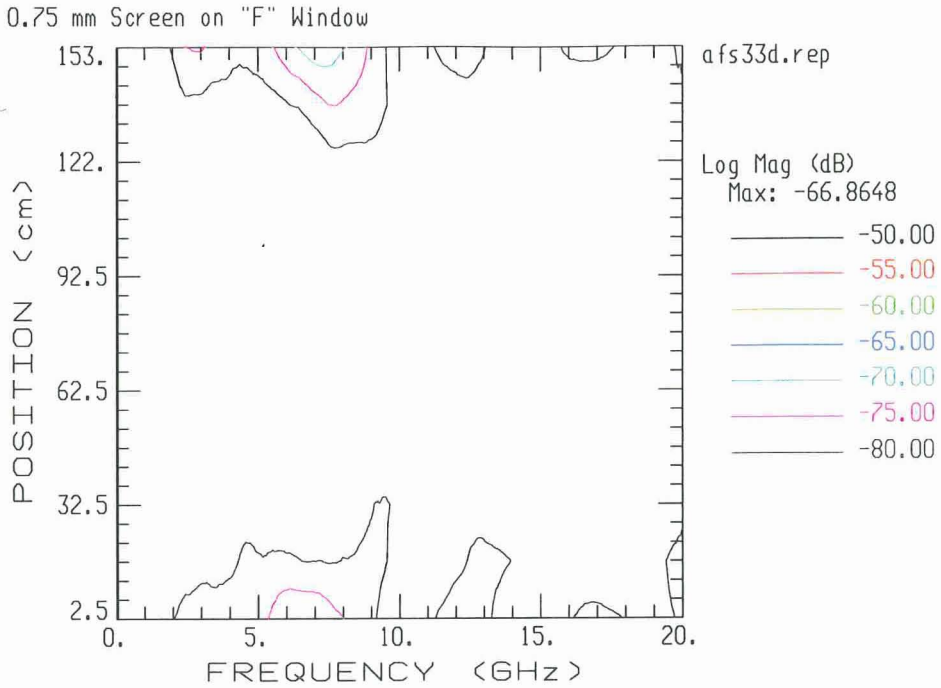

Figure 4.97: The S_{12} between the simulated PED and the external antenna when window "F" is screened with a 0.75 mm brass mesh, and all other windows are sealed. The maximum coupling is reduced 36.2 dB compared to the case of window "F" open.

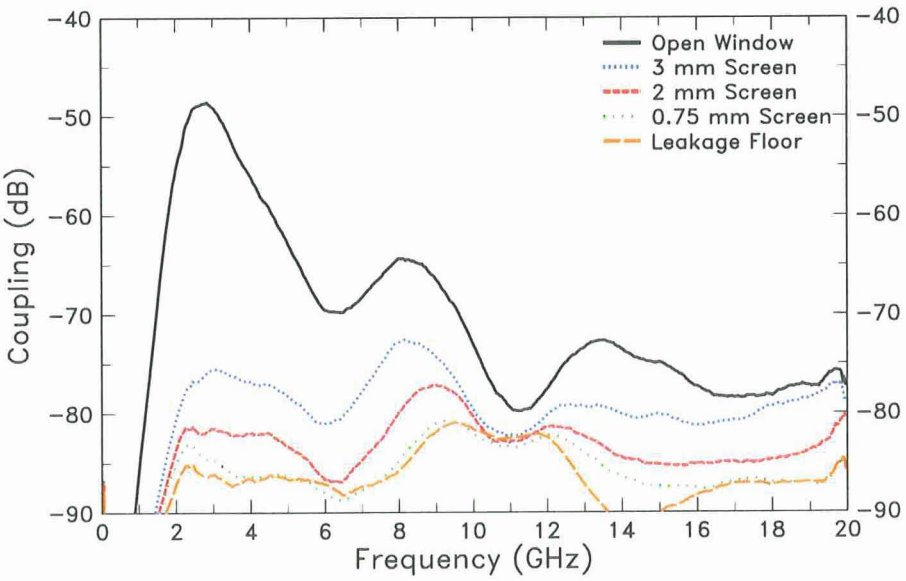

Figure 4.98: The coupling observed when external antenna is located at the same station as window "F" as a function of frequency for the three applied screens.

Chapter 5

Measured Shielding Effectiveness of the Cylindrical Fuselage Model

In addition to the rectangular simplified fuselage model, a cylindrical scale model fuselage was constructed, and a series of measurements have been performed. The cylindrical model was built to better simulate the fuselage part of an aircraft. The shielding effectiveness (SE) of the cylindrical fuselage is compared with that of the rectangular cross-section "Simplified Fuselage," and penetration reduction effected via aperture screening is explored.

It was found that the shielding effectiveness of the cylindrical fuselage varies in the deterministic sense from that of the Simplified Fuselage, but is extremely similar in a quasi-statistical sense.

The application of screens to the apertures reduces the penetration of the fields into the cylindrical fuselage by a considerable amount. The SE of the cylindrical fuselage was measured for various screen configurations. While some configurations produced results that appear to be anomalous relative to other configurations, the trends were repeatable.

I. The Cylindrical Fuselage

To permit meaningful comparisons with the Simplified Fuselage, the cylindrical fuselage was designed to have the same length and volume as that previous model. To achieve this specific volume, an inside diameter of 24.7 cm is required. A metal

cylinder of the necessary diameter was not available "off the shelf." Instead, a custom fabrication shop was employed to butt weld the edges of a sheet of 0.06" thick aluminum to create a tube having the appropriate circular cross-section. This raw cylinder is shown in Figure 5.1.

The same size and number of cabin windows were cut into the sides of the cylinder, at approximately the same locations as for the Simplified Fuselage. A photograph showing the nine, 2 cm by 5 cm windows is seen in Figure 5.2. The cabin windows approximate the same aperture area per fuselage length as those of a Boeing 757 (1:20 scale).

Flanged aluminum caps were machined to fit into each end of the cylinder (Figure 5.3). In one of the end caps, an 8 cm x 18 cm "cockpit" window was cut. The end caps not only finish the enclosure but also help to support its circular cross section. During measurements, copper tape is applied at the interfaces between the cylinder and end caps.

The physical realization of the cylindrical fuselage deviates somewhat from its design. The cylinder is not perfectly circular in cross section due to deformations that are nearly inherent to the welding process. It is very nearly circular, but with some deviation in the immediate vicinity of the weld, which is located on the starboard side. The weld protrudes from the surrounding surface of the metal, both inside and out. No attempt was made to blend the weld on the inside of the cylinder, but it was ground down on the outside to be nearly flush with the surface. Unfortunately, some errors were made by the ASU metal shop in cutting the cabin windows. In particular, one of the windows is located nearly 1 cm from its intended station. Finally, the end caps are much thicker than desired. They are as thin as practical according to the opinion of the machinist. There is one flaw in the design. The waterline of the cabin windows are only a few centimeters above the vertical center of the fuselage, as compared to 5 cm in the case of the Simplified Fuselage. However, since the cabin windows would be more on top of the cylindrical fuselage than on the sides if they were located any higher, the design flaw is more correctly attributed to the Simplified Fuselage's cabin windows being too high.

For the initial measurements, a 6 cm long wire probe was installed in the bottom of the fuselage, 50 cm from the nose. The probe consists of the non-captured center

Figure 5.1: The cylindrical fuselage began as a sheet of aluminum that was custom welded into a tube.

conductor of an sma flange connector, with a piece of 0.045″ diameter brass wire soldered to it. The body of the connector is silver epoxied to the outside surface of the fuselage. This probe configuration conforms to that used in the shielding effectiveness measurements of the Simplified Fuselage.

II. Shielding Effectiveness Measurements

The methodology of the shielding effectiveness measurements is nearly identical to those previously performed, but is described here for completeness.

The conventional definition of shielding effectiveness is the ratio of the electric field strength at a point in free space under plane wave illumination, to the electric field strength at that same point in space when surrounded by an enclosure under test and while subjected to the same illumination. For low levels of field penetration into the enclosure, the shielding effectiveness is high. For non-spherically symmetrical enclosures, the shielding effectiveness is a function of incidence angle of the illuminating

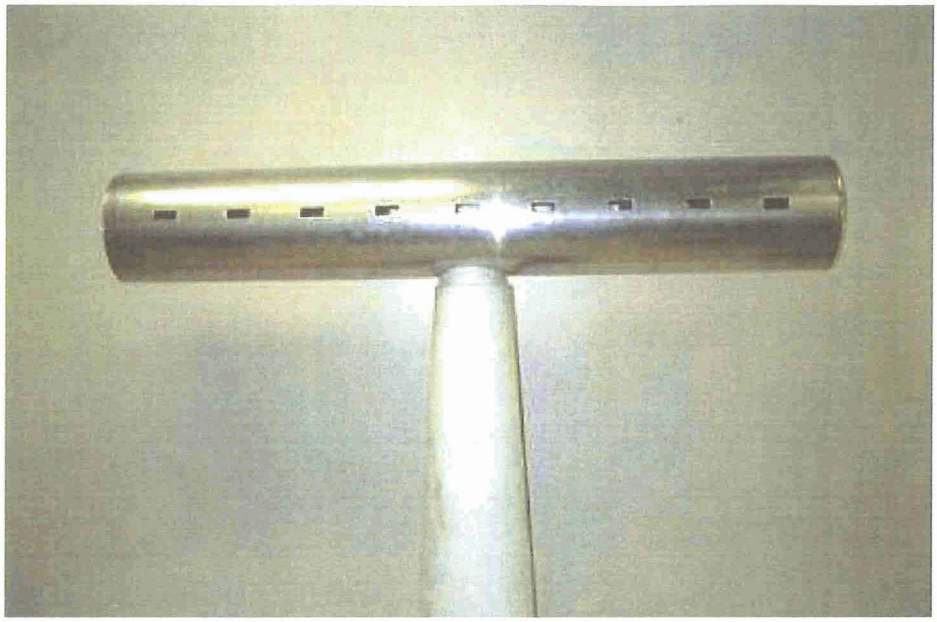

Figure 5.2: The cabin windows were designed to be the same number and configuration as those in the Simplified Fuselage. However, some discrepancies occurred in the physical realization.

Figure 5.3: Aluminum caps were machined to fit within the ends of the cylinder. The nose end cap features the same 8 cm by 18 cm "cockpit window" as the Simplified Fuselage.

plane wave, and of the location of the observation point relative to the enclosure.

The above definition is realizable in the computation realm, but not in the physical world. Some sort of probe with which to measure the electric fields is required. The presence, frequency response, and radiation pattern of the probe can have a profound impact on the resulting shielding effectiveness. Therefore, while the use of a probe in the measurements is unavoidable, all of the particulars of the probes used must be disclosed. At the ElectroMagnetic Anechoic Chamber (EMAC) facility, the probe used for the "free space fields" part of the shielding effectiveness has become standardized as a 6 cm long monopole mounted on a 20 cm square ground plane. The monopole is oriented parallel to the incident E field (usually vertical), with the edges of the ground plane orthogonal to the propagation vector. The radiation pattern of this monopole on a ground plane has relative nulls in this direction at approximately 0.9, 4.5, and 9.5 GHz, resulting in pronounced dips in the shielding effectiveness at these frequencies. Thus the measured shielding effectiveness is not particularly useful in the absolute sense of the conventional definition, but is suitable for our purposes of relative comparison and verification of numerical predictions (provided that the predictions conform to the measurements in the use of the monopole as a reference).

Similarly, a probe must be employed within the enclosure with which to measure the penetrating fields. It is understood that the probe will perturb those fields. Furthermore, the necessity of a ground plane and cable imposes limitations on the placement of the probe. It is generally convenient to use a monopole for the interior probe as well.

Finally, the shielding effectiveness is redefined to accommodate the necessities of the measurements as the ratio of the frequency response of the monopole on the square ground plane to the frequency response of the probe located within the enclosure.

A. Measurements

The measurements were performed in ASU's anechoic chamber in a direct illumination configuration. The cylindrical fuselage was placed on expanded polystyrene supports near one end of the chamber, and an auxiliary antenna was placed approximately 5.8 m from the model and at the same height above the floor as the model, also supported

with expanded polystyrene. This separation distance satisfies the far-field criterion for a 25 cm diameter target up to 14 GHz. A 1.2 m square baffle comprised of carbon-loaded foam microwave absorber was placed behind the auxiliary antenna, between it and the compact range reflector to reduce its illumination by the back lobes of the antenna. The auxiliary antenna was oriented so that its boresight was in the direction of the center of the model, and the model was oriented so that the incident fields from the auxiliary antenna were normally incident on the model's "cockpit window."

For these nose incident measurements, the separation distance between the model and the auxiliary antenna is minimized so as to maximize the directly incident field strength relative to any stray energy scattered from the room. It is important that the ratio of desired to undesired signal strength be maximized because time-domain filtering techniques (gating) cannot be used to remove the unwanted signals on this type of a structure. Due to the long ring-down time of this resonant cavity, its response is appreciably extended in the time domain. If a time-domain gate is used that is small enough to reject the stray signals scattered from the room, then part of the time-domain response of the model will also be rejected, thus distorting its frequency-domain response. For near oblique (to the length of the fuselage) incident angles, near-field to far-field techniques would be required.

The HP8510 network analyzer can acquire 801 frequency points per measurement. This resolution is insufficient to accurately sample the rapid variations in the frequency response of the model that occur between 400 MHz and 13 GHz. Therefore, the measurements were performed in 1 GHz bands of 801 frequency points. Four antennas were needed to cover this frequency range: one from 400 MHz to 4 GHz, another from 4 to 6 GHz, one to cover 6 to 8 GHz and a final horn to provide 8 to 13 GHz coverage. The microwave source was operated in synthesizer mode at an output power of +10 dBm. An IF averaging factor of 4096 was used.

B. Results

The first measurement, shown in Figure 5.4, is the shielding effectiveness of the cylindrical fuselage as a function of frequency, from 0.4 to 13 GHz, compared to that of the Simplified Fuselage. The SE of the cylindrical fuselage exhibits the same extremely

rapid variations with frequency that were seen with the Simplified Fuselage. Detailed comparison is impossible on this scale. To better see the typical differences between the SE of the two models, the scale is expanded in Figure 5.5 to 0.5 to 1.5 GHz. It is not terribly surprising that there are no correlations in the peaks and nulls between the SEs of the two models. However, if the SE is smoothed by 3% with respect to frequency, the SE of the cylindrical fuselage agrees well in this averaged sense to that of the Simplified Fuselage (Figure 5.6). One difference between the two is the cutoff frequency of the cylindrical model is lower than that of the Simplified Fuselage. Another difference evident in Figure 5.6 is the depth of the relative nulls. The depth of the nulls is related to the overall shape of the shielding effectiveness which is dominated by the frequency response of the reference monopole. These relative nulls are deeper in the SE of the Simplified Fuselage. The differences are small, but it is somewhat interesting to explain them by relating the differences in technique used in measuring the frequency response of the monopole. The uninitiated might assume that, because it is a simple target, the monopole would be easy to accurately measure. This is not true. Because the monopole accepts energy almost equally from nearly all directions, it is particularly susceptible to error from fields scattered by the surrounding environment. Furthermore, it seems to couple to nearby objects. In fact, it is rather difficult to accurately measure the frequency response of the monopole, particularly at low frequencies. A great deal of time was expended in making the monopole measurements for the case of the Simplified Fuselage. In those measurements, no time-domain gating was used. Instead, considerable experimentation was made in the placement of the monopole and the auxiliary antenna relative to one another and relative to the anechoic chamber to control and minimize the environmental scattering. Also, the microwave absorber configuration was explored extensively, to the extent of borrowing some ferrite tiles with which to line the floor immediately beneath the monopole (where the most severe problems were found to reside). In contrast, a different approach was used when measuring the monopole for the cylindrical fuselage case. The decision was made to use time-domain gating in this case. However, time-domain gating, when the filter is narrow, has the effect of distorting the resulting frequency response. In particular, the ends of each frequency band are often significantly distorted. To work around the band edge distortion, twice as many

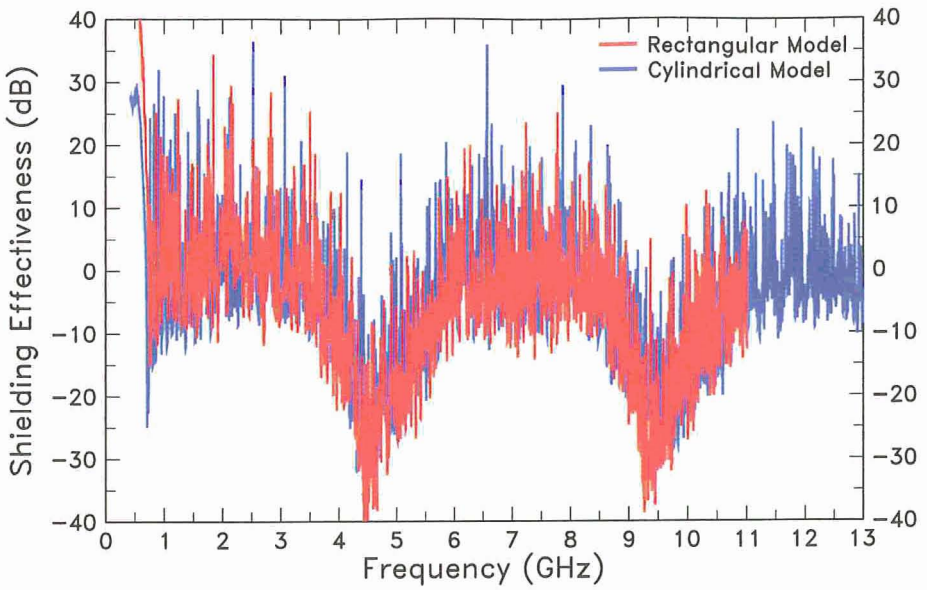

Figure 5.4: The shielding effectiveness (relative to a monopole) of the cylindrical fuselage (blue) compared to that of the Simplified Fuselage (red), at nose incidence and observed at a point 50 cm from the nose.

overlapping frequency bands were measured of the monopole. For example: 1.0 - 2.0 GHz, 1.5 - 2.5 GHz, 2.0 - 3.0 GHz, 2.5 - 3.5 GHz, and so on. After applying the time-domain gate, the central parts of each of the overlapping frequency bands were assembled into a complete frequency response, and the individual band edges were discarded. The net effects can be seen in Figure 5.6: the (smoothed) SE of the cylindrical fuselage is smoother that that of the Simplified Fuselage, does not extend quite as low in frequency, and the relative nulls are slightly filled or raised in amplitude (another result of the narrow time-domain gate used).

III. Shielding Effectiveness Improvement

Can the shielding effectiveness of an aircraft fuselage be improved? To explore that question, a number of measurements were performed with various treatments on the apertures. In the first of this series of measurements, the cockpit window was sealed with a brass plate copper taped to the nose of the fuselage, as seen in Figure 5.7. The resulting shielding effectiveness is compared to that without aperture treatment in Figure 5.8. From this point on, all of the shielding effectiveness plots are smoothed

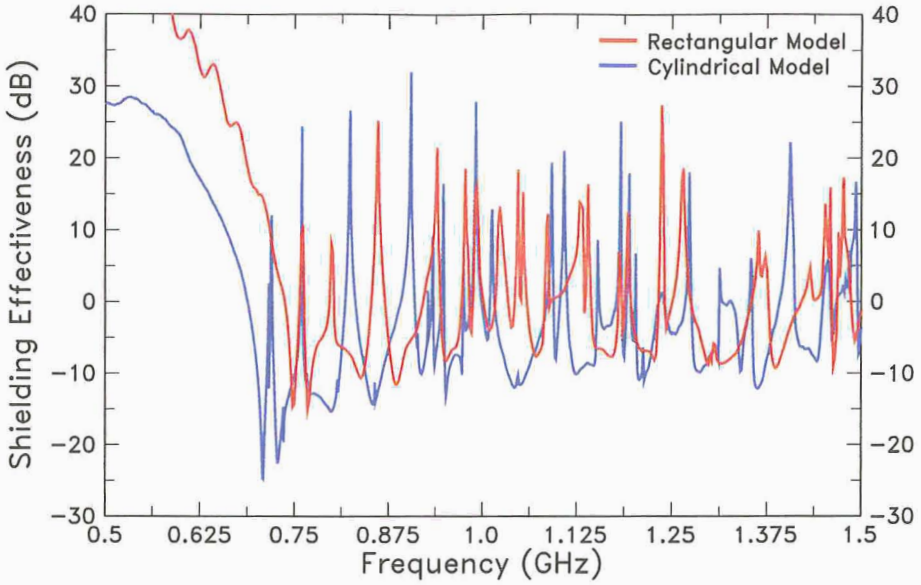

Figure 5.5: A detailed view of the comparison between the cylindrical fuselage and the Simplified Fuselage shielding effectiveness between 0.5 GHz and 1.5 GHz. No correlation in the peaks and nulls are observed.

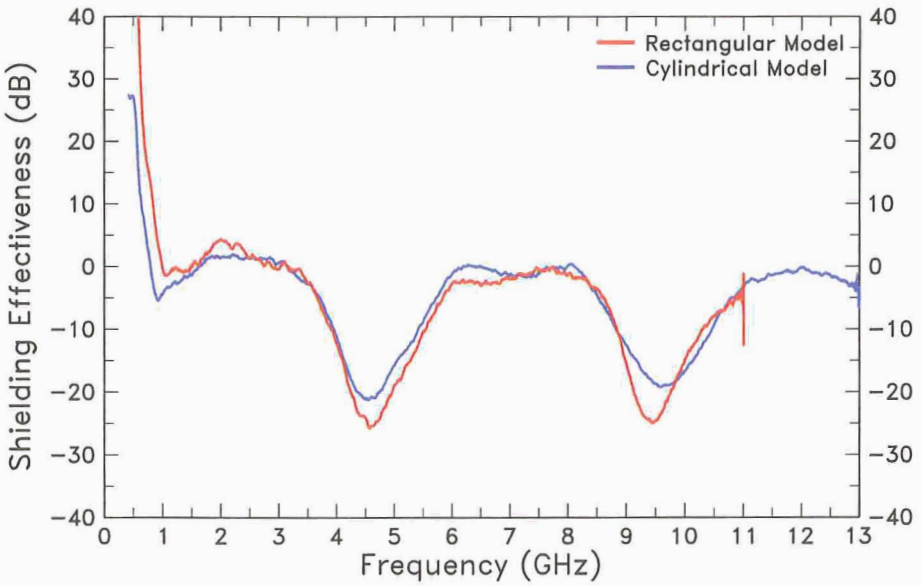

Figure 5.6: With the shielding effectiveness smoothed by 3% (with respect to frequency), it is more evident that the SE of the cylindrical fuselage is nearly identical to that of the Simplified Fuselage in this averaged, quasi-statistical sense.

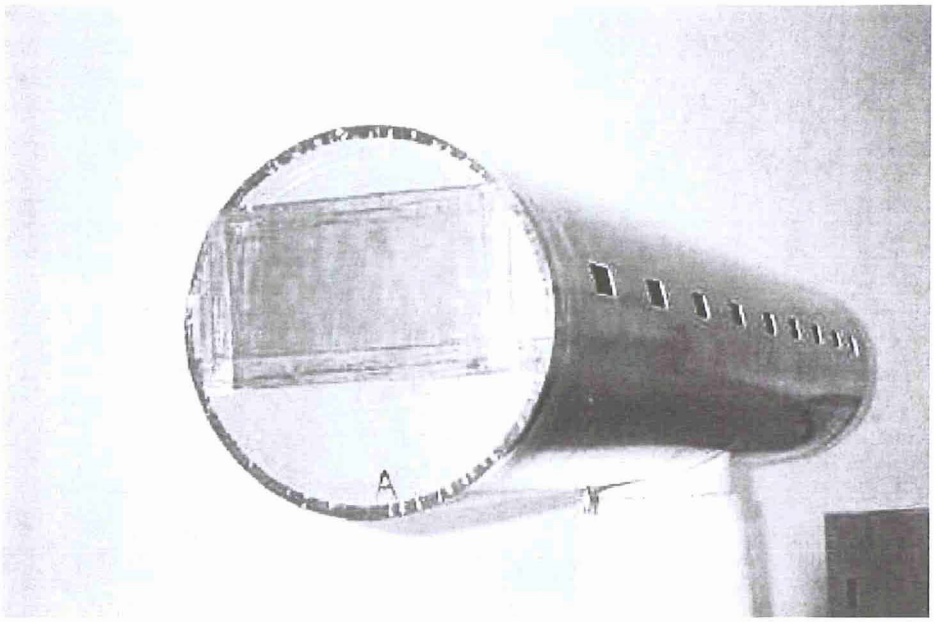

Figure 5.7: Shielding effectiveness measurements were made with the cockpit window sealed with a brass plate and copper tape to observe the relative penetration through this aperture, and as a comparison for when the cockpit window is covered with a wire screen.

by 3% to facilitate the comparisons. The improvement in SE effected by sealing the cockpit window is pronounced: an increase of approximately 20 dB. We will see that the majority of the energy penetrates through the cockpit window. This appears to be a statement of the obvious, since all of the cases in this study are at nose incidence. However, it was found in previous studies of Portable Electronic Devices (PEDs) that the large cockpit window provides the dominant penetration mechanism. When an external antenna and simulated PED were located at a station near the rear of the fuselage, adjacent to one of the cabin windows, the penetration through the cockpit window was found to be much larger than that through the cabin window.

It has been known for many decades that a mesh or screen having wire spacing that is small relative to the wavelength is a very good approximation to a solid sheet of conductor. Let us now replace the brass plate with an aluminum wire screen, as seen in Figure 5.9. This is standard home window screening which has a center-to-center wire spacing of approximately 1.94 mm. Repeating the measurements results in the shielding effectives curves of Figure 5.10. Indeed, the screen is only slightly

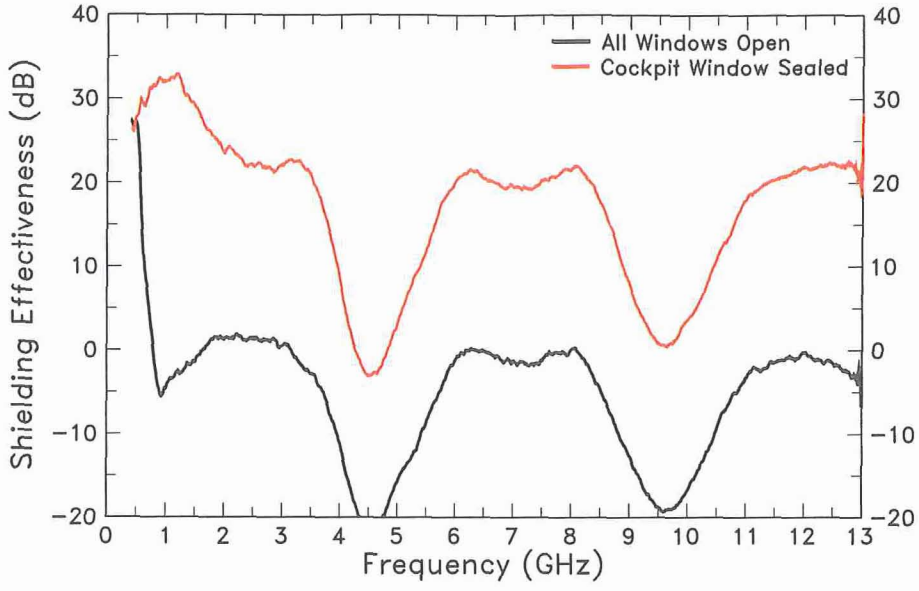

Figure 5.8: The shielding effectiveness increased by approximately 20 dB by sealing the cockpit window.

less effective than the brass plate at reducing the penetration of the fields into the fuselage.

Well, the penetration should be reduced to nearly nothing if all of the apertures are screened... right? A photograph of the cylindrical fuselage with all of the windows screened is shown in Figure 5.11. A screened cabin window is seen close up in Figure 5.12. Again, the shielding effectiveness was measured at nose incidence. While the penetration was reduced at frequencies below about 4 GHz, the penetration *increased* for frequencies above 4.5 GHz, as seen in Figure 5.13.

It is not clear why the penetration increased when the cabin windows were screened. However, when the cockpit window is sealed while the cabin windows are screened (Figure 5.14), the shielding effectiveness is higher (except above 11.5 GHz) than when the cockpit window is sealed and the cabin windows are open, as expected (Figure 5.15).

Perhaps the distribution of the residual energy that has penetrated through the cockpit screen is altered by the cabin window screens to be higher at the observation point than when the cabin windows are open. To test this theory, the window treatment series of measurements were repeated for an observation point 1.25 m from the

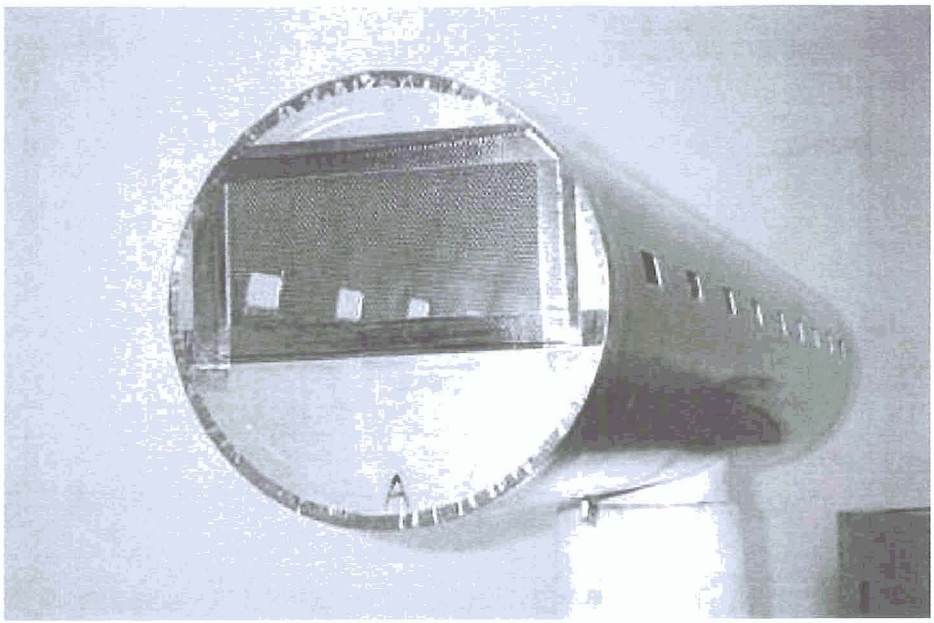

Figure 5.9: Replacing the brass with an aluminum wire screen should still be effective at reducing the penetration into the fuselage, if the screen wire spacing is small relative to the wavelength.

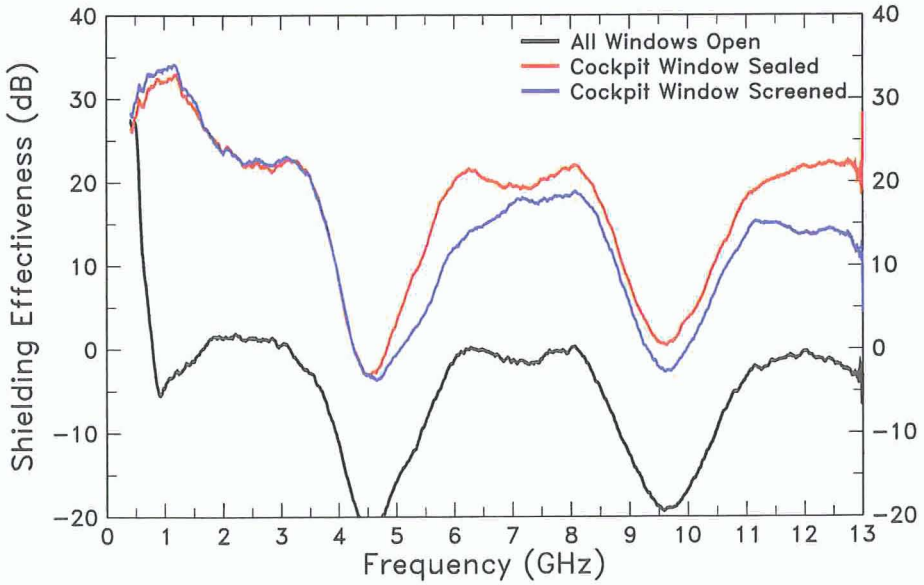

Figure 5.10: As the frequency goes up, the shielding effectiveness of the wire screen decreases, but it is just as effective as the brass plate below 4.5 GHz.

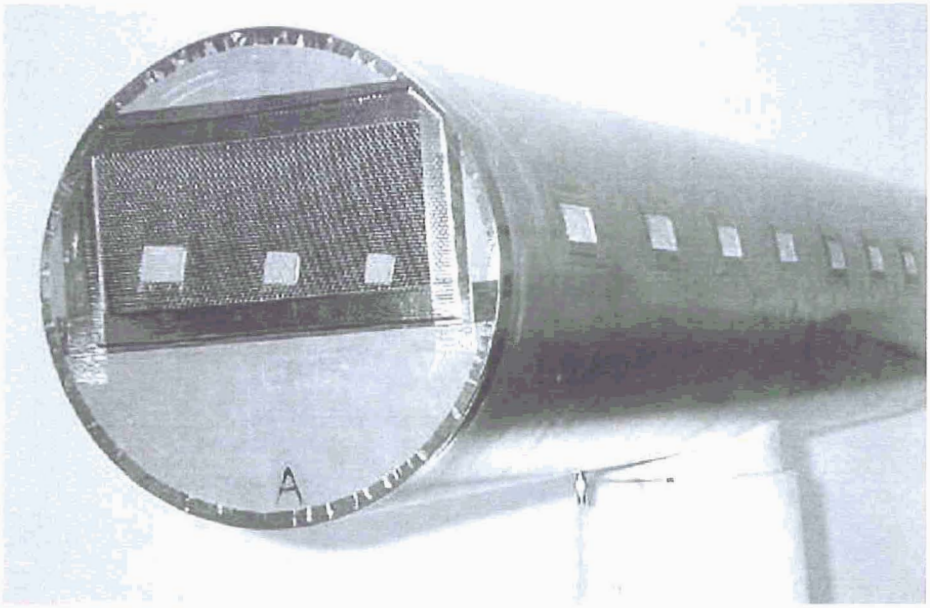

Figure 5.11: Adding the wire screens to the cabin windows should reduce the penetration into the fuselage still further.

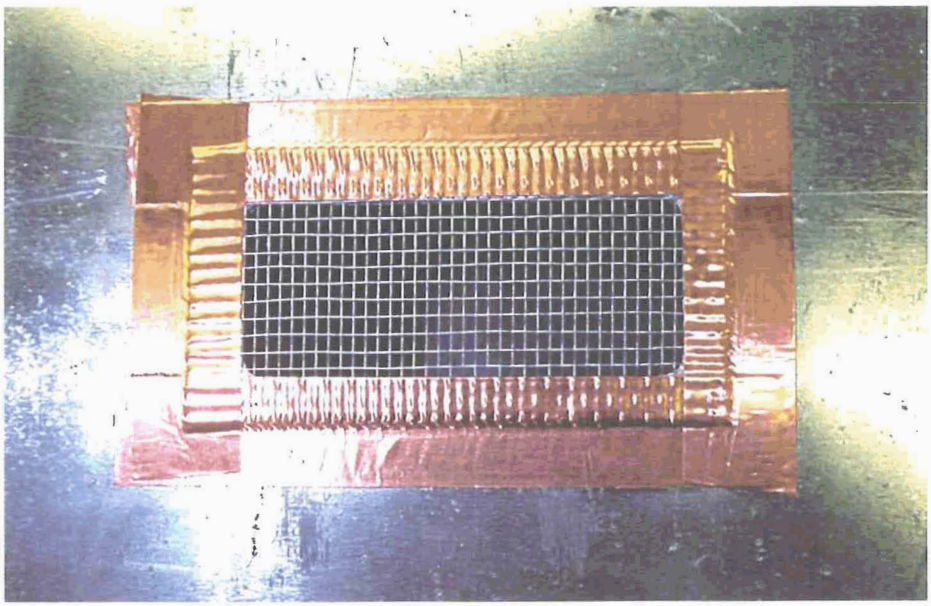

Figure 5.12: A close-up view of the screen applied to the cabin windows.

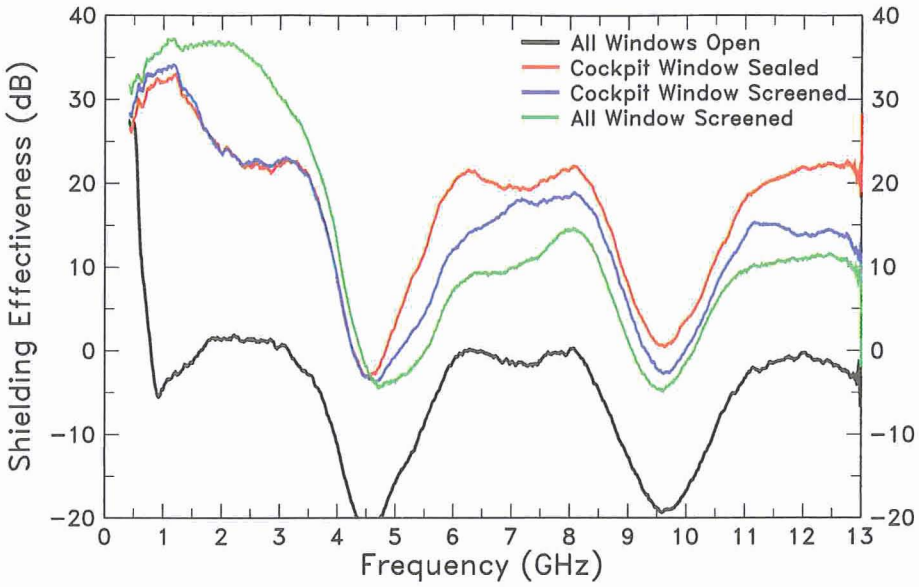

Figure 5.13: But curiously, at frequencies above 4.5 GHz, the shielding effectiveness actually decreases.

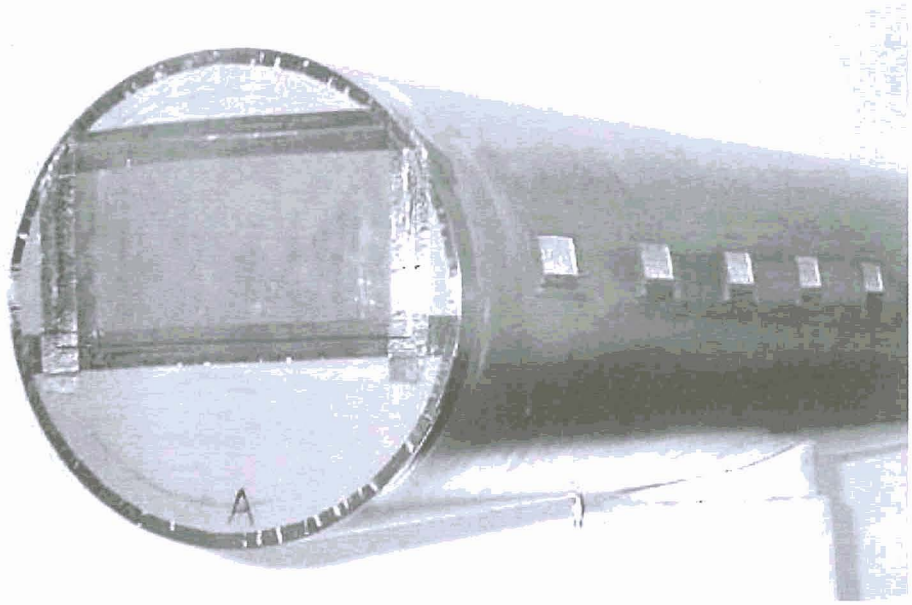

Figure 5.14: The cockpit window screen was replaced with the brass plate, in an attempt to better understand this seemingly anomalous behavior.

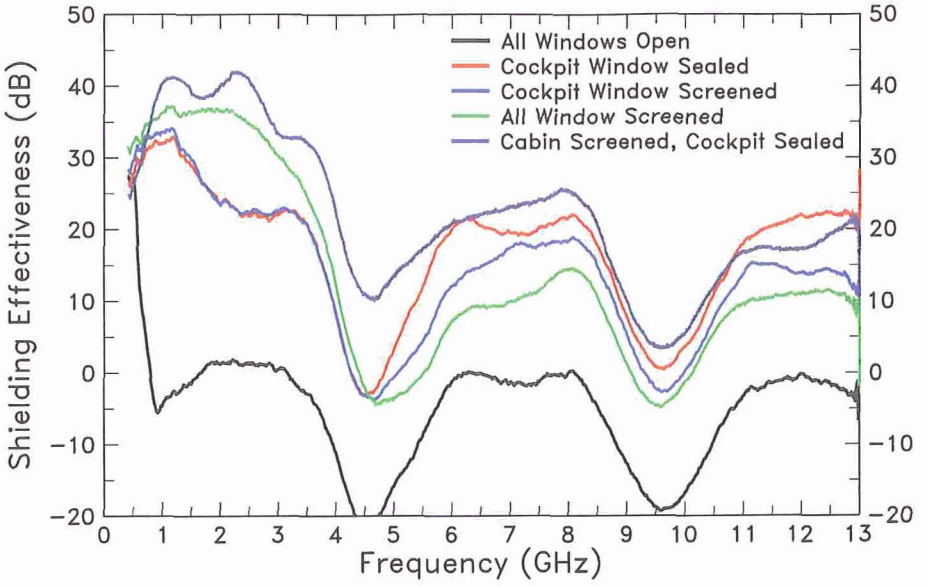

Figure 5.15: Now the shielding effectiveness has increased above that for the case of the cabin windows open and the cockpit window sealed, as expected.

nose (Figure 5.16). The same relative trend is observed at this observation point, as shown in Figure 5.17, and the reason why the penetration increased when all of the windows were screened as compared to when only the cockpit window was screened remains somewhat of a mystery.

IV. FDTD Predictions

In this section predictions of the shielding effectiveness for the simplified fuselage are presented. All the predictions are performed using the standard second-order accurate both in time and space FDTD(2,2) method. Three different cell sizes are used depending on the frequency range of the predictions. Predictions are performed for nose incidence. The computations of shielding effectiveness (SE) are based on the definition described by *procedure* #2 presented in [144]. This procedure is in accordance with measurements. The CAD model of the simplified fuselage is illustrated in Fig. 5.18 through Fig. 5.19

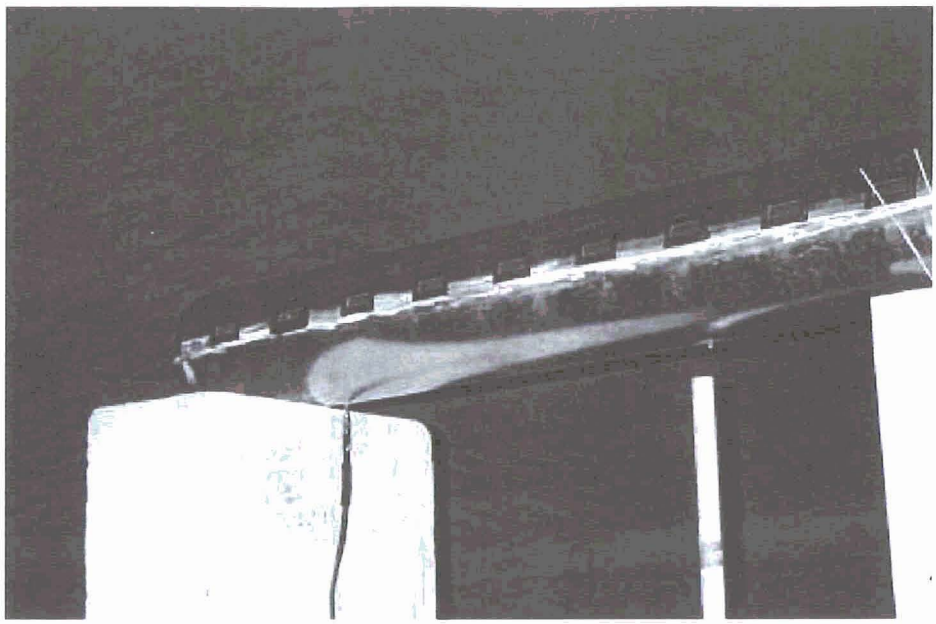

Figure 5.16: The entire window treatment series of measurements was repeated with the observation point moved to 1.25 m from the nose.

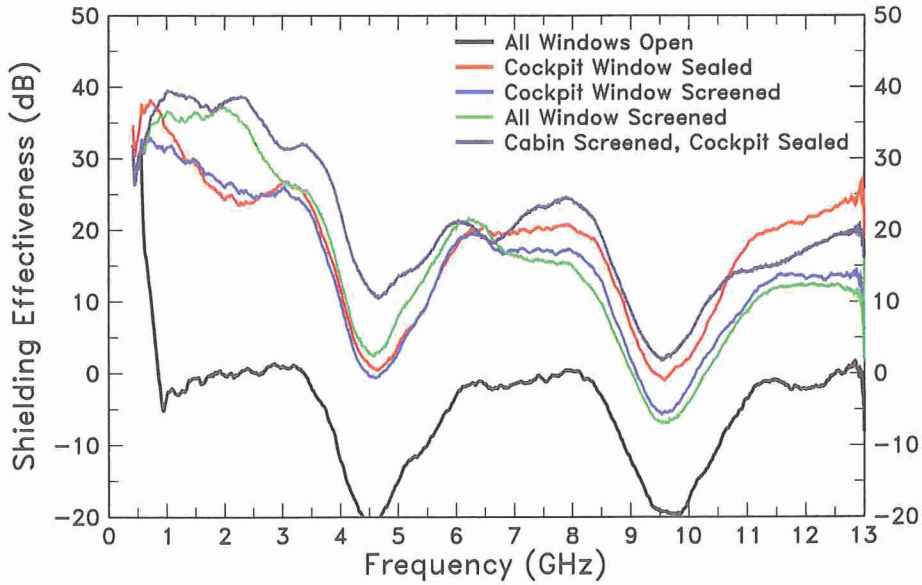

Figure 5.17: The resulting SE plots demonstrate that the same trends occur as when the observation point was at 50 cm from the nose.

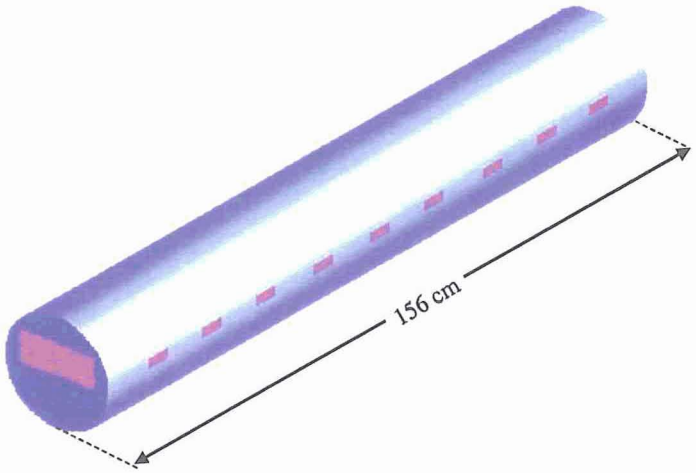

Figure 5.18: Geometry of the cylindrical fuselage

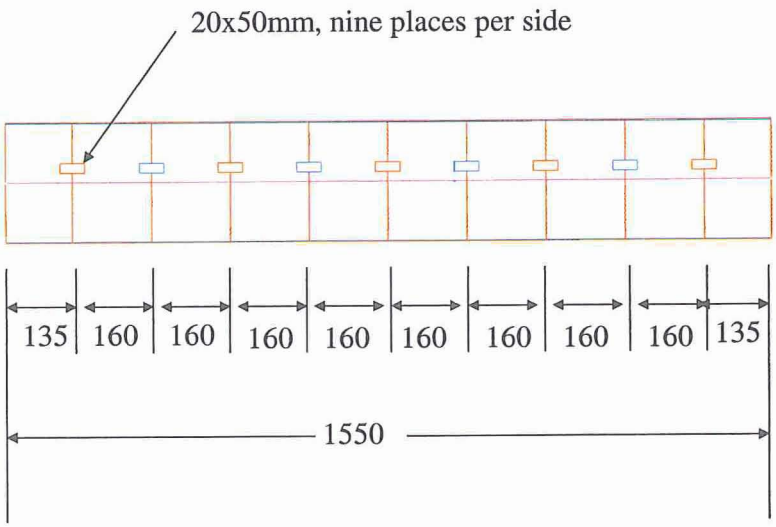

Figure 5.19: Side view of the cylindrical fuselage

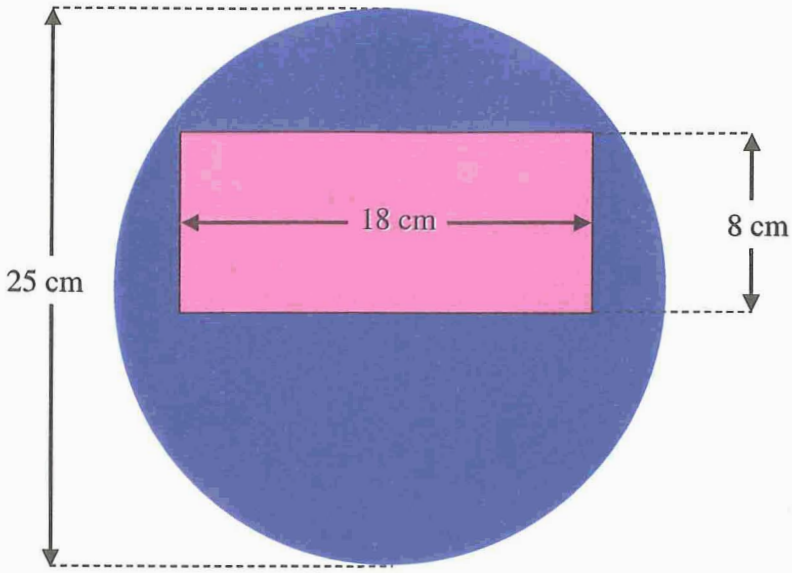

Figure 5.20: Front view of the cylindrical fuselage

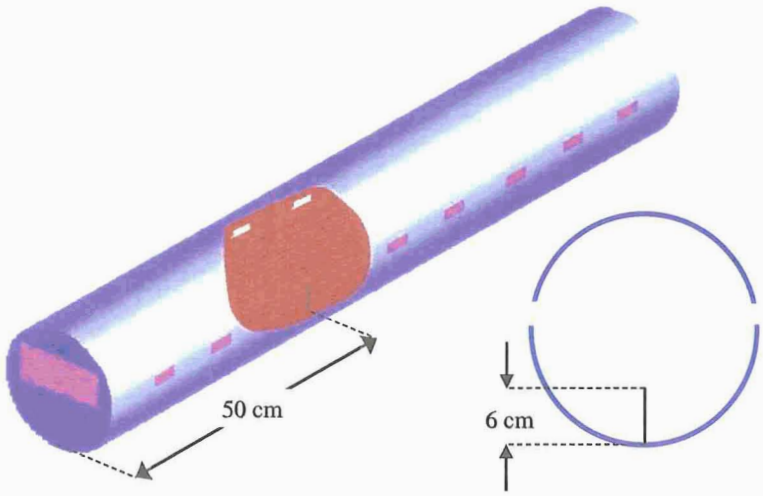

Figure 5.21: Probe location in the cylindrical fuselage

A. Cell size of 10 mm

Initially, all FDTD predictions are performed using a cell size of 10 mm (or $\lambda/10$ at 3 GHz). Therefore it is expected that these FDTD calculations will provide accurate results at most up to 3 GHz. SE predictions are computed for an azimuthal angle of incidence of 0° (nose incidence). The results of the FDTD method are illustrated in Fig. 5.22 through Fig. 5.25. Fig. 5.22 depicts SE in the entire frequency range of $0-2.8$ GHz, whereas Figs. 5.23, 5.24 and 5.25 provide three zoom views in the bands $0.7-1.4$ GHz, $1.4-2.1$ GHz and $2.1-2.8$ GHz, respectively. It can be seen that the FDTD predictions are in good agreement with the measurements. Discrepancies between the measurements and the predictions are observed in all frequency bands but especially in the last one. these inaccuracies are attributed to FDTD dispersion errors. Even though the cell size of 10 mm corresponds to $\lambda/10$ at 3 GHz, this mesh is proven insufficient for the last frequency band. This happens because the domain of the fuselage is electrically large causing accumulation of dispersion errors which significantly restrict FDTD accuracy. Another cause for these discrepancies is that the curved surface of the fuselage is impossible to be accurately modeled by the cubical cells of the standard FDTD scheme. The use of cubical cells results in a staircased model geometry which is quite different from the actual one and therefore the predicted penetrated field differs from measurements.

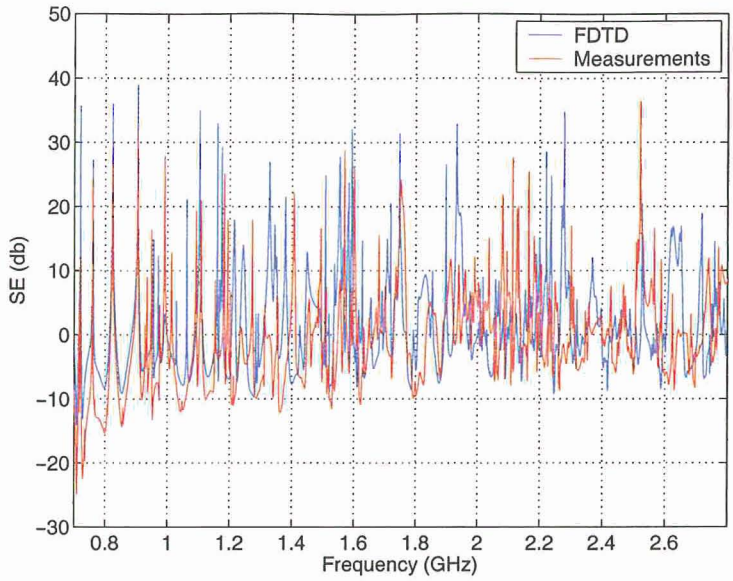

Figure 5.22: Shielding effectiveness of the scaled fuselage for azimuthal incident angle of 0°, cell size 10 mm

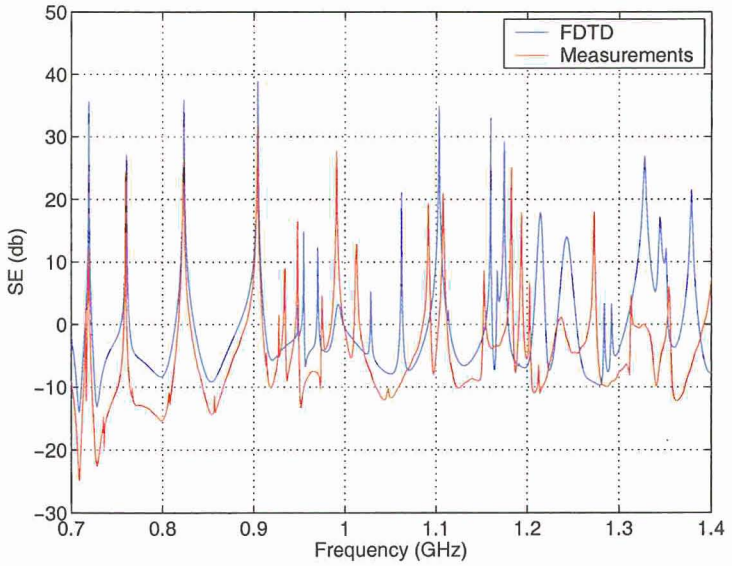

Figure 5.23: Shielding effectiveness of the scaled fuselage for azimuthal incident angle of 0°, cell size 10 mm

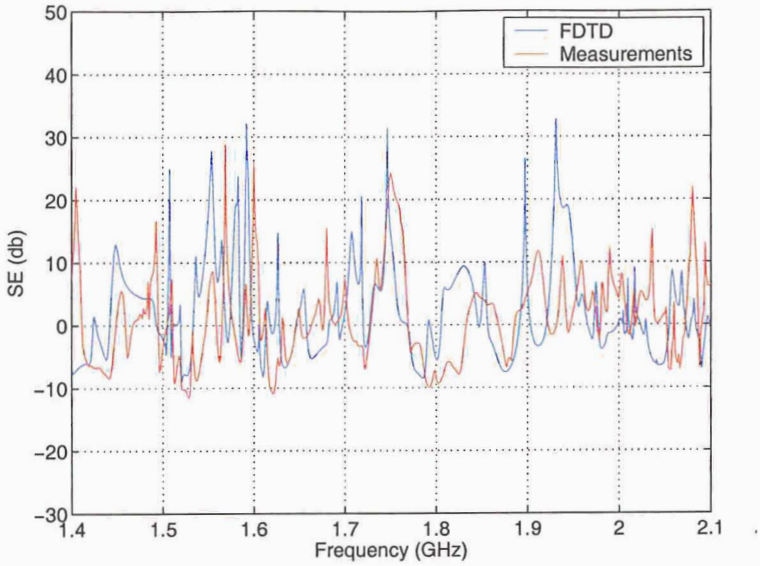

Figure 5.24: Shielding effectiveness of the scaled fuselage for azimuthal incident angle of 0°, cell size 10 mm

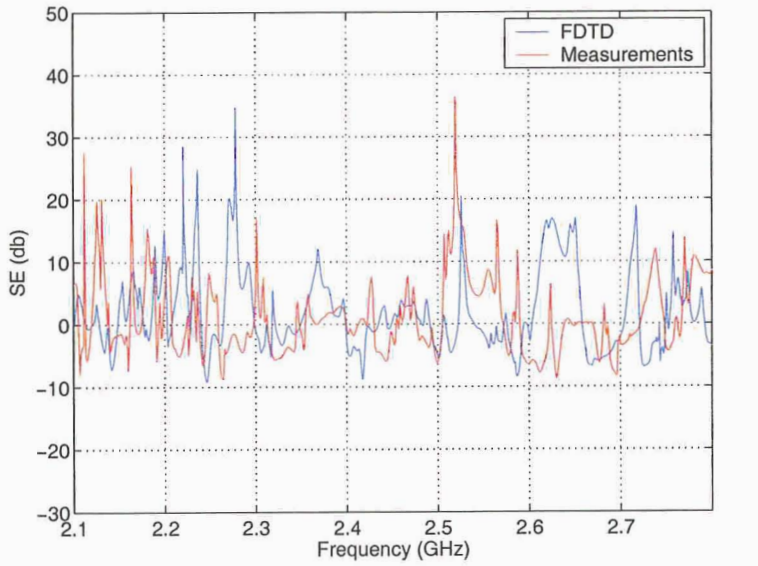

Figure 5.25: Shielding effectiveness of the scaled fuselage for azimuthal incident angle of 0°, cell size 10 mm

B. Cell size of 5 mm

The inaccuracies of the FDTD computations shown above were attributed to dispersion errors. In order to reduce dispersion errors and improve the accuracy of the FDTD predictions at higher frequency bands, finer meshes have to be used. Finer meshes provide more accurate results but they yield large computational domains which require significant computational resources. Here, all FDTD predictions are performed using a cell size of 5 mm (or $\lambda/10$) at 6 GHz. Therefore it is expected that these FDTD calculations will provide accurate results at most up to 6 GHz. The FDTD computations are shown and compared to measurements in Fig. 5.26 through Fig. 5.29. It can be observed that the numerical results agree very well with measurements up to 3.5 GHz. However their accuracy is already degraded in the last frequency band, even though the cell size of 5 mm corresponds to $\lambda/15$ at 4 GHz. In an electrically large space such as a simplified fuselage, the accumulation of phase errors due to dispersion becomes significant and deteriorates the accuracy of the FDTD solution. The simplified fuselage has electrical dimensions of approximately $31\lambda \times 4\lambda \times 5\lambda$ at 6 GHz, which make the fuselage an electrically large domain. This explains the inaccurate results of FDTD in the last frequency band. However, the finer mesh of 5 mm, used here, provides predictions that exhibit better accuracy than that of the predictions performed for a cell size of 10 mm. This can be observed by comparing Figs. 5.25 and 5.27. Also, it has to be mentioned that the staircasing error still exists in this case, which affects the accuracy of the computations. Of course, this staircased surface is less rough than the previous but still differs from the physical model.

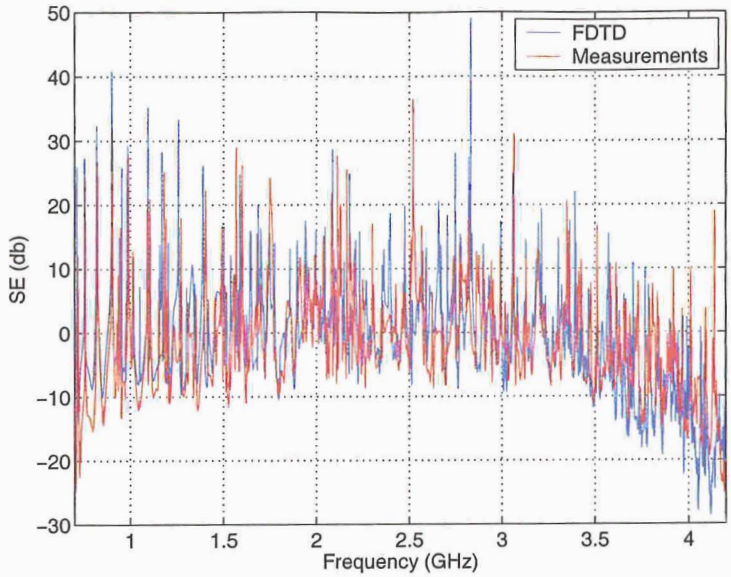

Figure 5.26: Shielding effectiveness of the scaled fuselage for azimuthal incident angle of 0°, cell size 5 mm

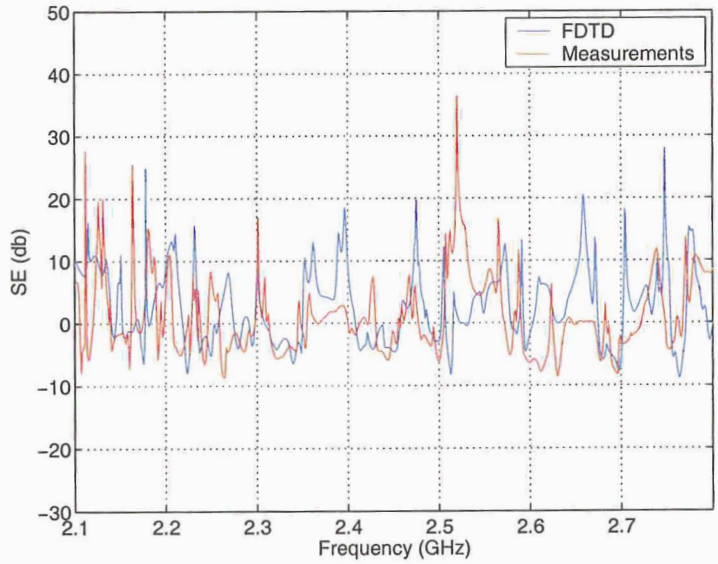

Figure 5.27: Shielding effectiveness of the scaled fuselage for azimuthal incident angle of 0°, cell size 5 mm

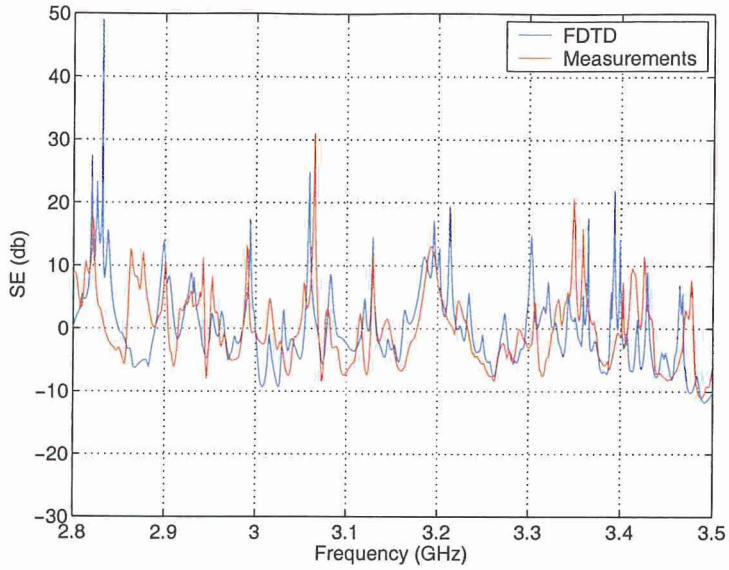

Figure 5.28: Shielding effectiveness of the scaled fuselage for azimuthal incident angle of 0°, cell size 5 mm

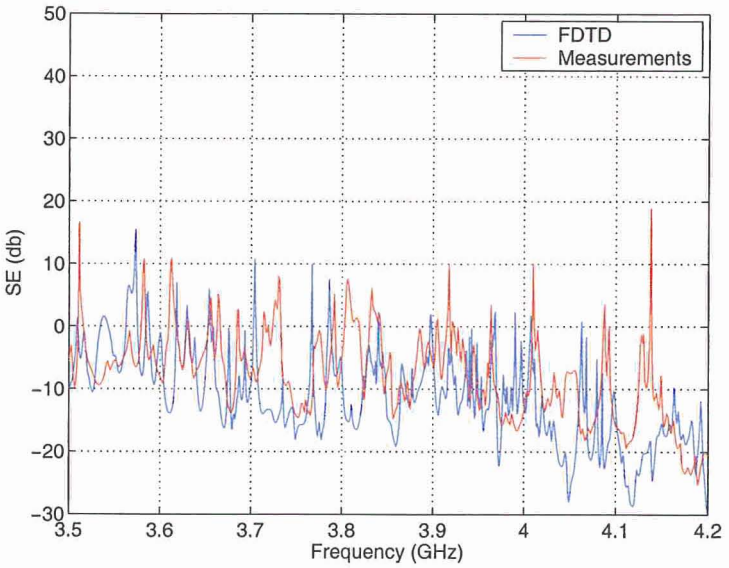

Figure 5.29: Shielding effectiveness of the scaled fuselage for azimuthal incident angle of 0°, cell size 5 mm

C. Cell size of 2.5 mm

In the previous sections, the FDTD mesh was refined from 10 mm to 5 mm and this refined mesh provided results of improved accuracy. In order to reduce even further the dispersion error and improve the accuracy of the FDTD predictions at higher frequencies, the mesh is again refined. Here, all FDTD predictions are performed using a cell size of 2.5 mm (or $\lambda/13$ at 9 GHz). Therefore, it is expected that these FDTD calculations will provide accurate results at most up to 9 GHz. Moreover, the new finer cell size, improves the modeling accuracy of the fuselage curved surface, therefore a general improvement in all frequency bands is expected. Of course the staircasing error still exists but the discontinuities that it creates are smoother. The FDTD computations are shown and compared to measurements in Fig. 5.30 through Fig. 5.40. It can be observed that the numerical results agree very well with measurements up to 5.6 GHz and the agreement in these frequency bands has been improved. However, the accuracy is already degraded in the higher frequency bands. Again even though the discretization is at least $\lambda/13$ at 9 GHz, the accumulation of phase errors through the domain make this discretization insufficient. Note that the simplified fuselage has electrical dimensions of approximately $47\lambda \times 6\lambda \times 7\lambda$ at 9 GHz, which make the fuselage an extremely electrically large domain.

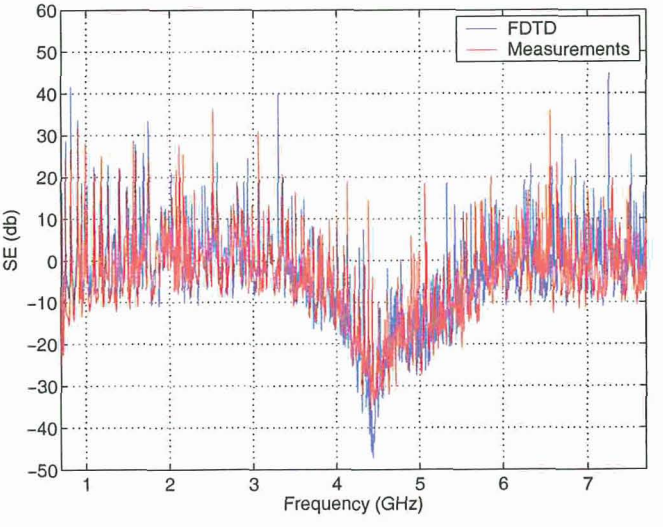

Figure 5.30: Shielding effectiveness of the scaled fuselage for azimuthal incident angle of 0°, cell size 2.5 mm

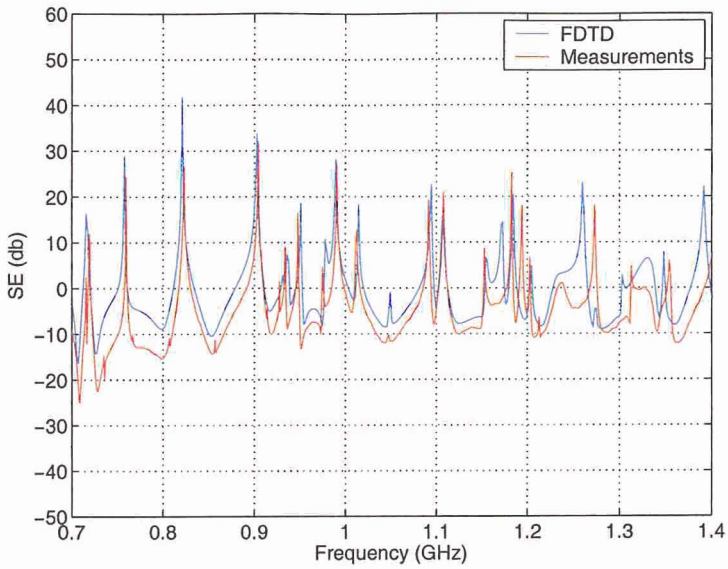

Figure 5.31: Shielding effectiveness of the scaled fuselage for azimuthal incident angle of 0°, cell size 2.5 mm

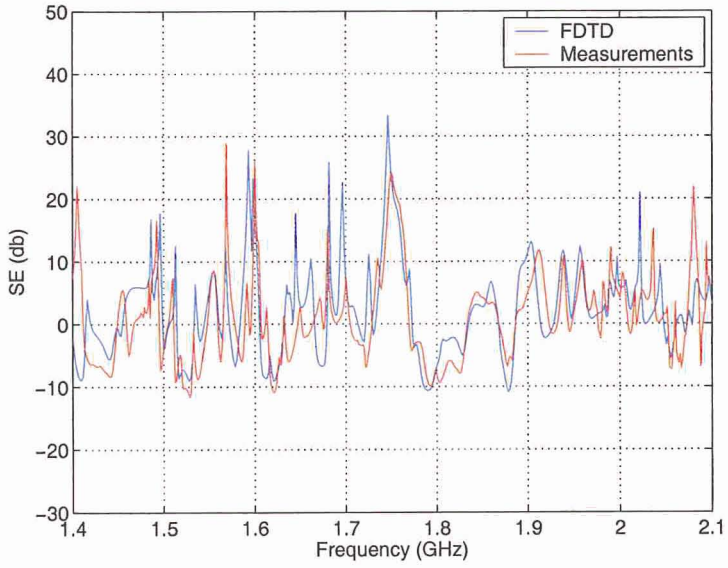

Figure 5.32: Shielding effectiveness of the scaled fuselage for azimuthal incident angle of 0°, cell size 2.5 mm

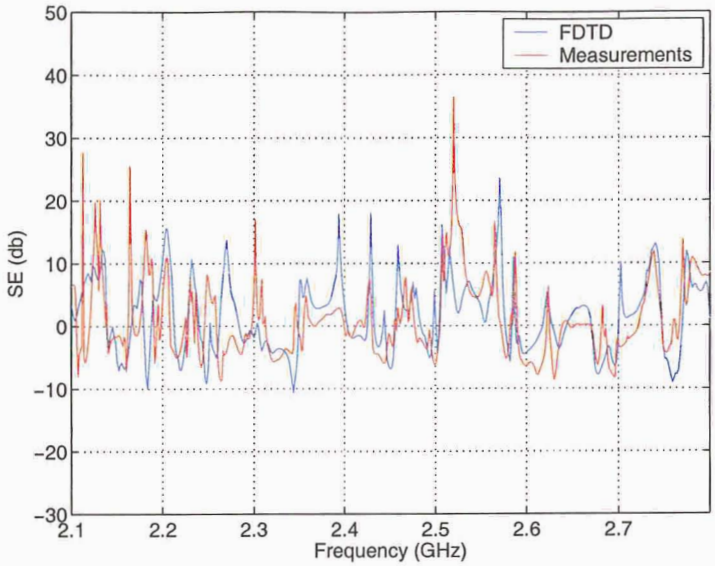

Figure 5.33: Shielding effectiveness of the scaled fuselage for azimuthal incident angle of 0°, cell size 2.5 mm

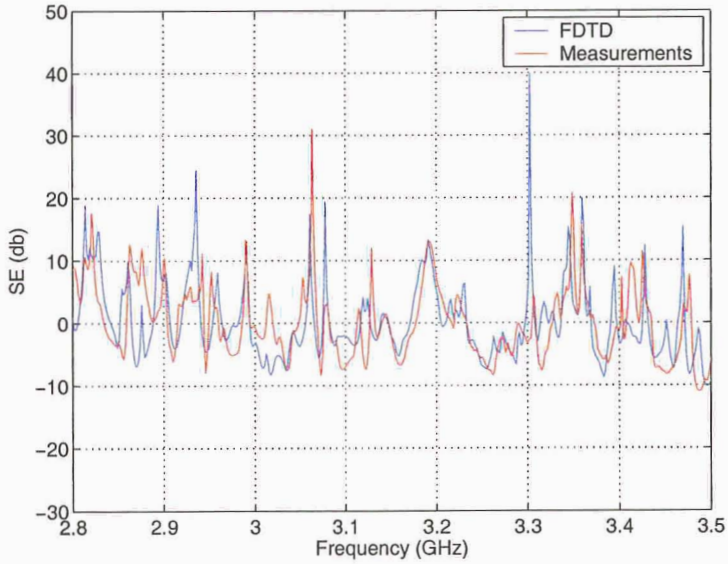

Figure 5.34: Shielding effectiveness of the scaled fuselage for azimuthal incident angle of 0°, cell size 2.5 mm

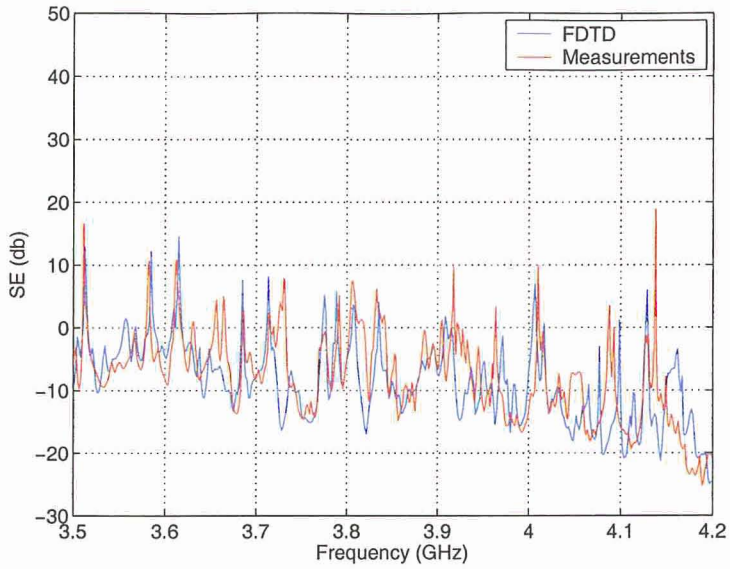

Figure 5.35: Shielding effectiveness of the scaled fuselage for azimuthal incident angle of 0°, cell size 2.5 mm

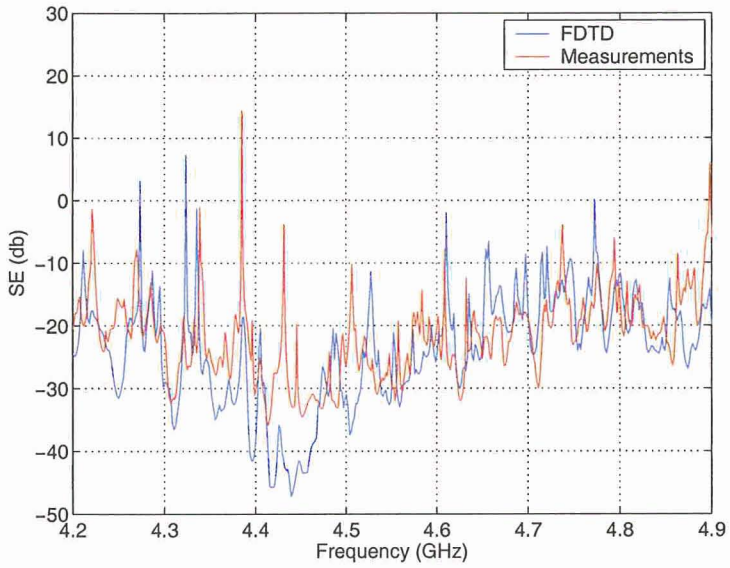

Figure 5.36: Shielding effectiveness of the scaled fuselage for azimuthal incident angle of 0°, cell size 2.5 mm

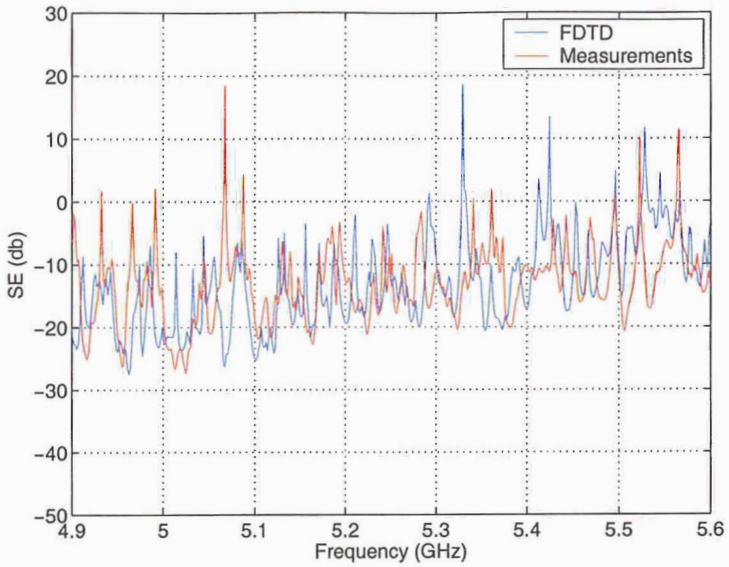

Figure 5.37: Shielding effectiveness of the scaled fuselage for azimuthal incident angle of 0°, cell size 2.5 mm

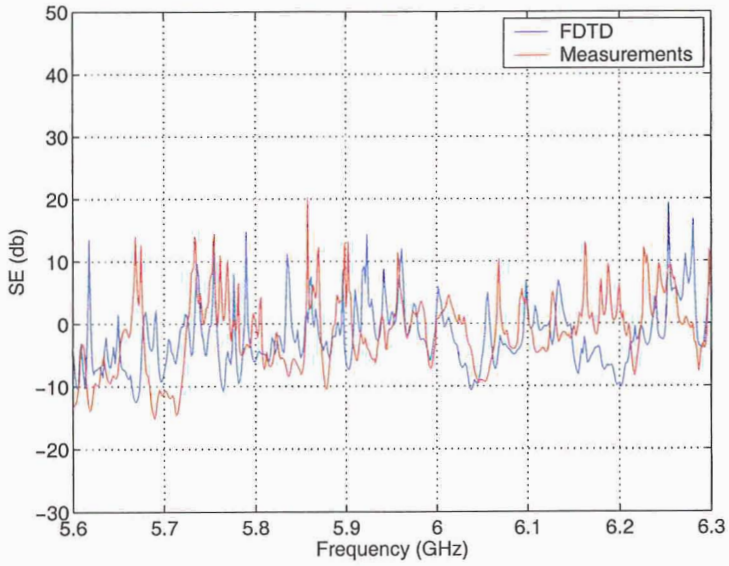

Figure 5.38: Shielding effectiveness of the scaled fuselage for azimuthal incident angle of 0°, cell size 2.5 mm

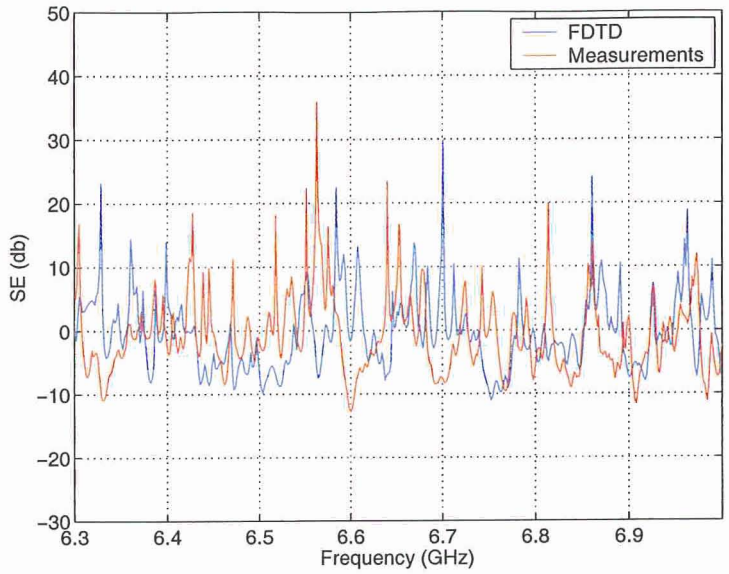

Figure 5.39: Shielding effectiveness of the scaled fuselage for azimuthal incident angle of 0°, cell size 2.5 mm

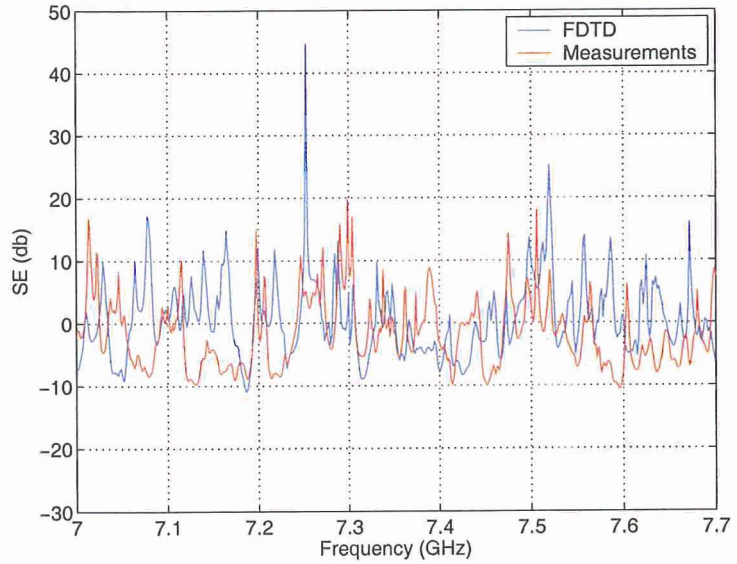

Figure 5.40: Shielding effectiveness of the scaled fuselage for azimuthal incident angle of 0°, cell size 2.5 mm

V. Conclusions

The construction of the cylindrical fuselage was successfully completed, with some small deviations from its intended design as a circular cross section version of the Simplified Fuselage.

While the shielding effectiveness measurements at a point 50 cm from the cylindrical fuselage's nose do not correlate in a deterministic sense to those of the Simplified Fuselage, the two are very similar in an averaged sense. Thus, a rectangular cross-section fuselage model can be a good approximation (in a quasi-statistical sense) to a curved fuselage of the same interior volume.

Application of screens to the cabin and cockpit windows has a pronounced effect in increasing the shielding effectiveness of the structure. Shielding effectiveness improvements of 10 to 40 dB were observed when screens having wire spacing of (full scale) 1.5" were applied. However, the full scale diameter of the wire in the aluminum screens is 0.18". This is obviously much larger than could be used in practice. The improvement in shielding would be lessened in the case of a finer diameter wire. On the other hand, the aluminum screen used was simply woven, and the contact impedance of aluminum is not particularly low. Screens specifically intended for electromagnetic shielding would likely have bonded wires which improves their effectiveness.

The shielding effectiveness of the structure increased at frequencies below 4.5 GHz when screens were added to the cabin windows, as compared to the case of only the cockpit window being screened. Oddly, the shielding effectiveness simultaneously decreased at frequencies above 4.5 GHz. While no satisfactory explanation is proposed, the same trend was observed when the observation point was moved to the rear of the fuselage (at 1.25 m from the nose).

The standard FDTD scheme was used to compute the SE of the circular cross section scale model fuselage. The domain was discretized using three different cell sizes, 10 mm, 5 mm and 2.5 mm. Predictions was compared with measurements and they were in very good agreement while significant improvement was observed as the mesh was refined. Moreover the observed discrepancies were attributed to staircasing errors as well as phase error accumulation.

Chapter 6

Statistics of the Electromagnetic (EM) Field Inside the Simplified Fuselage

In this chapter, a statistical analysis is presented of the HIRF penetration problem for a simplified scale model fuselage. A reverberation chamber (RC) approach is examined. A rotatable scatterer (mode-stirrer) is inserted into the fuselage and measurements are performed at different locations for different mode-stirrer orientations. From the collected set of data, statistical quantities are calculated. Moreover, probabilistic models that have been derived for RCs are compared with the statistical field distributions in the fuselage.

I. Introduction

Until now, the problem of calculating the SE of a simplified fuselage model has been extensively studied with great success using deterministic methods, although the results are subject to previously mentioned limitations. To overcome these limitations, a statistical approach is recommended. This requires the insertion of a mode stirrer inside the simplified fuselage model. The mode-stirrer, with its four uneven paddles, has the capability to rotate and thus to simulate the numerous field configurations/modes inside the cavity.

In the following sections an overview is given of the RC technique for immunity tests. The principles of RC construction and operation are described while the prob-

abilistic model that governs the field distributions is presented. Thereafter, the ASU approach is presented where a mode-stirrer was constructed and placed inside the fuselage. Measurements were performed for different mode-stirrer orientations and the statistical distributions of the selected data were calculated. Goodness-of-Fit tests are performed between the experimental data distributions and the theoretical probabilistic models.

II. Reverberation Chambers (RCs)

A. Principles of Operation

Conventional immunity tests are performed using anechoic chambers or open-area test sites. In anechoic chambers, the equipment under test (EUT) is exposed to a controlled EM environment and its coupling with the radiating source is studied. However anechoic chambers can simulate only *free space* environments without interferences from external sources, not to mention that the radiated signal is approximately a *plane wave*. Moreover, in a real environment, there is no reason to expect a specific field configuration and a pre-determined type of source. In contrast, in a real environment, the direction, polarization and frequency of the incident fields are random. Also the evolution of modern communication systems and the plethora of electronic devices has resulted in a more "hostile" ambient environment increased in density and intensity.

All the aforementioned factors have resulted in more strict EMI regulations which necessitated the need for testing techniques that resemble realistic conditions. An alternative method of EMI testing is to use a reverberation chamber (RC) (or mode-stirred chamber). Although the concept of RCs is rather old [145], recently they have been widely accepted from the EMC/EMI community as a valid and reliable susceptibility, vulnerability and SE measurement technique. The geometry of an RC is shown in Fig. 6.1. As can be seen, RCs are large cavities consisting of metal walls along with a metallic paddle, denoted as mode-stirrer, which has the ability to rotate. The rotation property of the stirrer, its shape as well as its size are all of great importance for the proper operation of the RC. When the stirrer rotates, the boundary conditions on the chamber continuously vary and the inevitable standing

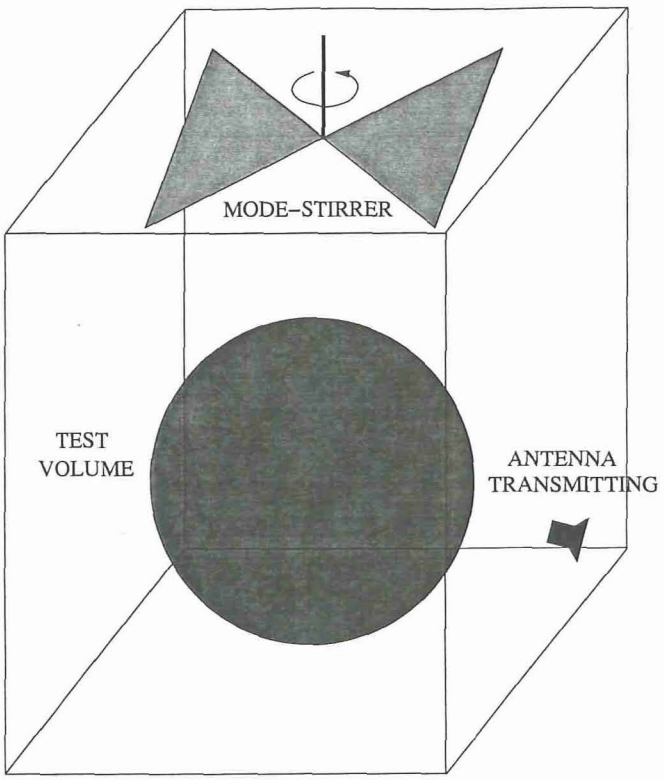

Figure 6.1: Reverberation Chamber geometry.

waves that occur inside the chamber are stirred. Therefore the EM energy that is injected onto the RC corner, from the transmitting antenna, is allowed to reflect off the six faces and the stirrer. So the incident waves at a point in the chamber have both continuously changing amplitude and phase. This is because the rotating tuner changes the number of reflections and the length of the reflected paths before the incident waves arrive at that point. As a, consequence the sharp nulls, of the standing wave field configuration smooth out while for the TEST VOLUME part of the chamber, the field is characterized by *statistical isotropy*, *random polarization* and *uniformity*. At this point it is appropriate to mention that regarding to the stirrer way of rotation there are two competing philosophies. The Italian philosophy, supported by P. Corona [146], is known as "stirring" and recommends a continuously turning paddle. The alternative philosophy, supported by J. Laudbury [146], is known as "tuning" and recommends discrete stirrer rotation.

As mentioned before, the choice of shape and size for the stirrer are very important for its effectiveness. It is recommended [147] that the shape of the stirrer should be as irregular as possible so that the field can be scattered evenly in all directions. Also, multiple tuners may be used [148], which are typically mounted on opposite walls to improve the stirring of the fields. This is more important in the case of flat tuners that they act as scatterers in only one plane. With respect to size, the stirrer should be electrically large or greater than $\frac{\lambda}{2}$ at the lowest frequency of operation [147]. Also Wu and Chang in [149] examined ways to achieve sufficient eigenfrequency shifting, and thus randomness of the field, in a 2-D cavity with an 1-D perturbing body. They concluded that the key mechanism that causes uniformly random field distribution is a form of random modulation, both in amplitude and frequency, that can be achieved only if the rotating scatterer is large enough. Concluding, a typical test to determine the effectiveness of a mode-stirrer is to measure the ratio of the maximum to minimum received power as a function of stirrer orientation. A reasonable guideline for proper operation of the tuner is a minimum tuning ratio of 20 dB.

Among other characteristics, the total possible number of modes in an RC is also of great interest. A good approximation for the number of eigenmodes as a function of frequency is given by [150],

$$N(f) = \underbrace{\frac{8\pi}{3} a\,b\,c\,\frac{f^3}{c^3}}_{1} - \underbrace{(a+b+c)\,\frac{f}{c} + \frac{1}{2}}_{2} \tag{6.1}$$

where c is the speed of light in free space, while a, b and c are the chamber dimensions. Note that the first term of (6.1) coincides with Weyl's [151], [152] asymptotic expression which is proportional to the volume abc of the chamber. The second term is the "edge term" which modifies Weyl's result, especially in the lower frequencies range. It should be noted that (6.1) is applicable in the frequency range

$$\frac{2\pi}{\lambda} \min\{a, b, c\} \geq \pi \tag{6.2}$$

The efficiency of an RC strongly depends on the number of modes N, existing at a specific frequency or in a frequency range. As a matter of fact, the higher the N the better is the efficiency of the chamber. Therefore mode degeneracy has to be seriously taken into account. Many RC designers [147], [150] suggest that

the ratio of their dimensions should be as non-rational as possible while a cubical chamber should be definitely avoided. As an example, the NBS chamber dimensions are $2.74\,m \times 3.05\,m \times 4.57\,m$. The previous remarks reveal an intrinsic limitation of RCs. Because N increases with frequency, it is more difficult to perform immunity tests at the lower frequency range since the chamber would not operate properly. Therefore EM interference from low frequency threats is difficult to test using RCs. Several studies have been reported dealing with the lowest usable frequency (LUF) of an RC and suggestions have been made on how to calculate it [153] and on how to perform measurements below the LUF level [154].

As mentioned before, the main objective when using an RC is to create a delta correlated stochastic electromagnetic field in it, which implies that there are no strong elementary sources. Therefore, the transmitting and receiving antennas should be properly placed and oriented inside an RC so that there would be no line-of-sight between them. In order to achieve that, the following receiving-transmitting antenna configurations are recommended:

a. Position the transmitting and receiving antennas in different corners of the chamber, oriented toward the corners

b. Position one of the antennas in a corner oriented toward the corner, while the other one is sufficiently far away and oriented toward the tuner

c. Position the two antennas with line-of-sight but keep them cross-polarized.

Although the development of RCs statistical theory requires that there are no dominating field components, recently new studies have been reported [155], [156], [157] that present alternative statistical theories for this RC mode of operation, while also their usefulness for immunity testing is discussed.

B. Statistical Characterization

In this section, probabilistic models are presented for various field quantities in an RC. Probability density functions (PDFs) as well as cumulative density functions (CDFs) are derived for the magnitude of the electric field components, the received power in each direction as well as the SE of a single spatial point. Moreover, the

stirrer efficiency is studied with respect to the number of steps that are required to obtain uncorrelated field measurements. For the analysis of the next sections, the following assumptions are made:

a. There is no line-of-sight between the transmitting and receiving antennas

b. In the RC perfect more-stirring has been achieved

1. General Statistical properties of the EM field in an RC

The electric field $\boldsymbol{E}$ at location $\boldsymbol{r}$ in the TEST VOLUME of the RC can be represented as an integral of plane waves [158] over all real angles (θ, ϕ), or

$$\boldsymbol{E} = \iint_{\Omega} \boldsymbol{A}(\Omega)\, \mathrm{e}^{-\mathrm{j}\,\boldsymbol{k}\cdot\boldsymbol{r}}\, \mathrm{d}\Omega \tag{6.3}$$

where the solid angle Ω is given by $\Omega = \sin\theta \mathrm{d}\theta \mathrm{d}\phi$ while $\boldsymbol{k}$ is the vector wavenumber. The angular spectrum $\boldsymbol{A}(\Omega)$ can be written in terms of its orthogonal components, as

$$\boldsymbol{A}(\Omega) = \hat{\boldsymbol{a}}_\theta\, A_\theta(\Omega) + \hat{\boldsymbol{a}}_\phi\, A_\phi(\Omega) \tag{6.4}$$

where $\hat{\boldsymbol{a}}_\theta$ and $\hat{\boldsymbol{a}}_\phi$ are the unit vectors along the elevation and azimuthal directions. Moreover, each one of $A_\theta(\Omega)$ and $A_\phi(\Omega)$ is a complex quantity and can be written in terms of their real and imaginary parts

$$A_\theta(\Omega) = A_{\theta r}(\Omega) + \mathrm{j}\, A_{\theta i}(\Omega) \tag{6.5}$$

$$A_\phi(\Omega) = A_{\phi r}(\Omega) + \mathrm{j}\, A_{\phi i}(\Omega) \tag{6.6}$$

The geometry for a plane wave component is shown in Fig. 6.2.

For a statistical field, as generated in a reverberation chamber, the angular spectrum is taken to be a random variable which depends on stirrer position. In a typical RC measurement, the statistical ensemble is generated by rotating the stirrer. The starting point for the statistical analysis is to select statistical properties for the angular spectrum that are representative of a well-stirred field. Appropriate statistical

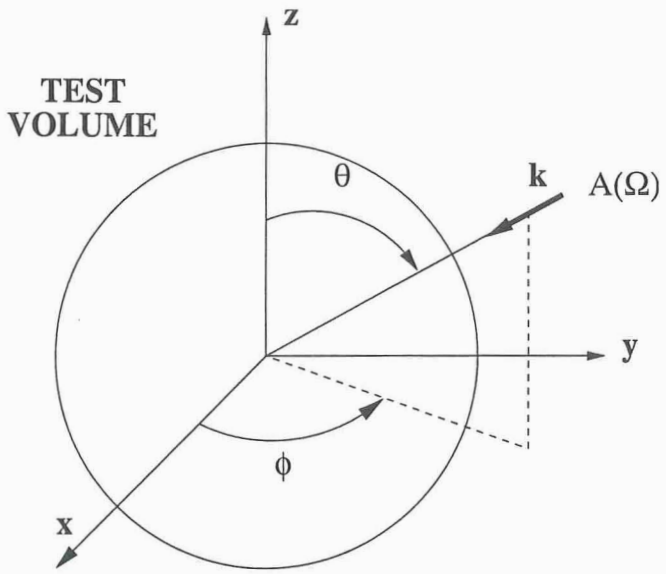

Figure 6.2: One vector component of the angular spectrum of the electric field.

assumptions for such field configuration are the following mean values [1] :

$$\langle \boldsymbol{A}_\theta(\Omega) \rangle = \langle \boldsymbol{A}_\phi(\Omega) \rangle = 0 \tag{6.7}$$

$$\begin{aligned} \langle \boldsymbol{A}_{\theta r}(\Omega_1)\, \boldsymbol{A}_{\theta i}(\Omega_2) \rangle &= \langle \boldsymbol{A}_{\phi r}(\Omega_1)\, \boldsymbol{A}_{\phi i}(\Omega_2) \rangle \\ &= \langle \boldsymbol{A}_{\theta r}(\Omega_1)\, \boldsymbol{A}_{\phi r}(\Omega_2) \rangle \\ &= \langle \boldsymbol{A}_{\theta r}(\Omega_1)\, \boldsymbol{A}_{\phi i}(\Omega_2) \rangle \\ &= \langle \boldsymbol{A}_{\theta i}(\Omega_1)\, \boldsymbol{A}_{\phi r}(\Omega_2) \rangle \\ &= \langle \boldsymbol{A}_{\theta i}(\Omega_1)\, \boldsymbol{A}_{\phi i}(\Omega_2) \rangle = 0 \end{aligned} \tag{6.8}$$

[1] The *mean value* or *expected value* of a random variable $\mathbf{x}$ is defined as:

$$\langle \mathbf{x} \rangle = \mathcal{E}\{\mathbf{x}\} = \int_{-\infty}^{+\infty} x\, f_{\mathbf{x}}(x) \mathrm{d}x$$

where $f_{\mathbf{x}}(x)$ is the probability density function of $\mathbf{x}$.

and

$$\begin{aligned}\langle \boldsymbol{A}_{\theta r}(\Omega_1)\, \boldsymbol{A}_{\theta r}(\Omega_2)\rangle &= \langle \boldsymbol{A}_{\theta i}(\Omega_1)\, \boldsymbol{A}_{\theta i}(\Omega_2)\rangle \\ &= \langle \boldsymbol{A}_{\phi r}(\Omega_1)\, \boldsymbol{A}_{\theta r}(\Omega_2)\rangle \\ &= \langle \boldsymbol{A}_{\phi i}(\Omega_1)\, \boldsymbol{A}_{\phi i}(\Omega_2)\rangle \\ &= C\,\delta(\Omega_1 - \Omega_2)\end{aligned} \tag{6.9}$$

where δ is the Dirac delta function and C is a constant.

The physical justifications for the above assumptions are as follows. Since the angular spectrum is a result of many rays with random phases, the mean value should be zero, as indicated in (6.7). Moreover, since multi-path scattering changes the phase and rotates the polarization many times, angular spectrum components with orthogonal polarizations or quadrature phase have to be uncorrelated, as indicated in (6.8). Furthermore, since angular spectrum components arriving from different directions have taken "very different" multiple scattering paths, they have to be uncorrelated as indicated by the delta function on the right hand side of (6.9).

From (6.8) and (6.9) and after some straightforward manipulations, the following relations can be obtained

$$\left\langle \boldsymbol{A}_{\theta}(\Omega_1)\boldsymbol{A}^{*}_{\phi}(\Omega_2)\right\rangle = 0 \tag{6.10}$$

$$\langle \boldsymbol{A}_{\theta}(\Omega_1)\boldsymbol{A}^{*}_{\theta}(\Omega_2)\rangle \;=\; \left\langle \boldsymbol{A}_{\phi}(\Omega_1)\boldsymbol{A}^{*}_{\phi}(\Omega_2)\right\rangle = 2C\delta(\Omega_1 - \Omega_2) \tag{6.11}$$

where * denotes complex conjugate.

Now, a number of interesting and useful field properties are derived using all the

above assumptions. The mean value of the electric field is equal to

$$\langle \boldsymbol{E}(\boldsymbol{r}) \rangle = \iint_{\Omega} \langle \boldsymbol{A}(\Omega) \rangle \, \mathrm{e}^{-\mathrm{j}\boldsymbol{k}\cdot\boldsymbol{r}} \mathrm{d}\Omega$$

$$= \iint_{\Omega} \langle (\hat{\boldsymbol{a}}_\theta \, A_\theta(\Omega) + \hat{\boldsymbol{a}}_\phi \, A_\phi(\Omega)) \rangle \, \mathrm{e}^{-\mathrm{j}\boldsymbol{k}\cdot\boldsymbol{r}} \mathrm{d}\Omega \tag{6.12}$$

$$= \hat{\boldsymbol{a}}_\theta \iint_{\Omega} \langle A_\theta(\Omega) \rangle \, \mathrm{e}^{\mathrm{j}\boldsymbol{k}\cdot\boldsymbol{r}} \mathrm{d}\Omega + \hat{\boldsymbol{a}}_\phi \iint_{\Omega} \langle A_\phi(\Omega) \rangle \, \mathrm{e}^{-\mathrm{j}\boldsymbol{k}\cdot\boldsymbol{r}} \mathrm{d}\Omega \overset{(6.7)}{=} 0$$

From the last result we conclude that the mean value of the electric field in an RC is zero. This is expected because a well-stirred field is the sum of a large number of multi-path rays with random phases.

Another interesting property is obtained if we calculate the mean value of the electric field squared, $\langle |\boldsymbol{E}(\boldsymbol{r})|^2 \rangle$. The electric field squared in terms of its angular spectrum is given by

$$\begin{aligned} |\boldsymbol{E}(\boldsymbol{r})|^2 &= \boldsymbol{E}(\boldsymbol{r}) \, \boldsymbol{E}^*(\boldsymbol{r}) \\ &= \iint_{\Omega} \iint_{\Omega} \boldsymbol{A}(\Omega_1) \cdot \boldsymbol{A}^*(\Omega_2) \mathrm{e}^{-\mathrm{j}(\boldsymbol{k}_1 - \boldsymbol{k}_2)\cdot\boldsymbol{r}} \mathrm{d}\Omega_1 \mathrm{d}\Omega_2 \end{aligned} \tag{6.13}$$

while its mean value is calculated with the aid of (6.10) and (6.11) which lead to

$$\begin{aligned} \langle |\boldsymbol{E}(\boldsymbol{r})|^2 \rangle &= 4C \iint_{\Omega} \iint_{\Omega} \delta(\Omega_1 - \Omega_2) \mathrm{e}^{-\mathrm{j}(\boldsymbol{k}_1 - \boldsymbol{k}_2)\cdot\boldsymbol{r}} \mathrm{d}\Omega_1 \mathrm{d}\Omega_2 \\ &= 4C \iint_{\Omega} \mathrm{d}\Omega_2 = 16\pi C \equiv E_o^2 \end{aligned} \tag{6.14}$$

This is the uniformity property of an RC and states that the mean square value of the electric field is constant and independent of position. Similarly, it can be shown the following property, known as isotropy, or

$$\langle |\boldsymbol{E}_x|^2 \rangle = \langle |\boldsymbol{E}_y|^2 \rangle = \langle |\boldsymbol{E}_z|^2 \rangle = \frac{E_0^2}{3} \tag{6.15}$$

All the above properties have been experimentally verified at the NBS RC [147].

Another important quantity that gives insight to the response in an RC is the spatial correlation function [159]. It is given by the expression

$$\rho(\boldsymbol{r}_1, \boldsymbol{r}_2) = \frac{\langle \boldsymbol{E}(\boldsymbol{r}_1) \cdot \boldsymbol{E}^*(\boldsymbol{r}_2) \rangle}{\sqrt{\langle |\boldsymbol{E}(\boldsymbol{r}_1)|^2 \rangle \; \langle |\boldsymbol{E}(\boldsymbol{r}_2)|^2 \rangle}} \tag{6.16}$$

where $\boldsymbol{r}_1$ and $\boldsymbol{r}_2$ are two locations in the chamber. The numerator of (6.16) is the mutual coherence function, which has been used to describe multiple scattering phenomena [160]. After some manipulations, it can be shown that the spatial correlation function for an ideally operating RC is given by

$$\rho(\boldsymbol{r}_1, \boldsymbol{r}_2) = \frac{\sin(k|\boldsymbol{r}_1 - \boldsymbol{r}_2|)}{k|\boldsymbol{r}_1 - \boldsymbol{r}_2|} \tag{6.17}$$

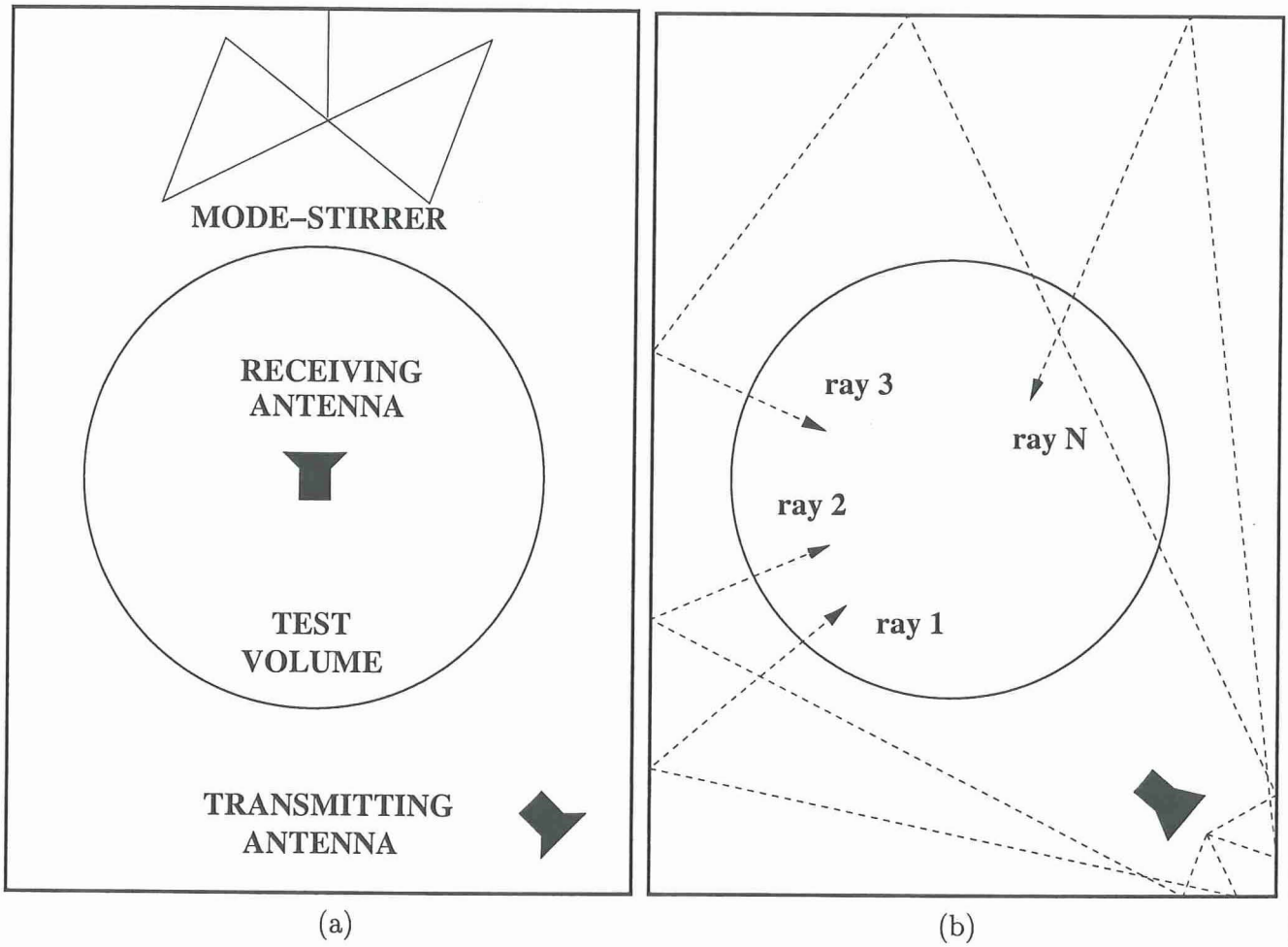

Figure 6.3: Reverberation Chamber: (a) Top view (b) Side view.

2. Probability distribution of $|E_z|^2$ inside an RC

First the PDF of the electric field component E_z in an RC is derived. The PDF of this quantity is important because it is proportional to power and because in our experiments a z-oriented monopole was used as the receiving antenna. In terms of its quadrature components, E_z is given by

$$E_z = E_{zr} + \mathrm{j}\, E_{zi} = A \exp(\mathrm{j}\, \phi) \tag{6.18}$$

where $E_{zr} = A \cos(\phi)$ and $E_{zi} = A \sin(\phi)$. Now, the field E_z is a sum of all possible scattered fields inside the RC, as shown in Fig. 6.3; therefore it can be written as

$$E_z = \sum_{n=1}^{N} A_n \exp(\mathrm{j}\, \phi_n) = \sum_{n=1}^{N} (E_{zr,n} + \mathrm{j}\, E_{zi,n}) \tag{6.19}$$

From the Central Limit Theorem [161] we have that, given n independent random variables $\mathbf{x}_i$ with mean μ_i and variance σ_i^2, respectively, their sum

$$\mathbf{x} = \mathbf{x}_1 + \mathbf{x}_2 + \cdots + \mathbf{x}_n \tag{6.20}$$

is also a random variable normally distributed with mean and variance

$$\mu = \sum \mu_i \quad \text{and} \quad \sigma^2 = \sum \sigma_i^2 \tag{6.21}$$

respectively. It is appropriate to mention that the above theorem is valid regardless of the probability distribution of each random variable.

For completeness, we mention that a random variable $\mathbf{x}$ is normally distributed with mean value μ and standard deviation σ when its probability density function (PDF) is given by

$$f_{\mathbf{x}}(x) = \frac{1}{\sqrt{2\pi}\sigma} \mathrm{e}^{-\frac{(x-\mu)^2}{2\sigma^2}} \tag{6.22}$$

or in symbolic form

$$\mathbf{x} \sim \mathcal{N}\left(\mu, \sigma^2\right) \tag{6.23}$$

The corresponding Cumulative Distribution Function (CDF) of a PDF is given by

$$F_{\mathbf{x}}(x) = \Pr\left[\mathbf{x} \leq x\right] = \int_{-\infty}^{x} f_{\mathbf{x}}(z)\, \mathrm{d}z \tag{6.24}$$

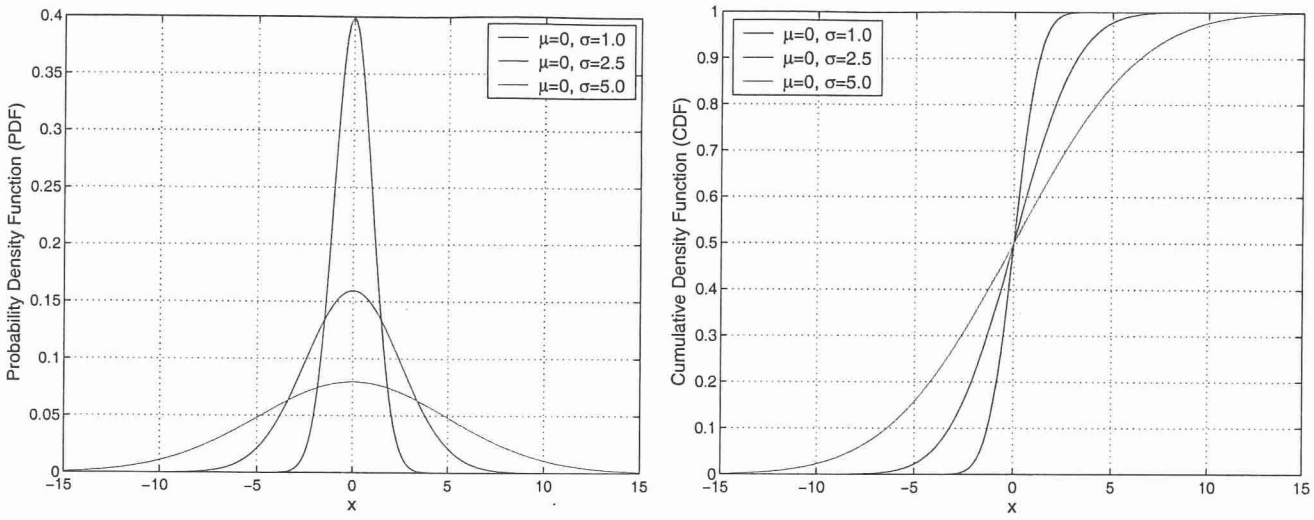

(a) (b)

Figure 6.4: Normal/Gaussian distributions: (a) probability density functions (b) cumulative density functions .

where in the case of a normal distribution the above integral yields

$$F_{\mathbf{x}}(x) = 1 - \frac{1}{2}\text{erfc}\left(\frac{x-\mu}{\sigma}\right) \tag{6.25}$$

In Fig. 6.4 there are the PDF plots of three zero mean Gaussian distributions with different standard deviation constants as well as the corresponding CDF plots.

Provided that for each n all $E_{zr,n}$ as well as all $E_{zi,n}$ are independent, then we can claim that both

$$E_{zr} = \sum_n E_{zr,n} \quad \text{and} \quad E_{zr} = \sum_n E_{zi,n} \tag{6.26}$$

are normally distributed. In an RC, the main objective is to create a uniform field distribution. Therefore a direct illumination (line-of-sight) of the receiving antenna from the transmitting one is avoided so that there will be no dominating field component. Based on that, we can claim that the mean value of both quantities E_{zr} and E_{zr} is zero. Moreover, since the scattering mechanism is identical, it is reasonable to assume that both quantities are characterized by the same standard deviation σ.

In what follows we use the following notation

$$\mathbf{x}_1 \equiv E_{zr}$$

$$\mathbf{x}_2 \equiv E_{zi}$$

where

$$\mathbf{x}_i \sim \mathcal{N}\left(0, \sigma^2\right) \qquad i = 1, 2 \tag{6.27}$$

Since the quantity of interest is $|E_z|^2$, the PDF of random variable $\mathbf{x}$ will be derived, where

$$\mathbf{x} = \mathbf{x}_1^2 + \mathbf{x}_2^2 \tag{6.28}$$

under the assumption of (6.27). In order to do that, we recall that [161], given n independent and identically distributed random variables $\mathbf{x}_i \sim \mathcal{N}(0, \sigma^2)$, then the distribution of the random variable which equals to the sum of their squares, that is

$$\mathbf{x} = \mathbf{x}_1^2 + \ldots + \mathbf{x}_n^2 \tag{6.29}$$

is chi-square distributed with n degrees of freedom, or

$$f_{\mathbf{x}}(x) = \frac{1}{2\sigma^2} x^{\frac{n}{2}-1} \mathrm{e}^{-\frac{x}{2\sigma^2}}, \qquad x > 0 \tag{6.30}$$

The distribution of (6.30) is designated as $\chi^2(\nu)$. In Fig. 6.5(a) there are the plots of chi-square PDFs for three different degrees of freedom while in Fig. 6.5(b) there are the corresponding CDFs. When $n = 2$, the distribution of $\mathbf{x}$

$$f_{\mathbf{x}}(x) = \frac{1}{2\sigma^2} \mathrm{e}^{-\frac{x}{2\sigma^2}}, \qquad x > 0 \tag{6.31}$$

which is the exponential distribution with parameter $\alpha \equiv \frac{1}{2\sigma^2}$. Therefore, we conclude that quantity $|E_z|^2$ in an RC is exponentially distributed. The same conclusions can be drawn for $|E_x|^2$ and $|E_y|^2$.

Of great importance is the calculation of the exponential distribution parameter, given a set of experimental data $\boldsymbol{x} = (x_1, x_2, \ldots, x_N)$. In order to do that, we make use of the maximum-likelihood estimator (MLE) [161]. According to the theory of

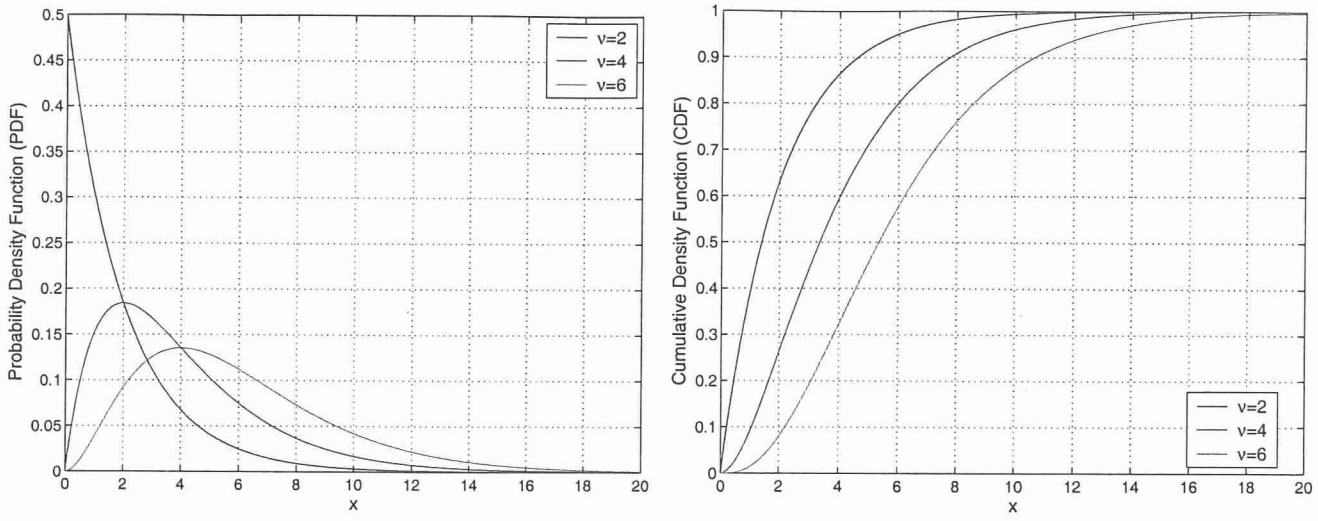

(a) (b)

Figure 6.5: Chi-square distributions: (a) probability density functions (b) cumulative density functions.

MLEs, an estimation of a PDF parameters $\boldsymbol{\alpha} = (\alpha_1, \alpha_2, \ldots, \alpha_M)$ can be made if the quantity

$$L(\mathbf{x}; \boldsymbol{\alpha}) = \prod_{i=1}^{N} f_{\mathbf{x}}(x_i; \alpha) \tag{6.32}$$

is maximized with respect to α, where N is the number of experimental data. In our case the above expression becomes

$$\begin{aligned} L(\mathbf{x}; \hat{\sigma}^2) &= \prod_{i=1}^{N} f_{\mathbf{x}}(x_i; \hat{\sigma}^2) = \\ &= \left(\frac{1}{2\hat{\sigma}^2}\right)^N \mathrm{e}^{-\frac{\sum_{i=1}^{N} x_i}{2\hat{\sigma}^2}} \end{aligned} \tag{6.33}$$

As mentioned before, the parameter $\hat{\sigma}^2$ is such that it maximizes the corresponding likelihood function. Therefore, for its evaluation we solve

$$\frac{\partial}{\partial \hat{\sigma}^2} L(\mathbf{x}; \hat{\sigma}^2) = 0 \tag{6.34}$$

or

$$\frac{\partial}{\partial \hat{\sigma}^2} \ln\left[L(\mathbf{x}; \hat{\sigma}^2)\right] = 0 \tag{6.35}$$

since the logarithm is a monotonic function. From the previous equation, we easily obtain [162]

$$\hat{\sigma}^2 = \frac{\sum_{i=1}^{N} x_i}{2N} = \frac{\bar{\mathbf{x}}}{2} \tag{6.36}$$

3. Probability distributions of $|E_z|$ and $\arg[E_z]$ inside an RC

In order to calculate the PDF of $|E_z|$ the following property of RVs is used [161]:

Given the joint probability density function of the RVs $\mathbf{x}$ and $\mathbf{y}$, $f_{\mathbf{xy}}(x, y)$, then the joint PDF of $\mathbf{z} = \mathbf{g}(\mathbf{x}, \mathbf{y})$ and $\mathbf{w} = \mathbf{h}(\mathbf{x}, \mathbf{y})$ is given by

$$f_{\mathbf{zw}}(z, w) = \frac{f_{\mathbf{xy}}(x_1, y_1)}{|J(x_1, y_1)|} + \ldots + \frac{f_{\mathbf{xy}}(x_n, y_n)}{|J(x_n, y_n)|} \tag{6.37}$$

where $J(x_i, y_i)$ is the Jacobian of the transformation, defined as

$$J(x_i, y_i) = \begin{vmatrix} \frac{\partial z}{\partial x_i} & \frac{\partial z}{\partial y_i} \\ \frac{\partial w}{\partial x_i} & \frac{\partial w}{\partial y_i} \end{vmatrix} \tag{6.38}$$

Recall that, in our case the RV of interest is $|E_z|$ which can be written in terms of its real and imaginary parts as

$$|E_z| = \sqrt{E_{zr}^2 + E_{zi}^2} \tag{6.39}$$

or according to the convention of the previous section

$$|E_z| = \sqrt{\mathbf{x}_1^2 + \mathbf{x}_2^2} \tag{6.40}$$

Hence, given that RVs $\mathbf{x_1}$, $\mathbf{x_2}$ are independent and identically distributed, with Gaussian PDF of zero mean value and equal variance σ^2, their joint PDF is given by

$$f_{\mathbf{x_1 x_2}}(x_1, x_2) = \frac{1}{2\pi\sigma^2} \mathrm{e}^{-\frac{\mathbf{x}_1^2 + \mathbf{x}_2^2}{2\sigma^2}} \tag{6.41}$$

In order to calculate the PDF of the RV $\mathbf{z} = \sqrt{\mathbf{x}_1^2 + \mathbf{x}_2^2}$, we write it in terms of polar coordinates, or

$$\begin{aligned} x_1 &= \rho \sin\phi \\ x_2 &= \rho \cos\phi \end{aligned}$$

Then, from (6.37) and (6.38) we get

$$f_{\rho\phi}(\rho,\phi) = \frac{f_{\mathbf{xy}}(x,y)}{|J(x,y)|} \Rightarrow$$

$$f_{\rho\,\phi}(\rho,\phi) = \frac{1}{2\pi\sigma^2}\,\rho\,\mathrm{e}^{-\frac{\rho^2}{2\sigma^2}} \tag{6.42}$$

From the above equation, we can easily obtain the PDFs of RVs ρ and ϕ by calculating the following integrals[2]:

$$f_\rho(\rho) = \int_0^{2\pi} f_{\rho\phi}(\rho,\phi)\mathrm{d}\phi \tag{6.43}$$

and

$$f_\phi(\phi) = \int_0^{+\infty} f_{\rho\phi}(\rho,\phi)\mathrm{d}\rho \tag{6.44}$$

which lead to

$$f_\rho(\rho) = \frac{1}{\sigma^2}\,\rho\,\mathrm{e}^{-\frac{\rho^2}{2\sigma^2}} \tag{6.45}$$

$$f_\phi(\phi) = \frac{1}{2\pi} \tag{6.46}$$

From the above analysis, the following conclusions can be drawn:

a. RVs $|\mathbf{E_z}| \equiv \rho$ and $\arg[\mathbf{E_z}] \equiv \phi$ are independent since their joint PDF can be written as

$$f_{\rho\phi}(\rho,\phi) = f_\rho(\rho)\, f_\phi(\phi) \tag{6.47}$$

b. The PDF of RV $|\mathbf{E_z}|$, given by (6.45), is chi-square with 2 degrees of freedom $\chi^2(2)$ which is the same as the Rayleigh distribution. The same result can be obtained in several ways[3].

c. The PDF of RV $\arg[\mathbf{E_z}]$, given by (6.46), is uniform over the interval $[0, 2\pi]$

[2]For two independent RVs $\mathbf{x}$ and $\mathbf{y}$, we can calculate the marginal PDF of $\mathbf{x}$ by intergrating their joint PDF with respect to y, i.e $f_x(x) = \int_{-\infty}^{+\infty} f_{xy}(x,y)\,dy$

[3]If RV $\mathbf{x}$ is exponentially distributed, or

$$f_{\mathbf{x}}(x) = \mathrm{e}^{-x/2}, \quad x > 0$$

4. Probability distribution of $|E_z|^2$ inside an RC when there is direct illumination between the transmitting and receiving antennas

The case of direct illumination between the transmitting and receiving antennas inside an RC has recently been investigated [155], [156], [157] and probabilistic expressions have been derived for the field distributions which are in very good agreement with the corresponding measurements. Although in our project such case was not of primary interest, a brief analysis will be given and the probabilistic expressions for the field distribution will be presented.

In [161] it is proven that given two independent normally distributed random variables with the same variance but nonzero mean values, then the probability density function of the random variable

$$\mathbf{y} = \sqrt{\mathbf{x}_1^2 + \mathbf{x}_2^2} \tag{6.49}$$

is the following

$$f_{\mathbf{y}}(y) = \frac{y}{\sigma^2}\, \mathrm{e}^{-\frac{y^2+\mu}{2\sigma^2}}\, I_0\left(\frac{\sqrt{\mu}y}{\sigma^2}\right), \qquad y > 0 \tag{6.50}$$

where $\mu = \mu_1^2 + \mu_2^2$ and $I_0(\cdot)$ is the modified Bessel function of the zeroth-order. Notice that in this case, $\mathbf{x}_1$ and $\mathbf{x}_2$ are normally distributed with *non-zero* mean which is due to the dominant electric field component created by the direct illumination of the two antennas. Now, in order to calculate the probability density function of $\mathbf{x} \equiv \mathbf{y}^2$ we use the following transformation

$$f_{\mathbf{x}}(x) = f_{\mathbf{y}}\left(g^{-1}(x)\right)\left|\frac{g^{-1}(x)}{x}\right| \tag{6.51}$$

---

then the distribution of the RV

$$\mathbf{y} = \sqrt{\mathbf{x}} = \sqrt{\mathbf{z}_1^2 + \mathbf{z}_2^2}$$

is given from the following transform

$$f_{\mathbf{y}}(y) = f_{\mathbf{x}}\left(g^{-1}(y)\right)\left|\frac{dg^{-1}(y)}{dy}\right|$$

In our case $g(x) = \sqrt{x}$ and $g^{-1}(y) = y^2$. So the distribution of RV $\mathbf{y}$ is

$$f_{\mathbf{y}}(y) = 2y\,\mathrm{e}^{-\frac{y^2}{2}}, \quad y > 0 \tag{6.48}$$

which is the Rayleigh distribution.

which is valid provided that

- g is $1-1$ in $S = \{x \in \mathbb{R} : f(x) > 0\}$
- g^{-1} has continuous first derivative in $T = g(S)$

In our case

$$x = g(y) = y^2, \qquad y > 0 \tag{6.52}$$

or

$$y = g^{-1}(x) = \sqrt{x}, \qquad x > 0 \tag{6.53}$$

where it is obvious that both g and g^{-1} satisfy the above conditions. Therefore the probability density function of random variable y is

$$f_{\mathrm{x}}(x) = \frac{1}{2\sigma^2} \mathrm{e}^{-\frac{x+\mu}{2\sigma^2}} I_0\left(\frac{\sqrt{\mu x}}{\sigma^2}\right), \qquad x > 0 \tag{6.54}$$

Thus, we conclude that under the assumption that a line-of-sight exists, the probability density function of $|E_z|^2$ is the one given from (6.54). Notice that the above formula has two parameters to be estimated, μ and σ^2. Therefore the calculation of their MLEs is a rather complicated and difficult task which involves the solution of a system of differential equations with the unknowns being arguments of Bessel functions.

5. Stirrer Efficiency

In this section the relation between the number of stirrer positions and data independence is studied. It can be proved [161] that for large number of data the estimator for the exponential distribution parameter, as given from (6.36), approaches a normal distribution with mean and variance

$$\mathrm{mean}[\hat{\sigma}^2] = \sigma^2 \quad \text{and} \quad \mathrm{var}[\hat{\sigma}^2] = \frac{\sigma^4}{n} \tag{6.55}$$

respectively. Therefore the probability that $\hat{\sigma}^2$ is within k standard deviations $(\frac{\sigma^2}{\sqrt{n}})$ of its mean is given by

$$\Pr\left[|\hat{\sigma}^2 - \sigma^2| < k\frac{\sigma^2}{\sqrt{n}}\right] = \Pr\left[\frac{|\hat{\sigma}^2 - \sigma^2|}{\sigma^2}\sqrt{n} < k\right] = \gamma \tag{6.56}$$

The values of gamma correspond to the desired level of confidence. In probability theory the most common values for γ are 0.99, 0.95 and 0.90. From the normal distribution tables, we get the values of k corresponding to the above values for γ. These values are listed in Table 6.1.

$\gamma = 2\upsilon - 1$	υ	$Z_\upsilon \equiv k$
0.99	0.995	2.58
0.95	0.975	1.96
0.90	0.950	1.65

Table 6.1: Normal distribution, $\Pr[x < k] = \gamma,\ x \sim N(\mu, \sigma^2)$.

Therefore, requiring $\hat{\sigma}^2$ to be within a confidence interval of d dB, we have that

$$d\,\mathrm{dB} = 10 \log \frac{1 + k/\sqrt{n}}{1 - k/\sqrt{n}} \tag{6.57}$$

The above equation is plotted in Fig. 6.6. As expected, the width of the confidence interval approaches 0 dB as the number of independent stirrer positions increases.

Moreover, in order to evaluate that a stirrer provides independent samples, the correlation coefficient is usually calculated. It has to be mentioned that although independent data are also uncorrelated, the opposite is not necessarily true unless the data are normally distributed [161]. The correlation coefficient $\rho_0(r)$ where r is the angular distance between two stirrer positions is calculated according to

$$\rho_0(r) = \frac{1}{N-1} \frac{\sum_N (x_i - \overline{x})(x_{i+r} - \overline{x})}{\sigma_x^2} \tag{6.58}$$

where N is the total number of samples and with $\bar{\cdot}$ we denote ensemble average. The quantitative significance of a measured correlation coefficient ρ_0 can be evaluated by calculating the probability that N measurements of two uncorrelated variables would give correlation coefficients ρ larger than ρ_0. This probability is given by [163], [164]

$$\Pr\left[|\rho| \geq |\rho_0|\right] = \frac{2\Gamma\left(\frac{N-1}{2}\right)}{\sqrt{\pi}\Gamma\left(\frac{N-2}{2}\right)} \int_{|\rho_0|}^{1} \left(1 - \rho^2\right)^{\frac{N-4}{4}} \mathrm{d}\rho \tag{6.59}$$

where N is the number of stirrer positions. Thus if we obtain a correlation coefficient ρ_0 for which $\Pr\left[|\rho| \geq |\rho_0|\right]$ is small, it is unlikely that our variables are uncorrelated,

that is, a correlation is indicated. In particular, if $\Pr[|\rho| \geq |\rho_0|] \leq 0.05$, the correlation is called significant, while if it is less than 0.01, the correlation is called highly significant [163].

In Fig. 6.7 the probability of (6.59) is plotted versus number of stirrer positions N. The value of ρ_0 is equal to e^{-1} because for practical purposes this is the threshold for uncorrelated data. As was expected, the probability to get highly significant correlated data decreases as N increases.

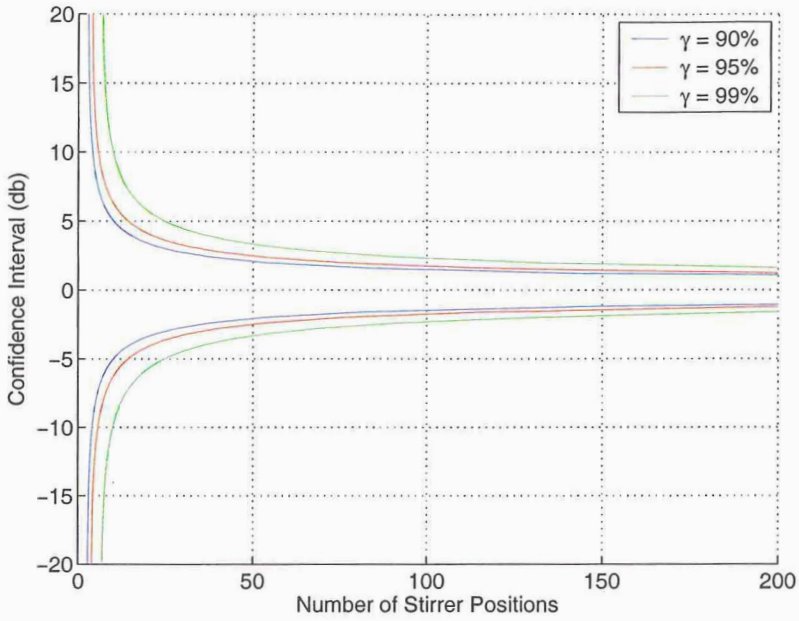

(a) (b)

Figure 6.6: Confidence Interval vs. Stirrer Positions.

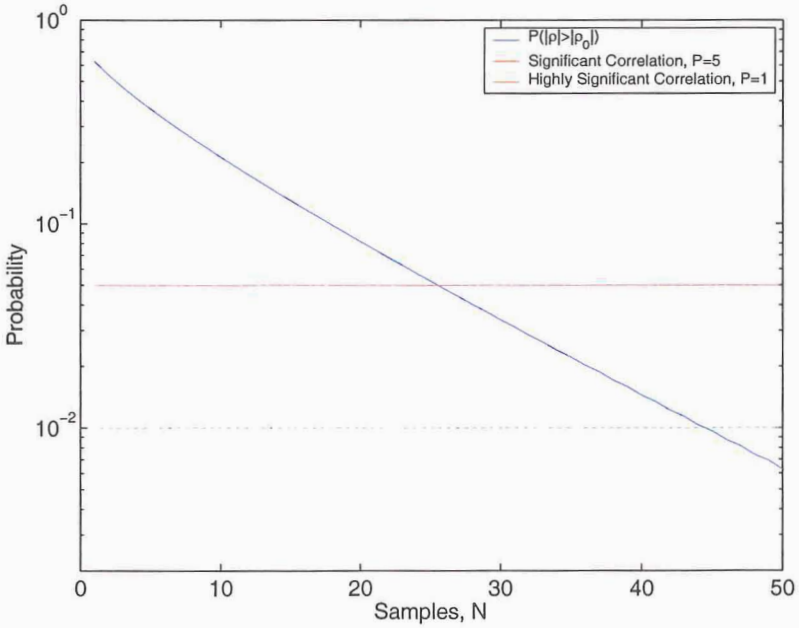

(a) (b)

Figure 6.7: Probability for $|\rho| > |\rho_0| = e^{-1}$.

III. Mode-Stirrer Construction and Measurements

A. Introduction

In past reports, we have demonstrated the ability to perform shielding effectiveness (SE) predictions of the "Simplified Fuselage" scale model using the Finite-Difference Time-Domain (FDTD) method which agreed closely to measurements up to approximately 5 GHz. At higher frequencies, the predictions no longer agreed with the measurements in a precise deterministic sense. There are a number of reasons for the discrepancies between the predictions and measurements at the higher frequencies. The primary factor is the limited FDTD discretization. It was found that the FDTD cell size must be less than $\lambda/16$ for highly accurate predictions on this type of resonant cavity. This is due to the accumulation of phase errors associated with the long propagation distances of the fields "bouncing around" within the cavity. Because the prediction is sensitive to the phaser sum of the reverberating fields, the dispersion errors must be held to a higher tolerance than for most other structures. Since the computer memory requirements using the FDTD increase at a rate approximately proportional to the cube of the cell size (every time the cell size is halved, the solution space increases by a factor of 8), the limits of one's computational resources are quickly reached. Research conducted at ASU into time-domain windowing and the use of sub-cell gridding combined with a hybrid second/fourth-order FDTD has shown promise, but the state-of-the-art FDTD methods and computers are still insufficient to deterministically predict field penetration into a full-scale airliner at frequencies higher than about 1.5 GHz. However, it was found that while the FDTD predictions diverged in the deterministic sense from measured shielding effectiveness at higher frequencies, the predictions continued to exhibit trends (average and peak SE) that were in close agreement with the measurements at frequencies far beyond the previously mentioned 5 GHz. Furthermore, the practical application of High Intensity Radiated Fields (HIRF) studies is not dependent on deterministic accuracy. Thus, a branch of the HIRF research is directed toward a statistical approach.

Currently, our statistical approach is being modeled after reverberation chamber techniques and associated formulation. Our model of an aircraft fuselage is a highly resonant cavity that should be amenable to mode stirring techniques to explore the

statistics of the penetrated fields. This section of the report relates the experimental portion of the mode-stirred shielding effectiveness study conducted with the Simplified Fuselage.

A mode stirrer has been constructed and installed in the Simplified Fuselage. Shielding effectiveness measurements have been performed as a function of mode stirrer orientation over a wide range of frequencies for nose-incident illumination. The resulting SE measurements exhibit promising variation with respect to mode stirrer orientation. These measurements are available for further validation of the FDTD predictions, but also represent a substantial resource of data that could be applied to an experimental consideration of the statistics of the HIRF penetration.

B. The Mode Stirrer

The mode stirrer is comprised of four blades mounted on a "X"-shaped cross piece that is subsequently mounted atop a shaft which passes through the floor of the Simplified Fuselage.

The blades of the mode stirrer are shown in Figure 6.8. They are $0.010''$ thick brass plates which measure $6X10$ cm, $6X12$ cm, $6X14$ cm, and $6X16$ cm. The blades were designed to be asymmetrical to enhance their randomizing effects on the penetrated fields. The edges of the blades are soldered to short lengths of circular-cross-section brass tubing, at 8 cm from one end of each blade. The brass tubing is a tight slip fit into the 0.5 cm square brass tubing cross piece shown in Figure 6.9. This construction enables each blade to be individually oriented in elevation as seen in Figures 6.10 and 6.11, in these measurements and predictions however, the blades are oriented parallel to the shaft. A flat washer was soldered to the circular cross section shaft (also seen in Figures 6.10 and 6.11 at a location along its length which fixes the height of the cross piece at the vertical center of the Simplified Fuselage. A hole was drilled through the floor of the Simplified Fuselage through which the mode stirrer shaft passes. This hole is located at the port / starboard center, 50 cm from the nose. After the shaft passes through the hole in the floor, a spring is passed over the end and is captured by a small rod that fits through a hole in the shaft. The spring holds the entire assembly tightly against the floor of the model. The rod not only captures the spring,

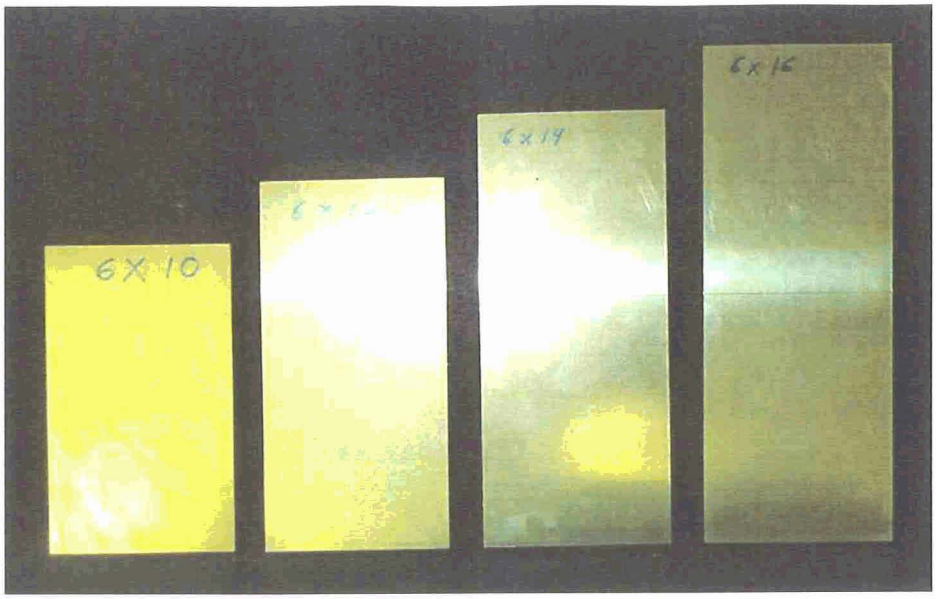

Figure 6.8: The mode stirrer blades are made from 0.010″ thick brass. Their asymmetrical dimension are intended to enhance the randomization of the penetrated fields.

but also acts as an external indicator of the mode stirrer's orientation, and as part of the interface to the positioner turntable for automation of the mode stirrer orientation.

C. Measurements

Yet again, the mode-stirred shielding effectiveness measurements were performed in much the same manner as described in previous reports and in the section of this report concerning the measurements of the cylindrical fuselage.

The two significant differences between these and previous measurements are the calibration and the use of the mode stirrer. In previous measurements, the results could only be formulated in terms of shielding effectiveness because the penetration and the frequency response of the reference monopole were not calibrated measurements. The frequency responses of the feed antennas, cabling, instrumentation, etc. were normalized out when the ratio of the monopole measurements to the penetration measurements were made to form the shielding effectiveness. In contrast, a set of calibration coefficients were computed from measurements of gain standards. These

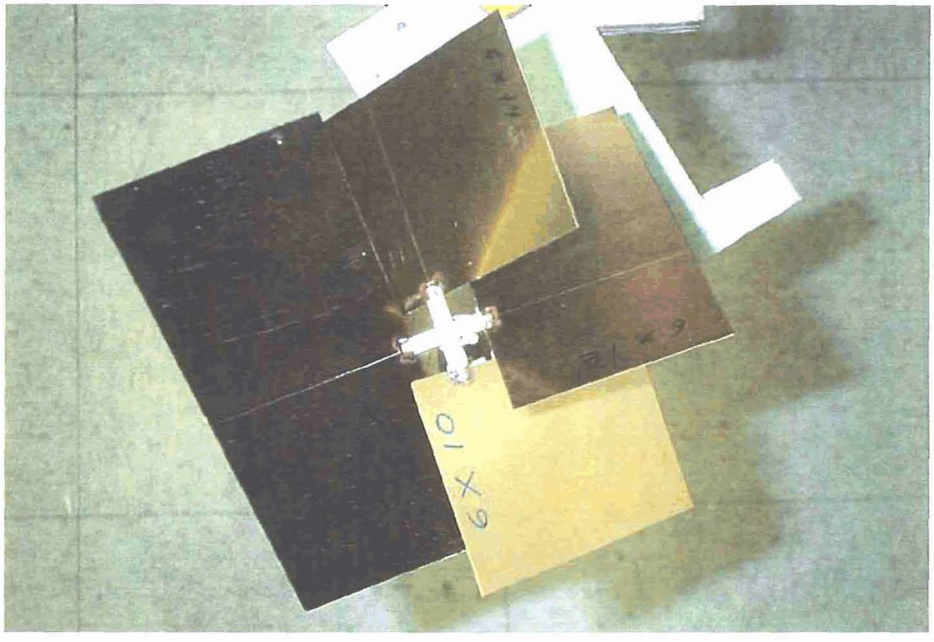

Figure 6.9: The brass cross piece is constructed with 0.5 cm square tubing. Short lengths of brass tubing soldered to the edges of each blade are tight slip fits into the ends of the cross piece.

calibration coefficients can be applied to the monopole and Simplified Fuselage measurements to compute absolute far-field gain values. In other words, if desired, both the measurements and predictions can be formulated as the far-field gain, in the nose direction, as a function of mode stirrer orientation when the interior probe is excited. This is clearly the reciprocal of the penetration observed at the probe location when the model is illuminated from the far field and from the nose direction. What is not clear is how to relate this far-field gain to penetration field values in volts/meter. However, the far-field gain can be computed directly with the FDTD, and it is directly proportional to the penetration.

The other substantial difference is the implementation of the mode stirrer. Changes in the mode stirrer orientation were automated by interfacing it with the azimuthal turntable of the positioner. One end of a dielectric shaft was connected to the turntable, the other end was slotted to accept the metal bar through the brass shaft of the mode stirrer. A photograph of the set up is shown in Figure 6.12. The measurements were performed in one-gigahertz bands up to 13 GHz, where each band contains 801 frequency points.

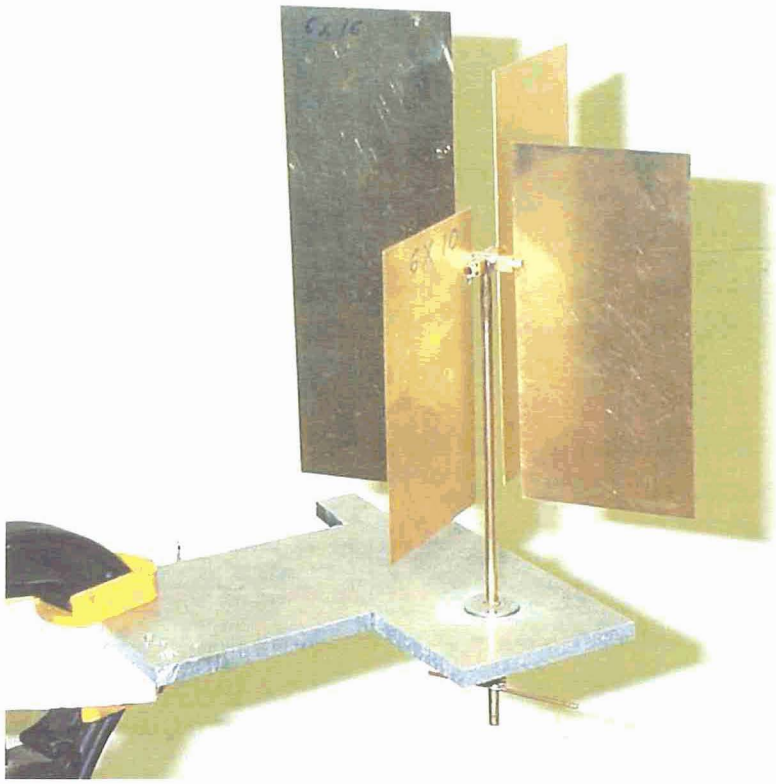

Figure 6.10: The construction was designed to enable the variable orientation of each blade in elevation.

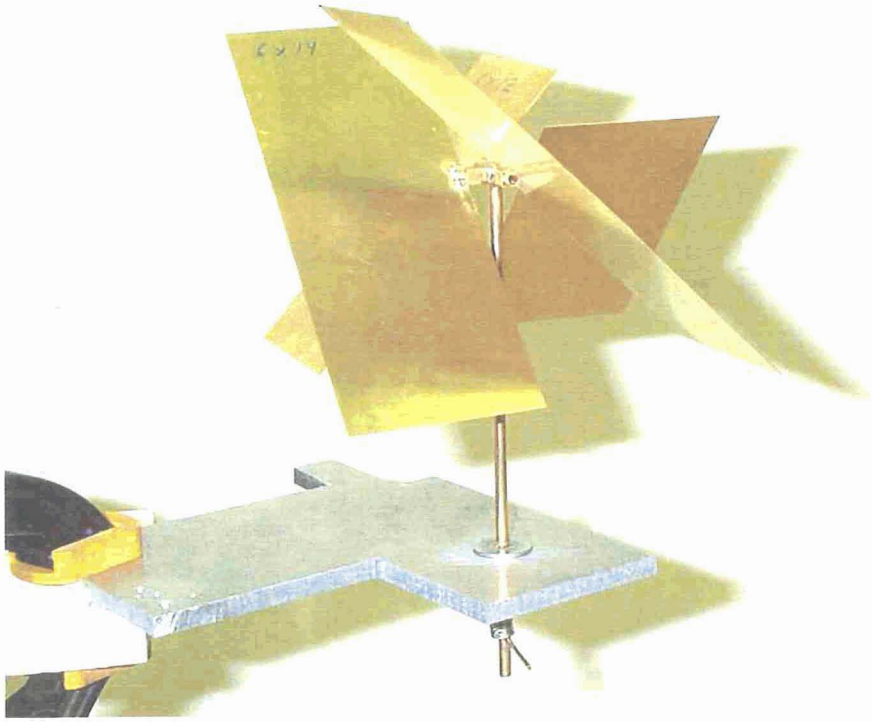

Figure 6.11: Here, the blades are shown at approximately 45° elevation angle.

The penetration was measured using 6 cm long vertical wire probes installed in the floor of the model. Three of the probes were installed on the port / starboard center at distances from the nose of 25 cm, 100 cm, and 125 cm (designated Probes A, C, and D, respectively). A fourth probe was installed at 100 cm from the nose and 5 cm to the port of center. This probe is designated as Probe B. All four probes were present during the measurements.

Some examples of the measured variations in relative field penetration as a function of mode stirrer orientation are shown in Figures 6.13 and 6.14. The calibrated penetration versus frequency at probe B and with the mode stirrer fixed at 0° is shown in Figure 6.15.

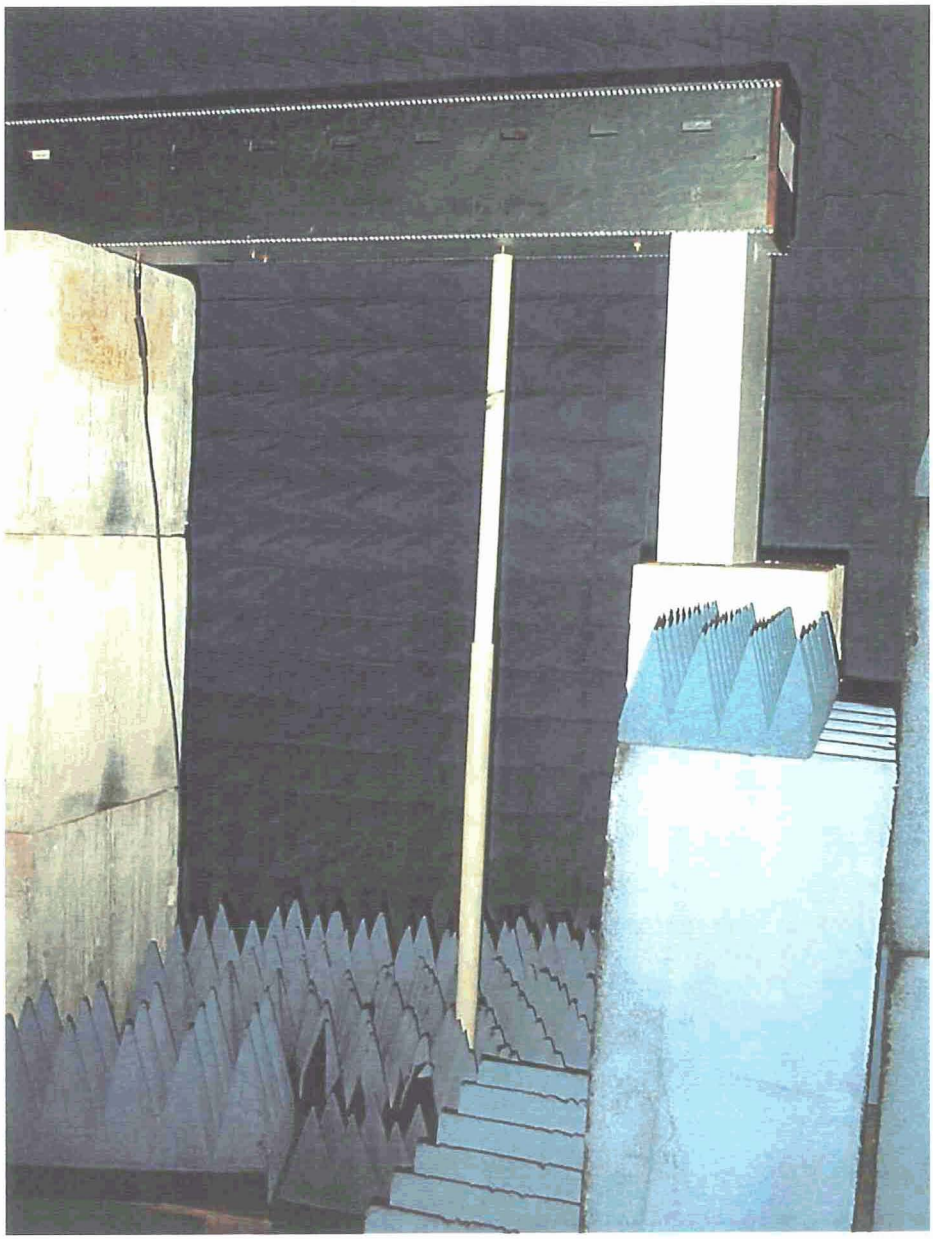

Figure 6.12: This photograph shows the expanded polystyrene blocks supporting the Simplified Fuselage, and the dielectric shaft which connects the positioner to the mode stirrer.

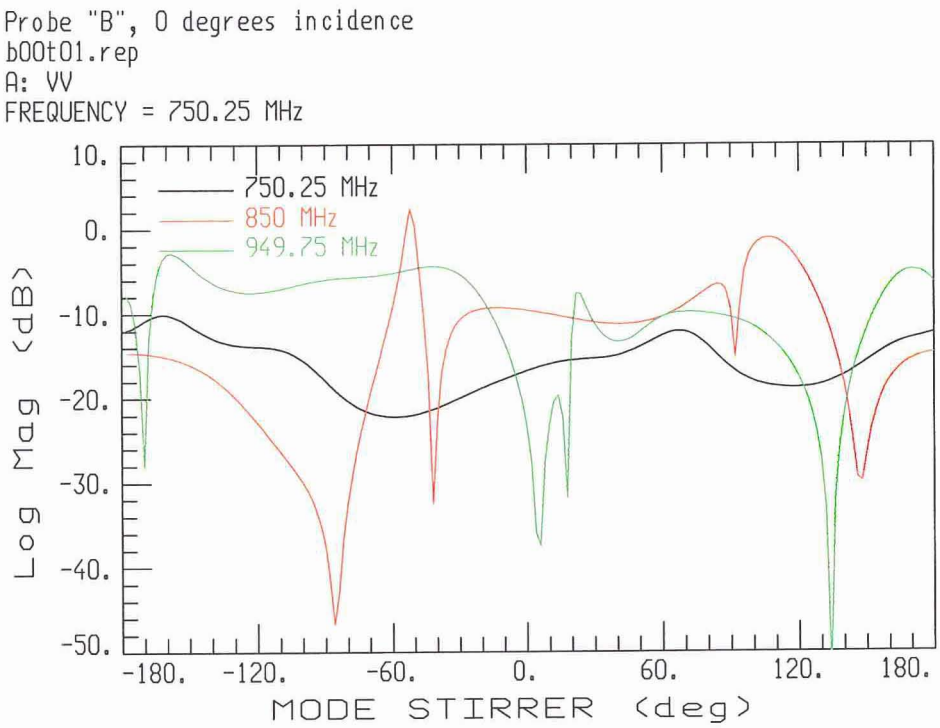

Figure 6.13: The measured relative variations of field penetration at Probe B with respect to mode stirrer orientation.

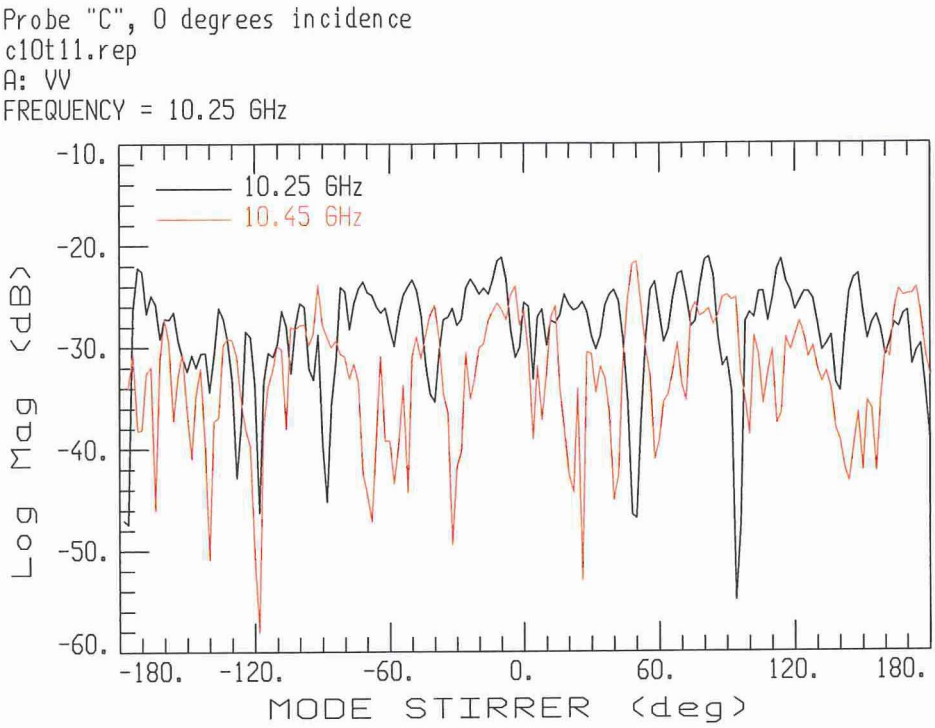

Figure 6.14: The measured relative variations, with respect to mode stirrer orientation, of the field penetration at Probe C.

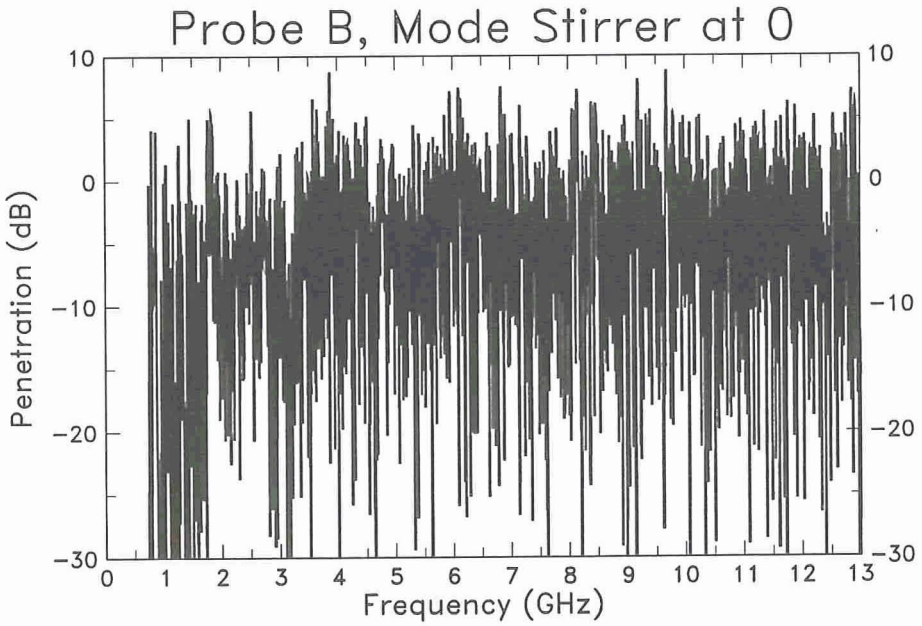

Figure 6.15: The calibrated penetration measured at probe B when the mode stirrer orientation is fixed at 0° versus frequency.

D. Predictions and Comparisons

In this section, predictions of the shielding effectiveness for the simplified fuselage with the mode-stirrer are presented. All the predictions are performed using the standard FDTD scheme, and they are compared with measurements. Predictions are performed for an azimuthal angle of 0° (nose incidence) and with the mode-stirrer at its initial position. Predictions and measurements are compared for probe locations A, B, C and D. The CAD model of the simplified fuselage with the mode-stirrer along with the four probes is shown in Fig. 6.16 while the measurement setup at the ASU EMAC is shown in Fig. 6.17. The comparisons of shielding effectiveness (SE) are based on the definition described by *procedure* #2 presented previously in this report. All FDTD predictions are performed using a cell size of 2.5 mm (or $\lambda/10$ at 12 GHz). Therefore it is expected that these FDTD calculations will provide accurate results at most up to 12 GHz. Due to the special geometrical features of our model (shaft, cross holding the paddles), we were required to use such a fine discretization in order to model accurately enough the geometry. The results are illustrated in Fig. 6.18 through Fig. 6.33. It can be seen that the FDTD results are in very good agreement with the measurements up to 6 GHz for all four points. Discrepancies between the measurements and the predictions are observed in the last frequency bands [see Figs. 6.21(a) and (b), Figs. 6.25(a) and (b), Figs. 6.29(a) and (b), Figs. 6.25(a) and (b)]. These inaccuracies are attributed to FDTD dispersion errors. This happens because the fuselage is electrically large causing accumulation of dispersion errors which significantly restrict the accuracy of the computational method. Also it has to be mentioned that the stirrer geometry is very complicated and hence difficult to be modeled accurately. Furthermore, during the measurements, the mode-stirrer may not have been totally aligned and set exactly at its initial position. All these are possible reasons that create extra discrepancies between predictions and measurements.

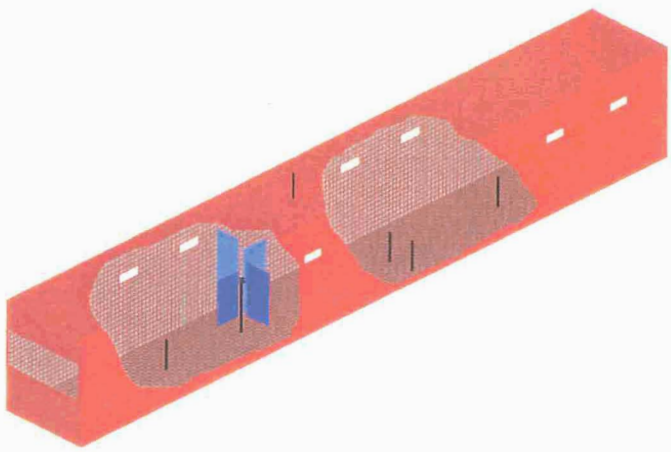

Figure 6.16: Simplified scale model fuselage with the mode-stirrer and the four probes

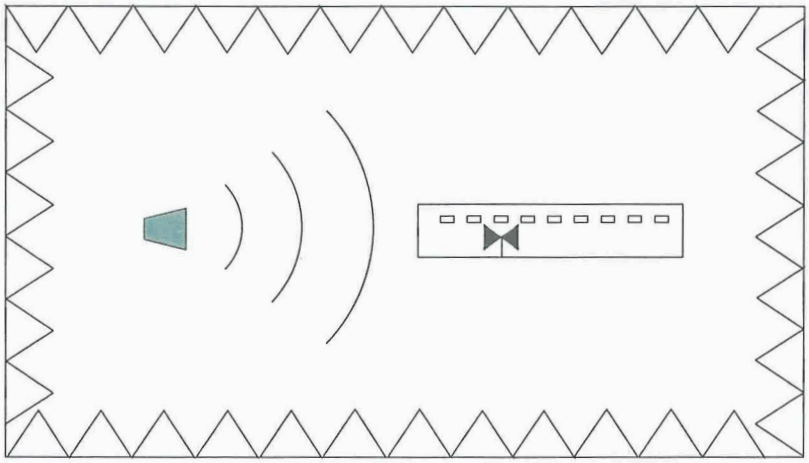

Figure 6.17: Measurement setup at ASU EMAC

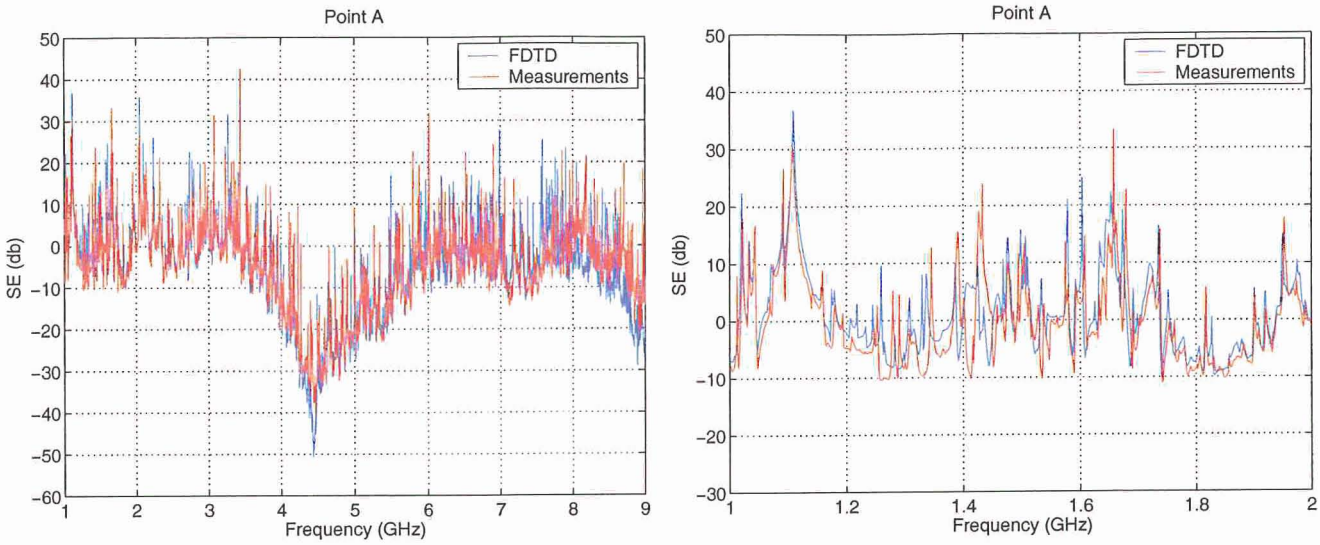

(a) (b)

Figure 6.18: Shielding effectiveness of the scaled fuselage with the mode-stirrer for azimuthal incident angle of 0° at probe A

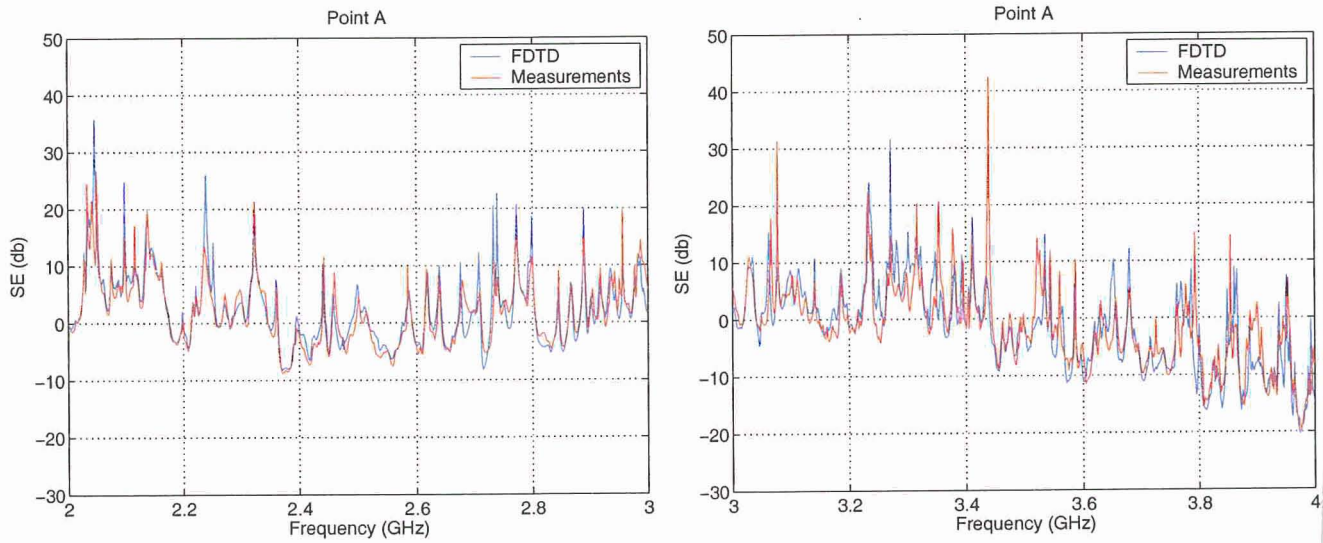

(a) (b)

Figure 6.19: Shielding effectiveness of the scaled fuselage with the mode-stirrer for azimuthal incident angle of 0° at probe A

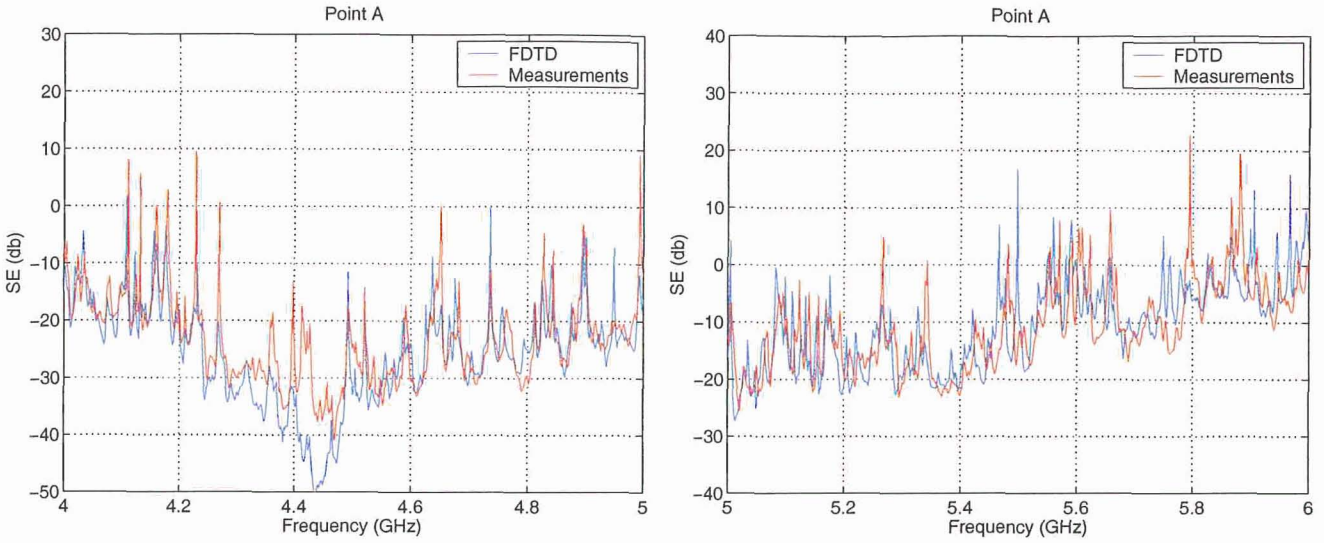

(a) (b)

Figure 6.20: Shielding effectiveness of the scaled fuselage with the mode-stirrer for azimuthal incident angle of 0° at probe A

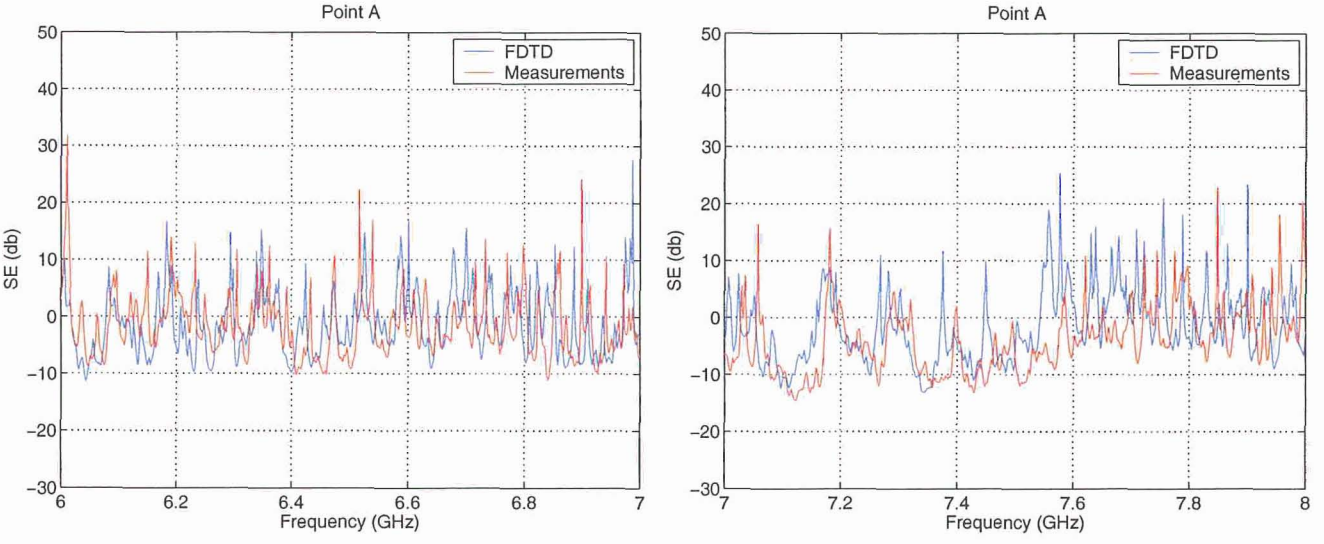

(a) (b)

Figure 6.21: Shielding effectiveness of the scaled fuselage with the mode-stirrer for azimuthal incident angle of 0° at probe A

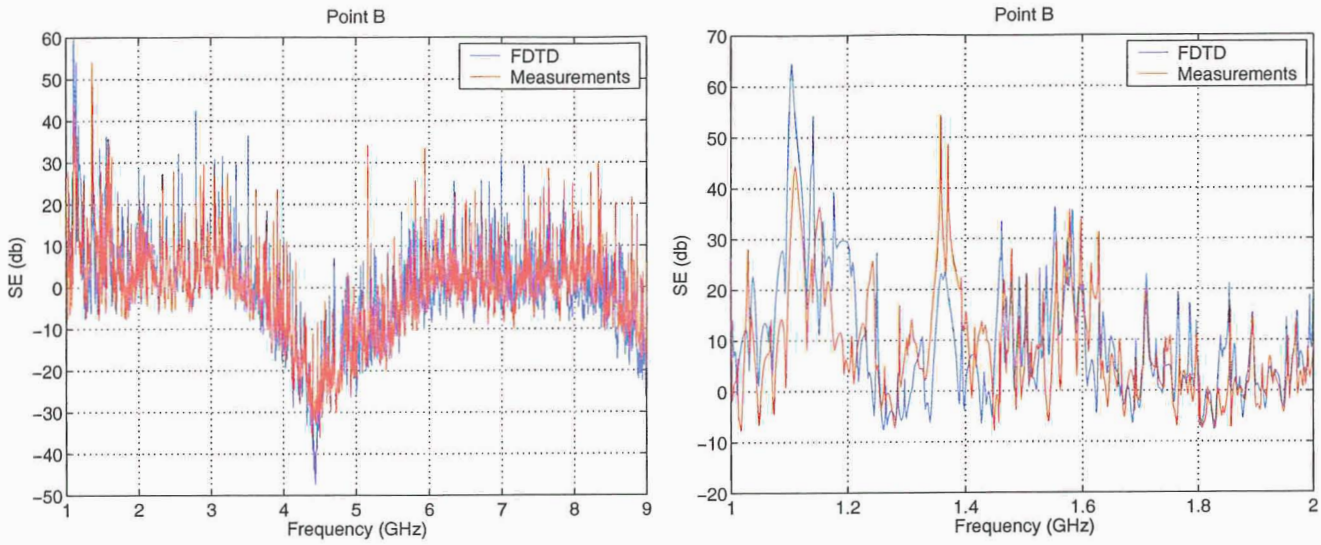

(a) (b)

Figure 6.22: Shielding effectiveness of the scaled fuselage with the mode-stirrer for azimuthal incident angle of 0° at probe B

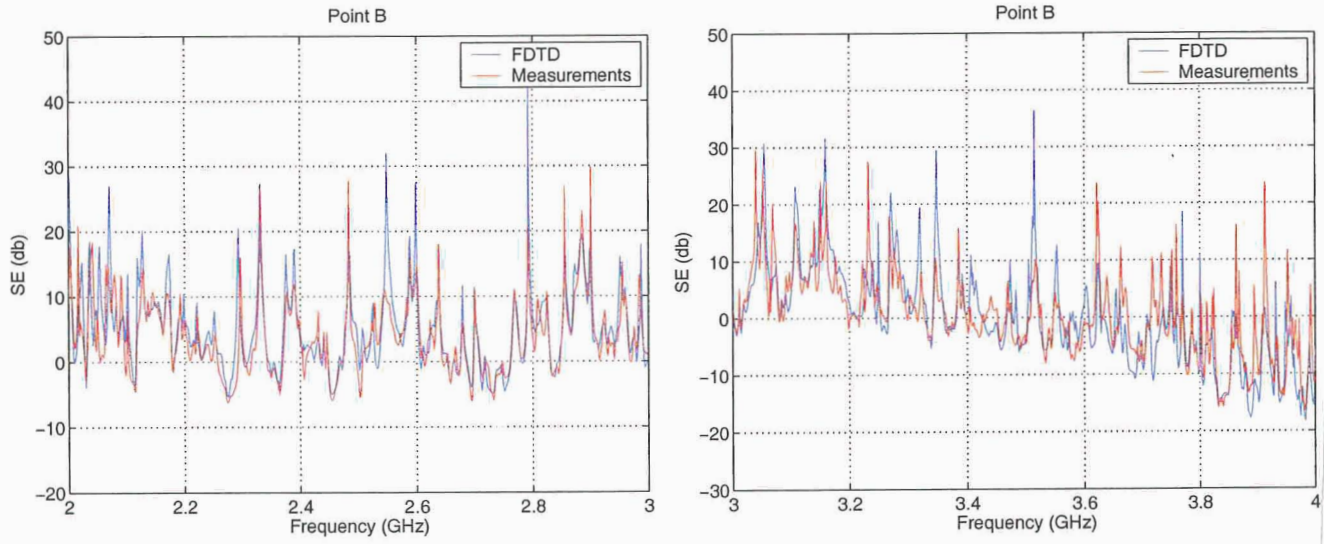

(a) (b)

Figure 6.23: Shielding effectiveness of the scaled fuselage with the mode-stirrer for azimuthal incident angle of 0° at probe B

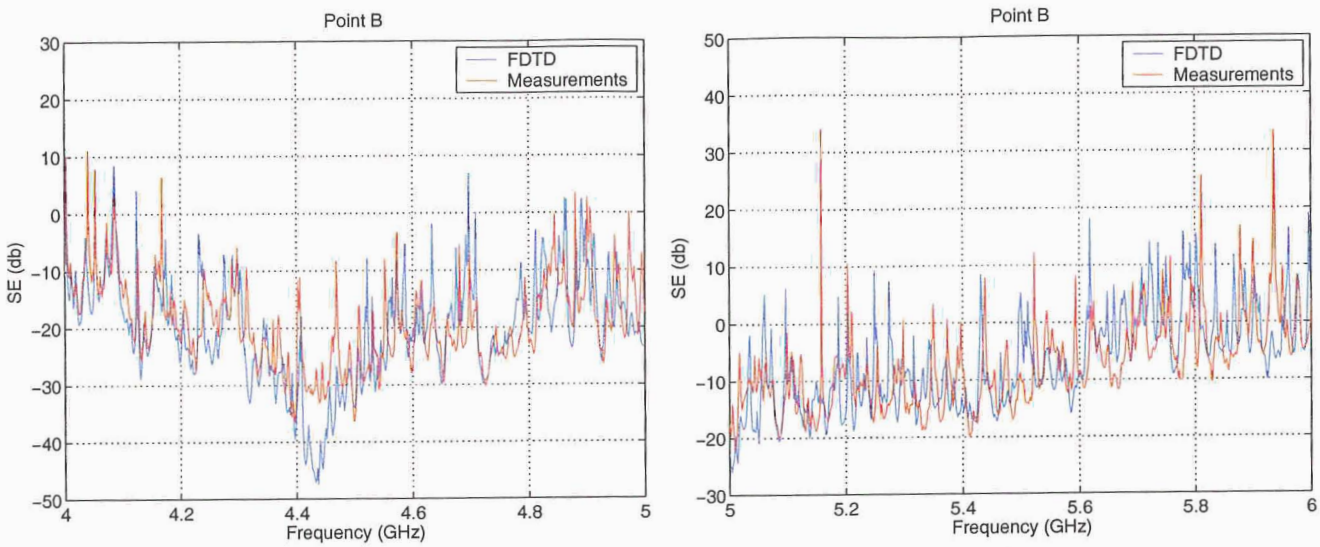

(a) (b)

Figure 6.24: Shielding effectiveness of the scaled fuselage with the mode-stirrer for azimuthal incident angle of 0° at probe B

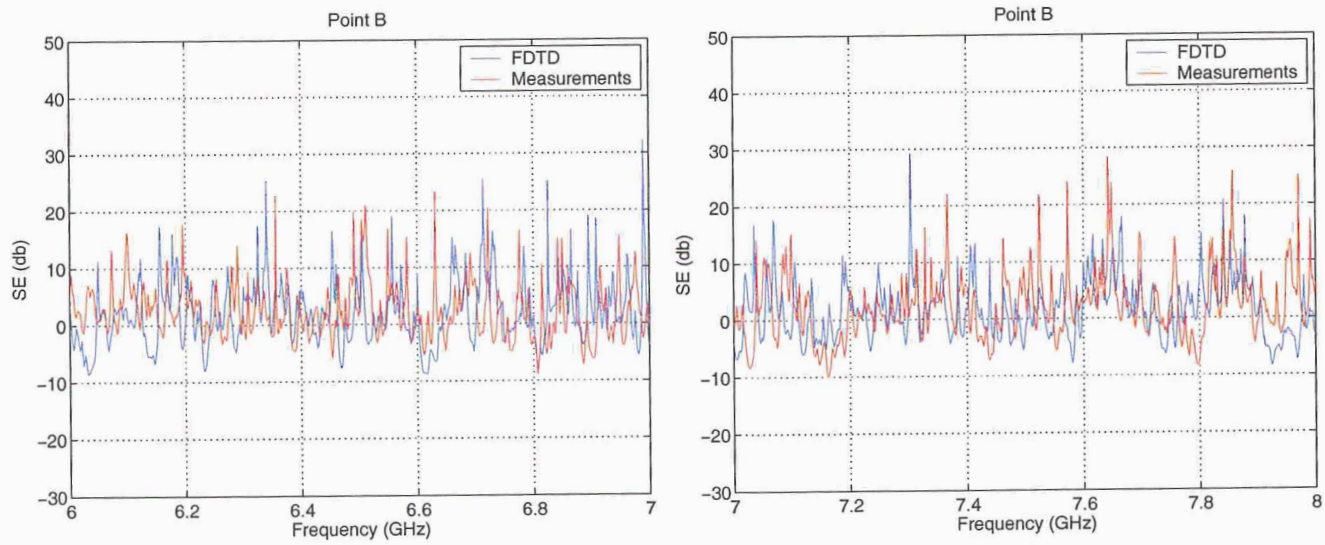

(a) (b)

Figure 6.25: Shielding effectiveness of the scaled fuselage with the mode-stirrer for azimuthal incident angle of 0° at probe B

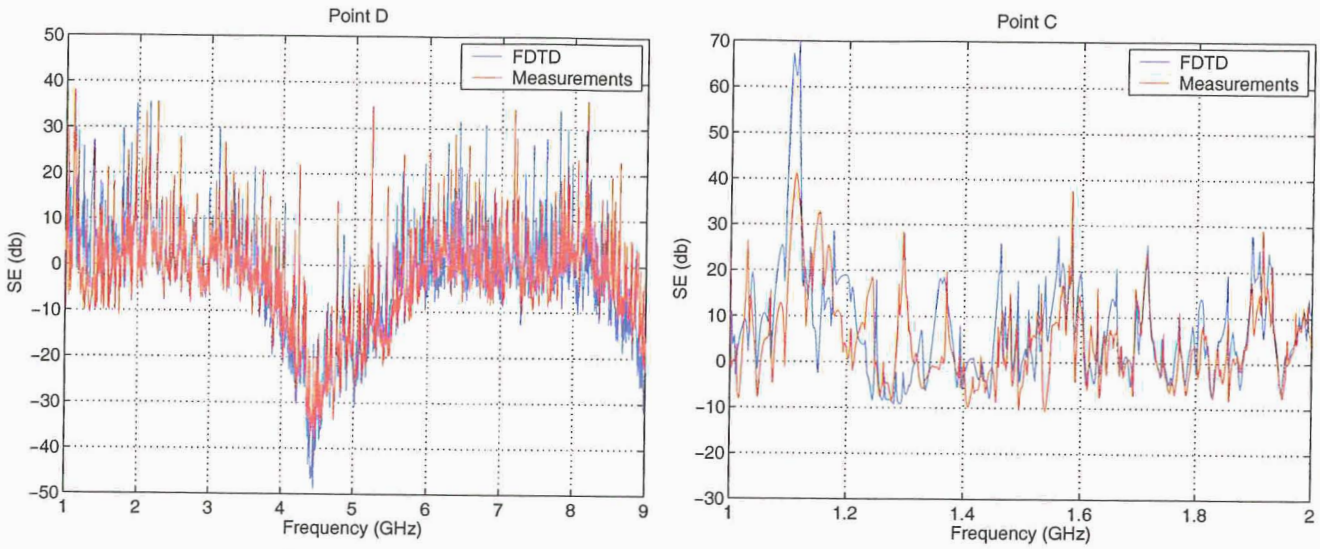

(a) (b)

Figure 6.26: Shielding effectiveness of the scaled fuselage with the mode-stirrer for azimuthal incident angle of 0° at probe C

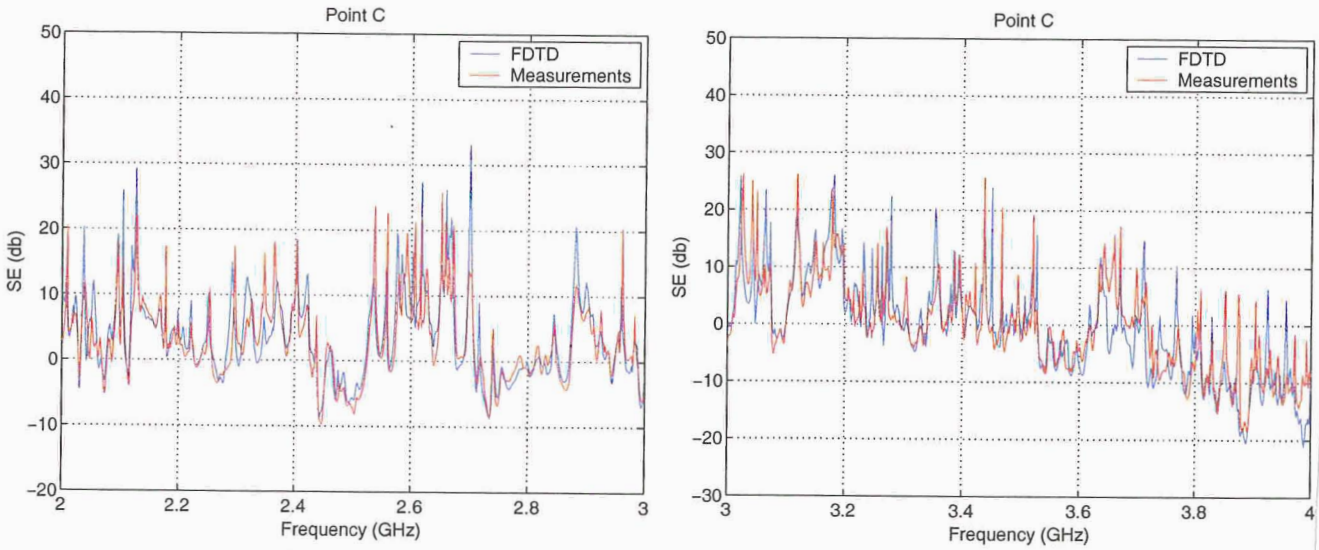

(a) (b)

Figure 6.27: Shielding effectiveness of the scaled fuselage with the mode-stirrer for azimuthal incident angle of 0° at probe C

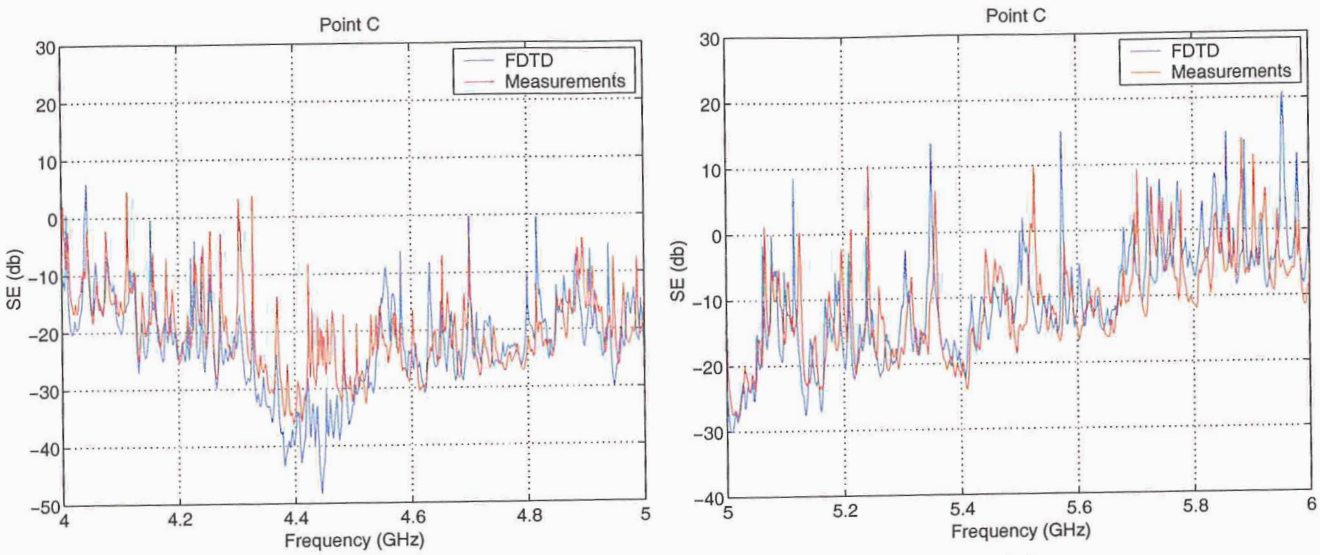

Figure 6.28: Shielding effectiveness of the scaled fuselage with the mode-stirrer for azimuthal incident angle of 0° at probe C

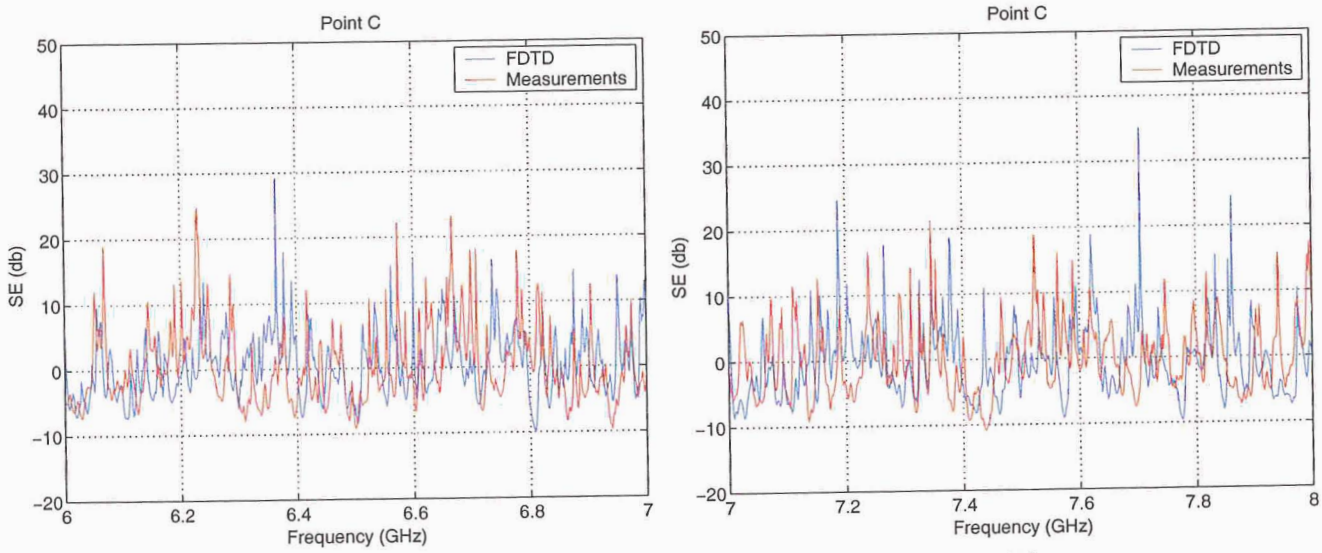

Figure 6.29: Shielding effectiveness of the scaled fuselage with the mode-stirrer for azimuthal incident angle of 0° at probe C

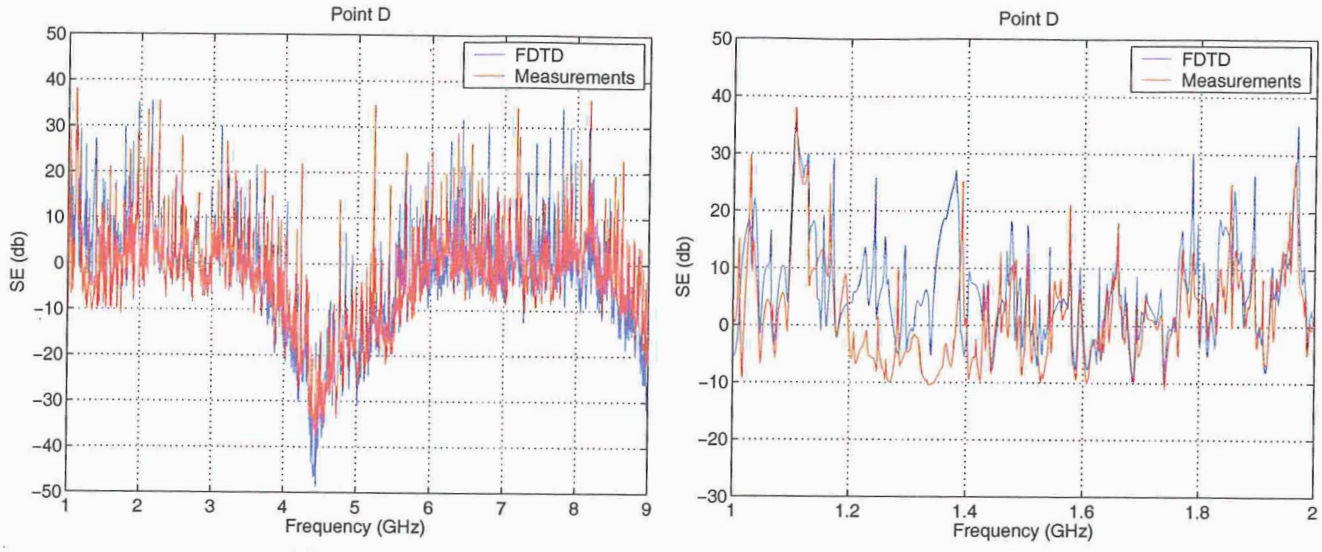

(a) (b)

Figure 6.30: Shielding effectiveness of the scaled fuselage with the mode-stirrer for azimuthal incident angle of 0° at probe D

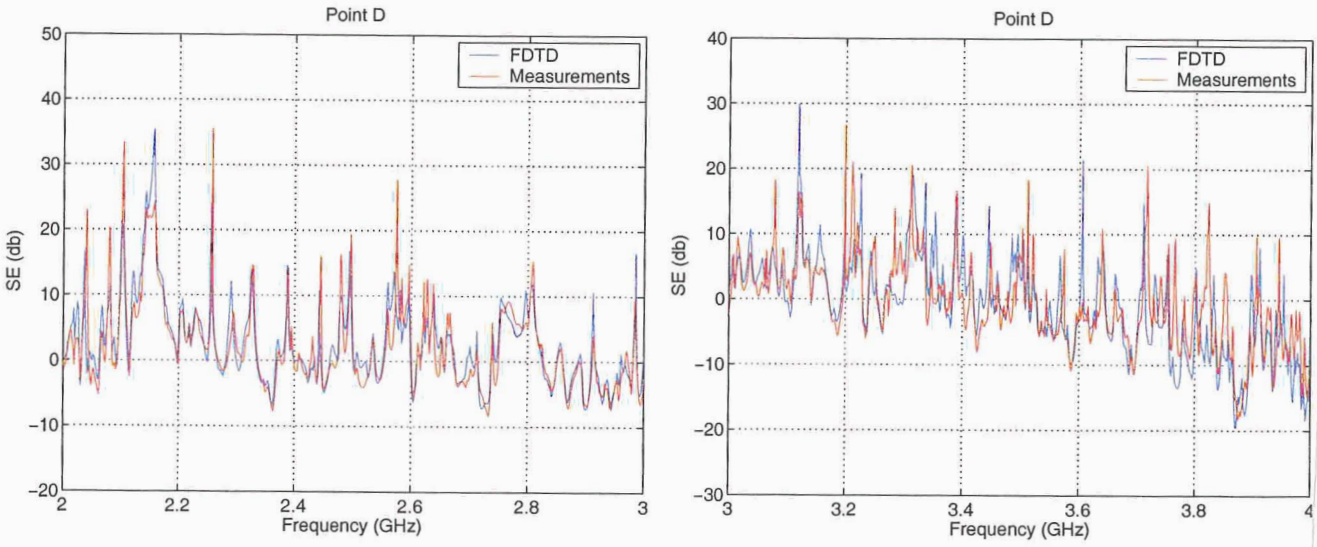

(a) (b)

Figure 6.31: Shielding effectiveness of the scaled fuselage with the mode-stirrer for azimuthal incident angle of 0° at probe D

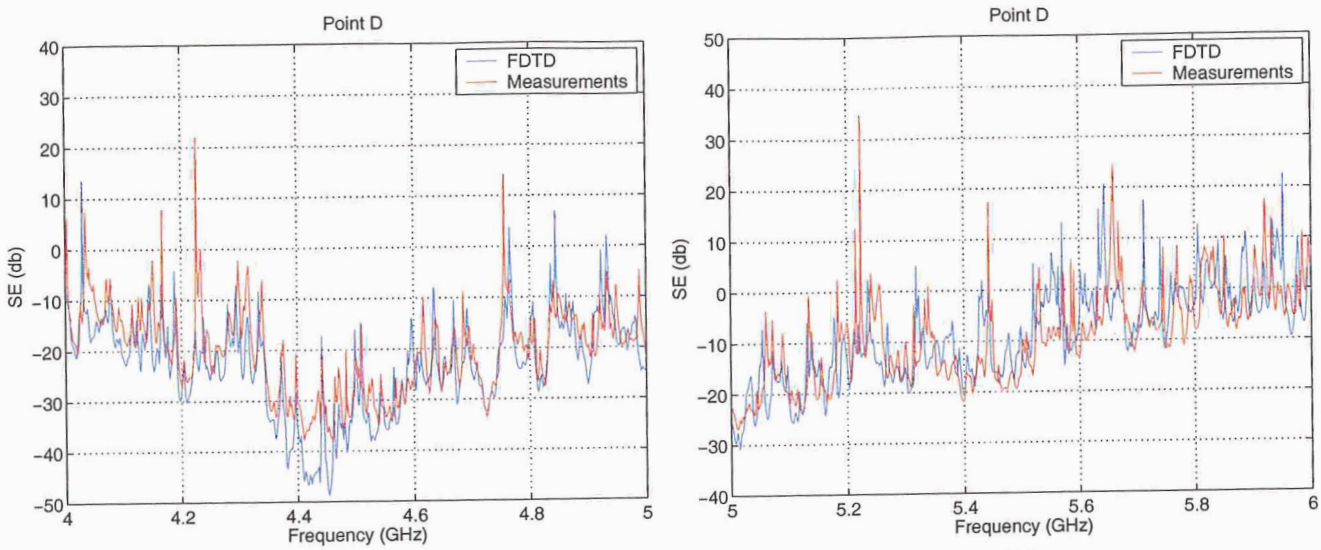

(a) (b)

Figure 6.32: Shielding effectiveness of the scaled fuselage with the mode-stirrer for azimuthal incident angle of 0° at probe D

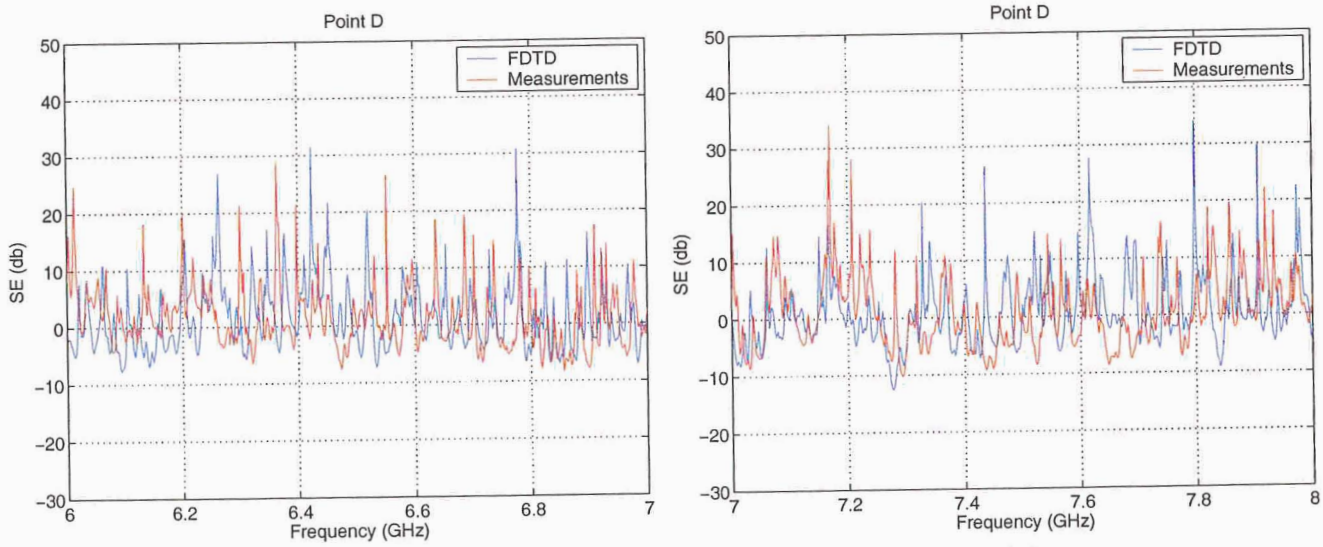

(a) (b)

Figure 6.33: Shielding effectiveness of the scaled fuselage with the mode-stirrer for azimuthal incident angle of 0° at probe D

IV. Statistical and Probabilistic Analysis of Measurements

A. Introduction

In this section, data obtained from measurements are statistically processed and results are presented. Initially, a basic statistical analysis is performed where the maximum, mean and minimum value of data obtained from measurements are calculated. Results are presented in tabular, as well as in graphical form. Moreover, two alternative definitions for SE are proposed. The first one, is based on the maximum observed cavity response, over all stirrer positions, while the second one is based on the mean value, of the measurements over all stirrer positions. The new SE definitions are designated as SE_{max} and SE_{mean}, respectively. The SE for each probe location is calculated, using both definitions, and the results are plotted versus frequency. Furthermore, the mode-stirrer effectiveness is demonstrated. In order to do that, the SE at each probe location is compared, after being calculated with two different ways. The first one is according to the standard SE calculation methodology, as described in previous chapters, and it is performed without the mode-stirrer installed. The second one is based on SE_{max}, as described above.

Next, a more advanced statistical analysis is presented, based on probability theory. Data independency test is performed and from the results the ability of the mode-stirrer to create a sufficient reverberant electromagnetic environment is demonstrated. Also, the theoretical principles of the independence test are briefly discussed. Moreover, elements of RC theory, as presented in the previous section, are used in order to test whether our data is distributed according to the theoretical expected distributions. Theoretical expected distributions and experimental data distributions are compared using a goodness-of-fit test. Results are presented in tabular form while a brief description of the goodness-of-fit test theory is given. In addition, the distribution of SE is investigated. The formula of its distribution is derived and plotted along with the distribution of experimental data.

B. Basic Statistical Processing

In this section, basic statistical quantities are calculated which give an indication of the stirrer effectiveness, as well as the field fluctuation, versus stirrer position and frequency, in the fuselage. First the maximum, mean average and standard deviation were computed for each probe location, for certain frequencies, over all stirrer orientations. For 1, 2, 3, 4, 5, 6, 7 and 8 GHz the results are analytically presented in Table 6.2, while in Figs. 6.34 and 6.35 the variations of the maximum and minimum electric field values are plotted versus frequency for all probe locations. It is really impressive that the maximum field value is almost constant for all frequencies that the stirrer is effective enough (greater than 1 GHz). Also, it can be observed that for the same probe location, the mean average values differ only a few dBs ($< 5\,\text{dB}$) between different frequencies, while same observations can be made for the mean value variations for different probe locations but fixed frequency.

In Table 6.3, the mean values of the maximum electric field along with its standard deviations are summarized. As mentioned before, the difference between the mean values at each point is less than 2 dB. This is an indication that field in the fuselage is characterized by the same mean value. Also, notice the standard deviation of the field is almost the same at all four points which is an evidence that the field fluctuations are the same at the four different probe locations. Of course this result cannot be used *a priori* for any location in the fuselage. The fuselage geometry is rather asymmetrical compared to that of an actual RC; therefore, the uniformity property is not "by default" applicable to our case. More probing locations and in different orientations may give more information regarding to the behavior the mean value everywhere in the fuselage, given that a volume analogous to the RC TEST VOLUME cannot be created in the fuselage, strictly speaking.

C. Shielding Effectiveness: The Statistical Approach

An intrinsic limitation of the SE, as has been defined so far, is that it is not representative of the overall cavity shielding because it strongly depends on frequency, position and angle of incidence. In order to overcome the limitations of position and incidence angle, two alternative and more general SE definitions are introduced. The first one, is based on the maximum measured electric field value, over all stirrer

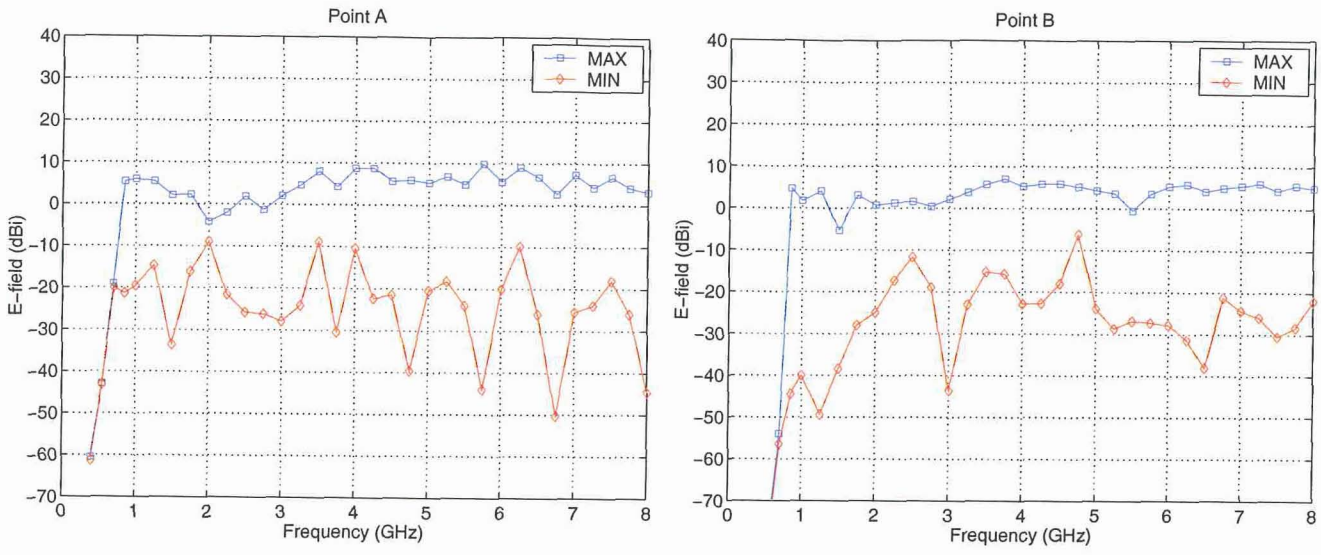

Figure 6.34: Maximum and minimum E-field variation vs. frequency for points A and B.

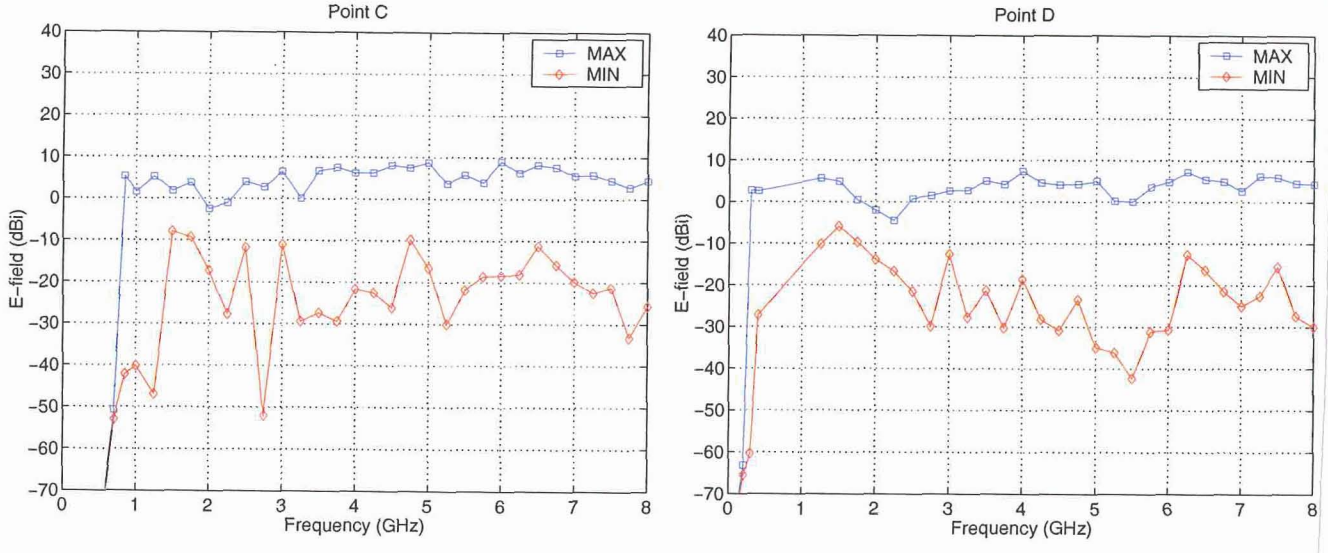

Figure 6.35: Maximum and minimun E-field variation vs. frequency for points C and D.

	Frequency (GHz)	Maximum (dB)	Minimum (dB)	Mean average (dB)	Standard deviation (dB)
Point A	1	6.12	-19.28	3.99	0.44
	2	-4.04	-8.78	-5.28	-12.08
	3	2.12	-28.60	-4.21	-4.97
	4	8.44	-10.32	3.56	2.23
	5	5.19	-20.36	-1.78	-1.48
	6	4.57	-19.08	-1.19	-2.36
	7	7.33	-24.55	0.80	0.71
	8	2.21	-29.67	-3.26	-3.72
Point B	1	2.03	-41.32	-6.60	-4.07
	2	0.86	-24.44	-5.89	-5.45
	3	2.18	-41.75	-4.59	-4.40
	4	4.91	-23.62	-0.89	-1.64
	5	4.17	-24.44	-2.17	-2.31
	6	4.56	-24.03	-0.54	-1.30
	7	5.55	-24.50	-3.03	-2.53
	8	4.56	-16.09	-2.05	-2.39
Point C	1	1.77	-41.67	-5.78	-4.02
	2	-2.27	-17.00	-6.64	-8.75
	3	6.52	-11.04	-0.93	-0.52
	4	6.05	-22.42	0.37	-0.09
	5	8.64	-17.15	2.69	1.75
	6	8.26	-12.28	3.11	1.49
	7	5.72	-19.46	-1.88	-2.32
	8	5.88	-41.05	-1.36	-1.40
Point D	1	2.78	-27.04	-4.20	-3.00
	2	-1.81	-13.74	-4.61	-8.13
	3	2.69	-12.55	-1.11	-3.98
	4	7.23	-20.00	-0.15	0.11
	5	4.88	-35.07	-2.48	-1.93
	6	4.06	-46.20	-2.39	-2.97
	7	2.76	-24.56	-3.70	-4.18
	8	5.48	-32.07	-3.18	-2.44

Table 6.2: Maximum, minimum, mean average and standard deviation, over all stirrer positions, of the electric field for points A, B, C and D, for different frequencies.

Point	mean average (dB)	standard deviation (dB)
A	5.23	3.44
B	3.68	6.15
C	4.35	5.29
D	4.23	5.59

Table 6.3: Mean average and standard deviation values of the maximum electric field value.

positions, while the second is based on the mean average value over all stirrer positions. The modified SEs are given from the following formulas:

$$SE_{max} = 20 \log \left(\frac{\text{empty space frequency response}}{\text{problem space frequency } \mathbf{max} \text{ response}} \right) \tag{6.60}$$

and

$$SE_{mean} = 20 \log \left(\frac{\text{empty space frequency response}}{\text{problem space frequency } \mathbf{mean} \text{ response}} \right) \tag{6.61}$$

For each probe location, the SE was calculated based on the above formulas and corresponding plots are shown in Figs. 6.36 and 6.37. It can be observed that for certain frequencies the SE_{max} is 10 dB less than SE_{mean}. This observed difference is the advantage that this pair of definitions offers. More precisely, this difference between SE_{max} and SE_{mean}, for a certain frequency, can be used as a benchmark for an EMC engineer, in order to have electronic equipment working within a safety margin that will assure its immunity. It has to be mentioned that for more accurate prediction of this safety margin, a more effective mode-stirrer should be designed and used. A mode-stirrer is considered effective when it can scatter fields *evenly* in all directions. Also, the higher maximum field values can be achieved inside the cavity the more effective the stirrer is. In what follows, two figures-of-merit regarding mode-stirrer effectiveness are presented. As a final comment on the variations of the maximum and minimum field values, it can be observed that for low frequencies the two values are almost identical which is an indication that the stirrer is not that effective in these frequencies. Moreover, all four points exhibit almost the same maximum and mean values.

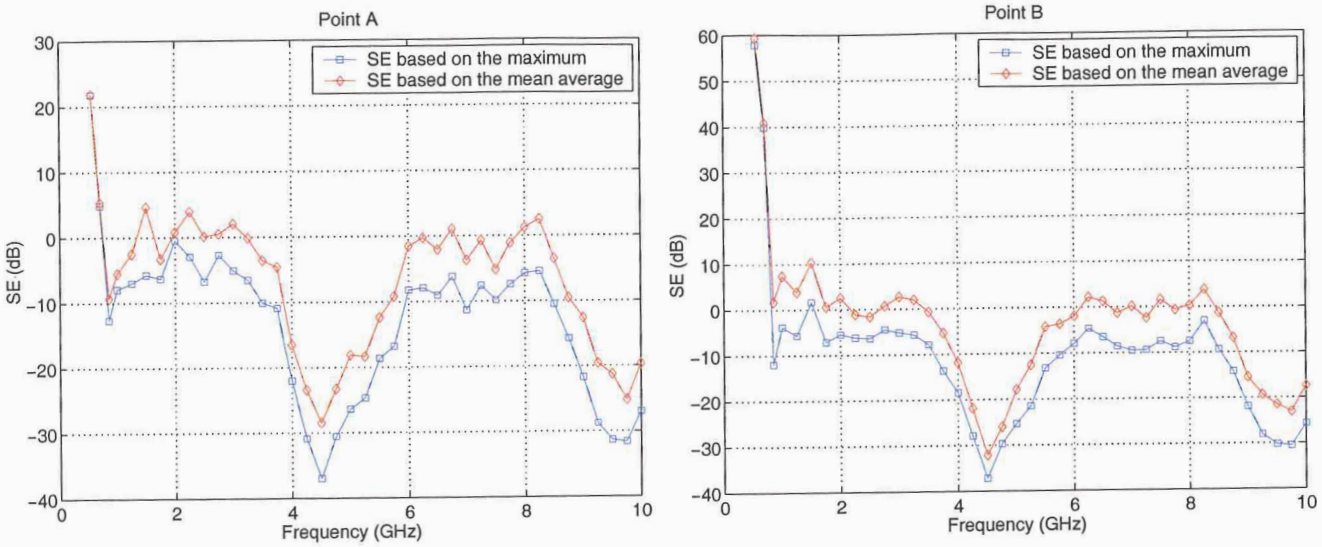

Figure 6.36: Maximum and mean SE variation versus frequency, points A and B.

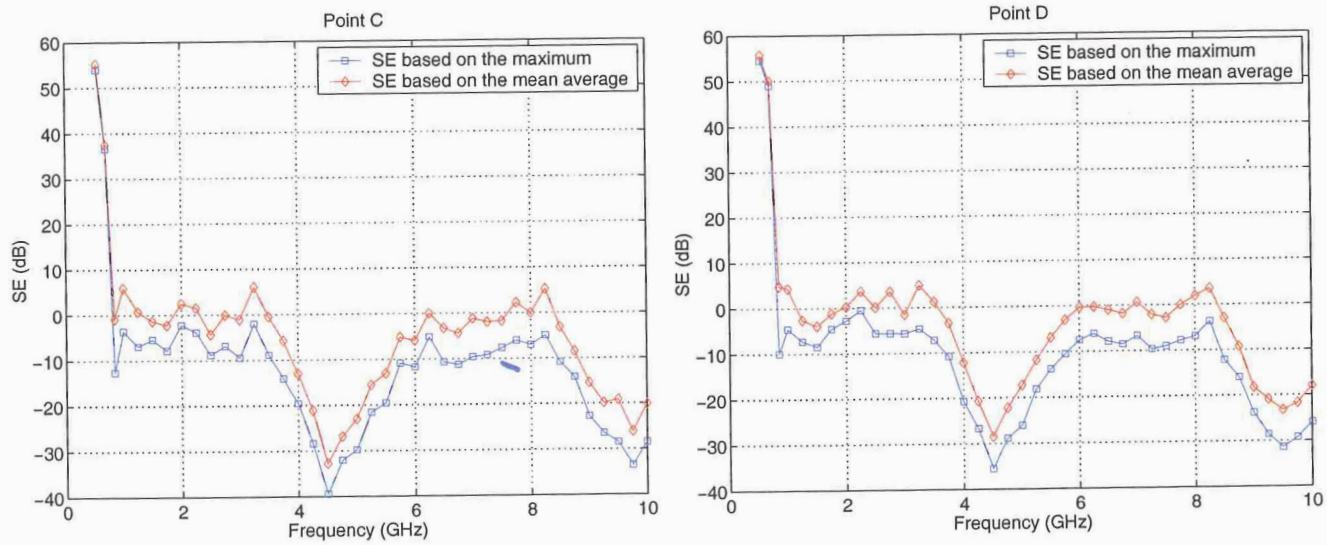

Figure 6.37: Maximum and mean SE variation versus frequency, points C and D.

Two methods were used to demonstrate the mode-stirrer effectiveness. According to the first one, the SE at all four points was calculated without the mode-stirrer in the simplified fuselage. Then, for the same points, their SE was calculated based on the SE_{max} definition. This test is performed in an attempt to gain more insight about the aircraft shielding. The interior of an aircraft, under real conditions of operation, is not static. In contrast, inside a real aircraft during flight there are moving passengers and stewards, as well as baggages and personal belongings. All these factors increase the fuselage geometry complexity, and they are expected to change its SE. With the rotating mode-stirrer, we attempt to simulate real life conditions in an aircraft. The results are illustrated in Figs. 6.38 through 6.39. It is obvious that the level of SE, which is based on the RC approach, is significantly smaller than the one which is based on the deterministic approach, for most of the frequencies. The bigger differences are observed for 4.5 GHz and 9.5 GHz, and they are around 20 dB. For the remaining frequencies, the difference is equal or less than 5 dB while for 3.8, 7.2 and 9.1 GHz the SE based on the deterministic definition is smaller than the SE based on the RC approach. The same conclusions can be drawn for all four probe locations. Therefore, we can conclude that the more complex the fuselage becomes (i.e. mode-stirrer insertion), the smaller is its SE. This can be attributed to the fact that random scatterers, scatter the field towards directions where without them the field would not have been scattered.

Another quantity of interest, when working with RCs, is its *Stirring Ratio* (SR) [147]. SR is defined as the ratio of the maximum over the minimum measured field value over all stirrer positions for a fixed frequency, or

$$SR(f) = \frac{\max_{\phi} |E_z|^2}{\min_{\phi} |E_z|^2} \tag{6.62}$$

In Figs. 6.40 and 6.41 the SR of points A, B, C and D is plotted versus frequency. The dashed curve in each plot represents is the 20 dB level above which, effective stirring has been achieved [147]. It can be observed that all points above 4 GHz exhibit very good SR, which is an indication that the mode-stirrer is sufficiently effective.

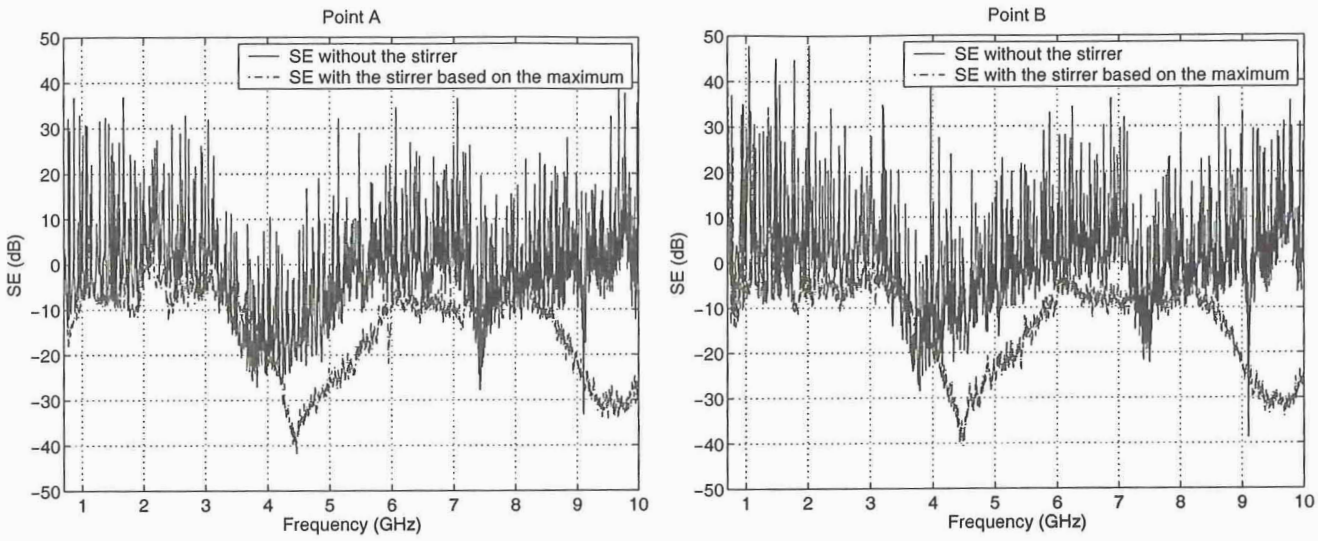

Figure 6.38: Stirrer effectiveness, points A and B.

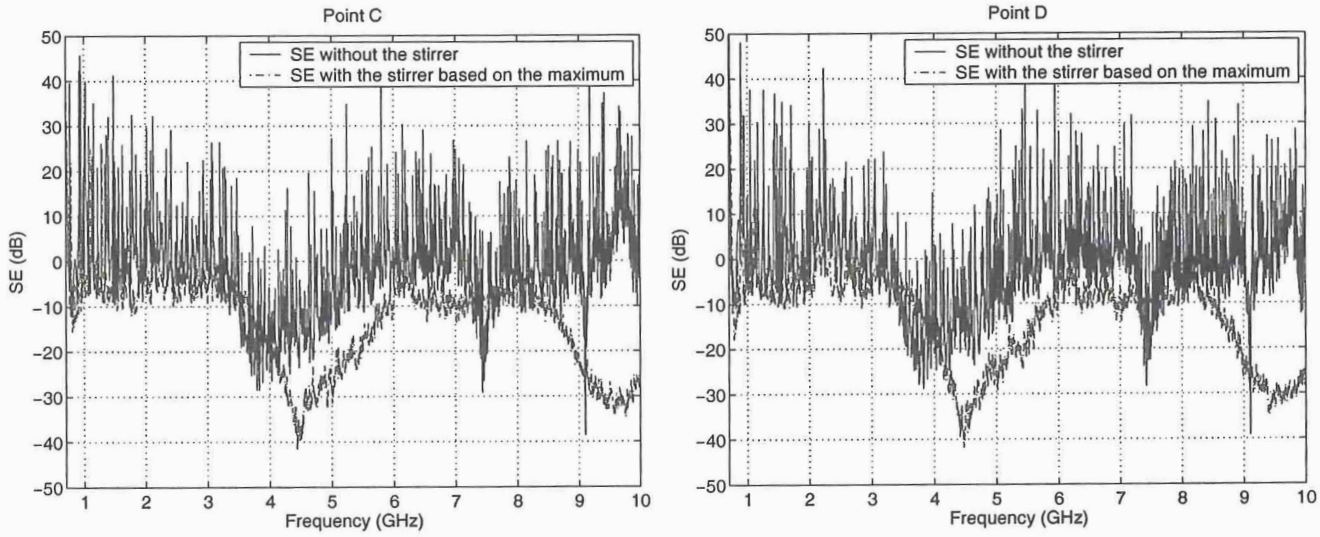

Figure 6.39: Stirrer effectiveness, points C and D.

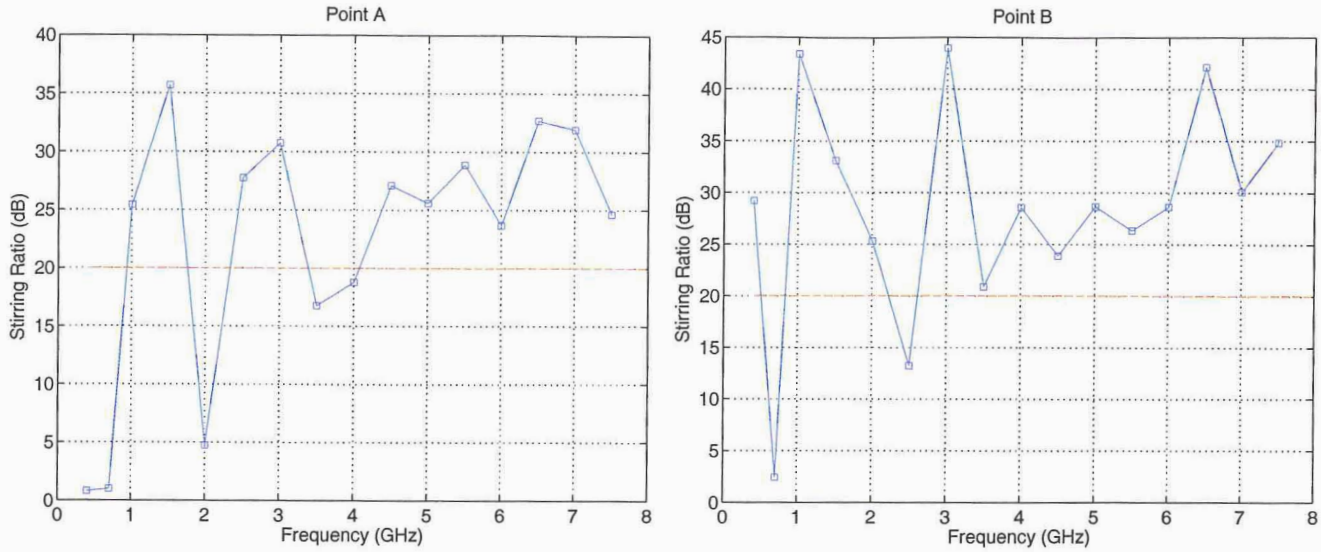

Figure 6.40: Stirring ratio of points A and B.

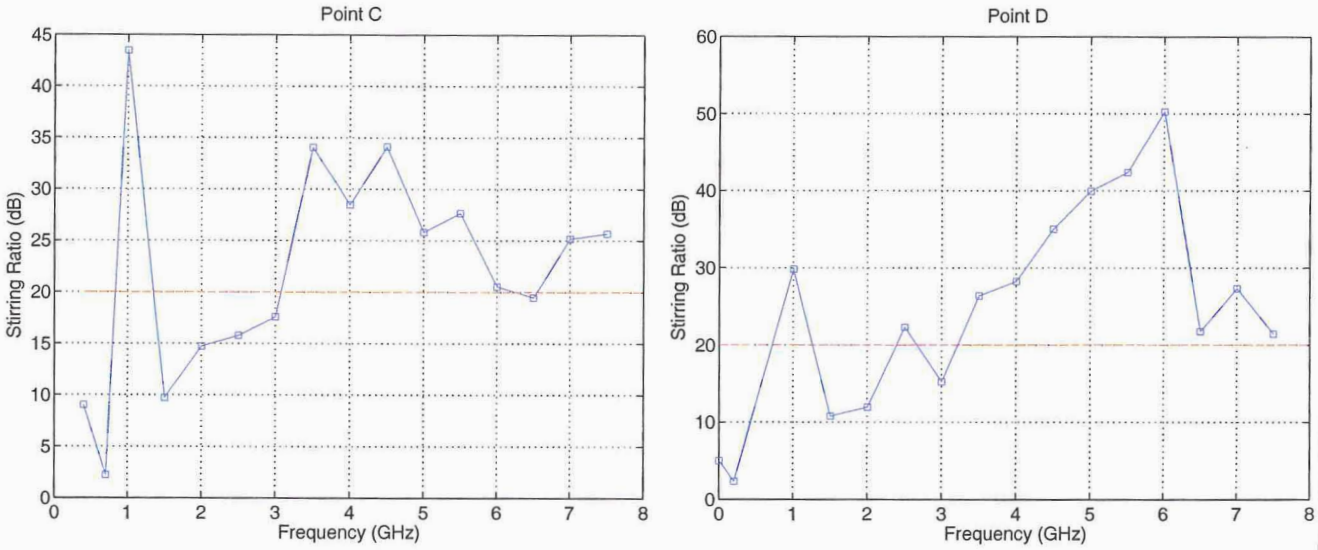

Figure 6.41: Stirring ratio of points C and D.

D. Data Statistical Independence

Since basic statistical data processing has been completed, we proceed with more advanced probabilistic analysis. Prior to any further discussion, some preliminary tests have to be performed. The first, and most important test, to be performed is a data randomness or data statistical independence test. This is because all the theoretical RC probability models that will be employed later assume that the set of data to be processed is statistically independent. Therefore, in order to assure the models' validity, the above test must be performed. The statistical independence of data can be tested using either the *run-test* or the *reverse arrangement test* [165] - [166]. For the purposes of this project, the run-test was used. The run-test is based on the well known *Bernoulli trials*, and it is an elegant method to test how fair a random event is. According to a run-test, a given set of data (or a sequence of events) $x_1, x_2, \ldots x_M$ is grouped, with respect to their median, x_m, as follows:

- When a set element is greater or equal than the median, it is identified with the plus (+) sign, or

$$x_i \geq x_m \Rightarrow x_i \longrightarrow (+)$$

- When a set element is lower than the median it is identified with the minus (-) sign, or

$$x_i < x_m \Rightarrow x_i \longrightarrow (-)$$

Then, the set of data is serially processed, and the above rule is applied. This procedure is schematically illustrated in Fig. 6.42. A *run* is defined as "a sequence of identical observations (sequential data greater or lower than the median) followed by a different observation or no observation at all". The total number of runs r equals the number of sign alternations. It has been proven that r is a random variable (RV) while its distribution is well tabulated. The criterion for data independence is the following inequality

$$r_{N/2;1-\alpha/2} < r \leq r_{N/2;\alpha/2} \tag{6.63}$$

where N is the number of data, α is the significance level and $r_{N/2;1-\alpha/2}$, $r_{N/2;\alpha/2}$ are obtained from the tables of r distribution. The run-test was performed with our

data above 5 GHz, and they are clearly independent with 95% confidence level. As mentioned before, this was expected because the stirrer becomes more effective as the frequency increases and as a consequence, the interior of the fuselage becomes more reverberant.

In order to give a more illustrative representation of data independence, in Figs. 6.43 and 6.44 the distributions of our data are displayed in scatter-plot form, for point A at 1 and 8 GHz. It can be observed that at 1 GHz the data is very correlated, which was expected since they do not pass the independence test. In contrast, at 8 GHz data is significantly less correlated. It should be pointed out that in order to achieve data independence, even for lower frequencies, different mode-stirrer geometries should be attempted or even multiple mode-stirrers which would scatter the field more evenly towards all possible directions in the fuselage. In our case, this scenario is not feasible because of the fuselage geometry limitations.

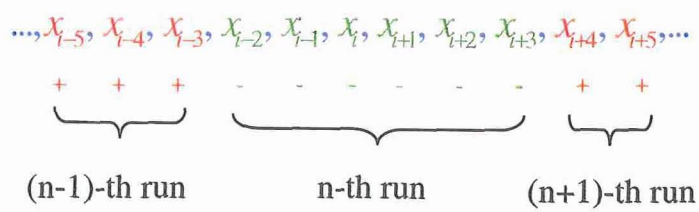

Figure 6.42: Schematic representation of data clustering for the run-test.

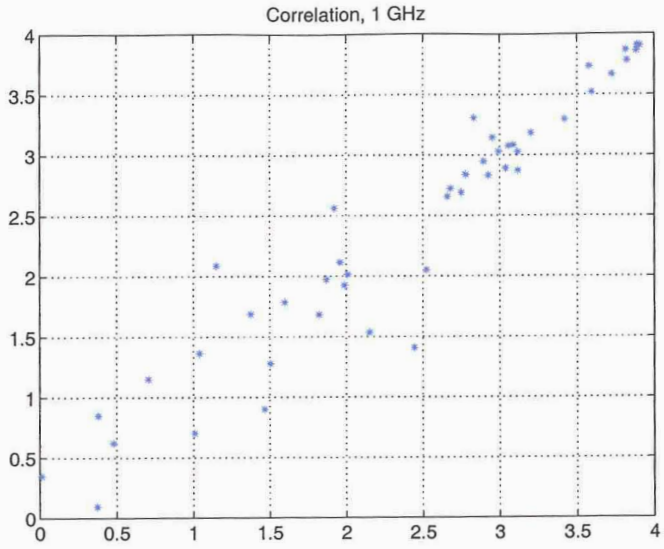

Figure 6.43: Scatter plot for point A at 1 GHz.

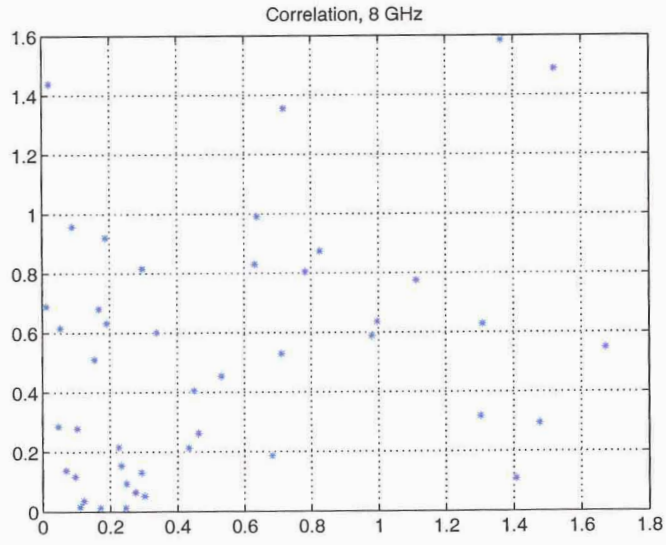

Figure 6.44: Scatter plot for point A at 8 GHz.

E. CDFs and PDFs of Experimental Data

In this section, CDFs and PDFs of experimental data are presented. In particular, elements of RC theory, as presented in previous section, are employed and empirical CDFs are compared with the theoretical expected ones. In order to perform these comparisons, the Kolmogorov-Smirnov goodness-of-fit test is utilized. In what follows, a brief description of the aforementioned test is given and then the corresponding results are presented. Finally, once the preliminary tests have been performed and the validity of our statistical assumptions has been assured, PDFs and CDFs of various field quantities are presented.

1. The Kolmogorov-Smirnov (K-S) Goodness-of-fit Test

Goodness-of-fit tests are performed, in order to check the hypothesis that a set of data is distributed according to a particular statistical model. Such tests are the Chi-Square and the K-S. In this project only the latter is used. As mentioned before the K-S test is used to decide if a sample comes from a population of a specific distribution, and its methodology is as follows.

Let us have a set of N measurements. These measurements in our case correspond to some field quantity, and they are a function of stirrer position. Also, let $F(x)$ be the hypothesized CDF of these measurements and $F^*(x)$ be the actually measured CDF. Then, for each of the N measurements, we define the following quantities:

$$d_n = |F(x_n) - F^*(x_n)| \tag{6.64}$$

and

$$D_N = \max_n d_n \tag{6.65}$$

As an intermediate step we introduce the K-S distribution [167]

$$Q(\lambda) = \sum_{k=-\infty}^{+\infty} (-1)^k \, \mathrm{e}^{-2k^2\lambda^2} \tag{6.66}$$

Now, if $F^*(x)$ is represented by $F(x)$ with 90% confidence, then 90% of the time D_N will be less than $\lambda/\sqrt{N}$. For a general confidence level $1 - Q(\lambda)$, the above statement

can be written as

$$\Pr\left[D_N > \lambda/\sqrt{N}\right] = Q(\lambda) \tag{6.67}$$

or

$$\Pr\left[D_N < \lambda/\sqrt{N}\right] = 1 - Q(\lambda) \tag{6.68}$$

Therefore, if the desired confidence level is known, then by either inverting (6.67) or from look-up tables, one can decide whether the measurements are distributed according to the hypothetised CDF.

2. K-S Test Results

After having performed the K-S test to our data, the corresponding results are presented in this section. In our case the experimental data under test is the set of measurements collected from all four probes for 180 stirrer positions. The confidence level of the test was set to 95%. The quantity whose distribution was tested is $|E_z|^2$. In our case, $F^*(x)$ is the empirical CDF of measurements. Moreover, from RC theory we recall that, ideally $|E_z|^2$ is exponentially distributed with parameter α, or

$$f_{\mathbf{x}}(x) = \frac{1}{\alpha} \mathrm{e}^{-\frac{x}{\alpha}}, \quad x > 0 \tag{6.69}$$

where $x \equiv |E_z|^2$. Therefore, the hypothetised CDF of $F(x)$ is an exponential CDF, that is

$$F(x) = 1 - \mathrm{e}^{-\frac{x}{\alpha}} \tag{6.70}$$

Parameter α of $F(x)$ has to be estimated and according to maximum likelihood estimator (MLE) theory an estimation is given by

$$\hat{\alpha} = \bar{x} \tag{6.71}$$

where $\bar{x}$ is the mean average of our measurements.

The test was performed for data at 1, 2, ... 8 GHz and the results are shown in Table 6.4. It can seen the hypothesis that $|E_z|^2$ measurements are exponentially distributed was rejected for all frequencies below 6 GHz, while it was not rejected

for higher frequencies. In the same table, for each frequency the estimated value of α, as well s the numbers of modes existing in the cavity, are indicated. They are calculated according to Weyl's formula. Also, it has to be mentioned that a more relaxed estimation of the exponential distribution parameter leads to a hypothesis acceptance for lower frequencies. The fact that experimental data pass the test for higher frequencies can be attributed to the size of the stirrer that becomes electrically larger and thus more effective. Moreover, as frequency increases, the number of modes in the fuselage cavity increases which is also a requirement for good mode-stirring. It can be observed that as the number of modes increases, measurements pass the K-S test. This is in accordance with our initial statement that, in order for the RC statistics to be reliable, the Central Limit Theorem has to be valid, and this is the case only when a large number of modes co-exists in the chamber.

Frequency (GHz)	K-S test result	Number of modes	$\hat{\alpha}$
1	Fail	22	0.8432
2	Fail	183	0.5646
3	Fail	622	0.1647
4	Fail	1476	0.4912
5	Fail	2884	0.9028
6	Pass	4985	0.6508
7	Pass	7917	1.1102
8	Pass	11818	0.5775

Table 6.4: Kolmogorov-Smirnov test results.

3. PDFs and CDFs of $|E_z|^2$

In Figs. 6.45 - 6.47 there are in bar-form $|E_z|^2$ distributions, based on measirements as well as their empirical CDFs along with the theoretical ones. These plots correspond to data obtained at 1 and 8 GHz, respectively. It can be observed that at 1 GHz the two curves are in poor agreement while at 8 GHz they agree very well. As mentioned before, this behavior is attributed to the fact that the stirrer becomes more effective for higher frequencies. The importance of CDF plots is that one can read what the probability is that the field value does not exceed a certain level. Also, CDF plots are considered as "universal" curves of a cavity's response. Therefore, they can be

used as guidelines from EMC engineers when sensitive electronic equipment inside an aircraft has to be properly shielded.

4. PDFs and CDFs of SE

Another field quantity whose distribution is of great importance for every EMC design is that of SE. In this section, based on the PDF of $|E_z|^2$, we derive the PDF of SE. In order to do that, the following observations are made. SE, as has been defined up to now, is proportional to the following quantity:

$$SE \sim \frac{|E_z|^2_{\text{free space}}}{|E_z|^2_{\text{cavity}}} \tag{6.72}$$

Notice that the numerator of the above fraction is constant over all stirrer positions while the denominator is a random variable. Using random variable transformations, and the methodology described previously, it is straightforward to show that given an exponentially distributed random variable or

$$f_{\mathrm{x}}(x) = \frac{1}{2\sigma^2} \mathrm{e}^{-\frac{x}{2\sigma^2}} \tag{6.73}$$

then the distribution of c/x (which is also a random variable), where c is a constant, is given by

$$f_{\mathrm{x}}(x) = \frac{c}{2\sigma^2 x^2} \mathrm{e}^{-\frac{c}{2\sigma^2 x}} \tag{6.74}$$

Based on the above derivation, the theoretical CDF of SE, is plotted along with the empirical CDF obtained from measurements. The results are illustrated in Figs. 6.49 - 6.52. It is observed that measurements and theory are in very good agreement. As mentioned before, SE CDF plots give an indication of the probability that a certain SE value exists in the fuselage. The observations that can be made from such plots can be used as benchmarks for an efficient EMC/EMI design.

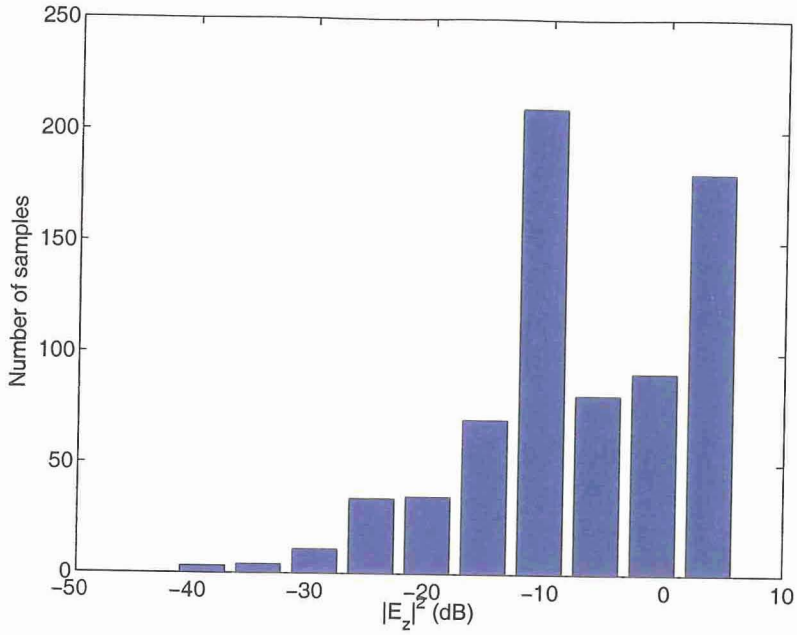

Figure 6.45: PDF of $|E_z|^2$ at 1 GHz.

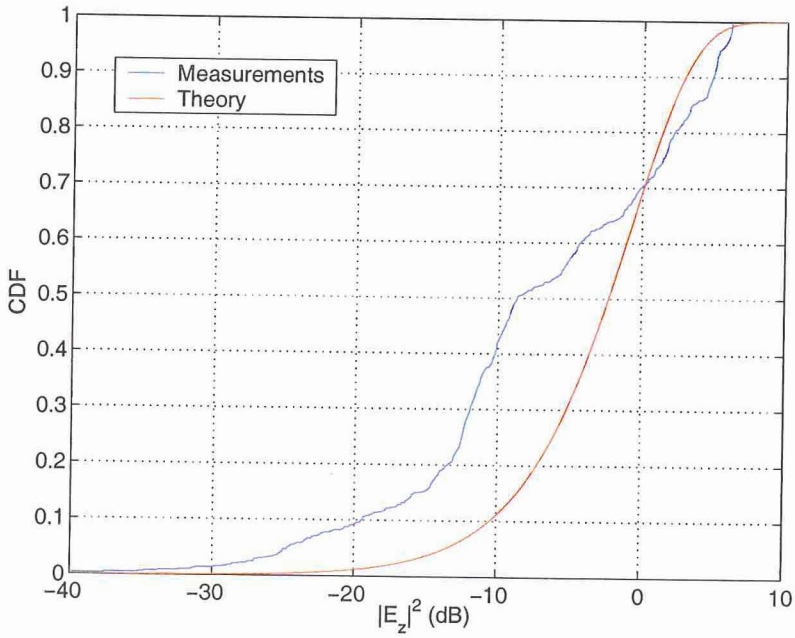

Figure 6.46: CDF of $|E_z|^2$ at 1 GHz.

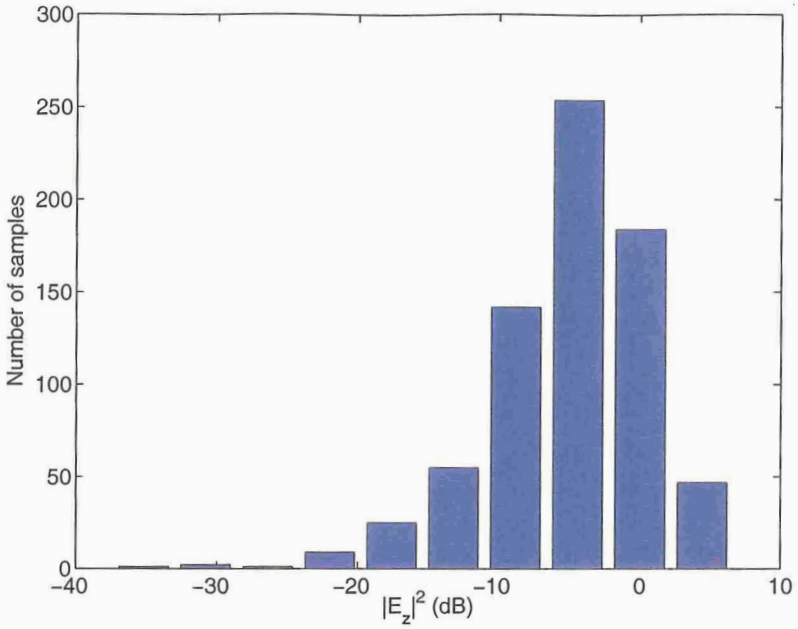

Figure 6.47: PDF of $|E_z|^2$ at 8 GHz.

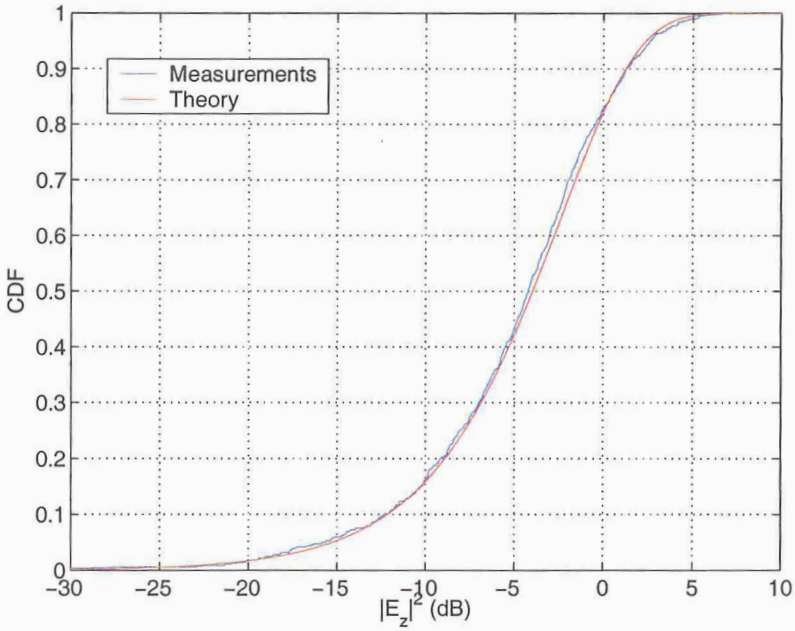

Figure 6.48: CDF of $|E_z|^2$ at 8 GHz.

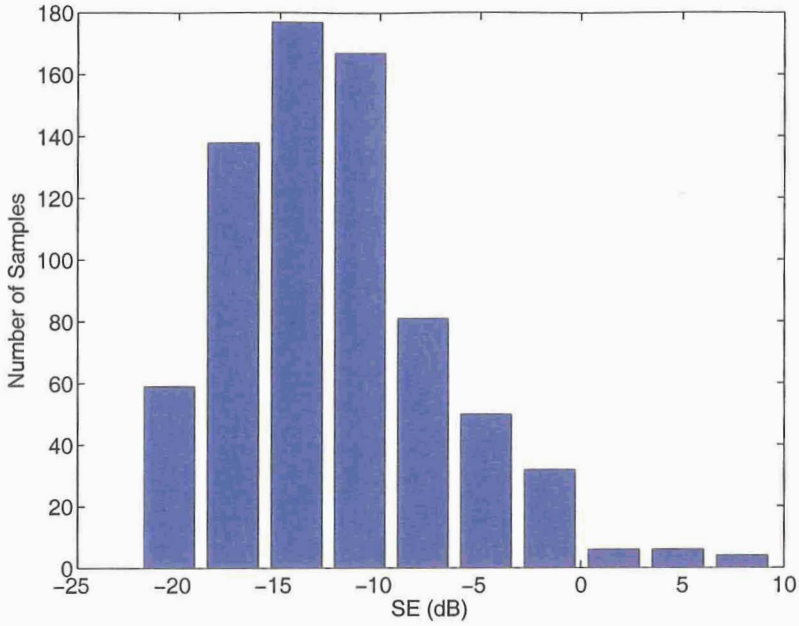

Figure 6.49: PDF of SE at 5 GHz.

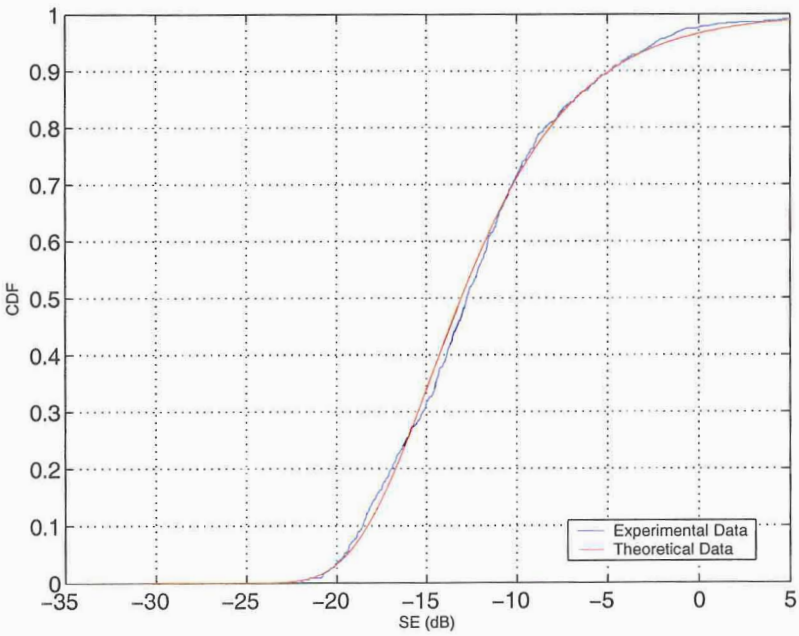

Figure 6.50: CDF of SE at 5 GHz.

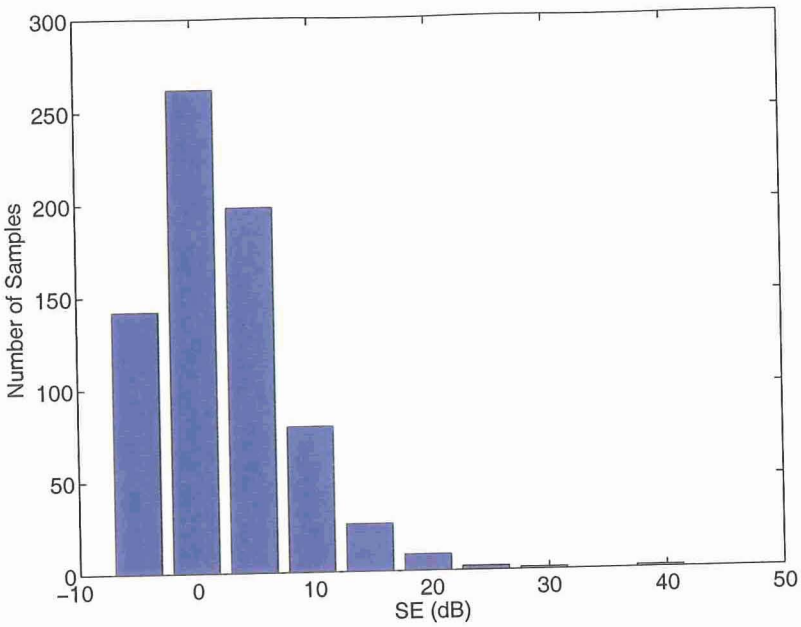

Figure 6.51: PDF of SE at 8 GHz.

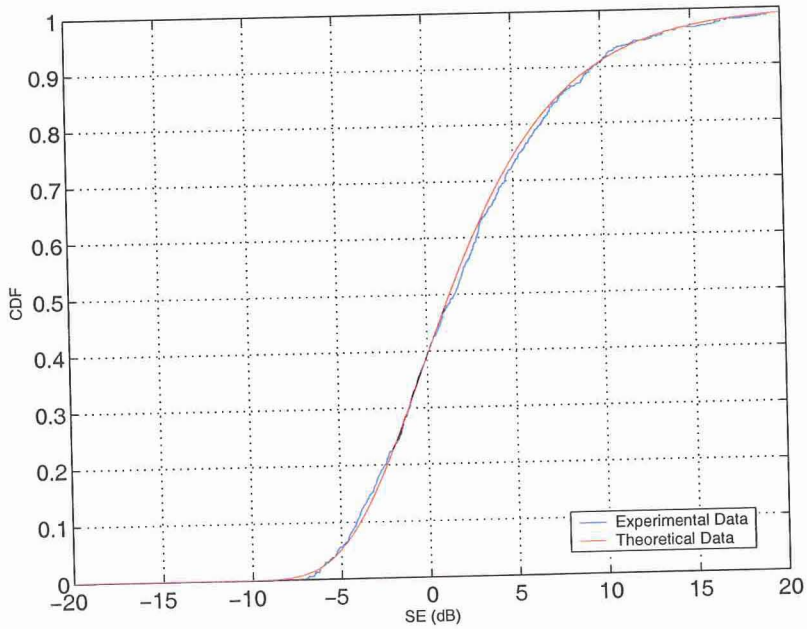

Figure 6.52: CDF of SE at 8 GHz.

Chapter 7

Statistical Properties of an Overmoded Cavity as a Function of Frequency

I. Introduction

A reverberation chamber approach was employed in the previous chapter in order to get more insight into the HIRF penetration problem. It was demonstrated that the installation and operation of a rotatable scatterer (mode-stirrer) in the fuselage resulted in an electromagnetic field configuration that is stochastic in nature. More precisely, it was shown that the value of the electromagnetic field, as a function of mode-stirrer orientation, is a random variable which exhibits statistical properties that are related to the Chi-square (χ^2) distribution.

In this chapter, the field statistics inside the fuselage are examined from a different point of view. This investigation is based on the theoretical and experimental studies of the field statistical distribution in complex cavities, as presented in Price *et al.* [5]. In their work it is demonstrated that under external continuous wave illumination, the power received by a dipole antenna in an overmoded cavity is exponentially distributed, whether the observations are made at a fixed spatial point while frequency is swept or whether the observations are made at a fixed frequency while the probe is translated in position. The work of Price *et al.* was motivated by the observation that field values within cavities vary extremely rapidly. More precisely, if a single mode is excited in a cavity and the field power at an arbitrary location within it is measured,

the result will be a value equal or less than the true mode amplitude at that location (less in the case of a lossy cavity). Moreover, if the frequency of operation changes, then another mode will be excited and a different mode configuration will be created. Consequently, the measurement point will be at a different position relative to the peaks and nulls of the cavity. The value of the field power at the new frequency of operation will be, as before, equal or less than the mode amplitude but unrelated to that of the previous mode. The aforementioned scenario becomes more complicated if many modes are excited simultaneously in the cavity and thus the measured power is the sum of contributions of all modes. Moreover, if the shape of the cavity is irregular, the field polarization for a certain mode can be a function of position. It becomes obvious that the deterministic approach is not the optimum one for predicting the field penetration in a complex cavity and therefore, conventional methods to characterize the response of a cavity under external illumination, such as shielding effectiveness (SE) measurements, are not sufficient. In addition, the computational costs of modeling fine geometrical details, which may have significant effects on the spatial distributions of the fields within the cavity, are often prohibitive. Furthermore, it is unrealistic to model the locations and movement of people, for example within the cabin of an airliner.

The pioneering work of Price *et al.* takes into account the statistical nature of the problem and depends only on general properties of the system. Although it was recognized empirically that the cumulative distribution functions (CDFs) of measured fields are less sensitive to experimental parameters and were characterized as "universal" curves in [168], it was Price *et al.* that developed the necessary theoretical justification for the above assumption. Their work involves a thorough derivation of the statistics responsible for the exponential distribution [$\chi^2(2)$ chi-square with two degrees of freedom], of the power in a complex cavity. Nevertheless, it is rather complicated: it is written using physicist's notation while some errors, which have been reported [169], [6], make it difficult to be followed. A more smooth and detailed description of this work has been given by Holland and John [6]. Not only have they revised and corrected it, but they have also expanded it.

In what follows, a brief description will be given of the statistical theory of complex cavities. Afterward, the Kolmogorov-Smirnov test will be used to test whether data

obtained from measurements is distributed according to the theoretical expected ones.

II. Statistical Field Theory of Complex Cavities

In this section, the principles of the statistical field theory of externally illuminated complex overmoded cavities are presented. We describe as complex any irregularly shaped or leaky cavity such as the interior of an aircraft or a satellite. An overmoded cavity is characterized as one within which several modes are simultaneously excited. Another requirement in order for a cavity to be considered as overmoded is that the width of each excited mode is larger than the mode spacing [170]. According to Warne *et al.*, the degree of spectral overlap is given by the following parameter α:

$$\alpha = \frac{k^3 V}{2\pi Q} \tag{7.1}$$

where V is the volume of the cavity and Q its quality factor. It is obvious that this parameter is the ratio of the energy stored in the cavity modes over a narrow spectral bandwidth (containing many complete modes) to the same energy if the field amplitude is fixed at the average peak level. If the cavity is undermoded (discrete mode spectrum), $\alpha \ll 1$; if the cavity is overmoded (overlapping mode spectrum), $\alpha \gg 1$. Another way to interpret (7.1) is the following. According to the Rayleigh-Jeans law for the equilibrium radiation of an absolutely black body, the density of the modes $\mathrm{d}N(f)$ excited in the frequency range $(f, f + \Delta f)$ is given by [171]

$$\frac{\mathrm{d}N(f)}{\mathrm{d}f} = \frac{8\pi V}{c^3} f^2 \tag{7.2}$$

where V is the cavity volume and c is the speed of light. Moreover, the cavity quality factor in terms of the operating frequency is given by

$$\frac{\Delta f}{f} = \frac{1}{2Q} \tag{7.3}$$

By combining (7.2) and (7.3) we get

$$N_s = \frac{\mathrm{d}N}{\mathrm{d}f}\Delta f = \frac{8\pi V}{\lambda^3 Q} \tag{7.4}$$

The above quantity is called *specific mode density*, and it is analogous to (7.1). Although numerous modes are excited in a cavity by a monochromatic source, the specific mode density is a measure of the number of modes which contain the majority of the energy in the cavity.

In order to derive the field distributions inside a complex cavity, we follow the Price *et al.* formulation, as documented in [5]. According to this formulation the electric and magnetic fields in a cavity can be decomposed into contributions from each of the cavity's eigenmodes so that the magnetic and electric fields internal to the cavity can be written, respectively, as

$$\mathbf{B}(\mathbf{r},t) = \sum_i \mathbf{B}_i(\mathbf{r},t) \tag{7.5a}$$

$$\mathbf{E}(\mathbf{r},t) = \sum_i \mathbf{E}_i(\mathbf{r},t) \tag{7.5b}$$

Each of the eigenmodes $\mathbf{B}_i$ and $\mathbf{E}_i$ satisfies Maxwell's equations, within the cavity domain, along with the boundary conditions associated with the cavity walls. It has to be mentioned that during this formulation, the explicit coordinate system chosen is not important since only the general properties of the eigenmodes are important. Now, each of the eigenmodes is separated into a product of five functions, each one corresponding to a different field property. Consequently, the electric field of the ith eigenmode is written as

$$\mathbf{B}_i(\mathbf{r},t) = B_{0i}(\omega)\,\widehat{\mathbf{b}}_i(\mathbf{r})\,g_i(\mathbf{r})\,f_i(\mathbf{r})\,\sin(\omega t+\phi_i) \tag{7.6a}$$

$$\mathbf{E}_i(\mathbf{r},t) = E_{0i}(\omega)\,\widehat{\mathbf{e}}_i(\mathbf{r})\,g_i(\mathbf{r})\,h_i(\mathbf{r})\,\cos(\omega t+\phi_i) \tag{7.6b}$$

The first function, $B_{0i}(\omega)$, is the scalar amplitude of the magnetic field of the ith eigenmode averaged over the cavity volume, such that

$$U_i = \frac{B_{0i}^2\,V}{2\,\mu_0} \tag{7.7}$$

where U_i is the total energy in the cavity in the ith eigenmode. The second function, $\hat{\mathbf{e}}_i(\mathbf{r})$, is a unit vector which points along the electric field of the ith mode at each point in the cavity. The third and fourth functions correspond to the slowly and rapidly

varying parts of the spatial distribution. Although the product representation of the eigenfuctions, as given by (7.6a) and (7.6b), is not of apparent purpose, it is very significant for the work of Price. A possible explanation is the one given by Holland [6], according to which $g_i(\mathbf{r})$ is attributed to slowly varying effects or "trends", such as the frequency dependent cavity quality factor. Function $g_i(\mathbf{r})$ is defined as the amplitude of $B_i(\mathbf{r}, t)$ averaged over time and the phase volume, or

$$g_i(\mathbf{r}) = \left[\frac{2}{B_{0i}^2 \, V_{ph}(\mathbf{r})} \int_{V_{ph}(\mathbf{r})} \overline{\mathbf{B}_i^2(\mathbf{r}', t)} \mathrm{d}\mathbf{r}' \right]^{\frac{1}{2}} \tag{7.8}$$

where $V_{ph}(\mathbf{r})$ is a sphere of radius $\lambda/2$.

The fourth function, f_i, is as mentioned before, the rapidly varying part of the original ith eigenfunction. It is obtained by taking the spatially dependent magnitude of the ith eigenfunction and dividing it by $B_{0i}(\omega)$ and $g_i(\mathbf{r})$, as follows

$$f_i(\mathbf{r}) = \frac{2 \, \widehat{\mathbf{b}}_i \cdot \overline{\mathbf{B}_i(\mathbf{r}, t)}}{B_{0i} \, g_i(\mathbf{r})} \tag{7.9}$$

The overbar in the previous equations indicates mean square average over the temporal dependence. Finally, the fifth function is just the time dependence of the ith eigenmode including its phase, ϕ_i. The frequency is determined by the external exciting field and is the same for all excited modes.

The properties that the eigenfunctions components must satisfy are the following:

1. The integral of $f_i(\mathbf{r})$ squared over the phase volume is unity, or

$$\frac{1}{V_{ph}(\mathbf{r})} \int_{V_{ph}(\mathbf{r})} f_i^2(\mathbf{r}) \, \mathrm{d}\mathbf{r}' = 1$$

2. The integral of g_i^2 over the cavity volume is equal to the volume, or

$$\int_V g_i^2(\mathbf{r}) = V$$

3. The eigenfunctions form an orthogonal basis set, or

$$\int_V \widehat{b}_i \, g_i \, f_i \cdot \widehat{b}_k \, g_k \, f_k \, \mathrm{d}\mathbf{r} = V \, \delta_{ik}$$

Although the reason for imposing the above conditions is not apparent at this stage, they are of great importance for the development of the statistical field theory of complex cavities as developed by Price et al. [5].

If we measure the electromagnetic field power along the $\hat{a}$ direction, at point $\mathbf{r}$ in the cavity using a square-law detector, it will be proportional to the following quantity

$$P \sim \overline{[\hat{\mathbf{a}} \cdot \mathbf{B}(\mathbf{r}, t)]^2} \tag{7.10}$$

Using (7.5a) and (7.6a), the right hand side of (7.10) can be written as follows

$$P \sim \left[\sum_i B_{0i} \left(\hat{\mathbf{a}} \cdot \hat{\mathbf{b}}_i \right) g_i f_i \sin(\omega t + \phi_i) \right]^2 =$$

$$= \sum_i B_{0i}^2 \left(\hat{\mathbf{a}} \cdot \hat{\mathbf{b}}_i \right)^2 g_i^2 f_i^2 + \sum_{\substack{i,k \\ i \neq k}} B_{0i} B_{0k} \left(\hat{\mathbf{a}} \cdot \hat{\mathbf{b}}_i \right) \left(\hat{\mathbf{a}} \cdot \hat{\mathbf{b}}_k \right) g_i g_k f_i f_k \cos(\phi_i - \phi_k) \tag{7.11}$$

From the above equation we see that P is positive definite and of quadratic form. The random vector f_i, as given by (7.9), is a time-average of a stationary process. The central limit theorem assures that the vector has an asymptotic Gaussian distribution. The asymptotic distribution of the quadratic form can then be approximated by a Γ distribution [172] with probability distribution function

$$f(x) = \frac{x^{\alpha-1} \, \mathrm{e}^{-\frac{x}{\beta}}}{\Gamma[\alpha] \, \beta^{\alpha}}, \quad x \geq 0 \tag{7.12}$$

where α and β are parameters to be determined. It can be proved that for a large cavity, where the specific mode density becomes large, α goes to zero while β is equal to the average power over all frequencies. For these specific values for α and β, $f(x)$ reduces to a chi-square distribution with two degrees of freedom [$\chi^2(2)$].

III. Statistical Analysis of Experimental Data

In this section the empirical cumulative distribution function (CDF) of measurement data is compared with the theoretical expected field CDF as developed previously. The measurement procedure has been described in detail in a previous chapter but for completeness a brief description is also given here. The fuselage geometry is shown in Fig. 7.1. The penetrated field was probed at four points designated as A, B, C and D, using vertically oriented monopole antennas. During the measurements the mode-stirrer was present in the fuselage but was not rotated. The mode-stirrer breaks degeneracy and makes the chi-square statistics more applicable. The collected data was in the frequency range from 1 GHz up to 8 GHz with 5607 intermediate frequency points.

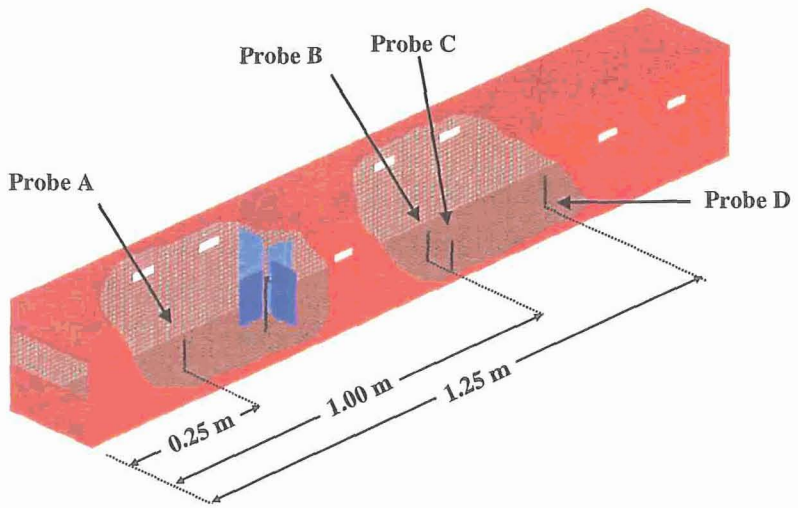

Figure 7.1: Fuselage geometry along with the mode-stirrer and the four probes.

Regarding the measurements setup, the following remarks have to be made. The basic assumptions, in order to develop a statistical theory for the field distributions inside a complex cavity, are that there are no observation points located where there is line-of-sight illuminated by the driving source through a large aperture, and there are no small shield rooms inside a big shield room. In our case, the simplified scaled model fuselage was illuminated directly through the main aperture. This excitation scenario is not a perfect match with the above assumptions. In particular, the entire fuselage

interior is in direct line-of-sight with the source. Also, the front aperture (cockpit window) is so large that the high Q requirement for the analysis of an overmoded cavity may not be met. Lastly, the excitation is primarily dominated by the front large aperture and secondarily by the small ones located along the sides of the fuselage. Despite these violations, the fuselage interior is proved to be characterized by the proposed field statistics, as will be demonstrated.

The measured quantity under test is $|E_z|^2$, and according to the previous theoretical formulation it should be exponentially distributed

$$f_{\mathbf{x}}(x) = \frac{1}{\alpha} \mathrm{e}^{-\frac{x}{\alpha}} \tag{7.13}$$

with parameter α. In order to calculate this parameter, the maximum likelihood estimator (MLE) theory is employed, according to which an estimation of α is given by

$$\widehat{\alpha} = \overline{x} \tag{7.14}$$

where the over-bar indicates averaging over all frequency points.

For each of the points A, B, C and D, an estimate for α was made, and the corresponding theoretical CDFs were computed. Then, in order to test if the empirical CDFs of measurement data match the theoretical CDFs, goodness-of-fit tests were performed. The Kolmogorov-Smirnov goodness-of-fit test was performed to our data with a 95% confidence level. Data from all points successfully passed this test.

In Figs. 7.2 - 7.9, the results of this statistical analysis are presented. For each observation point, the $|E_z|^2$ variations versus frequency are plotted. The empirical CDF based on measured data (solid curve), along with the theoretical expected CDF (dashed curve), are also presented. It can be observed that for all points, empirical and theoretical CDFs are in very good agreement, although at the upper and lower "tails" there are some discrepancies. In the next section, another statistical model for the field distribution inside a complex cavity is presented which gives better agreement even at the lower and upper "tails".

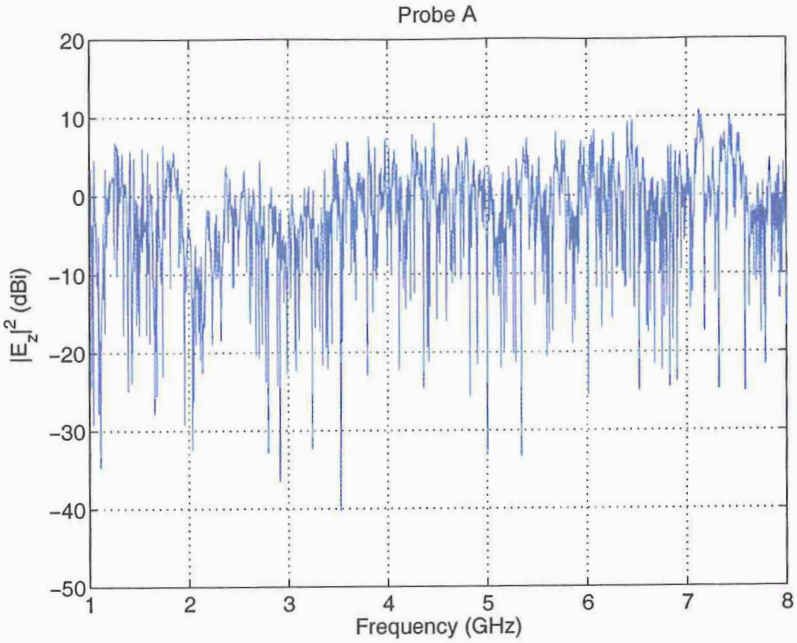

Figure 7.2: $|E_z|^2$ vs. frequency, point A.

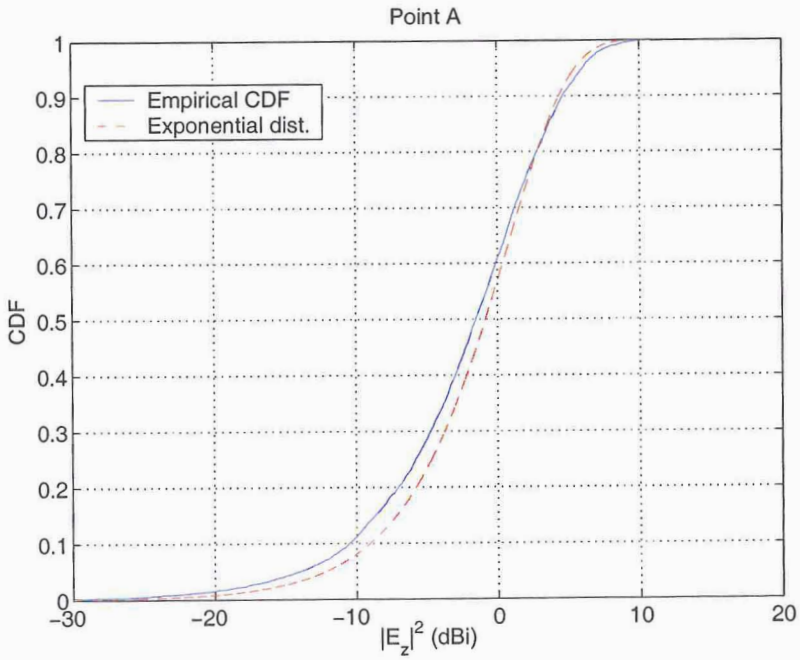

Figure 7.3: Empirical and theoretical-exponential CDFs at point A.

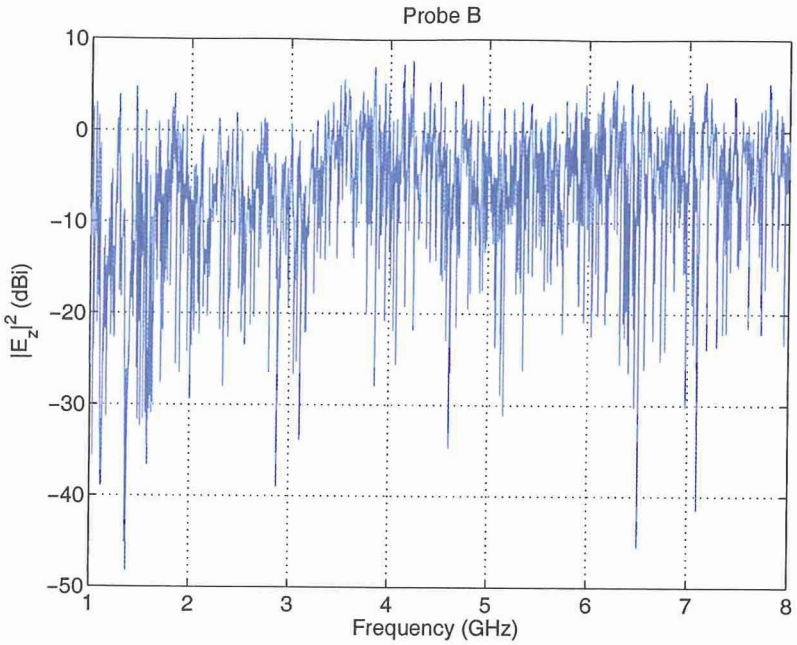

Figure 7.4: $|E_z|^2$ vs. frequency, point B.

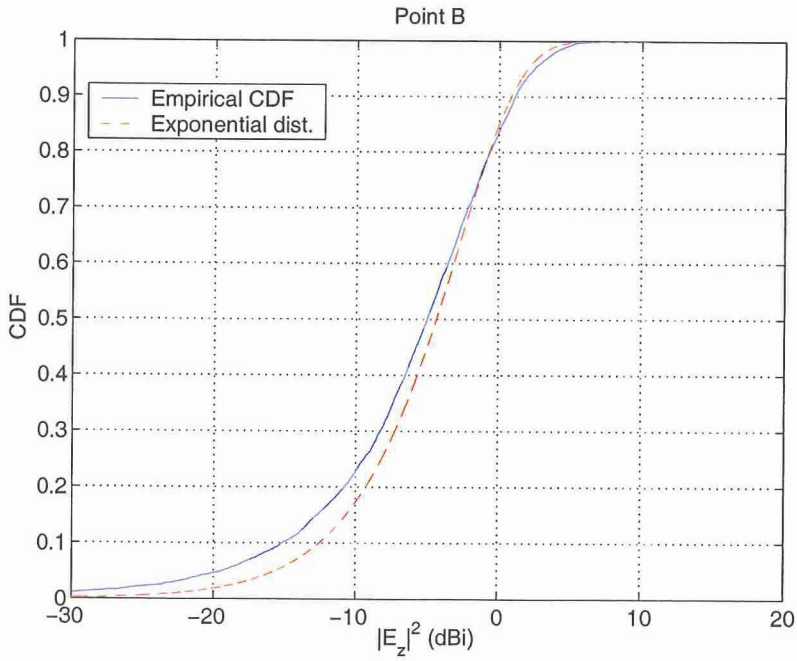

Figure 7.5: Empirical and theoretical-exponential CDFs at point B.

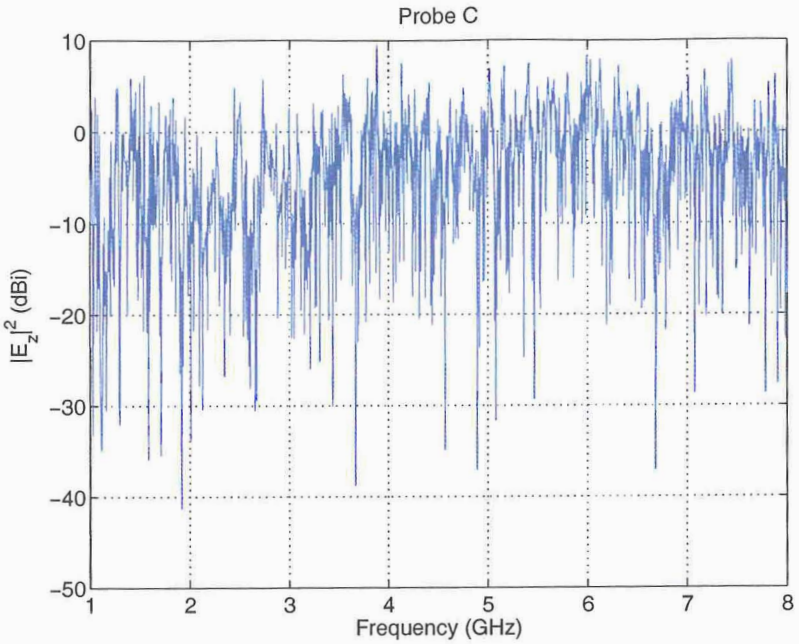

Figure 7.6: $|E_z|^2$ vs. frequency, point C.

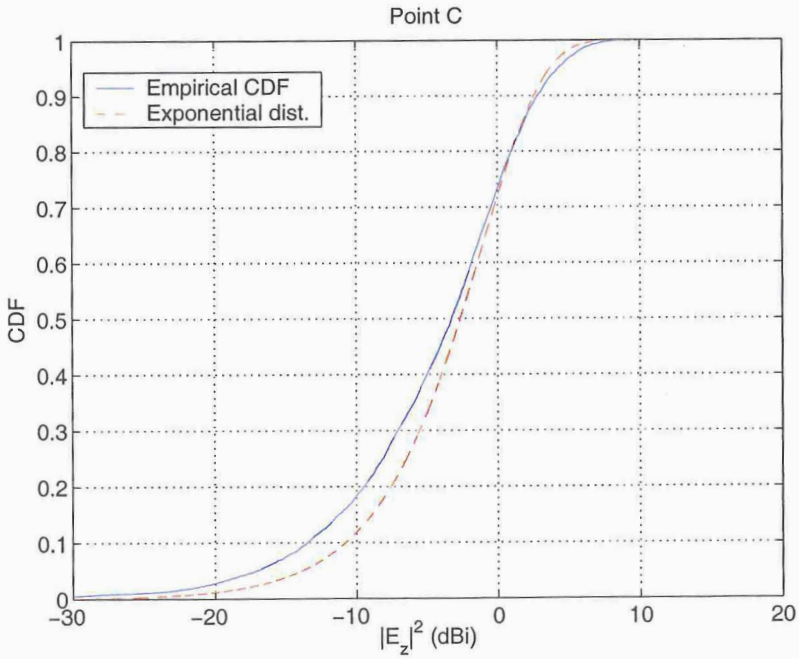

Figure 7.7: Empirical and theoretical-exponential CDFs at point C.

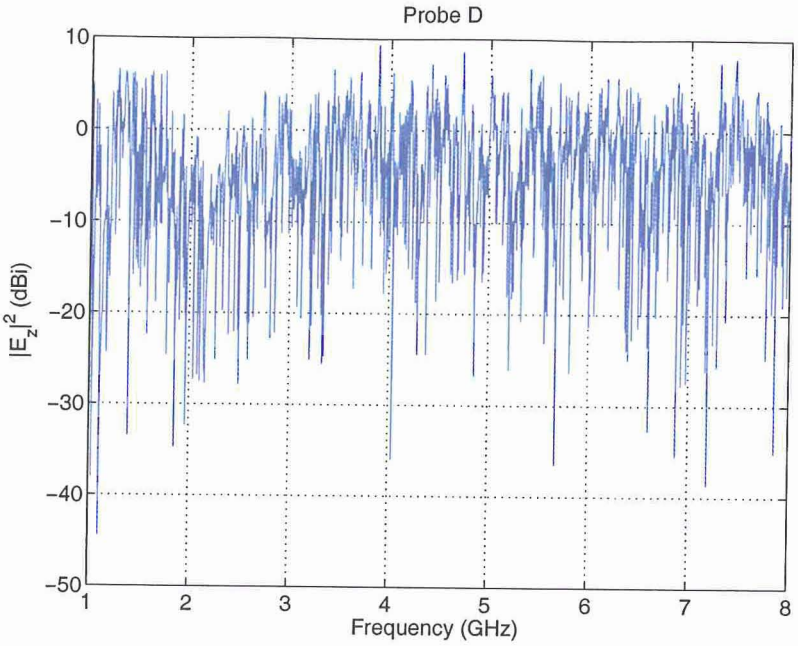

Figure 7.8: $|E_z|^2$ vs. frequency, point D.

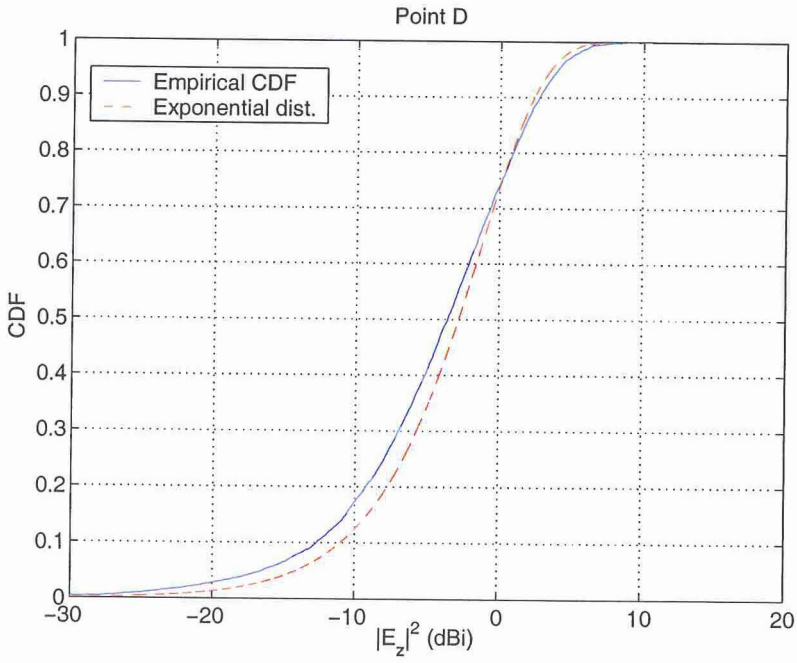

Figure 7.9: Empirical and theoretical-exponential CDFs at point D.

IV. The Lehman Model

A great debt for understanding the electromagnetic field statistical behavior of complex cavities is owed to Lehman [173]. This is because he first observed that the interior of a cavity has physical properties that make the electromagnetic power-flux density be exponentially distributed. However, he also observed that a leaky enclosure can be illuminated from three different directions, with two possible quadrature polarizations for each different direction. He concluded that the power flux inside an externally illuminated leaky cavity, as projected in an internal dipole antenna, should also have attributes of a chi-square distribution with six degrees of freedom. Therefore he proposed a new distribution for the power-flux density known as the Lehman distribution [6]. In what follows, the Lehman distribution is briefly presented. Then it is used to perform goodness-of-fit tests and finally the results are presented.

As mentioned before, it was proposed by Lehman that the field external to a leaky cavity can illuminate its apertures from any of three directions having two possible polarizations. This will result in inward power leakage which is chi-square distributed with six degrees of freedom. Moreover the internal cavity response model dictates that the power flux distribution is chi-square distributed with two degrees of freedom. Therefore, from the above assumptions, it can be concluded that the overall internal cavity response should have a power-flux probability density function which is the product of these two distributions, that is

$$x = x_2\, x_6 \tag{7.15}$$

where x_2 is the chi-square with two degrees of freedom variation while x_6 is the chi-square with six degrees of freedom. The probability density function of x is given by [161]

$$l(x) = \int_0^{+\infty} \frac{1}{z}\, \chi_2^2\left(\frac{x}{z}\right)\, \chi_6^2(z)\, \mathrm{d}z \tag{7.16}$$

which after some manipulations reduces to

$$l(x) = \Lambda^2\, x\, K_2\left(2\sqrt{\Lambda x}\right) \tag{7.17}$$

where $K_2(\cdot)$ is the second order modified Bessel function of the second kind. Therefore

the cumulative density function of $l(x)$, or the Lehman distribution, is given by

$$\begin{aligned} L(x) &= \int_0^x l(z)\mathrm{d}z \\ &= 1 - (\Lambda x)^{3/2}\, K_3\left(2\sqrt{\Lambda x}\right) \end{aligned} \tag{7.18}$$

where $K_3(\cdot)$ is the third order modified Bessel function of the second kind. It is obvious that Lehman is a single parameter distribution. Parameter Λ can be calculated according to the average and standard deviation of the distribution using the following formulas

$$\mu = \frac{3}{\Lambda}, \qquad \sigma = \frac{\sqrt{15}}{\Lambda} \tag{7.19}$$

Goodness-of-fit tests were performed between data empirical CDFs and theoretical CDFs as provided from the Lehman distribution. The confidence level was set to 95% and measurements from all four points successfully passed the test. In Figs. 7.10 and Figs. 7.11 the empirical CDFs of data from all four points are presented along with the theoretical expected ones as provided by the Lehman and the exponential distribution. It is apparent that the Lehman model is in better agreement with measurements than the exponential one. The important achievement is that the Lehman model exhibits better agreement with measurements on the upper "tail" of the distribution, because this is where harmful effects will occur. Therefore it provides better guidelines for an efficient EMC design.

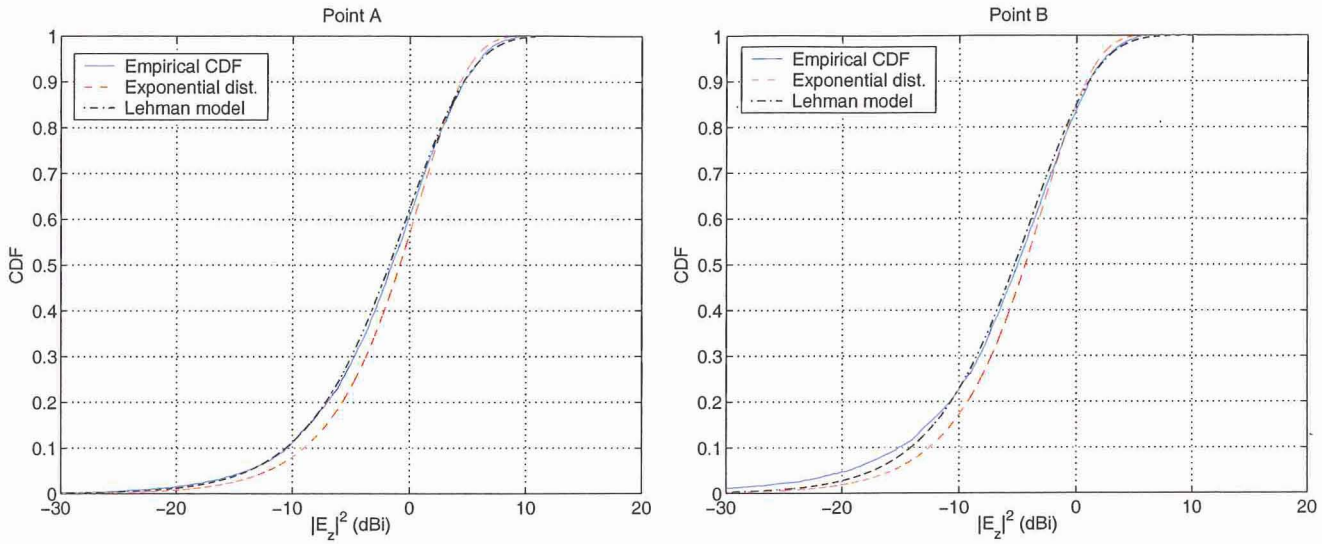

(a) (b)

Figure 7.10: Empirical and theoretical (exponential and Lehman) CDFs : (a) Point A (b) Point B.

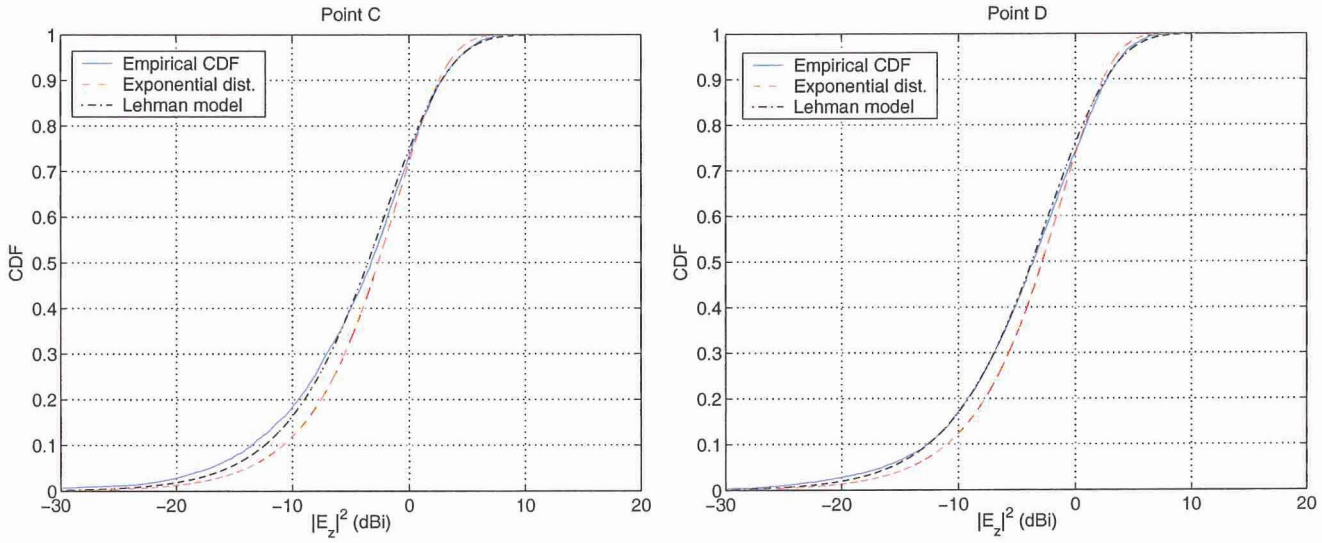

(a) (b)

Figure 7.11: Empirical and theoretical (exponential and Lehman) CDFs : (a) Point C (b) Point D.

Chapter 8

Frequency Stirring for Reverberation Chambers

I. Introduction

Reverberation Chambers (RCs) are an attractive alternative method to perform EMI susceptibility tests. Their main advantage over conventional immunity test methods is that a stochastic in nature field configuration can be established inside them and hence model "real-world" EMI conditions. As has been described in Chapter 6, an RC is a large metallic enclosure within which the boundary conditions continuously change with respect to time. This is accomplished with the operation of a rotating metallic paddle, usually referred to as mode–stirrer. By perturbing the boundary conditions of the RC, the spatial field pattern inside it continuously changes, and hence randomness is induced in the field variations. The random field configuration inside an RC is characterized by the following properties: uniformity, isotropy and random polarization. It has to be mentioned that these properties are valid everywhere inside the RC's cavity except for locations close to the walls and the source. Moreover, the aforementioned properties are considered figures-of-merit of an RC's performance, while their establishment ensures its successful operation.

The above conditions make the design of an RC an extremely tedious procedure, and in general, not an easy task to perform, therefore several design considerations have to be taken seriously into account for a successful RC operation. The most important of all is the choice the mode-stirrer's shape and size. Not only has the mode-stirrer to be electrically large, in order to create sufficient mode agility, but it has

also to be irregularly shaped in order to scatter the impinging on it electromagnetic waves evenly towards all directions. Crawford and Koepke [147] have provided useful guidelines for the design of a mode-stirrer. For example, they recommend that its size should be at least $\lambda/2$ at the lowest frequency of operation. Nevertheless, in general, the design of a mode-stirrer can be described as "a trial-and error, experimental process", as has been stated by Wu and Chang [149]. Moreover, RC operation is further dependent on the mode-stirrer, since it is required that data be taken over many stirrer positions in order to ensure that the test object has been exposed to all possible field levels.

An alternative method to create an RC environment inside a conducting box, without the aid of a mode-stirrer is by *electronic mode-stirring* or *frequency stirring*. It was initially proposed by Loughry [174] as an alternate to mechanical mode-stirring for the conduct of susceptibility tests. The idea behind frequency stirring is to keep the boundary conditions of the chamber constant and to inject in it a proper band-limited signal which will evenly excite all the corresponding eigenmodes. This is accomplished by properly modulating band–limited white Gaussian noise to microwave frequencies. By using band–limited modulated white Gaussian noise, the energy of the signal is spread over a narrow frequency bandwidth while the modes of the cavity which lie within this bandwidth are randomly excited.

In what follows, the basic aspects of the frequency stirring technique are presented. A review on the properties of noise is given that to emphasize its importance for the realization of the frequency stirring technique. Then, the method is used in the case of a 2-D as well as a 3-D cavity. For both cases, the cavities' responses are simulated using FDTD, when the excitation source is the one mentioned previously. Tests for the homogeneity of the electromagnetic field are performed; furthermore its statistical properties are presented.

II. Frequency stirring

As has been mentioned before, the conventional method of mode-stirring uses a rotating metallic paddle which either continuously or discretely changes the boundary conditions within the RC, while maintaining a constant excitation frequency. In such way, at a given point in the chamber, field homogeneity is achieved by averaging

the contribution of many different eigenmodes. In contrast, according to frequency stirring, the boundary conditions are maintained constant while the frequency varies over a narrow bandwidth around some center frequency. The obvious advantage of frequency stirring over mode stirring is that it ensures the simultaneous excitation of many modes in the cavity by utilizing a proper excitation source.

Before proceeding with more details about the implementation of the frequency stirring technique, let us first give a qualitative explanation of how RC operation introduces randomness to the field variations. This explanation, apart from giving insight to the phenomenon under investigation, it will also reveal the direct connection between mechanical mode-stirring and frequency stirring.

Consider a rectangular cavity with walls of finite conductivity, the geometry of which is shown in Fig. 8.1(a). For the case of TE^z modes, it is well known that the electric and magnetic vector potentials are given respectively by [175]:

$$\mathbf{F} = \widehat{\mathbf{a}}_z \, F_z(x,y,z) \tag{8.1}$$

$$\mathbf{A} = \mathbf{0} \tag{8.2}$$

where F_z is a solution to the Helmholtz equation, and it is given by

$$F_z(x,y,z) = A_{mnp} \cos(\beta_x \, x) \, \cos(\beta_y \, y) \, \sin(\beta_z \, z) \tag{8.3}$$

The corresponding electric and magnetic field components can be expressed in terms of F_z as:

$$E_x = -\frac{1}{\varepsilon} \partial_y F_z \qquad H_x = -\mathrm{j} \frac{1}{\omega \mu \varepsilon} \partial_{xz}^2 F_z \tag{8.4}$$

$$E_y = -\frac{1}{\varepsilon} \partial_x F_z \qquad H_y = -\mathrm{j} \frac{1}{\omega \mu \varepsilon} \partial_{yz}^2 F_z$$

$$E_z = 0 \qquad H_z = -\mathrm{j} \frac{1}{\omega \mu \varepsilon} \left(\partial_{zz}^2 + \beta^2 \right) F_z$$

In addition, the electric field must satisfy the following boundary condition on each of the cavity walls:

$$\widehat{\mathbf{n}} \times \mathbf{E} = \mathbf{0} \tag{8.5}$$

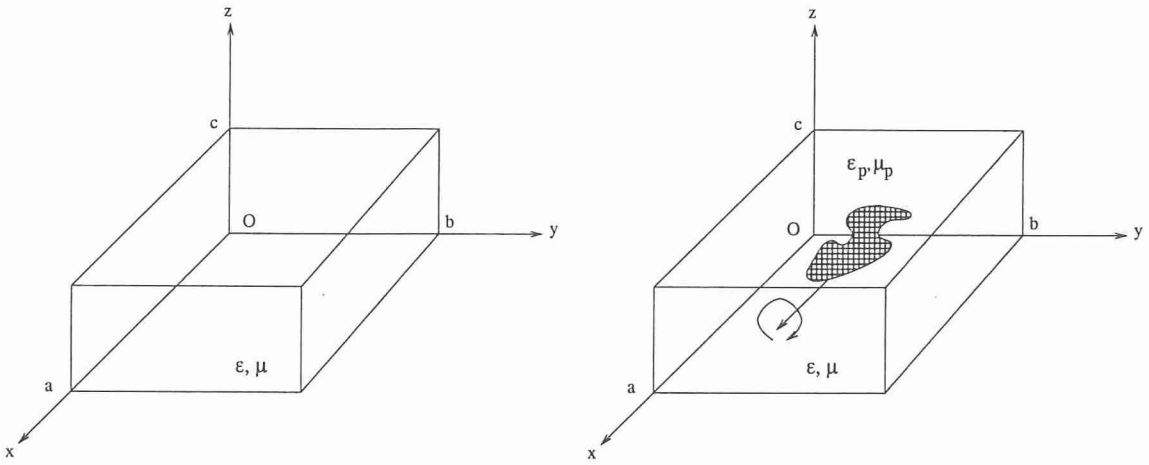

Figure 8.1: Cavity geometries. (a) Empty (unperturbed). (b) With a rotating perturbing body.

The quantities β_x, β_y and β_z are the wavenumbers along the x, y and z directions, respectively. Since the solution space is bounded, the wavenumbers are allowed to take only discrete values, while they are subjected to the constraint equation shown below:

$$\beta_x^2 + \beta_y^2 + \beta_z^2 = \beta^2 = \omega^2 \mu \varepsilon \tag{8.6}$$

where

$$\left.\begin{array}{rcl} \beta_x & = & \frac{m\pi}{a} \\ \beta_y & = & \frac{n\pi}{b} \\ \beta_z & = & \frac{p\pi}{c} \end{array}\right\} \begin{array}{l} m, n \in \mathbb{Z}_+ \quad \text{and} \quad m = n \neq 0 \\ p \in \mathbb{Z}_+^* \end{array} \tag{8.7}$$

Now consider the same cavity with a rotating perturbing body included in it, as shown in Fig. 8.1(b). The electromagnetic field expressions can be obtained by employing perturbation techniques, as described in [176], according to which the presence of the perturbing body in the cavity is dealt as a spatial variation of the material properties in it. In principle, the electromagnetic field can be expressed using a set of perturbed eigenfunctions. For the new field configuration, the wavenumbers can be written in terms of the ones corresponding to the empty cavity as:

$$\widetilde{\beta}_k = \beta_k + \Delta\beta_k \tag{8.8}$$

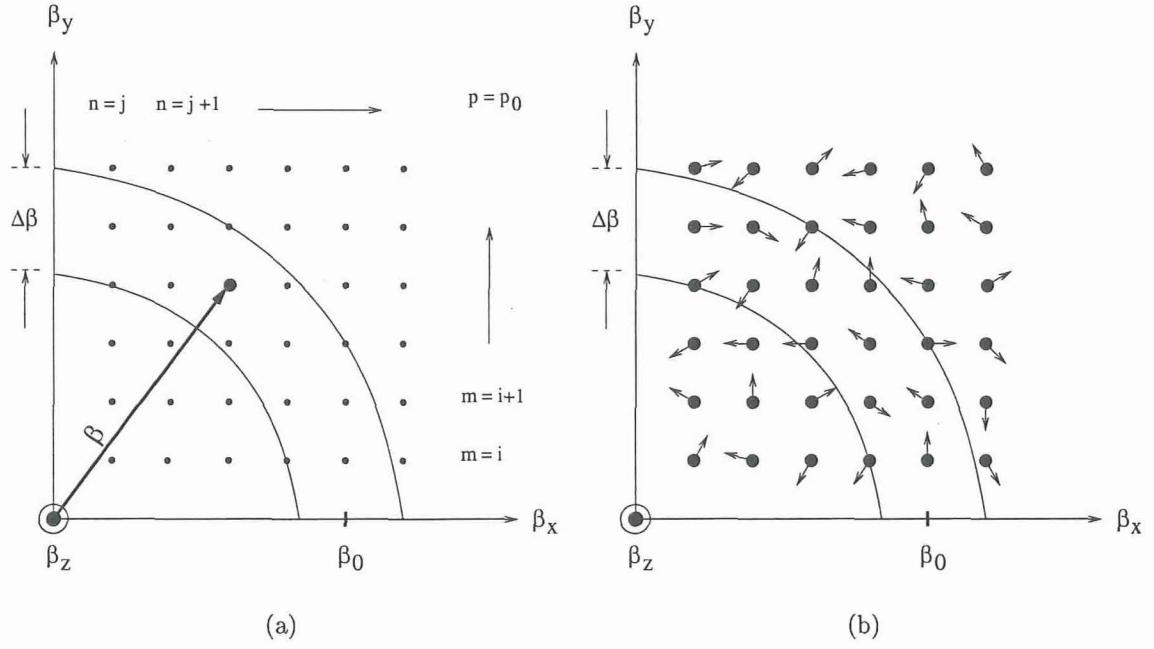

Figure 8.2: Mode distributions. (a) Empty cavity. (b) Cavity including perturb body.

where $k \in \{x,\ y,\ z\}$. From the above equation, it is obvious that the presence of the perturbing body results to an eigenfrequency–shift determined by the quantity $\Delta\beta_k$. The amount of wavenumber shift strongly depends on the size of the perturbing body since each mode's configuration is a function of space. Therefore, a large perturbing body will result to a pronounced wavenumber (eigenfrequency) shift. Nonetheless, it is the overall time-dependent behavior of $\Delta\beta_k$ that creates the desired mode agility and certifies an efficient RC operation. More precisely, a wavenumber shift with the proper time variation, will be continuously creating new modes. Certainly, in an overmoded cavity where mode spacing is small, a properly shaped stirrer makes the phenomenon more intense, and under certain conditions it has the ability to introduce randomness into the system.

To better illustrate wavenumber shifting, a pictorial presentation of the phenomenon is given. In Fig. 8.2(a) there is the mode distribution on a constant β_z plane of the discrete wavenumber space. For a constant excitation frequency f_0, the

bandwidth of operation is given by

$$\Delta f = \frac{f_0}{Q} \tag{8.9}$$

The cavity Q in the above equation is given by [177]

$$Q = \frac{3\,V}{2\,S\,\mu_r\,\delta} \tag{8.10}$$

where V is the volume of the cavity, S is the surface of the walls, δ is the skin depth and μ_r the relative permeability of the wall material. For a frequency f_0 and a corresponding bandwidth Δf, the excited modes are contained in a spherical shell of thickness $\Delta\beta$, a cross-section of which is the circular section shown in Fig. 8.2(a).

Now, if a perturbing body is placed inside this cavity, a wavenumber shift of the already existing modes will occur. However, if the size of the perturbing body is small, the amount of shift will be negligible. Consequently, when the mode-stirrer starts to rotate, the excited modes will barely start moving, and hence little mode agility will be achieved. In contrast, if the size of the body is large, the wavenumber shift will be significant, although this is not enough. For example, a large spherical body will definitely create a sufficient shift but its rotation, due to symmetry, will have no further effect; i.e. no mode agility will occur. Therefore , in addition the perturbing body has to be as irregularly shaped as possible. If all the above conditions for the scatterer are satisfied, eigenmodes will start to move in and out from the bandwidth zone, as shown in Fig. 8.2(b), resulting to the desired simultaneous mode excitation.

From the preceding analysis, the following conclusions can be drawn:

a. The "in–and–out" motion of the eigenmodes, which in a sense resembles a random-walk [161], results in the random excitation of the perturbed modes which is the key factor in order to introduce randomness in the cavity.

b. Although the term "randomness" is very common in the RC nomenclature, the actual randomness of the fields inside an RC may be questionable. An objection could be raised since the calculation of the field variations inside a cavity is a purely deterministic procedure that requires, in general, the superposition of several wave equation solutions. Therefore, how can the superposition of purely deterministic quantities, yield a random one? The answer to this question is

based on one of the very first assumptions that was made in order to develop the RC theory; that is, the perturbing rotating body, apart from being large enough, it should also be as asymmetrical as possible. The scatterer's asymmetry is equivalent to the height fluctuations of a rough surface that can only be described in a statistical sense. As a matter of fact, the height of a rough surface $z = z(x, y)$ can be expressed as a $2 - D$ Fourier series [1] [160]

$$z(x, y) = \sum_{m,n} P(m, n)\, e^{j\left(\frac{2\pi m}{L}x + \frac{2\pi n}{L}y\right)} \tag{8.11}$$

where $P(m, n)$ is a zero mean *random variable* whose values are uncorrelated for different spatial frequencies [2]. Furthermore, in order to describe the scattering field from surfaces such as the above, probability density functions of its amplitude and phase are employed [160]. From all the above, the inherent random nature of the electromagnetic field involved in such phenomena is apparent.

III. Stochastic processes and noise

In this section a brief overview of some basic properties of noise signals is given. Although the theory of stochastic processes is very documented in classic references such as [161], [178] and [179], for completeness some important details of it are repeated here.

A. Properties of white gaussian noise

Stochastic processes are random phenomena whose statistical properties are functions of time. For instance, the thermal noise voltages generated in the resistors of an electronic device is a typical example of a stochastic process. Notice that if several voltage measurements are performed, a different waveform will occur each time. Each of these voltage waveforms is a *sample function* while the set of all possible sample functions constitute an ensemble of sample functions or a stochastic process [161], [180].

A more mathematically consistent definition of a stochastic process is the following [161]: a stochastic process $\mathbf{x}(t)$ is a rule which assigns a function $\mathbf{x}(t, \zeta)$ to each

[1] L is the side length of a rough surface the height of which is given by $z(x, y)$

[2] $W(m, n)$ is the spectral density of the rough surface height function

outcome ζ of an experiment of luck. Therefore, a stochastic process is a family of time functions depending on the parameter ζ. In Fig. 8.3 there is a graphical representation of a stochastic process. As a matter of fact there are three realizations of the stochastic process $\mathbf{x}(t,\zeta)$ corresponding, respectively, to parameter values ζ_k, ζ_{k+1} and ζ_{k+2}. A property of particular interest is that, for a fixed time value t_o, the sequence $\{\mathbf{x}(t_0,\zeta_i)\}_{i=1}^{i=N}$ is a random variable.

For the purposes of this research, our interest was confined to band–limited white Gaussian noise, the properties of which are presented below. First of all noise is an ergodic random process. Ergodicity is a special case of stationarity. Although stationarity is defined in the strict sense as well as in the wide sense, we are interested only in the latter because of its attractive properties which are very helpful for our study. More specifically, a random process is called wide sense stationary if its expected value is constant; i.e., independent of time:

$$\mathcal{E}\{\mathbf{x}(t)\} = c, \quad \forall\, t \tag{8.12}$$

and its autocorrelation [or correlation between random variables $x(t_1,\zeta)$ and $x(t_2,\zeta)$] depends only on $\tau = t_1 - t_2$:

$$\mathcal{E}\{\mathbf{x}(t_1)\,\mathbf{x}(t_2)\} = R(t_1 - t_2) = R(\tau) \tag{8.13}$$

Ergodic are the stationary random processes whose statistical characteristics (n-th order moments) can be estimated from time–averages of a single sample function. For example, the expected value of random variable $\mathbf{x}(t)$, at any time instant $\mathcal{E}\{\mathbf{x}(t)\}$, is equal to the time average $\overline{\mathbf{x}(t)}$ or

$$\mathcal{E}\{\mathbf{x}(t)\} = \overline{\mathbf{x}(t)} = c \tag{8.14}$$

Moreover the autocovariance of $\mathbf{x}(t)$ [or the covariance of random variables $x(t_1,\zeta)$ and $x(t_2,\zeta)$] is given by:

$$C(t_1,t_2) = R(t_1,t_2) - n(t_1)\,n(t_2) \tag{8.15}$$

where $n(t_1) = \mathcal{E}\{\mathbf{x}(t_1)\}$ and $n(t_2) = \mathcal{E}\{\mathbf{x}(t_2)\}$. Since we have assumed wide sense stationarity (8.15), yields

$$C(\tau) = R(\tau) - n^2 \tag{8.16}$$

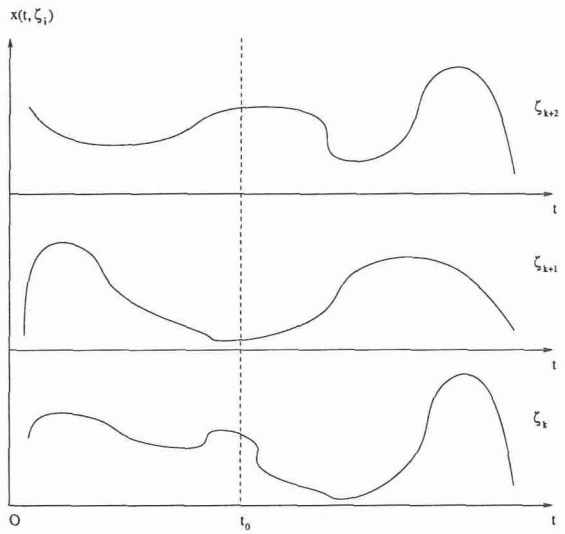

Figure 8.3: Three realizations of a stochastic process.

In addition a stochastic process $\mathbf{x}(t)$ is called white noise if the random variables $\mathbf{x}(t_i)$ and $\mathbf{x}(t_j)$ are uncorrelated for every $t_i \neq t_j$ or

$$C\left(t_i, t_j\right) = 0 \tag{8.17}$$

Furthermore, for a wide sense stationary white noise the following condition holds

$$C\left(\tau\right) = q\delta\left(\tau\right) \tag{8.18}$$

Therefore, from (8.16) and (8.18), we get that

$$R(\tau) = q\delta(t) \tag{8.19}$$

The above property uniquely characterizes a white noise while its importance will become apparent later where the spectral characteristics of noise are presented.
Finally, it is common to assume, since it is convenient calculation-wise, that the random variables $\mathbf{x}(t_i)$ are distributed according to a zero mean Gaussian distribution, or

$$\mathbf{x}(t_i) \sim N(0, \sigma^2) \tag{8.20}$$

B. Filtering and spectral characteristics of band–limited white gaussian noise

A very important property of white Gaussian noise is its delta-correlation, as shown in (8.19). In order to demonstrate the importance of this property, let us compute the Fourier transform of $R(\tau)$ or the power spectral density of white Gaussian noise:

$$S(\omega) = \int_{-\infty}^{+\infty} R(\tau) \mathrm{e}^{-\mathrm{j}\omega\tau} \mathrm{d}\tau = \frac{N_0}{2} \tag{8.21}$$

where we set $q \equiv \frac{N_0}{2}$. In Fig. 8.4(a) there is a graphical representation of the result obtained in (8.21). As can be observed, power is evenly distributed over all frequencies, a feature that perfectly matched to the requirements of frequency stirring. Moreover, the uniform distribution of power justifies the use of the term "white". It is used in analogy with white light, which is a superposition of all visible spectral components.

Let us now examine the effect of filtering on noise. Our analysis is similar to the one presented in [181]. First, we will demonstrate that if Gaussian noise $n_i(t)$ is applied to the input of a filter, as shown in Fig. 8.4(b), the output $n_o(t)$ is also Gaussian noise. If the impulse response of the filter is $h(t)$, then its output is given by:

$$n_o(t) = \int_{-\infty}^{+\infty} n_i(\tau) h(t-\tau)\, \mathrm{d}\tau \tag{8.22}$$

For the purposes of our analysis it is more convenient to rewrite the above equation as:

$$n_o(t) = \lim_{\Delta\tau \to 0} \sum_{k=-\infty}^{+\infty} n_i\left(k\Delta\tau\right) h\left(t - k\Delta\tau\right) \Delta\tau \tag{8.23}$$

From (8.23) it is apparent that the filter output is a superposition of impulses, each one of strength $n_i(k\Delta\tau)\Delta\tau$. Now, since the input signal is Gaussian noise, at two arbitrary time instances $k\Delta\tau$ and $l\Delta\tau$, the corresponding noise values $n_i(k\Delta\tau)$ and $n_i(l\Delta\tau)$ will be uncorrelated, independent Gaussian distributed random variables with zero mean and with the same variance. Consequently, for any time instant t_o, the filter output $n_o(t_o)$ is a linear superposition of independent random variables and hence, according to the Central Limit Theorem, $n_o(t_o)$ will also be Gaussian distributed with

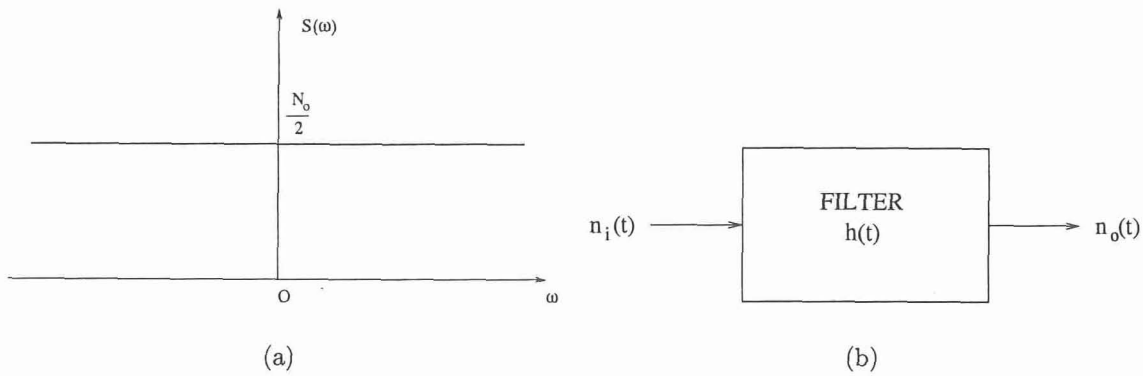

Figure 8.4: Noise band-pass filtering. (a) Power spectral density of white noise. (b) Block diagram of noise filtering.

zero mean and with variance the same as that of $n_i(t_o)$, where $n_o(t)$ is the output noise signal and it will be a Gaussian stochastic process.

After demonstrating that filtering does not alter the statistical characteristics of Gaussian noise, the effect of filtering on its spectral characteristics is further examined. In order to do that, first a frequency representation of noise is established. Consider a sample function of noise $n(t)$ where from this sample the section corresponding to the time interval $(-T/2, T/2)$ is selected. Let $n_T(t)$ be the periodic expansion of the selected section. Then, since $n_T(t)$ is periodic, it can be represented as a Fourier series expansion:

$$n_T(t) = \sum_{k=1}^{+\infty} [a_k \cos(2\pi k \Delta f t) + b_k \sin(2\pi k \Delta f t)] \tag{8.24}$$

where $\Delta f = 1/T$. Notice that if we let $T \to +\infty$ (or $\Delta f \to 0$), then $n_T(t)$ reverts to the actual noise sample function $n(t)$:

$$n(t) = \lim_{T \to +\infty} n_T(t) \tag{8.25}$$

$$= \lim_{T \to +\infty} \sum_{k=1}^{+\infty} [a_k \cos(2\pi k \Delta f t) + b_k \sin(2\pi k \Delta f t)]$$

Given the validity of (8.25), it is expected that when noise is passed through a band-pass filter, the transfer function of which is shown in Fig. 8.5(a), it is expected

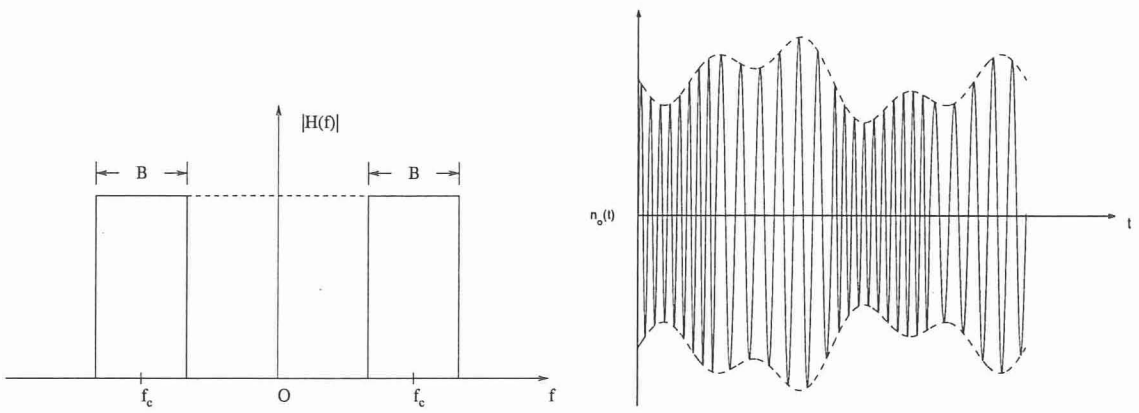

(a) (b)

Figure 8.5: Noise band-pass filtering. (a) Band-pass filter transfer function. (b) Time response of noise band-pass filtering.

that the output of the filter will be a combination of sinusoids in the frequency range $(f_c - B/2, f_c + B/2)$, while its amplitude will vary randomly [181]. A waveform of the output is shown in Fig. 8.5(b) where different frequency components as well as random fluctuations of the envelope's amplitude can be observed. Furthermore, Wu and Chang [149] studied the effect of a mode-stirrer in the response of a cavity, and they concluded that the "action of a large rotating scatterer in a cavity has the same effect as a signal that has been both frequency and amplitude modulated". This last comment implies that the system "mode-stirrer cavity" is described by a transfer function which randomly modulates both in amplitude and frequency the input signal. This conclusion proves that mechanical mode-stirring of cavities is equivalent to frequency stirring or to band–limited noise excitation of cavities. Also the amplitude modulation effect on electromagnetic fields due to a rotating body has been studied in [182] and [183].

Finally, it can be easily proved that if a stochastic process $\mathbf{x}(t)$ is applied to the input of linear time-invariant filter, then the output is also a stochastic process while their power spectral densities are related according to

$$S_{\mathbf{y}}(f) = |H(f)|^2 \, S_{\mathbf{x}}(f) \tag{8.26}$$

where $H(f)$ is the filter's transfer function. The power of the output signal is given

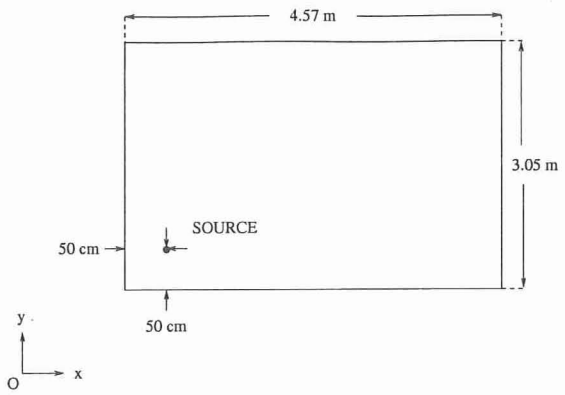

Figure 8.6: Two dimensional cavity geometry.

by:

$$P(f) = \int_{-\infty}^{+\infty} S_{\mathbf{y}}(f)\mathrm{d}f \tag{8.27}$$

Thus, if the input is white Gaussian noise, then the power of the output noise signal is equal to:

$$P(f) = N_0 B \tag{8.28}$$

where B is the band–pass filter's bandwidth.

IV. Two-dimensional cavity excitation

In this section frequency stirring of a 2-D conducting cavity is studied. A 2-D cavity was selected to begin our simulations instead of a 3-D one, because it is a considerably less complicated problem. In addition, a simple case is also the recommended one in order to get familiar with a new technique; i.e., frequency stirring. In what follows, initially an overview of the simulation set-up is given while afterwards the corresponding results are presented.

A. Simulation set-up

The geometry of the cavity that was modeled is shown in Fig. 8.6, and as can be seen its dimensions are 4.57 m $\times$ 3.05 m while the conductivity of its walls was set equal to aluminum's conductivity, that is 3.816×10^7S/m. Notice that the cavity's

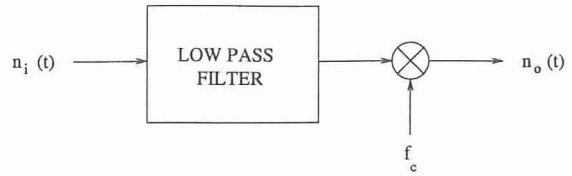

Figure 8.7: Excitation signal generation.

dimensions are the same as the ones from the RC of NIST [147]. Furthermore, the cavity was excited with an infinite line source located 50cm from the left and bottom walls.

Of particular importance for the success of our simulations was the proper choice of the excitation signal. Obviously, the latter would be band–limited white Gaussian noise; however, the center frequency, as well as the bandwidth, had to be determined by us. Based on useful hints from already existing studies on the same topic [174], [184] and [185], it was decided to perform our simulations at an operating frequency of 1 GHz and 4 GHz and for five different bandwidths of 0 MHz, 1 MHz, 5 MHz, 10 MHz and 50 MHz. It has to be mentioned that the criterion for choosing the operating frequency is to create a sufficiently overmoded cavity. In particular the cavity's under test electrical size at 1 GHz and 4 GHz is approximately $15\lambda \times 10\lambda$ and $46\lambda \times 31\lambda$, respectively, which based on the 6λ empirical criterion [169] is undoubtedly a well-overmoded cavity. The reason for choosing several frequency bandwidths was in an effort to study the ability to create a homogeneous field configuration as a function of frequency bandwidth.

In order to simulate the electromagnetic field variations inside the cavity, a 2-D standard FDTD code [186] was developed. Since the excitation was a z directed infinite in extent current source, the TM^z (E_z, H_x, H_y) field configuration was modeled. The choice of the discretization cell size was based on the operating frequency. Therefore, for the 1 GHz case a 10–mm cell size was chosen, while for the 4 GHz one a 5–mm cell size was selected. Based on the $\lambda/10$ criterion, those cell sizes provide sufficiently accurate results up to 3 GHz and 6 GHz, respectively. It has to be mentioned that all of the performed simulations were computationally intensive. As an indication, we mention that for 2^{18} time-steps and a 10–mm cell size, almost half a day simulation time was required while for the same number of time-steps and a

5–mm cell size, the simulation was significantly longer, nearly 5 days. All simulations were performed at a four PENTIUM 2.2 GHz processor machine, with 6 Gb of RAM, running under LINUX OS.

The excitation signal $n_o(t)$ was generated following the procedure shown in the block diagram of Fig. 8.7. As can be seen, white Gaussian noise $n_i(t)$ was first passed through a low-pass filter whose bandwidth corresponds to the bandwidth of interest, i.e. 0 MHz, 1 MHz, 5 MHz, 10 MHz and 50 MHz. For the implementation of the low-pass filter, we used the raised-cosine function [180]:

$$x(t) = \frac{\sin(\pi t/T)}{\pi t/T} \frac{\cos(\pi \beta t/T)}{1 - 4\beta^2 t^2/T^2} \tag{8.29}$$

Notice that $x(t)$ is also dependent on the parameter β which is referre to as the roll-off factor and takes values in the range $0 \leq \beta \leq 1$. By properly choosing the value of β, the raised-cosine's spectrum can be adjusted and create nearly ideal low–pass filters that do not suffer from the Gibb's phenomenon. The time dependent waveforms of a raised-cosine along with the corresponding spectrum for three different values of β are shown in Figs. 8.8(a)-8.8(b). For our simulations, the roll-off factor was set to 0.1.

Afterwards the filtered signal was modulated to the operating frequency of interest f_c. The modulation scheme was double sideband, suppressed carrier, amplitude modulated (AM-DSB-SC) [181]. The spectrum of the resulting output signal $n_o(t)$ for an operating frequency of 1 GHz, and four different bandwidths, are shown in Figs. 8.9(a)-8.9(d). It has to be mentioned that the creation of the excitation signal was performed using *MATLAB*, and the output was stored in a text file. Then the FDTD code, written in *FORTRAN*, was properly modified so that each time an excitation source value was needed it could be obtained from the text file.

Finally, 135 locations inside the cavity were chosen and the values of the E_z component were observed. The probing locations were divided in groups of 45. Each group's points were distributed equidistantly along the $y = 1.0$ m, $y = 1.5$ m and $y = 2.0$ m axis, respectively. In each row the spacing between two successive observations points was 10 cm. After the end of each simulation, the following data post–processing was performed in order to compute field homogeneity:

1. Compute the Fourier transform of E_z at an observation point based on the its

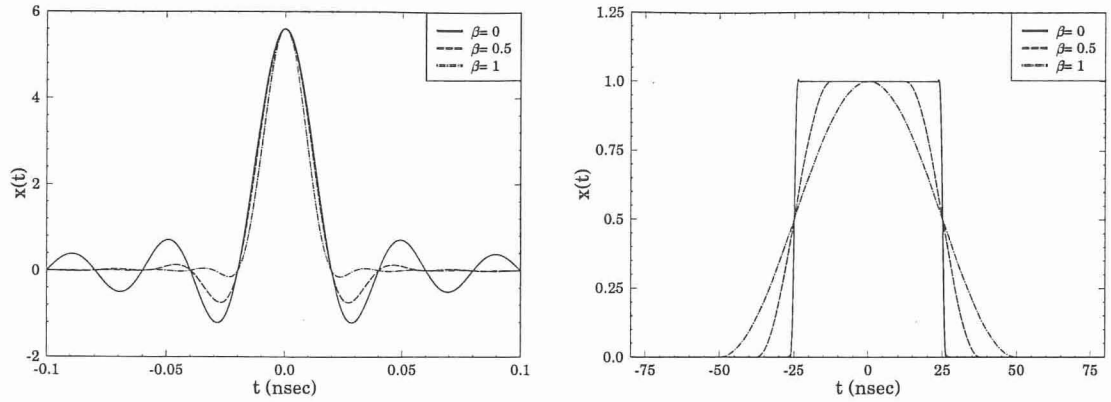

(a) (b)

Figure 8.8: Raised cosine pulse. (a) Time waveform. (b) Spectrum.

time-response as predicted from FDTD.

2. Select those values of the frequency response which lie within the bandwidth of the excitation signal.

3. Calculate the average square E_z frequency response at the point of interest for an operation frequency f_c and a bandwidth BW, using the following formula:

$$|E_z(f_c)|^2_{av} = \frac{1}{BW}\sum_i |E_z(f_i)|^2 \Delta f_i, \quad |f_i - f_c| \leq \frac{BW}{2} \tag{8.30}$$

B. Simulation Results

In this section results from homogeneity tests are presented. In Figs. 8.10(a)–8.11(d) the average electric field frequency response is shown as a frequency of position. In particular Figs. 8.10(a)–8.10(d) correspond to excitation signals bandwidths 1 MHz, 5 MHz, 10 MHz and 50 MHz, respectively, at a center frequency of 1 GHz. Results for the same excitation signal bandwidths, but for a 4 GHz center frequency, are shown in Figs. 8.11(a)–8.11(d). Notice that the average E_z frequency response for each bandwidth has been plotted along

with the response corresponding to a zero-bandwidth excitation signal. The latter was chosen as a reference because, according to the frequency stirring methodology, it is considered as the worst excitation scenario. Moreover, all the results presented here

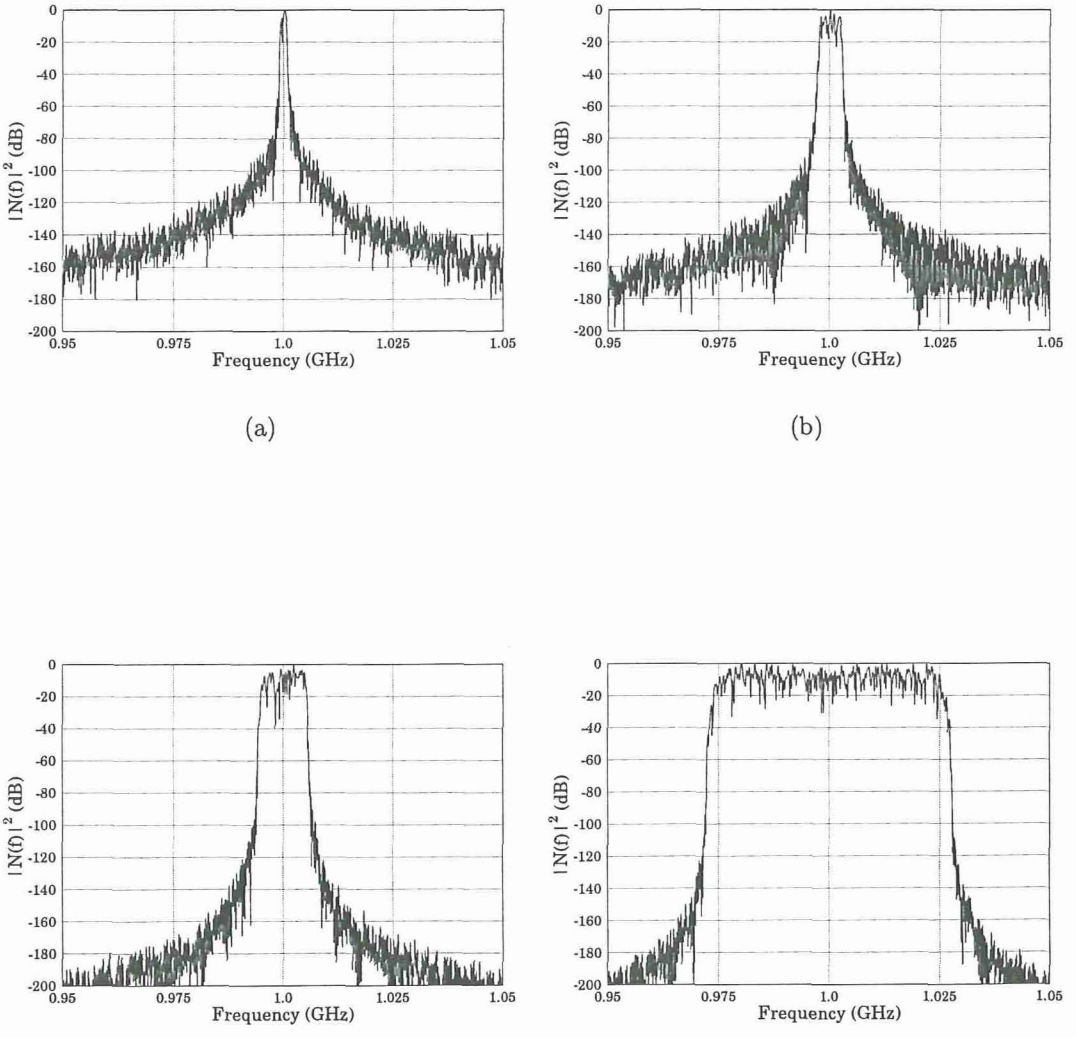

Figure 8.9: Spectrum of excitation signal. (a) 1 MHz bandwidth. (b) 5 MHz bandwidth. (c) 10 MHz bandwidth. (d) 50 MHz bandwidth.

correspond to observations made at the group of points distributed along the middle row ($y = 1.5$ m). Finally, it has to be mentioned that all the frequency responses have been normalized to their mean value versus position.

From both groups of figures [Figs. 8.10(a)–8.10(d) and Figs. 8.11(a)–8.11(d)] it is apparent that field variations versus position significantly decrease as bandwidth increases. As a matter of fact the standard deviation of the field fluctuations for a zero–bandwidth excitation signal is 8.7 dB, while for a 50 MHz it reduces to 0.8 dB. The standard deviation of the electric field variations decreases gradually and the amount of decrease is proportional to the bandwidth of the excitation signal.

However, when the center frequency increases, from 1 GHz to 4 GHz, it is observed that relatively good electric field spatial uniformity is established for smaller bandwidths of the excitation signal. More precisely, for a 5 MHz bandwidth at 1 GHz the standard deviation of the electric field is 3.5 dB while for the same bandwidth at 4 GHz it reduces to 1.7 dB. This was expected since as frequency increases the number of the excited modes in the cavity becomes larger. For example, for the previous excitation scenarios, the modes in the cavity are 5 and 19, respectively. At this point it has to be mentioned that the cavity's dimensions have been chosen so that the ratio of its sides' lengths is an irrational number. In such a case, mode degeneracy is avoided and each mode individually contributes to the field uniformity. Consequently, the number of the excited modes in the cavity is an important quantity which determines the field homogeneity.

Finally, in Figs. 8.12(a)-8.12(b) the average electric field frequency response is plotted for three different y positions. More precisely, in Fig. 8.12(a) for a center frequency of 1 GHz and a bandwidth of 50 MHz, the average electric field is plotted as a function of x for $y = 1.0$ m, $y = 1.5$ m and $y = 2.0$ m. In Fig. 8.12(b) the same curves are plotted for 4 GHz. It is apparent that the three curves, for both frequencies, are characterized by the same statistics. This last result is very important because it proves that spatial uniformity is not established locally but everywhere in the cavity. All the above observations are summarised in Table 8.1.

		Lower row $y = 1.0$ m		Middle row $y = 1.5$ m		Upper row $y = 2.0$ m	
Center frequency	BW (MHz)	STD (dB)	Number of modes	STD (dB)	Number of modes	STD (dB)	Number of modes
1 **GHz**	1	6.57	1	8.52	1	8.71	1
	5	3.50	5	2.53	5	3.89	5
	10	1.88	10	1.74	10	2.13	10
	50	0.83	49	0.95	49	0.89	49
4 **GHz**	1	3.15	4	4.34	4	3.44	4
	5	1.70	19	2.20	19	1.85	19
	10	1.50	39	1.85	39	1.52	39
	50	1.00	195	0.91	195	1.09	195

Table 8.1: Standard deviation and number of modes for different bandwidths, excitation frequencies and positions.

V. Three-dimensional cavity excitation

In this section the frequency stirring technique is further investigated by examining its implementation for the case of a 3-D cavity. This is a significantly more complicated problem to be studied; however its successful modeling is equivalent to the simulation of a real RC's operation. This would offer great advantages since a "virtual" RC facility will be available

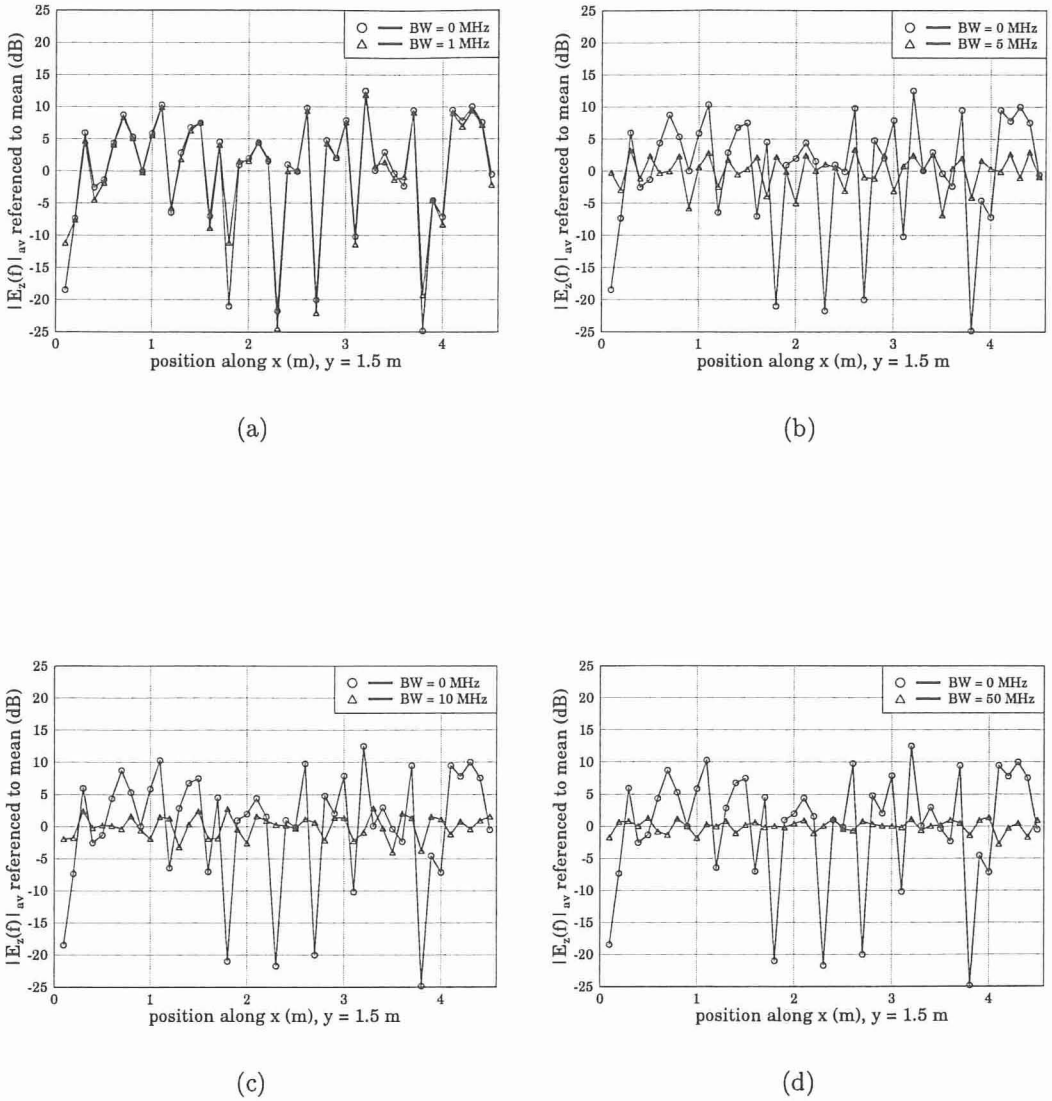

Figure 8.10: Electric field homogeneity at 1 GHz for different noise bandwidths. (a)0 MHz versus 1 MHz. (b) 0 MHz versus 5 MHz. (c) 0 MHz versus 10 MHz. (d) 0 MHz versus 50 MHz.

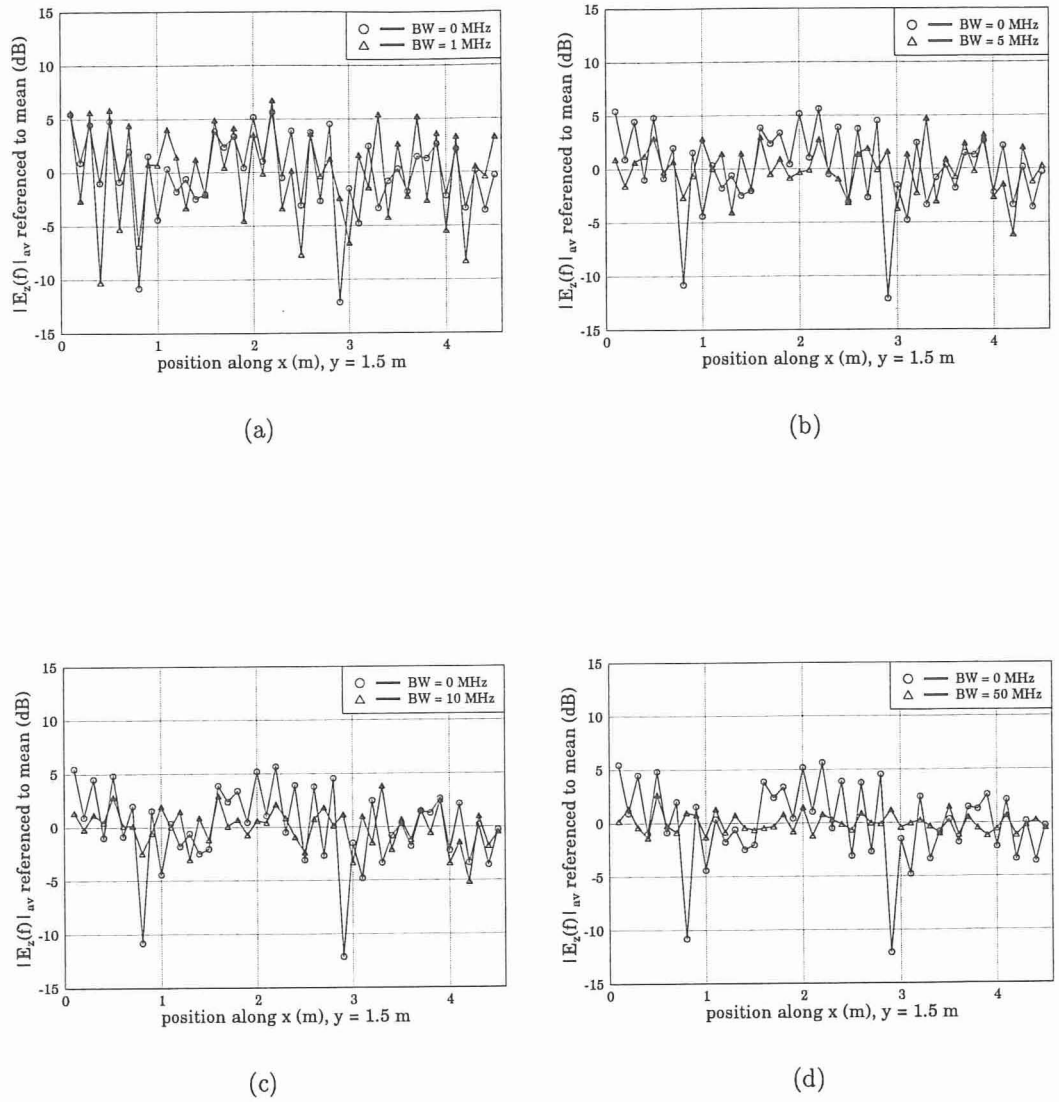

Figure 8.11: Electric field homogeneity at 4 GHz for different noise bandwidths. (a)0 MHz versus 1 MHz. (b) 0 MHz versus 5 MHz. (c) 0 MHz versus 10 MHz. (d) 0 MHz versus 50 MHz.

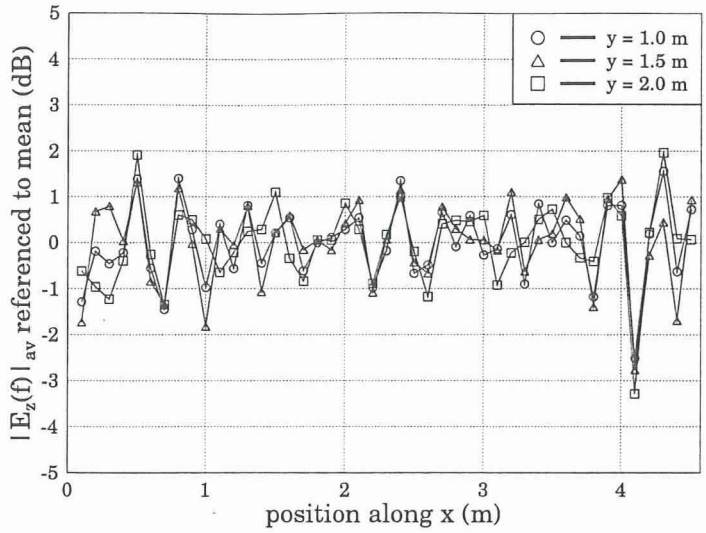

(a)

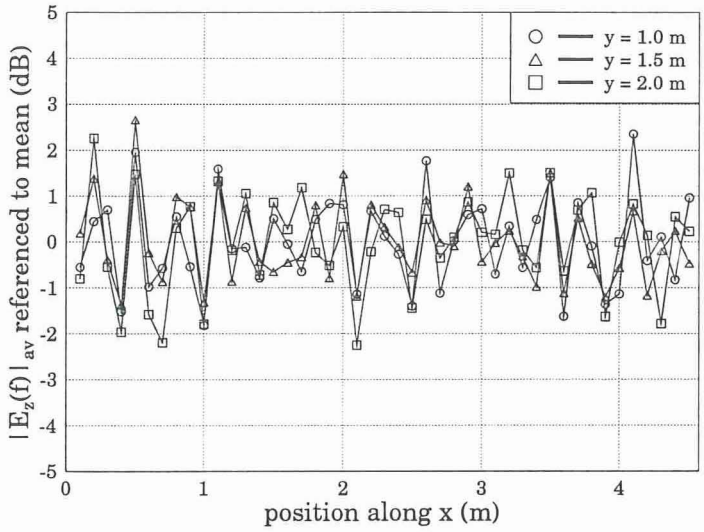

(b)

Figure 8.12: Electric field homogeneity for different y positions. (a) Center frequency 1 GHz and bandwidth 50 MHz. (b) Center frequency 4 GHz and bandwidth 50 MHz.

for vulnerability testing of various, sensitive to EMI, equipment. As will be shown later, the electromagnetic field inside the 3-D cavity, except for its uniformity it will also be tested for its isotropy. As has been described in Chapter 6, an electromagnetic field configuration is described as isotropic when its energy is equally distributed among the three electric or magnetic field components. Uniformity along with isotropy are very important properties which uniquely characterize the electromagnetic field inside an RC. In what follows, an overview is given of the simulation set-up with a particular emphasis on the radiation element's design, which is of great importance for the methods effectiveness. Afterwards, the corresponding test results are presented.

A. Simulation set-up

The geometry of the cavity that was modeled is shown in Fig. 8.13(a), and as can be seen its dimensions are 2.05 m $\times$ 1.50 m $\times$ 1.30 m while the conductivity of its walls was set equal to aluminum's conductivity, that is 3.816×10^7S/m. Notice that the cavity's dimensions have been chosen so that the ratio of its sides' lengths is an irrational number. As a result degeneracy is avoided and each excited mode is distinct.

In the same figure, it can also be seen the antenna configuration used for our simulations, in order to inject electromagnetic energy inside the cavity. A more detailed description of the antenna geometry is given in Fig. 8.13(b). The antenna consists of a hollow right wedge with a vertical dipole placed in it. The top and bottom faces of the wedge are right isosceles triangles whose right edges are 30 cm long, as is its height. Both the top and bottom faces of the wedge are parallel to the cavity's top and bottom walls. The dipole is 11 cm high [Fig. 8.14(a)] and it has been placed 10 cm away from the cavity's right edges [Fig. 8.14(b)]. Notice that the wedge has been positioned inside the cavity so that its open face directs the electromagnetic energy, emanating from the dipole, towards one of the cavity's edges.

As has been mentioned previously, the choise of the antenna for the excitation of an RC is a very crusial issue, about which several design guidelines have been suggested [147], [174], [184]. In these references it is recommended that the appropriate transmittimg antennas for an effective RC operation are horn type [45], oriented to-

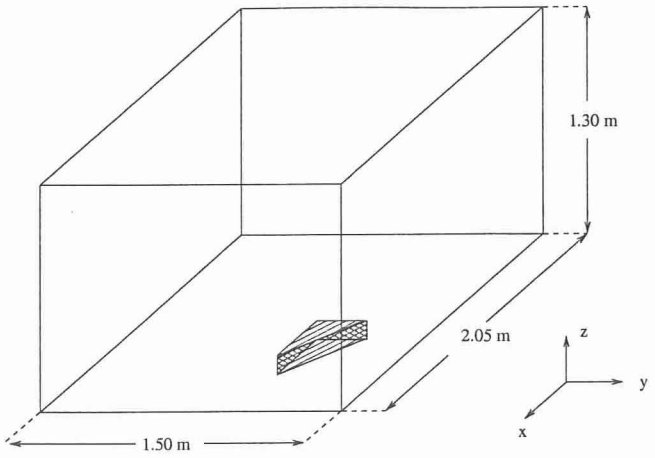

(a) Perspective view.

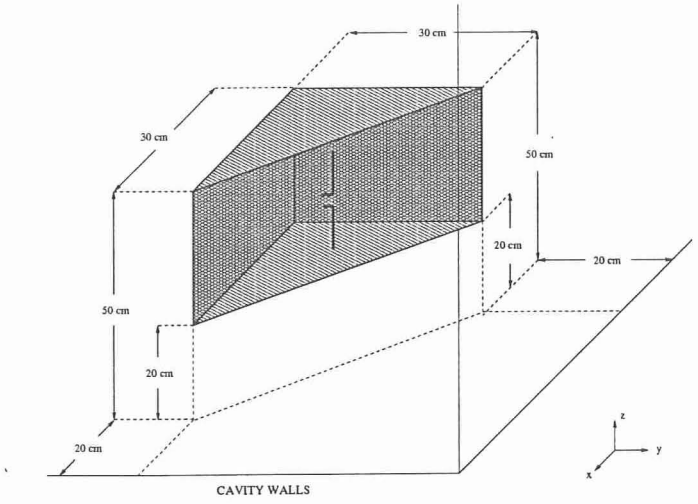

(b) Antenna details.

Figure 8.13: Three dimensional cavity.

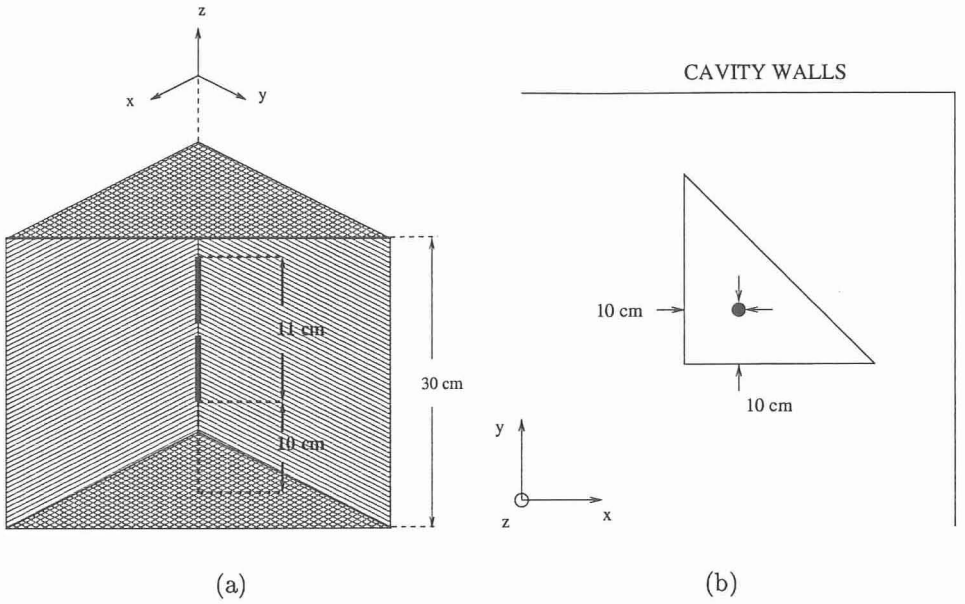

(a) (b)

Figure 8.14: Dipole details. (a) Front view. (b) Top view.

wards one of its vertices. In such way the elimination of dominant field compoments is ensured (no line-of-sight between the antenna and the observation points) while the field is allowed to spread evenly towards all directions inside the cavity and hence a random field configuration is established. Given all the above, as well as the inherent limitation of FDTD to accurate model geometries including tilted surfaces (it introduces staircasing), the choise of the above radiating configuration is considered optimal because it complies with RC design guidelines and it can be easily modeled using FDTD.

The excitation signal was band-limited white Gaussian noise; the generation of the excitation signal was performed as described for the 2-D cavity. However, simulations were performed only for a center frequency of 3 GHz and for bandwidths of 0 MHz, 10 MHz and 50 MHz. For this particular frequency, the cavity's electrical size is $20\lambda \times 15\lambda \times 13\lambda$ which based on the 6λ empirical criterion [169] it can definitely be characterised as well-overmoded.

In order to simulate the electromagnetic field variations inside the cavity, a 3-D standard FDTD code was used. The choice of the discretization cell size was based on the operating frequency, therefore a 10–mm cell size was chosen. Based on the $\lambda/10$

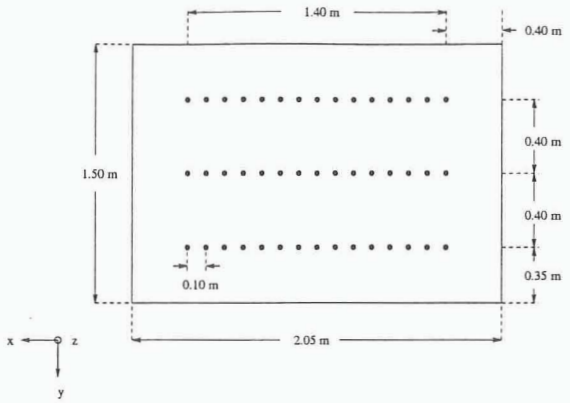

Figure 8.15: Observation points.

criterion, this cell size provides sufficiently accurate results up to 3 GHz. It has to be mentioned that all of the performed simulations were computationally intensive. As an indication, we mention that for 2^{18} time-steps, the simulation time was nearly 7 days. All simulations were performed at a four PENTIUM 2.2 GHz processor machine with 6 Gb of RAM running under LINUX OS.

Finally, 42 locations inside the cavity were chosen and the values of the E_x, E_y and E_z electric field components were observed. All the observation points are along the $z = 0.80$ m plane while they are divided in groups of 14 as shown in Fig. 8.15. Each group's points are distributed equidistantly along the $y = 0.35$ m, $y = 0.75$ m and $y = 1.15$ m axis, respectively. In each row the spacing between two successive observations points is 10 cm. After the end of each simulation, the collected data were post–processed and uniformity, as well as isotropy tests, were performed.

B. Simulation results

In this section results from homogeneity and isotropy tests are presented. In Figs. 8.16(a)-8.16(b) the average $|E_z|$ frequency response as a function of frequency is shown, for a 10 MHz and 50 MHz excitation signal bandwidth, respectively. Notice that the average E_z frequency response for each bandwidth has been plotted along with the response corresponding to a zero-bandwidth excitation signal. The latter was chosen as a reference because, according to the frequency stirring methodology, it is considered as the worst excitation scenario. Moreover, all the results presented here

correspond to observations made at the group of points distributed along the middle row ($y = 0.75$ m). Finally, it has to be mentioned that all the frequency responses have been normalized to their mean value versus position.

From both figures it is apparent that field variations versus position significantly decrease as the bandwidth increases. As a matter of fact the standard deviation for a zero-bandwidth excitation signal is 4.184 dB, while for a 10 MHz and 50 MHz bandwidth, it reduces down to 1.182 dB and 0.432 dB, respectively. It is apparent that frequency stirring is able to create the desired field homogeneity inside the 3-D cavity. It can also be observed that the standard deviation of the electric field variations decrease gradually and the amount of decrease is proportional to the bandwidth of the excitation signal. The same conclusions can be drawn for the electromagnetic field homogeneity based on observations made along the lower ($y = 0.35$ m) and the upper ($y = 1.15$ m) rows. In Fig. B., the average electric field frequency response is plotted for the three different rows. It is apparent that the three curves are characterised by the same statistics. This last result is very important because it proves that spatial uniformity is not a local phenomenon in the cavity.

Finally, in Fig. B. the electric field isotropy is presented. As can be seen, the average frequency response of $|E_x|$, $|E_y|$ and $|E_z|$ are plotted as a function of position. All three plots correspond to observations made along the middle row ($y = 0.75$ m) for an excitation signal of a 50 MHz bandwidth. It can be observed that at each observation point, along each direction, the electric field is characterised by nearly the same average frequency response (differences > 3 dB). This is a clear indication that the electromagnetic field is isotropic and consequently, if an equipment under test is placed inside it, it will be subjected to the same field values in the x, y and z directions. All the above observations are summarised in Table 8.2.

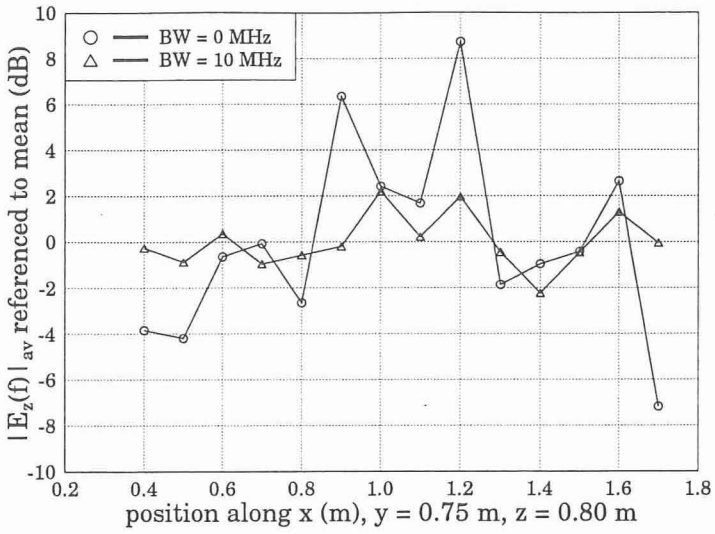

(a)

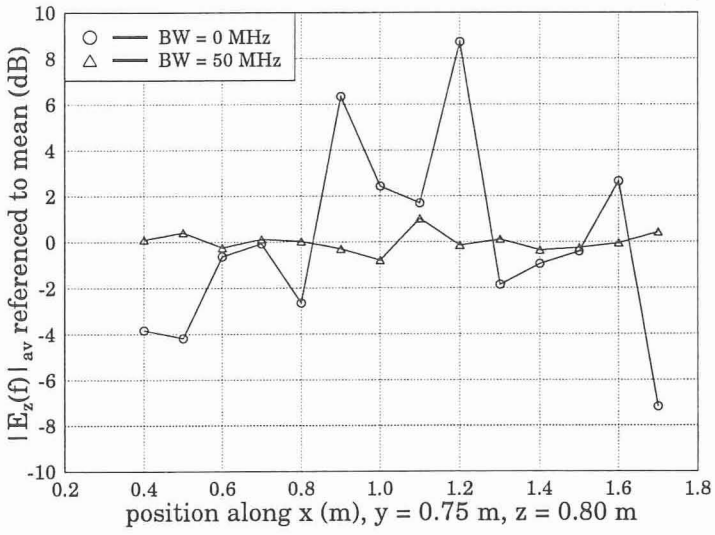

(b)

Figure 8.16: Electric field homogeneity at 3 GHz for different noise bandwidths. (a) Center frequency 3 GHz and bandwidth 10 MHz. (b) Center frequency 3 GHz and bandwidth 50 MHz.

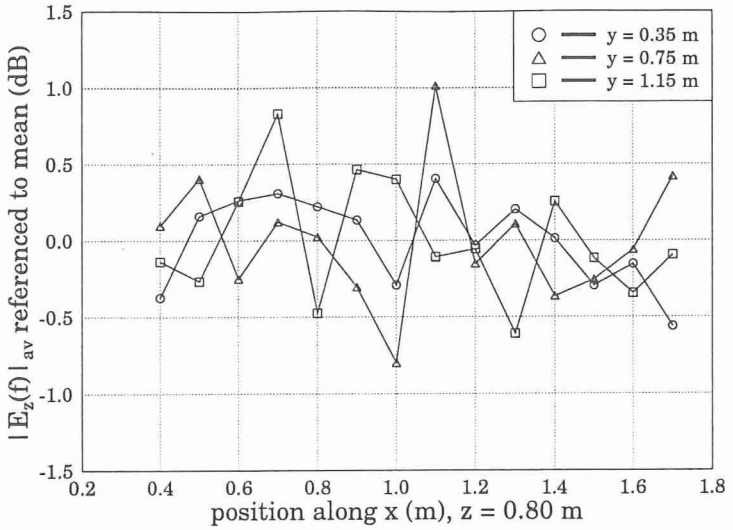

Figure 8.17: Electric field homogeneity for different y positions. Center frequency 3 GHz and bandwidth 50 MHz.

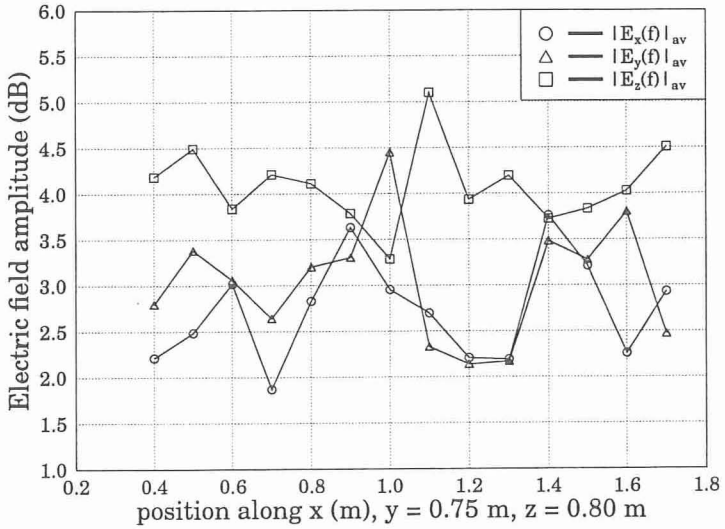

Figure 8.18: Electric field isotropy. Center frequency 3 GHz and bandwidth 50 MHz.

			Lower row $y = 0.35$ m	Middle row $y = 0.75$ m	Upper row $y = 1.15$ m
Field Component	BW (MHz)	Number of modes	STD (dB)	STD (dB)	STD (dB)
E_x	10	335	0.95	1.28	0.78
	50	1675	0.82	0.57	0.55
E_y	10	335	1.21	1.39	1.68
	50	1675	0.62	0.66	0.53
E_z	10	335	1.43	1.18	1.39
	50	1675	0.29	0.43	0.40

Table 8.2: Standard deviation and number of modes for different bandwidths, excitation frequencies,electric field components and positions.

Chapter 9

Summary and Conclusions

One of the main objectives of this research was the investigation and development of low dispersion methods that can accurately, as well as efficiently, solve electrically large problems. It is of great interest in many applications, such as antenna analysis or scattering and penetration, to be able to analyze electrically large problems. Traditional finite methods, such as the FDTD and the FEM methods, are second-order accurate, thereby significantly restricting the size of the structures that can be handled. Dispersion is an inherent characteristic of these methods that also corrupts the numerical solutions with errors, and it becomes even more important for electrically large domains. One way of dealing with these problems is to use higher-order finite-difference (FD) methods that exhibit less dispersion and can analyze more efficiently such domains.

Higher-order FDTD schemes were examined and implemented into three dimensional general codes which can handle arbitrary geometries and can perform numerous types of analysis, such as antenna, coupling, and penetration analysis. Specifically, a second-order accurate in time and fourth-order accurate in space scheme FDTD(2,4) was mainly used throughout this report. In order to solve "open-space" problems absorbing boundary conditions (ABCs) had to be formulated and applied in the context of FDTD(2,4). The perfectly matched layer (PML) was chosen as ABCs due to its excellent performance compared to other types of ABCs. Various difficulties of the implementation of higher-order schemes, such as boundary conditions and discontinuities, were extensively discussed and resolved. Additionally, two different hybrid methods between the subgrid FDTD(2,2) and FDTD(2,4) were developed and

formulated.

The second main objective of this research was to analyze three very important and complex practical problems. The first problem concerned analysis of cavity-backed slot (CBS) antennas with particular emphasis on different coupling reduction techniques. The second problem involved shielding effectiveness analysis of conducting enclosures with apertures, and it related to penetration of High Intensity Radiated Fields (HIRF) into airplane fuselages. Finally, the third problem consisted of the analysis of EMI generated by personal electronic devices (PEDs) in the cabin of fuselages. In the following paragraphs, the conclusions of this research are presented in more detail.

This research was initiated by examining the basic characteristics of FDTD(2,4). Dispersion as well as stability characteristics of both FDTD(2,2) and FDTD(2,4) were analytically formulated, numerically computed, and compared. It was shown that FDTD(2,4) outperforms FDTD(2,2) in terms of dispersion errors. Therefore, FDTD(2,4) can be used to accurately model electrically larger domains than the ones that can be simulated by FDTD(2,2). Then, one-dimensional domains were analyzed using both FDTD(2,2) and FDTD(2,4) to qualitatively access the performance characteristics of FDTD(2,4) and compare them to the ones of FDTD(2,2). In free space simulations, it was found that a 20 wavelengths long domain was simulated accurately by FDTD(2,4) when a discretization of a tenth of a wavelength ($\Delta x/10$) was used. However, this discretization of the domain ($\Delta x/10$) yielded inaccurate results in the case of FDTD(2,2) due to large dispersion errors of FDTD(2,2).

Furthermore, FDTD(2,4) was applied to perfect conductor discontinuities (PEC) analysis, and it was found that FDTD(2,4) exhibits an inherent artificial penetration through thin PEC films. This is attributed to the length of the FDTD(2,4) stencil which allows fields from one side of the PEC to couple on the other side of the PEC. Two ways to resolve this problem were proposed in the one-dimensional formulation. These two ways were found to be effective for most two-dimensional problems but unstable or ineffective for most practical three-dimensional problems where PEC planes are not infinite in extent. As far as dielectric discontinuities, numerical analysis on one-dimensional domains illustrated that FDTD(2,4) was able to accurately simulate the transition from one dielectric to the other.

In order to solve unbounded problems, such as radiation, scattering, etc., absorbing boundary conditions had to be implemented in FDTD(2,4). The perfectly matched layer (PML) method was chosen. Specifically, the anisotropic PML technique was used to terminate FDTD(2,2) and FDTD(2,4) lattices. The anisotropic PML does not use the split formulation of the fields presented in the original PML by Berenger thereby being more consistent with the Maxwell's equations. It was found that PML is a very effective truncation technique, and it performs equivalently on either FDTD(2,2) or FDTD(2,4) for two- and three-dimensional computational grids.

Moreover, the FDTD(2,4) method was used to solve two simple 3-D problems of engineering interest. It was shown that FDTD(2,4) was far more accurate in predicting the pattern of an array consisting of two elements and calculating the resonances of a rectangular cavity. A discretization with cell size of $\lambda/10$ was found to be adequate for domains as large as 20 wavelengths. Also, radiation pattern analysis of monopoles on helicopter airframes, as well as rectangular boxes, was performed by FDTD(2,4). The accuracy of FDTD(2,4) was again better than the accuracy of FDTD(2,2).

Boundary conditions in the context of higher-order schemes were also discussed. Boundary conditions represent one of the most important challenges in higher-order methods. An extensive literature review of this issue was presented, and most of the existing research has been generated in the fields of computational physics and mathematics. This line of research, which is related to boundary conditions and higher-order schemes, supports the fact that it is very challenging to design accurate as well as stable higher-order boundary conditions. In particular, stability is the most difficult problem. Even though many efforts to formulate stable schemes have been attempted, only few and simple one- and two-dimensional problems have been analyzed using higher-order boundary conditions. However, when the analysis is extended to systems of equations which are multi-dimensional (especially three-dimensional), higher-order boundary conditions, that can be applied in a stable way, do not exist. In addition, most of the known research has dealt with boundary conditions on the exterior boundary of computational domains whereas in most practical engineering problems boundary conditions have to be applied to the interior of the domain. This makes the problem of boundary conditions even more difficult.

One very important issue related to boundary conditions is the ability of a method to simulate thin geometric features, meaning features that are much smaller in size than all other dimensions of the geometry, and they cannot be discretized using a reasonable cell size. The issues of boundary conditions and thin geometric features in the context of FDTD(2,4) were illustrated through simulation of two monopole antennas on finite ground planes.

Initially, FDTD(2,4) was applied alone without being able to simulate the radius of the wires. The S-parameters computed in this case by FDTD(2,4) were more accurate than FDTD(2,2). However, the input impedance FDTD(2,4) calculations were not as accurate as the ones of FDTD(2,2) since FDTD(2,4) did not simulate the radius of the wires. Then, FDTD(2,4) was combined with the FDTD(2,2) thin wire model and the S-parameters computed in this case were not as accurate as the ones that used only FDTD(2,4). In addition, the input impedance calculations exhibited improved accuracy in this case compared to the ones that used FDTD(2,4) alone. Basically, when FDTD(2,4) was combined with the FDTD(2,2) thin wire model, it provided results very similar to the calculations of FDTD(2,2) alone. This can be attributed to the fact that the FDTD(2,2) thin wire model is second-order accurate thereby degrading the accuracy of FDTD(2,4). Also, one-sided differences were applied around each wire but they were found unstable. After long experimentation with various one-sided schemes, it was decided to pursue other ways to expand the capabilities of FDTD(2,4). In conclusion, it was clear that there was a need for a higher-order method that can simulate thin geometric features without loosing its high-order of accuracy.

Furthermore, a method that benefits from the advantages of both FDTD(2,2) and FDTD(2,4) was presented. The new method is a hybrid of FDTD(2,4) with a subgrid FDTD(2,2). Subgrid techniques utilize two grids; a fine one and a coarse one. The ratio between the coarse and the fine grid cell sizes was chosen to be 1:3. All odd integer-cell ratios have the advantage of exhibiting fields in the coarse and fine grids which stay synchronized in time and collocated in space. On the fine grid, the standard FDTD(2,2) is used to handle any of the fine features of the structure, such as thin wires, thin slots, etc, whereas on the coarse grid FDTD(2,4) was used. Therefore, existing and validated thin (subcell) models, that have been developed in

the context of FDTD(2,2), can be used on the fine grid to simulate such thin geometric features. In addition, on the coarse mesh, away from phenomena associated with the complex structure, FDTD(2,4) is used to mainly simulate the wave propagation in homogeneous media. Following this approach, high accuracy is obtained both around fine geometric features, such as thin wires, thin slots, etc., as well as in the wave propagation which is simulated by a higher-order scheme, i.e., FDTD(2,4).

The new hybrid technique was applied to the analysis of two monopoles on a ground plane. The results were compared to FDTD(2,2) computations and measurements. It was illustrated that great computational savings both in memory as well as execution time are achieved when the hybrid FDTD(2,4)/Subgrid FDTD(2,2) method is used. Moreover, this hybrid approach is very promising for other practical situations because of the flexibility for the inclusion of all existing thin and sub-cell models with FDTD(2,2). Simultaneously, the method offers the high accuracy of FDTD(2,4) for the propagation of waves over electrically large distances.

Besides the first hybrid method of FDTD(2,4) with a subgrid FDTD(2,2), a second hybrid technique was presented. The new hybrid method combined FDTD(2,4) and subgrid FDTD(2,2) in a reverse fashion. Therefore, its name [subgrid FDTD(2,2)/ FDTD(2,4)] was the reverse of the name of the original hybrid technique [FDTD(2,4)/ subgrid FDTD(2,2)]. After completing the formulation of the hybrid technique, it was shown that its use yields tremendous memory savings when domains become large in all three directions. This new hybrid method was also applied to practical engineering problems and the conclusions related to that analysis will be presented later in this section.

Applications of both FDTD(2,2) and FDTD(2,4) were also presented. Initially, an improved thin wire model was discussed and compared to the delta-gap feed model. The improved thin wire model was found to be far more accurate than the delta-gap feed model for input impedance calculations. The discrete Fourier transform (DFT) was also compared to the fast Fourier transform (FFT). It was shown that for certain applications such as computations of patterns at multiple frequencies, DFT is far more efficient than FFT.

Moreover, analysis of cavity-backed slot (CBS) was performed. Different numerical issues related to the modeling of such antennas were described. It was found

that the use of a voltage source with an internal resistance in FDTD is indispensable for efficient computations. Both FDTD and FEM/MoM were used to compute the input impedance of a single CBS antenna, and coupling between two elements, and they compared very well with measurements. However, it was found that for coupling versus distance calculations, the hybrid FEM/MoM is faster than the pure FDTD. This is attributed to the fact that FEM/MoM does not discretize the space between the two cavities but rather treats the open-space interaction within the MoM formulation. Therefore, the FEM/MoM computational space remains constant because only the CBS antennas need to be discretized in the hybrid methodology. On the contrary, FDTD has to also account for the space between the two antennas thereby yielding very large domains especially for large distances.

A very comprehensive study of coupling between two CBS antennas was also performed through measurements and simulations. The dependence of coupling on the separation distance between the two antennas was investigated. Disorienting the antennas was also found to be a very effective method of coupling reduction. Specifically, the H-plane configuration exhibited significantly smaller levels of coupling than the E-plane configuration. Moreover, other alternative methods of reducing coupling were examined including incorporation of lossy superstrates as well as ground plane discontinuities, such as slits. It was illustrated that lossy material superstrates can be very effective in decreasing the coupling between two antennas, but they cause a reduction of the antenna gain. Therefore, in a practical design, there is always a compromise between reduction of coupling and maintenance of a sufficiently high gain.

Shielding effectiveness analysis was also performed for cavities with apertures. Various acceleration techniques were presented. The probe excitation by a voltage source with an internal resistance enabled the analysis of highly resonant structures. Also, the introduction of small artificial loss proved to be very useful when analyzing high Q structures using the plane wave excitation.

Furthermore, issues related to the Fourier transform of time-domain data were discussed. Windowing approaches were introduced and applied in FDTD computations. Different windows were presented and their advantages as well as their drawbacks were reported. Also, general guidelines for choosing windows were analyzed and ex-

plained in detail. It was found that windowing can be very useful, especially when FFTs of time-domain data that have not converged to zero are performed. Windows reduce the discontinuities at the boundaries of data sets and effectively resolve problems associated with spectral leakage. It was illustrated that even when severe discontinuities occur at the end of time-domain data sets, windowing can be used and provide very accurate results as long as the set of data is sufficiently long to describe the response of a structure. Windowing can be particularly beneficial in the analysis of both large and high Q structures where the transients need a prohibitive simulation time to decay. In such cases windowing is probably the only way that can provide predictions of reasonable accuracy.

Moreover, different possible shielding effectiveness definitions in the context of FDTD were presented and compared. Their respective pros and cons were analyzed. All numerical results were compared with measurements and exhibited excellent agreement. Shielding effectiveness was computed and measured for different incident angles at a band of frequencies covering up to 1.5 GHz.

After validating the accuracy of FDTD(2,2) for shielding effectiveness (SE) calculations, SE analysis was extended to more complicated problems. Specifically, SE analysis was performed for a simplified scaled model of a Boeing 757 aircraft. It was shown that this geometry generates very large computational domains especially as the frequency of interest increases and the mesh becomes finer. For example, the simplified fuselage has electrical dimensions of approximately $47\lambda \times 6\lambda \times 7\lambda$ at 9 GHz, which make the fuselage an extremely electrically large domain. This domain, discretized with a cell size of 2.5 mm (or $\lambda/13$ at 9 GHz), yields a very large computational domain; $620 \times 80 \times 96$ cells.

First, the standard FDTD(2,2) was used to compute the SE of the scaled fuselage, and it was found to be very accurate when the cell size was chosen fine enough for the frequency band of interest. However, as the mesh became finer the memory requirements became significantly larger, i.e., every time the mesh is refined by a factor of 2, the memory requirements just for the electric and magnetic field components that describe the fuselage become larger by a factor of $2^3 = 8$. It should also be pointed out that the SE waveform consisted of rapid frequency variations with multiple peaks and valleys. This is due to the electrical dimensions of the simplified fuselage which

establish several resonances in the frequency band of interest. These rapid frequency variations complicate even more the analysis of this problem. The levels of the SE varied from as low as -50 dB to as high as 50 dB. Low levels of SE represent a high amount of penetration into the fuselage which can potentially affect the operation of the aircraft's electronic systems.

Then, the second hybrid method of subgrid FDTD(2,2)/FDTD(2,4) was applied to the analysis of HIRF penetration into the scaled model of a Boeing 757 aircraft. Significant memory savings were achieved when the hybrid formulation was used compared to the memory requirements of the standard FDTD(2,2) alone. This happens because the largest part of the computational domain is the interior of the fuselage, and the problem of boundary conditions arises only near the walls of the enclosures. Therefore, it is desired to simulate the propagation inside the fuselage using a higher-order method such as FDTD(2,4). In addition, near the walls of the fuselage a subgrid FDTD(2,2) method should be used in order to represent accurately the PEC boundary conditions, and successfully simulate the penetration mechanisms. All these features are implemented by the hybrid approach. The accuracy of subgrid FDTD(2,2)/FDTD(2,4) was the same with the accuracy exhibited by the FDTD(2,2) scheme alone when the same fine grid cell size was used.

Another very important EMI problem for all commercial aviation is interference that can be generated on-board by various personal electronic devices (PEDs). This research examined the EMI produced by a PED antenna mounted inside a scaled model of a Boeing 757 near one of the windows, and received by an antenna mounted on the top exterior of the scaled model's fuselage. This type of interaction corresponds to interference that can be potentially generated by a passenger's cellular phone and can be received by antennas belonging to the communication and/or navigation systems of airplanes. Initially, FDTD(2,2) was applied to predict this EMI and the numerical computations compared very well with the measurements up to frequencies for which the discretization was fine enough. These results validate for first time the ability of FDTD(2,2) to accurately simulate coupling in a complex geometrical setting. Furthermore, the fuselage is electrically very large thereby allowing a plethora of modes and resonances to be established. All these issues make the modeling of coupling even more challenging. However, FDTD(2,2) was proven very accurate for

the analysis of such problems. In addition, the hybrid method was also applied to this problem. As mentioned above, the use of the hybrid subgrid FDTD(2,2) and FDTD(2,4) method yields significant memory savings. Therefore, the hybrid method was used in order to be validated in the context of the PED analysis. Again, the hybrid method was found to be as accurate as the FDTD(2,2) scheme alone when the same fine grid cell size was used. As far as the PED coupling levels, they exhibited a highly oscillatory behavior due to the large number of resonances present inside the fuselage. Also, the maximum level of coupling was -30 dB and occured at several frequencies. This level of -30 dB can represent a threat to the communication systems of the airplane. However, the definite interpretation of effects of such coupling levels are left to the engineers that deal with, and design the communication systems of the aircraft.

In addition to the rectangular simplified fuselage model, a cylindrical scale model fuselage was constructed, and a series of measurements were performed. The cylindrical model was built to better simulate the fuselage part of an aircraft. In addition, the standard FDTD scheme was used to compute the SE of the cylindrical scaled fuselage. FDTD predictions were found to be very accurate when the cell size was chosen fine enough for the frequency band of interest. Three different cell sizes, of 10, 5 and 2.5 mm were used. The 2.5 mm cell size gave results which were in better agreement with measurements for all frequency bands. It has to be mentioned that even for the finest cell size, discrepancies were observed which were attributed to staircasing errors as well as phase error accumulation due to the electrically large geometry.

Finally, a statistical approach was investigated for the HIRF penetration problem for the simplified scale model fuselage. This statistical approach utilized a reverberation chamber (RC) technique. A mode-stirrer was constructed and inserted into the fuselage. Measurements were performed while the mode-stirrer was rotating and the field inside the fuselage was probed at different locations. Thereafter, the collected data was statistically processed. Initially a basic statistical analysis was performed. The maximum, minimum and mean average values of the electric field over all stirrer positions were calculated versus frequency for all probe locations. It was discovered that measurements from all probes exhibit similar statistical properties. Furthermore,

another interesting observation was that, for each point, the maximum electric field value was almost constant versus frequency, while the maximum electric field level was on average, the same for all probes.

Moreover, two alternative SE definitions were proposed which are based on the maximum and the mean average observed value over all stirrer positions. It was observed that SE values obtained from the new definitions were smaller that the ones that the traditional definition provides. Moreover the stirrer effectiveness was studied using two different methods. The fist method is based on the ability of the stirrer to create higher electric field values than the one that can be established in the empty fuselage. The second one is based on stirring ratio, which is an RC figure-of-merit. Both methods showed that the mode-stirrer was very effective. Afterwards a more advanced statistical analysis was performed which utilized elements of probability and RC theory. Data statistical independence, as well as goodness-of-fit tests, were performed. The run test was employed in order to test data randomness. Measurements were found to provide independent data for frequencies higher than 6 GHz with a confidence level of 95%. As regards to the goodness-of-fit test, the Kolmogorov-Smirnov (K-S) test was used. Empirical cumulative density functions (CDFs) for experimental data were proven to be in very good agreement with theoretical expected CDFs as provided from RC theory. Measurement data above 5 GHz clearly passed this test with a 95% confidence level. Furthermore, the K-S test was used to test if SE CDFs of experimental data match theoretical SE CDFs as provided from probability and RC theories. The confidence level was again set to 95%, and it was shown that experimental SE CDFs were in excellent agreement with the theoretical expected SE CDFs. As a concluding remark, the cavity of a simplified fuselage, along with the mode-stirrer, exhibit statistical properties very similar to those of an actual RC. This is of great importance because electronic systems of an aircraft can be tested for their immunity individually inside an RC. Therefore it is not necessary to construct large anechoic chambers where a entire aircraft needs to be inserted into the facility.

The statistical properties of the penetrated fields were investigated with frequency the independent variable. CDFs were computed using the scale model penetration measurements collected at the four monopole locations within the "Simplified Fuselage." This empirical data was tested using the Kolnogorov-Smirnov criterion, which

demonstrated that it is exponentially distributed with a 95% confidence level over the frequency range of 1 to 9 GHz. The measured CDFs were compared to the theoretical CDFs of Price and Lehman. While both are in very good agreement with measurement, it was found that the Lehman distributions are the more accurate of the two, particularly at the upper ends of the curves at which the peak power levels are described.

Chapter 10

Conclusions

In this project the penetration of High Intensity Radiated Fields (HIRF) into general aviation aircraft was investigated. Several methods and techniques were studied and implemented and much progress was made in the understanding of the behavior of the penetrated electromagnetic field. In what follows the skeleton of the research procedure and tactics that were followed is presented. For each of the step of this procedure comments are made regarding its importance and its contribution to the achievement of the final result. Also, several "hints" are given that could serve as a valuable source of information for anyone interested in EMC and EMI of aircrafts. Finally, it should be mentioned that the purpose of the following presentation is twofold. First of all it is an overview of a rather large and full of details technical report. Second, it is a "navigator" for someone who wishes to conduct research in the same or related areas.

For the purposes of this research both deterministic and statistical approaches were attempted. The main objective of the deterministic part was to demonstrate that the penetrated electromagnetic field inside an aircraft fuselage can be predicted using some numerical technique, which in our case was the Finite Difference Time Domain (FDTD). In order to do that the cavity under test is placed inside an anechoic chamber where it is illuminated by a plane wave and the field penetrated inside the cavity is measured. Afterwards the same scattering scenario is modeled using FDTD and predictions of the penetrated electromagnetic field are made. The ability to match measurements with the corresponding predictions will validate the accuracy of the numerical technique and consequently the accuracy of its predictions. Prior

to any measurements or predictions, the measured quantity has to be chosen. In our case, it was the cavity's shielding effectiveness (SE) and since there are many ways to define it, we chose the one which was in accordance with the measurements.

As an introductory stage, measurements and predictions were performed in simple geometries such as small conducting boxes with apertures. The advantage of working with such geometries is that they can be both easily measured and modeled. Therefore, several experiments were performed within a reasonable period of time while much knowledge is gained about the HIRF penetration problem, and hence prepared us in order to study more complex geometries such that of an aircraft. The second step of the deterministic approach was to construct a simplified scale model fuselage. The construction of the simplified fuselage is a very important issue because the less its imperfections the closer the FDTD modeled geometry will be to the real one. Such imperfections can be misalignment of the fuselage walls or cracks along the joints of the walls which may result in field leakage. Once the simplified fuselage was constructed measurements were performed as well as predictions, and they were found to be in excellent agreement through a wide frequency range and for different incidence angles. From this first part of our research, it was shown that FDTD is able to predict the SE of a complex cavity very accurately. The importance of this accomplishment is that there is no need to use large testing facilities, wherein an aircraft can fit, in order to perform immunity tests. Instead, a simple FDTD simulation is sufficient to give all the information needed about an aircraft's SE. From our studies it was also shown that a $\lambda/10$ discretization, at the maximum frequency of interest, is sufficient for accurate results. Moreover, it became apparent that dispersion errors are unavoidable when FDTD predictions are performed at electrically large geometries, resulting in degradation of the results accuracy. Finally it has to be mentioned that the numerical simulation of such problems is computationally consuming. As a benchmark, the time required to run the entire simplified fuselage ($1.55 \times 0.24 \times 0.20\,\mathrm{m}^3$) with a uniform discretisation in all directions using a 2.5 mm cell size for $100,000$ time steps requires almost 3 days at a 2 processor (PENTIUM 2.2 GHz), 6 GB of RAM, LINUX machine.

During the first part of our research a simplified scale model fuselage was constructed. It is a rather oversimplified model of an aircraft but sufficient for our pur-

poses. Of course if somebody wants more realistic results about the penetrated field in an aircraft, a more detailed and refined scale model has to be constructed. Unfortunately, if one tried to model the geometry of a fuselage taking into account all the details of a real aircraft's interior it would be concluded that it is an unrealistic task to perform. This is because modeling of fine geometrical features requires small cell sizes which result in huge computational domains. Furthermore, even if it was possible to model an aircraft exactly it would be impossible to model the time dependent geometrical features of an aircraft interior such as moving passengers, the existence of which significantly affects the spatial pattern of the field inside the fuselage.

Therefore it is obvious that another approach should be followed which will take into account all the factors that the deterministic approach cannot. Also, since the field value inside a fuselage cavity changes rapidly with respect to space, it would be more useful to know its mean average value and its variance. So, we concluded that a statistical approach is the appropriate one to be attempted. The first requirement in order to perform a statistical approach is to create inside the scale model fuselage the randomly varying environment of a real aircraft. In order to do that, a rotatable scatterer (mode-stirrer) was constructed and inserted in the fuselage. The scatterer consists of four uneven paddles and its purpose is to scatter field in all directions and hence create in the cavity all the possible field configurations. Measurements were performed and while the scatterer was rotating, the field was measured at four different locations. In order to statistically process the collected data, a certain theoretical background was necessary. This theoretical background is provided by the reverberation chamber (RC) theory. RCs are large metallic cavities within which a stochastic in nature electromagnetic field can be established. The stochastic electromagnetic field inside RCs has been studied and probabilistic models have been derived that govern the field distribution. So, based on this theory, we investigated whether the fields inside the fuselage are similarly distributed.

The first set of data to be examined consisted of single point measurements over all stirrer positions for a fixed frequency. As a matter of fact, measurements from all four probe locations were grouped in order to average their contributions and create a large amount of data. It has to be mentioned that the mode-stirrer was rotating stepwise with a 2° step resulting in 180 data values per obsrvation point. Other ways

to increase the number of data and have a more reliable statistical analysiswould be to use multiple stirrers or just increase the number of probes. RC theory has been developed based on the assumption that the field distribution in them is random or delta correlated. This is a very important condition because it makes possible the employment of probability theory theorems (central limit theorem) with the aid of which field probability models can be derived. Therefore a preliminary test is to examine our data for their randomness-independence. There are many tests for such purpose, but we chose the run-test which is based on Bernoulli trials. It was shown that the collected data pass this test for frequencies greater than 4 GHz. The independence test, apart from setting the foundations for the following statistical analysis, gives us also an indication of how effective the mode-stirrer is. Afterwards a goodness-of-fit test has to be performed on the collected data in order to test how good they match with the field probability models that RC theory suggests. In our case the Kolmogorov-Smirnov goodness-of-fit test was employed, and it was found that our data are distributed according to the theoretical expected distributions. Therefore, cumulative distribution function plots can be created for the field variations within the cavity. Based on these plots the probability that the field value will exceed a certain level can be calculated and hence provide guidelines for effective EMC/EMI design.

Apart from the probabilistic analysis an elementary statistical analysis was also performed. Field quantities, such as the maximum, minimum and mean average over all stirrer positions, can be easily computed and give an indication of the field fluctuations within the fuselage. Moreover, another figure-of-merit of the mode-stirrer's effectiveness is the calculation of the stirring ratio. Stirring ratio is defined as the maximum over the minimum over all stirrer positions observed value. Values of the stirring ratio above 20 dB correspond to a well stirred electromagnetic environment. General observations from this analysis are that for higher frequencies better field uniformity is obtained. Also, the average value of the penetrated field varies with respect to the frequency of the impinging wave and the maximum field value is almost constant with respect to frequency.

Furthermore the statistical properties of the penetrated electromagnetic field were studied as a function of frequency. Changes of the excitation frequency result in dif-

ferent field spatial patterns in the cavity. It has been proved that inside a complex cavity field measurements at a single point over a wide frequency range should be χ^2 distributed. FDTD predictions were made for the penetrated field at several points inside the fuselage over a wide frequency range. Goodness-of-fit tests were performed to our data, and it was found to be in excellent agreement with the theoretical expected distributions. Also it was found that different positions inside the fuselage are characterized by the same statistical properties and hence predictions from one point can provide information for the field distribution in the entire fuselage. Moreover, a parametric study was performed for different cockpit windows and different angles of incidence and it was found that the statistical properties of the penetrated field were varying.

Finally, the excitation of conducting cavities using band-limited white Gaussian noise was examined. This technique is also known as frequency stirring. The method was validated by implementing it for 2D and 3D cavities. As a matter of fact the method's effectiveness was tested for different bandwidths and center frequencies of the excitation signal. It was concluded that, using frequency stirring, it is possible to create inside a cavity a spatially uniform electromagnetic field distribution similar to the one inside reverberation chambers. Also, as the excitation frequency increases, the statistical properties of the electromagnetic field are closer to the ones of an ideally operating reverberation chamber. Finally, it has to be mentioned that a great advantage of this method is that it allows the accurate vulnerability testing of any EMI sensitive equipment inside a reverberation chamber using solely numerical techniques. Consequently, an actual reverberation chamber does not have to be built. Moreover, numerical simulations are easier to control and repeat several times and hence give flexibility to the investigation.

As a concluding remark we could say that, although deterministic methods are very accurate, they are subjected to many limitations that make them impractical. On the other hand, statistical methods are more appropriate for the modeling of the HIRF penetration problem because they provide with results which are subjected to less constraints. More specifically, there is not a general statistical theory that can describe the field variations inside any type of cavity. The existing statistical theories are applicable only to cavities with certain geometrical specifications. Therefore,

in the case of an externally illuminated aircraft cavity it is unlikely to develop a statistical model that would describe the field distribution at any spatial point inside it, for any frequency of the impinging wave and any angle of incidence.

Bibliography

[1] *NPRM applicable to FAR Part 25: Transport Category Airplanes, FAA, ARAC EEHWG Document WG-278.* March 1998.

[2] *American National Standard Dictionaty for Technologies of Electromagnetic Compatibility (EMC), Electromagnetic Pulse (EMP), ans Electrostatic Discharge (ESD).* 1998.

[3] G. Ballas, *Simulation of lightning effects on aircraft using the finite-difference time domain method.* Master's thesis, Arizona State University, Tempe, AZ, 2000.

[4] M. A. Gkatzianas, *Lightning and shielding effectiveness modeling using the finite-difference time-domain method.* Master's thesis, Arizona State University, Tempe, AZ, 2002.

[5] R. H. Price, H. T. Davis, and E. P. Wennas, "Determination of the statistical distribution of electromagnetic-field amplitudes in complex cavities," *Physical Review E*, vol. 48, pp. 4716–4729, December 1993.

[6] R. Holland and R. S. John, *Statistical Electromagnetics.* Philadelphia: Taylor and Francis, 1999.

[7] K. S. Yee, "Numerical solution of initial boundary value problems involving Maxwell's equations in isotropic media," *IEEE Trans. Antennas Propagat.*, vol. 14, no. 3, pp. 302–307, 1966.

[8] R. Holland, L. Simpson, and R. H. St. John, "Code optimization for solving large 3D EMP problems," *IEEE Trans. Nuclear Sci.*, vol. 26, no. 6, pp. 4964–4969, 1979.

[9] K. S. Kunz and L. Simpson, "A technique for increasing the resolution of finite-difference solutions of the Maxwell's equation," *IEEE Trans. Electromagn. Compat.*, vol. EMC-23, no. 4, pp. 419–422, 1981.

[10] D. E. Merewether, R. Fisher, and F. W. Smith, "On implementing a numeric Huygen's source scheme in a finite difference program to illuminate scattering bodies," *IEEE Trans. Nuclear Sci.*, vol. 27, no. 6, pp. 1829–1833, 1980.

[11] A. C. Cangellaris and R. Lee, "On the accuracy of numerical wave simulations based on finite methods," *J. Electromagnetic Waves and Applications*, vol. 6, no. 12, pp. 1635–1653, 1992.

[12] K. L. Shlager, J. G. Maloney, S. L. Ray, and A. F. Peterson, "Relative accuracy of several finite-difference time-domain methods in two and three dimensions," *IEEE Trans. Antennas Propagat.*, vol. 41, no. 12, pp. 1732–1737, 1993.

[13] J. Fang, *Time Domain Finite Difference Computation for Maxwell's Equations.* PhD thesis, University of California at Berkeley, Berkeley, CA, 1989.

[14] T. Deveze, L. Beaulie, and W. Tabbara, "A fourth order scheme for the FDTD algorithm applied to Maxwell equations," in *IEEE Antennas and Propagat. Soc. Int. Symposium*, (Chicago, IL), pp. 346–349, July 1992.

[15] P. G. Petropoulos, "Phase error control for FD-TD methods," in *Ultra-Wideband Short-Pulse Electromagnetics*, (H. L. Bertoni, L. Carin, and L. B. Felsen, eds.), pp. 359–366, Plenum Press, 1993.

[16] D. W. Zingg, "Higher-order finite-difference methods in computational electromagnetics," in *IEEE Antennas and Propagat. Soc. Int. Symposium*, (Montréal, Canada), pp. 110–113, July 1997.

[17] M. F. Hadi and M. Piket-May, "A modified FDTD (2,4) scheme for modeling electrically large structures with high-phase accuracy," *IEEE Trans. Antennas Propagat.*, vol. 45, no. 2, pp. 254–264, 1997.

[18] A. Taflove and M. E. Brodwin, "Numerical solution of steady-state electromagnetic scattering problems using the time-dependent Maxwell's equations," *IEEE Trans. Microwave Theory Tech.*, vol. MTT-23, no. 8, pp. 623–630, 1975.

[19] A. Taflove, *Computational Electrodynamics: The Finite-Difference Time-Domain Method.* Boston, MA: Artech House, 1995.

[20] G. Haussmann, *A Dispersion Optimized Three-Dimensional Finite-Difference Time-Domain Method for Electromagnetic Analysis.* PhD thesis, University of Colorado at Boulder, 1998.

[21] B. Engquist and A. Majda, "Absorbing boundary conditions for the numerical simulation of waves," *Math. Comp.*, vol. 31, pp. 629–651, 1977.

[22] G. Mur, "Absorbing boundary conditions for the finite-difference approximation of the time-domain electromagnetic-field equations," *IEEE Trans. Electromagn. Compat.*, vol. EMC-23, no. 4, pp. 377–382, 1981.

[23] P. A. Tirkas, C. A. Balanis, and R. A. Renaut, "Higher order absorbing boundary-conditions for the finite-difference time-domain method," *IEEE Trans. Antennas Propagat.*, vol. 40, no. 10, pp. 1215–1222, 1992.

[24] E. L. Lindman, ""Free-space" boundary conditions for the time dependent wave equation," *J. Comput. Phys.*, vol. 18, pp. 66–78, 1975.

[25] R. L. Higdon, "Absorbing boundary conditions for difference approximations to the multi-dimensional wave equation," *Math. Comput.*, vol. 47, no. 176, pp. 437–459, 1986.

[26] R. L. Higdon, "Numerical absorbing boundary conditions for the wave equation," *Math. Comput.*, vol. 49, no. 179, pp. 65–90, 1987.

[27] L. Halpern and L. N. Trefethen, "Wide angle one-way wave equations," *Journal of the Acoustical Society of America*, vol. 84, pp. 1397–1404, Oct. 1988.

[28] R. A. Renaut and J. Petersen, "Stability of wide-angle absorbing boundary conditions for the wave equation," *Geophysics*, vol. 54, pp. 1153–1165, Sept. 1989.

[29] J.-P. Berenger, "A perfectly matched layer for the absorption of electromagnetic waves," *J. Comput. Phys.*, vol. 114, no. 1, pp. 185–200, 1994.

[30] D. S. Katz, E. T. Thiele, and A. Taflove, "Validation and extension to three dimensions of the Berenger PML absorbing boundary condition for FD-TD meshes," *IEEE Microwave Guided Wave Lett.*, vol. 4, no. 8, pp. 268–270, 1994.

[31] W. V. Andrew, C. A. Balanis, and P. A. Tirkas, "A comparison of the Berenger perfectly matched layer and the Lindman higher-order ABC's for the FDTD method," *IEEE Microwave Guided Wave Lett.*, vol. 5, no. 6, pp. 192–194, 1995.

[32] U. Pekel and R. Mittra, "A finite element method frequency domain application of the perfectly matched layer (PML) concept," *Microwave and Opt. Technol. Lett.*, vol. vol. 9, no. 3, pp. 117–122, June 1995.

[33] U. Pekel and R. Mittra, "An application of the perfectly matched layer (PML) concept to the finite element method frequency domain analysis of scattering problems," *IEEE Microwave and Guided Wave Lett.*, vol. 5, no. 8, pp. 258–260, Aug. 1995.

[34] Z. S. Sacks, D. M. Kingsland, R. Lee, and L. J. F., "A perfectly matched anisotropic absorber for use as an absorbing boundary condition," *IEEE Trans. Antennas Propagat.*, vol. 43, pp. 1460–1463, Dec. 1995.

[35] L. Zhao and A. C. Cangellaris, "A general approach for the development of unsplit-field time-domain implementations of perfectly matched layers for FDTD grid truncation," *IEEE Microwave Guided Wave Lett.*, vol. 6, no. 5, pp. 209–211, 1996.

[36] L. Zhao and A. C. Cangellaris, "GT-PML: Generalized theory of perfectly matched layers and its application to the reflectionless truncation of finite-difference time-domain grids," *IEEE Trans. Microwave Theory Tech.*, vol. 44, no. 12, pp. 2555–2563, 1996.

[37] S. D. Gedney, "An anisotropic perfectly matched layer-absorbing medium for the truncation of FDTD lattices," *IEEE Trans. Antennas Propagat.*, vol. 44, no. 12, pp. 1630–1639, 1996.

[38] A. Taflove, ed., *Advances in Computational Electrodynamics: The Finite-Difference Time-Domain Method.* Boston, MA: Artech House, 1998.

[39] A. C. Polycarpou, M. R. Lyons, and C. A. Balanis, "A two-dimensional finite element formulation of the perfectly matched layer," *IEEE Microwave and Guided Wave Lett.*, vol. 6, pp. 338–340, Sep. 1996.

[40] A. C. Polycarpou and C. A. Balanis, "An optimized anisotropic PML for the analysis of microwave circuits," *IEEE Microwave and Guided Wave Lett.*, vol. 8, pp. 30–32, Jan. 1997.

[41] A. R. Roberts and J. Joubert, "PML absorbing boundary condition for higher-order FDTD schemes," *Electron. Lett.*, vol. 33, no. 1, pp. 32–34, 1997.

[42] P. G. Petropoulos, "The application of pml abcs in higher-order fdtd schemes," in *13th Annual Review of Progress in Applied Computational Electromagnetics*, (Monterey, CA), pp. 884–890, March 1997.

[43] M. Hadi, *A Modified (2,4) Scheme For Modeling Electrically Large Structures with High Phase Accuracy.* PhD thesis, University of Colorado at Boulder, 1996.

[44] T. G. Moore, J. G. Blaschak, A. Taflove, and G. A. Kriegsmann, "Theory and application of radiation boundary operators," *IEEE Trans. Antennas Propagat.*, vol. 36, no. 12, pp. 1797–1812, 1988.

[45] C. A. Balanis, *Antenna Theory: Analysis and Design.* New York: John Wiley and Sons, 1997.

[46] C. A. Balanis, *Advanced Engineering Electromagnetics.* New York: John Wiley and Sons, 1989.

[47] B. Gustafsson, "The convergence rate for difference approximations to general mixed initial boundary value problems," *SIAM J. Numer. Anal.*, vol. 18, pp. 179–179, 1981.

[48] M. H. Carpenter, D. Gottlieb, and S. Abarbanel, "The stability of numerical boundary treatments for compact high-order finite-difference schemes," *J. Comput. Phys.*, vol. 108, pp. 272–295, 1993.

[49] B. Gustafsson, H. O. Kreiss, and A. Sundstrom, "Stability theory of difference appoximations for mixed initial boundary value problems II," *Math. Comp.*, vol. 26, pp. 649–686, 1972.

[50] M. H. Carpenter, D. Gottlieb, and S. Abarbanel, "Time-stable boundary conditions for finite-difference schemes solving hyperbolic systems: Methodology and application to high-order compact schemes," *J. Comput. Phys.*, vol. 111, pp. 220–236, 1994.

[51] B. Strand, "Summation by parts for finite difference approximations for d/dx," *J. Comput. Phys.*, vol. 110, pp. 47–67, 1994.

[52] S. S. Abarbanel and A. E. Chertock, "Strict stability of high-order compact implicit finite-difference schemes: The role of boundary conditions for hyperbolic pdes, I," *J. Comput. Phys.*, vol. 160, pp. 42–66, 2000.

[53] S. S. Abarbanel, A. E. Chertock, and A. Yefet, "Strict stability of high-order compact implicit finite-difference schemes: The role of boundary conditions for hyperbolic pdes, II," *J. Comput. Phys.*, vol. 160, pp. 67–87, 2000.

[54] M. H. Carpenter, J. Nordstrom, and D. Gottlieb, "A stable and conservative interface treatment of arbitrary spatial accuracy," Tech. Rep. 98-12, ICASE, Feb. 1998.

[55] D. Darmofal, "Eigenmode analysis of boundary conditions for the one-dimensional preconditioned euler equations," Tech. Rep. 98-51, ICASE, Nov. 1998.

[56] J. Nordstrom and M. H. Carpenter, "Boundary and interface conditions for high order finite difference methods applied to the euler and navier-stokes equations," Tech. Rep. 98-19, ICASE, May 1998.

[57] B. Sjögreen, "High-order centered difference methods for the compressible navier-stokes equations," *J. Comput. Phys.*, vol. 117, pp. 67–78, 1995.

[58] J. L. Young, D. Gaitonde, and J. S. Shang, "Toward the construction of a fourth-order difference scheme for transient EM wave simulation: Staggered grid approach," *IEEE Trans. Antennas Propagat.*, vol. 45, pp. 1573–1580, Nov. 1997.

[59] J. S. Shang, "High-order compact-difference schemes for time-dependent maxwell equations," *J. Comput. Phys.*, vol. 153, pp. 312–333, 1999.

[60] D. Gottlieb and E. Turkel, "Dissipative two-four methods for time-dependent problems," *Math. Comp.*, vol. 30, pp. 703–723, Oct. 1976.

[61] E. J. Caramana, M. J. Shashkov, and P. P. Whalen, "Formulations of artificial viscocity for multi-dimensional shock wave computations," *J. Comput. Phys.*, vol. 144, pp. 70–97, 1998.

[62] R. C. Swanson, R. Radespiel, and E. Turkel, "On some numerical dissipation schemes," *J. Comput. Phys.*, vol. 147, pp. 518–544, 1998.

[63] D. Furihata, "Finite difference schemes for $\partial u/\partial t = (\partial u/\partial x)^a \delta g/\delta u$ that inherit energy conservation or dissipation property," *J. Comput. Phys.*, vol. 156, pp. 181–205, 1999.

[64] A. Yefet and P. G. Petropoulos, "A non-dissipative staggered fourth-order accurate explicit finite difference scheme for the time-domain Maxwell's equations," Tech. Rep. NASA/CR-1999-209514, Institute for Computer Applications in Science and Engineering, Aug. 1999.

[65] S. V. Georgakopoulos, C. A. Balanis, and C. R. Birtcher, "Coupling between transmission line antennas: Analytic solution, FDTD, and measurements," *IEEE Trans. Antennas Propagat.*, vol. 47, pp. 978–985, June 1999.

[66] I. S. Kim and W. J. R. Hoefer, "A local mesh refinement algorithm for the time domain-finite difference method using Maxwell's curl equations," *IEEE Trans. Microwave Theory Tech.*, vol. 38, no. 6, pp. 812–815, 1990.

[67] S. S. Zivanovic, K. S. Yee, and K. K. Mei, "A subgridding method for the time-domain finite-difference method to solve Maxwell's equations," *IEEE Trans. Microwave Theory Tech.*, vol. 39, no. 3, pp. 471–479, 1991.

[68] D. T. Prescott and N. V. Shuley, "A method for incorporating different sized cells into the finite-difference time-domain analysis technique," *IEEE Microwave Guided Wave Lett.*, vol. 2, no. 11, pp. 434–436, 1992.

[69] M. W. Chevalier, R. J. Luebbers, and V. P. Cable, "FDTD local grid with material traverse," *IEEE Trans. Antennas Propagat.*, vol. 45, no. 3, pp. 411–421, 1997.

[70] W. K. Gwarek, "Analysis of arbitrarily shaped two-dimensional microwave circuits by finite-difference time-domain method," *IEEE Trans. Microwave Theory Tech.*, vol. 35, no. 4, pp. 738–744, 1988.

[71] D. M. Sheen, S. M. Ali, M. D. Abouzahra, and J. A. Kong, "Application of the three-dimensional finite-difference time-domain method to the analysis of planar microstrip circuits," *IEEE Trans. Microwave Theory Tech.*, vol. 38, no. 7, pp. 849–857, 1990.

[72] T. Shibata and E. Sano, "Characterization of MIS structure coplanar transmission lines for investigation of signal propagation in integrated circuits," *IEEE Trans. Microwave Theory Tech.*, vol. 38, no. 7, pp. 881–890, 1990.

[73] J.-G. Yook, N. I. Dib, and L. P. B. Katehi, "Characterization of high frequency interconnects using finite difference time domain and finite element methods," *IEEE Trans. Microwave Theory Tech.*, vol. 42, no. 9, pp. 1727–1736, 1994.

[74] P. Mezzanotte, M. Mongiardo, L. Roselli, R. Sorrentino, and W. Heinrich, "Analysis of packaged microwave integrated circuits by FDTD," *IEEE Trans. Microwave Theory Tech.*, vol. 42, no. 9, pp. 1796–1801, 1994.

[75] K.-L. Wu, C. Wu, and J. Litva, "An application of FD-TD method for studying the effects of packages on the performance of microwave and high speed digital circuits," *IEEE Trans. Microwave Theory Tech.*, vol. 42, no. 10, pp. 2007–2009, 1994.

[76] K. Naishadham and X. P. Lin, "Application of spectral domain Prony's method to the FDTD analysis of planar microstrip circuits," *IEEE Trans. Microwave Theory Tech.*, vol. 42, no. 12, pp. 2391–2398, 1994.

[77] B.-Z. Wang, "Small-hole formalism for the FDTD simulation of small-hole coupling," *IEEE Microwave Guided Wave Lett.*, vol. 5, no. 1, pp. 15–17, 1995.

[78] X. Zhang and K. K. Mei, "Time-domain finite difference approach to the calculation of the frequency-dependent characteristics of microstrip discontinuities," *IEEE Trans. Microwave Theory Tech.*, vol. 36, no. 12, pp. 1775–1787, 1988.

[79] J. C. Olivier and D. A. McNamara, "Finite-difference time-domain (FD-TD) analysis of discontinuities in homogeneous, dispersive waveguides," *Electron. Lett.*, vol. 25, no. 15, pp. 1006–1007, 1989.

[80] G.-C. Liang, Y.-W. Liu, and K. K. Mei, "Full-wave analysis of coplanar waveguide and slotline using the time-domain finite-difference method," *IEEE Trans. Microwave Theory Tech.*, vol. 37, no. 12, pp. 1949–1957, 1989.

[81] S.-T. Chu and S. K. Chaudhuri, "A finite-difference time-domain method for the design and analysis of guided-wave optical structures," *J. Lightwave Technol.*, vol. 7, no. 12, pp. 2033–2038, 1989.

[82] D. T. Prescott and N. V. Shuley, "Reducing solution time in monochromatic FDTD waveguide simulations," *IEEE Trans. Microwave Theory Tech.*, vol. 42, no. 8, pp. 1582–1584, 1994.

[83] F. Moglie, T. Rozzi, and P. Marcozzi, "Wideband matching of waveguide discontinuities by FDTD methods," *IEEE Trans. Microwave Theory Tech.*, vol. 42, no. 11, pp. 2093–2098, 1994.

[84] J. C. Olivier and D. A. McNamara, "Analysis of multiport discontinuities in waveguide using a pulsed FDTD approach," *IEEE Trans. Microwave Theory Tech.*, vol. 42, no. 12, pp. 2229–2238, 1994.

[85] D. M. Sullivan, O. P. Gandhi, and A. Taflove, "Use of the finite-difference time-domain method in calculating EM absorption in man models," *IEEE Trans. Biomed. Eng.*, vol. 35, no. 3, pp. 179–186, 1988.

[86] C.-Q. Wang and O. P. Gandhi, "Numerical simulation of annular phased arrays for anatomically based models using the FDTD method," *IEEE Trans. Microwave Theory Tech.*, vol. 37, no. 1, pp. 118–126, 1989.

[87] J.-Y. Chen and O. P. Gandhi, "RF currents induced in an anatomically-based model of a human for plane-wave exposures (20-100 MHz)," *Health Physics*, vol. 57, no. 1, pp. 89–98, 1989.

[88] R. J. Spiegel, M. B. A. Fatmi, S. S. Stuchly, and M. A. Stuchly, "Comparison of finite-difference time-domain SAR calculations with measurements in a heterogeneous model of a man," *IEEE Trans. Biomed. Eng.*, vol. 36, no. 8, pp. 849–855, 1989.

[89] D. Sullivan, "Three-dimensional computer simulation in deep regional hyperthermia using the finite-difference time-domain method," *IEEE Trans. Microwave Theory Tech.*, vol. 38, no. 2, pp. 204–211, 1990.

[90] C. M. Furse, J. Y. Chen, and O. P. Gandhi, "The use of the frequency-dependent finite-difference time-domain method for induced current and SAR calculations for a heterogeneous model of the human body," *IEEE Trans. Electromagn. Compat.*, vol. 36, no. 2, pp. 128–133, 1994.

[91] H. Y. Chen and H. H. Wang, "Current and SAR induced in a human head model by electromagnetic fields irradiated from a cellular phone," *IEEE Trans. Microwave Theory Tech.*, vol. 42, no. 12, pp. 2249–2254, 1994.

[92] P.-Y. Cresson, C. Michel, L. Dubois, M. Chive, and J. Pribetich, "Complete three-dimensional modeling of new microstrip-microslot applicators for microwave hyperthermia using the FDTD method," *IEEE Trans. Microwave Theory Tech.*, vol. 42, no. 12, pp. 2657–2666, 1994.

[93] A. Taflove and K. R. Umashankar, "The finite-difference time-domain (FD-TD) method for numerical modeling of electromagnetic scattering," *IEEE Trans. Magnet.*, vol. 25, no. 10, pp. 3086–3091, 1989.

[94] V. Shankar, W. F. Hall, and A. Mohammadian, "A time-domain differential solver for electromagnetic scattering problems," *Proc. IEEE*, vol. 77, no. 5, pp. 709–721, 1989.

[95] M. A. Strickel and A. Taflove, "Time-domain synthesis of broad-band absorptive coatings for two-dimensional conducting targets," *IEEE Trans. Antennas Propagat.*, vol. 38, no. 7, pp. 1084–1091, 1990.

[96] C. M. Furse, S. P. Mathur, and O. P. Gandhi, "Improvements to the finite-difference time-domain method for calculating the radar cross section of a perfectly conducting target," *IEEE Trans. Microwave Theory Tech.*, vol. 38, no. 7, pp. 919–927, 1990.

[97] A. Reineix and B. Jecko, "Analysis of microstrip patch antennas using finite difference time domain method," *IEEE Trans. Antennas Propagat.*, vol. 37, no. 11, pp. 1361–1369, 1989.

[98] J. G. Maloney, G. S. Smith, and W. R. Scott, Jr., "Accurate computation of the radiation from simple antennas using the finite-difference time-domain method," *IEEE Trans. Antennas Propagat.*, vol. 38, no. 7, pp. 1059–1068, 1990.

[99] J. C. Olivier and D. A. McNamara, "Analysis of edge slots in rectangular waveguide using finite-difference time-domain method," *Electron. Lett.*, vol. 26, no. 15, pp. 1135–1136, 1990.

[100] D. S. Katz, M. J. Piket-May, A. Taflove, and K. R. Umashankar, "FDTD analysis of electromagnetic wave radiation from systems containing horn antennas," *IEEE Trans. Antennas Propagat.*, vol. 39, no. 8, pp. 1203–1212, 1991.

[101] C. W. Penney and R. J. Luebbers, "Input impedance, radiation pattern, and radar cross-section of spiral antennas using FDTD," *IEEE Trans. Antennas Propagat.*, vol. 42, no. 9, pp. 1328–1332, 1994.

[102] V. A. Thomas, K. M. Ling, M. E. Jones, B. Toland, J. Lin, and T. Itoh, "FDTD analysis of an active antenna," *IEEE Microwave Guided Wave Lett.*, vol. 4, no. 9, pp. 296–298, 1994.

[103] A. Navarro, M. J. Nuñez, and E. Martin, "Study of TE_0 and TM_0 modes in dielectric resonators by a finite difference time-domain method coupled with the discrete fourier transform," *IEEE Trans. Microwave Theory Tech.*, vol. 39, no. 1, pp. 14–17, 1991.

[104] J. M. Jarem, "A method of moments analysis and a finite-difference time-domain analysis of a probe-sleeve fed rectangular waveguide cavity," *IEEE Trans. Microwave Theory Tech.*, vol. 39, no. 3, pp. 444–451, 1991.

[105] J. A. Pereda, L. A. Vielva, A. Vegas, and A. Prieto, "Computation of resonant frequencies and quality factors of open dielectric resonators by a combination of the finite-difference time-domain (FDTD) and Prony's methods," *IEEE Microwave Guided Wave Lett.*, vol. 2, no. 11, pp. 431–433, 1992.

[106] J. A. Pereda, L. A. Vielva, A. Vegas, and A. Prieto, "The finite-difference time-domain (FDTD) method applied to the computation of resonant frequencies and quality factors of open dielectric resonators," *J. de Physique III*, vol. 3, no. 3, pp. 539–551, 1993.

[107] R. Mittra and P. H. Harms, "A new finite-difference time-domain (FDTD) algorithm for efficient field computation in resonantor narrow-band structures," *IEEE Microwave Guided Wave Lett.*, vol. 3, no. 9, pp. 316–318, 1993.

[108] M. F. Iskander, R. L. Smith, A. O. M. Andrade, H. Kimrey, Jr., and L. M. Walsh, "FDTD simulation of microwave sintering of ceramics in multimode cavities," *IEEE Trans. Microwave Theory Tech.*, vol. 42, no. 5, pp. 793–800, 1994.

[109] S. Watanabe and M. Taki, "An improved fdtd model for the feeding gap of a thin-wire antenna," *IEEE Microwave Guided Wave Lett.*, vol. 8, no. 4, pp. 152–154, 1998.

[110] R. F. Harrington, *Field Computations by Moment Methods.* New York: Macmillan, 1968.

[111] C. M. Furse and O. P. Gandhi, "Why the DFT is faster than the FFT for FDTD time-to-frequency domain conversions," *IEEE Microwave Guided Wave Lett.*, vol. 5, no. 10, pp. 326–328, 1995.

[112] J. Calejs, "Admittance of a rectangular slot which is backed by a rectangular cavity," *IEEE Trans. on Antennas and Propagation*, pp. 119–126, March 1963.

[113] A. T. Adams, "Flush mounted rectangular cavity slot antennas- Theory and design," *IEEE Trans. on Antennas and Propagation*, pp. 342–351, May 1967.

[114] H. Moheb, J. Shaker, and S. L., "Numerical and experimental investigation of cavity-backed arbitrary antennas," *Canadian Journal of Physics*, vol. 74, no. 3-4, pp. 122–131, 1996.

[115] M. Omiya, T. Hikage, N. Ohno, K. Horiguchi, and K. Itoh, "Design of cavity-backed slot antennas using the finite-difference time-domain technique," *IEEE Trans. Antennas Propagat.*, vol. 46, no. 12, pp. 1853–1858, 1998.

[116] A. J. Parfitt and T. S. Bird, "Computation of aperture antenna mutual coupling using FDTD and Kirchhoff field transformation," *Electron. Lett.*, vol. 34, no. 12, pp. 1167–1168, 1998.

[117] H. Yokoi and H. Fukumuro, "Low sidelobe paraboloidal antenna with microwave absorber," *Trans. IECE*, vol. 54-B, pp. 619–624, Oct. 1971. (in Japanese).

[118] C. M. Knop, Y. B. Cheng, and E. L. Ostertag, "An absorber-wall parallel-plate waveguide," *IEEE Trans. Microwave Theory Tech.*, vol. 34, pp. 773–785, July 1986.

[119] C. M. Knop, Y. B. Cheng, and E. L. Ostertag, "On the fields in a canonical horn having arbitrary wall impedance," *IEEE Trans. Antennas Propagat.*, vol. 34, pp. 1092–1098, Sep. 1986.

[120] J. Siller C. A., "An experimental investigation of wide-angle sidelobe suppression in a pyramidal horn-reflector antenna," *Bell Lab. Tech. J.*, vol. 63, pp. 531–544, Apr. 1984.

[121] C. S. Lee, S. W. Lee, and D. W. Justice, "A simple circular-polarized antenna: Circular waveguide horn coated with lossy magnetic material," *IEEE Trans. Antennas Propagat.*, vol. 36, pp. 297–300, Feb. 1988.

[122] P. A. Tirkas and C. A. Balanis, "Contour path FDTD methods for analysis of pyramidal horns with composite inner E-plane walls," *IEEE Trans. Antennas Propagat.*, vol. 42, no. 11, pp. 1476–1483, 1994.

[123] H. J. Stalzer, A. Fathy, A. Hessel, and J. Smoys, "Effect of lossy ground performance of planar and cylindrical arrays," *Radio Sci.*, vol. 25, pp. 133–147, Mar.-Apr. 1990.

[124] K. Yoshitomi and H. Sharobim, "Radiation from a rectangular waveguide with a lossy flange," *IEEE Trans. Antennas Propagat.*, vol. 42, no. 10, pp. 1398–1403, 1994.

[125] M. Piket-May, A. Taflove, and J. Baron, "FD-TD modeling of digital signal propagation in 3-D circuits with passive and active loads," *IEEE Trans. Microwave Theory Tech.*, vol. 42, no. 8, pp. 1514–1523, 1994.

[126] R. J. Luebbers and H. S. Langdon, "A simple feed model that reduces time steps needed for FDTD antenna and microstrip calculations," *IEEE Trans. Antennas Propagat.*, vol. 44, no. 7, pp. 1000–1005, 1996.

[127] A. Polycarpou, *Finite-Element Analysis of Microwave Passive Devices and Ferrite Tuned Antennas.* PhD thesis, Arizona State University, 1998.

[128] D. M. Pozar, "Input impedance and mutual coupling of rectangular microstrip antennas," *IEEE Trans. Antennas Propagat.*, vol. 30, pp. 1191–1196, Nov. 1982.

[129] K. J. Moeller, *Characterization of the electromagnetic environment inside an airliner due to exterior sources.* PhD thesis, Arizona State University, 1999.

[130] H. A. Mendez, "Shielding theory of enclosures with apertures," *IEEE Trans. Electromagn. Comp.*, vol. 20, no. 2, pp. 296–305, 1978.

[131] G. Ceri, R. De Leo, and V. M. Primiani, "Theoretical and experimental evaluation of the electromagnetic radiation from apertures in shielding enclosures," *IEEE Trans. Electromagn. Comp.*, vol. 34, no. 24, pp. 423–432, 1992.

[132] M. Robinson, T. Benson, C. Christopoulos, J. Dawson, M. Ganley, A. Marvin, S. Porter, and D. Thomas, "Analytical formulation for the shielding effectiveness of enclosures with apertures," *IEEE Trans. Electromagn. Comp.*, vol. 40, no. 3, pp. 240–247, 1998.

[133] F. Olyslager, E. Laermans, D. D. Zutter, S. Criel, R. D. Smedt, N. Lietaert, and A. D. Clercq, "Numerical and experimental study of the shielding effectiveness of a metallic enclosure," *IEEE Trans. Electromagn. Comp.*, vol. 41, no. 3, pp. 202–212, 1999.

[134] A. Taflove, "Application of the finite-difference time-domain method to sinusoidal steady-state electromagnetic-penetration problems," *IEEE Trans. Electromagn. Compat.*, vol. EMC-22, no. 2, pp. 191–202, 1980.

[135] A. Taflove and K. Umashankar, "A hybrid moment method/finite-difference time-domain approach to electromagnetic coupling and aperture penetration into complex geometries," *IEEE Trans. Antennas Propagat.*, vol. 30, no. 4, pp. 617–627, 1982.

[136] K. R. Umashankar, A. Taflove, and B. Beker, "Calculation and experimental validation of induced currents on coupled wires in an arbitrary shaped cavity," *IEEE Trans. Antennas Propagat.*, vol. 35, no. 11, pp. 1248–1257, 1987.

[137] A. Taflove, K. R. Umashankar, B. Beker, F. Harfoush, and K. S. Yee, "Detailed FD-TD analysis of electromagnetic fields penetrating narrow slots and lapped joints in thick conducting screens," *IEEE Trans. Antennas Propagat.*, vol. 36, no. 2, pp. 247–257, 1988.

[138] K. P. Ma, M. Drewniak, Li, J. L., T. H. Hubing, and T. P. Doren, "Comparison of FDTD algorithms for subcellural modeling of slots in shielding enclosures," *IEEE Trans. Electromagn. Comp.*, vol. 39, no. 2, pp. 147–155, 1997.

[139] M. Li, S. Radu, J. Nuebel, J. L. Drewniak, T. H. Hubbing, and T. P. VanDoren, "Design of airflow aperture arrays in shielding enclosures," in *IEEE International EMC Symposium*, (Denver, CO), pp. 1059–1063, Aug. 1998.

[140] S. V. Georgakopoulos, C. R. Birtcher, and C. A. Balanis, "Coupling modeling and reduction techniques of cavity-backed slot antennas: FDTD vs. measurements," *IEEE Trans. Electromagn. Compat.*, vol. 43, pp. 261–272, Aug. 2001.

[141] F. J. Harris, "On the use of windows for harmonic analysis with the discrete Fourier transform," in *Proceedings of the IEEE*, pp. 51–83, Jan. 1978.

[142] A. C. Polycarpou, "Advanced helicopter electromagnetics methods for helicopter applications," Tech. Rep. No. TRC-EM-CAB-0001, Telecommuncations Research Center, Arizona State University, 2000.

[143] S. V. Georgakopoulos, *Coupling Between Multiple Wire Antennas on Complex Structures.* Master's thesis, Arizona State University, 1998.

[144] C. A. Balanis *et al.*, "Penetration of high intensity radiated fields (hirf) into aircraft," Tech. Rep., Telecommunication Research Center, Arizona State University, Jun. 1, 2001 - Nov. 31, 2001.

[145] P. Corona, G. Latmiral, E. Paolini, and L. Piccioli, "Use of a reverberating enclosure for measurements of radiated power in the microwave range," *IEEE Trans. Electromag. Compat.*, vol. 18, pp. 54–59, 1976.

[146] P. Corona, J. Ladbury, and G. Latmiral, "Reverberation-chamber research-then and now: A review of early work and comparison with current understanding," *IEEE Trans. on Electromag. Compat.*, vol. 44, pp. 87–94, February 2002.

[147] M. L. Crawford and G. H. Koepke, "Design, evaluation and use of a reverberation chamber for performing electromagnetic susceptibility/vulnerability measurements," Technical Note 1092, National Bureau of Standards, April 1986.

[148] P. Corona, G. Ferrara, and M. Migliaccio, "Reverberating chambers as sources of stochastic electromagnetic fields," *IEEE Trans. on Electromag. Compat.*, vol. 38, pp. 348–356, August 1996.

[149] D. I. Wu and D. C. Chang, "The effect of an electrically large stirrer in a mode-stired chamber," *IEEE Trans. on Electromag. Compat.*, vol. 31, pp. 164–169, May 1989.

[150] B. H. Liu and D. C. Chang, "Eigenmodes and the composite quality factor of a reverberating chamber," NBS Tech. Note 1066, Nat. Bureau of Stand., August 1983.

[151] H. Weyl, "Das asymptotische verteilungsgesetz der eigenwerte linearer partialler differentialgleichungen (mit einer anwendung auf die theorie der hohlraumstrahlung)," *Math. Annalen*, no. 71, pp. 441–479, 1912.

[152] H. Weyl, "Ü die abhängigkeit der eigenschwingungen einer membran von deren begrenzung," *J. reine u. angew. Math.*, no. 141, pp. 1–11, 1912.

[153] L. R. Arnaut, "Operation of electromagnetic reverberation chambers with wave diffractors at relatively low frequencies," *IEEE Trans. on Electromag. Compat.*, vol. 43, pp. 637–653, November 2001.

[154] C. E. Goldblum, D. Lane, J. L. Press, L. Rayadurga, and L. Cohen, "Evanescent modes in a unique mode-stirred chamber -the advanced technology chamber (atc)- design, construction, operation and data," in *Proc. IEEE Int. Symp. Electromagnetic Compatibility*, pp. 180–184, 1996.

[155] P. Corona, G. Ferrara, and M. Migliaccio, "Reverberating chamber electromagnetic field in the presence of an unstirred component," *IEEE Trans. on Electromag. Compat.*, vol. 42, pp. 111–115, May 2000.

[156] M. Migliaccio, "On the phase statistics of the electromagnetic field in reverberating chambers," *IEEE Trans. on Electromag. Compat.*, vol. 43, pp. 694–695, November 2001.

[157] N. K. Kouveliotis, P. T. Trakadas, and C. N. Capsalis, "Theoretical investigation of the field conditions in a vibrating reverberation chamber with an unstirred component," *IEEE Trans. on Electromag. Compat.*, vol. 45, pp. 77–81, February 2003.

[158] D. A. Hill, "Plane wave integral representation for fields in reverberation chambers," *IEEE Trans. on Electromag. Compat.*, vol. 40, pp. 209–217, August 1998.

[159] D. A. Hill, "Spatial correlation function for fields in a reverberation chamber," *IEEE Trans. on Electromag. Compat.*, vol. 37, p. 138, February 1995.

[160] A. Ishimaru, *Wave propagation and scattering in random media.* Vol. 2, Academic Press, 1978.

[161] A. Papoulis, *Probability, Random Variables, and Stochastic Processes.* McGraw Hill, 3rd ed., 1991.

[162] A. H. Panaretos, "Reverberation chamber theory," 2002. Personal notes.

[163] J. R. Taylor, *An introduction to error analysis.* University Science Books, 1982.

[164] E. M. Pugh and G. H. Winslow, *The analysis of physical measurements.* Addison-Wesley, 1966.

[165] J. S. Bendat and A. G. Piersol, *Random Data, Analysis and Measurement Procedures.* A-Wiley Interscience Publication, 1986.

[166] O. Kempthorne and L. Folks, *Probability, Statistics and Data Analysis.* The Iowa State univesity Press, 1st ed., 1971.

[167] B. P. Roe, *Probability and Statistics in experimental Physics.* Springer-Verlag, 2nd ed., 2001.

[168] R. H. Price, H. T. Davis, R. H. Bonn, E. P. Wenaas, R. Achenbach, V. Gieri, R. Thomas, J. Alcala, J. Hanson, W. Haynes, C. McCrea, C. Montano, R. Peterson, B. Trautlein, and R. Umber, "Determination of the statistical distribution of electromagnetic field amplitudes in complex cavities," Tech. Rep. 88JAL129, JAYCOR, NM, June 1988.

[169] R. Holland and R. H. S. John, "Statistical response of em-driven cables inside an overmoded enclosure," *IEEE Trans. Electromagn. Compat.*, vol. 40, pp. 311–324, November 1998.

[170] L. K. Warne, K. S. H. Lee, H. G. Hudson, W. A. Johnson, R. E. Jorgenson, and S. L. Stronach, "Statistical properties of linear antenna impedance in an electrically large cavity," *IEEE Trans. Antennas Propagat.*, vol. 51, pp. 978–992, May 2003.

[171] Y. P. Terletskii, *Statistical Physics.* North-Holland, Amsterdam, 1971.

[172] N. G. Gamkrelidze and V. I. Rotar', "On the rate of convergence in the limit theorem for quadratic forms," *SIAM J. Theory Probab. Appl.*, vol. 22, pp. 394–397, 1977.

[173] T. H. Lehman, "A statistical theory of electromagnetic fields in complex cavities," Interaction Note 494, Air Force Res. Lab., May 1993.

[174] T. A. Loughry, "Frequency stirring: An alternate approach to mechanical mode-stirring for the conduct of electromagnetic susceptibility testing," Tech. Rep. PL-TR-91-1036, Philips Laboratory, NM, Nov. 1991.

[175] C. A. Balanis, *Advanced Engineering Electromagnetics.* New York: John Wiley and Sons, 1989.

[176] G. Goubau, *Electromagnetic waveguides and cavities.* New York: Pergamon Press, 1961.

[177] J. M. Dunn, "Local, high-frequency analysis of the fields in a mode-stirred chamber," *IEEE Trans. Electromagn. Compat.*, vol. 32, pp. 53–58, Feb. 1990.

[178] W. B. Davenport and W. L. Root, *An introduction to the theory of random signals and noise.* New York: IEEE Press, 1987.

[179] S. M. Ross, *Stochastic Processes.* John Wiley and Sons, 2nd ed., 1995.

[180] J. G. Proakis, *Digital Communications.* McGraw-Hill, 4th ed., 2001.

[181] H. Taub and D. L. Schilling, *Principles of communication systems.* McGraw-Hill, 2nd ed., 1986.

[182] C. W. Chuang, P. H. Pathak, and C. C. Huang, "On wave modulation by a rotating object," *IEEE Trans. Antennas Propagat.*, vol. 30, pp. 486–489, May 1982.

[183] I. J. Lahaie and D. L. Sengupta, "Scattering of electromagnetic waves by a slowly rotating rectangular metal plate," *IEEE Trans. Antennas Propagat.*, vol. 27, pp. 40–45, Jan. 1976.

[184] M. L. Crawford, T. A. Loughry, M. O. Hatfield, and G. J. Freyer, "Band-limited, white gaussian noise excitation for reverberation chambers and applications to radiated susceptibility testing," Tech. Rep. 1375, NIST, Boulder, CO, Jan. 1996.

[185] D. A. Hill, "Electronic mode stirring for reverberating chambers," *IEEE Trans. on Electromag. Compat.*, vol. 36, no. 4, pp. 294–299, 1994.

[186] A. T. Taflove and S. C. Hagness, *Computational Electrodynamics: The Finite-Difference Time-Domain Method.* Artech House, 2nd ed., 2000.